NASA CP-2001

ADVANCES IN ENGINEERING SCIENCE

Volume 3

13th Annual Meeting
Society of Engineering Science
Sponsored by JIAFS
Hampton, VA, November 1–3, 1976

NASA
National
Aeronautics and
Space
Administration

Society of
Engineering Science

NASA Conference Publications (CP Series) contain compilations of scientific and technical papers or transcripts arising from conferences, workshops, symposia, seminars, and other professional meetings that NASA elects to publish.

The text of these proceedings was reproduced directly from author-supplied manuscripts for distribution prior to opening of the meeting. NASA has performed no editorial review of the papers other than those contributed by its employees or contractors.

NASA CP-2001

Advances In Engineering Science

Volume 3

13th Annual Meeting
Society of Engineering Science
Hampton, VA, November 1—3, 1976

Sponsored by Joint Institute for Advancement of Flight Sciences
NASA Langley Research Center
and
George Washington University

National
Aeronautics and
Space
Administration

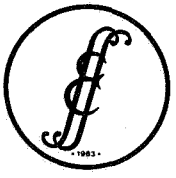

Society of
Engineering Science

For sale by the National Technical Information Service
Springfield, Virginia 22161
Price – $11.50

PREFACE

The technical program of the 13th Annual Meeting of the Society of Engineering Science, Inc., consisted of 159 invited and contributed papers covering a wide variety of research topics, a plenary session, and the Annual Society of Engineering Science Lecture. Thirty-three of the technical sessions contained invited and/or contributed papers while two of the sessions were conducted as panel discussions with audience participation.

These Proceedings, which contain the technical program of the meeting, are presented in four volumes arranged by subject material. Papers in materials science are contained in Volume I. Volume II contains the structures, dynamics, applied mathematics, and computer science papers. Volume III contains papers in the areas of acoustics, environmental modeling, and energy. Papers in the area of flight sciences are contained in Volume IV. A complete Table of Contents and an Author Index are included in each volume.

We would like to express particular appreciation to the members of the Steering Committee and the Technical Organizing Committee for arranging an excellent technical program. Our thanks are given to all faculty and staff of the Joint Institute for Advancement of Flight Sciences (both NASA Langley Research Center and The George Washington University) who contributed to the organization of the Meeting. The assistance in preparation for the meeting and this document of Sandra Jones, Virginia Lazenby, and Mary Torian is gratefully acknowledged. Our gratitude to the Scientific and Technical Information Prgrams Division of the NASA Langley Research Center for publishing these Proceedings is sincerely extended.

Hampton, Virginia 1976

J. E. Duberg

J. L. Whitesides

Co-Chairmen

J. E. Duberg
NASA Langley Research Center

J. L. Whitesides
The George Washington University

Steering Committee

W. D. Erickson, NASA Langley Research Center
P. J. Bobbitt, NASA Langley Research Center
H. F. Hardrath, NASA Langley Research Center
D. J. Martin, NASA Langley Research Center
M. K. Myers, The George Washington University
A. K. Noor, The George Washington University
J. E. Duberg, NASA Langley Research Center, Ex-officio
J. L. Whitesides, The George Washington University, Ex-officio

Technical Organizing Committee

C. L. Bauer, Carnegie-Mellon University
L. B. Callis, NASA Langley Research Center
J. R. Elliott, NASA Langley Research Center
K. Karamcheti, Stanford University
P. Leehey, Massachusetts Institute of Technology
J. S. Levine, NASA Langley Research Center
R. E. Little, University of Michigan-Dearborn
J. M. Ortega, Institute for Computer Applications in Science and Engineering
E. M. Pearce, Polytechnic Institute of New York
A. D. Pierce, Georgia Institute of Technology
E. Y. Rodin, Washington University
L. A. Schmit, University of California at Los Angeles
G. C. Sih, Lehigh University
E. M. Wu, Washington University

SOCIETY OF ENGINEERING SCIENCE, INC.

The purpose of the Society, as stated in its incorporation document, is "to foster and promote the interchange of ideas and information among the various fields of engineering science and between engineering science and the fields of theoretical and applied physics, chemistry, and mathematics, and, to that end, to provide forums and meetings for the presentation and dissemination of such ideas and information, and to publish such information and ideas among its members and other interested persons by way of periodicals and otherwise."

OFFICERS

L. V. Kline, President
IBM Corporation

S. W. Yuan, First Vice President and Director
The George Washington University

C.E. Taylor, Second Vice President and Director
University of Illinois

E. Y. Rodin, Second Vice President and Director
The George Washington University

R. P. McNitt, Secretary
Virginia Polytechnic Institute and State University

J. Peddieson, Treasurer
Tennessee Technological University

DIRECTORS

B. A. Boley, Northwestern University
G. Dvorak, Duke University
T. S. Chang, Massachusetts Institute of Technology
E. Montroll, University of Rochester
J. M. Richardson, North American Rockwell Corp.
E. Saibel, Army Research Office
J. W. Dunkin, Exxon Production Research Co.
J. T. Oden, University of Texas

CORPORATE MEMBERS

Chevron Oil Field Research Company
Exxon Production Research Company
IBM Corporation
OEA Incorporated

CONTENTS

VOLUME I

ANNUAL SOCIETY OF ENGINEERING SCIENCE LECTURE

MATERIALS SCIENCE I
Chairmen: C. L. Bauer and E. Pearce

MATERIALS SCIENCE II
Chairman: R. E. Little

MATERIALS SCIENCE III
Chairman: J. H. Crews, Jr.

COMPOSITE MATERIALS
Chairman: E. M. Wu

DYNAMIC FRACTURE MECHANICS
Chairman: G. C. Sih

FRACTURE MECHANICS
Chairman: H. F. Hardrath

IMPACT AND VIBRATION
Chairman: H. L. Runyan, Jr.

VOLUME II

STRUCTURAL DYNAMICS I
Chairman: L. D. Pinson

STRUCTURAL DYNAMICS II
Chairman: S. Utku

APPLIED MATHEMATICS
Chairman: J. N. Shoosmith

ADVANCES IN COMPUTER SCIENCE
Chairman: J. M. Ortega

VOLUME III

AEROACOUSTICS I
Chairman: D. L. Lansing

AEROACOUSTICS II
Chairman: A. Nayfeh

WAVE PROPAGATION
Chairman: E. Y. Rodin

ATMOSPHERIC SOUND PROPAGATION
Chairman: M. K. Myers

STRUCTURAL RESPONSE TO NOISE
Chairman: L. Maestrello

ENVIRONMENTAL MODELING I
Chairman: L. B. Callis

ENVIRONMENTAL MODELING II
Chairman: M. Halem

PLANETARY MODELING
Chairman: J. S. Levine

ENERGY RELATED TOPICS
Chairman: W. D. Erickson

VOLUME IV

INVISCID FLOW I
Chairman: F. R. DeJarnette

INVISCID FLOW II
Chairman: P. J. Bobbitt

VISCOUS FLOW I
Chairman: S. Rubin

VISCOUS FLOW II
Chairman: D. M. Bushnell

AIRCRAFT AERODYNAMICS
Chairman: R. E. Kuhn

EXPERIMENTAL FLUID MECHANICS
Chairman: J. Schetz

PROPULSION AND COMBUSTION
Chairman: A. J. Baker

FLIGHT DYNAMICS AND CONTROL I
Chairman: A. A. Schy

FLIGHT DYNAMICS AND CONTROL II
Chairman: M. J. Queijo

HOW DOES FLUID FLOW GENERATE SOUND?

Alan Powell
Technical Director
David W. Taylor Naval Ship R&D Center

The development of the understanding of flow-generated sound is traced, with emphasis on the development of various theories of the mechanism involved, both of the flow itself and that by which acoustic energy is generated. Examples of the former include the long history of resonating or whistling flows, aeolian tones, jet noise, and boundary-layer noise. The pertinent features of the sound-generation mechanism, in terms of quadrupole, dipole, and monopole theories, and variations thereupon, are pointed out. Some of the situations that have given rise to interesting and apparently divergent views are described from the point of view of present understanding.

SOUND PROPAGATION THROUGH NONUNIFORM DUCTS*

Ali Hasan Nayfeh
Virginia Polytechnic Institute and State University

SUMMARY

A critical review is presented of the state of the art regarding methods of determining the transmission and attenuation of sound propagating in nonuniform ducts with and without mean flows. The approaches reviewed include purely numerical techniques, quasi-one-dimensional approximations, solutions for slowly varying cross sections, solutions for weak wall undulations, approximation of the duct by a series of stepped uniform cross sections, variational methods, and solutions for the mode envelopes.

INTRODUCTION

The prediction of sound propagation in nonuniform ducts is a problem whose solution has application to the design of numerous facilities, such as central airconditioning and heating installations, loud speakers, high-speed wind tunnels, aircraft engine-duct systems, and rocket nozzles.

The mathematical statement of sound propagation in a nonuniform duct that carries compressible mean flows can be obtained as follows. Each flow quantity $q(\vec{r},t)$ can be expressed as the sum of a mean flow quantity $q_0(\vec{r})$ and an acoustic quantity $q_1(\vec{r},t)$, where $\vec{r}$ is a dimensionless position vector and t is a dimensionless time. In nonuniform ducts, $q_0(\vec{r})$ is a function of the axial dimensionless coordinate z as well as the transverse dimensionless coordinates x and y. Substituting these representations into the equations of state and conservation of mass, momentum, and energy and subtracting the mean quantities, we obtain

$$\frac{\partial \rho_1}{\partial t} + \nabla \cdot (\rho_0 \vec{v}_1 + \rho_1 \vec{v}_0) = NL \tag{1}$$

$$\rho_0\left(\frac{\partial \vec{v}_1}{\partial t} + \vec{v}_0 \cdot \nabla \vec{v}_1 + \vec{v}_1 \cdot \nabla \vec{v}_0\right) + \rho_1 \vec{v}_0 \cdot \nabla \vec{v}_0 + \nabla p_1 = \frac{1}{Re} \nabla \cdot \underline{\underline{\tau}}_1 + NL \tag{2}$$

$$\rho_0\left(\frac{\partial T_1}{\partial t} + \vec{v}_0 \cdot \nabla T_1 + \vec{v}_1 \cdot \nabla T_0\right) + \rho_1 \vec{v}_0 \cdot \nabla T_0 - (\gamma-1)\left(\frac{\partial p_1}{\partial t} + \vec{v}_0 \cdot \nabla p_1 + \vec{v}_1 \cdot \nabla \rho_0\right) = \frac{1}{Re}\left[\frac{1}{Pr} \nabla \cdot (\kappa_0 \nabla T_1 + \kappa_1 \nabla T_0) + (\gamma-1)\Phi_1\right] + NL \tag{3}$$

*Work supported by the NASA Langley Research Center under Contract No. NAS 1-13884: Dr. Joe Posey, Technical Monitor. The comments of Dr. J. E. Kaiser are greatly appreciated.

$$\frac{p_1}{p_0} = \frac{\rho_1}{\rho_0} + \frac{T_1}{T_0} \tag{4}$$

where $\underline{\underline{\tau}}_1$ and Φ_1 are the linearized viscous stress tensor and dissipation function and NL stands for the nonlinear terms in the acoustic quantities. These equations are supplemented by initial and boundary conditions.

No solutions to eqs. (1)-(4) subject to general initial and boundary conditions are available yet. To determine solutions for the propagation and attenuation of sound in ducts, researchers have used simplifying assumptions. In the absence of shock waves, the viscous acoustic terms produce an effective admittance at the wall that leads to small dispersion and attenuation (ref. 1). For lined ducts, this admittance produced by the acoustic boundary layer may be neglected, but it cannot be neglected for hard-walled ducts as demonstrated analytically and experimentally by Pestorius and Blackstock (ref. 2).

Most of the existing studies neglect the nonlinear acoustic terms in eqs. (1)-(4) and the boundary conditions. However, the assumption of linearization is not valid for high sound pressure levels. The effects of the nonlinear acoustic properties of the lining material become significant when the sound pressure level exceeds about 130 dB (re 0.0002 dyne/cm^2), while the gas nonlinearity becomes significant when the sound pressure level exceeds about 160 dB. In particular, the nonlinearity of the gas must be included when the mean flow is transonic.

Another popular assumption is that the mean flow is incompressible. Theories based on this assumption will not be applicable to evaluating the promising approach to the reduction of inlet noise by using a high subsonic inlet, or partially choked inlet, in conjunction with an acoustic duct liner. Numerous experimental investigations (refs. 3-20) of various choked-inlet configurations have been reported. Most, but not all, of these investigations have noted significant reductions of the noise levels when the inlet is choked. Further, most of the potential noise reduction is achieved by operation in the partially choked state (mean Mach number in the throat of 0.8 - 0.9). Some investigators (e.g. ref. 9) report the possibility of substantial "leakage" through the wall boundary layers, whereas others (e.g. ref. 12) report that leakage is minor. To evaluate these effects, one cannot neglect the viscous terms in the mean flow and perhaps in the acoustic equations. Since the mean flow is transonic at the throat, one has to include the nonlinear terms also because the linear acoustic solution is singular for sonic mean flows.

A fourth assumption being employed in analyzing sound propagation in ducts is the characterization of the effects of the linear by an admittance that is deterministic and homogeneous. On inspection of any liner, one can easily see that this is not the case. The analysis of the effects of stochastic admittances is in its infancy (ref. 21).

A fifth assumption which is usually employed is that of parallel mean flow in which the boundary layer is fully developed and the duct walls are parallel to the mean flow (ref. 22). Further, in some analyses, the fully developed mean flow is replaced by a plug flow, thereby neglecting the refractive effects of

the mean boundary layer which become increasingly more significant as the sound frequency increases. Certainly, theories based on the parallel flow assumption will not be capable of determining the attenuation and propagation characteristics in nonuniform ducts (ducts whose cross-sectional area changes along their axes). Recently, a number of approaches have been developed to treat sound propagation in nonuniform ducts. Each approach has unique characteristics and advantages as well as obvious limitations, either of a numerical or a physical nature. Some of these approaches were reviewed in reference 22. The purpose of the present paper is to present an updated critical review of these approaches.

DIRECT NUMERICAL TECHNIQUES

Direct numerical methods based on finite differences have been proposed (refs. 23-25). However, these methods have been restricted to simple cases of no-mean flow or one-dimensional mean flow and/or plane acoustic waves and promise to become unwieldy for more general cases. Methods were also based on finite elements (refs. 26 and 27). These purely numerical techniques would be impractical because of the excessive amount of computation time and the large round-off errors. The latter is a result of the necessity of using very small axial and transverse steps or very small finite elements to represent the axial oscillations and the rapidly varying shapes of each mode. In fact, a computational difficulty exists even in calculating the higher-order Bessel functions that represent the mode shapes in a uniform duct carrying uniform mean flow unless asymptotic expansions are used. Moreover, the axial step or finite element must be much smaller than the wavelength of the lowest mode in order to be able to determine the axial variation. These small steps and finite elements would cause the error in the numerical solution to increase very rapidly with axial distance and sound frequency.

To simplify the computation of the axial variation of the lowest mode in a two-dimensional duct with constant cross-sectional area but varying admittance, Baumeister (ref. 28) expressed the pressure as

$$p(x,y,t) = P(x,y)\exp[i(kx - \omega t)]$$

where k is the propagation constant corresponding to a hard-walled duct. Then, he used finite differences to solve for the "so-called" envelope P(x,y). This approach is suited for the lowest mode.

QUASI-ONE-DIMENSIONAL APPROXIMATIONS

The earliest studies of sound propagation in ducts with varying cross sections stemmed from the need to design efficient horn loudspeakers. Such horns are essentially acoustic transformers of plane waves and their efficiency depends on the throat and mouth area, the flare angle (wall slope), and the frequency of the sound. The walls of the horns are perfectly rigid and they do not flare so rapidly to keep the sound guided by the horn and prevent its spread-

ing out as spherical waves in free space.

For the case of no-mean flow, one writes the quasi-one-dimensional equivalent of eqs. (1)-(4). Combining these equations, he obtains Webster's equation (ref. 29).

$$\frac{1}{S}\frac{\partial}{\partial x}\left(S\frac{\partial p_1}{\partial x}\right) = \frac{\partial^2 p_1}{\partial t^2} \tag{5}$$

where S is the cross-sectional area of the duct. This equation can be derived alternatively as the first term in an expansion of the three-dimensional acoustic equations in powers of the dimensionless frequency (ref. 30). It can also be derived by integrating the acoustic equations across the duct. Solutions of equation (5) have been obtained and verified by many researchers (ref. 22). Using the method of multiple scales (ref. 31), Nayfeh (ref. 32) obtained an expansion for equation (5) with the nonlinear terms retained; the solution shows the variation of the position of the shock with the cross-sectional area.

In the case of mean flow, one writes the quasi-one-dimensional equivalent of equations (1)-(4). For linear waves and sinusoidal time variations, the resulting equations describing the axial variations were solved for a special duct geometry for which the equations have constant coefficients (ref. 33), for the case of short waves by using the WKB approximation (ref. 34), and for general duct geometry by using numerical techniques (refs. 35 and 36). The nonlinear case was treated by Whitham (ref. 37), Rudinger (ref. 38), Powell (refs. 39 and 40), and Hawkings (41).

In this quasi-one-dimensional approach, one can determine only the lowest mode in ducts with slowly varying cross sections and cannot account for transverse mean-flow gradients or large wall admittances.

SOLUTIONS FOR SLOWLY VARYING CROSS-SECTIONS

For slowly varying cross sections, the mean flow quantities are slowly varying functions of the axial distance; that is, $q_0 = q_0(z_1,x,y)$, where $z_1 = \varepsilon z$ with ε being a small dimensionless parameter that characterizes the slow axial variations of the cross-sectional area. For linear waves and sinusoidal time variations, the method of multiple scales (ref. 31) is used to express the acoustic quantities which are expressed in the form

$$q_1(x,y,z,t) = \sum_{n=0}^{N} \varepsilon^n Q_n(x,y,z_1,z_2,z_3,\ldots,z_N)\exp(i\phi) + O(\varepsilon^{N+1}) \tag{6}$$

where $z_n = \varepsilon^n z$ and

$$\frac{\partial\phi}{\partial t} = -\omega, \quad \frac{\partial\phi}{\partial z} = k_0(z_1) \tag{7}$$

Expressing each acoustic quantity as in equation (6), substituting these expressions into equations (1)-(4) and the boundary conditions, and equating co-

efficients of equal powers of ε yield equations to determine successively the Q_n. The zeroth-order problem is the same as the problem for a duct that is locally parallel with z_1 appearing as a parameter. The solution for the acoustic pressure can be expressed as

$$Q_0(x,y,z_1,z_2,\ldots,z_N) = A(x,y,z_1,z_2,\ldots,z_N)\psi(x,y,z_1) \tag{8}$$

where $\psi(x,y,z_1)$ is the quasi-parallel mode shape corresponding to the propagation constant $k_0(z_1)$. The function A is still undetermined to this level of approximation; it is determined by imposing the so-called evaluable conditions at the higher levels of approximation. To first order, one obtains the following equation for A:

$$f(z_1)\frac{dA}{dz_1} + g(z_1)A = 0 \tag{9}$$

where $f(z_1)$ and $g(z_1)$ are obtained numerically from integrals across the duct of ψ, q_0, k_0, and their derivatives.

Equation (9) has the solution

$$A(z_1) = A_0\exp[i\varepsilon\int k_1(z_1)dz] \tag{10}$$

where $k_1 = ig(z_1)/f(z_1)$. To first order, A_0 is a constant to be determined from the initial conditions. Then, to the first approximation,

$$p_1 = A_0\psi(x,y;z_1)\exp\left\{i\int[k_0(z_1) + \varepsilon k_1(z_1)]dz - i\omega t\right\} + O(\varepsilon) \tag{11}$$

According to this approach, one can determine the transmission and attenuation for all modes for hard-walled and soft-walled ducts with no-mean flow (ref. 42), two-dimensional ducts carrying incompressible and compressible flows (refs. 43 and 44), and annular ducts (ref. 45). Thus, in this approach one can include transverse and axial gradients, slow variations in the wall admittances, and boundary-layer growths, but the technique is limited to slow variations and the expansion needs to be carried out to second order in order to determine reflections of the acoustic signal.

WEAK WALL UNDULATIONS

In this approach, one assumes that the cross section of the duct deviates slightly from a uniform one. For example, the dimensionless radius of a cylindrical duct can be expressed as

$$R(z) = 1 + \varepsilon R_1(z) \tag{12}$$

and the dimensionless positions of the walls of a two-dimensional duct can be expressed as

$$\begin{aligned} y &= 1 + \varepsilon d_1(z) \\ y &= 1 + \varepsilon d_2(z) \end{aligned} \tag{13}$$

where ε is a small dimensionless parameter and R_1, d_1, and d_2 need not be slowly varying functions of z.

Taking advantage of the small deviation of the duct cross-section from a uniform one, a number of researchers (refs. 46-49) sought straightfoward expansions (called Born approximations in the physics literature). For two-dimensional ducts and sinusoidal time variations, the expansions have the form

$$q_1(y,z,t) = \exp(i\omega t) \sum_{n=1}^{N} \varepsilon^n Q_n(y,z) + O(\varepsilon^N) \qquad (14)$$

Substituting expressions like equation (14) for each flow quantity in equations (1)-(4) and the boundary conditions and expanding the results for small ε, one obtains equations and boundary conditions for the successive determination of the Q_n.

Isakovitch (ref. 46), Samuels (ref. 47), and Salant (ref. 48) obtained straightforward expansions for waves propagating in two-dimensional ducts when d_1 and d_2 vary sinusoidally with z. Under these conditions, first-order expansions are unbounded for certain frequencies called the resonant frequencies; hence, the straightforward expansion is invalid near these resonant frequencies. Nayfeh (ref. 50) used the method of multiple scales and obtained an expansion that is valid near these resonant frequencies. He pointed out that resonances occur whenever the wavenumber of the wall undulations is equal to the difference of the wavenumbers of two propagating modes. These results show that these two modes interact and neither of them exists in the duct without strongly exciting the other modes. These results were extended by Nayfeh (ref. 51) to the case of two-dimensional ducts carrying uniform mean flows in the absence of the wall undulations.

Tam (ref. 49) obtained a first-order expansion for waves incident in the upstream direction on a throat or a constriction in a cylindrical duct. His results show that substantial attenuation of wave energy is possible for an axial flow Mach number of about 0.6 and throats of reasonable area reduction. It should be noted that the straightforward expansion is not valid for long distances and it might break down near resonant frequencies. These deficiencies can be removed by using the method of multiple scales. Then, one can account for all effects except large axial variations.

APPROXIMATIONS BY STEPPED UNIFORM SECTIONS

In this approach, one analyzes the effects of the continuous variations in the wall admittance and/or the cross-sectional variations by approximating the duct by a series of sections, each with a uniform admittance (refs. 52 and 53) and a uniform cross-section (ref. 54). Then, one matches the pressure and the velocity at all interfaces of the different uniform sections. Hogge and Ritzi (ref. 55) approximated the duct by a series of cylindrical and conical sections and matched the pressure and velocity at the approximate interfaces between sections. Since the end surfaces of the conical sections are spherical rather

than planar, the interfaces between sections do not match exactly and some error is introduced.

This approach is most suited for cases in which the wall liner consists of a number of uniform segments (refs. 52,53,56-61) and/or cases in which the duct cross-section consists of uniform but different segments (ref. 62). In the latter case, determining the mean flow can be a formidable problem if viscosity is included. In approximating a duct with a continuously varying cross-sectional area by a series of stepped uniform ducts, a large number of uniform segments are needed to provide sufficient accuracy for the solution when the axial variations are large.

VARIATIONAL METHODS

In the variational approach, one uses either the Rayleigh-Ritz procedure, which requires the knowledge of the Lagrangian describing the problem, or the method of weighted residuals (ref. 63). Since the Lagrangian is not known yet for the general problem, the Galerkin procedure (a special case of the method of weighted residuals) is the only applicable technique at this time. According to this approach, one chooses basis functions (usually the mode shapes of a quasi-parallel problem) and represents each flow quantity as

$$q_1(x,y,z,t) = \sum \psi_n(z)\phi_n(x,y)\exp(i\omega t) \tag{15}$$

where the ϕ_n are the basis functions, which, in general, do not satisfy the boundary conditions. On expressing each flow quantity as in equation (15), substituting the result into equations (1)-(4) and the boundary conditions, and using the Galerkin procedure, one obtains coupled ordinary-differential equations describing the ψ_n. These equations are then solved numerically.

Stevenson (ref. 64) applied this approach to the problem of waves propagating in hard-walled ducts with no-mean flow. Beckemeyer and Eversman (ref. 65) used the variational approach with the Lagrangian for waves propagating in hard-walled ducts with no-mean flow, Eversman, Cook, and Beckemeyer (ref. 66) applied the Galerkin approach to two-dimensional lined ducts with no-mean flow, and Eversman (ref. 67) applied it to ducts carrying mean flows.

Since the $\psi_n(z)$ vary rapidly even for a uniform duct, $\psi_n(z) \propto \exp(ik_n z)$ and k_n can be very large for the lower modes, very small axial steps must be used in the computations resulting in large computation time, which increases very rapidly with axial distance and sound frequency.

THE WAVE ENVELOPE TECHNIQUE

According to this approach, one uses the method of variation of parameters to change the dependent variables from the fast varying variables to others that vary slowly. Thus, each acoustic quantity q_1 is expressed as

$$q_1(x,y,z,t) = \sum_{n=1}^{N} A_n(z)\exp[i\int k_n(z)dz - i\omega t]Q_n(x,y,z)$$

$$+ \tilde{A}_n(z)\exp[-i\int k_n(z)dz - i\omega t]\tilde{Q}_n(x,y,z) \qquad (16)$$

where the $Q_n(x,y,z)$ are the quasi-parallel modes corresponding to the quasi-parallel propagation constants $k_n(z)$, the tilde refers to upstream propagation, N is the number of modes used, and $A_n(z)$ is a complex function whose modulus and argument represent, in some sense, the amplitude and the phase of the nth mode. Since k_n is complex, the exponential factor contains an estimate of the attenuation rate of the nth mode. Thus,

$$|A_n|\exp[-\int \alpha_n(z)dz]$$

is the envelope of the nth mode.

To use this method, one determines first the functions $\psi_n^{(1)}(x,y,z)$, $\psi_n^{(2)}(x,y,z)$, $\psi_n^{(3)}(x,y,z)$, $\psi_n^{(4)}(x,y,z)$, and $\psi_n^{(5)}(x,y,z)$ which are solutions of the adjoint quasi-parallel problem corresponding to the propagation constant k_n. Multiplying equations (1)-(4), respectively, by $\psi_n^{(1)}$, $\psi_n^{(2)}$, $\psi_n^{(3)}$, $\psi_n^{(4)}$, and $\psi_n^{(5)}$, adding the resulting equations, integrating the result by parts across the duct to transfer the transverse derivatives from the dependent variables to the ψ's, and using the boundary conditions, one obtains 2N integrability conditions (constraints), one corresponding to each k_n. Substituting the truncated expansion (eq. 16) into these integrability conditions, one obtains 2N first-order ordinary differential equations for the A_n. Then, these equations are solved numerically.

This technique has been applied by Kaiser and Nayfeh (ref. 68) to the propagation of multimodes in two-dimensional, nonuniform, lined ducts with no-mean flow. The results show that the present technique is superior to the variational approach especially for large sound frequencies and axial distances. This approach is being applied to the inlet problem by Nayfeh, Shaker, and Kaiser.

REFERENCES

1. Nayfeh, A. H.: Effect of the Acoustic Boundary Layer on the Wave Propagation in Ducts. The Journal of the Acoustical Society of America, Vol. 54, No. 6, Dec. 1973, pp. 1737-1742.

2. Pestorius, F. M. and Blackstock, D. T.: Non-Linear Distortion in the Propagation of Intense Acoustic Noise. Interagency Symposium on University Research in Transportation Noise Proceedings, Vol. II, March 1973, Stanford, Calif., pp. 565-577.

3. Sobel, J. A. and Welliver, A. D.: Sonic Block Silencing for Axial and Screw-Type Compressors. Noise Control, Vol. 7, No. 5, pp. 9-11, Sept/

Oct. 1961.

4. Hawthorne, J. M., Morris, G. J., and Hayes, C.: Measurement of Performance, Inlet Flow Characteristics, and Radiated Noise for a Turbojet Engine Having Choked Inlet Flow. NASA TN D-3929, 1967.

5. Chestnutt, D.: Noise Reduction by Means of Inlet-Guide-Vane Choking in an Axial-Flow Compressor. NASA TN D-4683, 1968.

6. Higgins, C. C., Smith, J. N., and Wise, W. H.: Sonic Throat Inlets. NASA SP-189, pp. 197-215, 1968.

7. Large, J. B., Wilby, J. F., Grande, E., and Anderson, A. O.: The Development of Engineering Practices in Jet, Compressor, and Boundary Layer Noise. Proc. AFOSR-UTIAS Symp. on Aerodynamic Noise, pp. 43-67, 1968.

8. Putnam, T. W. and Smith, J. N.: XB-70 Compressor Noise Reduction and Propulsion System Performance for Choked Inlet Flow. NASA TN D-5692, 1970.

9. Chestnutt, D. and Clark, L. R.: Noise Reduction by Means of Variable-Geometry Inlet Guide Vanes in a Cascade Apparatus. NASA TN X-2392, 1971.

10. Lumsdaine, E.: Development of a Sonic Inlet for Jet Aircraft. Internoise '72 Proceedings, pp. 501-506, 1972.

11. Benzakein, M. J., Kazin, S. B., and Savell, C. T.: Multiple Pure-Tone Noise Generation and Control. AIAA Paper No. 73-1021, October 1973.

12. Klujber, F.: Results of an Experimental Program for the Development of Sonic Inlets for Turbofan Engines. AIAA Paper No. 73-222.

13. Putnam, T. W.: Investigation of Coaxial Jet Noise and Inlet Choking Using an F-111A Airplane. NASA TN-D-7376, 1973.

14. Koch, R. L., Ciskowski, T. M., and Garzon, J. R.: Turbofan Noise Reduction Using a Near Sonic Inlet. AIAA Paper No. 74-1098.

15. Klujber, F. and Okeefe, J. V.: Sonic Inlet Technology Development and Application to STOL Propulsion. Society of Automotive Engineers Paper No. 74-0458.

16. Savkar, S. D. and Kazin, S. B.: Some Aspects of Fan Noise Suppression Using High Mach Number Inlets. AIAA Paper No. 74-554.

17. Groth, H. W.: Sonic Inlet Noise Attenuation and Performance with a J-85 Turbojet Engine as a Noise Source. AIAA Paper No. 74-91.

18. Abbott, J. M.: Aeroacoustic Performance of Scale Model Sonic Inlets - Takeoff/Air Approach Noise Reduction. AIAA Paper No. 75-202.

19. Lumsdaine, E., Cherng, J. G., Tag, I., and Clark, L. R.: Noise Suppression

with High Mach Number Inlets. NASA CR-143314, July 1975.

20. Miller, B. A.: Experimentally Determined Aeroacoustic Performance and Control of Several Sonic Inlets. AIAA Paper No. 75-1184.

21. Yu, J. C., Smith, C. D., and Munger, P.: Acoustic Wave Propagation in a Lined Duct with Non-Uniform Impedance. AIAA Paper No. 75-515.

22. Nayfeh, A. H., Kaiser, J. E., and Telionis, D. P.: Acoustics of Aircraft Engine-Duct Systems. AIAA Journal, Vol. 13, 1975, pp. 130-153.

23. Baumeister, K. J. and Rice, E. J.: A Difference Theory for Noise Propagation in an Acoustically Lined Duct with Mean Flow. AIAA Paper No. 73-1007.

24. Quinn, D. W.: A Finite Difference Method for Computing Sound Propagation in Non-Uniform Ducts. AIAA Paper No. 75-130.

25. King, L. S. and Karamcheti, K.: Propagation of Plane Waves in the Flow Through a Variable Area Duct. AIAA Paper No. 73-1009.

26. Kapur, A. and Mungur, P.: Duct Acoustics and Acoustic Finite Element Method. AIAA Paper No. 75-498.

27. Sigmann, R., Majjegi, R. K., and Zinn, B: Private Communication.

28. Baumeister, K. J.: Generalized Wave Envelope Analysis of Sound Propagation in Ducts with Variable Axial Impedance and Stepped Noise Source Profiles. AIAA Paper No. 75-518.

29. Webster, A. G.: Acoustical Impedance and the Theory of Horns and of the Phonograph. Proceedings of the National Academy of Science, Vol. 5, July 1919, pp. 275-282.

30. Peube, J. L. and Chasseriaux, J.: Nonlinear Acoustics in Ducts with Varying Cross Section. Journal of Sound and Vibration, Vol. 27, No. 4, 1973, 533-548.

31. Nayfeh, A. H.: Perturbation Methods. New York: Wiley-Interscience, 1973, Chap. 6.

32. Nayfeh, A. H.: Finite-Amplitude Plane Waves in Ducts with Varying Properties. Journal of the Acoustical Society of America, Vol. 57, pp. 1413-1415.

33. Eisenberg, N. A. and Kao, T. W.: Propagation of Sound Through a Variable-Area Duct with a Steady Compressible Flow. The Journal of the Acoustical Society of America, Vol. 49, No. 1, 1971, pp. 169-175.

34. Huerre, P. and Karamcheti, K.: Propagation of Sound through a Fluid Moving in a Duct of Varying Area. Interagency Symposium of University Research in Transportation Noise Proceedings, Vol. II, 1973, Stanford University, Stanford, Calif., pp. 397-413.

35. Davis, S. S. and Johnson, M. L.: Propagation of Plane Waves in a Variable Area Duct Carrying a Compressible Subsonic Flow. Presented at the 87th Meeting of the Acoustical Society of America, New York, 1974.

36. Kooker, D. E., and Zinn, B. T.: Use of a Relaxation Technique in Nozzle Wave Propagation Problems. AIAA Paper 73-1011, Seattle, Wash., 1973.

37. Whitham, G. B.: On the Propagation of Shock Waves Through Regions of Non-Uniform Area of Flow. Journal of Fluid Mechanics, Vol. 4, Pt. 4, 1958, pp. 337-360.

38. Rudinger, G.: Passage of Shock Waves Through Ducts of Variable Cross Section. Physics of Fluids, Vol. 3, No. 3, 1960, pp. 449-455.

39. Powell, A.: Propagation of a Pressure Pulse in a Compressible Flow. The Journal of the Acoustical Society of America, Vol. 31, No. 11, 1959, pp. 1527-1535.

40. Powell, A.: Theory of Sound Propagation through Ducts Carrying High-Speed Flows. The Journal of the Acoustical Society of America, Vol. 32, No. 12, 1960, pp. 1640-1646.

41. Hawkings, D. L.: The Effects of Inlet Conditions on Supersonic Cascade Noise. Journal of Sound and Vibration, Vol. 33, 1974, pp. 353-368.

42. Nayfeh, A. H. and Telionis, D. P.: Acoustic Propagation in Ducts with Varying Cross-Sections. The Journal of the Acoustical Society of America, Vol. 54, No. 6, 1973, pp. 1654-1661.

43. Nayfeh, A. H., Telionis, D. P., and Lekoudis, S. G.: Acoustic Propagation in Ducts with Varying Cross Sections and Sheared Mean Flow. AIAA Paper No. 73-1008, Seattle, Wash., 1973.

44. Nayfeh, A. H. and Kaiser, J. E.: Effect of Compressible Mean Flow on Sound Transmission Through Variable-Area Plane Ducts. AIAA Paper No. 75-128.

45. Nayfeh, A. H., Kaiser, J.E. and Telionis, D. P.: Transmission of Sound Through Annular Ducts of Varying Cross Sections and Sheared Mean Flow. AIAA Journal, Vol. 13, No. 1, 1975, pp. 60-65.

46. Isakovitch, M. A.: Scattering of Sound Waves on Small Irregularities in a Wave Guide. Akusticheskii Zhurnal, Vol. 3, 1957, pp. 37-45.

47. Samuels, J. S.: On Propagation of Waves in Slightly Rough Ducts. The Journal of the Acoustical Society of America, Vol. 31, 1959, pp. 319-325.

48. Salant, R. F.: Acoustic Propagation in Waveguides with Sinusoidal Walls. The Journal of the Acoustical Society of America, Vol. 53, 1973, pp. 504-507.

49. Tam, C. K. W.: Transmission of Spinning Acoustic Modes in a Slightly Non-uniform Duct. Journal of Sound and Vibration, Vol. 18, No. 3, 1971, pp. 339-351.

50. Nayfeh, A. H.: Sound Waves in Two-Dimensional Ducts with Sinusoidal Walls. The Journal of the Acoustical Society of America, Vol. 56, No. 3, 1974, pp. 768-770.

51. Nayfeh, A. H.: Acoustic Waves in Ducts with Sinusoidally Perturbed Walls and Mean Flow. Journal of the Acoustical Society of America, Vol. 57, 1975, pp. 1036-1039.

52. Zorumski, W. E. and Clark, L. R.: Sound Radiation from a Source in an Acoustically Treated Circular Duct. NASA Paper presented at 81st Aeroacoustical Society Meeting (Washington, D.C.), 1971.

53. Lansing, D. L. and Zorumski, W. E.: Effects of Wall Admittance Changes on Duct Transmission and Radiation of Sound. Journal of Sound and Vibration, Vol. 27, No. 1, 1973, pp. 85-100.

54. Alfredson, R. J.: The Propagation of Sound in a Circular Duct of Continuously Varying Cross-Sectonal Area. Journal of Sound and Vibration, Vol. 23, No. 4, 1972, pp. 433-442.

55. Hogge, H. D. and Ritzi, E. W.: Theoretical Studies of Sound Emission from Aircraft Ducts. AIAA Paper 73-1012.

56. Zorumski, W. E.: Acoustic Theory of Axisymmetric Multisectioned Ducts-Reduction of Turbofan Engine Noise. NASA TR-R-419, 1974.

57. Quinn, D. W.: Attenuation of the Sound Associated with a Plane Wave in a Multisection Cylindrical Duct. AIAA Paper No. 75-496.

58. Arnold, W. R.: Sparse Matrix Techniques Applied to Modal Analysis of Multisection Duct Liners. AIAA Paper No. 75-514.

59. Lester, H. C.: The Prediction of Optimal Multisectioned Acoustical Liners for Axisymmetric Ducts. AIAA Paper No. 75-521.

60. Motsinger, R. E., Kraft, R. E., Zwick, J.W., Vukelich, S. I., Minner, G. L., and Baumeister, K. J.: Optimization or Suppression for Two Element Treatment Liners for Turbomachinary Exhaust Ducts. NASA CR-134997, April 1976.

61. Sawdy, D. T., Beckeyer, R. J., and Patterson, J. D.: Analytical and Experimental Studies of an Optimum Multisegment Phased Liner Noise Suppression Concept. NASA CR-134960, 1976.

62. Miles, J.: The Reflection of Sound due to a Change in Cross-Section of a Circular Tube. The Journal of the Acoustical Society of America, Vol. 26, No. 3, 1954, pp. 1419.

63. Finlayson, B. A.: The Method of Weighted Residuals and Variational Principles. Academic Press, New York, 1972.

64. Stevenson, A. F.: Exact and Approximate Equations for Wave Propagation in Acoustic Horns. Journal of Applied Physics, Vol. 22, No. 12, 1951, pp. 1461-1463.

65. Beckemeyer, R. J. and Eversman, W.: Computational Methods for Studying Acoustic Propagation in Nonuniform Waveguides. AIAA Paper 73-1006, Seattle, Wash., 1973.

66. Eversman, W., Cook, E.L., and Beckemeyer, R. J.: A Method of Weighted Residuals for the Investigation of Sound Transmission in Non-Uniform Ducts Without Flow. Journal of Sound and Vibration, Vol. 38, 1975, pp. 105-123.

67. Eversman, W.: A Multimodal Solution for the Transmission of Sound in Non-uniform Hard Wall Ducts with High Subsonic Flow. AIAA Paper No. 76-497.

68. Kaiser, J. E. and Nayfeh, A. H.: A Wave Envelope Technique for Wave Propagation in Nonuniform Ducts. AIAA Paper No. 76-496.

EXPERIMENTAL PROBLEMS RELATED TO JET NOISE RESEARCH*

John Laufer
Department of Aerospace Engineering
University of Southern California

ABSTRACT

Sound generation by turbulence is a rather unique problem of physics for several reasons:

1.) the generation mechanism is a highly non-linear problem and, therefore, different from classical acoustics;

2.) conventional experimental techniques developed either in acoustics or in fluid mechanics, are not best suited for studying this question. Consequently, jet noise research presents a great challenge to the experimentalists. The presentation will attempt to give an account of what the specific difficulties are and the various techniques used so far in studying the problem.

Formulation of the Experimental Problem. In considering the nature of the problem one finds that, in general, it is not at all obvious what the experimental approach should be and, in particular, what measurements to make. The sound intensity at a fixed point in the far field is the sum total of the pressures arriving simultaneously to that point due to radiation by unknown acoustic sources of the turbulent flow distributed over a volume. Thus, far field measurements alone cannot give sufficient information about these sources and inversely, the "acoustic source nature" of the flow cannot be detected directly by one or two point measurements in the turbulent layer. A number of approaches have been used in the past; some attack only certain aspects of the problem, others have a more ambitious aim. These will be discussed in detail.

Far Field Measurements. Historically, the earliest experiments consisted of conventional intensity and directivity measurements. These measurements clarified the general nature of the far field and pointed to some of the strengths and weaknesses of the existing theories. However, with the exception indicating consistency with the quadrupole nature of the sources as predicted by Lighthill's theory, they could give no additional information about the radiation. Subsequently, two point correlation measurements provide indication of the possible presence of large-scale structures as sources.

With the development of a highly directional microphone, the source

*This research was supported by the National Science Foundation under Grant NSF-ENG 75-19741.

strength distribution along the axis, as seen from a far-field point, could be obtained. Such a technique has the potential of giving considerably more information about the nature of the sources.

Near-Field Measurements. A great deal of experimental work has been done on the fluctuation field within a turbulent layer in connection with studying the turbulent flow itself. It is questionable whether "conventional" turbulence measurements would shed much light on the "acoustic source nature" of the flow. Speculation of the type of measurements one might need here will be given in some detail. In particular, the use of artificial flow excitation will be discussed.

Simultaneous Near- and Far-Field Measurements. This is an area where considerable work has been done using various techniques. The advantages and shortcomings of these methods will be considered and some general comments on future work will be made.

NONLINEAR PERIODIC WAVES*

Lu Ting

Courant Institute of Mathematical Sciences
New York University

ABSTRACT

A review of systematic perturbation procedures for the analysis of nonlinear problems is presented. The cases when the multiplicity of an eigenvalue is finite or infinite are treated for self-sustained and for forced oscillations. The possibility of the formation of shock waves is discussed. Applications to acoustic problems are presented.

INTRODUCTION

Most of the problems in acoustics can be treated successfully by the linearized theory since the nonlinear terms in the governing equations are in general of higher order. The linearized theory predicts the natural frequencies. When there is only one eigenfunction associated with a natural frequency, we say the eigenvalue is simple and the mode of the free oscillation is given by the eigenfunction times a constant, the amplitude a, which is undefined. For forced oscillations the amplitude becomes infinite when the forcing term is in resonance.

When the small nonlinear terms are included, the periodic solutions can be constructed by the perturbation theory. The linear problem will yield the first term in the perturbation expansion of the solution, and further terms will also be determined by linear problems. This theory is based upon the original discovery by Lindstedt and Poincare that, to avoid the occurrence of secular terms in applying perturbation theory to periodic motions in celestial mechanics, it is necessary to make a perturbation expansion of the period of motion. This theory is frequently used for problems involving nonlinear ordinary differential equations. It has been applied systematically to periodic free vibration problems involving nonlinear partial differential equations by Keller and Ting (ref. 1). The solution and the frequency are assumed to be regular functions of a small parameter ε, the order of magnitude of the nonlinear terms.

When the eigenvalue is simple in the linear problem, the orthogonality of the eigenfunction with the inhomogeneous terms in the governing equation for the next order solution, and those for the higher ones, removes the secular terms and also defines the amplitude of the oscillation as a function of the frequency.

* This paper is supported by NASA Grant NSG 1291

When the multiplicity of an eigenvalue in the linear problem is equal to k, there are k linearly independent eigenfunctions. The linear solution is a linear combination of those k eigenfunctions. The orthogonality of the inhomogeneous terms of the governing equations for the higher solutions with k eigenfunctions yields k equations to relate the k coefficients in the linear combinations to the frequency. The nonlinear analyses define not only the amplitude but also specify the mode of the linear oscillation to one special linear combination of the k eigenfunctions.

When the multiplicity of an eigenvalue is infinite, the linear solution can be represented as an infinite series of the eigenfunctions. The orthogonality conditions with the eigenfunctions yield infinite numbers of equations for the coefficients in the series. The solution of these equations becomes very difficult, in general. Of course, we can construct an approximate solution by truncating the infinite series to a finite number of terms and imposing only a finite number of orthogonality conditions. This approximate solution will be useful only when the infinite series happens to converge very fast.

For a slightly nonlinear wave equation without dispersion, the multiplicity of each eigenvalue is infinite. The general solution of the linear wave equation can be represented by forward and backward waves with unknown wave forms. The orthogonality conditions were shown to be equivalent to an integral condition by Keller and Ting (ref. 1) and by Hale (ref. 2). Using the integral condition Fink, Hall, and Khalili (ref. 3) showed that it leads to a functional differential equation for the wave form and obtained explicit solutions in terms of elliptic functions for three types of nonlinear forcing terms. Generalization of the analysis and the establishment of an integral solvability condition for n-dimensional space have been made by Ting (ref. 4).

The systematic perturbation theory was applied to several interesting nonlinear boundary value problems by Millman and Keller (ref. 5). They also presented a systematic procedure for the construction of solutions of forced oscillations. The amplitude of the forcing term and the energy of the system are assigned. The solutions and the frequency are again regular functions of the small parameter ε . The energy equation guarantees the boundedness of the solution. With a simple eigenvalue, we obtain the finite amplitude solution of free oscillation when the forcing function is in resonance while its amplitude vanishes. When the eigenvalue is not simple, the force function can be any linear combination of the eigenfunctions with assigned amplitudes, and the solution of the forced oscillation will remain finite due to the energy condition. However, in order to recover the finite amplitude solution of free oscillation, the forcing function has to be a linear combination of all the eigenfunctions with all the coefficients approaching zero simultaneously while their ratios, which remain constant, are specified by the energy equation so that the wave form of the forcing function will be related to that of the free oscillation.

The procedures for the construction of the perturbation solutions and the statements regarding the solutions will be demonstrated in the following two sections for slightly nonlinear one dimensional wave equations with or without a finite dispersion term. When there is a finite dispersion term, the eigenvalue of the linear equation is simple. Without the dispersion term, the

multiplicity of the eigenvalue is infinite. For each case, we will treat the problem of the free oscillations first and then that of forced oscillations.

The author wishes to acknowledge Prof. Joseph B. Keller for valuable discussions regarding this paper.

SYMBOLS

A	amplitude of the forcing function
a	amplitude of the oscillation
b_j	coefficients of linear combinations in eq. (31)
C_{jk}	coefficients of in eq. (15)
E	energy of the system
f	nonlinear term
g, G	the wave form of the solution and the forcing term respectively
j, k, m, n	positive integers
t	time
u	the solution of the nonlinear equation
x	space variable
α	dispersion coefficient
β	defined in eq. (28)
γ	coefficient in the nonlinear term when $f(u) = \gamma u^3$
ε	small dimensionless parameter denoting the order of magnitude of the nonlinear terms
λ	eigenvalue or ω^2
ξ	the phase variable
τ	integration variable
ω	frequency
$(\cdot)$	differentiation with respect to ε at $\varepsilon = 0$

Subscripts:

o	the leading term, i.e., when $\varepsilon = 0$
x,t	partial derivatives with respect to x or t

NONLINEAR WAVE EQUATION FOR A DISPERSIVE SYSTEM

Analysis of Free Oscillations

Let us construct the periodic solution of the nonlinear equation with a finite dispersion coefficient,

$$u_{tt} - u_{xx} + \alpha u = \varepsilon f(u) \quad 0 < x < \pi \tag{1}$$

subjected to the periodicity and boundary conditions,

$$u(x, t + 2\pi/\omega) = u(x,t) \tag{2}$$

$$u(0,t) = u(\pi,t) = 0 \tag{3}$$

ε is a prescribed small parameter and $\varepsilon f(u)$ represents the nonlinear force. ω is an undetermined angular frequency. Let us introduce $t' = \omega t$ and $u'(x,t') = u(x,t)$ in eqs. (1),(2),(3) so that the period in the new time variable is 2π. We will drop the primes and eqs. (1),(2), (3) become

$$\omega^2 u_{tt} - u_{xx} + \alpha u = \varepsilon f(u) \tag{4}$$

$$u(x,t + 2\pi) = u(x,t) \tag{5}$$

$$u(0,t) = u(\pi,t) = 0 \tag{6}$$

We shall seek a solution $u(x,t,\varepsilon)$ and a corresponsing angular frequency $\omega(\varepsilon)$ which are representable by finite Taylor series in ε, i.e.

$$u(x,t,\varepsilon) = u_0(x,t) + \varepsilon \dot{u}(x,t) + \tfrac{1}{2}\varepsilon^2 \ddot{u} + \ldots \tag{7}$$

and $$\lambda(\varepsilon) = \omega^2(\varepsilon) = \omega_0^2 + \varepsilon\dot{\lambda} + \tfrac{1}{2}\varepsilon^2 \ddot{\lambda} + \ldots. \tag{8}$$

where $u_0 = u(x,t,o)$, $\omega_0 = \omega(0)$ and $(\dot{})$ denotes differentiation with respect to ε at $\varepsilon = 0$.

By setting $\varepsilon = 0$, eq. (4) becomes the linear equation for the zero-order solution u_0, i.e.,

$$\omega_o^2 u_{ott} - u_{oxx} + \alpha u_0 = 0 \tag{9}$$

and the same periodicity and boundary conditions eqs. (5), (6) hold for u_0. By choosing the origin of t appropriately we can require $u_t = 0$ at $t = 0$ and write these solutions as

$$u_0 = a \sin nx \cos t \tag{10}$$

$$\lambda_0 = \omega_0^2 = \alpha + n^2, \quad n = 1, 2, \ldots. \tag{11}$$

For each integer n, ω_0 or the eigenvalue λ_0 is defined. When α is an irrational number we can show that there is only one eigenfunction, namely sin nx cos t. The amplitude a is undetermined so far.

We differentiate eqs. (4), (5), (6) with respect to ε and set $\varepsilon = 0$ to obtain the equations for the next order solution u. They are:

$$\omega_o^2 \dot{u}_{tt} - \dot{u}_{xx} + \alpha \dot{u} = - \dot{\lambda} u_{o_{tt}} + f(u_o) \tag{12}$$

and eqs. (5) and (6) with u replaced by $\dot{u}$. They will have a solution (ref. 1) if the inhomogeneous part is orthogonal to the eigenfunction, i.e.

$$\frac{2}{\pi^2} \int_0^{2\pi} dt \int_0^{\pi} dx \quad [-\dot{\lambda} u_{o_{tt}} + f(u_o)] \quad \sin nx \cos t = 0. \tag{13}$$

We will give a physical meaning to this condition. The inhomogeneous term in the linear equation for $\dot{u}$ can be considered as the forcing term. The solution will be finite only when the forcing term is not in resonance with the normal mode of the homogeneous system. In other words, the coefficient of the Fourier component, sin nx cos t, of the forcing term should vanish as expressed by condition (13).

The solution is

$$\dot{u} = \sum_{k=0}^{\infty} \sum_{j=1}^{\infty}{}' C_{jk} \sin j x \cos kt/[j^2 + \alpha - \omega_o^2 k^2] \tag{14}$$

The prime over the summation sign means $j \neq n$ when $k = 1$. The coefficients C_{jk} are defined by:

$$f(u_o) = \sum_{k=0}^{\infty} \sum_{j=1}^{\infty} C_{jk} \cos kt \sin jx \qquad 0<x<\pi \tag{15}$$

The denominator in eq. (14) can be rewritten as $j^2 - n^2k^2 + \alpha(1-k^2)$ which will not vanish since α is an irrational number and $j \neq n$ when $k = 1$. Eq. (13) in turn yields the first order frequency-amplitude relationship,

$$\omega^2 - \omega_o^2 = \varepsilon\dot{\lambda} + O(\varepsilon^2) = - C_{n1}/a + O(\varepsilon^2) \tag{16}$$

For the special case of $f(u) = - u^3$, we have

$$C_n = -(9/16)a^3$$

and $$\omega^2 = \alpha + n^2 + \varepsilon(9/16)a^2 + O(\varepsilon^2) \tag{17}$$

Figure 1 shows the amplitude-frequency curves for $\alpha = \sqrt{2}$, $\varepsilon = 0.1$ in the neighborhood of the first two natural frequencies, i.e., n = 1,2,

Analysis of Forced Oscillations

We will modify the preceding problem by adding the distributed forcing function A sin j x cos ω t where j is a positive integer and A is the amplitude of the forcing function. The differential equation, eq. (4), must be changed to:

$$\omega^2 u_{tt} - u_{xx} + \alpha u - \varepsilon f(u) = A \sin jx \cos t \tag{18}$$

while eqs. (5) and (6) remain unchanged.

We will now establish the energy equation. We multiply eq. (18) by u_t, integrate with respect to x from 0 to π and carry out integration by parts for the second term with the aid of eqs. (5) and (6). We obtain

$$\frac{dE}{dt} = \frac{d}{dt}\int_0^{\pi} \tfrac{1}{2}\{\omega^2 u_t^2 + u_x^2 + u^2\alpha - 2\varepsilon \int_0^u f(u)du - A\int_0^t u(k,\tau)\sin jx \cos\tau\, d\tau\}dx = 0$$

Therefore the energy E is a constant and in particular at t = 0, we have

$$\tfrac{1}{2}\int_0^{\pi} [\omega^2 u_t^2 + u_x^2 + u^2\alpha - 2\varepsilon \int_0^u f(u)\, du]dx\Big|_{t=0} = E \tag{19}$$

We will prescribe the energy E and consider u and ω to be functions of E, A and ε . We will then represent u and ω as finite Taylor series in ε as in eqs. (7) and (8). Letting ε = 0 in eqs. (18), (19), (5) and (6), we obtain

$$\omega_o^2 u_{ott} - u_{oxx} + \alpha u_o = A \sin jx \cos t \tag{20}$$

and

$$\tfrac{1}{2}\int_0^{\pi} [\omega_o^2 u_{o_t}^2 + u_{ox}^2 + \alpha u_o^2]\Big|_{t=0} dx = E \tag{21}$$

while eqs. (5) and (6) hold for u_o. The solution of eqs. (20), (5) and (6) is

$$u_o = a \sin jx \cos t \tag{22}$$

where

$$a = A/[j^2 + \alpha - \omega_o^2] \tag{23}$$

ω_o is related to the energy E by eq. (21),

$$E = \pi a^2(j^2 + \alpha)/4 = (\pi/4)A^2(j^2 + \alpha)/(j^2 + \alpha - \omega_o^2)^2 \tag{24}$$

Since α is an irrational number, the forcing term is in resonance with the linear system only at the jth natural frequency. With $\omega_o^2 = j^2 + \alpha$, the amplitude a and the energy E in the linearized theory become infinite. For the nonlinear theory, we prescribe the amplitude A and the energy E and define $\omega_o^2(A,E,\varepsilon)$,

from eq. (24). We will then proceed to determine $\omega^2(A,E,\varepsilon)$ from the next order analysis.

We differentiate eqs. (18) and (19) with respect to ε and the set $\varepsilon = 0$ to obtain

$$\omega^2_o \dot{u}_{tt} - \dot{u}_{xx} + \alpha \dot{u} = - \dot{\lambda} u_{o_{tt}} + f(u_o) \tag{25}$$

and

$$\int_0^{\pi} [u_o \dot{u}_\alpha + u_{ox} \dot{u}_x - \int_0^{u_o} f(u)du]_{t=0} \, dx = 0 \tag{26}$$

We make use of the fact that $u_{ot} = 0$ at $t = 0$. Again eqs. (5) and (6) hold also for $\dot{u}$. The solution of eqs. (25), (5), and (6) is

$$\dot{u} = \frac{\dot{\lambda} a + C_{j1}}{j^2 - \omega_o^2 + \alpha} \sin j x \cos t \tag{27}$$

$$+ \sum_{m=0}^{\infty} \sum_{k=1}^{\infty}{}' \frac{C_{km}}{k^2 + \alpha - \omega^2_o m^2} \sin k x \cos mt$$

The symbol ($'$) means that $k \neq j$ when $m = 1$. Here the coefficients C_{km} are defined by eq. (15). Insertion of eq. (27) into eq. (26) yields

$$\dot{\lambda} = \frac{-1}{a} \Big\{ C_{j1} + (j^2 + \alpha - \omega_o^2) \Big[\sum_{\substack{m=0 \\ m \neq 1}}^{\infty} \frac{C_{jm}}{j^2 + 1 - \omega_o^2 m^2} \tag{28}$$

$$- \frac{2}{\pi a (j^2 + \alpha)} \int_0^{\pi} dx \int_0^{\beta} f(u)du \Big] \Big\}$$

where $\beta = u_o(x,0) = a \sin jx$. Use of eq. (28) in eq. (8) yields ω^2 in terms of A and E to the first order in ε.

From eq. (24) it is clear that for a nontrivial solution, $a \neq 0$ and E is positive. We can solve for ω_o^2,

$$\omega^2_o = j^2 + \alpha \pm [\pi A^2 (j^2 + \alpha)/(4E)]^{\frac{1}{2}} \tag{29}$$

In the limit $A \to 0$, we obtain the results for free oscillations,

$$\omega_o^2 \to j^2 + \alpha$$

and

$$\dot{\lambda} \to - C_{j1}/a$$

since $f(u_o)$ is finite. These results are in agreement with the results of eqs. (11), (14) and (16) obtained in the preceding subsection by a different procedure.

Since the amplitude a of the solution is equal to $\{4E/[\pi(j^2 + \alpha)]\}^{\frac{1}{2}}$ we will plot a vs ω^2 for each constant forcing amplitude A instead of E vs ω^2 Fig. 2 shows the curves for A = 0, 0.2, 1 with $\alpha = \sqrt{2}$, $\varepsilon = 0.1$, j = 1, $f(u) = -u^3$. Of course, the curve for A = 0 agrees with the curve in Fig. 1 near the first natural frequency.

We will now explain why these two apparently different methods for the construction of finite amplitude free oscillations are equivalent.

In the first method, the underlying principle is that the solution u or u_0, $\dot{u}$ etc., have to be finite. The orthogonality condition eq. (13) guarantees that u is finite since the eigenvalue is simple and the solution $\dot{u}$ in eq.(14) is therefore not in resonance with the natural mode which is proportional to u_0. In the second method, we note that u_0 is finite for finite energy E. Hence $f(u_0)$ is finite, and the first order energy equation (26) says that the part of $\dot{u}_x$ which is orthogonal to u_{0x} has to be finite. u_0 is an eigen-solution. Since the eigenvalue is simple, eq. (26) is sufficient to guarantee that $\dot{u}$ is finite. When the eigenvalue is not simple, and the forcing function contains only one of the eigenfunctions, eq. (26) is not sufficient to insure that $\dot{u}$ is finite although eq. (26) will produce a relationship between ω^2 and E for A = 0. Of course, if we continue to the second order energy equation, the appearance the $\dot{u}_x^2$ term would then require $\dot{u}$ to be finite. The procedures for handling the problems with nonsimple eigenvalues are described in the next section.

NONLINEAR WAVE EQUATION FOR A NONDISPERSIVE SYSTEM

Analysis of Free Oscillation

The governing equations (4), (5), (6) in the preceding section remain applicable when we set $\alpha = 0$. The perturbation expansions eqs. (7) and (9) are the same. The governing equations for the zero order solution are

$$\omega^2_0 \, u_{ott} - u_{oxx} = 0 \tag{30}$$

and eqs. (5) and (6) with u replaced by u_0. Again we choose the origin of t such that $u_t = 0$ at t = 0, the solution for a given integer n can be written as

$$u_0 = a \left[\sum_{j=1}^{\infty} b_j \sin nj\, x \cos njt\right] \tag{31}$$

with

$$\lambda_0 = \omega^2_0 = n^2 \tag{32}$$

u_0 is expressed in terms of a linear combination of all the eigenfunctions associated with λ_0. Since we factor out the amplitude a, we can impose a condition on b_j's, say

$$\sum_{1}^{\infty} b_j^2 \, j^2 = 1 \tag{33}$$

The governing equations for the next order solution $\dot{u}$ are eqs. (12), (5), and (6) with $\alpha = 0$. The solution $\dot{u}$ is bounded when the inhomogeneous part of eq. (12) is orthogonal to all the eigenfunctions $\sin njx \cos njt$ for all j. The results are

$$\dot{\lambda} a b_j + \frac{2}{\pi^2} \int_0^{2\pi} dt \int_0^{\pi} dx\, f(u_0) \sin njx \cos njt = 0 \tag{34}$$

for $j = 1, 2, \ldots$. Eqs. (34) and (33) are the equations for all the b_j's and a in terms of λ. They are difficult to solve.

It was observed in ref. 4 that at least for the special case of $f(u) = \gamma u^3$ where γ is a constant, the approximate solution which was obtained by keeping only two terms in eq. (31) and applying eq. (34) for j = 1 and 2 differs from the exact solution by less than 0.1%. The construction of the approximate solution is the same as if the multiplicity of the eigenvalue were finite (say equal to 2). For a general nonlinear problem, it would be advisable to construct the exact solution by the following procedure.

The general solution of eqs. (30), (5), and (6) with $\lambda_0 = n^2 = 1$, can be written as

$$u(x,t) = \tfrac{1}{2} a\, [g(t + x) - g(t - x)] \tag{35}$$

with

$$g(\xi + 2\pi) = g(\xi) \tag{36}$$

where g is the unknown wave form. We introduce an extra factor a so that a normalization condition on g can be introduced, say

$$\frac{1}{\pi} \int_0^{2\pi} [g'(\xi)]^2 d\xi = 1 \tag{37}$$

The series eq. (31) can be identified with g as

$$g(\xi) = \sum_1^{\infty} b_j \operatorname{Sin} j\xi. \tag{38}$$

The orthogonality condition of eq. (34) can now be replaced by an integral equation for the wave form g (ref. 1, 2)

$$-\frac{a\pi}{2}\dot{\lambda}\, g(t) + \int_0^{\pi} f[u_0(t-x, x)]\, dx = 0 \tag{39}$$

For the case of $f = \gamma u^3$, eq. (39) is reduced to a functional differential equation for g and the solution is an elliptic function (ref. 3). Consequently all the coefficients b_j in eqs. (38) or (31) are defined. Eq. (39) also provides a relationship between a and λ, i.e., the amplitude frequency relationship.

Analysis of Forced Oscillation

If we introduce a distributed forcing term proportional to an eigenfunction

say the first one $\sin x \cos t$, eq. (30) becomes

$$\omega_o^2 u_{ott} - u_{oxx} = A \sin x \cos t \tag{40}$$

The solution of eqs. (40), (5), and (6) is

$$u_o = a \sin x \cos t \tag{41}$$

where $$a = A/[1 - \omega_o^2] \tag{42}$$

The energy equation is eq. (21) with $\alpha = 0$. Letting $\varepsilon = 0$, we relate ω_o to E

$$E = \pi a^2/4 = (\pi/4)\, A^2/(1 - \omega_o^2)^2 \tag{43}$$

or

$$\omega_o^2 = 1 \pm [\pi A^2/(4E)]^{\frac{1}{2}}$$

When the amplitude of the forcing function A and the energy E are non-zero, the amplitude a and the frequency ω_o are defined by eqs. (42) and (43). In particular $\omega_o^2 \neq 1$; therefore, a is finite.

The next order differential equation and energy equation for $\dot{u}$ and $\dot{\lambda}$ are given by eqs. (25) and (26) with $\alpha = 0$. Their solutions are given by eqs. (27) and (28) with $\alpha = 0$ and $j = 1$. In particular for $f(u) = -u^3$, we have

$$\dot{u} = \frac{\dot{\lambda} a - 9\, a^3/16}{1 - \omega_o^2} \sin x \cos t - \frac{3\, a^3}{16(1 - 9\omega_o^2)} \sin 3x \cos 3t + \frac{3\, a^3}{16(9 - \omega_o^2)} \sin 3x \cos t + \frac{9\, a^3}{16(1 - \omega_o^2)} \sin 3x \cos 3t \tag{44}$$

and

$$\dot{\lambda} = (9\, a^2/16)\,[1 + 3\omega_o^2 \quad (1 - \omega_o^2)/(1 - 9\omega_o^2)] \tag{45}$$

In the limit of $A \to 0$ and $\omega_o^2 \to 1$ such that the energy A and also the amplitude a remain constant, we obtain $\dot{\lambda} = 9a^2/16$ while $\dot{u}$ becomes unbounded because of the last term in eq. (44) unless $E = a = 0$.

In order to obtain nontrivial free oscillations as a limiting case of the forced oscillations, the forcing function should contain all the eigenfunctions in the form of an infinite series eq. (31) or be represented as general solution eq. (35) for $\lambda_o = 1$. Eq. (40) should now be

$$\omega_o^2 u_{o_{tt}} - u_{oxx} = (A/2)[G(t + x) - G(t - x)] \tag{46}$$

The solution u_o is

$$u_o = (a/2)[g(t + x) - g(t - x)] \tag{47}$$

where $$a = A/(1 - \omega_o^2) \tag{48}$$

$$g''(\xi) = -G(\xi) \tag{49}$$

with $g(\xi + 2\pi) = g(\xi)$ and $g(0) = 0$. Since we introduce an extra factor A we can normalize G or g by eq. (37). The energy is related to a or A by eq. (43).

In the limiting case of $\omega^2 \to 1$ and $A \to 0$, while E and a remain finite, u_0 in eq. (47) is of the same form as eq. (35) for the free oscillation. The governing equation for $\hat{u}$ is also the same as that for the free oscillation. On account of the next order energy equation, the part of $\hat{u}$ which is infinite has to be orthogonal to all the eigenfunctions. Therefore, $\hat{u}$ is finite and the wave form $g(\xi)$ will be the same as that for the finite free oscillation in ref. 3. The wave form for forcing term is in turn defined by eq. (49) as $A \to 0$.

CONCLUDING REMARKS

The perturbation theories for nonlinear free and forced oscillations are reviewed. In the case that the eigenvalue for the linear problem is simple, the solution for the forced oscillation yields that of free oscillation when the forcing term is in resonance while its amplitude approaches zero accordingly. This statement remains true when the multiplicity of the eigenvalue is finite or infinite provided that the forcing function is a linear combination of all the eigenfunctions. Their amplitudes vanish in such a menner that the wave form of the forcing function is defined by that for the free oscillation.

From eq. (24) we see that for a special combination of E and A, $k^2+\alpha-\omega^2m^2$ vanishes for a pair of (k,m) and the solution $\hat{u}$ given by eq. (27) becomes infinite. We should then add a free oscillation mode b sin k x cos mt to u_0 and the amplitude b is determined from the energy equation so that the secular term associated with the mode (k,m) in $\hat{u}$ vanishes. Similar modifications should be made to avoid the appearance of a secular term of higher mode for the solution of a forced oscillation of a nondispersive system.

When the perturbation theory for the free oscillations yields only a trivial solution, we conclude that the small amplitude periodic solution which splits off from the state of rest does not exist. The longitudinal vibrations of a uniform bar with fixed or free ends are examples mentioned in ref. 1. This result is verified in ref. 1 by the method of characteristics. It yields a stronger result that, for certain initial boundary value problems, every nontrivial solution becomes singular in a finite time. Shock waves are formed afterwards. This result is the same as that of Lax but the proof is somewhat different (ref. 6). This result was also applied (ref. 1) to show that there are no nonsingular (shockless) finite amplitude sound waves in a closed tube. For long tubes with open ends, it can be extended to a problem periodic in x if the simple boundary condition of constant pressure is imposed. Consequently we can conclude again the nonexistence of nonsingular periodic solution. However, the realistic boundary condition for an open end of a long pipe should be imposed based on the analysis of Levine and Schwinger (ref.7). The reflection coefficient is not equal to -1. It depends on the wave number and furthermore its

absolute value is less than unity due to the loss of energy propagated to infinity. Therefore an initial wave in an open tube will decay and a periodic free oscillation cannot be sustained. Detailed studies for this problem will be reported elsewhere.

REFERENCES

1. Keller, J.B., and Ting. L.: Periodic Vibrations of Systems Governed by Nonlinear Partial Differential Equations. Commun. on Pure and Appl.Math. Vol. XIX, No. 4, Nov. 1966, pp. 371-420.

2. Hale, J.K.: Periodic Solutions of a Class of Hyperbolic Equations Containing a Small Parameter. Arch. Rational Mech. Anal., Vol. 23, No. 5, September 1967, pp. 380-398.

3. Fink, J.P.; Hall, W.S.; and Khalili, S.: Perturbation Expansions for Some Nonlinear Wave Equations, SIAM, J. Appl. Math. Vol. 24, No. 4, Jan.1973, pp. 575-595.

4. Ting, L.: Periodic Solutions of Nonlinear Wave Equations in N-dimensional Space. To appear in SIAM J. Appl. Math., Part A, 1977.

5. Millman, M.H. and Keller, J.B.: Perturbation Theory of Nonlinear Boundary Value Problems. J. of Math. Phys. Vol. 10, No. 2., Feb. 1969, pp.342-361.

6. Lax, P.D.: Development of Singularities of Solutions of Nonlinear Hyperbolic Partial Differential Equations. J. Math. Phys., Vol. 5, No. 5., May 1964, pp. 611-613.

7. Levine, H. and Schwinger, J.: On the Radiation of Sound from an Unflanged Circular Pipe. Phys. Review., Vol. 73, No. 4., Feb. 1948, pp.383-406.

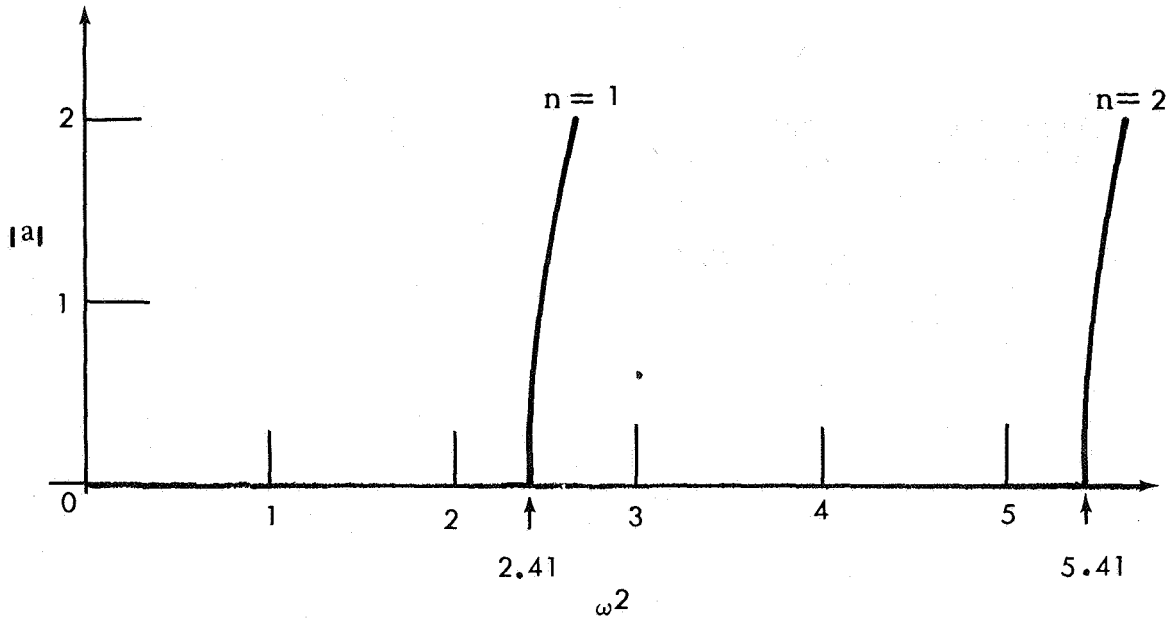

Figure 1.- Amplitude-frequency curve for free oscillations.

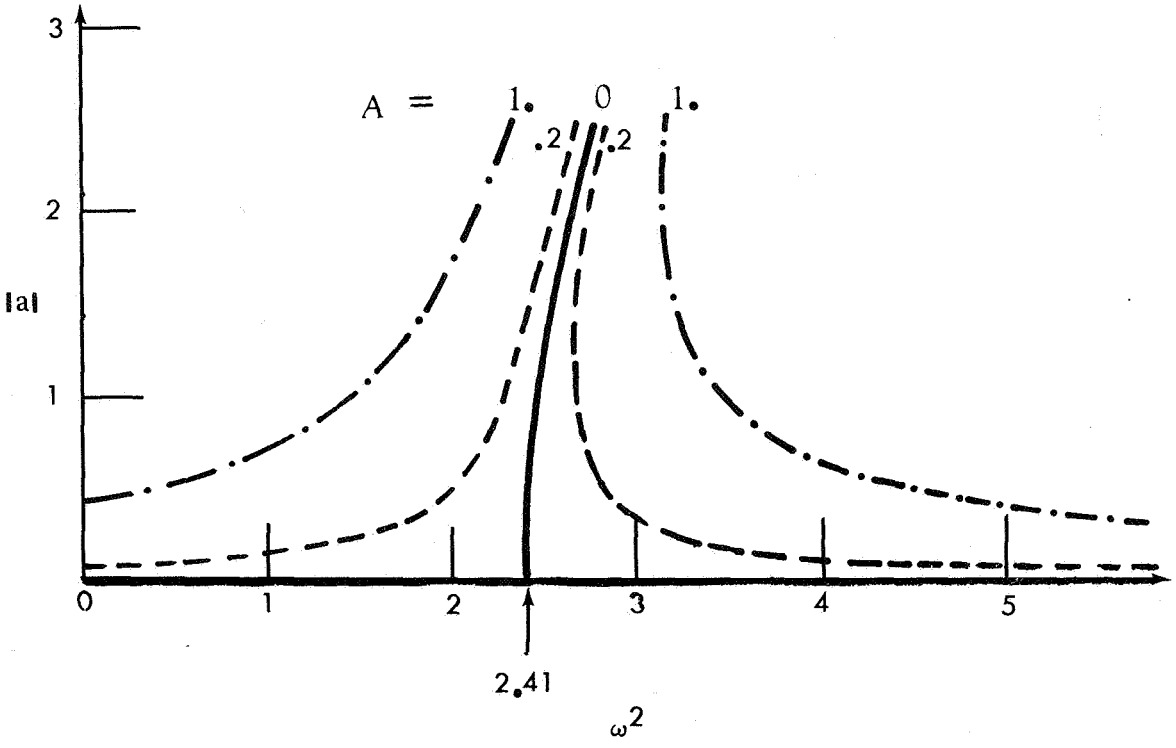

Figure 2.- Amplitude-frequency curve for forced oscillations.

FEATURES OF SOUND PROPAGATION THROUGH AND STABILITY OF A FINITE SHEAR LAYER*

S. P. Koutsoyannis
Stanford University

SUMMARY

The plane wave propagation, the stability and the rectangular duct mode problems of a compressible inviscid linearly sheared parallel, but otherwise homogeneous flow, are shown to be governed by Whittaker's equation. The exact solutions for the perturbation quantities are essentially the Whittaker M-functions $M_{i\tau,\pm 3/4}(4i\tau\eta^2)$ where the non-dimensional quantities τ, η and $4\tau\eta^2$ have precise physical meanings. A number of known results are obtained as limiting cases of our exact solutions. For the compressible finite thickness shear layer it is shown that no resonances and no critical angles exist for all Mach numbers, frequencies and shear layer velocity profile slopes except in the singular case of the vortex sheet.

INTRODUCTION AND BACKGROUND

Studies on compressible free shear layers have not been extensive. In fact with the exception of the earlier work of Graham and Graham (ref. 1) who studied sound propagation through a finite linearly sheared layer in the low-frequency limit, it has been only recently that Blumen et al (ref. 2) obtained an exact solution for the stability of the shear layer with an hyperbolic tangent profile with the significant result that this shear layer is unstable to two dimensional disturbances for all Mach numbers whereas the vortex sheet is known to be unstable only for $M<2\sqrt{2}$, a result that cautions against modeling real sheared flows with vortex sheets, as has been the practice in a number of recent noise research studies, since, as the authors point out, even the long wavelength characteristics of finite thickness shear layers may be quite different from the corresponding properties of the analogous vortex sheet. In this study we consider sound propagation and stability in linearly sheared parallel compressible inviscid homogeneous flows. Work relating to the solutions of the pressure perturbation equation has been that of Küchemann (ref. 3) who also considered the stability of a boundary layer approximated by a linear velocity profile, the study of Pridmore-Brown (ref. 4) and that of Graham and Graham (ref. 1).

Küchemann (ref. 3) obtained a formal series solution for the density perturbation equation and he also arrived at a solution supposedly valid for large values of (our) parameter $\eta = \frac{1}{K} - M$. His series solution, although it is given in a cumbersome and lengthy form, is correct but his asymptotic solution is in

*Work supported under NASA Grants NASA 2007 and NASA 676 to the Joint Institute of Aeronautics and Astronautics.

serious error. Pridmore-Brown (ref. 4) solved the pressure perturbation equation in the short wavelength approximation, i.e., for large values of (our) parameter $\tau = \frac{\omega}{4b} K$. His asymptotic solutions may also be in error. Graham and Graham (ref. 1) studied the problem of a plane wave incident on a linear velocity profile free shear compressible inviscid layer. They used entirely a series solution of the density perturbation equation which they independently rederived apparently unaware of the earlier work of Küchemann. Because they used the series solution only, they were unable to give proofs for the range of the parameters τ and η for which ordinary, total or amplified reflection occurs, although correctly identified the regions intuitively. More importantly and for the same reasons, they could neither prove the existence or non-existence of reasonances or critical angles, but for the case of "sufficiently thin -- but not zero thickness -- shear layer" nor could they draw any conclusions for either the large Mach number M or large τ cases.

SYMBOLS

a	Speed of sound of the homogeneous fluid
b	Velocity profile slope of the shear layer
c	Disturbance phase speed (in general complex)
$\vec{e}_f$	Unit vector in the direction of the mean flow
f,g	Independent solutions of equation (1)
k,k_o	Wave numbers of incident wave
m	Second index of the Whittaker M-functions
n	Index of refraction
$\vec{n}$	Wave normal unit vector
$p^{(1)}$ &$p^{(2)}$	Linear combinations of f and g in equation (5)
q	Parameter of transformation in equation (1)
$w(\vec{r})$	z-component of the velocity perturbation
x,y,z	Rectanular coordinates
z_1	Shear layer thickness
A,B,C,D	Functions of f, g and their derivatives in equation (7)
A,B	Functions of A,B,C and D in equation (9)
H	Heaviside function
K	Inverse of the x-component of the disturbance Mach number
$\vec{M}_d$	Disturbance vector Mach number
$\vec{M}_f$	Mean flow vector Mach number
M(z)	Mean flow Mach number
R.P.	"Real part of"

R	Reflection coefficient
R_1, R_2	In and out of phase component of R
T	Transmission coefficient
T_1, T_2	In and out of phase component of T
$\vec{U}(z)$	Mean velocity
W	Dependent variable in Whittaker's equation
α	x-component of the wave vector of the pressure disturbance
η	Non-dimensional variable in equation (2)
θ, θ_o	Angle of incidence of plane wave
ξ	Independent variable in Whittaker's equation
τ	Non-dimensional parameter in equation (2)
Φ_u & Φ_ℓ	Perturbation velocity potentials
ω	Disturbance frequency

SOLUTION OF THE PRESSURE PERTURBATION EQUATION

In a homogeneous inviscid compressible parallel shear flow having a linear velocity profile in the z-direction only, i.e., $U = U(z) = bz$, it may be easily shown that, starting either from the linearized equations of motion or directly using the appropriate linearized form of the convective wave equation, the z-dependent part $p(z)$ of the pressure perturbation $p(\vec{r})$ is governed by the equation:

$$p_{\eta\eta} - \frac{2}{\eta} p_\eta + (4\tau)^2 (\eta^2 - 1) p = 0 \qquad (1)$$

where

$$\eta = \frac{1}{K} - M, \quad 4\tau = \frac{\omega}{b} K, \quad \text{and} \quad M = M(z) = \frac{bz}{a}. \qquad (2)$$

M is the local Mach number and K and ω acquire the following meanings depending on the problem at hand:

(i) Free Shear Layer: Propagation of a plane wave of wave vector $\vec{k}$ and frequency ω impinging on the shear layer from a half-space ($z<0$) of relative rest and at an angle θ measured from the z-axis ($-\frac{\pi}{2} \leq \theta \leq +\frac{\pi}{2}$):

$$K = \frac{1}{\sin\theta}$$

(ii) Free Shear Layer: Stability for assumed disturbances of the form $p(\vec{r}) = p(z)\, e^{i\alpha(x-ct)}$ (α and c possibly complex):

$$K = \frac{a}{c} \quad \text{and} \quad \omega = ac$$

(iii) Sound Propagation in Rectangular Ducts: Modes for assumed disturbances of the form $p(\vec{r}) = p(z)\, e^{i\alpha(kx-\omega t)}$ (k and ω real):

$$K = \frac{ak}{\omega}$$

The transformation $p = \eta^{\frac{1}{2}} W(\xi), \xi = q\eta^2$ with $q = 4i\tau$, reduces equation (1) into Whittaker's equation for W, so that the two independent solutions f and g of equation (1) are:

$$\begin{Bmatrix} f \\ g \end{Bmatrix} = (4i\tau)^{-\frac{1}{2}\pm m} M_{i\tau, \mp m}(4i\tau\eta^2) \quad , \quad m = \frac{3}{4} \tag{3}$$

Where M are the Whittaker M-functions and τ, η, K are defined following equation (2). It is easily shown that for τ and η real, the functions f and g are also real with f being even and g odd functions of η whereas both f and g are even functions of τ. Moreover series and asymptotic expansions for f and g are readily obtainable from the known properties of the Whittaker M-functions (ref. 5 and 6). The series expansion agrees with the series obtained by Küchemann (ref. 3) and Graham and Graham (ref. 1) although the form that results from equation (3) above is not only more compact, but also faster converging. The asymptotic forms of f and g and their derivatives with respect to η are obtained in terms of I_{2m}, I_{2m+1} with $m = \pm \frac{3}{4}$ using Oliver's method (ref. 5 and 6) and they are in disagreement with both the results of Küchemann (ref. 3) and Pridmore-Brown (ref. 4). This was expected as mentioned in the introduction since Küchemann essentially seeking an expression for large η neglected 1 compared to η^2 in the last term of our equation (1) which is tantamount to setting $\tau = 0$ in Whittaker's equation, whereas Pridmore-Brown by applying Langer's method obtained only a non-uniform leading term of an asymptotic expansion in terms of Airy functions. These and other details may be found in reference 7.

THE FINITE THICKNESS LAYER

Plane Wave Propagation

We consider the two-dimensional finite inviscid compressible shear layer of thickness z_1 with velocity profile

$$\begin{aligned} U &= bz_1 && z \geq z_1 \\ &= bz && z_1 \geq z \geq 0 \\ &= 0 && 0 \geq z \end{aligned} \tag{4}$$

in the (x,z) plane and a time-harmonic monochromatic plane wave incident from the $z<0$ half-space with wave vector $\vec{k}$ and wave number $k = \frac{\omega}{a}$, in the (rest) frame of reference of the stationary fluid at $z<0$, in an otherwise homogeneous fluid in the entire (x,z) plane. The velocity potentials in the lower region (of relative rest) and the upper region of uniform flow are:

$$\Phi_{\ell} = \text{R.P.} \left\{ \mp i \left[e^{\pm ik(x\sin\theta + z\cos\theta - at)} + Re^{\pm ik(x\sin\theta - z\cos\theta - at)} \right] \right\}, z \leq 0$$

$$\underset{u}{\Phi} = \text{R.P.}\left\{\mp iTe^{\pm ik\left[x\sin\theta \pm (z-z_1)\left|\sin\theta\right|(\eta^2-1)^{\frac{1}{2}} - at\right]}\right\}, \quad z \gtrless z_1$$

where R.P. denotes "real part of"; the first term in equation (5) represents the incident wave coming from the half-space $z \lessgtr 0$ and R and T are respectively the complex reflection and transmission coefficients for the velocity potential, and the upper signs are taken for $\eta > 0$.* In the middle (shear layer) region with the velocity profile equation (4) the pressure perturbation $p(\vec{r})$ and the z-component $w(\vec{r})$ of the velocity perturbation are given by:

$$p(\vec{r}) = p^{(1)}(\eta)\sin\left[k(x\sin\theta - at)\right] + p^{(2)}(\eta)\cos\left[k(x\sin\theta - at)\right]$$

$$w(\vec{r}) = \frac{a}{4\tau\eta}\left\{p_\eta^{(1)}(\eta)\cos\left[k(x\sin\theta - at)\right] - p_\eta^{(2)}(\eta)\sin\left[k(x\sin\theta - at)\right]\right\}$$

where $p^{(1)}(\eta)$ and $p^{(2)}$ are linear combinations of the independent solution f and g, equation (3), of equation (1), i.e.

$$p^{(1)}(\eta) = a_{11}f + a_{12}g, \qquad p^{(2)}(\eta) = a_{21}f + a_{22}g \tag{5}$$

with a_{ij} constants. Writing also $R = R_1 + iR_2$, $T = T_1 + iT_2$ for the complex reflection and transmission coefficients R and T respectively and applying the boundary conditions (continuity of the pressure perturbation $p(\vec{r})$ and z-component $w(\vec{r})$ of the velocity perturbation) at the interfaces $z=0$ and $z=z_1$, and after separating real and imaginary parts in the resulting equations one obtains a system of eight linear algebraic equations for the determination of the eight unknowns a_{ij}, R_i, T_i. After somewhat tedious but straightforward algebra the following expressions for the reflection and transmission coefficients are obtained:

$$1 - R^2 = \pm\frac{72}{\left|\sin 2\theta\right|}\cdot\frac{\eta_1^2\sqrt{\eta_1^2 - 1}}{(A \mp B)^2 + (C \mp D)^2} = \pm\left|\tan\theta\right|\sqrt{\eta_1^2 - 1}\;T^2 \tag{6}$$

for $|\eta_1| > 1$, $-\frac{\pi}{2} \lessgtr \theta \lessgtr \frac{\pi}{2}$, R_i, T_j real, and

$|R_1|^2 = 1$, $T = T_1 = T_2 = 0$, for $|\eta_1| < 1$, $-\frac{\pi}{2} < \theta < \frac{\pi}{2}$, R_i, T_j complex

---

*This representation used by Miles (ref. 8) and Graham and Graham (ref. 1) is consistent with the radiation condition as postulated by Miles. Actually Sommerfeld's radiation condition does not apply for plane waves and the difficulties arising in such a case have been discussed by Lighthill (ref. 9). At any rate these representations for the velocity potentials insure that the reflected and transmitted waves are outgoing in a reference frame fixed in the upper fluid and are consistent with Miles's postulate and Ribner's intuitive picture (ref. 10).

with,

$$
\begin{aligned}
A &= \frac{1}{4\tau}\frac{K}{\sqrt{1-K^2}}\left[f_\eta(0)g_\eta(1) - f_\eta(1)g_\eta(0)\right] \\
B &= (4\tau)(\mathrm{sgn}K)\sqrt{\eta_1^2-1}\left[f(1)g(0) - f(0)g(1)\right] \\
C &= \frac{K}{\sqrt{1-K^2}}(\mathrm{sgn}K)\sqrt{\eta_1^2-1}\left[f(1)g_\eta(0) - f_\eta(0)g(1)\right] \\
D &= f_\eta(1)g(0) - f(0)g_\eta(1)
\end{aligned}
\qquad (7)
$$

with $K = \sin\theta$

The upper signs in equation (6) hold for $\eta_1>1$ and the lower signs for $\eta_1<-1$, in both cases $|\eta|>1$. In equation (7) we used the notation 0 and 1 in the arguments of f and g and their derivatives with the understanding that 0 designates evaluation at $\eta=\eta_0=\eta\big|_{z=0}=\frac{1}{\sin\theta}$ and 1 designates evaluation at $\eta=\eta_1=\eta\big|_{z=z_1}=\frac{1}{\sin\theta}-M_1$, i.e., at the two edges of the shear layer.

It is clearly seen from equations (6) that the various reflection regimes are:

$$
\begin{aligned}
&\eta_1>1 \quad , \quad R^2<1 \quad : \quad \text{Ordinary Reflection} \\
&-1<\eta_1<+1 \quad , \quad R^2=1 \quad : \quad \text{Total Reflection} \\
&\eta_1<-1 \quad , \quad R^2>1 \quad : \quad \text{Amplified Reflection}
\end{aligned}
\qquad (8)
$$

These regimes are quite analogous to the three regimes found by Miles (ref. 8) and Ribner (ref. 10) for the vortex sheet case and intutively arrived at by Graham and Graham (ref. 1). The above conditions in equation (8) imply that although the values of the reflection and transmission coefficients depend on the frequency ω and the velocity profile slope b, the dependence is only through the angle of incidence θ, and the two parameters $\tau=\frac{\omega}{b}\sin\theta$ and $\eta_1=\frac{1}{\sin\theta}-M_1$, whereas the conditions for the three reflection regimes are independent of ω or b and depend only on η_1 which is the Mach number $\frac{1}{\sin\theta}$ of the x-component of the phase velocity of the incident wave front relative to the relative Mach number M_1 of the two uniform flows confining the shear layer.

The limiting case of the vortex sheet is easily obtained in the limit $\tau\to 0$ (high-frequency or long acoustic wavelength limit) whereas the low-frequency or short wavelength limit is obtained by letting $\tau\to\infty$ in equation (6); in the former case:

$$
1-R^2 = \pm 4\,\frac{|\tan\theta|\,\eta_1^2\sqrt{\eta_1^2-1}}{\left(\sin^2\theta\,\eta_1^2 \pm |\tan\theta|\sqrt{\eta_1^2-1}\right)^2}, \quad \tau\to 0
$$

which agrees with the results of Miles (ref. 8) and Ribner (ref. 10), whereas in the short wavelength case $1-R^2$ becomes the Heaviside function H:

$$1-R^2 = H\,(1-\eta_1), \qquad \tau\to\infty$$

Resonances and Critical Angles

In this section we give a formal proof that in the amplified reflection regime, $\eta_1<-1$, there are no resonances and in the ordinary reflection regime, $\eta_1>+1$, there are no cricital angles.

First it is easily deduced from equation (6) that excluding the singular cases of $\theta\to 0$ or $M\to\infty$ (in special ways) we may assume that neither A=C=0 or B=D=0, nor all four A,B,C and D may be zero simultaneously. It is next seen from equation (6) that resonances exist if the denominator in the expression for R^2 is zero in the amplifying regime $\eta_1<-1$, i.e., if

$$\Delta = \mathbf{A}^2 + \mathbf{B}^2 = 0, \quad \mathbf{A} = A+B \text{ and } \mathbf{B} = C+D \tag{9}$$

with A,B,C, and D given by equations (7). But Δ in equation (9) above is just the determinant of the coefficients a_{ij} in equations (5) of the system of the four equations determining a_{ij}. Since only the first equation of that system is inhomogeneous with right hand side proportional to τ, a solution for the a_{ij} exists if and only if either $\Delta = \mathbf{A}^2 + \mathbf{B}^2 + \neq 0$ and $\tau \neq 0$ or $\Delta = \mathbf{A}^2 + \mathbf{B}^2 \to 0$ and $\tau\to 0$. It thus follows that equation (9) has solutions, only for $\tau\to 0$, and this is precisely the limiting case of the vortex sheet; i.e., resonances are possible only for the vortex sheet. One may also obtain the same result by algebraic manipulation of the general expressions for R_1 and R_2:

$$R_1 = \frac{B^2-A^2+D^2-C^2}{\Delta}, \quad R_2 = \frac{2}{\Delta}(AD - BC), \quad \Delta = (A \mp B)^2 + (C \mp D)^2 \tag{10}$$

for the case of amplified reflection (lower signs).

For the critical angles we use the expressions in equation (10) with the upper signs (ordinary reflection $\eta_1>1$). If critical angles exist, then $R_1=R_2=0$ and using equation (10) we may easily deduce that for $B\neq 0$, $D\neq 0$ the ratio $\frac{A}{B} = \frac{C}{D}$ may then only attain the value -1 for zero reflection. But this implies that A+B=C+D=0 which is precisely the condition for the existence of resonances equation (9) which we have just shown that do not exist for a finite thickness shear layer.

THE FINITE THICKNESS LAYER

Stability Considerations

For the layer equation (4) the boundary value problem leads to the following equation:

$$i(A + B) + (C - D) = 0 \tag{11}$$

where A,B,C, and D in general complex are given by equation (7) with $K = \frac{a}{c}$ and with (sgn K) ommitted in the expressions for B and C. The roots of the above equation give the dependence of the phase speed c, or of the frequency αc, on the wavenumber α. For temporal amplification α is real and positive, c and $\omega=\alpha c$ are real. For the neutral stability line however, in either case $c=c_r+ic_i$

with $c_i=0$, i.e., c is real, thus K is real and one may distinguish the cases $K\gtrless 1$, $|\eta|\lessgtr 1$ corresponding to supersonic (upper signs) or subsonic (lower signs) disturbances and relative Mach numbers respectively.

Comparing equation (11) and equation (9) we see that the resonances, were they to exist, would obey the system of equations A+B=0, C+D=0 whereas the neutral stability characteristics are determined by the system of equations A+B=0, C-D=0, with A,B,C,D real. Thus, in general one does not expect any connection between resonances and neutral stability eigenvalues except in the singular case of the compressible vortex sheet case which is discussed below.

Special Case: The Compressible Vortex Sheet

As before, we let $\tau\to 0$ in equation (11) and (7) to obtain

$$(1-\frac{1}{K^2})^{\frac{1}{2}} K^2\eta^2 + (1-\eta^2)^{\frac{1}{2}} = 0 \qquad (12)$$

where η and K may be complex. Excluding the singular cases $K\to 1$ and $\eta\to 1$, as well as $K = \frac{a}{c}\to\infty$, we consider the case where the square root terms in equation (7) have the same signs, i.e., the cases $K<1, |\eta|>1$ or $K>1, |\eta|<1$. The formal solution of equation (12) above is

$$\frac{1}{K} = \frac{c}{a} = \frac{1}{2}\left\{M\pm\left[M^2+4\mp 4\sqrt{1+M^2}\right]^{\frac{1}{2}}\right\},$$

which is in agreement with the results of Landau (ref. 11). It is a matter of simple algebra to show that in order to satisfy the inequalities $|\eta|\gtrless 1$ only the upper (minus) sign in the square root term in the above equation for the eigenvalues should be retained. Thus two neutral eigenvalues are not permissible which is precisely the result of Miles (ref. 12) which he arrived at in a totally different way, namely by considering the vortex sheet stability as an initial value problem. It is finally worth noting that for the vortex sheet case the stability equation (11) for neutral eigenvalues, becomes C-D=0, whereas for the plane wave propagation case as we saw previously equation (9) for the resonances becomes C+D=0, since for the vortex sheet, $\tau\to 0$, and A and B are $O(\tau)$ whereas C and D are O(1). Thus it is only for the vortex sheet that resonances and neutral stability eignevalues are given by the same equation i.e. $C^2 = D^2$. For the finite shear layer the roots of equation (9) and (11) the two equations are in general different. In fact, we have shown that although equation (9) may have real roots, there are <u>no</u> resonances for the finite thickness compressible shear layer.

PHYSICAL MEANING OF $\eta, \frac{\omega}{b}$, τ and $4\tau\eta^2$.

<u>Variable</u> $\eta = \frac{1}{K} - M$. $1/K$ is $\frac{1}{\sin\theta}$, $\frac{c}{a}$, $\frac{\omega/k}{a}$ for plane wave propagation, stability and rectangular duct mode studies respectively, and we may thus write for η:

$$\eta = (\vec{M}_d - \vec{M}_r)\cdot\vec{e}_f$$

Thus η is a relative Mach number measure i.e., it is the parallel to the mean flow component of the disturbance (phase speed based) vector Mach number $\vec{M}_d$, relative to the (relative) mean flow Mach number and thus it is a measure of the components of the relative speeds of the disturbance and the mean flow in the direction of the mean flow.

Parameter $\frac{\omega}{b}$: $\frac{\omega}{b}$ acquires the simple meaning of a characteristic Strouhal number of the flow by writing:

$$S = \frac{\text{(Shear layer thickness) x (Disturbance frequency)}}{\text{Mean Flow Speed}} = \frac{z\omega}{bz} = \frac{\omega}{b}$$

Parameters τ and $4\tau\eta^2$: For propagation of a plane wave incident from a homogeneous half-space ($z<o$) at an angle θ_o ($-\frac{\pi}{2}<\theta_o<+\frac{\pi}{2}$) with the z-axis, it is easy to show that the wave normals $\vec{n}$ are independent of x, i.e., that all wave normals of a given z-stratum are parallel. Thus defining an index of refraction $n = (1+\vec{M}_f\cdot\vec{n})^{-1} = (1+M\sin\theta)^{-1}$, it is easy to show that $n = 1-M\sin\theta_o = \sin\theta_o\eta$, $n = n\sin\theta\eta$. Using these relations we may write:

$$\frac{\text{Local disturbance wavelength}}{\text{Relative refraction index change}} = \frac{k_o n}{|\nabla n|/n} = \frac{\omega}{b}\sin\theta_o\eta^2 = 4\tau\eta^2, \text{ and } 4\tau\eta^2 \text{ is the}$$

argument of the Whittaker M-functions in our general solutions f and g of the pressure perturbation equation. τ itself also attains the simple meaning

$$\tau = \frac{\omega}{b}K = \frac{\omega/b}{1/K} \quad \frac{\text{Characteristic Strouhal Number}}{\text{Parallel component of the disturbance Mach number}}$$

CONCLUSIONS

In this paper we have examined some aspects of plane wave propagation and stability of compressible inviscid homogeneous flows characterized by a linear velocity profile. The focus of this study has been on the search for exact solutions of the perturbation equations which bring forth the salient common features of all such parallel flows. The essential conclusions of this study are: (1) The z-dependent part of the pressure (or density) disturbance of such flows is governed by Whittaker's equation with independent solutions $\eta^{\frac{1}{2}}M_{i\tau,\pm m}(4i\tau\eta^2)$, with $m = \frac{3}{4}$ where M are the Whittaker M-functions and η,τ, and $4\tau\eta^2$ admit the following interpretations:

$\eta = (\vec{M}_d-\vec{M}_f)\cdot\vec{e}_f$ = Relative Mach number parallel to mean flow

$\tau = \frac{\omega/b}{\vec{M}_d\cdot\vec{e}_f}$ = Strouhal number / Disturbance Mach number component in the direction of the mean flow

$4\tau\eta^2 = \frac{k_o n}{|\nabla n|/n}$ = Local disturbance wavelength / Relative refractive index change

(2) Solutions to a number of other parallel flow problems may be obtained as limiting cases from our exact solutions. Such flows include the compressible vortex sheet ($\tau\to o$), the incompressible vortex sheet ($\tau\to\infty$, $\eta\to o$, $(\tau\eta)\to o$), the incompressible shear layer ($\tau\to\infty$,$\eta\to o$, $(\tau\eta)$-finite), and the short wavelength approximation of the compressible finite shear layer ($\tau\to\infty$). (3) The compressible finite thickness layer has no resonances and no critical angles for all

Mach numbers, frequencies, shear layer thicknesses and shear profile slopes except for combinations of the singular values of 0 or ∞ for, ω and b; two such combinations ($b\to\infty$, $z_1\to 0$ but bz_1 finite or $\omega\to\infty$) constitute the compressible vortex sheet case.

REFERENCES

1. Graham, E.W. and Graham, B.B.: The Effect of a Shear Layer on Plane Waves of Sound in a Fluid. Boeing Scientific Research Laboratories Document 01-82-0823, November 1968.

2. Blumen, W., Drazin, P.G., and Billings, D.F.: Shear Layer Instability of a Compressible Fluid. Part 2, J. Fluid Mech., Vol. 71, 1975, p.p. 305-316.

3. Küchemann, Dietrich: Störungsbewegungen in einer Gasström mit Grenzchicht. ZAMM, Vol. 18, 1938, p.p. 207-222.

4. Pridmore-Brown, D.C.: Sound Propagation in a Fluid Flowing Through an Attenuating Duct. J. Fluid Mech., Vol. 4, 1958, p.p. 393-406.

5. Oliver, F.W.J.: The Asymptotic Solution of Linear Differential Equations of the Second Order in a Domain Containing one Transition Point. Phil. Trans. Roy. Soc. (London) A249, 1956, p.p. 65-97; see also Skovgaard, Helge: Uniform Asymptotic Expansions of Confluent Hypergeometric Functions and Whittaker Functions. Jul. Gjellerups Forlag, Copenhagen, 1966.

6. Buchholz, Herbert: Die Konfluente Hypergeometrische Function mit besonderer Beruchsichtigung ihrer Anwendungen. Ergebnisse der Angewanten Mathematic, Bd. 2, Springer-Verlag, Berlin, 1953.

7. Koutsoyannis, S.P.: Sound Propagation and Stability in Parallel Flows with Constant Velocity Gradient. Joint Institute for Aeronautics and Acoustics Report No. 6, Sept. 1976.

8. Miles, J.W.: On the Reflection of Sound at an Interface of Relative Motion. J. Acoust. Soc. Am., Vol. 29, 1957, p.p. 226-228.

9. Lighthill, M.J.: Studies on Magneto-Hydrodynamic Waves and Other Anisotropic Wave Motions, Phil, Trans. Roy. Soc. (London) A252, 1960, p.p. 397-430; see also Lighthill, M.J.: The Fourth Annual Fairey Lecture: The Propagation of Sound Through Moving Fluids. J. Sound. Vibr., Vol. 24, 1972, p.p. 471-492.

10. Ribner, Herbert S.: Reflection, Transmission, and Amplification of Sound by a Moving Medium. J. Acoust. Soc. Am., Vol. 29, 1957, p.p. 435-441.

11. Landau, L.: Stability of Tangential Discontinuities in Compressible Fluid. Akad. Nauk. S.S.S.R., Comptes Rendus (Doklady), Vol. 44, 1944, p.p. 139-141.

12. Miles, J.W.: On the Disturbed Motion of a Plane Vortex Sheet. J. Fluid Mech. Vol. 4, 1958, p.p. 538-552.

EFFECTS OF HIGH SUBSONIC FLOW ON SOUND PROPAGATION IN A VARIABLE-AREA DUCT*

A. J. Callegari
State University of New York at Purchase, and
Courant Institute of Mathematical Sciences, New York University

M. K. Myers
Joint Institute for Advancement of Flight Sciences
The George Washington University

SUMMARY

The propagation of sound in a converging-diverging duct containing a quasi-one-dimensional steady flow with a high subsonic throat Mach number is studied. The behavior of linearized acoustic theory at the throat of the duct is shown to be singular. This singularity implies that linearized acoustic theory is invalid. The explicit singular behavior is determined and is used to sketch the development (by the method of matched asymptotic expansions) of a non-linear theory for sound propagation in a sonic throat region.

1. INTRODUCTION

Observations of a correlation between axial Mach number and attenuation of sound radiated upstream from so-called sonic engine inlets have recently focused attention on the acoustic behavior of variable-geometry ducts (refs. 1 and 2). For high-subsonic flows in these ducts, non-linear transonic effects become of major interest. In the linear case, a fully three-dimensional theory presents formidable computational difficulties, and a study of possible non-linear effects is, of course, even more complicated. Thus, it is natural, in undertaking such an effort, to restrict attention initially to a quasi-one dimensional model: the simplest case likely to lead to results of some practical interest. Many earlier authors have studied linear quasi-one dimensional duct acoustics (see refs. 2-6, for example), but, in general, these studies have not been concerned with either the behavior or the validity of the linerized solution as the axial Mach number approaches unity.

The present paper presents some results of an ongoing analytical study of quasi-one dimensional acoustics in converging-diverging ducts with high-subsonic throat Mach numbers. The problem is inherently nonlinear, much like steady

---

*This work was supported by NASA Langley Research Center through the Acoustics Branch, ANRD.

transonic flow theory, but the nonlinear behavior occurs only in a narrow region surrounding the throat section. Linearized theory yields a singular solution in this region, and the current study is employing the method of matched asymptotic expansions to determine the proper solution. However, in order to apply any asymptotic method to correct a solution which is not uniformly valid, it is necessary to know in detail the singular behavior of the defective solution.

Thus, it is the major purpose of this paper to study the nature of the singularity of linearized theory at a sonic throat. To correct the defect using asymptotic methods requires an intricate analysis; the problem depends crucially on two small parameters, and the nonlinear correction to the defect in linearized theory involves a distinguished limit for small values of these parameters. The results obtained here are necessary preliminaries in this analysis. However, they also are of independent interest and do not appear to have been discussed previously.

The analysis presented in sections 3 and 4 naturally suggests that linearization is inappropriate in a small region near the throat of the duct. The detailed results concerning the singular behavior of the linear solution lead to an appropriate stretching of the space variable and a corresponding inner expansion of the dependent variables which does not suffer a singularity at the throat. In the final section of this work the equations describing this inner nonlinear theory are presented, although the details of the expansion process are omitted for brevity. The solution of these nonlinear equations is the subject of current research and will appear in subsequent publications.

2. FORMULATION AND ACOUSTIC PERTURBATION

We consider the propagation of sound in a variable area duct carrying a homentropic inviscid ideal gas flow. The acoustic wavelength is assumed sufficiently large, and the area variation sufficiently slow, that the field can be described by the equations of quasi-one dimensional gas dynamics (ref. 7):

$$
\begin{aligned}
&c_s\bar{\rho}_t + \bar{u}\bar{\rho}_x + \bar{\rho}\bar{u}_x + \bar{\rho}\bar{u}(A'/A) = 0 \\
&c_s\bar{u}_t + \bar{u}\bar{u}_x + (1/\bar{\rho})\,\bar{p}_x = 0 \\
&\bar{p}/\bar{\rho}^{\gamma} = \text{constant} = B
\end{aligned}
\qquad (2.1)
$$

In equations (2.1) $\bar{p}$, $\bar{\rho}$, and $\bar{u}$ are the total fluid pressure, density, and axial velocity, and A(x) is the duct cross sectional area. The dimensionless independent variables x and t are measured in units of L and L/c_s respectively, where L is a characteristic length associated with the area variation, and c_s is the stagnation value of sound speed in the gas. The geometry of the problem is as indicated in figure 1 where the origin of x corresponds to a throat: $A'(0)=0$.

If the velocity and density in the basic steady flow in the duct are denoted by $U(x)$ and $R(x)$ respectively, then from (2.1),

$$UR' + RU' + RU(A'/A) = 0 \quad , \quad \text{and} \quad UU' + \gamma BR^{\gamma-2}R' = 0 \tag{2.2}$$

where the energy relation in equations (2.1) has been used to eliminate the pressure from the system. We intend to seek solutions to the system (2.1) which are small perturbations about the steady values U and R, and it is convenient at the outset to define dimensionless variables $u(x,t)$ and $\rho(x,t)$ according to

$$\bar{u}(x,t) = U(x)[1+u(x,t)] \quad , \quad \text{and} \quad \bar{\rho}(x,t) = R(x)[1+\rho(x,t)] \tag{2.3}$$

Substituting (2.3) into (2.1) and employing the steady relations (2.2) yields the system of equations on u and ρ in the form

$$\begin{aligned} &G^{\frac{1}{2}}\rho_t + M[(1+u)\rho_x+(1+\rho)u_x] = 0 \\ &G^{\frac{1}{2}}u_t + M(1+u)u_x+(1/M)(1+\rho)^{\gamma-2}\rho_x+(M'/G)[(1+u)^2-(1+\rho)^{\gamma-1}] = 0 \end{aligned} \tag{2.4}$$

In equations (2.4), $M(x)$ is the flow Mach number $U(x)/c(x)$, $c(x)$ is the speed of sound in the steady flow ($c^2=\gamma BR^{\gamma-1}$), and

$$G(x) = (c_s/c)^2 = 1 + (\gamma-1)M^2/2 \tag{2.5}$$

the latter expression following from the Bernoulli relation implied by the second of equations (2.2). Equations (2.4) are equivalent to those used by Cheng and Crocco in reference 3.

We introduce a small dimensionless parameter δ, which measures the strength of the source of sound in the duct, and is assumed given from the boundary conditions associated with the system (2.1). Then $u(x,t)=u(x,t;\delta)$, $\rho(x,t)=(x,t;\delta)$ which we assume to have expansions for $\delta<<1$ of the form

$$u = \delta\mu(x,t) + \ldots \quad , \quad \rho = \delta r(x,t) + \ldots \tag{2.6}$$

Substituting (2.6) into (2.4) and neglecting all but first-order terms we obtain the linearized acoustic equations:

$$\begin{aligned} &G^{\frac{1}{2}}r_t + M(r_x+\mu_x) = 0 \\ &G^{\frac{1}{2}}\mu_t + M\mu_x + (1/M)r_x+(M'/G)[2\mu-(\gamma-1)r] = 0 \end{aligned} \tag{2.7}$$

Equations (2.7), subject to appropriate boundary conditions, generally must be solved numerically because of their variable coefficients. It is the purpose of the present work to analyze the behavior of solutions to (2.7) in the vicinity of the throat of the duct when the throat Mach number $M(0)$ is close to unity. It is well known that the system (2.7) is singular at any point where $M(x)=1$. This can be seen most simply by subtracting the two equations; the resulting equation has no μ_x term, and the coefficient of r_x becomes $(M^2-1)/M$, which

vanishes as M→1. This can only occur at x=0 for the duct of Fig. 1. The singularity at x=0 implies that, in general, the acoustic quantities r and μ will be singular when the flow is sonic there. Thus, as we shall see in what follows, r and μ generally become arbitrarily large near x=0 as M(0) approaches unity, thereby violating the assumptions made in deriving (2.7) that μ, μ_x, r, and r_x all remain bounded.

As a result of the singular behavior of the system (2.7) for high subsonic Mach numbers in the throat region, linearized acoustic theory is inadequate to describe sound propagation in the duct; we must re-formulate the perturbation scheme to take into account nonlinear terms in the system (2.4) which were neglected in (2.7). However, in order to make progress in this direction it is necessary to know precisely the nature of the singular behavior of the solutions μ and r to (2.7). This behavior has been recognized, but never resolved, in previous treatments of the system (2.7) (refs. 4,5). In section 4 of this paper we construct an analytical general solution for the linear system (2.7) which displays explicitly the nature of its solutions at x=0 when M(0) is near unity. Before constructing this solution, however, we must discuss the behavior as M(0)→1 of the solutions to the steady flow equations (2.2) in some detail in the following section.

3. BASIC STEADY FLOW

As we have seen, the acoustic equations of motion are singular at x=0 when M(0)=1. It is useful, therefore, to introduce a parameter ε=1-M(0) into our discussion and to consider both the basic steady flow quantities and the acoustic quantities as functions of ε; i.e., U(x)=U(x;ε), μ(x,t)=μ(x,t;ε), and so on. The parameter ε can be considered as having been introduced through the unstated boundary conditions on the steady flow.

The elementary equations of quasi-one dimensional flow (2.2) are discussed in detail in numerous texts; for example, a particularly comprehensive treatment is given by Crocco (ref. 8). It is straightforward to express any of the fluid quantities in terms of the duct area A(x) or, equivalently, in terms of the Mach number M(x;ε). However, the behavior of M explicitly as a function of x and ε does not, to our knowledge, appear in the literature, and it is the purpose of the present section to determine this.

We begin with the well-known relation implied by equation (2.2),

$$M' = -MGA'/(1-M^2)A \tag{3.1}$$

which becomes, after integration,

$$\alpha^s M^s(x)[1+(\gamma-1)M^2(0)/2] = M^s(0)[1+(\gamma-1)M^2(x)/2] \tag{3.2}$$

where, in equation (3.2) we have defined,

$$A(x)/A(0) = \alpha(x), \quad s = 2(\gamma-1)/(\gamma+1) \tag{3.3}$$

Figure 2 shows a sketch of typical integral curves of equation (3.1) assuming $A''(0)\neq 0$. We are interested in a curve such as AB in figure 2, for which M remains less than unity for all x. Since $1-M(0)=\varepsilon$ is assumed small it is natural to seek an expansion of $M(x;\varepsilon)$ in the form

$$M(x;\varepsilon) = M_0(x) + \varepsilon M_1(x) + \varepsilon^2 M_2(x) \ldots \tag{3.4}$$

where $M_0(0)=1$. Substituting (3.4) into (3.2) and equating like powers of ε we find that $M_0(x)$ must satisfy

$$(\gamma+1)\alpha^s M_0^s /2 = 1+(\gamma+1)M_0^2/2 \tag{3.5}$$

while $M_1(x)=0$, and

$$M_2(x) = - 2M_0[1+(\gamma-1)M_0^2/2]/(\gamma+1)(1-M_0^2) \tag{3.6}$$

Obviously, as can also be inferred from the integral curves of figure 2, the expansion (3.4) is not uniformly valid near x=0: the third term is as large as the first whenever $1-M_0(x)$ is as small as ε.

It remains to find $M_0(x)=M(x;0)$ in terms of x; i.e., to solve equation (3.5). We express $\alpha(x)$ as a power series

$$\alpha(x) = 1 + ax^2 + \ldots$$

where we assume $a=A''(0)/2A(0)\neq 0$. Then $M_0(x)$ can be determined after some algebra in the form:

$$M_0(x) = 1 - ((\gamma+1)a/2)^{\frac{1}{2}}|x| + \ldots \tag{3.7}$$

Thus, the leading term of $M(x;\varepsilon)$ behaves as a piecewise linear function of x near the throat so long as $a\neq 0$. If a=0 we find that $M_0(x)$ is smooth at x=0, but this case will not be discussed further in this paper.

4. SINGULARITY OF THE ACOUSTIC SOLUTION

We shall now analyze the acoustic equations (2.7) in order to exhibit explicitly the singular behavior of their solutions in the vicinity of the throat as M(0) approaches unity. Since the steady flow depends on the parameter $\varepsilon=1-M(0)$, the coefficients in the acoustic equations and hence the acoustic quantities μ and r are functions of ε. For $\varepsilon<<1$ we look for solutions of the acoustic equations in the form

$$r=r_0(x,t)+\varepsilon r_1(x,t)+ \ldots , \quad \mu=\mu_0(x,t)+\varepsilon\mu_1(x,t)+ \ldots \tag{4.1}$$

Inserting equation (4.1) into equation (2.7) and using expansion (3.4) for the coefficients, we get, after neglecting higher order terms,

$$G_0^{\frac{1}{2}} r_{0_t} + M_0(r_{0_x} + \mu_{0_x}) = 0$$
$$G_0^{\frac{1}{2}} \mu_{0_t} + M_0 \mu_{0_x} + (1/M_0) r_{0_x} + (M'_0/G_0)(2\mu_0 - (\gamma-1) r_0) = 0 \qquad (4.2)$$

We recall that $M_0(x)$ is any Mach number distribution which yields a sonic velocity at the throat and a subsonic velocity throughout the remainder of the duct. These equations are singular at x=0 since $M_0(0)=1$ *. This is most directly seen by subtracting the two equations.

Analytical solutions of the system (4.2) cannot be found for arbitrary $M_0(x)$ and arbitrary time dependence. However for harmonic time dependence the system can be reduced to a system of ordinary differential equations with a singular point at x=0 and no other singular points within the duct. The nature of this singular point will determine the singular behavior in the time harmonic acoustic quantities. Explicit analytical results concerning the exact nature of the singular point and the dependence on $M_0(x)$ or $U_0(x)$ can be found by use of series solution methods for linear ordinary differential equations. We do not present the general results of this analysis in the current paper. Instead, we shall illustrate the singular behavior of a general solution of the system (4.2) corresponding to a specific steady flow. We assume that the time dependence is harmonic and that the steady velocity distribution is given by a piecewise linear function of x:

$$U_0(x) = c^*(1-K|x|) \qquad |x| < (1/K) \qquad (4.3)$$

where c^* is the critical sound speed and K is a positive constant. This velocity distribution corresponds to a reasonably shaped duct with $A'(0)=0$ and $A''(0)\neq 0$. Equation (3.7) leads us to observe that for any duct with $A'(0)=0$ and $A''(0)\neq 0$, $U_0(x)$ will be given by equation (4.3) for x sufficiently close to the throat. Thus results of this section will be generally applicable to the throat region of many ducts of practical interest. The Mach number distribution associated with equation (4.3) is

$$M_0(x) = (1-K|x|)[(\gamma+1)/2 - (\gamma-1)(1-K|x|)^2/2]^{-\frac{1}{2}} \qquad (4.4)$$

A general solution of the system (4.2) with $M_0(x)$ given by equation (4.4) can be constructed by judicious use of an analytical solution found by Crocco and Cheng (ref. 3). In effect, they obtained a general solution to the system (4.2) with

$$r_0(x,t) = r_0(x)\exp(i\Omega t) \ , \ \mu_0(x,t) = \mu_0(x)\exp(i\Omega t) \qquad (4.5)$$

where $\Omega = \beta K(2/\gamma+1)^{\frac{1}{2}}$ and

$$U_0(x) = c^*(1+Kx) \ , \ -(1/K) < x \qquad (4.6)$$

---

*They are also singular since M_0' has a jump discontinuity at x=0. This does not affect the dominant singular behavior in the solution and would not be present if we had chosen $A''(0)=0$.

Their treatment involves introduction of the new independent variable $z=(1+Kx)^2$. Inserting equations (4.5) and (4.6) into the system (4.2) and introducing z and $\sigma(z)=r_0(x(z))$, $\nu(z)=\mu_0(x(z))$ we obtain, after elimination of $\nu(z)$,

$$z(1-z)d^2\sigma/dz^2-2[1+i\beta/(\gamma+1)]z\ d\sigma/dz - [i\beta(2+i\beta)/2(\gamma+1)]\sigma=0 \qquad (4.7)$$

and

$$\nu(z) = [(\gamma-1+i\beta)\sigma-(\gamma+1)(1-z)\ d\sigma/dz]/(2+i\beta) \qquad (4.8)$$

Equation (4.7) is a hypergeometric equation with complex coefficients. Two linearly independent solutions are

$$\sigma_1=F(a,b,d;1-z) \quad \text{and} \quad \sigma_2=(1-z)^{1-d}F(-b,-a,2-d;1-z) \qquad (4.9)$$

where

$$d = 2 + 2i\beta/(\gamma+1)\ , \quad a+b+1 = d\ , \quad ab = i\beta(2+i\beta)/2(\gamma+1) \qquad (4.10)$$

and F is the standard hypergeometric function (ref. 9).

Since the velocity distribution used by Cheng and that in equation (4.3) are identical for $x<0$, equation (4.9) provides a general solution to our problem for $x<0$. Of course, Cheng's solution for $x>0$ corresponds to a supersonic steady flow and is not relevant to our discussion. In order to obtain a solution when $U_0(x)$ is given by equation (4.3) for $x>0$ we observe that the acoustic equations in this case reduce to equations (4.7) and (4.8) if β is replaced by $-\beta$. Thus we have found a general solution to the acoustic equation corresponding to $U_0(x)$ given by equation (4.3) for both $x<0$ and $x>0$.

The singularity at $x=0$ can be found explicitly by examining the solutions σ_1 and σ_2 of equation (4.9) and the corresponding functions when β is replaced by $-\beta$. Clearly σ_1 is analytic at $z=1(x=0)$ and the singular behavior is due to σ_2. The leading term in σ_2 for z near unity is given by

$$\sigma_2 \sim (1-z)^{1-d}F(a,b,d;0) = [\cos(q\ell n(1-z)) \mp i\ \sin(q\ell n(1-z))]/(1-z) \qquad (4.11)$$

where $q=2\beta/(\gamma+1)$ and the - and + signs hold for $x<0$ and $x>0$, respectively (ref. 9). For general acoustic boundary conditions both σ_1 and σ_2 appear in the acoustic solution, and the amplitudes of the acoustic quantities will approach infinity as x^{-1} when $x\to 0$. In addition their phases have an oscillatory discontinuity at $x=0$. Figure 3 shows an example typical of the behavior of the acoustic quantities (pressure, in this case) for small ε. The rapid rise in the vicinity of the throat is indicative of the developing singularity in the linearized acoustic quantities as $\varepsilon\to 0$. For the typical case shown a pressure wave of magnitude unity was incident from the left on a converging-diverging section situated in an otherwise uniform duct.

Since any duct with a tnroat at which $A''(0)\neq 0$ will have a locally (near $x=0$) piecewise linear steady velocity distribution, the acoustic quantities in such a duct will have the singular behavior given in equation (4.11). In this

circumstance the linear theory governing expansion (2.6) fails for any nonzero δ, no matter how small. Nonlinear effects become appreciable in the throat region. In the next section, an approach is outlined which applies the method of matched asymptotic expansions to study the nonlinear effect in the region near the throat.

5. NONLINEAR PERTURBATION EQUATIONS

In this section we set forth in summary the theory describing sound propagation near the throat as $M(0)\to 1$. We regard the expansion indicated by equations (2.3) and (2.6) as an outer expansion valid as $\delta\to 0$ for fixed values of x, t, and ε; i.e.,

$$\begin{aligned} \bar{u}(x,t;\varepsilon,\delta) &= U(x;\varepsilon)[1 + \delta\mu(x,t;\varepsilon) + \ldots] \\ \bar{\rho}(x,t;\varepsilon,\delta) &= R(x;\varepsilon)[1 + \delta r(x,t;\varepsilon) + \ldots] \end{aligned} \tag{5.1}$$

From the details of the previous section we know that in general μ and r become arbitrarily large in the limit as x and ε approach zero, being expected to grow as x^{-1}.

Therefore we introduce an inner variable $X=[(\gamma+1)/2]^{\frac{1}{2}}(x/\varepsilon)$ and assume that $\bar{u}$ and $\bar{\rho}$ behave asymptotically as $\varepsilon\to 0$ with X, t fixed as:

$$\begin{aligned} \bar{u} &= \bar{u}^i(X,t;\varepsilon) = U^i(X;\varepsilon)[1+\varepsilon\mu^i(X,t) + \ldots] \\ \bar{\rho} &= \bar{\rho}^i(X,t;\varepsilon) = R^i(X;\varepsilon)[1+\varepsilon r^i(X,t) + \ldots] \end{aligned} \tag{5.2}$$

where ε is assumed to be a function of δ which vanishes as $\delta\to 0$ and is to be determined by asymptotic matching of (5.2) with (5.1). In addition we expand the steady flow quantities in the form:

$$U^i(X;\varepsilon)=U_0^i(X)+\varepsilon U_1^i(X)+\ldots,\quad R^i(X;\varepsilon)=R_0^i(X)+\varepsilon R_1^i(X)+\ldots \tag{5.3}$$

Equations (5.3) could be combined directly with (5.2) as one inner expansion, but we find that it simplifies the considerable algebra involved to retain the dimensionless perturbations μ and r and to multiply the separate expansions as indicated in equation (5.2).

The steady flow quantities in equation (5.3) are known if the corresponding expansion of the Mach number is known. We assume an expansion for M of the same form as (5.3), substitute this expansion into equation (3.1), transform to the inner variable X, and solve the successive differential equations which result. After matching with the outer expansion (3.4) we find

$$M(x;\varepsilon) = M^i(x;\varepsilon) = 1 - \varepsilon\ (1+aX^2)^{\frac{1}{2}} + \ldots \tag{5.4}$$

where $a=A''(0)/2A(0)$ as before. Using (5.4) we find the coefficients in the expansions (5.3) by use of the steady flow relations between M and U or R.

Next we carry out the same process on system (2.4) using $u=\varepsilon\mu^i+\ldots$, $\rho=\varepsilon r^i+\ldots$, and substituting equation (5.4) in the coefficients. This yields the system of inner equations satisfied by μ^i and r^i in the form:

$$\eta_t + [\zeta+\eta-(1+aX^2)^{\frac{1}{2}}]\,\eta_X - \frac{aX}{(1+aX^2)^{\frac{1}{2}}}(\zeta+\eta) = 0$$
$$\zeta_X = 0 \qquad (5.5)$$

where in equations (5.5) we have defined

$$\zeta = (3-\gamma)(\mu^i+r^i)/4 \quad \text{and} \quad \eta = (\gamma+1)(\mu^i-r^i)/4$$

Equations (5.5) are the nonlinear equations which, to first order in ε, govern sound propagation through a throat as the Mach number there approaches unity. The lengthy details of solving the system will not be presented here. However, certain important conclusions can be made at this stage. The quantities η and ζ are related to the Riemann invariants of system (2.4), η representing the upstream and ζ the downstream propagating portions of the solution to (2.4). Considerations of asymptotic matching between expansions (5.1) and (5.2) lead to the conclusion that, to first order in ε, ζ actually vanishes. Thus, as is often argued from physical considerations, the lowest order nonlinear effect of the sonic throat is on the upstream propagating waves alone.

A final observation which we make here is that matching considerations indicate that, in the distinguished limit implied by the inner expansion (5.2), ε is to be taken equal to $\delta^{\frac{1}{2}}$. Hence we conclude that, given an acoustic source strength δ, nonlinear effects on sound arise for throat Mach numbers as far away from unity as $\delta^{\frac{1}{2}}$. This would explain why marked sonic throat effects are observed experimentally for throat Mach numbers as low as 0.75-0.8.

References

1. Chestnutt, D., and Clark, L.: Noise Reduction by Means of Variable Geometry Inlet Guide Vanes in a Cascade Apparatus. NASA TM X-2392, October 1971.

2. Nayfeh, A.; Kaiser, J.; and Telionis, D.: Acoustics of Aircraft Engine-Duct Systems. AIAA Journal, vol. 13, no. 2, February 1975, pp. 130-153.

3. Crocco, L., and Cheng, S. I.: Theory of Combustion Instability in Liquid Propellant Rocket Motors. Butterworths, London, 1956, Appendix B.

4. Davis, S., and Johnson, M.: Propagation of Plane Waves in a Variable Area Duct Carrying a Compressible Subsonic Flow. J. Acoust. Soc. Am., vol. 55, S574(A), 1974.

5. Eisenberg, N.,and Kao, T.: Propagation of Sound Through a Variable Area Duct with a Steady Compressible Flow. J. Acoust. Soc. Am., vol. 49, no. 1 (part 2), January 1971, pp. 169-175.

6. King, L., and Karamcheti, K.: Propagation of Plane Waves in Flow Through a Variable Area Duct. Aeroacoustics: Jet and Combustion Noise; Duct Acoustics, H. Nagamatsu, ed., AIAA/MIT, 1975, pp. 403-418.

7. Liepmann, H., and Roshko, A.: Elements of Gasdynamics. John Wiley, New York, 1957, Ch. 2.

8. Crocco, L.: One Dimensional Treatment of Steady Gas Dynamics. Fundamentals of Gas Dynamics, H. Emmons, ed., Princeton Univ. Press, 1958, pp. 64-349.

9. Abramowitz, M., and Stegun, I.: Handbook of Mathematical Functions. Nat. Bur. Standards, 1964, Ch. 15.

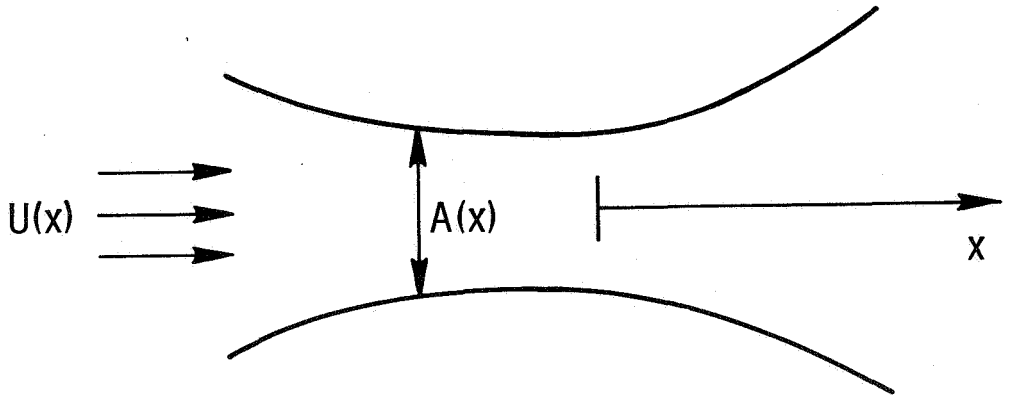

Figure 1.- Sketch of typical duct geometry.

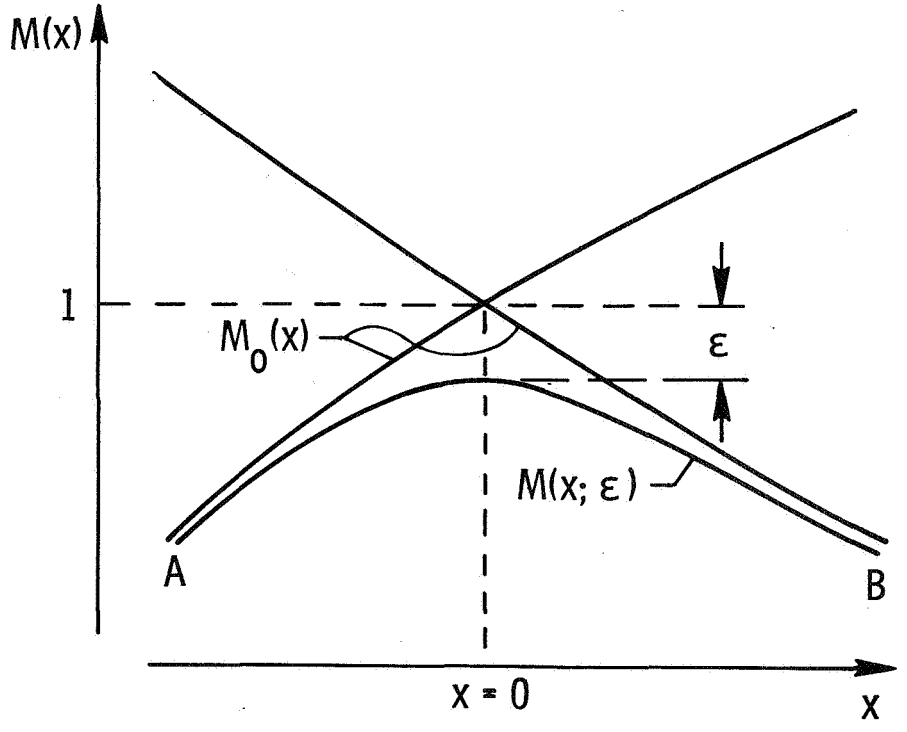

Figure 2.- Typical steady flow integral curves. Curve AB is described by equations (3.4) and (5.4).

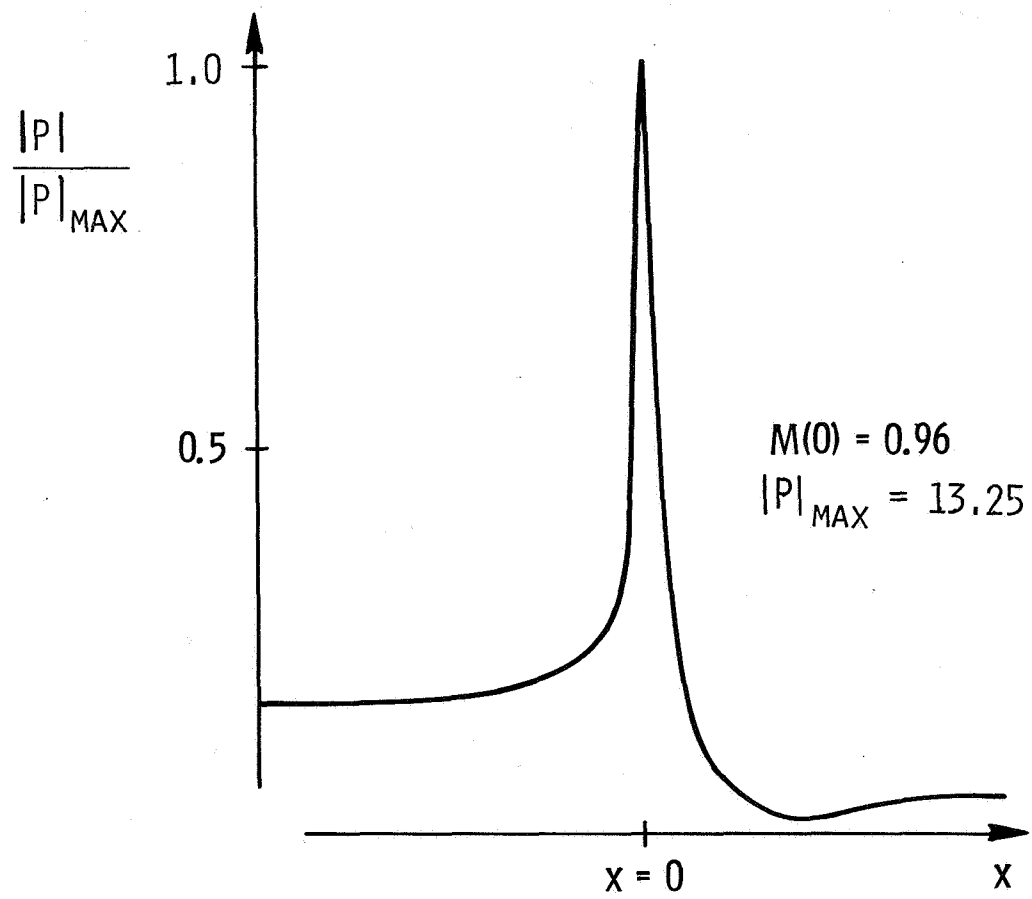

Figure 3.- Typical behavior of linearized pressure magnitude for high subsonic throat Mach numbers.

EFFECTS OF MEAN FLOW ON DUCT MODE OPTIMUM SUPPRESSION RATES

Robert E. Kraft
General Electric Co.

William R. Wells
University of Cincinnati

SUMMARY

The nature of the solution to the convected acoustic wave equation and associated boundary conditions for rectangular ducts containing uniform mean flow is examined in terms of the complex mapping between the wall admittance and characteristic mode eigenvalues. It is shown that the Cremer optimum suppression criteria must be modified to account for the effects of flow below certain critical values of the nondimensional frequency parameter of duct height divided by sound wavelength. The implications of these results on the design of low frequency suppressors is considered.

INTRODUCTION

The lining of duct walls with acoustic treatment is a standard practice in the jet engine industry for obtaining suppression of turbomachine noise. The design of this acoustic treatment depends upon a number of factors in addition to acoustic performance, including weight, structural integrity, length restrictions, and ability to withstand severe environments. The design goal of obtaining a maximum of suppression with a minimum of panelling requires a thorough knowledge of the acoustic propagation phenomena in ducts in the presence of complex sound sources and mean flow, among other effects. This paper is aimed at increasing the understanding of a vital element in the prediction of sound suppression in ducts with mean flow, the nature of the eigenvalue problem.

In Reference 1 the general problem of the modal solution to acoustic wave propagation in multi-segment ducts with mean flow has been considered. The success of a modal analysis prediction program such as the one developed in Reference 1 is strongly dependent upon the ability to obtain an accurate and complete set of eigenvalues for each section of the duct. It is felt that greater appreciation of the nature of the propagation process can be gained through detailed examination of complex contour plots of the eigenvalue-admittance relationship for particular cases. The basic theory and equations used in this paper are presented in Reference 1.

A useful acoustic treatment design criteria which has been in use for a number of years is the least attenuated mode theory developed by Cremer (Reference 2). Although it is gradually being replaced by the more accurate

multi-mode prediction procedures, it is still of practical value for preliminary designs and the evaluation of basic trends. The Cremer theory is based on the location of branch points (or critical points) of the complex eigenvalue-admittance mapping, and the consequences of this criteria, particularly for low values of the frequency parameter (ratio of duct height to sound wavelength)

$$\eta = H/\lambda \tag{1}$$

are examined. It is shown how the theory must be modified for very low η-values.

The results of this study are applied to the specific case of ducts with rectangular cross section. The methods will find direct application to other cross-sectional geometries with the proper generalization of the characteristic duct modes.

SYMBOLS

c - speed of sound

f - frequency

H - duct height

i - $\sqrt{-1}$

k - wave number

M_o - mean flow Mach number

n - exponent in boundary condition

t - time

Z_{opt} - wall impedance (optimum)

β - wall admittance (dimensionless)

γ - nondimensional duct eigenvalue

κ - axial propagation constant

η - nondimensional frequency parameter, Hf/c

λ - sound wavelength

ρ_o - ambient density of air

ω - circular frequency, $2\pi f$

RECTANGULAR DUCT MODAL SOLUTION

The method of separation of variables is applied to the convected acoustic wave equation under the assumption of uniform mean flow and rectangular duct geometry. In this study, consideration will be limited to duct treatment sections with the same treatment on opposite sides of the duct.

Substitution of the general solution of the differential equation into the boundary condition leads to two different expressions

$$\beta kH = \frac{i\gamma}{\left(1 - M_o \frac{\kappa}{k}\right)^n} \frac{1 - \cos\gamma}{\sin\gamma} \tag{2}$$

and

$$\beta kH = \frac{-i\gamma}{\left(1 - M_o \frac{\kappa}{k}\right)^n} \frac{1 + \cos\gamma}{\sin\gamma} \qquad (3)$$

where β is the acoustic admittance at the wall, based on $e^{-i\omega t}$ time dependence. These are complex, transcendental equations for the eigenvalue, γ. Their solution leads to two distinct sequences of eigenvalues, the symmetric mode eigenvalues and the antisymmetric mode eigenvalues, respectively. For simplicity, the two sequences can be combined into a single set of eigenvalues.

NATURE OF THE BOUNDARY CONDITIONS

The boundary condition expressions (2) and (3) must be solved by numerical methods if the eigenvalues are desired for given admittances. The admittance, however, can be isolated as a function of the eigenvalue, making it susceptible for plotting contours of constant magnitude and phase of the quantity βkH in the complex eigenvalue plane. The graphical representation of the relationship between the admittance and the eigenvalue is considered in detail in Reference 3, in which detailed contour plots are shown for a variety of conditions. From these plots, it is possible to obtain the sequences of eigenvalues which determine the characteristic duct modes for a given wall admittance.

It is shown in Reference 3 that the boundaries separating eigenvalue regions for different modes in the eigenvalue plane are branch cuts of the admittance-eigenvalue contour mapping. One point on the branch cut is a branch point, or critical point, of the mapping, at which the eigenvalues for two adjacent modes coalesce, giving a double-value. By considering plots of lines of constant attenuation superimposed on the eigenvalue-admittance mapping, it has been shown by Cremer (Reference 2), and is illustrated in Reference 3, that adjacent modes, in particular the first and second modes, attain nearly the same attenuation rate at the branch point. Cremer proposed the choice of the admittance at the branch point of the first mode as a design criteria which optimizes suppression for the least attenuated mode.

For symmetric modes in the duct with the same liner on both sides, at Mach 0.0, the optimum admittance for the least attenuated mode is (in polar form)

$$\beta kH = (5.28, -38.7^o) \qquad (4)$$

Transforming this to an impedance ($e^{+i\omega t}$ convention) design criteria, we get

$$\frac{Z_{opt}}{\rho_o c} = (0.93 - 0.74i)\eta \qquad (5)$$

Although useful for preliminary design, the attenuation rate of a single mode or even a pair of modes is not sufficient to predict attenuation or to design optimum treatment for finite length ducts with arbitrary sources at higher η-values. In these cases, the impedance must be chosen to maximize suppression for a particular combination of modes, and may turn out to be nowhere near the classical Cremer optimum.

The assumption of uniform mean flow requires that a physically unrealistic slip-flow condition must be postulated to occur at the wall surface. It can be shown that the surface flow convection effect leads to an anomaly in the boundary conditions, such that two different conditions can be obtained depending on whether continuity of particle displacement or continuity of particle velocity is assumed to hold at the wall. Based on the analysis of Reference 4, the current most widely accepted condition is that of particle displacement continuity. For this reason, and since it causes the more drastic effect of the two conditions, particle displacement continuity is assumed in this study. The most fortuitous choice of these conditions for any given flow, frequency, or duct height is yet to be resolved.

The effect of flow on the modal maps is to cause a distortion of the βkH magnitude and phase contours from the Mach 0.0 case. Since the propagation constant κ is a function of kH as well as γ, the eigenvalue relationships can no longer be made independent of kH, and a separate mapping must be made at each Mach number and value of η (since $\eta = kH/2\pi$).

A branch point of the mapping of the complex function βkH on the complex γ-plane is the point at which the derivative of βkH with respect to γ is zero. Equation (2) was used to determine the location of the branch point for arbitrary values of kH and mean flow Mach number. The desired value of γ is the root which corresponds to the branch point between first and second modal regions for each case. These roots were extracted using a simple Newton-Raphson iteration scheme. The branch points for the Mach 0.0 case were used as initial values to provide accuracy in the fourth decimal place.

When the values of the eigenvalue at the branch points are determined, the optimum admittance (or impedance) can be found from Equation (2) and the optimum suppression rate can be found from the axial propagation constant. Figures 1 and 2 show the dependence of the optimum specific resistance R and reactance X, respectively, on η with Mach number M_o as a parameter. The impedance components have been divided by the η-value, which makes the Mach 0.0 curve a straight line with zero slope, that is, independent of η. Figure 3 shows the optimum attenuation rate for each of the impedances as a function of η.

The optimum suppression rates appear to be independent of Mach number for η-values higher than about 2, but diverge from the Mach 0.0 case below $\eta = 2$, as the region of high suppression rates is entered. Higher optimum attenuations can be obtained for propagation against the flow for these low η-values than for propagation with the flow.

In the low η regions, the optimum resistance undergoes a rather bizarre behavior. For a given Mach number, there is an η-value below which the optimum resistance tends to negative values. A negative resistance, or active, liner is one which tends to generate energy, as opposed to a passive, positive resistance liner which can only absorb energy. At first sight, this phenomenon

appears to be physically unreasonable, possibly indicating a basic flaw in the theory.

It must be kept in mind that the optimum impedance criteria to this point has been based on the branch point criteria developed by Cremer. In the no-flow or high η-value cases, this criteria is unambiguous, but for low η-values it will be shown that the flow-induced distortion of the modal maps is so severe as to cause significant changes in the nature of the problem. It will be shown that, if one will admit the existence of active (negative resistance) wall liners, two suppression criteria must be provided, one for passive liners and one for active liners. The strange behavior is caused by the

$$\frac{1}{\left(1 - M_o \frac{\kappa}{k}\right)^2}$$

factor in the particle displacement continuity boundary condition, when κ/k begins to get large in magnitude.

MODIFIED OPTIMUM CRITERIA FOR LOW η-VALUES

Choosing a Mach number of -0.4, modal maps of the lowest order symmetric mode region were plotted for successively lower η-values, according to the following list:

Figure 4	$\eta = 0.36$
Figure 5	$\eta = 0.3$
Figure 6	$\eta = 0.15$

Note in Figure 4 that the -90^o phase lines have left the real and imaginary γ-axes and are converging on the branch point. The branch cut which defines the region of passive impedance for the lowest order mode now consists of just a short length of line of constant magnitude of βkH ($|\beta kH| = 1.37$), with the rest of the cut being comprised of $\pm 90^o$ phase lines. This η-value is just above the value for which the optimum impedance goes negative. In Figure 5, the -90^o lines have passed through the branch point, which now has a phase of less than -90^o, giving a negative resistance. The lowest order mode region has become isolated from the second order mode region, and contains no branch point. The optimum impedance for the lowest order mode is now defined as the point at which the highest valued curve of constant attenuation touches the boundary of the modal region.

At the branch point, a higher positive suppression is predicted than in the modal region, in spite of the negative resistance. This implies that an active liner would provide more suppression than a passive liner, if designed with the branch point impedance components. This unexpected behavior may be possibly understood in terms of the modal "cut-off" phenomenon, for which modes below their cut-off frequency decay exponentially in the duct. Apparently the effects of cut-off are so strong that even an active impedance leads to strong

decay in the presence of uniform flow.

At sufficiently low η, the modal regions reunite on the right-hand-side of the real γ axis, where a new branch point appears, as shown in Figure 6, providing a new optimum criteria. Figure 7 shows the revised optimum impedance and suppression curves for Mach -0.4 and n = 2 where only passive liners are allowed. The region between $0.20 < \eta < 0.36$ is where the lowest order mode exists in isolation of the second mode. Note the substantial drop-off in optimum attenuation below $\eta = 0.36$. Figure 8 shows the revised optimum resistance, reactance, and suppression curves for the Mach +0.4 case. Note the decrease in suppression below $\eta = 0.2$.

CONCLUSIONS

The Cremer optimization theory for least attenuated modes has been modified to account for the effects of mean flow at low η-values. It is seen that the branch point criteria no longer holds below certain critical η-values, and the optimum passive liner impedance must be determined from the modal maps. Revised optimum impedance and suppression curves have been presented for Mach ± 0.4. In future studies, it would be useful to provide experimental verification of the revised optimum criteria. In particular, investigation of the active liner concept might prove of practical value, if such a device can be shown to exist.

REFERENCES

1. Motsinger, R.E., Kraft, R.E., and Zwick, J.W., "Design of Optimum Acoustic Treatment for Rectangular Ducts with Flow", ASME paper 76-GT-113, March, 1976.

2. Cremer, L., "Theory of Sound Attenuation in a Rectangular Duct with an Absorbing Wall and the Resultant Maximum Attenuation Coefficient", McDonnell-Douglas Corp. Report No. MDC-J6630, July, 1974, translated from Akustische Beihefte of Acustica, Hef 42, 1953, pp. 249-263.

3. Kraft, R.E., "Theory and Measurement of Acoustic Wave Propagation in Multi-Segmented Rectangular Flow Ducts", Ph. D. dissertation, University of Cincinnati, Department of Aerospace Engineering, June 1976.

4. Eversman, W., and Beckemeyer, R.J., "Transmission of Sound in Ducts with Thin Shear Layers - Convergence to the Uniform Flow Case", Journal of the Acoustical Society of America, Vol. 52, No. 1, pt. 2, 1972.

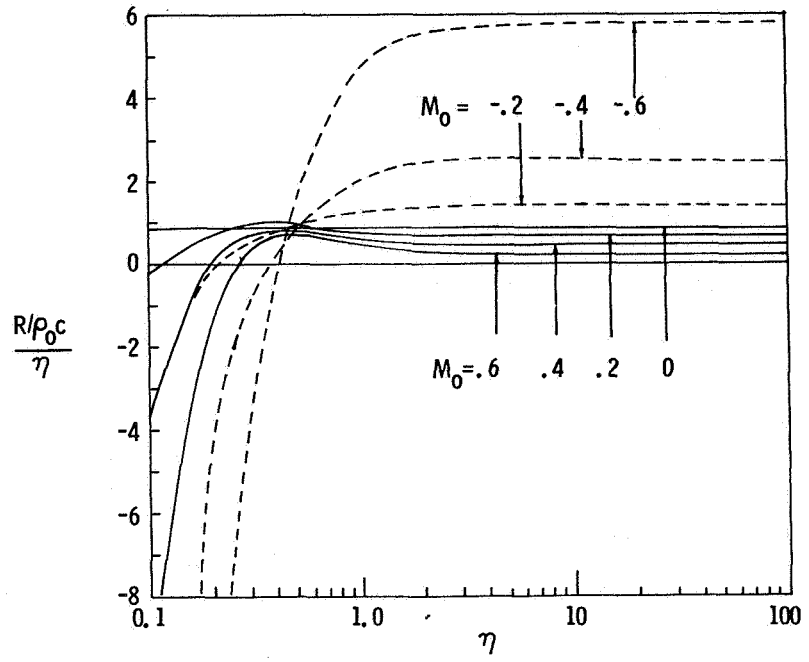

Figure 1.- Optimum resistance for lowest order mode as a function of η, for various Mach numbers, based on Cremer optimum criteria.

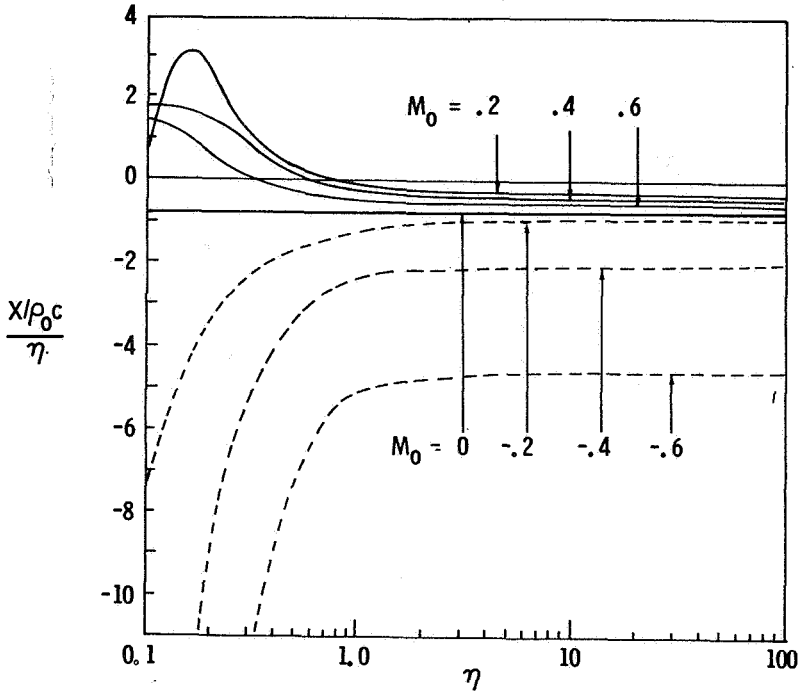

Figure 2.- Optimum reactance for lowest order mode as a function of η, for various Mach numbers, based on Cremer optimum criteria.

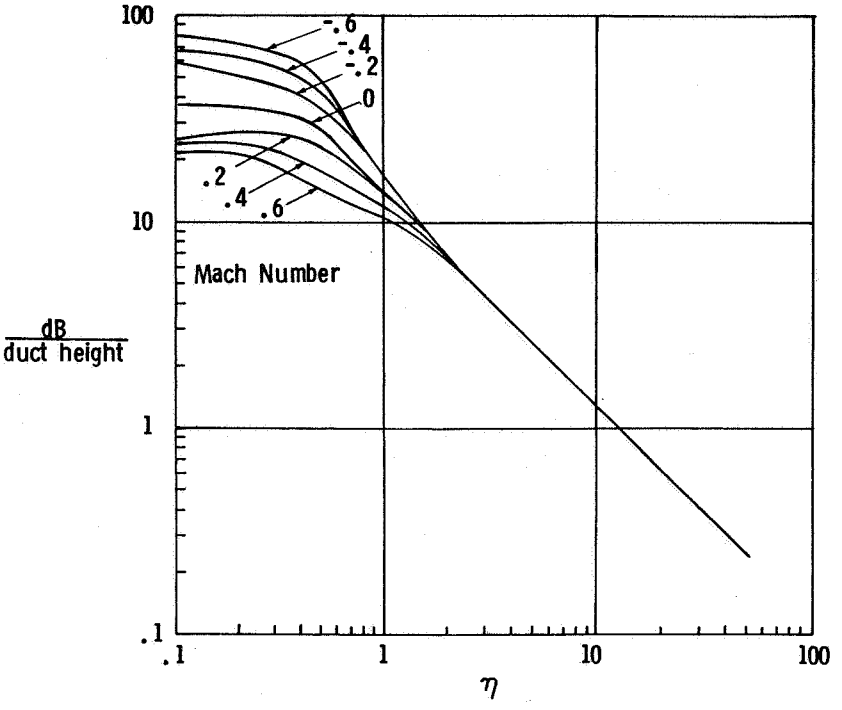

Figure 3.- Optimum attenuation as a function of η for various Mach numbers for lowest order mode, based on Cremer optimum criteria.

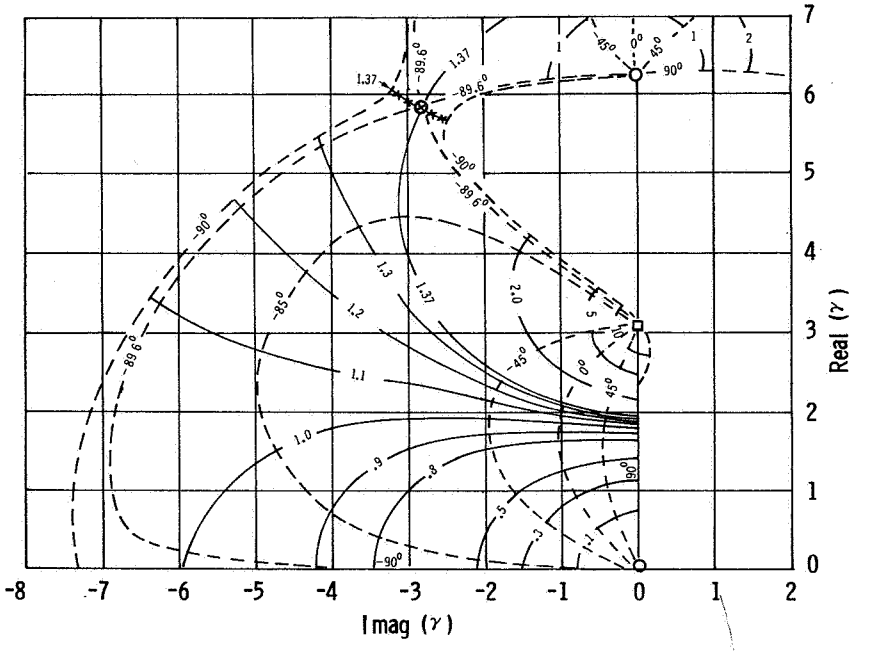

Figure 4.- Complex eigenvalue-admittance mapping for symmetric modes; Mach -0.4; kH = 2.2619; (η = 0.36); Continuity of Particle Displacement. ——— Constant |βkH|, ----- Constant Phase (βkH).

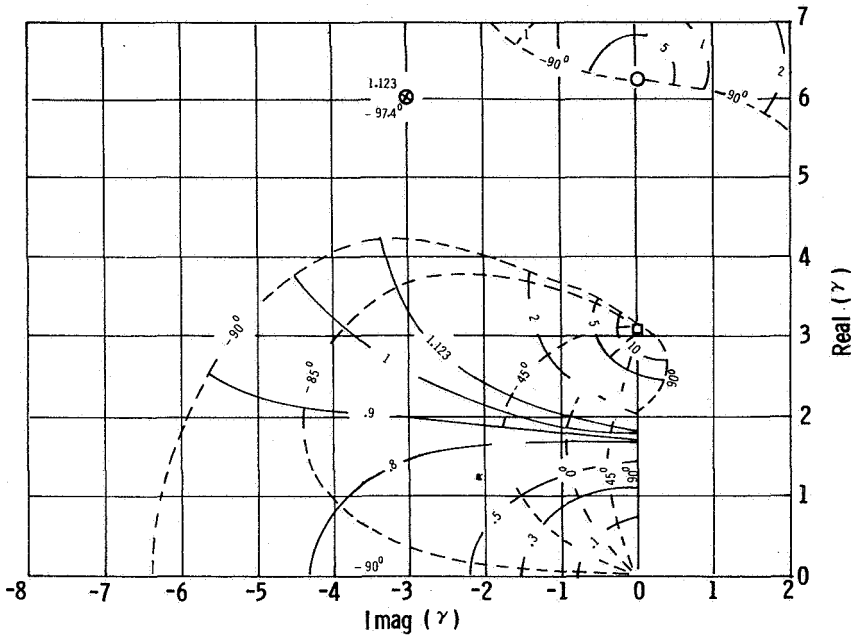

Figure 5.- Complex eigenvalue-admittance mapping for symmetric modes; Mach -0.4; kH = 1.885; (η = 0.3); Continuity of Particle Displacement. ——— Constant $|\beta kH|$, ----- Constant Phase (βkH).

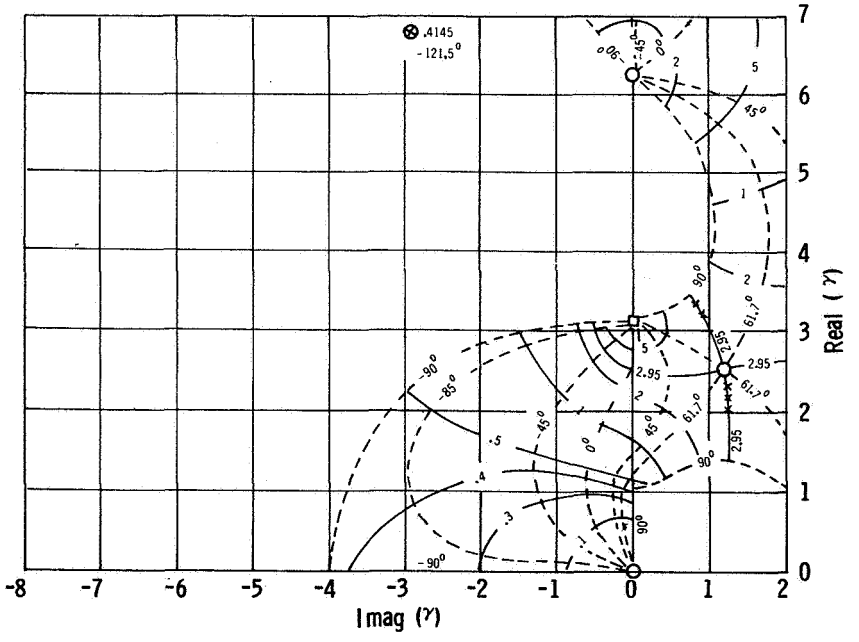

Figure 6.- Complex eigenvalue-admittance mapping for symmetric modes; Mach -0.4; kH = 0.9425; (η = 0.15); Continuity of Particle Displacement. ——— Constant $|\beta kH|$, ----- Constant Phase (βkH).

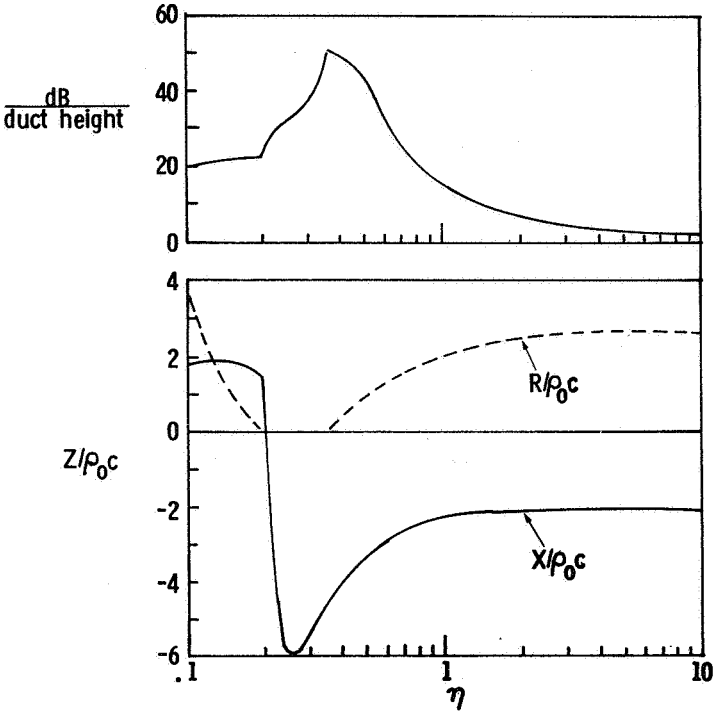

Figure 7.- Lowest order mode optimum suppression rate and impedances as a function of η for passive liners, Mach -0.4.

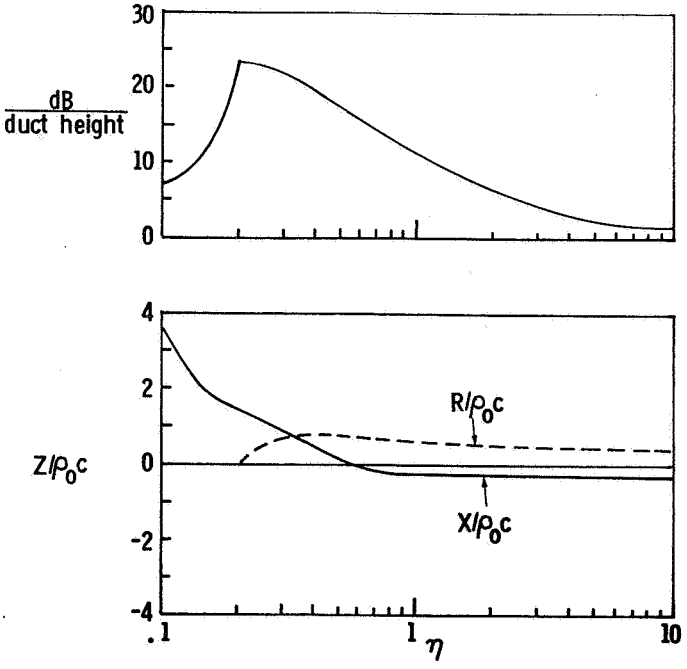

Figure 8.- Lowest order mode optimum suppression rates and impedances as a function of η for passive liners, Mach +0.4.

INLET NOISE SUPPRESSOR DESIGN METHOD BASED UPON THE DISTRIBUTION OF ACOUSTIC POWER WITH MODE CUTOFF RATIO

by Edward J. Rice
NASA Lewis Research Center

SUMMARY

Higher order spinning modes must be considered in the design of efficient noise suppressors with outer wall treatment such as in an engine inlet. These modes are difficult to measure and are in fact impossible to resolve with flush mounted wall microphones. An alternative liner design procedure is presented here which potentially circumvents the problems of resolution in modal measurement. The method is based on the fact that the modal optimum impedance and the maximum possible sound power attenuation at this optimum can be expressed as functions of cutoff ratio alone. Modes with similar cutoff ratios propagate similarly in the duct and in addition propagate similarly to the far field. Thus there is no need to determine the acoustic power carried by these modes individually, and they can be grouped together as one entity. With the optimum impedance and maximum attenuation specified as functions of cutoff ratio, the off-optimum liner performance can be estimated using a previously published approximate attenuation equation.

INTRODUCTION

The need to consider higher order spinning modes in the design of aircraft inlet suppressors with wall treatment only has been demonstrated in references 1 and 2. Using spinning modes in the propagation theory to simulate an engine inlet requires information on the modal power distribution, which is very difficult to measure. Assumptions of equal modal amplitude (ref. 3) or equal modal power (refs. 1 and 4) have been made. These assumptions may be valid for static test data (ref. 5) where the dominant source of noise may be from the interaction of the rotor with random inflow disturbances. However, in flight the character of the noise source changes considerably (ref. 6) and the modal structure giving valid liner designs has yet to be established.

Because of the difficulty of modal measurement, an alternative and more easily used method has been proposed (ref. 7). This method involves the use of the distribution of acoustic power as a function of mode cutoff ratio (hereafter called acoustic power-ξ distribution) rather than the actual modal power distribution itself. This is much simpler since many modes may have nearly the same cutoff ratio and need not be separated because they all behave the same when liner design is considered. This similar behavior is demonstrated by showing that the optimum wall impedance and the maximum possible sound power attenuation obtained at this optimum can be expressed as functions of cutoff ratio alone.

When these quantities are expressed in this way there is only a very small residual modal dependence (lobe m and radial mode μ), which can be ignored in a multimodal liner design.

It was established in reference 7 that modal optimum wall impedance was intimately related to cutoff ratio. The reference also implied that maximum attenuation and the radiation pattern were dependent upon cutoff ratio. In this paper the method will be developed into a quantitative tool useable for liner design. Approximate expressions are provided in terms of cutoff ratio for the optimum impedance and the maximum possible attenuation. Since no explicit modal identity occurs in these required inputs, modal decomposition of the noise source is replaced by the acoustic power-ξ distribution which treats all similarly propagating modes as a single entity. These equations also contain the usual input quantities such as flow Mach number, boundary layer thickness, noise frequency, and duct dimensions. Since all of the correlated quantities mentioned above involve only the optimum quantities, an off-optimum estimate procedure is also provided. This involves the approximate equation of reference 8 in which the off-optimum behavior is shown to be uniquely determined by the optimum impedance and damping along with the actual off-optimum wall impedance. The procedure outlined in this paper requires only the addition of the quantifying of the acoustic power-ξ distribution.

Methods for estimating the acoustic power-ξ distribution from the far field directivity pattern are nearing completion and should be available soon. A more desirable method using direct duct measurements with flush-mounted wall pressure transducers is currently being studied.

The problem of changes in acoustic power-ξ distribution in going from a hardwall duct to a soft wall section is discussed.

SYMBOLS

A	function of eigenvalue phase angle, eq. (15)
c	speed of sound, m/sec
D	duct diameter, m
ΔdB	sound power attenuation, dB
ΔdB_m	maximum possible sound power attenuation, dB
F	boundary-layer refraction function, eq. (11)
f	frequency, Hz
G	function of maximum possible attenuation, eq. (18)
J_m	Bessel function of first kind, order m
K	wave number, $k\tau$
k	ω/c, m^{-1}
L	acoustic liner length, m
M_0	axial steady flow Mach number, free-stream uniform value
m	spinning mode lobe number (circumferential order)
N	normalized expected number of modes versus cutoff ratio
P	acoustic pressure, N/m^2
R	amplitude of eigenvalue α
R_{HW}	hardwall eigenvalue
r	radial coordinate, m
r_0	circular duct radius, m
t	time, sec
v_g	group velocity ($\partial\omega/\partial K$)
x	axial coordinate, m
α	complex radial eigenvalue ($\alpha = Re^{i\phi}$)

β	$\Delta dB_m/\Delta dB$	μ	radial mode number
δ	boundary-layer thickness, m	ξ	cutoff ratio
ε	dimensionless boundary-layer thickness, δ/r_0	ξ_{HW}	cutoff ratio in hardwall duct
		σ	attenuation coefficient
ζ_m	optimum specific acoustic impedance	τ	propagation coefficient
		Φ	angular coordinate, rad
ζ_{m0}	optimum specific acoustic impedance for $\varepsilon = 0$	ϕ	phase angle of eigenvalue, deg
		χ	specific acoustic reactance
η	frequency parameter, fD/c	χ_m	optimum specific acoustic reactance
θ	specific acoustic resistance		
θ_m	optimum specific acoustic resistance	ω	circular frequency, rad/sec

DEFINITION OF THE CUTOFF RATIO

Some preliminary expressions are given here to establish the notation and terminology. The modal pressure solutions are given by (in the uniform flow region)

$$P = J_m\left(\frac{\alpha r}{r_0}\right) e^{i\omega t - im\Phi - k(\sigma + i\tau)x} \tag{1}$$

where P, α, σ, and τ should actually have m, μ subscripts to associate them with the m, μ mode. For soft walled ducts the radial eigenvalue is complex and is given by

$$\alpha = Re^{i\phi} \tag{2}$$

The damping and propagation coefficients are given by

$$\sigma + i\tau = \frac{-iM_0 + i\sqrt{1 - (1 - M_0^2)\left(\frac{\alpha}{\pi\eta}\right)^2}}{1 - M_0^2} \tag{3}$$

or

$$\sigma + i\tau = \frac{-iM_0 + i\sqrt{1 - (1 - M_0^2)\left(\frac{R}{\pi\eta}\right)^2 (\cos 2\phi + i \sin 2\phi)}}{1 - M_0^2} \tag{4}$$

where η is the frequency parameter given by

$$\eta = fD/c \tag{5}$$

For hardwall duct the definition of cutoff ratio is quite direct since the eigenvalue α is real and can be given by (in a manner similar to ref. 9),

$$\xi_{HW} = \frac{\pi\eta}{R_{HW}\sqrt{1 - M_0^2}} \tag{6}$$

This definition causes the expression in the radical of equation (4) (with $\phi = 0$) to change sign at $\xi_{HW} = 1$ and causes the pressure to be damped with distance for $\xi < 1$.

For soft walled ducts the definition of cutoff ratio is not so simple. The modes possess propagating characteristics at all frequencies so there is no precise cutoff. A definition of cutoff ratio used in reference 7 was

$$\xi = \frac{\pi\eta}{R\sqrt{(1 - M_0^2)\cos 2\phi}} \tag{7}$$

which causes the real part of the radical in equation (4) to be zero at $\xi = 1$. The definition was quite arbitrary with the only advantage being that it reduced to the hardwall definition when $\phi \to 0$. A better definition might be

$$\xi = \frac{\pi\eta\sqrt{\cos\frac{2\phi}{3} - \sqrt{3}\sin\frac{2\phi}{3}}}{R\sqrt{1 - M_0^2}} \tag{8}$$

which is thought to be a new result. This was derived by insuring that the group velocity ($v_g = \partial\omega/\partial K$) be at a minimum when $\xi = 1$, which implies a minimum acoustic power propagation. Fortunately there is not much difference between the ξ definitions for the small angles ϕ encountered at the optimum impedance. For the largest difference ξ from equation (8) is about 0.87 of that from equation (7). Thus the calculated results of reference 7 are used here without modification.

MODE CUTOFF RATIO AS THE BASIC PROPAGATION PARAMETER

In this section the cutoff ratio will be shown to be the basic parameter governing noise propagation in acoustically lined ducts. This will be done by showing that the optimum wall impedance for all of the modes can be accurately correlated by the cutoff ratio alone and that the maximum attenuation at this optimum can be adequately correlated by the cutoff ratio. All of the calculations presented here were obtained using the calculation procedure of reference 10. A uniform flow region was assumed in the duct interior with a boundary layer present near the wall. The classic uniform-flow sound propagation solutions were coupled to a Runge-Kutta integration solution through the boundary layer. The definition of modal optimum impedance is the same as in references

2 and 10 as well as that of reference 11 but with the additional considerations of Mach number, boundary-layer thickness, and higher order modes.

Optimum Wall Impedance

The discovery that the optimum liner wall impedance depends only on mode cutoff ratio was documented in reference 7. Figure 1 is repeated from reference 7 for completeness. Figure 1 shows sample optimum impedance calculations plotted in the wall impedance plane. The conditions used are those for a General Electric TF-34 engine. Note that a common locus of optima is evident despite the wide range of modes used. Only the first radial of each of the higher lobe number modes deviates from this common line, and this deviation is quite small. (The first radial is the furthest point toward the left side for a given lobe number.) Two coincident modes are singled out and compared in the insert table. The only thing these two modes have in common is the cutoff ratio. Additional results were shown in reference 7 which illustrated the excellent correlation of optimum impedance with cutoff ratio.

Maximum Possible Sound Power Attenuation

The maximum possible sound power attenuation is generally expressed as $\Delta dB/(L/D)$ and plotted against the frequency parameter ($\eta = fD/c$) as in figure 5 of reference 2. This type of plot has been recast in terms of the cutoff ratio (fig. 2). Several radial modes ($\mu = 1$, 2, 5, and 10) for lobe numbers of $m = 1$, 7, and 20 are shown. In each case for a given m, the $\mu = 1$ curve is the lowest and the attenuation increases monotonically with increasing μ. Except for the first two radial modes of the lowest lobe number ($m = 1$), the curves cluster together. If an average curve is used through the cluster of curves, most of the modes will be adequately represented with the maximum error deviation from the average being about a factor of two for the lowest order modes. In a multimodal liner design, this error in only a few of the lower order modes is not anticipated to be significant. In those cases where a few low-order modes are known to carry the bulk of the acoustic power, the method proposed in this paper should not be used since for these conditions the direct modal approach is both simpler and more accurate.

With the exception noted previously, the maximum attenuation of the multitude of modes can be adequately represented by a single function of the cutoff ratio alone. The equations involved with the attenuation will be given in the next section where approximate correlations are discussed.

APPROXIMATE CORRELATING EQUATIONS

In this section approximate equations are developed for the optimum impedance and the maximum possible attenuation. The correlation between exactly

calculated optimum impedance and cutoff ratio is considered to be firmly established, but the optimum impedance correlation equation given here must be considered preliminary. If more exact results are required at this time, the complete calculation procedure of reference 10 is suggested with a representative mode used at each cutoff ratio value under consideration.

Optimum Impedance Correlation Equation

The correlating equation was derived using the approximate equation of reference 10 as a starting point, which in turn was derived from the thin boundary-layer approximation theory of reference 12. The starting point from reference 10 is

$$\zeta_m = \frac{(1 + \varepsilon)\zeta_{m0}}{1 - iF\zeta_{m0}} = \theta_m + i\chi_m \tag{9}$$

where ζ_m is the optimum impedance with a boundary layer and where

$$\zeta_{m0} = \theta_{m0} + i\chi_{m0} \tag{10}$$

is the optimum impedance with the boundary-layer thickness $\varepsilon = \delta/r_0 = 0$. The quantity F is given by

$$F = \left(\frac{\varepsilon\pi\eta M_0}{4}\right)\left(1 + \frac{4}{\xi^4}\right) \tag{11}$$

where the first term is the simplest form of the equation in reference 10 and the second is an empirical correction needed in the vicinity of unity cutoff ratio. This correction is needed since the results of reference 10 and thus presumably reference 12 are not valid near cutoff.

The quantities in equation (10) must now be cast in terms of the cutoff ratio ξ if equation (9) is to be a function of cutoff ratio as it is known to be from the exact calculations. Because of limited space, the derivations can not be included here. Equations (21) to (23), (30) and (31) of reference 8 along with equation (31) of reference 2 were used. The variables M_0 and η on which boundary-layer refraction effects strongly depend (ref. 10) were carried intact through the derivation. Certain liberties were taken with the other variables such as replacing nearly first or second powers of the mode numbers with first and second powers of the eigenvalue. The eigenvalue had to be recovered in the equations in order to introduce the cutoff ratio from equation (8). The final equation, which must be considered as empirical, is

$$\zeta_{m0} \approx \frac{\xi}{(1 + M_0)}\left[\sqrt{\frac{1 - M_0}{1 + M_0}} - i0.84\ (1 - M_0)\ \frac{\xi}{\eta}\right] \tag{12}$$

Equation (12) is surprisingly accurate for the zero boundary-layer thickness optimum resistance, but large percent errors can occur in the reactance for very small values of reactance.

With equations (11) and (12) used in equation (9) the optimum wall impedance with a boundary layer can be calculated as a function of cutoff ratio. These approximate calculations are compared with the exact calculations (from ref. 7) in figures 3 and 4. The approximations predict the gross behavior of the exact calculations and are probably accurate enough for most liner design studies.

Maximum Attenuation Correlation

An expression for maximum possible sound power attenuation can be derived by using the real part σ of equation (4) and the cutoff ratio from equation (8) in the following expression (ref. 2)

$$\frac{\Delta dB_m}{L/D} = -17.4\pi\eta\sigma \tag{13}$$

which then yields

$$\frac{\Delta dB_m}{L/D} = \frac{-17.4R}{\sqrt{2(1 - M_0^2)}} \left[\left(\frac{\xi}{A}\right)^2 \sqrt{1 - 2\left(\frac{A}{\xi}\right)^2 \cos 2\phi + \left(\frac{A}{\xi}\right)^4} + \cos 2\phi - \left(\frac{\xi}{A}\right)^2 \right]^{1/2} \tag{14}$$

where A is given by

$$A \equiv \sqrt{\cos \frac{2\phi}{3} - \sqrt{3} \sin \frac{2\phi}{3}} \tag{15}$$

Equation (14) was used to generate the curves in figure 2 with the eigenvalues (R, ϕ) used for each mode and with $M_0 = 0$. An averaged equation can be obtained by using the values of R and ϕ near the center of the cluster of curves such as the 20, 1 (m, μ) mode ($R = 26.662$, $\phi = 5.46°$) or the 7, 10 mode ($R = 41.881$, $\phi = 3.53°$). An approximate form of equation (14) can be derived for large ξ as

$$\frac{\Delta dB_m}{L/D} \approx \frac{-8.7RA \sin 2\phi}{\xi\sqrt{1 - M_0^2}} \approx \frac{-40}{\xi\sqrt{1 - M_0^2}} \tag{16}$$

where the average-curve values of R and ϕ were used to arrive at the final expression. This compares favorably with the expression in reference 7 except that the term $\sqrt{1 - M_0^2}$ is missing in reference 7. When expressed on a modal basis, the Mach number would not appear in equation (16) as discussed in reference 2, but it is reinserted along with the cutoff ratio when equation (8) is used. Equation (16) is valid for the linear portion of the curves in figure 2 but it will underpredict the maximum attenuation near $\xi = 1$.

OFF-OPTIMUM ATTENUATION

As seen in figure 1 for any chosen impedance, at best only one value of cutoff ratio would be at an optimum. Since a distribution of modes and their associated cutoff ratios would be the usual case encountered, off-optimum damping must be considered. Since the optimum impedance and maximum damping are now known for any cutoff ratio value, the approximate attenuation equation of reference 8 is ideally suited for use here. This equation is expressed as

$$\theta^2 - 2\theta[\theta_m + G(\beta - 1)] + \left(\chi - \frac{\chi_m}{\beta}\right)^2 + \frac{\theta_m(3\beta - 1)}{\beta(\beta + 1)}\left[\frac{\theta_m(2\beta^2 - \beta + 1)}{\beta(\beta + 1)} + 2G(\beta - 1)\right] = 0 \qquad (17)$$

where

$$G = \frac{8.7\ L/D}{\Delta dB_m(1 + M_0)^2} \qquad (18)$$

and

$$\beta = \frac{\Delta dB_m}{\Delta dB} \qquad (19)$$

The off-optimum attenuation to be solved for is ΔdB occuring at an impedance given by θ and χ with optimum input values θ_m, χ_m, and ΔdB_m and with the usual design inputs of L, D, and M_0. When operating off-optimum ΔdB cannot exceed ΔdB_m, and β is always greater than unity. Thus a possible procedure for solving equation (17) is to increment β upward from unity until the equation is satisfied and then solve for ΔdB from equation (19).

OUTLINE OF USE OF THE ACOUSTIC LINER DESIGN PROCEDURE

In the example that follows the use of the equations presented in the preceding sections will be illustrated. The final element of the technique that is needed is the distribution of acoustic power as a function of cutoff ratio. Because of space limitation as well as the preliminary state of the development of this subject, the equations will be presented without proof and are intended for illustrative purposes only.

The modal population density as a function of cutoff ratio is expressed as

$$\frac{dN}{d\xi} = \frac{2}{\xi^3} \qquad (20)$$

If equation (20) is integrated between ξ_1 and ξ_2, the normalized number of modes between these limits is

$$N = \frac{1}{\xi_1^2} - \frac{1}{\xi_2^2} \tag{21}$$

Note that N is normalized since, if $\xi_1 = 1$ and $\xi_2 = \infty$, then $N = 1$. For simplicity equal energy per mode will be used, which may be a reasonable assumption for static test data (ref. 5). Then the acoustic power between ξ_1 and ξ_2 is also given by equation (21). Next, choose 10 increments so that 0.1 of the power falls in each interval with 0.05 of the power on each side of the interval center. The 10 ξ intervals thus have centers located at $\xi = 1.026$, 1.085, 1.155, 1.24, 1.35, 1.49, 1.69, 2, 2.58, and 4.47.

Now the attenuation calculation can be made for each value of cutoff ratio ξ at the desired values of resistance θ and reactance χ. Assume that boundary-layer thickness ε, Mach number M_0, frequency parameter η, and the allowable duct diameter D and length L are known from other considerations. For each center value of ξ, then, calculate the optimum impedance components θ_m and χ_m from equation (9) using equations (11) and (12). Next, calculate the maximum possible attenuation ΔdB_m for each ξ from equation (14) using equation (15) and the R and ϕ values given just after equation (15). Now all the inputs are available (θ, χ, θ_m, χ_m, ΔdB_m) to calculate β from equation (17) and then ΔdB from equation (19), again, for each of the 10 values of ξ. The estimated liner output acoustic power can then be calculated, and an overall ΔdB calculated by applying the ΔdB for each ξ catagory to its respective input power, summing the output powers, and comparing this sum with the total input power. The calculation is now complete at the selected value of θ and χ. If a multimodal optimization study is being made, new values of θ and χ would be selected, and the calculations repeated until the total attenuation is maximized.

CONCLUDING REMARKS

The acoustic liner evaluation method presented in this paper should provide a useful alternative to the more usual modal analysis approach. Some of the problems in the modal approach, which are not problems in the present approach, are as follows: The phase speed of a mode is inversely proportional to the propagation coefficient τ given by equation (3). If the cutoff ratio from equation (6) is used in equation (3), the term $\sqrt{1 - 1/\xi^2}$ will be found to contain all of the modal information. For well propagating modes ($\xi >> 1$) this radical is essentially equal to one and the axial phase speed of all these modes is nearly identical. Also in a multimodal situation several modes may have almost equal cutoff ratios even though $\xi \approx 1$. These modes would also be indistinguishable in an axial direction since they have the same axial phase velocity. Thus the modal acoustic power can not be uniquely determined by using axial microphone traverses, and radial traverses (which are undesirable) must be used. Modes with nearly coincident cutoff ratios do not present a problem to the method of this paper since they all behave similarly in the acoustic liner (with respect to optimum impedance and maximum attenuation) and are thus lumped together.

Some simplifying conditions have been tacitly assumed to hold in the development of the technique presented here. It has been assumed that modal cross coupling is not important in the attenuation calculations in the lined duct section; that is, the reduction of acoustic power of each mode can be calculated independently of all the other modes. Theoretically, the cross coupling should be considered (refs. 13 and 14), but for practical purposes this coupling might be negligible (0.5-dB error in the results of ref. 15). Although not directly affecting the results presented here, the problem of a possible change in acoustic power-ξ distribution in going from a hard walled section to a soft walled section must be recognized. Could a power density distribution determined in a hard duct be used for attenuation calculations in the lined duct section or what modifications must be made? This can not be answered definitely at this time, but some insight can be offered. The cutoff ratio should be related to the angle of incidence with the duct wall. If modes are available in the soft duct with angles similar to those in the hard duct, then these modes should be excited. Thus angle of incidence is preserved in much the same way as the lobe numbers are preserved. This analogy is not exact since modes with exactly the same lobe number are available in both duct sections while angles of incidence can only be approximately the same. Thus some scattering of acoustic power among the various cutoff ratios should occur, but in a multimodal situation this is not suspected to be an extremely important effect. A notable singular exception occurs when a plane wave in the hard duct reaches the soft walled section. The plane wave with $\xi = \infty$ is scattered into several soft wall modes with finite and possibly even small cutoff ratios (depending on frequency parameter). This situation does not comply with the conditions assumed earlier, since there is no mode in a very soft duct that matches the angle of incidence of the plane wave. Perhaps the most serious assumption of all is that an acoustic power-ξ distribution is more available than an acoustic power-modal distribution. In reference 7 it was implied that the far-field directivity pattern is intimately related to the acoustic power-ξ distribution. This approach, which has been pursued and is nearing completion, should allow at least a crude approximation to the power distribution. Also, the present method offers the potential for avoiding some of the problems associated with modal measurement. Measurements of the acoustic power-ξ distribution using wall mounted microphones in the duct should be developable and ultimately available.

REFERENCES

1. Yurkovich, R.: Attenuation of Acoustic Modes in Circular and Annular Ducts in the Presence of Uniform Flow. AIAA Paper 74-552, June 1974.
2. Rice, Edward J.: Spinning Mode Sound Propagation in Ducts with Acoustic Treatment. NASA TN D-7913, 1975.
3. Ko, S. H.: Theoretical Prediction of Sound Attenuation in Acoustically Lined Annular Ducts in the Presence of Uniform Flow and Shear Flow. J. Acoust. Soc. Amer., vol. 54, no. 6, June 1973, pp. 1592-1606.
4. Yurkovich, R.: Attenuation of Acoustic Modes in Circular and Annular Ducts in the Presence of Sheared Flow. AIAA Paper 75-131, Jan. 1975.
5. Saule, A. V.: Modal Structure Inferred from Static Far-Field Noise Directivity. AIAA Paper 76-574, 1976.

6. Feiler, C. E.; and Merriman, J. E.: Effects of Forward Velocity and Acoustic Treatment on Inlet Fan Noise. AIAA Paper 74-946, Aug. 1974.
7. Rice, E. J.: Acoustic Liner Optimum Impedance for Spinning Modes with Mode Cutoff Ratio as the Design Criterion. AIAA Paper 76-516, 1976.
8. Rice, Edward J.: Attenuation of Sound in Ducts with Acoustic Treatment - A Generalized Approximate Equation. NASA TM X-71830, 1975.
9. Sofrin, T. G.; and McCann, J. J.: Pratt and Whitney Experience in Compressor-Noise Reduction. Preprint 2D2, Acoust. Soc. Amer., Nov. 1966.
10. Rice, E. J.: Spinning Mode Sound Propagation in Ducts with Acoustic Treatment and Sheared Flow. AIAA Paper 75-519, Mar. 1975.
11. Cremer, Von Lothar: Theory of Sound Attenuation in a Rectangular Duct with an Absorbing Wall and the Resultant Maximum Coefficient. Acoustica, vol. 3, no. 2, 1953, pp. 249-263.
12. Eversman, W.; and Beckemeyer, R. J.: Transmission of Sound in Ducts with Thin Shear Layers - Convergence to the Uniform Flow Case. Acoust. Soc. Amer., vol. 52, no. 1, July 1972, pp. 216-220.
13. Rice, Edward J.: Attenuation of Sound in Soft-Walled Circular Ducts. Symposium on Aerodynamic Noise, H. S. Ribner, ed., Univ. Toronto Press, 1969, pp. 229-249.
14. Rice, Edward J.: Propagation of Waves in an Acoustically Lined Duct with a Mean Flow. Basic Aerodynamic Noise Research. Ira A. Schwartz, ed., NASA SP-207, 1969, pp. 345-355.
15. Snow, D. J.: Influence of Source Characteristics on Sound Attenuation in a Lined Circular Duct. J. Sound Vibration, vol. 37, no. 4, 1974, pp. 459-465.

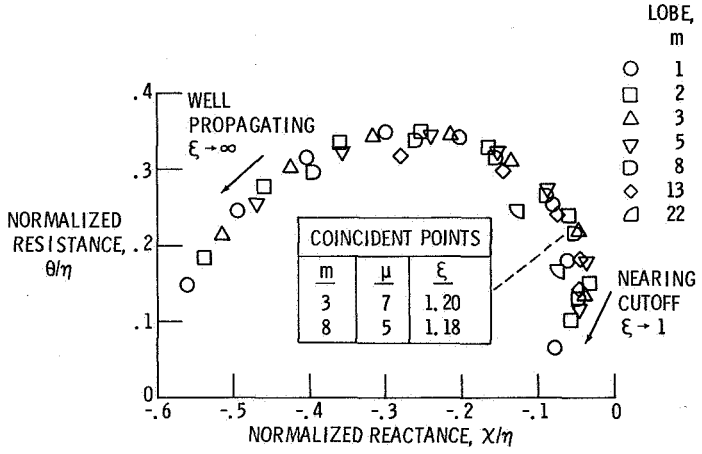

Figure 1. - Example higher order spinning mode optimum impedance locus. Frequency, 2890 hertz; frequency parameter, 9.47; Mach number, -0.36; boundary layer, $\delta/r_0 = 0.059$.

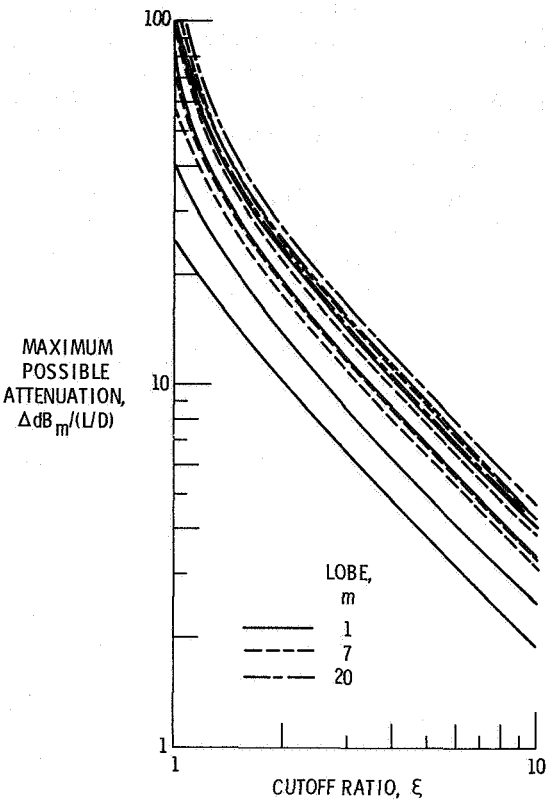

Figure 2. - Maximum possible attenuation as function of mode cutoff ratio. Zero Mach number.

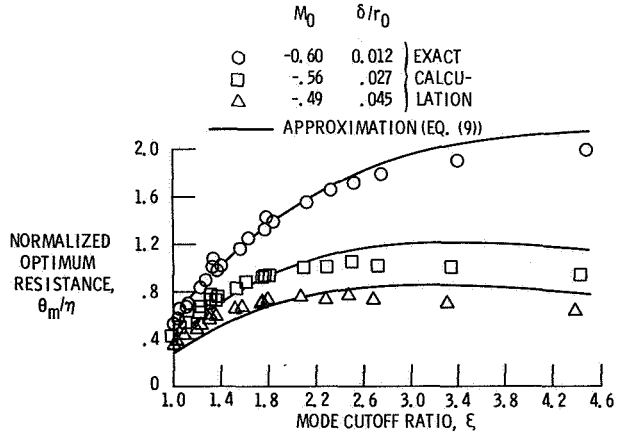

Figure 3. - Resistance correlation compared with exact calculations.

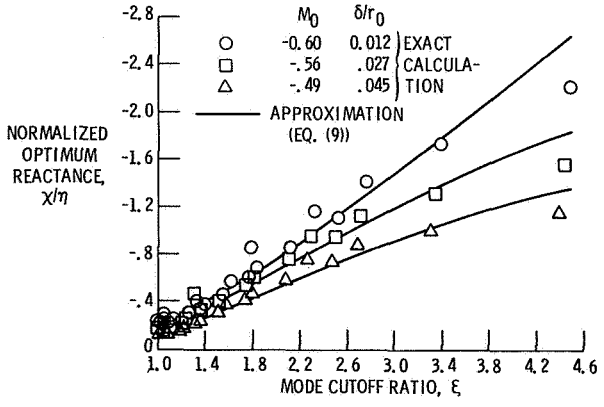

Figure 4. - Reactance correlation compared with exact calculations.

ORIFICE RESISTANCE FOR EJECTION INTO A GRAZING FLOW

Kenneth J. Baumeister
NASA Lewis Research Center

SUMMARY

Experiments have shown that the resistance for ejection from an orifice into a grazing flow can be less than for the no-flow case over a range of orifice velocities. To explain this decrease in orifice resistance with the addition of grazing flow, the flow from the orifice was modeled by using the inviscid analysis of Goldstein and Braun, which is valid when the orifice-flow total pressure is nearly the same as the free-stream grazing-flow total pressure. For steady outflow from an orifice into a grazing flow, the orifice flow can enter the main grazing flow in an inviscid manner without generating large eddies to dissipate the kinetic energy of the jet. From the analysis, a simple closed-form solution was developed for the steady resistance for ejection from an orifice into a grazing-flow field. The calculated resistances compare favorably with the previously published data of Rogers and Hersh in the flow regime where the total pressure difference between the grazing flow and the orifice flow is small.

INTRODUCTION

Perforated plates with back cavities are commonly used in flow ducts to dissipate acoustic energy. To predict the amount of acoustic energy absorbed by the liner, the impedance of the liner must be estimated. Either a theoretical or an empirical model is required to relate the wall impedance to the construction of the liner, the magnitude of the grazing flow, and the sound pressure level.

Many investigations of grazing-flow impedance have been performed that lead to impedance models for use in duct sound-propagation studies. Recent visual simulation studies (ref. 1) have revealed the basic physical flow process that occurs at the orifice in the presence of grazing flow. These visual studies have led to both empirical (ref. 2) and theoretical (refs. 3 and 4) impedance models both without and with grazing flow.

The theoretical studies of references 3 and 4 predict the resistance and reactance for oscillatory flow into an orifice. As yet, however, no theoretical model has been proposed for that portion of the oscillatory flow cycle where fluid is ejected from the orifice into the grazing-flow field. For steady orifice flows in the presence of a grazing flow, reference 2 presents an expression for the steady orifice resistance for small inflows or outflows. The present study develops a potential flow model for predicting the resistance of

an orifice during steady outflow in the presence of grazing flow. A simple closed-form solution is presented, and the calculated resistances are compared with measured values for the case where the total pressures of the orifice and main grazing flows are nearly the same.

SYMBOLS

C_D	discharge coefficient
c	speed of sound
d	width of orifice
H	width of channel, fig. 2
h	width of orifice jet at infinity, fig. 2
M_∞	grazing-flow Mach number, v_∞/c
P_c	total chamber pressure
P_∞	total grazing-flow pressure
p_∞	static grazing-flow pressure
S_e	slip factor
v_e^+	jet velocity upstream
v_e^-	grazing-flow velocity upstream
$\overline{v}_{jet}$	average jet velocity equal to total flow rate divided by actual area of hole
v_∞	grazing-flow velocity
z	impedance
δ	boundary-layer thickness
ε	total pressure difference parameter, eq. (8)
θ	steady orifice specific resistance
θ_p	steady orifice specific resistance predicted by inviscid flow theory
ρ	density

STEADY FLOW MODELS

Zorumski and Parrot (ref. 5) found for thin perforated plates that the instantaneous acoustic orifice resistance without a grazing flow is equivalent to the flow resistance of the orifice. The flow resistance is defined as the ratio of the steady pressure drop across a material to the steady velocity through the material. Feder and Dean (ref. 6) also show a close correspondence between the acoustic and steady flow resistances in the presence of a grazing flow.

Figure 1 shows, schematically, typical steady resistance data for airflow through an orifice both with and without a grazing airflow. The symmetrical straight lines represent resistance for flow into and out of the orifice with no grazing flow. Without grazing flow, vortex rings form at the orifice lip (see insert photographs in fig. 1). For either inflow or outflow with no grazing flow, nearly all the kinetic energy of the jet passing through the orifice is lost. In this simple case the resistance θ can be correlated by considering the one-dimensional energy equation (ref. 2)

$$\theta \equiv \frac{p_c - p_\infty}{\rho c \overline{v}_{jet}} = \frac{1}{2c} \frac{\overline{v}_{jet}}{C_D^2} \tag{1}$$

where the symbols are defined in the preceding section. The discharge coefficient C_D is equal to the actual area of the flow divided by the area of the hole.

In the more general case with grazing flow, the kinetic energy of the jet (assumed to be equivalent to the instantaneous acoustic energy from ref. 5) will be dissipated into heat by friction or transferred back into the mean flow field through the interaction between the jet and the grazing flow.

POTENTIAL OUTFLOW MODEL

Experiments (ref. 2) have shown that the steady outflow resistance of an orifice with grazing flow can be less than for the no-flow case over a range of orifice velocities. This is shown in figure 1 by the schematic representation of the steady orifice resistance as a function of the jet velocity and the grazing-flow Mach number. As shown in the lower left photograph of figure 1, the resistance is less with grazing than without grazing flow.

The photographic inserts in figure 1 indicate the nature of the flow fields. As reported in reference 1, dyes were injected in the vicinity of the orifice and the motion of the fluid (water) was observed. As shown in the upper left photograph of figure 1, for no grazing flow, ejection from the orifice forms large eddies around the exit lip of the orifice, resulting in the dissipation of the kinetic energy of the jet. On the other hand, with ejection from the orifice into a grazing flow, the lower left photograph in figure 1 shows much smoother flow patterns. The flow leaves the orifice, is turned by the grazing flow, and blends in with the grazing flow.

With the sharp-edge orifice under consideration here, some separation and associated vorticity are generated immediately downstream of the orifice. However, under the condition where the total pressure of the jet and the total pressure of the grazing flow are equal, the orifice flow can enter the main grazing flow in a nearly inviscid manner (refs. 7 to 9) without the generation of large eddies to dissipate the kinetic energy of the jet. Therefore, the flow from the orifice is now modeled by using the steady inviscid analysis of Goldstein and Braun (refs. 7 and 8), which is valid when the orifice-flow total pressure is nearly the same as the free-stream grazing-flow total pressure.

To determine the specific orifice steady flow resistance as defined in equation (1), the relation between the driving pressure difference ΔP and the average jet velocity $\bar{v}_{jet}$ must be determined. This relation was estimated based on an inviscid flow model shown pictorially in figure 2.

The one-dimensional continuity equations can be written across the two cell boundaries as shown in figure 2

$$v_\infty H = v_e^-(H - h) \qquad \text{(Negative domain)} \tag{2}$$

$$\bar{v}_{jet}\, d = v_e^+ h \qquad \text{(Positive domain)} \tag{3}$$

Combining equations (2) and (3) yields

$$\bar{v}_{jet} = v_\infty \frac{H}{H-h} \frac{h}{d} \frac{v_e^+}{v_e^-} \tag{4}$$

The ratio of v_e^+ to v_e^- is defined as the slip factor S_e, and the ratio h/d is defined as the contraction ratio. These factors are estimated from the inviscid theory of reference 7, which presents a solution for the injection of an attached steady-flow inviscid jet into a moving stream. The analytical solution in reference 7 applies to a two-dimensional (slot), inviscid, incompressible jet injected into a semi-infinite moving stream. The solution uses small-perturbation theory; consequently, the solution is valid when the difference between the total pressure in the main stream is not too large. Also, losses at sharp corners, in turning, and in generating eddies have been neglected. The agreement between theory and experiment will be used to justify these simplifications.

The duct flow area is assumed to be large in comparison with the total orifice flow area, so that for a typical flow duct (such as in ref. 2, to which the theory will be compared)

$$\frac{H}{H-h} \approx 1 \qquad \frac{h}{H} \ll 1 \tag{5}$$

For this condition, the semi-infinite model of reference 7 should apply. Therefore, equation (4) becomes

$$\bar{v}_{jet} = v_\infty \frac{h}{d} S_e \tag{6}$$

By using the graphical results of figure 11(e) of reference 7, the extrapolated values of the slip factor far downstream from the orifice slot can be correlated as a function of the difference between the total pressure and the total upstream pressure, as follows:

$$S_e = \frac{v_e^+}{v_e^-} \approx \frac{v_e^+}{v_\infty} = (1 + \varepsilon)^{1/2} \tag{7}$$

where

$$\varepsilon \equiv \frac{P_c - P_\infty}{\frac{1}{2}\rho v_\infty^2} \tag{8}$$

Here, ε is a small perturbation parameter that can be legitimately varied between +0.2 and -0.2. For $\varepsilon = 0$, the slip is zero (ref. 8, eq. (4)) along the entire length of the interface between the grazing- and jet-flow streams. Thus, the generation of vorticity in a real fluid will be minimized for this condition.

By using the results of figure 9 of reference 7, the ratio of the final height of the jet to the slot width h/d can be correlated as a function of ε

$$\frac{h}{d} = 0.8\left(1 + \frac{\varepsilon}{2}\right) \tag{9}$$

Substituting equations (7) and (9) into equation (6) yields

$$\bar{v}_{jet} = 0.8\, v_\infty \left(1 + \frac{\varepsilon}{2}\right)(1 + \varepsilon)^{1/2} \tag{10}$$

Since the analysis performed in reference 7 is valid for only a first-order power of ε, equation (10) can be simplified to

$$\bar{v}_{jet} \approx 0.8\, v_\infty\left(1 + \frac{\varepsilon}{2}\right)\left(1 + \frac{\varepsilon}{2}\right) \approx 0.8\, v_\infty\left(1 + \varepsilon\right) \tag{11}$$

Recall that the steady orifice resistance is defined as the ratio of the pressure difference $P_c - p_\infty$ to the jet velocity $\bar{v}_{jet}$. Since the relation of total to static pressure is defined as

$$P_\infty = p_\infty + \frac{1}{2}\rho v_\infty^2 \tag{12}$$

it follows that

$$\theta = \frac{P_c - p_\infty}{\rho c \bar{v}_{jet}} = \frac{P_c - P_\infty + \frac{1}{2}\rho v_\infty^2}{\rho c \bar{v}_{jet}} \tag{13}$$

From the definition of ε, equation (8), the specific orifice steady-flow resistance can also be written as

$$\theta = \frac{v_\infty^2\,(\varepsilon + 1)}{2c\bar{v}_{jet}} \tag{14}$$

Substituting the expression for $\bar{v}_{jet}$ from equation (11) yields

$$\theta_p = \frac{M_\infty}{1.6} \tag{15}$$

where M_∞ is the Mach number of the grazing flow upstream of the orifice, assuming a uniform flow in the duct. Equation (15) cannot be applied to the zero-grazing-flow case since the assumed flow model does not apply. The subscript p has been added to θ to indicate that this resistance has been evaluated by using a potential flow model. Significantly, the resistance θ_p is only a function of the grazing-flow Mach number and is independent of ε in this linearized theory.

The theoretical equation (15) is based on an inviscid model for which no boundary layer exists up- or downstream of the orifice. In the next section this model is compared with the data of Rogers and Hersh (ref. 2) in which the ratio of boundary-layer thickness δ, to orifice hole diameter is less than 1 ($\delta/d = 0.71$). A word of caution is necessary; for actual inlets with large δ/d, a correction for boundary-layer thickness would most likely be required. For example, for a δ/d of 4.09, the data of reference 2 show that the acoustic resistance could increase from 5 to 25 percent depending on the ratio of jet to grazing (mean) flow velocity. For applications of equation (15) to large δ/d ratios, it is suggested, therefore, that an empirical correction factor be used based on data such as those presented in reference 2.

Equation (15) is a theoretical expression for the resistance of an orifice to steady outflow. Equation (15) is a priori limited to small ε, that is, small differences between the cavity and free-stream total pressures. However, as shown in the next section, the theory does fortuitously seem to correlate the data for negative values of ε. As shown in figure 3, the close proximity of the wall prevents wave growth and thereby reduces the losses of the jet, making inviscid theory more appropriate. For large positive pressure differences (positive ε), as shown in figure 3, eddies form at the interface between the jet and the stream. Obviously, the flow cannot be assumed inviscid in this case.

EXPERIMENTAL COMPARISON

The expression for the specific orifice resistance θ_p given by equation (15) is now compared with the measured airflow data from reference 2.

Case a: Jet- and Grazing-Flow Total Pressures Equal ($\varepsilon = 0$)

The theory is first compared to the experimental data for $\varepsilon = 0$. In this case, the slip along the streamline separating the jet and grazing flow is zero; thus, vorticity generation should be at a minimum. Therefore, the inviscid theory would be best applied for this case. As seen in figure 4, the simple inviscid theory for the orifice resistance gives excellent agreement with experiment over the range of grazing-flow Mach numbers tested in reference 2.

Case b: $\varepsilon > 0$

The theory is now compared to the data of reference 2 for a range of ε. For large ε, the jet will interact with the grazing flow and generate waves and associated vorticity at the interface. Inviscid theory should not be expected to work in this range. As seen in figure 5, for the $\varepsilon > 0$ points on the data curves, the deviation between theory and experiment increases with ε.

Case c: $\varepsilon < 0$

For the case where the chamber pressure is less than the free-stream total pressure ($\varepsilon < 0$), the flow from the orifice is observed to be a smooth thin flow with no visible wave growth along the interface. The close proximity of the wall to the jet–grazing-flow interface reduces the growth rate of the waves. Reducing wave amplitude (ref. 9, p. 83) reduces the rate at which the energy of the jet is dissipated. This could explain why the inviscid theory and experiment still agree (which may be fortuitous) for large negative values of ε, as shown in figure 5.

DISCUSSION OF RESULTS

The acoustic flow resistance at a suppressor wall can be related to a transfer of acoustic energy across the boundary of the duct. Normally, the acoustic energy lost by the suppressor is assumed to be dissipated into heat inside or in the near field of the absorber. In this paper, an inviscid flow model is used to predict the steady orifice-flow resistance for ejection from an orifice into a grazing flow. This inviscid flow resistance is commonly used as part of the resistive component of the wall impedance in an acoustic suppressor analysis. How can an inviscid (frictionless) flow resistance account for the energy dissipation associated with the acoustic resistance?

A possible explanation is that the steady outflow resistance into a grazing flow is not related to the instantaneous acoustic resistance. However, many investigators assume that these resistances are related. An argument to support the latter assumption follows.

Acoustic energy can be dissipated (in a resonator for example), sent through some flanking path into the surrounding environment (such as through the structure), or transformed into a mean flow field. The last case is now considered in detail. In an acoustic field, the acoustic energy can be transformed directly into the mean grazing-flow field only in the presence of vorticity (eq. (1.87) of ref. 10). However, for $\varepsilon = 0$, the asymptotic value of the jet velocity leaving the orifice will be equal (ref. 7, eq. (4)) to the grazing-flow velocity. Therefore, the jet kinetic energy (usually assumed to represent the induced acoustic jet velocity) effectively becomes a part of the grazing-flow field, since the two fluids are now indistinguishable. Since the marging of the two streams occurs in an irrotational manner, the flow field in the vicinity of the orifice is not acoustic. In fact, the orifice velocities

generated by the far-field acoustic pressures can be described by the incompressible momentum equations (refs. 3 and 4).

The flow field near the wall, therefore, is termed the nonacoustic boundary region (fig. 6). The acoustic flow region is adjacent to this region, as shown in figure 6. It is commonly assumed that the pressure and velocity at the boundary of the nonacoustic region (dashed line in fig. 6) are valid boundary conditions for the region where the acoustic equations apply. The ratio of pressure to velocity at this boundary is defined as the impedance z. In addition, the steady flow resistance is assumed to be equal to the instantaneous acoustic resistance (real part of impedance).

From the preceding discussion, the interpretation of a dissipative, resistive boundary condition developed by an inviscid theory must imply that the acoustic energy is lost by a process other than frictional dissipation. In this case (fig. 6), the kinetic energy of the acoustic jet becomes part of the steady grazing flow in the nonacoustic region adjacent to the orifice. Since this transfer of energy occurs outside the acoustic field, the usual acoustic flow laws (requiring vorticity for energy transfer to a grazing flow) are not violated. Therefore, there is no conceptual problem in relating a frictionless steady flow resistance to an acoustic resistance.

In summary, sound impinging on a resonator cavity is partially reflected and partially absorbed. During the positive portion of the sound pressure cycle (with or without grazing flow), the nonreflected potential energy of the impinging pressure wave induces flow into the orifice. The kinetic energy of the induced flow is stored in the back cavity (system reactance) and partially dissipated by viscous scrubbing and flow expansion. During the negative portion of the sound pressure wave, the cavity gives up its stored energy and drives the fluid out. In the absence of grazing flow, the kinetic energy of the acoustic jet undergoes an abrupt change in flow area that leads to dissipation of its kinetic energy. With grazing flow, some of the kinetic energy of the jet can be diverted back into the grazing flow. In both cases, all the kinetic energy of the jet is lost to the acoustic field.

CONCLUSIONS

Experiments have shown that the resistance for ejection from an orifice with grazing flow can be less than for the no-flow case over a range of orifice velocities. A simple closed-form inviscid solution was shown to explain the decrease in orifice resistance with grazing flow.

REFERENCES

1. Baumeister, Kenneth J.; and Rice, Edward J.: Visual Study of the Effect of Grazing Flow on the Oscillatory Flow in a Resonator Orifice. NASA TM X-3288, 1975.

2. Rogers, T.; and Hersh, A. S.: The Effect of Grazing Flow on the Steady-State Resistance of Isolated Square-Edged Orifices. AIAA Paper 75-493, Mar. 1975.

3. Hersh, A. S.; and Rogers, T.: Fluid Mechanical Model of the Acoustic Impedance of Small Orifices. AIAA Paper 75-495, Mar. 1975.

4. Rice, Edward J.: A Theoretical Study of the Acoustic Impedance of Orifices in the Presence of a Steady Grazing Flow. NASA TM X-71903, 1976.

5. Zorumski, William E.; and Parrot, Tony L.: Nonlinear Acoustic Theory for Rigid Porous Materials. NASA TN D-6196, 1971.

6. Feder, Ernest; and Dean, Lee W., III: Analytical and Experimental Studies for Predicting Noise Attenuation in Acoustically Treated Ducts for Turbofan Engines. NASA CR-1373, 1969.

7. Goldstein, Marvin E.; and Braun, Willis: Injection of an Attached Inviscid Jet at an Oblique Angle to a Moving Stream. NASA TN D-5501, 1969.

8. Goldstein, M. E.; and Braun, Willis: Inviscid Interpenetration of Two Streams with Unequal Total Pressures. J. Fluid Mech., vol. 70, pt. 3, Aug. 1975, pp. 481-507.

9. Bird, R. B.; et al.: Lectures in Transport Phenomena. Continuing Education Series 4, Am. Inst. Chem. Engrs., 1969.

10. Goldstein, Marvin E.: Aeroacoustics. McGraw-Hill Book Co., Inc., 1976.

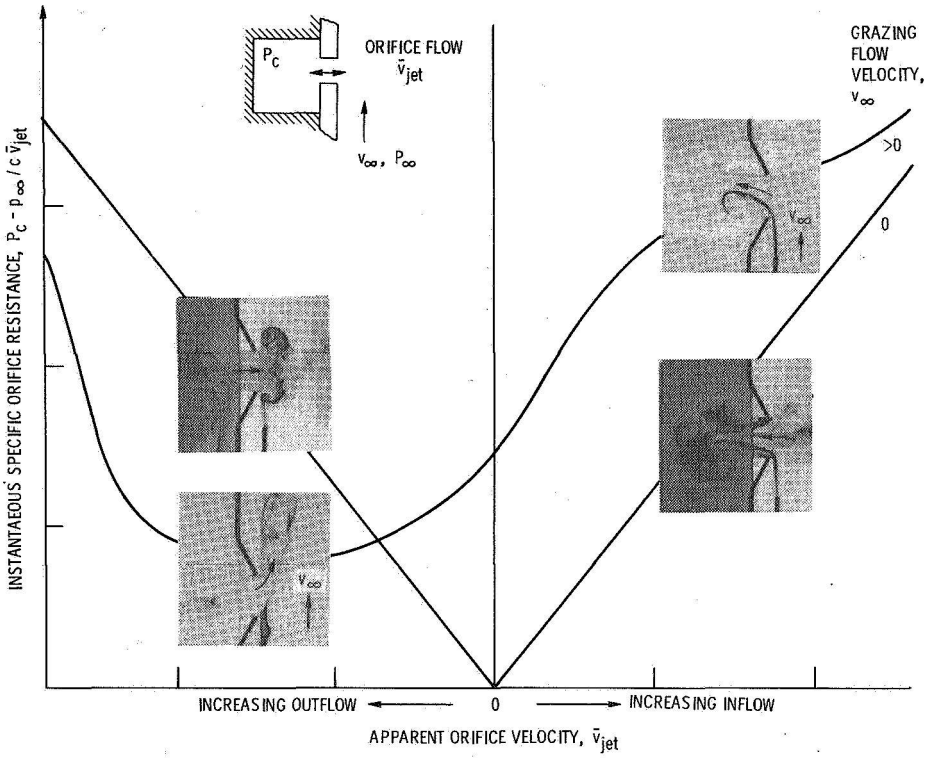

Figure 1. - Effect of sinusoidally varying orifice flow rate on instantaneous specific orifice resistance and flow profiles.

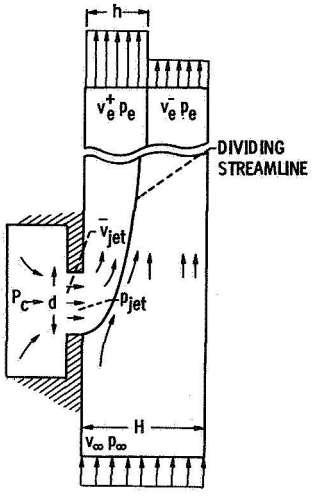

Figure 2. - Flow injection model of attached inviscid jet at right angle to moving stream.

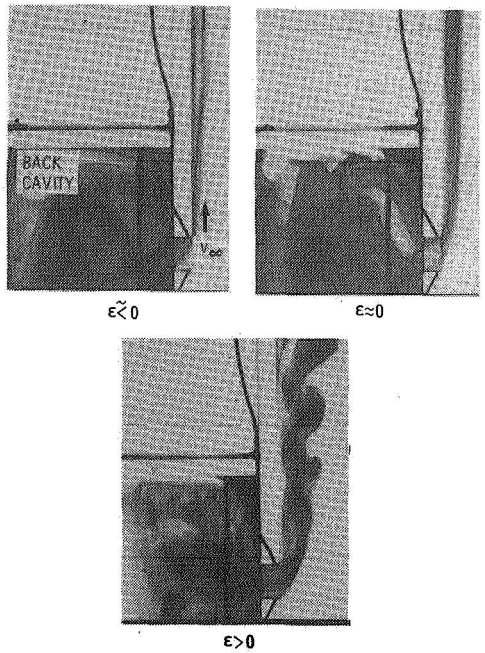

Figure 3. - Effect of increasing chamber pressure on shape of flow field.

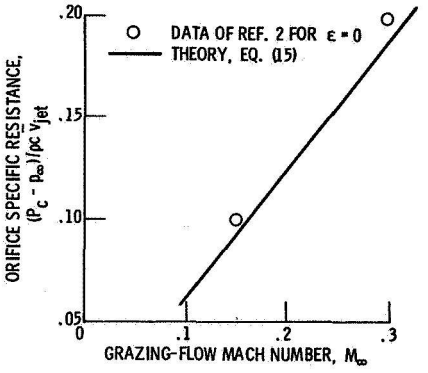

Figure 4. - Steady flow resistance as calculated from potential flow theory compared with data for total pressure difference parameter $\epsilon = 0$.

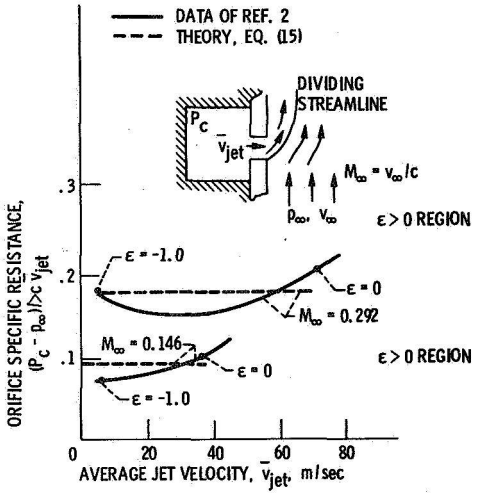

Figure 5. - Steady flow resistance as calculated from potential flow theory compared with data.

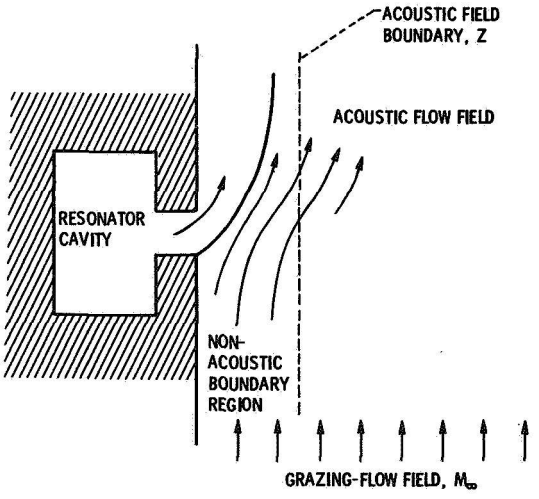

Figure 6. - Flow regimes in vicinity of orifice.

A SIMPLE SOLUTION OF SOUND TRANSMISSION THROUGH AN ELASTIC WALL TO A RECTANGULAR ENCLOSURE, INCLUDING WALL DAMPING AND AIR VISCOSITY EFFECTS

Amir N. Nahavandi, Benedict C. Sun, and W. H. Warren Ball
New Jersey Institute of Technology

SUMMARY

This paper presents a simple solution to the problem of the acoustical coupling between a rectangular structure, its air content, and an external noise source. This solution is a mathematical expression for the normalized acoustic pressure inside the structure. The paper also gives numerical results for the sound-pressure response for a specified set of parameters.

INTRODUCTION

The formulation of the problem is based on the following assumptions:

1. The structure consists of a three-dimensional chamber, oriented with respect to a Cartesian coordinate system as shown in figure 1. The boundaries of the chamber are rigid except for an elastic wall, of homogeneous material, exposed to an external noise source and clamped at all edges.

2. The external noise source is assumed to be a pure-tone (i.e., single-frequency) signal of known amplitude and frequency.

3. The air inside the chamber is considered to behave as a compressible viscous fluid undergoing oscillations of small magnitude.

4. The elastic wall is considered to behave as a vibrating plate with linear damping.

The external, incident noise-pressure disturbance causes the elastic wall to vibrate in the transversal direction, inducing pressure fluctuations inside the chamber with a subsequent internal pressure loading on the elastic wall. The solution for the acoustic pressure inside the chamber, when damping and viscous effects are neglected, has been presented in reference 1; the effects of air viscosity and wall damping are included in the analysis given in this paper.

SYMBOLS

a,b,c	height, width, and length of the chamber
a_{ij}	coefficients in the expression for the elastic-wall deflection
C	speed of sound
D	elastic-wall bending stiffness; $D = Eh^3/12(1-\sigma^2)$
E	Young's modulus for the elastic wall
f	a function of $\bar{\alpha}$, $\bar{\beta}$, $\bar{\gamma}$, and $\bar{\delta}$, defined by equation (28)
h	thickness of the elastic wall
i	$i^2 = -1$
k_a	air viscosity damping coefficient
$K_1 \ldots K_6$	constants of integration
K_{mn}	coefficients in the expression for the acoustic pressure
p	sound-pressure level inside the chamber
p_c	sound-pressure level at $z = c$
$p_{c/2}$	sound-pressure level at $z = c/2$
p_o	external sound-pressure level acting on the elastic wall
P_o	amplitude of the time-harmonic, external sound-pressure level
R	weighting function used in the weighted-residual method
t	time
v_x, v_y, v_z	components of air velocity inside the chamber
W	deflection of the elastic wall in the positive z-direction
w	mode shape of the elastic wall
x,y,z	Cartesian coordinates
$\bar{\alpha}$	wall-to-air mass ratio
$\bar{\beta}$	wall-to-air stiffness ratio
$\bar{\gamma}$	wall-to-air interaction damping ratio
$\bar{\delta}$	dimensionless air viscosity damping
∇^4	$= \frac{\partial^4}{\partial x^4} + 2\frac{\partial^4}{\partial x^2 \partial y^2} + \frac{\partial^4}{\partial y^4}$
ζ_w	wall damping coefficient
η	chamber width-to-height ratio
λ,μ,ν	separation constants
ν_{mn}	separation constants in the expression for the acoustic pressure

ξ dimensionless parameter defined by equation (29-b)

ρ density

σ Poisson's ratio for the elastic wall

ω circular frequency of the external noise

Subscripts:

a refers to the air inside the chamber

max denotes "maximum value"

w refers to the elastic wall

Superscript:

- refers to dimensionless quantities

MATHEMATICAL FORMULATION

The governing dynamic equation for the elastic wall is:

$$\nabla^4 W + \frac{\zeta_w}{D}\frac{\partial W}{\partial t} + \rho_w \frac{h}{D}\frac{\partial^2 W}{\partial t^2} = \frac{1}{D}(p_c - p_o) \tag{1}$$

The acoustic wave equation for the air contained in the chamber is:

$$\frac{\partial^2 p}{\partial x^2} + \frac{\partial^2 p}{\partial y^2} + \frac{\partial^2 p}{\partial z^2} = \frac{1}{C_a^2}\left(\frac{\partial^2 p}{\partial t^2} + k_a \frac{\partial p}{\partial t}\right) \tag{2}$$

The boundary conditions for the problem are as follows:

a) The edges of the elastic wall are considered to be clamped:

$$W(0,y,t) = W(a,y,t) = W(x,0,t) = W(x,b,t) = 0 \tag{3}$$

$$\frac{\partial W}{\partial x}(0,y,t) = \frac{\partial W}{\partial x}(a,y,t) = \frac{\partial W}{\partial y}(x,0,t) = \frac{\partial W}{\partial y}(x,b,t) = 0 \tag{4}$$

b) The normal component of the internal air velocity near a rigid boundary is zero:

$$v_x(0,y,z,t)=v_x(a,y,z,t)=v_y(x,0,z,t)=v_y(x,b,z,t)=v_z(x,y,0,t)=0 \tag{5}$$

c) The normal component of the internal air velocity near the elastic wall is equal to the wall velocity:

$$v_z(x,y,c,t)=\frac{\partial W}{\partial t} \tag{6}$$

The relationship between the internal air pressure and components of internal air velocity are:

$$\frac{\partial v_x}{\partial t} = -\frac{1}{\rho_a}\frac{\partial p}{\partial x} - k_a v_x \ , \quad \frac{\partial v_y}{\partial t} = -\frac{1}{\rho_a}\frac{\partial p}{\partial y} - k_a v_y \ , \quad \frac{\partial v_z}{\partial t} = -\frac{1}{\rho_a}\frac{\partial p}{\partial z} - k_a v_z \tag{7}$$

The external noise pressure is considered to be harmonic in time and expressed by:

$$p_o = P_o\, e^{i\omega t} \tag{8}$$

and the objective is to find:

$$W = W(x,y,t) \quad \text{and} \quad p = p(x,y,z,t) \tag{9}$$

The solution of equation (2), by separation-of-variables technique, is:

$$p(x,y,z,t) = e^{i\omega t}\sum_{m=0}^{\infty}\sum_{n=0}^{\infty} K_{mn}\ \mathrm{Cos}\frac{m\pi x}{a}\,\mathrm{Cos}\frac{n\pi y}{b}\,\mathrm{Cos}\ \nu_{mn} z \tag{10}$$

$$\text{where} \qquad \nu_{mn}^{\,2} = \frac{\omega^2 - i\omega k_a}{c_a^{\,2}} - \left(\frac{m\pi}{a}\right)^2 - \left(\frac{n\pi}{b}\right)^2 \tag{11}$$

Application of equations (6) and (7) yields:

$$\frac{\partial W}{\partial t} = \frac{e^{i\omega t}}{\rho_a(k_a + i\omega)}\sum_{m=0}^{\infty}\sum_{n=0}^{\infty} K_{mn}\,\nu_{mn}\,\mathrm{Cos}\frac{m\pi x}{a}\,\mathrm{Cos}\frac{n\pi y}{b}\,\mathrm{Sin}\ \nu_{mn} c \tag{12}$$

The value of $\frac{\partial W}{\partial t}$ is found by integrating equation (1) under the loading conditions as indicated below:

$$\nabla^4 W + \frac{\zeta_w}{D}\frac{\partial W}{\partial t} + \rho_{wD}\frac{h}{\partial}\frac{\partial^2 W}{\partial_t^{\,2}} = \frac{e^{i\omega t}}{D}\left[\left(\sum_{m=0}^{\infty}\sum_{n=0}^{\infty} K_{mn}\ \mathrm{Cos}\frac{m\pi x}{a}\,\mathrm{Cos}\frac{n\pi y}{b}\,\mathrm{Cos}\ \nu_{mn} c\right) - P_o\right] \tag{13}$$

For a solution of the form:

$$W(x,y,t) = w(x,y)e^{i\omega t} \tag{14}$$

equation (13) reduces to:

$$\nabla^4 w + \frac{i\omega\zeta_w}{D} w - \rho_w \omega^2 \frac{h}{D} w = \frac{1}{D}\left[\left(\sum_{m=0}^{\infty}\sum_{n=0}^{\infty} K_{mn}\ \mathrm{Cos}\frac{m\pi x}{a}\,\mathrm{Cos}\frac{n\pi y}{b}\,\mathrm{Cos}\ \nu_{mn} c\right) - P_o\right] \tag{15}$$

Galerkin's method is used to find an approximate solution to equation (15). In this method, an approximate solution which satisfies the boundary conditions of equations (3) and (4) is first assumed as follows:

$$w(x,y) = \sum_{i=1}^{M} \sum_{j=1}^{N} a_{ij} \left[1 - \cos\frac{(2i-1)2\pi x}{a}\right] \left[1 - \cos\frac{(2j-1)2\pi y}{b}\right] \tag{16}$$

Coefficients a_{ij} are found such that equation (16) satisfies equation (15) and the sum of the weighted residuals is identically zero over the region of integration, i.e.:

$$\int_0^a \int_0^b \left\{ \nabla^4 W + \frac{i\omega\zeta_w}{D} w - \rho_w \omega^2 \frac{h}{D} w - \frac{1}{D}\left[\left(\sum_{m=0}^{\infty}\sum_{n=0}^{\infty} K_{mn} \cos\frac{m\pi x}{a} \cos\frac{n\pi y}{b} \cos \nu_{mn} c\right) - P_o\right]\right\} R \, dxdy = 0 \tag{17}$$

This process is known as the weighted residual method and R is the weighting function. In Galerkin's method, the weighting function is made equal to the shape function defining the approximation. In general, this leads to the best approximation when

$$R = \left[1 - \cos\frac{(2i-1)2\pi x}{a}\right] \left[1 - \cos\frac{(2j-1)2\pi y}{b}\right] \tag{18}$$

Equation (17) applies for every pair of integers i and j. Generally there are $M \cdot N$ simultaneous equations of this form to be solved for the coefficients a_{ij}. For the case of low-frequency, normally-incident external noise only the diaphragm motion of the wall (first mode) will be excited. For this case, $M = 1$ and $N = 1$, and integration of equation (17) leads to:

$$a_{11} = \frac{\frac{K_{22}}{4} \cos \nu_{22} c - \frac{K_{20}}{2} \cos \nu_{20} c - \frac{K_{02}}{2} \cos \nu_{02} c + K_{00} \cos \nu_{00} c - P_o}{D\left\{\frac{3}{4}\left[\left(\frac{2\pi}{a}\right)^4 + \left(\frac{2\pi}{b}\right)^4\right] + \frac{1}{2}\left(\frac{2\pi}{a}\right)^2\left(\frac{2\pi}{b}\right)^2 - \frac{9}{4}\frac{\omega}{D}\left(\rho_w h\omega - i\zeta_w\right)\right\}} \tag{19}$$

and $$W(x,y,t) = a_{11}\left(1 - \cos\frac{2\pi x}{a}\right)\left(1 - \cos\frac{2\pi y}{b}\right) e^{i\omega t} \tag{20}$$

The values of K_{22}, K_{20}, K_{02}, and K_{00} are found by substituting the deflection from equation (20) into equation (12):

$$(-\omega^2 + ik_a\omega)\rho_a a_{11}\left(1-\cos\frac{2\pi x}{a}\right)\left(1-\cos\frac{2\pi y}{b}\right) = \sum_{m=0}^{\infty}\sum_{n=0}^{\infty} K_{mn} \nu_{mn} \cos\frac{m\pi x}{a} \cos\frac{n\pi y}{b} \sin \nu_{mn} c \tag{21}$$

When the left and right sides of equation (21) are equated term by term, it is found that all the constants K_{mn} are zero except K_{00}, K_{02}, K_{20}, and K_{22}. These are easily found and substituted in equation (19) to give:

$$a_{11} = -P_o \Big/ D \left\{ \frac{3}{4}\left[\left(\frac{2\pi}{a}\right)^4 + \left(\frac{2\pi}{b}\right)^4\right] + \frac{1}{2}\left(\frac{2\pi}{a}\right)^2\left(\frac{2\pi}{b}\right)^2 - \frac{9}{4}\frac{\omega}{D}\left(\rho_w h\omega - i\zeta_w\right) + \frac{\rho_a(\omega^2 - ik_a\omega)}{D}\left(\frac{\text{Cot } \nu_{22}c}{4\nu_{22}} + \frac{\text{Cot } \nu_{20}c}{2\nu_{20}} + \frac{\text{Cot } \nu_{02}c}{2\nu_{02}} + \frac{\text{Cot } \nu_{00}c}{\nu_{00}}\right)\right\} \tag{22}$$

Referring to equation (10), the acoustic pressure inside the chamber can now be written as:

$$p(x,y,z,t) = e^{i\omega t}\left(K_{00}\,\text{Cos}\,\nu_{00}z + K_{02}\,\text{Cos}\frac{2\pi y}{b}\,\text{Cos}\,\nu_{02}z + K_{20}\,\text{Cos}\frac{2\pi x}{a}\,\text{Cos}\,\nu_{20}z + K_{22}\,\text{Cos}\frac{2\pi x}{a}\,\text{Cos}\frac{2\pi y}{b}\,\text{Cos}\,\nu_{22}z\right) \tag{23}$$

To generalize the solution obtained above, the following dimensionless quantities are introduced:

$$\bar{x} = \frac{x}{c}, \quad \bar{y} = \frac{y}{c}, \quad \bar{z} = \frac{z}{c}, \quad \bar{a} = \frac{a}{c}, \quad \bar{b} = \frac{b}{c}, \quad \bar{c} = 1, \quad \bar{h} = \frac{h}{c} \tag{24}$$

$$\bar{t} = \frac{tC_a}{c}, \quad \bar{\omega} = \frac{\omega c}{C_a}, \quad \bar{C} = \frac{C_w}{C_a}, \quad \bar{p} = \frac{p}{P_o}, \quad \bar{D} = \frac{D}{P_o c^3} \tag{25}$$

$$\bar{a}_{11} = \frac{a_{11}}{c}, \quad \bar{\rho}_w = \frac{\rho_w C_a^2}{P_o} \quad \bar{\rho}_a = \frac{\rho_a C_a^2}{P_o}, \quad \bar{\rho} = \frac{\bar{\rho}_w}{\bar{\rho}_a}, \quad \bar{\delta} = \frac{k_a c}{C_a} \tag{26}$$

Using the above dimensionless quantities, equation (23) can be written as:

$$\bar{p}(\bar{x},\bar{y},\bar{z},\bar{t}) = e^{\bar{i}\bar{\omega}\bar{t}}\; f(\bar{\alpha},\bar{\beta},\bar{\gamma},\bar{\delta})\left[\frac{\text{Cos}\,\bar{z}\,\sqrt{\bar{\omega}^2 - i\bar{\delta}\bar{\omega}}}{\sqrt{\bar{\omega}^2 - i\bar{\delta}\bar{\omega}}\;\text{Sin}\sqrt{\bar{\omega}^2 - i\bar{\delta}\bar{\omega}}}\right.$$

$$+\frac{\text{Cos}\frac{2\pi\bar{y}}{\bar{b}}\,\text{Cos}\,\bar{z}\,\sqrt{\bar{\omega}^2 - \left(\frac{2\pi}{\bar{b}}\right)^2 - i\bar{\delta}\bar{\omega}}}{\sqrt{\bar{\omega}^2 - \left(\frac{2\pi}{\bar{b}}\right)^2 - i\bar{\delta}\bar{\omega}}\;\text{Sin}\sqrt{\bar{\omega}^2 - \left(\frac{2\pi}{\bar{b}}\right)^2 - i\bar{\delta}\bar{\omega}}} + \frac{\text{Cos}\frac{2\pi\bar{x}}{\bar{a}}\,\text{Cos}\,\bar{z}\,\sqrt{\bar{\omega}^2 - \left(\frac{2\pi}{\bar{a}}\right)^2 - i\bar{\delta}\bar{\omega}}}{\sqrt{\bar{\omega}^2 - \left(\frac{2\pi}{\bar{a}}\right)^2 - i\bar{\delta}\bar{\omega}}\;\text{Sin}\sqrt{\bar{\omega}^2 - \left(\frac{2\pi}{\bar{a}}\right)^2 - i\bar{\delta}\bar{\omega}}}$$

$$\left.-\frac{\text{Cos}\frac{2\pi\bar{x}}{\bar{a}}\,\text{Cos}\,\frac{2\pi\bar{y}}{\bar{b}}\,\text{Cos}\,\bar{z}\,\sqrt{\bar{\omega}^2 - \left(\frac{2\pi}{\bar{a}}\right)^2 - \left(\frac{2\pi}{\bar{b}}\right)^2 - i\bar{\delta}\bar{\omega}}}{\sqrt{\bar{\omega}^2 - \left(\frac{2\pi}{\bar{a}}\right)^2 - \left(\frac{2\pi}{\bar{b}}\right)^2 - i\bar{\delta}\bar{\omega}}\;\text{Sin}\sqrt{\bar{\omega}^2 - \left(\frac{2\pi}{\bar{a}}\right)^2 - \left(\frac{2\pi}{\bar{b}}\right)^2 - i\bar{\delta}\bar{\omega}}}\right] \tag{27}$$

where $f(\bar{\alpha},\bar{\beta},\bar{\gamma},\bar{\delta}) = -1 \Big/ \left\{ \frac{\bar{\beta}\xi}{\bar{\omega}^2 - i\bar{\delta}\bar{\omega}} - \frac{9\bar{\alpha}\bar{\omega}^2}{4(\bar{\omega}^2 - i\bar{\delta}\bar{\omega})} + i\frac{9\bar{\gamma}\bar{\omega}}{4(\bar{\omega}^2 - i\bar{\delta}\bar{\omega})} + \right.$

$$\frac{\text{Cot}\sqrt{\bar{\omega}^2 - \left(\frac{2\pi}{\bar{a}}\right)^2 - i\bar{\delta}\bar{\omega}}}{2\sqrt{\bar{\omega}^2 - \left(\frac{2\pi}{\bar{a}}\right)^2 - i\bar{\delta}\bar{\omega}}} + \frac{\text{Cot}\sqrt{\bar{\omega}^2 - \left(\frac{2\pi}{\bar{b}}\right)^2 - i\bar{\delta}\bar{\omega}}}{2\sqrt{\bar{\omega}^2 - \left(\frac{2\pi}{\bar{b}}\right)^2 - i\bar{\delta}\bar{\omega}}} + \tag{28}$$

$$\left. \frac{\text{Cot}\sqrt{\bar{\omega}^2 - \left(\frac{2\pi}{\bar{a}}\right)^2 - \left(\frac{2\pi}{\bar{b}}\right)^2 - i\bar{\delta}\bar{\omega}}}{4\sqrt{\bar{\omega}^2 - \left(\frac{2\pi}{\bar{a}}\right)^2 - \left(\frac{2\pi}{\bar{b}}\right)^2 - i\bar{\delta}\bar{\omega}}} + \frac{\text{Cot}\sqrt{\bar{\omega}^2 - i\bar{\delta}\bar{\omega}}}{\sqrt{\bar{\omega}^2 - i\bar{\delta}\bar{\omega}}} \right\}$$

and

$$\bar{\alpha} = \bar{\rho}\,\bar{h} = \frac{\rho_w h}{\rho_a c} \quad , \quad \bar{\beta} = \frac{(1 + 1.056\eta^5)\bar{\rho}\bar{c}^2\bar{h}^3}{0.0284\bar{b}^4} \quad , \quad \bar{\gamma} = \frac{\zeta_w}{\rho_a C_a} \tag{29-a}$$

$$\bar{\delta} = \frac{k_a c}{C_a} \quad , \quad \eta = \frac{b}{a} = \frac{\bar{b}}{\bar{a}} \quad , \quad \xi = \frac{0.9221(3\eta^4 + 2\eta^2 + 3)}{(1-\sigma^2)\ (1 + 1.056\eta^5)} \tag{29-b}$$

Equations (27), (28), and (29) constitute the analytical solution to the acousto-structural problem. These equations show that the normalized pressure distribution within the chamber is a harmonic function of time and depends on the following dimensionless parameters:

1) wall-to-air mass ratio, $\bar{\alpha}$
2) wall-to-air stiffness ratio, $\bar{\beta}$
3) wall-to-air interaction damping ratio, $\bar{\gamma}$
4) dimensionless air viscous damping, $\bar{\delta}$
5) dimensionless frequency, $\bar{\omega}$
6) dimensionless space coordinates, $\bar{x},\bar{y},\bar{z}$
7) enclosure dimensions, $\bar{a},\bar{b},\bar{c}$

NUMERICAL RESULTS

To obtain quantitative values of sound-pressure level as a function of external noise frequency, a cubical chamber (a=b=c) is assumed, and the amplitude of the dimensionless sound pressure at the center of the chamber (x=y=z=c/2) is found:

$$\bar{p}_{c/2_{max}} = \frac{\text{Numerator}}{\text{Denominator}} \tag{30}$$

$$\text{where, Numerator} = \frac{1}{2\sqrt{\bar{\omega}^2-i\bar{\delta}\bar{\omega}}\ \text{Sin}\tfrac{1}{2}\sqrt{\bar{\omega}^2-i\bar{\delta}\bar{\omega}}} + \frac{1}{\sqrt{\bar{\omega}^2-4\pi^2-i\bar{\delta}\bar{\omega}}\ \text{Sin}\tfrac{1}{2}\sqrt{\bar{\omega}^2-4\pi^2-i\bar{\delta}\bar{\omega}}}$$

$$+ \frac{1}{2\sqrt{\bar{\omega}^2-8\pi^2-i\bar{\delta}\bar{\omega}}\ \text{Sin}\tfrac{1}{2}\sqrt{\bar{\omega}^2-8\pi^2-i\bar{\delta}\bar{\omega}}} \qquad (30\text{-a})$$

$$\text{and Denominator} = \frac{3.94\bar{\beta}}{\bar{\omega}^2-i\bar{\delta}\bar{\omega}} - \frac{9\bar{\alpha}\bar{\omega}^2}{4(\bar{\omega}^2-i\bar{\delta}\bar{\omega})} + i\frac{9\bar{\gamma}\bar{\omega}}{4(\bar{\omega}^2-i\bar{\delta}\bar{\omega})} + \frac{\text{Cot}\sqrt{\bar{\omega}^2-i\bar{\delta}\bar{\omega}}}{\sqrt{\bar{\omega}^2-i\bar{\delta}\bar{\omega}}}$$

$$+ \frac{\text{Cot}\sqrt{\bar{\omega}^2-4\pi^2-i\bar{\delta}\bar{\omega}}}{\sqrt{\bar{\omega}^2-4\pi^2-i\bar{\delta}\bar{\omega}}} + \frac{\text{Cot}\sqrt{\bar{\omega}^2-8\pi^2-i\bar{\delta}\bar{\omega}}}{4\sqrt{\bar{\omega}^2-8\pi^2-i\bar{\delta}\bar{\omega}}} \qquad (30\text{-b})$$

The response of this "advanced" three-dimensional model, as given by equation (30), is compared with that of a "simplified" one-dimensional model obtained by replacing the elastic wall by a simple spring-mass system. For this simplified model the amplitude of the sound pressure at the center of the cubical chamber is:

$$\left(\bar{P}_{c/2}\right)^{s}_{\text{max}} = \frac{\dfrac{1}{2\sqrt{\bar{\omega}^2-i\bar{\delta}\bar{\omega}}\ \text{Sin}\tfrac{1}{2}\sqrt{\bar{\omega}^2-i\bar{\delta}\bar{\omega}}}}{\dfrac{\bar{\beta}}{\bar{\omega}^2-i\bar{\delta}\bar{\omega}} - \dfrac{\bar{\alpha}\bar{\omega}^2}{\bar{\omega}^2-i\bar{\delta}\bar{\omega}} + i\dfrac{\bar{\gamma}\bar{\omega}}{\bar{\omega}^2-i\bar{\delta}\bar{\omega}} + \dfrac{\text{Cot}\sqrt{\bar{\omega}^2-i\bar{\delta}\bar{\omega}}}{\sqrt{\bar{\omega}^2-i\bar{\delta}\bar{\omega}}}} \qquad (31)$$

If the effects of wall damping and air viscosity are neglected, the results given by equations (30) and (31) agree with the solution in reference 1, in which damping effects were not considered. Figures 2 and 3 show the frequency response, for a particular set of dimensionless parameters $\bar{\alpha}$ and $\bar{\beta}$, over the audio-frequency range, for the special case of $\bar{\gamma} = 0$ and $\bar{\delta} = 0$, i.e., when damping effects are neglected. These figures show that at intermediate frequencies and at the high-frequency end of the audible spectrum, the predictions of "advanced" and "simplified" models are quite similar.

When damping effects are included, i.e., when both $\bar{\gamma}$ and $\bar{\delta}$ are not zero, the digital computer program for the frequency response is very complicated, involving complex numbers and requiring double-precision (16 digits) accuracy. Results for this case will be published later.

REFERENCE

1. Nahavandi, A. N.; Sun, B. C.; and Ball, W. H. W.: A Simple Solution of Sound Transmission Through an Elastic Wall to a Rectangular Enclosure. Internoise 76 Proceedings, 1976 International Conference on Noise Control Engineering, April 5-7, 1976, pp. 251-254.

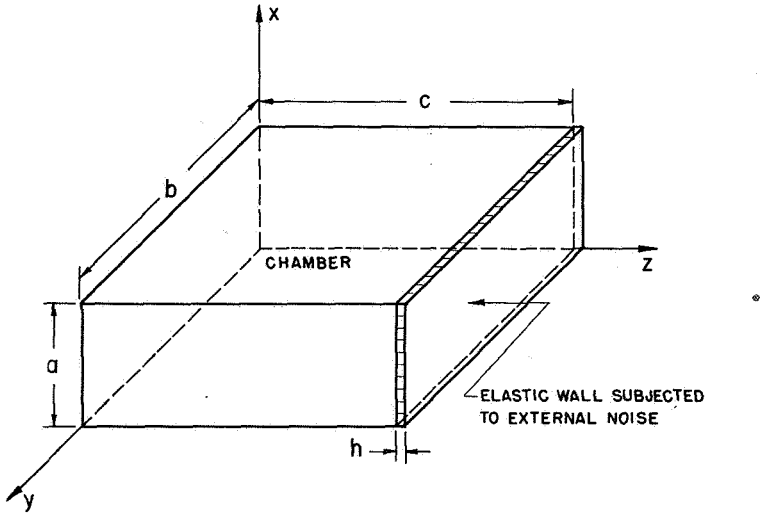

Figure 1.- Three dimensional model of sound transmission through an elastic wall to a rectangular chamber.

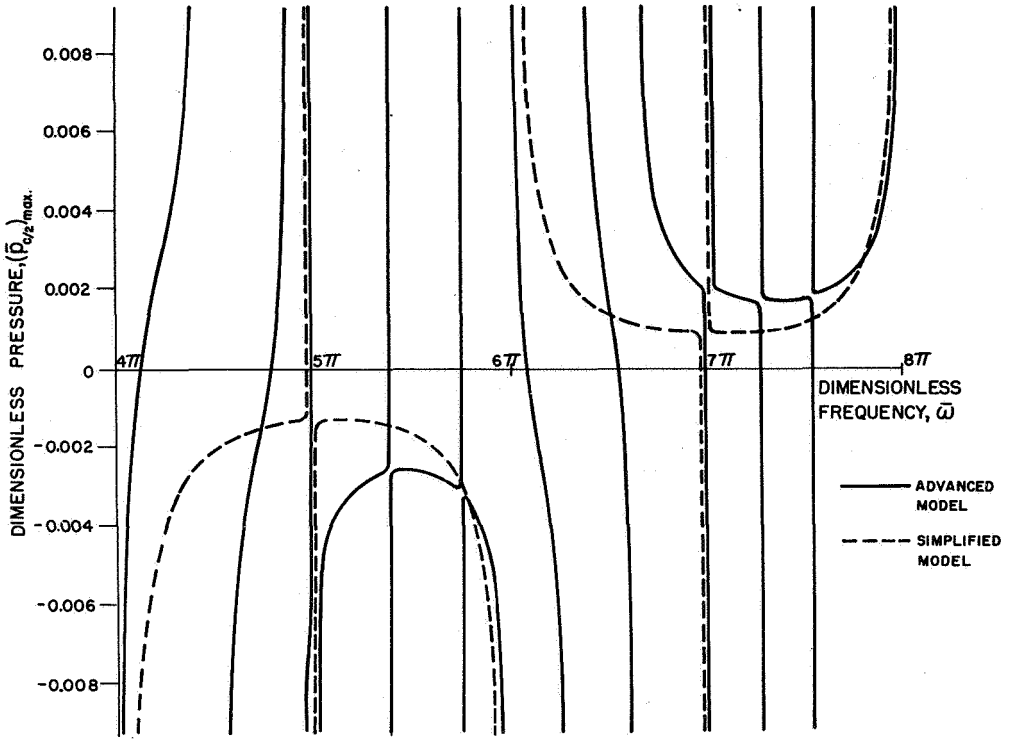

Figure 2.- Chamber frequency response to external noise source at low frequency for $\bar{\alpha} = 25$, $\bar{\beta} = 3.125$, $\bar{\gamma} = 0$, and $\bar{\delta} = 0$.

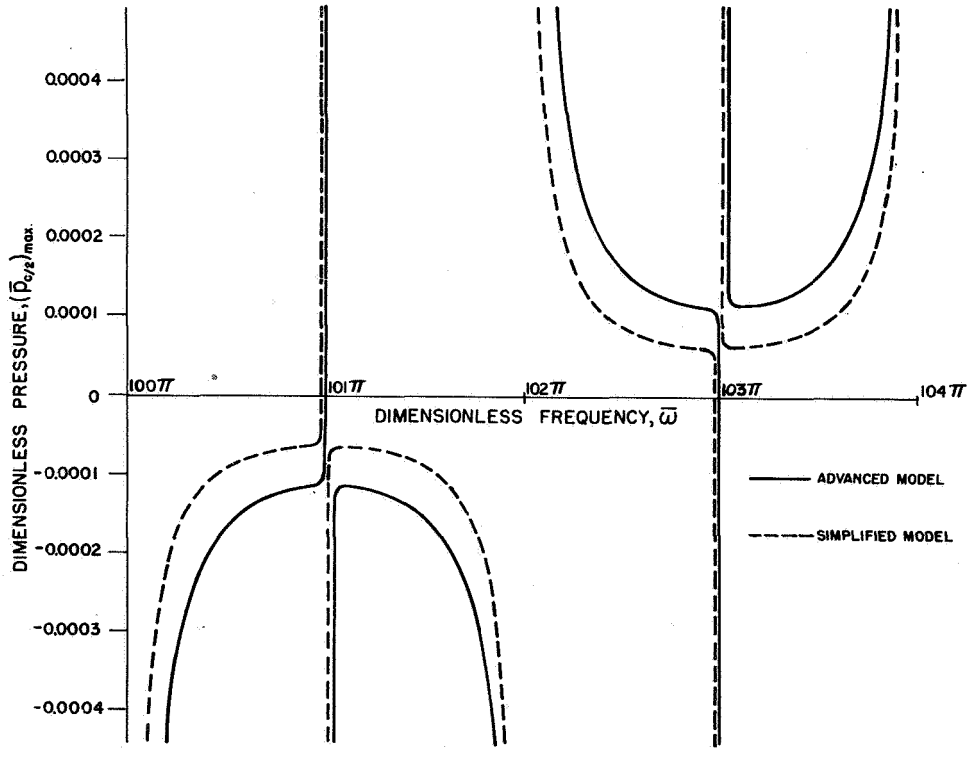

Figure 3.- Chamber frequency response to external noise source at high frequency for $\bar{\alpha} = 25$, $\bar{\beta} = 3.125$, $\bar{\gamma} = 0$, and $\bar{\delta} = 0$.

PARAMETRIC ACOUSTIC ARRAYS - A STATE OF THE ART REVIEW

Francis Hugh Fenlon
Applied Research Laboratory, The Pennsylvania State University

SUMMARY

Following a brief introduction to the concept of parametric acoustic interactions, the basic properties of Parametric Transmitting and Receiving Arrays are considered in the light of conceptual advances resulting from experimental and theoretical investigations that have taken place since Westervelt's (ref. 1) landmark paper in 1963.

INTRODUCTION

It is interesting to observe that the concept of a Parametric Acoustic Array which was first introduced by Westervelt (ref. 1) in 1963 can be viewed retrospectively as the inevitable consequence of his earlier investigations (ref. 2) of the scattering of sound by sound. Adopting this perspective as a framework for discussion, we begin by considering the propagation of isentropic finite-amplitude acoustical disturbances (i.e., waves of maximum Mach Number $\varepsilon_o < 0.1$) in an unbounded dispersionless, thermo-viscous fluid at rest. Such disturbances, as shown by Westervelt (ref. 3) are governed by a second-order nonlinear wave equation which can be derived from Lighthill's (ref. 4) 'acoustic analog equation' [i.e., a cleverly rearranged form of the Navier-Stokes (ref. 5) equations]. The excess pressure p' induced in the fluid by a finite-amplitude disturbance of initial peak pressure p_o is thus described by the equation,

$$\Box^2 P = -\frac{1}{2}\beta\varepsilon_o (P^2)_{tt} \qquad P(\underline{r},t) = p'/p_o \qquad \varepsilon_o = p_o/\rho_o c_o^2 \qquad (1)$$

where the coefficient of nonlinearity of the fluid (ref. 6) β has a value of ~3.5 in water at 20°C and atmospheric pressure. Taking the Fourier transform of eq. (1) gives,

$$(\nabla^2 + k^2)\tilde{P}_\omega = \frac{1}{2}\beta\varepsilon_o k^2 F_\omega\{P^2\} \qquad \tilde{P}_\omega(\underline{r}) = F_\omega\{P(\underline{r},t)\} \qquad k = \omega/c_o \qquad (2)$$

where the effect of viscous absorption can be included by treating k as a complex wavenumber.

If two finite-amplitude plane waves of initial peak amplitudes p_{o1}, p_{o2} and angular frequency-wavenumber pairs $(\omega_1,\underline{k}_1)$, $(\omega_2,\underline{k}_2)$, termed 'primary'

waves interact weakly (i.e., without incurring significant distortion) their combined field is obtained to a first-approximation via linear superposition giving,

$$P(r,t) = \mathrm{Re}\{P_{o1} \exp(j\omega_1 t - j\underline{k}_1 \cdot \underline{r}) + P_{o2} \exp(j\omega_2 t - j\underline{k}_2 \cdot \underline{r})\} + O(\varepsilon_o^{\,2}) \tag{3}$$

The right-hand-side of eq. (2) thus consists of forcing functions at the second harmonic and combination frequencies so that as in the case of a linear harmonic oscillator its response to any one of these applied forces remains small unless their frequencies coincide with characteristic frequencies of the homogeneous equation. For weakly interacting primary waves this occurs at the combination frequencies whenever the following 'resonance' conditions are satisfied (ref. 7):

$$\omega_1 \pm \omega_2 = \omega_{\pm} \qquad \underline{k}_1 \pm \underline{k}_2 = \underline{k}_{\pm} \tag{4}$$

Since the second of these conditions can be reexpressed for interaction in a dispersionless fluid (i.e., $\omega_1/k_1 = \omega_2/k_2 = \omega_{\pm}/k_{\pm} = c_o$) as,

$$\omega_1^{\,2} + \omega_2^{\,2} \pm 2\omega_1\omega_2 \cos\theta = \omega_{\pm}^{\,2}$$

where θ is the angle of intersection between the wave normals, it follows from the first condition that $\theta = 0$ is the only angle of intersection for which eq. (4) can be satisfied. As Westervelt (ref. 2) concluded therefore, two perfectly collimated overlapping finite-amplitude plane waves can only interact 'resonantly' when their wave vectors $\underline{k}_1$ and $\underline{k}_2$ are aligned in the same direction. On the other hand, it should be noted as Rudenko, et. al. (ref. 8) have shown that 'resonance' occurs at non-zero intersection angles in dispersive fluids.

In the case of 'non resonant' or 'asynchronous' interactions the combination tones are subject to spatial oscillations which inhibit their effective amplification. Alternatively, 'resonant' or 'synchronous' interactions result in continuous energy transfer from the primary waves to the nonlinearly generated 'secondary' waves (i.e., combination tones, etc.). If the initial amplitudes of the 'secondary' waves are zero they will thus grow linearly with range at the expense of the primary waves until the latter, and hence the amplitudes of the 'forcing functions' on the right-hand-side of eq. (2), are sufficiently diminished by this type of "finite-amplitude absorption" and by conventional 'linear' losses such as viscous absorption and spherical spreading. At distances from the source of the disturbance where the primary waves are no longer of

finite-amplitude, nonlinear interaction ceases, and the secondary waves formed in the "interaction zone" eventually decay at rates determined by their viscous attenuation coefficients and by spherical spreading losses. The range at which this occurs defines the 'far-field' of the secondary waves which is generally much greater than that of the primary waves. The interaction zone can thus be viewed as an extension of the source itself, the generation of secondary waves within it resulting from the establishment of volume distributed "virtual sources" created by the primary fields which formed as envisaged by Westervelt (ref. 1), a "virtual acoustic array". Moreover, the term 'parametric' which Westervelt (ref. 1) used to describe such arrays was chosen, by analogy with the concept of electrical parametric amplification, to convey the idea that their performance is dependent on parameters of the medium (i.e., β, ρ_o, c_o, attenuation characteristics, etc.) and of the source distribution (i.e., primary wave amplitudes, frequencies, and aperture dimensions). Since the spatial directivity of the secondary waves is in most instances equivalent to that of the primary waves, highly directive low frequency "parametric transmitting arrays" can thus be formed by bifrequency projectors simultaneously radiating highly directive primary waves of nearly equal frequencies to generate a low difference-frequency signal via nonlinear interaction in the medium. The converse task of directive low frequency reception, can likewise be accomplished by means of "parametric receiving arrays".

PARAMETRIC TRANSMITTING ARRAYS

When the primary waves are radiated by a plane piston projector of area A_o, they propagate as essentially collimated plane waves within their mean Rayleigh distance $r_o = A_o/\lambda_o$, λ_o being the mean primary wavelength, and as directive spherical waves beyond this range. If α_o is the mean primary wave attenuation coefficient, then $2\alpha_o r_o$ represents the total 'linear' loss incurred by the primary waves within r_o. Consequently, when $2\alpha_o r_o$ is such that the primary wave amplitudes are reduced to small-signal levels within r_o (i.e., $2\alpha_o r_o \gg 1$), a plane wave primary interaction of the type considered by Westervelt (ref. 1) occurs in the fluid. This type of parametric interaction, which is described as 'absorption-limited', results in the virtual sources being phased in such a manner that they form a "virtual-end-fire array whose 'far-field' spectrum contains only the difference-frequency (and possibly some of its harmonics). In most instances the latter signal overrides the primary waves and upper sideband components to survive in the far-field (i) because it has been amplified throughout the interaction zone and (ii) because of its significantly lower rate of viscous absorption. The 'far-field' pressure of an axially symmetric 'absorption-limited' parametric array obtained from eq. (2) thus becomes (refs. 1 and 9),

$$\tilde{p}_{\omega_-}(r,\theta) = D_-(\theta) \left(\frac{\omega_-^2 \beta p_{o1} p_{o2} A_o}{4\pi \rho_o c_o^4} \right) \left(\frac{1}{\alpha_T} \right) \frac{e^{-\alpha_- r - jk_- r}}{r} \qquad 2\alpha_o r_o \gg 1 \qquad (5)$$

where $\alpha_T = \alpha_1 + \alpha_2 - \alpha_- \simeq 2\alpha_o$ is the effective length of the virtual-end-fire-array and its directivity-function $D_-(\theta)$ is given by,

$$|D_-(\theta)| = \frac{|D_B(\theta)|}{\sqrt{1 + (2\alpha_T/k_-)^2 \sin^4(\theta/2)}} \qquad 2\alpha_o r_o >> 1 \qquad (6)$$

$D_B(\theta)$ being the far-field directivity function of the radiator at the difference-frequency - a necessary modification of Westervelt's (ref. 1) solution for $k_- a > 1$, introduced by Naze and Tjotta (ref. 9), where $2a$ is the characteristic dimension of the aperture. If $k_- a < 1$ then $D_B(\theta) \simeq 1$ over the angular domain of interest, so that in this instance the directivity function defined by eq. (6) assumes the form originally derived by Westervelt (ref. 1). This directivity function has no sidelobes, a most attractive feature of 'absorption-limited' parametric arrays, which has been confirmed experimentally by Bellin and Beyer (ref. 10), Berktay (ref. 11), Zverev and Kalachev (ref. 12), and by Muir and Blue (ref. 13). Using a 25 cm^2 square projector simultaneously radiating primary waves of frequencies 1.124 MHz and 0.981 MHz at finite-amplitudes in fresh water, the latter (ref. 13) showed that the far-field directivity function of the 143 kHz difference-frequency signal was in very good agreement with that predicted by eq. (6), thus demonstrating that in this instance the parametric array was capable of achieving the same directivity as a conventional source operating at 143 kHz, but with an aperture of characteristic dimension approximately eight times smaller.

If the near-field primary wave absorption loss $2\alpha_o r_o$ is very small (i.e., $2\alpha_o r_o << 1$), significant nonlinear interaction occurs beyond r_o where the primary fields propagate as directive spherical waves. A parametric array formed by this type of interaction is termed 'diffraction-limited' because the virtual-end-fire array which now extends beyond r_o is effectively truncated by spherical spreading losses at a distance $r_o' = r_o(\omega_o/\omega_-)$ where the half-power beamwidth of the virtual-end-fire-array begins to asymptotically approach that of the mean primary wave directivity function. Lauvstad and Tjotta (ref. 14), Cary (ref. 15), Fenlon (refs. 15 and 16), and Muir and Willette (ref. 17) have investigated the properties of 'diffraction-limited' parametric arrays, whose 'far-field' difference-frequency pressure for axially symmetric primary waves is given by eq. (2) as,

$$\tilde{p}_{\omega_-}(r,\theta) = -j\, D_-(\theta) \left(\frac{\omega_-^2\, \beta\, p_{o1} p_{o2}\, A_o}{4\pi\, \rho_o c_o^4} \right) \left(r_o' \ln \frac{1}{\alpha_T r_o'} \right) \frac{e^{-\alpha_- r - jk_- r}}{r}$$

$$2\alpha_o r_o << 1 \qquad (7)$$

the effective array length $r_o' \ln \frac{1}{\alpha_T r_o'}$ in this instance being considerably less than the 'absorption-limited' length $1/\alpha_T$. Moreover, as shown by

Fenlon (ref. 18) and Lockwood (ref. 19) the 'far-field' difference-frequency directivity function $D_-(\theta)$ for an axially symmetric diffraction-limited array is given by,

$$D_-(\theta) = D_1(\theta)\, D_2(\theta) \qquad 2\alpha_o r_o << 1 \tag{8}$$

where $D_i(\theta)$, $(i = 1,2)$ are the far-field primary wave directivity functions.

Combining the asymptotic solutions defined by eqs. (5)-(8), Fenlon (ref. 20), Berktay and Leahy (ref. 21), and (although not explicit in their analysis) Mellen and Moffett (ref. 22) have shown that the difference-frequency pressure in the 'far-field' of an axially symmetric parametric array can be expressed for all values of $2\alpha_o r_o$ as,

$$\left|\tilde{p}_{\omega_-}(r,\theta)\right| = D_-(\theta) \left(\frac{\omega_-}{\omega_o}\right)\left(\frac{\beta\, k_o\, p_{o1} p_{o2}\, r_o^2}{2\rho_o c_o^2}\right) R_L \frac{e^{-\alpha_- r}}{r} \tag{9}$$

where

$$R_L \to \frac{\omega_-/\omega_o}{\alpha_T r_o} \qquad \alpha_T r_o' >> 1 \tag{9a}$$

$$\to \ln \frac{1}{\alpha_T r_o'} \qquad \alpha_T r_o' << 1 \tag{9b}$$

$R_L = r_L/r_o'$ being the effective length of the parametric array r_L , normalized with respect to $r_o' = r_o(\omega_o/\omega_-)$. The dependence of R_L on $\alpha_T r_o'$ obtained from refs. 19 and 20 is shown in figure 1. Again, the general form of the difference-frequency directivity function $D_-(\theta)$ is obtained by convolving eqs. (6) and (8), as shown implicitly by Lauvstad and Tjotta (ref. 13) and explicitly by Blue (unpublished report). It should be noted that Berktay and Leahy (ref. 21) have evaluated the convolution integral numerically to obtain $D_-(\theta,\phi)$ for both axially symmetric and asymmetric 'diffraction-limited' arrays, the computed directivity functions being in excellent agreement with experimental results.

Returning to eq. (9) it is convenient to reexpress it in terms of the equivalent <u>peak</u> primary wave and difference-frequency source levels at 1m giving

$$\hat{SL}_- = \hat{SL}_1 + \hat{SL}_2 + 20 \log_{10}(\omega_-/2\pi \times 1\ \text{kHz}) + 20 \log_{10} R_L - 290\ \text{dB re 1 μPa at 1m in } \underline{\text{water}} \tag{10}$$

Since the dependence of R_L on $\alpha_T r_o'$ depicted in fig. 1 has been confirmed

experimentally (refs. 23 and 24) over the range $10^{-5} \leq \alpha_T r'_o \leq 10$, it follows that eq. (10) can be applied over the entire range of sonar frequencies provided that the combined peak primary wave pressure does not excede the shock threshold (i.e. the amplitude at which the primary waves become so distorted due to repeated self interaction that shock formation occurs within the interaction zone). Denoting the critical peak source level corresponding to the shock threshold as $\hat{SL}_{oc}$ it can be shown (ref. 20) that,

$$\hat{SL}_{oc} = 20 \log_{10} \sigma_{oc} - 20 \log_{10}(\omega_o/2\pi \times 1 \text{ kHz}) + 287 \text{ dB re 1 } \mu\text{Pa at 1m in water} \qquad (11)$$

where the parameter σ_{oc} is given as a function of $\alpha_o r_o$ in fig. 2 for a plane piston projector. It can also be shown that the half-power beamwidth $2\theta_-$ of the difference-frequency directivity function obtained from the convolution integral (refs. 13 and 21) is given to a good approximation by the expressions,

$$2\theta_- \simeq \frac{2\theta_o}{\sqrt{2}} \left\{ 1 + \sqrt{\alpha_T r'_o} \right\} \qquad 2\theta_o = \frac{0.88\,\lambda_o}{d} \qquad \text{for a square piston of side length } d \qquad (12a)$$

$$\simeq \frac{2\theta_o}{\sqrt{2}} \left\{ 1 + \frac{4}{\pi} \sqrt{\alpha_T r'_o} \right\} \qquad 2\theta_o = \frac{\lambda_o}{d} \qquad \text{for a circular piston of diameter } d\,. \qquad (12b)$$

Several examples illustrating the application of eqs. (10)-(12) to experiments reported in the literature are included in Tables 1a and 1b, the "frequency response index" $\bar{n}$ which appears in Table 1b being defined as,

$$\bar{n} = 1 + \frac{\ln\{R_L(\alpha_T r_o)/R_L(\alpha_T r'_o)\}}{\ln(\omega_o/\omega_-)} \qquad 1 \leq n \leq 2 \qquad (13)$$

where $R_L(\alpha_T r'_o)$ and $R_L(\alpha_T r_o)$ are both defined by the characteristic in fig. 1. It should be noted that from eq. (13), $\bar{n} \to 2$ for 'absorption-limited' arrays (i.e., $2\alpha_o r_o \gg 1$) and likewise $\bar{n} \to 1$ for 'diffraction-limited' arrays (i.e., $2\alpha_o r_o \ll 1$), as required. The difference-frequency pressure distribution in the 'near-field' of 'absorption-limited' parametric transmitting arrays has been analyzed by Berktay (ref. 25), Hobaek and Vestrheim (ref. 26) and by Novikov et. al. (ref. 27). A 'near-field' solution for 'diffraction-limited' arrays has also been obtained by Rolleigh (ref. 28) although it can be shown that this approximation is only valid for $10^{-2} \leq \alpha_T r'_o \leq 1$. A more comprehensive 'near-field' which include both 'absorption-limited' and 'diffraction limited' interactions has recently been derived by Mellen (ref. 29). However, this approximation has not as yet been sufficiently tested to confirm its applicability over a wide range of the parameter $\alpha_T r'_o$.

More complex parametric interactions between spatially separated primary sources have been treated analytically by Lauvstad (ref. 30) and by Cary and Fenlon (ref. 31).

An 'absorption-limited' parametric transmitting array was first formed in air by Bellin and Beyer (ref. 10) but the formation of 'diffraction-limited' arrays in air was only recently accomplished by Bennett and Blackstock (ref. 32) and independently by Muir (ref. 33). The latter, who made use of a small bifrequency transducer (i.e., operating simultaneously at 15.5 kHz and 16.5 kHz) located at the Newtonian focus of a 55.9 cm diameter parabolic reflector to form the primary waves, concluded from the success of his experiment that the advent of directional parametric megaphones is virtually assured.

Muir (ref. 33) also formed and successfully steered over a 36° sector a 21 kHz difference-frequency signal resulting from the interaction of primary waves (i.e., 185 kHz and 206 kHz) simultaneously radiated by small bifrequency transducers located on the focal surface of a 43 cm diameter solid polystyrene plastic refracting lens in water. Widener and Rolleigh (ref. 34) have subsequently shown that the difference-frequency pressure and directivity are not adversely affected by mechanically steered primary waves if the frequency of rotation is small compared to the difference-frequency.

In another recent experiment Ryder, Rogers, and Jarzynski (ref. 35) generated difference-frequencies of 10 kHz - 20 kHz via an 'absorption-limited' parametric transmitting array formed by primary waves of mean frequency 1.4 MHz propagating in a 16.5 cm diameter, 23 cm long silicone rubber cylinder immersed in water, the primary waves being radiated by 2 cm diameter circular piston centered at the back end of the cylinder. Although the axial field dependence of the difference-frequency signals was found to be in good agreement with eq. (5) when $1/\alpha_T$ was replaced by a 'slow-waveguide-antenna-absorption-distance-parameter', the 'far-field' difference-frequency directivity functions were much more directive than those predicted by eq. (6). However, despite the fact that the coefficient of nonlinearity in silicone rubber exceeds that of water by a factor of ~1.4 whilst its sound velocity is ~1.5 less than that of water, parametric arrays are formed less efficiently in this material because of its significantly greater rate of absorption per wavelength.

Attempts to address the problem of defining the maximum realizable conversion efficiency of parametric transmitting arrays have been made by Mellen and Moffett (ref. 22) and by Fenlon (ref. 36) via saturated parametric array models. Differences between these models at very high primary wave amplitudes however, have not yet been resolved experimentally.

Following Muir and Blue's (ref. 37) demonstration of the broadband (low Q) nature of parametric transmitting arrays, resulting from the transfer of primary wave bandwidths to the difference-frequency signal, it was evident that pulse compression techniques could be used, as in the case of peak-power-limited radars, to offset the poor conversion efficiency of these arrays.

Furthermore, when it was realized that the process of simultaneously radiating finite-amplitude tones of angular frequencies ω_1 and ω_2 each of initial amplitude P_o is equivalent to radiating a sinusoidal finite-amplitude carrier wave of angular frequency $\omega_o = (\omega_1 + \omega_2)/2$ and peak amplitude $2P_o$, modulated by a cosine envelope function of angular frequency $\Omega = (\omega_1 - \omega_2)/2$, it became obvious that parametric amplification is simply the converse of 'pulse demodulation' - a concept introduced by Berktay (ref. 11) and confirmed experimentally by Moffett, Westervelt, and Beyer (ref. 38) to explain the enhanced demodulation of a narrow-band-modulated finite-amplitude carrier resulting from propagation in a fluid (i.e., in addition to demodulation caused by viscous absorption) in terms of energy transferred by the carrier to its squared envelope frequency components. These components, being of lower frequency than the carrier survive the latter in the 'far-field' having been endowed with spatial directivities and bandwidths closely related to those of the carrier via angular and frequency convolution of the time waveform squared in the interaction zone. Eller (refs. 39 and 40) who investigated biased cosine modulation (i.e., a.m. with carrier) and narrow-band N-spectral line modulation showed, independently of Merklinger's (ref. 41) analysis of rectangular envelope modulation, that in principle, a maximum gain of 6 dB in conversion efficiency relative to that afforded by cosine modulation of angular frequency $\Omega/2$ could be realized for the same average carrier power by a periodic impulse function of repetition frequency Ω. In practice, however, since this form of modulation cannot be implemented by conventional band-limited, peak-power-limited acoustic sources, Merklinger (ref. 41) suggested the alternative of using a periodic rectangular envelope with a 25% 'mark-space-ratio' which results in a 5.1 dB gain in conversion efficiency for the same average power as a cosine modulated wave, provided that the source has sufficient bandwidth to form the rectangular envelope, and can at the same time sustain a 50% increase in peak pressure. On the other hand, if the source is peak-power-limited but not band-limited, a gain in conversion efficiency of 2.1 dB can still be realized for the same average power as a cosine modulated carrier, via periodic square wave modulation (i.e, rectangular modulation with a 50% mark-space-ratio) without incurring any increase in peak power. In general therefore, rectangular modulation is a very advantageous means of launching a parametric array, particularly as it can readily be implemented via switching amplifiers.

More recently, a procedure for optimizing the performance of parametric transmitting arrays by spectral design of the modulating envelope has been outlined in a preliminary study by Clynch (ref. 42).

PARAMETRIC RECEIVING ARRAYS

Parametric Receiving Arrays are formed in a fluid by projecting a finite-amplitude 'pump wave' of angular frequency ω_o into the medium to serve as a 'carrier' wave for a weak incoming signal of angular frequency ω_s, where in general $\omega_o/\omega_s \gg 1$. Since the pump wave is sufficiently intense to make the compressibility of the fluid amplitude dependent, the presence of any other wave,

such as the spatial component of a weak signal traveling along the pump axis, will result in a combined pressure field which is effectively squared by the inherent nonlinearity of the medium. The nonlinear interaction thus gives rise to sinusoidal modulation of the pump wave by the spatial component of the signal along its axis which in turn produces an intermodulation spectrum, the "sum" and "difference" components of angular frequencies $\omega_o \pm \omega_s$ being of greatest interest. For an efficient nonlinear interaction the 'resonance conditions' require that the spatial component of the signal along the pump axis be propagating in the same direction as the pump wave. On account of the fact that $\omega_o/\omega_s >> 1$ these sidebands are in close spectral proximity to the pump frequency, but unlike the latter, their directivity is equivalent to that of a virtual-end-fire line array of length L/λ_s (in wavelengths of the signal frequency), where L is the distance from the pump projector along its axis at which a receiving hydrophone resonant at $\omega_o + \omega_s$ or $\omega_o - \omega_s$ is located. Upon reception the "up-converted" signal is fed to a low pass filter to remove the pump frequency and recover the signal of frequency ω_s.

Although implicit in Westervelt's (ref. 2) work, the process of Parametric Reception was identified and made explicit by the extensive theoretical and experimental investigations of Berktay (ref. 43) who in cooperation with Al-Temimi (refs. 44, 45) and Shooter (ref. 46) considered the practical implications of the up-conversion process. Subsequent experimental work by Barnard et. al. (ref. 47) and by Berktay and Muir (ref. 48) has been directed to long wavelength up-conversion in fresh water lakes and to the consideration of arrays of parametric receivers, respectively, thus involving significant practical extensions of the original scaled laboratory experiments. Further theoretical extensions by Rogers et. al. (ref. 49) and by Truchard (ref. 50) have also been made to provide a more precise description of the pump fields radiated by practical sources and the resulting effect of such refinements upon the analytical form of solutions for the up-converted fields. More recently Goldsberry (ref. 51) and McDonough (ref. 52) have derived optimum operating conditions for parametric receiving arrays from systems analyses based on Berktay and Al-Temimi's analytical model (ref. 45) for a spherically spreading pump wave. It should be noted however, that Goldsberry's (ref. 51) analysis which attempts to include the effect of noise is much more realistic than that of McDonough (ref. 52) who neglected to include this vital effect. With the exception of a preliminary study by Bartram (ref. 53), no systematic analysis had been made prior to Fenlon and Kesner's analysis (ref. 54) of the effect of finite-amplitude absorption on the performance of parametric receivers, which although insignificant at low pump amplitudes, ultimately determines the maximum achievable efficiency of these arrays when the pump wave becomes saturated.

REFERENCES

1. Westervelt, P. J.: Parametric Acoustic Array. J. Acoust. Soc. Amer., vol. 35, no. 4, Apr. 1963, pp. 535-537.

2. Westervelt, P. J.: Scattering of Sound by Sound. J. Acoust. Soc. Amer., vol. 29, no. 2, Feb. 1957, pp. 199-203; vol. 29, no. 8, Aug. 1957, pp. 934-935; vol. 32, no. 7, July 1960, p. 934(A).

3. Westervelt, P. J.: Virtual Sources in the Presence of Real Sources. Proc. 2nd Int. Symp. Nonlinear Acoustics, The University of Texas at Austin, Nov. 1969 (AD 719936), pp. 165-181.

4. Lighthill, M. J.: On Sound Generated Aerodynamically. I. General Theory, Proc. Roy. Soc. (London), vol. A211, 1952, pp. 564-587.

5. Landau, L. D.; and Lifshitz, E. M.: Fluid Mechanics. Addison-Wesley, New York, 1959, p. 49.

6. Beyer, R. T.: Parameter of Nonlinearity in Fluids. J. Acoust. Soc. Amer., vol. 32, no. 6, June 1960, pp. 719-721.

7. Landau, L. D.; and Lifshitz, E. M.: Theory of Elasticity. Addison-Wesley, New York, 1964, pp. 115-117.

8. Rudenko, O. V.; and Soluyan, S. I.: The Scattering of Sound by Sound. Soviet Physics Acoustics, vol. 18, no. 3, Jan.-March 1973, pp. 352-355.

9. Naze, J.; and Tjotta, S. J.: Nonlinear Interaction of Two Sound Beams. J. Acoust. Soc. Amer., vol. 37, no. 1, Jan. 1965, p. 174(L).

10. Bellin, J. L. S.; and Beyer, R. T.: Experimental Investigation of an End-Fire Array. J. Acoust. Soc. Amer., vol. 34, no. 8, Aug. 1972, pp. 1051-1054

11. Berktay, H. O.: Possible Exploitation of Nonlinear Acoustics in Underwater Transmitting Applications. J. Sound Vib., vol. 2, no. 4, Oct. 1965, pp. 435-461.

12. Zverev, V. A.; and Kalachev, A. I.: Measurement of the Scattering of Sound by Sound in the Superposition of Parallel Beams. Soviet Physics Acoustics, vol. 14, no. 2, Oct.-Dec. 1968, pp. 173-178.

13. Muir, T. G.; and Blue, J. E.: Experiments on the Acoustic Modulation of Large-Amplitude Waves. J. Acoust. Soc. Amer., vol. 46, no. 1 (part 2), July 1969, pp. 227-232.

14. Lauvstad, V.; and Tjotta, S. J.: Nonlinear Interaction of Two Sound Beams. J. Acoust. Soc. Amer., vol. 35, no. 3, Mar. 1963, pp. 929-930(L).

15. Cary, B. B.; and Fenlon, F. H.: On the Exploitation of Parametric Effects in Acoustic Arrays. General Dynamics Technical Report, GDED 67-29 (1967).

16. Fenlon, F. H.: A Recursive Procedure for Computing the Nonlinear Spectral Interactions of Progressive Finite Amplitude Waves in Nondispersive Fluids. J. Acoust. Soc. Amer., vol. 50, no. 5 (part 2), Nov. 1971, pp. 1299-1312.

17. Muir, T. G.; and Willette, J. G.: Parametric Transmitting Arrays. J. Acoust. Soc. Amer., vol. 52, no. 5 (part 2), Nov. 1972, pp. 1481-1486.

18. Fenlon, F. H.: An Extension of the Bessel-Fubini Series for a Multiple Frequency CW Acoustic Source of Finite Amplitude. J. Acoust. Soc. Amer., vol. 51, no. 1 (part 2), Jan. 1972, pp. 284-289.

19. Lockwood, J. C.: Two Problems in High Intensity Sound. Ph.D. Thesis, The University of Rochester, New York, July 1971.

20. Fenlon, F. H.: On the Performance of a Dual Frequency Parametric Source via Matched Asymptotic Solutions of Burgers' Equation. J. Acoust. Soc. Amer., vol. 55, no. 1, Jan. 1974, pp. 35-46.

21. Berktay, H. O.; and Leahy, D. J.: Farfield Performance of Parametric Transmitters. J. Acoust. Soc. Amer., vol. 55, no. 3, Mar. 1974, pp. 539-546.

22. Mellen, R. H.; and Moffett, M. B.: A Model for Parametric Sonar Radiator Design. Naval Underwater Systems Center Tech. Memorandum No. PA 41-229-71 (1971).

23. Fenlon, F. H.; Thompson, J. H.; Konrad, W. L.; Douglas, G. R.; and Anderson, P. R.: On the Parametric Performance Potential of a Low Frequency Finite-Amplitude Source. Westinghouse Scientific Paper, 72-1M7-SONTR-P1, Oct. 1972.

24. Berktay, H. O.: Propagation Models for Parametric Transmitters. Proc. 6th Int. Symp. Nonlinear Acoustics, Moscow, U.S.S.R., 1975, pp. 228-231.

25. Berktay, H. O.: Near Field Effects in Parametric End Fire Arrays. J. Sound Vib., vol. 20, no. 2, Jan. 1972, pp. 135-143.

26. Hobaek, H.; and Vestrheim, M.: Axial Distribution of Difference Frequency Sound in a Collimated Beam of Circular Cross Section. Proc. 3rd Int. Symp. Nonlinear Acoustics, The University of Birmingham, England, April 1971; Proceedings of the British Acoustical Society, Jan. 1972, pp. 137-158.

27. Novikov, B. K.; Rudenko, O. V.; and Soluyan, S. I.: Parametric Ultrasonic Radiators. Soviet Physics Acoustics, vol. 21, no. 4, Feb. 1976, pp. 365-368.

28. Rolleigh, R. L.: Difference Frequency Pressure within the Interaction Region of a Parametric Array. J. Acoust. Soc. Amer., vol. 58, no. 5, Nov. 1975, pp. 964-971.

29. Mellen, R. H.: A Near-Field Model of the Parametric Radiator. J. Acoust. Soc. Amer., vol. 59, no. 1, April 1976, S28-29.

30. Lauvstad, V.: Nonlinear Interaction of Two Monochromatic Soundwaves. Acustica, vol. 16, no. 4, 1965/66, pp. 191-207.

31. Cary, B. B.; and Fenlon, F. H.: On the Near and Far-Field Radiation Patter Generated by the Non-Linear Interaction of Two Separate and Non-Planar Monochromatic Sources. J. Sound Vib., vol. 26, no. 2, Jan. 1973, pp. 209-222.

32. Bennett, M. B.; and Blackstock, D. T.: Parametric Array in Air. J. Acoust Soc. Amer., vol. 57, no. 3, Mar. 1975, pp. 562-568.

33. Muir, T. G.: A Survey of Several Nonlinear Acoustic Experiments on Travell Wave Fields. Proc. 5th Int. Symp. Nonlinear Acoustics, Copenhagen, Denmark 1973, I.P.C. Science and Technology Press, Guildford England 1973 pp. 119-125.

34. Widener, M. W.; and Rolleigh, R. L.: Dynamic Effects of Mechanical Angular Scanning of a Parametric Array. J. Acoust. Soc. Amer., vol. 59, no. 2, Feb. 1976, pp.

35. Ryder, J. D.; Rogers, P. H.; and Jarzynski, J.: Radiation of Difference-Frequency Sound Generated by Nonlinear Interaction in a Silicone Rubber Cylinder. J. Acoust. Soc. Amer., vol. 59, no. 5, May 1976, pp. 1077-1086

36. Fenlon, F. H.: Nonlinear Scaling for Saturation-Limited Parametric Arrays. J. Acoust. Soc. Amer., vol. 56, no. 6, Dec. 1974, p. 1957.

37. Muir, T. G.; and Blue, J. E.: Transient Response of The Parametric Acousti Array. Ibid. Ref. 3, pp. 227-255.

38. Moffett, M. B.; Westervelt, P. J.; and Beyer, R. T.: Large-Amplitude Pulse Propagation-A Transient Effect. J. Acoust. Soc. Amer., vol. 47, no. 5 (part 2), May 1970, pp. 1473-1474(L); vol. 49, no. 1 (part 2), Jan. 1971, pp. 339-343.

39. Eller, A. I.: Application of the USRD Type E8 Transducer as an Acoustic Parametric Source. J. Acoust. Soc. Amer., vol. 56, no. 6, Dec. 1974, pp. 1735-1739.

40. Eller, A. I.: Improved Efficiency of an Acoustic Parametric Source. J. Acoust. Soc. Amer., vol. 58, no. 5, Nov. 1975, p. 1093(L).

41. Merklinger, H. M.: Improved Efficiency in The Parametric Transmitting Arra J. Acoust. Soc. Amer., vol. 58, no. 4, Oct. 1975, pp. 784-787.

42. Clynch, J. R.: Optimal Primary Spectra for Parametric Transmitting Arrays. J. Acoust. Soc. Amer., vol. 58, no. 6, Dec. 1975, pp. 1127-1132.

43. Berktay, H. O.: Parametric Amplification by the Use of Acoustic Non-linearities and Some Possible Applications. J. Sound Vib., vol. 2, no. 4, Oct. 1965, pp. 462-470.

44. Berktay, H. O.; and Al-Temimi, C. A.: Virtual Arrays for Underwater Reception. J. Sound Vib., vol. 9, no. 2, Mar. 1969, pp. 295-307.

45. Berktay, H. O.; and Al-Temimi, C. A.: Up-Converter Parametric Amplification of Acoustic Waves in Liquids. J. Sound Vib., vol. 13, no. 1, Sept. 1970, pp. 67-88.

46. Berktay, H. O.; and Shooter, J. A.: Parametric Receivers with Spherically Spreading Pump Waves. J. Acoust. Soc. Amer., vol. 54, no. 4, Oct. 1973, pp. 1056-1061.

47. Barnard, G. R.; Willette, J. G.; Truchard, J. J.; and Shooter, J. A.: Parametric Acoustic Receiving Array. J. Acoust. Soc. Amer., vol. 52, no. 5 (part 2), Nov. 1972, pp. 1437-1441.

48. Berktay, H. O.; and Muir, T. G.: Arrays of Parametric Receiving Arrays. J. Acoust. Soc. Amer., vol. 53, no. 5, May 1973, pp. 1377-1383.

49. Rogers, P. H.; Van Buren A. L.; Williams, Jr., A. O.; and Barber, J. M.: Parametric Detection of Low-Frequency Acoustic Waves in the Nearfield of an Arbitrary Directional Pump Transducer. J. Acoust. Soc. Amer., vol. 55, no. 3, Mar. 1974, pp. 528-534.

50. Truchard, J. J.: Parametric Acoustic Receiving Array. J. Acoust. Soc. Amer., vol. 58, no. 6, Dec. 1975, pp. 1141-1150.

51. Goldsberry, T. G.: Parameter Selection Criteria for Parametric Receivers. J. Acoust. Soc. Amer., vol. 56, no. 6, Dec. 1974, p. 1959.

52. McDonough, R. N.: Long-Aperture Parametric Receiving Arrays. J. Acoust. Soc. Amer., vol. 57, no. 5, May 1975, pp. 1150-1155.

53. Bartram, J. F.: Saturation Effects in a Parametric Receiving Array. J. Acoust. Soc. Amer., vol. 55, no. 6, June 1974, p. 1382.

54. Fenlon, F. H.; and Kesner, W.: Saturated Parametric Receiving Arrays. Proc. 7th Int. Symp. Nonlinear Acoustics, Virginia Polytechnic Institute and State University, Blacksburg, Virginia, August 1976.

Table 1a

Experiment	f_1 kHz	f_2 kHz	f_o kHz	f_- kHz	f_o/f_-	A_o m^2	λ_o m	r_o m	α_o np/m	$\alpha_o r_o$ np	$\alpha_T r'_o$ np	σ_{oc}	R_L
Muir & Willette(ref. 17)	482	418	450	64	7.03	4.56×10^{-3}	3.33×10^{-3}	1.37	0.006	8.2×10^{-3}	0.116	0.3	1.9
Eller (ref. 39)	1460	1410	1435	50	28.7	3.14×10^{-3}	1.03×10^{-3}	0.304	0.04	1.2×10^{-2}	0.69	0.4	0.76

Table 1b

Experiment	$\hat{SL}_1$ dB µPam	$\hat{SL}_2$ dB µPam	$\hat{SL}_o$ dB µPam	$\hat{SL}_{oc}$ dB µPam	$\hat{SL}_-$ dB re 1µPam		θ_- degrees		$\bar{n}$	r_L m
					predicted via eq(10)	measured	predicted via eq(12)	measured		
Muir & Willette(ref. 17)	207.2	207.2	213.2	223.5	166	167	2.47	2.5	1.36	18.3
Eller (ref. 39)	206.7	206.7	212.7	215.9	155	154	4.32	4.5	1.44	6.5

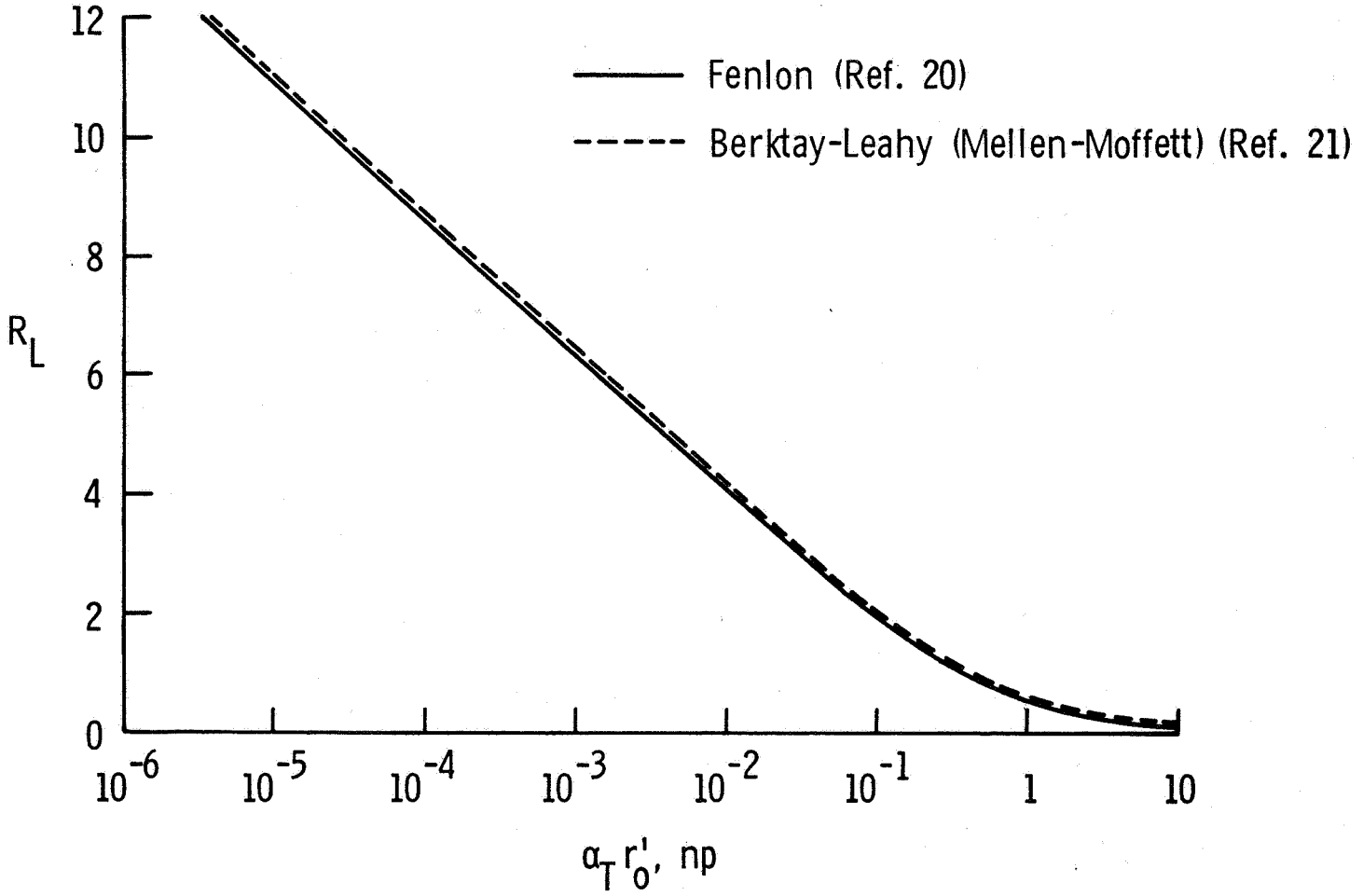

Figure 1.- Effective parametric array length characteristic.

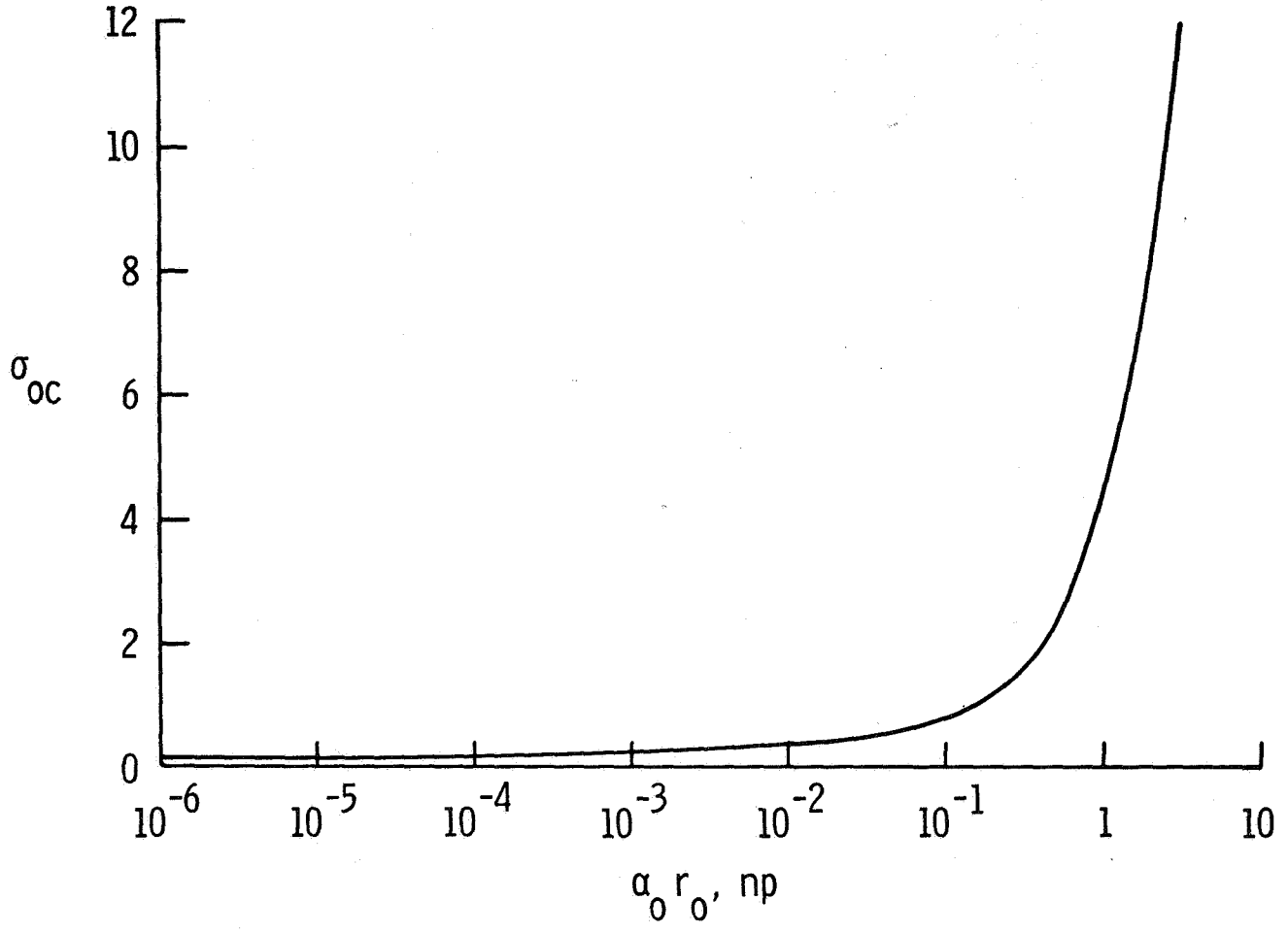

Figure 2.- Shock threshold characteristic.

NON-DIMENSIONAL GROUPS IN THE DESCRIPTION OF FINITE-AMPLITUDE SOUND PROPAGATION THROUGH AEROSOLS

David S. Scott
University of Toronto

SUMMARY

Several parameters, which have fairly transparent physical interpretations, appear in the analytic description of finite-amplitude sound propagation through aerosols. Typically, each of these parameters characterizes, in some sense, either the sound or the aerosol. It also turns out that fairly obvious combinations of these parameters yield non-dimensional groups which, in turn, characterize the nature of the acoustic-aerosol interaction. This theme is developed in order to illustrate how a quick examination of such parameters and groups can yield information about the nature of the processes involved, without the necessity of extensive mathematical analysis. This concept is developed primarily from the viewpoint of sound propagation through aerosols, although complimentary acoustic-aerosol interaction phenomena are briefly noted.

NOMENCLATURE

The nomenclature used is consistent with that of reference 1, from which the analytic results discussed in this paper were taken.

C	local wave propagation speed
c_o	infinitesimal sound speed in a clean gas $\equiv (\gamma RT_o)^{\frac{1}{2}}$
c	particulate specific heat
c_p	gas specific heat at constant pressure
H	c/c_v
l	dimensionless length $= \omega x/c_o$
l^*	dimensionless distance to shock formation
l^*_{cg}	dimensionless distance to shock formation in clean gas
m	mass of a single particle
M	equilibrium particulate mass loading $= mn_o/\rho_o$
n	particulate number density
r	radius of a single particle
R	ideal gas constant
T	temperature
U	gas velocity amplitude
u	dimensionless gas velocity
$u^{(i)}$	i^{th} order solution to u
x	dimensional distance
X_o	dimensional piston-displacement amplitude
γ	$= c_p/c_v$
$\delta_T c_o$	= local change in infinitesimal speed of sound due to temperature change
ε	acoustic Mach number $\equiv U/c_o$
μ	gas dynamic viscosity
ρ	gas density
ρ_p	particulate material density

τ particle momentum relaxation time $= (2\rho_p/9\mu)r^2$ ω frequency

INTRODUCTION

Interactions between sound and aerosols have received increasing scientific-engineering attention in recent years. Moreover, many of the more important applications involve high particulate load aerosols and intense acoustic fields. In regard to the latter, the intensities are often sufficiently high that finite-amplitude, or non-linear, effects become important.

Acoustic-aerosol interactions can be examined from two viewpoints. The first results from considering the effect of the aerosol media upon the sound which is propagating through that media. The second results from considering the effect of the acoustic field upon the aerosol itself. Illustrative applications of the former viewpoint include sound propagation through fogs in marine navigation and the attenuation of rocket or jet noise by particulate matter in the exhaust stream. From the latter viewpoint, the most remarkable result is an enhancement of the aerosol agglomeration rate; the result of a marked increase in aerosol particle-particle collision frequency. Perhaps the most promising application of this agglomeration phenomenon is in the conditioning of industrial atmospheric aerosol emissions (ref 2). Very recently, however, interesting prospects for application in the mitigation of LMFBR[+] accidents have appeared.

This paper will concentrate on the viewpoint of the influence of the aerosol upon sound propagation. It is this aspect which has succumbed most readily to theoretical treatment and hence presents greater opportunity for examination of meaningful analytical results. It can be our hope, however, that through gaining insight into the important parameters of acoustic-aerosol interactions from this viewpoint, we simultaneously identify those physical parameters of most importantance to phenomena associated with the effect of sound upon an aerosol.

FUNDAMENTAL PARAMETERS

To introduce our approach to the examination of acoustic-aerosol interactions, it is appropriate to first beiefly review what we mean by an aerosol and, secondly, to remind ourselves of the most well-known features of finite-amplitude acoustics. Such a review is worthwhile in itself. But it will also allow us to choose two parameters which we shall use to characterize the aerosol, and two further parameters which we shall use to characterize the acoustic field. Moreover, as we shall see, simple combinations of these parameters can then subsequently be used to allow physical interpretation of the acoustic-aerosol interactions.

[+]Liquid metal fast breeder reactor.

Of course to properly describe an aerosol or finite-amplitude acoustic field, many more than two parameters for each would be necessary. However, it is the theme of this paper that by choosing what might be considered the two "most important" parameters in each case, a non-rigorous, but interpretively useful, appreciation of the major processes can be gained.

Aerosol

An aerosol may be defined as a suspension of solid and/or liquid particulate matter in a gaseous media. Well-known examples include smokes, mists, fumes and atmospheric dust clouds. The author's preference is to consider an aerosol to be the combined particulate cloud and gaseous bath gas, rather than the particulate cloud itself. We shall use this interpretation through the remainder of this discussion.

The particulate component is typically characterized by classifications such as volatile or non-volatile, spherical or non-spherical particles, monodisperse or polidisperse particulate size distributions, etc. A monodisperse aerosol (sometimes also referred to as homogeneous) is one which contains particles of only one size (strictly speaking, in only one small size range). Next, in even the briefest outline of the nature of an aerosol, the remarkable phenomenon of continuous and spontaneous particulate agglomeration must be noted. The rate of agglomeration is proportional to the number density squared such that,

$$-\dot{n} \propto n^2. \tag{1}$$

Of course, the appropriate constant of proportionality depends upon several factors, such as, whether the aerosol is quiescent or in turbulent motion, electrical field and charge effects, particulate characterization and, what is of particular import to the phenomena we are treating, the absence or presence of acoustic fields and their nature. Figure 1, which has been abstracted from reference 3, is included to give some feel for the order of magnitudes involved in aerosol dynamics.

To facilitate selection of these parameters which we shall use to characterize the aerosol, it is expedient to choose a simply defined aerosol in order to focus on the major features of the acoustic-aerosol interaction. As such, we shall consider a monodisperse particulate cloud of spherical non-volatile particles, spacially uniformly dispersed throughout an inert, quiescent bath gas which will exhibit no molecular relaxation processes when under the influence of these acoustic fields we shall consider.

Clearly, a parameter of importance will be one which will characterize the size of individual particles, and do so in terms of the gas in which they are immersed, since any parameter chosen to characterize the aerosol must include features of both the particulate cloud and the carrier gas. Such a parameter is the momentum relaxation time, τ, which under assumptions consistent with the application of Stokes' Drag Law, becomes

$$\tau \equiv (2\rho_p/9\mu)r^2. \tag{2}$$

The obvious choice for the second aerosol parameter will be one which gives a measure of "how much" particulate matter is present. Again, the "how much" must be given in terms of the bath gas. As such, the natural choice is the mass loading ratio, M, given by,

$$M = (mn)/\rho. \tag{3}$$

We now have two very simple parameters which we shall use to characterize the aerosol. It is of interest to note that one of these, M, can be considered a "how much?" parameter, while the other, τ, is in some sense a "what type?" parameter. It will be useful to retain these simple "how much?" and "what type?" concepts when choosing the two parameters which shall represent the acoustic field.

Finite-Amplitude Sound

Consistent with our approach when we chose a simple aerosol as a vehicle to introduce the aerosol parameters, we shall now direct attention to a simple finite-amplitude acoustic field. In particular, we shall consider a plain progressive wavetrain generated by the sinusoidal motion of a piston at $x = 0$ and propagating into the semi-infinite region $x > 0$. By referring to figure 2, we can review the most well-known phenomenon associated with finite-amplitude sound propagation; that of the distortion of the initial sinusoidal wavetrain into a wavetrain more sawtooth in form containing higher harmonics.

There are two dominant mechanisms which cause this distortion and they do so through their effect on the local wave propagation velocity, C, at each point in the waveform. If we consider C at each point in the wave, we note that it is made up of the linear superposition of three velocities.

$$C = c_o + S_T c_o + u \tag{4}$$

Here, c_o is the quiescent speed of sound, that is the speed of infinitesimal-amplitude sound through the quiescent media. The second term accounts for changes in the local speed of sound due to variations in the temperature of the media caused by the presence of the acoustic field itself. The third term, u, is a convective term, resulting from the fact that the media itself is moving with a local velocity.

If we apply these physical considerations to determine the local speed of sound, C, at each of three points, x_1, x_2 and x_3, in the "early wave form" of figure 2, the mechanism of wave form distortion is easily understood. At x_3 compression effects have increased the temperature of that part of the wave above that in the quiescent gas. As such, $\delta_T C_o$, is positive. Moreover the convective velocity u is positive. Thus, C at x_3 is greater than c_o, and that "part" of the wave moves faster in the direction of propagation than would an infinitesimal amplitude wave. By similar arguments it is apparent that C at x_2 equals c_o and C at x_1 is less than c_o. These combined effects lead to the distortion shown by the "later wave form" of figure 2.

Now the important thing from our point of view is that both $\delta_T c_o$ and u are a *direct consequence* of the finite-amplitude nature of the acoustic field. As

such, in seeking parameters to characterize the acoustic field, we necessarily require a parameter which will measure the magnitude of finite-amplitude effects, or, the degree to which the field is a "finite-amplitude" field. The most appropriate parameter for this purpose is the acoustic Mach number, ε, given by,

$$\varepsilon = U/c_o. \tag{5}$$

Note that U is the acoustic velocity amplitude and not the local convective velocity, u, discussed earlier.

Now by comparison with the parameters introduced to describe the aerosol, it is evident that ε may be thought of as a "how much?" parameter. And this leaves us with the choice of a "what type?" parameter, which for the acoustic field is clearly ω, the fundamental sinusoidal frequency. Interestingly, in terms of the displacement amplitude, X_o, and for sinusoidal motion, the two acoustic parameters are related through the expression,

$$\varepsilon = (wX_o)/c_o. \tag{6}$$

Towards the end of this "early evolution" stage where non-linear effects bring about a relatively rapid transfer of energy from the fundamental to the higher harmonics, the waveform can resemble a series of low amplitude shocks. This distance to shock-formation has been given by Blackstock (ref 4) as,

$$1^*_{cg} = 2/(\gamma + 1)\varepsilon. \tag{7}$$

At shock-formation, the ratio of magnitudes of the fundamental to its harmonics are "semi-stable", resulting from a balance between the concomitant processes of energy flow from the lower harmonics to the higher harmonics, and the proportionally greater dissipation of the higher harmonics. This concept was first introduced by Fay (ref 5). The development of the wavetrain beyond the point of shock-formation to extinction might be thought of as the "late evolution" phase during which the progressive dissipation of the energy associated with the waveform causes the "semi-stable" waveform to decay to an infinitesimal sinusoidal form.

Before leaving the interpretation of these four parameters, it is appropriate to give some feeling for typical orders of magnitudes involved in units associated with either aerosol science or non-linear acoustics. This is presented in Table 1.

M	(grains/ft^3)	(gms/m^3)	ε	SPL(dB)	(Watts/m^2)	τ(sec)	r(μm)
10^{-4}	0.057	0.013	10^{-4}	114	2.5×10^{-1}	1.2×10^{-7}	0.1
10^{-3}	0.57	0.13	10^{-3}	134	2.5×10	1.2×10^{-5}	1
10^{-2}	5.7	1.3	10^{-2}	154	2.5×10^{3}	1.2×10^{-3}	10
10^{-1}	57	13	10^{-1}	174	2.5×10^{5}	1.2×10^{-1}	100

TABLE 1: Illustrative conversions of parameters M, ε and τ, for $\rho_p = 1$ gm/cm^3, $\rho_o = 1.29\times10^{-3}$ gm/cm^3, $\mu = 1.83\times10^{-4}$ poise.

INTERACTIONS

Intuitive

Of the four parameters, the two "what type?" parameters, $\tau[t]$ and $\omega[t^{-1}]$, have inverse units, and their simple product, $\omega\tau$, is a non-dimensional group which represents the physical ratio:

$$\omega\tau = \frac{\text{time of particle dynamic relaxation}}{\text{time of acoustic cycle}} . \tag{8}$$

As such, we expect the magnitude of $\omega\tau$ will tell us something about how effectively the aerosol and sound are coupled. In particular, as $\omega\tau \to 0$, the time of particle dynamic relaxation is very short with respect to the time of an acoustic cycle, and hence we expect the particles to behave much as if they were an element of fluid in the bath gas. That is, we expect their presence to play a minimal role affecting the sound being transmitted through the aerosol media. As $\omega \to 1$ the dynamic relaxation time of the aerosol particles is of the same order as the time of an acoustic cycle, and hence we might expect, in some sense, a maximum acoustic-aerosol interaction. As $\omega\tau \to \infty$, the long dynamic relaxation time with respect to an acoustic cycle indicates that the aerosol particles are essentially stationary. We therefore expect that the presence of the acoustic field has minimal effect upon the aerosol. We might further expect that although the aerosol could influence the sound, it would do so in only a minor way, since the sound can be expected to propagate primarily through the gaseous media in the interstices between particles, which is large w.r.t. the particle volume.

The two remaining "how much?" parameters combine to give a non-dimensional group, M/ε, even more simply interpreted. Specifically,

$$M/\varepsilon = \frac{\text{"how much?" particulate matter}}{\text{"how much?" sound}} . \tag{9}$$

With this interpretation, we expect that as $M/\varepsilon \to 0$, finite-amplitude sound effects will dominate processes of interest. As $M/\varepsilon \to 1$, we expect that finite-amplitude and aerosol effects influence various phenomena with approximately equal importance. As $M/\varepsilon \to \infty$, we expect that the presence of the aerosol, rather than that of finite-amplitude nature of the acoustic field, will be of predominant importance. Of course these M/ε interpretations should be viewed in terms of the magnitude of the associated $\omega\tau$ parameter which gives information on the effectiveness of the acoustic-aerosol interaction. That is, if the $\omega\tau$ product indicates a weak acoustic-aerosol coupling, the significance of the M/ε parameter might be unimportant *á priori*.

Analytic

We now consider the role of the preceeding acoustic-aerosol interaction parameters by examining the analytic results of reference 1. In particular, we shall examine the influence of the aerosol upon waveform distortion.

The assumptions and analytic details of the results we shall consider are presented in reference 1, and will not be repeated here. The work involved a perturbation solution of a set of equations and boundary conditions which described the attenuation, dispersion and harmonic growth, of an initially sinusoidal finite-amplitude plain progressive wavetrain propagating towards infinity. The solution, in terms of the dimensionless gas velocity, u, was given in the form:

$$u = \varepsilon u^{(1)} + \varepsilon^2 u^{(2)} + \varepsilon^3 u^{(3)} + \ldots \qquad (10)$$

Although not rigorously correct (see ref. 1), it is possible for the purposes of our discussion to consider each term in this expansion, $\varepsilon^i u^{(i)}$, to be the i^{th} harmonic. With this interpretation we consider the magnitude of waveform distortion by examining the evolution of $u^{(2)}$ with increasing distance from the initial sinusoidal motion.

First consider the case, shown in figure 3, where the $\omega\tau$ product is held constant at unity and M is increased from 0 to 10^{-1}. The M = 0 result corresponds to the growth of the second harmonic in a clean gas. As we increase the amount of particulate matter, the harmonic growth is retarded as the energy is removed from the harmonic by particulate-gas dissipative mechanisms.

Turning to the influence of the parameter $\omega\tau$, we can consider the case for which we hold the mass loading ratio constant at $M = 10^{-2}$. This is illustrated in figure 4 which shows the influence of the $\omega\tau$ parameter over the range $0 \leqq \omega\tau \leqq \infty$. In spite of the fact that the particulate loading is non-negligible, at $\omega\tau = 0$ the presence of the particulate matter does not alter the growth of the second harmonic from that which it would be in a clean gas. As the $\omega\tau$ product moves to $\omega\tau = 10^{-1}$, the acoustic-aerosol coupling improves, and the growth of the second harmonic is somewhat retarded over that which would be found in a clean gas. If we further increased $\omega\tau$ through unity to infinity, the maximum retardation of harmonic growth occurs at approximately $\omega\tau = 1$, after which the aerosol influence diminishes until, as $\omega\tau \to \infty$, the sound propagates as if there were no particulate matter present.

We see how the presence of particulate matter, as given by the mass loading ratio M, acts to *retard* the rate at which the growth of the second harmonic distorts the original sinusoidal waveform. But the effectiveness by which the aerosol retards the distortion is strongly affected by the effectiveness of the acoustic-aerosol coupling as indicated by the $\omega\tau$ parameter.

The next question which can be examined from this parametric approach is that of the distance to shock-formation. Or, what may be considered the same thing, the demarkation between the "early evolution" and "late evolution" stages of waveform development.

Analytically, this problem has been approached by comparing the magnitude of terms in the perturbation solution of equation (10). In reference 1 it is shown that, in an inviscid clean gas, the ratios of the second order solution to the first, and the third to the first, at the point of shock-formation, become,

$$\left|\varepsilon u^{(2)}/u^{(1)}\right| = \tfrac{1}{2} \qquad (11)$$

and

$$|\varepsilon^2 u^{(3)}/u^{(1)}| = 3/8 \qquad (12)$$

respectively. Either equation (11) or (12) may be used as a shock-formation criterion for the case M = 0. If, however, it is assumed that the relative amplitudes of the harmonics at the point of shock-formation in an aerosol are also given by equations (11) and (12), the difference between the two predictions will give some indication of the uncertainty associated with this assumption. This was the approach taken in reference 1 and the results are shown in figure 5.

We note that the distance to shock-formation in an aerosol is always greater than the distance to shock-formation in the clean gas. Thus, that which was indicated by figures 3 and 4 - that the presence of an aerosol retards the rate at which an initially monochromatic finite-amplitude wave distorts - is reinforced by the shock-formation distance results. But the matter of particular interest which is illustrated by figure 5, is the role played by the interaction parameters M/ε and $\omega\tau$.

If we direct attention to the case $\omega\tau = 1$, we note that at $M/\varepsilon \gg 1$ the distance to shock-formation in the aerosol is about 1.35 times that found in a clean gas. On the other hand, as M/ε decreases from unity the distance to shock-formation approaches that found in the clean gas, while as M/ε becomes greater than unity, the shock-formation distance rapidly approaches infinity and the system moves into a regime where shock-formation is precluded. Thus our earlier speculation, that the M/ε interaction parameter should be a measure of the relative importance of aerosol effects as compared to finite-amplitude effects is realized. Put simply, for the case $M/\varepsilon = 0.1$, the wave distortion proceeds essentially as if there were no aerosol present and is determined totally by the magnitude of the acoustic field. Conversely, for the case $M/\varepsilon \gg 10$, the acoustic field is damped out so rapidly by the presence of the aerosol that finite-amplitude distortion effects have no opportunity to significantly alter the harmonic ratios. In both cases, this is independent of the *absolute* magnitude of either M or ε.

Now consider the effect of the parameter $\omega\tau$, by examining the cases $\omega\tau = 0.1$ and $\omega\tau = 10$. As we move away from $\omega\tau = 1$, the coupling between the acoustic field and the aerosol becomes less effective, thereby weakening the influence of the aerosol upon waveform evolution, and allowing this evolution to proceed more closely to that which it would in a clean gas. Again, this conforms not only to the results of figures 3 and 4, but also to our intuitive expectations discussed earlier.

Before leaving figure 5, it should be noted that the two harmonic ratio criteria do predict somewhat different shock-formation distances. This discrepancy becomes marked as the ratio $l^*/l^*_{cg} \gtrsim 2$ or greater, and results from the fact that the semi-stable waveform characteristic of the newly formed shock can be quite different in an aerosol than in a clean gas. This, and other matters, will be mentioned briefly in the next section.

MORE GENERAL THEORIES AND ADDITIONAL PARAMETERS

The theme of this paper has been to introduce a means of performing order-of-magnitude evaluations of the relative importance of different processes in finite-amplitude sound propagation through aerosols, by means of quick examination of the four parameters, ω, τ, M and ε, as well as their combination in the interaction parameters M/ε and $\omega\tau$. Nevertheless, the subject should not be left without noting that additional parameters enter more general theories, and giving some indication of where these theories may be found in the literature.

The $\omega\tau$ product has been found in acoustic-aerosol literature for a number of years, and is perhaps best known from the monograph by Mednikov (ref 6) in which the motion of individual particles is given in terms of a *specified* acoustic field. This same parameter plays a major role in the formulation by Temkin and Dobbins (ref 7) of the attenuation and dispersion of infinitesimal-amplitude sound propagation through aerosols. In the event other transport phenomena play a role, such as heat or mass transfer, other "what type?" products, $\omega\tau_i$, where i corresponds to the transport process of interest, can become important. Sometimes, such as in the case of the theory drawn upon for the present paper, even though one of these transport processes cannot be neglected (heat transfer in the present case), the judicious choice of other parameters (in our case setting H = 1) can remove this additional dependence such that the problem collapses to a dependence on $\omega\tau$ only. In other cases, such as when volatile aerosols (ref 8) or compressibility of the particles (ref 9) are treated, it may be somewhat more difficult to collapse all "what type?" parameters into one.

The treatment of polydisperse aerosols is fairly readily accomplished by treatments analogous to those referred to here, by the introduction of integrals over the size distribtution using the appropriate size dependent parameter, such as τ, as a weighting function (e.g., references 1, 7, 10). If the semi-stable waveforms of the "late evolution" regime are of interest, in addition to the parameters we have introduced in the body of this paper, the parameter H plays a major role and cannot be neglected. This "late evolution" regime is treated by Davidson (ref 11).

CONCLUSIONS

It is the author's view that if an estimate of the relative magnitude, or importance, of different effects encountered in phenomena associated with finite-amplitude sound propagation through aerosols are of interest, a fairly quick appraisal of these can be made, by examining the magnitude of what are probably the two most important acoustic-aerosol interaction parameters M/ε and $\omega\tau$. In many cases, examination of these parameters will show that one or more effects will either dominate, or are unimportant, to the situation being considered. Moreover, it may be hoped that by considering these groups (which arise naturally in rigorous theoretical treatments) from the physical viewpoints discussed, the underlying physical mechanisms may be better appreciated.

REFERENCES

1. Davidson, G.A.; and Scott, D.S.: Finite-Amplitude Acoustics of Aerosols, J. Acoust. Soc. Amer., vol. 53, no. 6, June 1973, pp. 1717-1729.
2. Scott, D.S.: A New Approach to the Acoustic Conditioning of Industrial Aerosol Emissions, J. Sound Vib., vol. 43, no. 4, Dec. 1975, pp. 607-619.
3. Stanford Research Institute Journal, Third Quarter, 1961. (full chart reprints available from Dept. 300).
4. Blackstock, D.T.: J. Acoustic Soc. Amer., vol. 34, 1962, p. 9.
5. Fay, R.D.: J. Acoustic Soc. Amer., vol. 3, 1931, p. 222.
6. Mednikov, E.P.: Acoustic Coagulation and Precipitation of Aerosols, English translation; Consultants Bureau, N.Y., 1965.
7. Temkin, S.; and Dobbins, R.A.: Measurements of Attenuation and Dispersion of Sound by an Aerosol, J. Acoust. Soc. Amer., vol. 40, 1966, pp. 1016-24.
8. Cole, J.E.; and Dobbins, R.A.: Measurements of the Attenuation of Sound by a Warm Fog, J. Atmos. Sc., vol. 21, 1971, pp. 202-209.
9. Morfey, C.L.: Sound Attenuation by Small Particles in a Fluid, J. Sound Vib., vol. 8, 1968, pp. 156-170.
10. Davidson, G.A.; and Scott, D.S.: Finite-Amplitude Acoustic Phenomena in Aerosols from a Single Governing Equation, J. Acoust. Soc. Amer., vol. 54, no. 5, Nov. 1973, pp. 1331-1342.
11. Davidson, G.A.: A Burgers' Equation Approach to Finite-Amplitude Acoustics in Aerosol Media, J. Sound Vib., vol. 38, 1975, pp. 475-495.

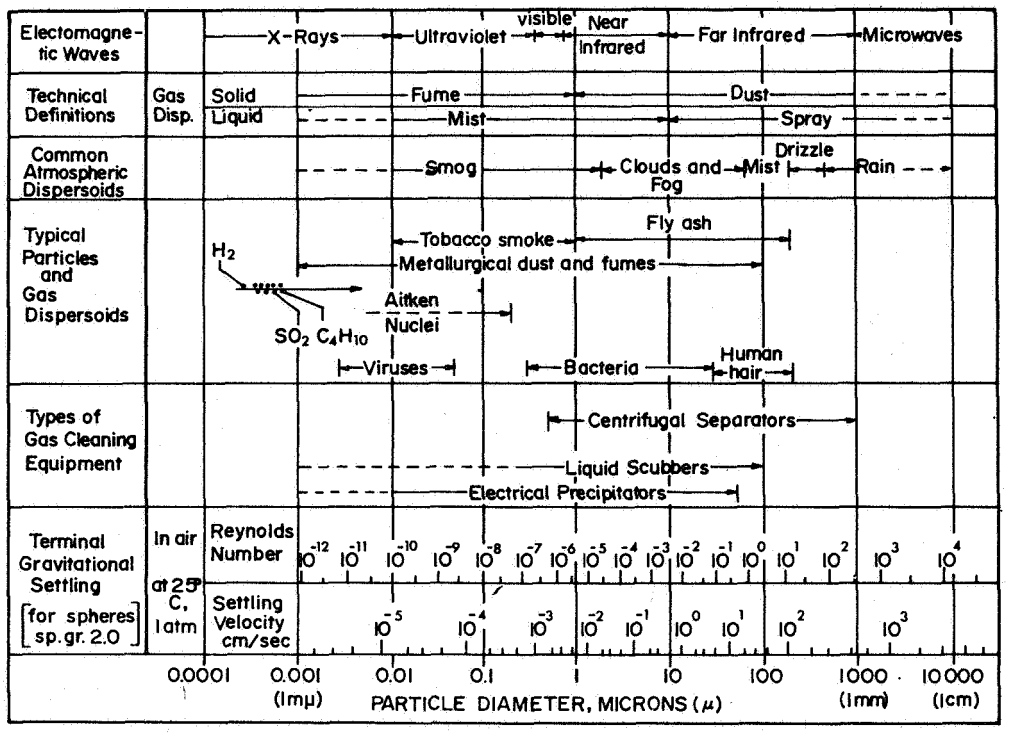

Figure 1.- Characterization of some aerosols.

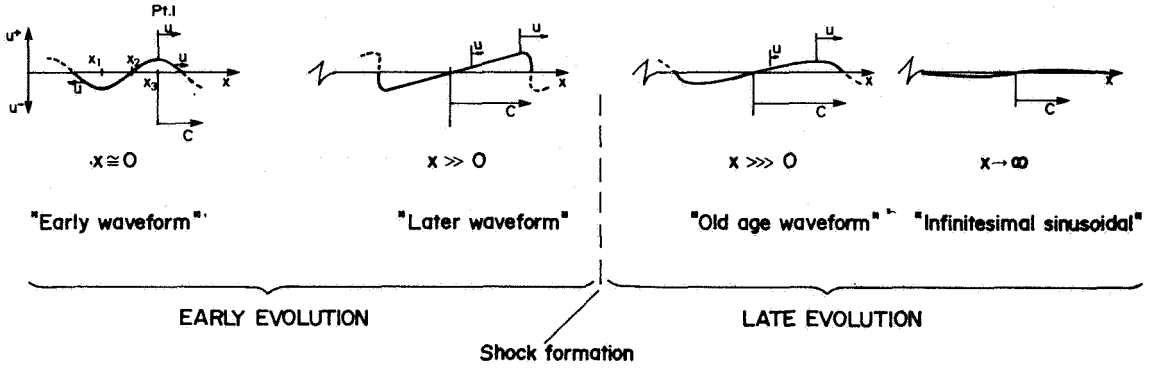

Figure 2.- Life-cycle of finite-amplitude progressive waves.

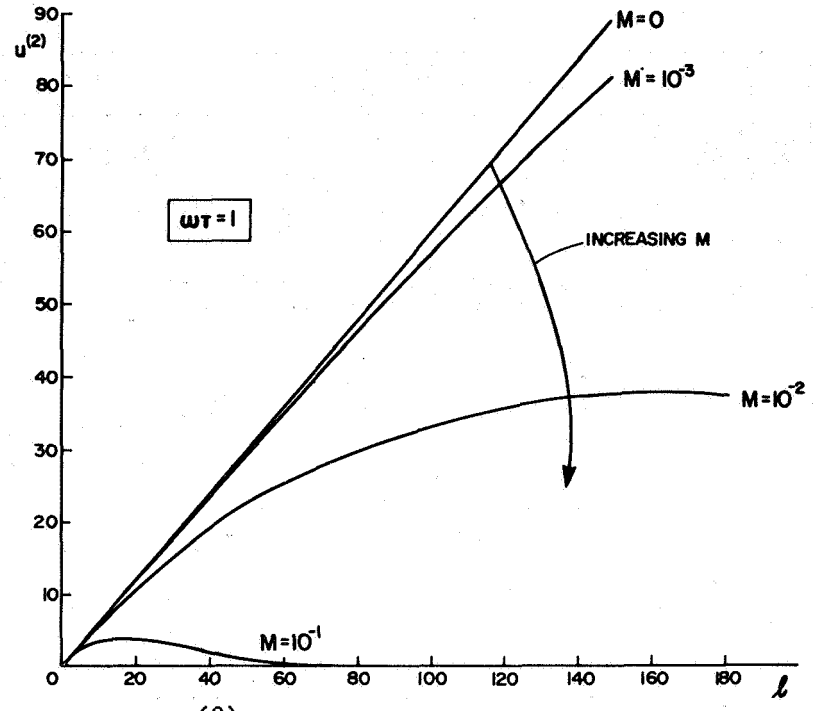

Figure 3.- Magnitude of $u^{(2)}$ versus dimensionless distance from wavetrain berth as finite-amplitude pure sinusoid showing functional dependence on M.

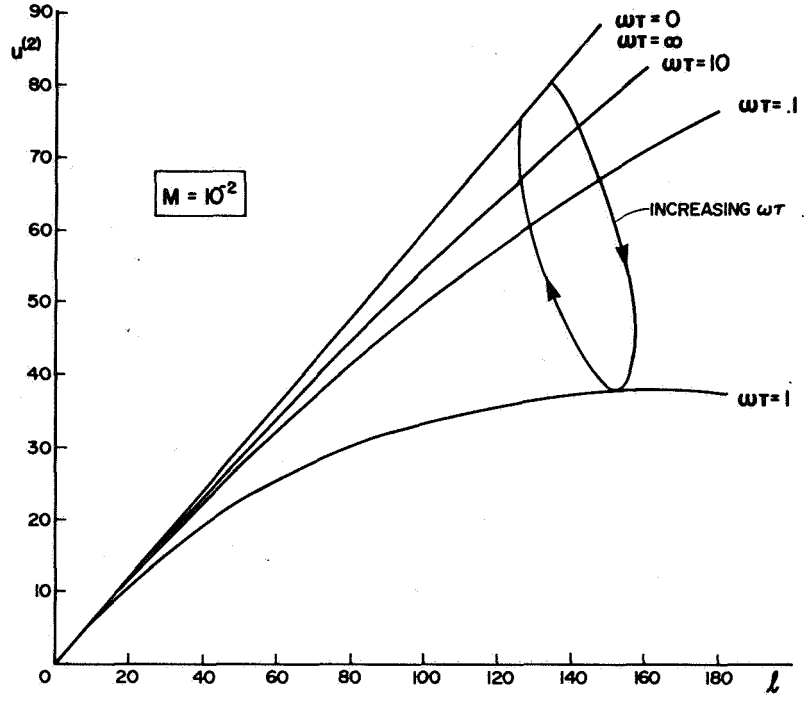

Figure 4.- Magnitude of $u^{(2)}$ versus dimensionless distance from wavetrain berth as finite-amplitude pure sinusoid showing functional dependence on $\omega\tau$.

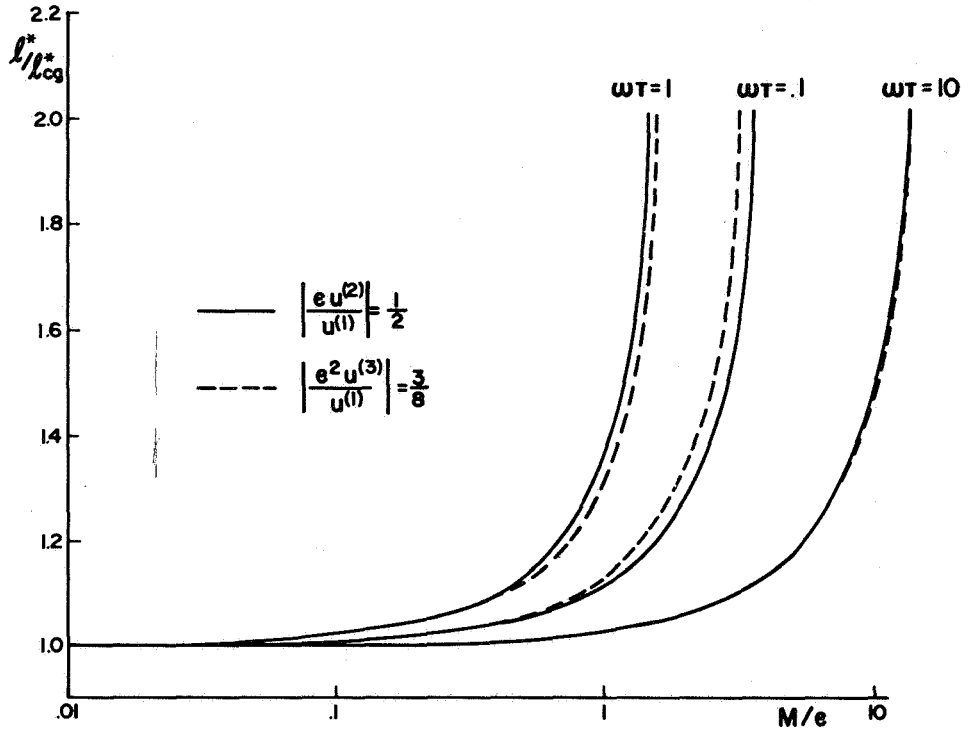

Figure 5.- Normalized dimensionless shock-formation distance versus M/ε parameter as a function of ωτ.

ONE-DIMENSIONAL WAVE PROPAGATION IN PARTICULATE SUSPENSIONS

Steve G. Rochelle and John Peddieson, Jr.
Tennessee Technological University

SUMMARY

One-dimensional small-amplitude wave motion in a two-phase system consisting of an inviscid gas and a cloud of suspended particles is analyzed using a continuum theory of suspensions. Laplace transform methods are used to obtain several approximate solutions. From these solutions are inferred some of the interesting properties of acoustic wave motion in particulate suspensions.

INTRODUCTION

This paper is concerned with small-amplitude wave propagation in a particulate suspension contained within a semi-infinite tube. Small-amplitude wave propagation in particulate suspensions is of interest because of applications to problems involving sound attenuation in fogs, flow visualization, nuclear reactor cooling systems, and combustion instabilities in rocket motors. Most previous work is devoted to various aspects of the problem of harmonic wave propagation in a suspension of infinite extent. Representative of early papers on this subject are those by Sewell (ref. 1), Epstein (ref. 2), and Epstein and Carhart (ref. 3). In these papers the flow past each particle was considered in detail, at least in principle. More recent calculations have employed two-phase continuum models of suspension behavior. In general, these models are appropriate when a representative volume element of the suspension, which is small compared to the characteristic dimensions of the flow field, contains an amount of fluid and an amount of particles sufficiently large to allow the formation of meaningful averages of the properties of the two phases within the volume element. Then the volume is treated as a differential element (a point) and the averages are treated as continuous variables. Representative of this approach to problems of small-amplitude wave propagation in suspensions are the work of Temkin and Dobbins (ref. 4), Morfey (ref. 5), Schmitt von Schubert (ref. 6), Marble and Wooten (ref. 7), Goldman (ref. 8), Mecredy and Hamilton (ref. 9), and the review articles by Marble (ref. 10), and Rudinger (ref. 11). Marble (ref. 10) points out that comparison of the predictions of continuum theories with the more detailed analysis given by Epstein and Carhart (ref. 3) shows that the continuum approach is completely adequate for wavelengths that are long compared to the particle dimensions.

In the present paper a simple continuum theory of particulate suspension behavior is applied to the problem of small-amplitude wave motion of a suspension in a semi-infinite tube. In contrast to the large amount of work on

harmonic wave propagation, there appears to be little (if any) work available on the propagation of non-harmonic waves. In order to focus attention on the basic relaxation mechanism inherent in such two-phase flows, several simplifying assumptions are made. These are: the motion is one-dimensional, the fluid phase can be modeled as an inviscid gas obeying a linear pressure-density relationship, the interphase force is directly proportional to the vector difference between the velocities of the two phases (thus, contributions due to added mass, history, etc. are neglected), and the volume fraction of the particle phase is small. The linear acoustic equations which follow from these assumptions are solved by the Laplace transform method for a step input of velocity at the end of the tube.

GOVERNING EQUATIONS

Let ρ_o be the initial gas-phase density, γ_o be the initial particle-phase density, a be the clean-gas speed of sound, U be the inlet gas velocity, $M = U/a$ be a Mach number, and τ be the relaxation time of the suspension (see Marble, reference 10). If the usual acoustic linearizations are made, the balance equations for mass and linear momentum and the equation of state take the dimensionless forms

$$\partial_t \rho + \partial_x u = 0, \quad \partial_t u = -\partial_x p + \kappa(v-u), \quad p = \rho \tag{1}$$

for the gas phase, and

$$\partial_t \gamma + \partial_x v = 0, \quad \partial_t v = u - v \tag{2}$$

for the particle phase. In equations (1) and (2) $a\tau x$ is the axial coordinate, $\tau\tau$ is time, Uu is the gas-phase velocity, Uv is the particle-phase velocity, $\rho_o M\rho$ is the difference between the current and initial gas densities, $\gamma_o M\gamma$ is the difference between the current and initial particle-phase densities, $\rho_o UaP$ is the difference between the current and initial pressures, and $\kappa = \gamma_o/\rho_o$. It can be seen that equations (1) and (2) are five equations involving five unknowns. Thus it is not necessary to consider the balance-of-energy equations for the two phases in order to determine the mechanical behavior. This is the reason for the second simplifying assumption discussed in the previous section.

Equations (1a), (1b), and (1c) can be combined to yield the modified wave equation

$$\partial_{tt} u = \partial_{xx} u + \kappa(\partial_t v - \partial_t u) \tag{3}$$

Equations (2b) and (3) can be solved simultaneously for u and v. Then equation (1a) can be solved for ρ and equation (2a) can be solved for γ.

It should be noted that the dimensional form of the equation of state is

$$(\rho_o Uap) = a^2(\rho_o M\rho) \tag{4}$$

Thus the dimensional clean-gas speed of sound is

$$d(\rho_o U a \rho)/d(\rho_o M \rho) = a^2 \tag{5}$$

as originally stated. Because of the way a was used in the nondimensionalization process it can be seen from equation (1c) that the dimensionless clean-gas speed of sound is

$$dp/d\rho = 1 \tag{6}$$

LAPLACE TRANSFORM OF SOLUTION

The suspension is contained in a semi-infinite pipe beginning at $x = 0$ and extending along the positive x axis. The suspension is at rest until $t = 0$ when a constant gas inlet velocity is suddenly created. Thus

$$u(0,t) = \Delta(t) \tag{7}$$

where the symbol $\Delta(\xi)$ is used to denote a unit step function. That is

$$\Delta(\xi) = \begin{cases} 0, & \xi < 0 \\ 1, & \xi > 0 \end{cases} \tag{8}$$

Taking the Laplace transforms of equations (1a), (1b), (2a), (2b), (3), and (7) one obtains

$$s\bar{\rho} + \bar{u}' = 0, \quad s\bar{\gamma} + \bar{v}' = 0$$

$$s^2\bar{u} = \bar{u}'' + \kappa s(\bar{v} - \bar{u}), \quad s\bar{v} = \bar{u} - \bar{v} \tag{9}$$

$$\bar{u}(0) = 1/s \tag{10}$$

where s is the Laplace transform parameter, a superposed bar denotes a Laplace transform, and a prime denotes differentiation with respect to x. Equations (9c) and (9d) can be combined to yield

$$\bar{u}'' - s^2 b^2 \bar{u} = 0 \tag{11}$$

where

$$b(s) = (1 + \kappa/(1 + s))^{\frac{1}{2}} \tag{12}$$

Solving equation (11) subject to equation (10) and the condition that $\bar{u}(x)$ should remain bounded for all $x > 0$, and substituting this solution into equations (9a), (9b), and (9d) leads to

$$\bar{u} = \exp(-sbx)/s, \quad \bar{v} = \exp(-sbx)/(s(1 + s))$$

$$\bar{\rho} = b \exp(-sbx)/s, \quad \bar{\gamma} = b \exp(-sbx)/(s(1 + s)) \tag{13}$$

It appears that no exact inversions of equations (13) can be obtained in terms of elementary functions. In subsequent sections several simple approximate inversions will be found and used to illustrate some of the properties of the solution to this problem.

INVERSION FOR SMALL TIMES

Approximate solutions for $t \ll 1$ can be obtained by expanding various functions appearing in equation (13) for $s \gg 1$. Expanding b (eq. (12)) in this way and retaining the first two terms leads to

$$b \doteq 1 + \kappa/(2s) \tag{14}$$

If only the first term in equation (14) is retained the corresponding inversions of equations (13) are (see Roberts and Kaufman, reference 12)

$$u \doteq \rho \doteq \Delta\,(t - x)$$

$$v \doteq \gamma \doteq (1 - \exp(-(t - x)))\Delta(t - x) \tag{15}$$

Equations (15a) and (15b) represent the solution for a clean gas. Thus immediately after the beginning of the motion, the motion is independent of the presence of the particles.

If the first two terms in equation (14) are retained the corresponding inversions are found to be

$$u \doteq \exp(-\kappa x/2)\Delta(t - x)$$

$$\rho \doteq \exp(-\kappa x/2)(1 + \kappa(t - x)/2)\Delta(t - x)$$

$$v \doteq \exp(-\kappa x/2)(1 - \exp(-(t - x)))\Delta(t - x)$$

$$\gamma \doteq \exp(-\kappa x/2)((1 - \kappa/2)(1 - \exp(-(t - x))) + \kappa(t - x)/2)\Delta(t - x) \tag{16}$$

Equations (16) illustrate the coupling between the motions of the two phases which manifests itself as the time since the beginning of the motion increases. To interpret these results most easily it is useful to remember that nonzero results are obtained only for $t > x$. Thus the condition $t \ll 1$ implies that equations (16) are valid only for $x \ll 1$ and $(t-x) \ll 1$. Simplifying equations (16c) and (16d) for $(t-x) \ll 1$ leads to

$$u \doteq \exp(-\kappa x/2)\Delta(t - x)$$

$$\rho \doteq \exp(-\kappa x/2)(1 + \kappa(t - x)/2)\Delta(t - x)$$

$$v \doteq \exp(-\kappa x/2)(t - x)\Delta(t - x)$$

$$\gamma \doteq \exp(-\kappa x/2)(t - x)\Delta(t - x) \tag{17}$$

Some observations based on equations (17) are as follows. For small t all disturbances propagate with the clean-gas wave speed 1. The amplitudes of all variables decrease with increasing x. For large values of the particle loading κ this effect can be significant. For a given value of $t-x$ (the time since the wave front passed position x) the degree of spatial attenuation increases with x. For a given value of x, the terms ρ, v, and γ are increasing functions of the time since passage of the wave front.

INVERSION FOR LARGE TIMES

Approximate solutions for $t \gg 1$ can be found by expanding the various functions appearing in equation (13) for $s \ll 1$. Expanding b (eq. (12)) in this way and retaining the first two terms gives

$$b \doteq (1 + \kappa) - \kappa s \tag{18}$$

Retaining only the first term in equation (18), substituting into equations (13), and inverting yields

$$u \doteq \Delta(t - (1+\kappa)^{\frac{1}{2}}x), \quad \rho \doteq (1+\kappa)^{\frac{1}{2}}\Delta(t-(1+\kappa)^{\frac{1}{2}}x)$$

$$v \doteq (1 - \exp(-(t-(1+\kappa)^{\frac{1}{2}}x)))\Delta(t-(1+\kappa)^{\frac{1}{2}}x)$$

$$\gamma \doteq (1+\kappa)^{\frac{1}{2}}(1-\exp(-(t-(1+\kappa)^{\frac{1}{2}}x)))\Delta(t-(1+\kappa)^{\frac{1}{2}}x) \tag{19}$$

It can be seen from equations (19) that for $t \gg 1$ all quantities propagate with wave speed $1/(1+\kappa)^{\frac{1}{2}}$. For values of x away from the wave front u and v are essentially equal as are ρ and γ. For values of x near the wave front differences between the velocities and densities remain for arbitrarily large values of t. In contrast to equation (17a), equation (19a) predicts that the gas velocity has a value of unity for all x. Thus the amplitude of u at a given x must increase with time. More insight into this matter will be provided by the results obtained in the next section.

It was attempted to invert equations (13) using the first two terms of the expansion of b for small s (eq. (18)). No inversion in terms of elementary functions could be found.

INVERSION FOR SMALL PARTICLE LOADING

Expanding equation (12) for $\kappa \ll 1$ and retaining the first two terms one gets

$$b \doteq 1 + \kappa/(2(1 + s)) \tag{20}$$

If equations (13) are inverted using only the first term of equation (20) the results are equations (15). For the important special case of negligible

particle loading equations (15) represent the exact solution. To find a correction for finite values of κ two terms of equation (20) must be retained. If equation (20) is substituted into equation (13) no simple inversion of the resulting expressions appears possible. Further simplification is achieved by expanding the exponentials involving b for small κ and keeping the first two terms. This results in

$$\bar{u} \doteq (1 - \kappa sx/(2(1 + s)))\exp(-sx)/s$$

$$\bar{\rho} \doteq (1 - \kappa(sx - 1)/(2(1 + s)))\exp(-sx)/s$$

$$\bar{v} \doteq (1 - \kappa sx/(2(1 + s)))\exp(-sx)/(s(1 + s))$$

$$\bar{\gamma} \doteq (1 - \kappa(sx-1)/(2(1 + s)))\exp(-sx)/(s(1 + s)) \qquad (21)$$

Inverting equations (21) yields

$$u \doteq (1 - \kappa x \exp(-(t - x))/2)\Delta(t - x)$$

$$\rho \doteq (1 + \kappa(1 - (1 + x)\exp(-(t - x)))/2)\Delta(t - x)$$

$$v \doteq (1 - \exp(-(t - x)) - \kappa x(t - x)\exp(-(t - x))/2)\Delta(t - x)$$

$$\gamma \doteq (1 - \exp(-(t - x)) + \kappa(1 - \exp(-(t - x))$$

$$- (1 + x)(t - x)\exp(-(t - x)))/2)\Delta(t - x) \qquad (22)$$

These expressions appear to be computationally useful for small x and all t. Equation (22a) shows that for a given x the value of u at the time of passage of the wave front is $1 - \kappa x/2$. (Note that this is the two-term expansion for small κ of the $\exp(-\kappa x/2)$ appearing in equation (16a)). As the time t-x since passage of the wave front increases, the amplitude of u increases to unity. Similarly it can be seen that the value of v for large t-x is unity while the values of both ρ and γ for large t-x are $1+\kappa/2$ which is the two-term expansion for small κ of the $(1+\kappa)^{\frac{1}{2}}$ appearing in equations (19b) and (19d). Thus the large-time limiting values predicted by equations (22) are consistent with those predicted by equations (19). Equations (22) do not predict the change in wave speed indicated by equations (19). It can be shown that this is due to the process of expanding the arguments of the exponentials appearing in equations (13) before inversion. For $\kappa << 1$ the difference between $(1+\kappa)^{\frac{1}{2}}$ and unity is small so this is not a serious matter.

DISCUSSION OF RESULTS

From the three sets of approximate solutions developed in the previous sections (eqs. (16), (19), and (22)) it is possible to put together a fairly complete picture of the wave motion produced by a step velocity input at x = 0. All waves travel with the same wave speed. For small times this is unity and for large times it is $1/(1+\kappa)^{\frac{1}{2}}$. The former is called the frozen wave speed. It is

the wave speed associated with the clean gas. The latter is called the equilibrium wave speed. It is the wave speed associated with wave motion in a gas having initial density equal to the initial suspension density. These results are to be expected on physical grounds. For small times the motion of the gas (through which the waves propagate) is independent of the presence of the particles as indicated by equations (15). For large times the velocities of both phases are essentially equal. Thus the suspension behaves like a gas with effective dimensionless density $1+\kappa$. The exact manner by which the transition from the frozen to the equilibrium wave speed is accomplished is not revealed by the approximate solutions obtained in this work.

The gas velocity u has the prescribed value of unity at the inlet and decreases to a minimum value at the wave front. The value of u at each point behind the wave front increases with time and eventually approaches unity. The particle velocity v and the fluid- and particle-density perturbations, ρ and γ respectively, are also decreasing functions of x. Their values for all values of x (including $x = 0$) increase with time. Finally ρ approaches a constant value throughout the region of motion while v and γ approach constant values except near the wave front. Because the step increase in gas velocity must be transmitted to the particles through the interphase-momentum-transfer mechanism the particles in the immediate vicinity of the wave front can never quite catch up to the gas.

It should be pointed out that for $t > 0$ a particle-free zone exists adjacent to the inlet. It can be shown that the speed of the forward boundary of this region is $O(M)$. Since the acoustic equations are valid only for small Mach numbers, and since the speed of the wave front is $O(1)$, the length of the particle-free zone is negligible compared to the length of the region of motion. For this reason the particle-free zone was neglected in this analysis. For waves of finite amplitude this could not be done. The position of the forward boundary of the particle-free zone would have to be computed as part of the solution. This would greatly increase the complexity of the analysis.

CONCLUSION

In this paper the problem of small-amplitude wave propagation in a particulate suspension was analyzed using a continuum theory of suspensions. The governing equations were solved approximately by the Laplace transform method. Three approximate inversions were developed and from these were inferred some of the properties of the wave motion.

REFERENCES

1. Sewell, C. J. F.: The Extinction of Sound in a Viscous Atmosphere by Small Obstacles of Cylindrical and Spherical Form. Phil. Trans. Roy. Soc. London, Series A, Math. Phys. Sciences, Vol. 210, 1910, pp. 239-270.

2. Epstein, P. S.: On the Absorption of Sound by Suspensions and Emulsions. Contributions to Applied Mechanics, Theodore von Karman Anniversary Volume. Calif. Inst. of Tech., 1941, pp. 162-188.

3. Epstein, P. S., and Carhart, R. R.: The Absorption of Sound in Suspensions and Emulsions, I. Water Fog in Air. J. Acoust. Soc. Am., Vol. 25, 1953, pp. 553-565.

4. Temkin, S., and Dobbins, R. A.: Attenuation and Dispersion of Sound by Particulate-Relaxation Processes. J. Acoust. Soc. Am., Vol. 40, 1966, pp. 317-324.

5. Morfey, C. C.: Sound Attenuation by Small Particles in a Fluid. J. Sound Vib., Vol. 8, 1968, pp. 156-170.

6. Schmitt von Schubert, B.: Schallwellen in Gasen Mit Festen Teilchen. ZAMP, Vol. 20, 1969, pp. 922-935.

7. Marble, F. E., and Wooten, D. C.: Sound Attenuation in a Condensing Vapor. Physics of Fluids, Vol. 13, 1970, pp. 2657-2664.

8. Goldman, E. B.: Absorption and Dispersion of Ultrasonic Waves in Mixtures Containing Volatile Particles. J. Acous. Soc. Am., Vol. 47, 1970, pp. 768-776.

9. Mecredy, R. C., and Hamilton, L. J.: The Effects of Nonequilibrium Heat, Mass, and Momentum Transfer on Two-Phase Sound Speed. Int. J. Heat Mass Transfer, Vol. 15, 1972, pp. 61-72.

10. Marble, F. E.: Dynamics of Dusty Gases. Annual Review of Fluid Mechanics, Vol. 2, 1970, pp. 397-447.

11. Rudinger, G.: Wave Propagation in Suspensions of Solid Particles in Gas Flow. Applied Mechanics Review, Vol. 26, 1973, pp. 273-279.

12. Roberts, G. E., and Kaufman, H.: Table of Laplace Transforms. W. B. Saunders Co., 1966, Part 2.

A CORRESPONDENCE PRINCIPLE FOR STEADY-STATE WAVE PROBLEMS*

Lester W. Schmerr
Iowa State University

SUMMARY

A correspondence principle has been developed for treating the steady-state propagation of waves from sources moving along a plane surface or interface. This new principle allows one to obtain, in a unified manner, explicit solutions for any source velocity. To illustrate the correspondence principle in a particular case, the problem of a load moving at an arbitrary constant velocity along the surface of an elastic half-space is considered.

INTRODUCTION

Certain problems in the linear theory of wave propagation are of fundamental importance to a wide variety of fields. One of these is the response of a plane interface between two different materials to moving transient sources of disturbance. The reflection and refraction of plane transient waves at an interface (refs. 1-3) and the generation of waves from specified sources moving at a constant velocity along an interface (refs. 4-7) are two important examples of this type of problem. In such cases it is usually assumed that the surrounding media is in plane motion and that a steady-state wave pattern exists relative to an observer moving with the source of disturbance. The resulting two-dimensional steady-state boundary value problem can then be solved either by transform techniques or by the use of complex function theory and the method of characteristics (see refs. 8 and 9).

In many problems, however, both of these traditional methods are very inefficient. This is because it is necessary to pose and solve separately the special cases when the source velocity is less than or greater than each of the characteristic wavespeeds in the surrounding media. This paper demonstrates that it is possible to treat all such special cases in a simple, unified manner through the application of a newly developed correspondence principle. In addition, this correspondence principle leads to a new and direct representation for the general solution of steady-state interface problems.

PROBLEM STATEMENT

Consider two homogeneous, isotropic semi-infinite media (either fluid or solid) which are in contact along the plane $\bar{y} = 0$ and which contain disturbances traveling at a constant velocity U in the negative $\bar{x}$-direction. We assume that these disturbances are uniform in the $\bar{z}$-direction and that a steady-state motion exists in the semi-infinite media. Under these conditions, the governing equations of motion in the two media reduce to (ref. 8):

*This work was supported by the Engineering Research Institute, Iowa State University.

$$(1 - U^2/c_m^2)\partial^2\phi_m/\partial x^2 + \partial^2\phi_m/\partial y^2 = 0 \qquad (m = 1,\ldots j) \tag{1}$$

in a set of moving coordinates (x,y,z) defined by $x = \bar{x} + Ut$, $y = \bar{y}$, $z = \bar{z}$. In equation (1), $\phi_m = \phi_m(x,y)$ and c_m are the displacement potentials and their corresponding wavespeeds, respectively, for the two media.

Along the surface $y = 0$, the ϕ_m must satisfy a certain set of boundary or continuity conditions which, in general, can be written in terms of the second order partial derivatives of the ϕ_m as

$$E_n(\partial^2\phi_m/\partial x^2,\ \partial^2\phi_m/\partial x\partial y,\ \partial^2\phi_m/\partial y^2) = P_n(x) \qquad (n = 1,\ldots j) \tag{2}$$

where the E_n also depend on the source speed U and the material properties of the two media and are linear functions of their arguments. The vector $\underline{P} = \{P_n(x)\}$ is determined by the values of the source disturbances along the plane $y = 0$ and is assumed to be given.

Since the linear operators which appear in equation (1) are hyperbolic if $U > c_m$ and elliptic if $U < c_m$, the steady-state solutions of these equations will depend on the relative size of U and the wavespeeds c_m. Consider first the "totally supersonic" (TSS) case (i.e. where $U > c_m$ is satisfied for all m in equation (1)).

Totally Supersonic Case

In the TSS case, the general solutions to the equations of motion (1) can be written as

$$\phi_m = F_m(x - \beta_m|y|) \tag{3}$$

where $\beta_m = (U^2/c_m^2 - 1)^{1/2}$ and the bars denote "absolute value of". In equation (3), solutions of the type $F_m(x + \beta_m|y|)$ have been rejected since they represent disturbances traveling in the positive x-direction and, hence, would violate the "radiation conditions" (ref. 8).

The second order partial derivatives of the ϕ_m then become

$$\left.\begin{aligned} \partial^2\phi_m/\partial x^2 &= F_m'' \\ \partial^2\phi_m/\partial x\partial y &= -\,\mathrm{sgn}(y)\beta_m F_m'' \\ \partial^2\phi_m/\partial y^2 &= \beta_m^2 F_m'' \end{aligned}\right\} \tag{4}$$

where F_m'' denote the second derivatives of F_m with respect to their arguments and sgn stands for "sign of". Placing equation (4) into equation (2) thus yields a set of linear equations in the F_m'' on $y = 0$, which using the summation convention can be written as

$$A_{nm}F_m''(x) = P_n(x) \qquad (n = 1,\ldots j) \tag{5}$$

Here, the $\tilde{A}$ is a real jxj matrix involving only the material properties of the given media and the disturbance speed U. Assuming that the matrix is non-singular, we can then solve for the F_m'', obtaining formally

$$F_m''(x) = A^{-1}_{mn}P_n(x) \tag{6}$$

and these results can be continued into the two media, using equation (3), to give:

$$\phi_m'' = A^{-1}_{mn}P_n(x - \beta_n|y|) \tag{7}$$

The stresses in each media can be obtained directly from equation (7) since they are simply linear functions of the ϕ_m''. The displacements or velocities, however, must be found from these results by a single integration. This TSS case is of fundamental importance for steady-state interface problems of the type we have been discussing because it contains implicitly, through equation (6), the solution for all other cases when this equation is interpreted in an operational sense. To prove this we now consider the general case.

General Case

Consider the general case when $U/c_m < 1$ for $m = 1,\ldots k$, where $k \leq j$. Then the governing equations (1) are hyperbolic for $m > k$ and elliptic for $m \leq k$, and their general solutions are

$$\left.\begin{aligned} \phi_m &= \mathrm{Re}\{G_m(x + i\bar{\beta}_m|y|)\} \qquad m \leq k \\ \phi_m &= F_m(x - \beta_m|y|) \qquad k < m \leq j \end{aligned}\right\} \tag{8}$$

where $\bar{\beta}_m = (1 - U^2/c_m^2)^{1/2}$, Re denotes "real part of", and the G_m for $m \leq k$ are analytic functions of the complex variables $x + i\bar{\beta}_m|y|$. For $m > k$, the second order partial derivatives of the ϕ_m are again given by equation (4). For $m \leq k$, we now obtain instead

$$\left.\begin{aligned} \partial^2\phi_m/\partial x^2 &= \mathrm{Re}\{G_m''\} \\ \partial^2\phi_m/\partial x\partial y &= -\,\mathrm{sgn}(y)\,\bar{\beta}_m\,\mathrm{Im}\{G_m''\} \\ \partial^2\phi_m/\partial y^2 &= -\,\bar{\beta}_m^2\,\mathrm{Re}\{G_m''\} \end{aligned}\right\} \tag{9}$$

where Im denotes "imaginary part of". However, on the boundary y = 0 the real and imaginary parts of these G_m'' satisfy a pair of Hilbert transforms

$$\mathrm{Re}\{G_m''\} = H[\mathrm{Im}\{G_m''\}]$$

$$\mathrm{Im}\{G_m''\} = -\,H[\mathrm{Re}\{G_m''\}]$$

where the Hilbert transform is

$$H[f] = 1/\pi \int_{-\infty}^{\infty} f d\xi/(\xi - x)$$

and the integral is understood to be taken in the principal value sense. Hence, the partial derivatives on y = 0 can be written in terms of $Re\{G_m''\}$ only as

$$\left.\begin{aligned} \partial^2\phi_m/\partial x^2 &= Re\{G_m''\} \\ \partial^2\phi_m/\partial x\partial y &= sgn(0\pm)\bar{\beta}_m H[Re\{G_m''\}] \\ \partial^2\phi_m/\partial y^2 &= -\bar{\beta}_m^2 Re\{G_m''\} \end{aligned}\right\} \qquad (10)$$

Note now that on the boundary y = 0, equations (4) and (10) will be identical if we make the following replacements in the TSS expressions (4) for $m \leq k$.

$$\beta_m \rightarrow -i\bar{\beta}_m \qquad (11)$$

and identify the F_m'' in the TSS case with the G_m'' in the general case through the additional replacements for $m \leq k$ given by:

$$\left.\begin{aligned} F_m'' &\rightarrow Re\{G_m''\} \\ iF_m'' &\rightarrow H[Re\{G_m''\}] \end{aligned}\right\} \qquad (12)$$

Thus, on the boundary y = 0 there is a one-to-one correspondence between the complex-valued TSS problem obtained by making the substitutions given by equation (11) and the general case problem if, as equation (12) shows, the appearance of the imaginary number i in the TSS problem is interpreted as representing the Hilbert transform operator in the general case. This correspondence also means that the complex-valued matrices $\underset{\sim}{A}$ and $\underset{\sim}{A}^{-1}$, which result in equations (5) and (6) from the substitutions given by equation (11), must be interpreted as representing matrix operators in the general case. In particular, breaking $\underset{\sim}{A}^{-1}$ into its real and imaginary parts, we have

$$A_{mn}^{-1} = a_{mn} + ib_{mn} \rightarrow a_{mn} + b_{mn}H[\cdot] \qquad (13)$$

where a_{mn} and b_{mn} are both real. Using this result and equations (6) and (12), we see that on y = 0 the general case solution is given by

$$\left.\begin{aligned} F_m''(x) &= a_{mn}P_n(x) + b_{mn}H[P_n(x)] \qquad k < m \leq j \\ Re\{G_m''(x)\} &= a_{mn}P_n(x) + b_{mn}H[P_n(x)] \qquad m \leq k \end{aligned}\right\} \qquad (14)$$

Since the general solutions for $m > k$ are constant along the real characteristics $x - \beta_m|y|$ (see equation (8)), the F_m'' can be continued directly into the adjacent media and the general case solution written as

$$\phi_m'' = a_{mn}P_n(x - \beta_n|y|) + b_{mn}H[P_n(x - \beta_n|y|)] \qquad k < m \leq j \tag{15}$$

For $m \leq k$, however, our problem consists of finding the functions $G_m''(x + i\bar{\beta}_m|y|)$ which are analytic in the upper half of the complex-plane and whose real part is given on the real axis by equation (14). This is a standard problem in analytic function theory whose solution may be written as

$$G_m'' = 1/i\pi \int_{-\infty}^{\infty} A_{mn}^{-1}P_n(\xi)d\xi/(\xi - z_m) \qquad m \leq k \tag{16}$$

provided the integral converges, where $z_m = x + i\bar{\beta}_m|y|$. As before, the stresses can be obtained directly from equations (15) and (16) although a further integration is necessary for displacements and velocities.

With the general solutions given by equations (15) and (16), it is now particularly easy to obtain the solution to steady-state interface problems for arbitrary source velocity. All that is needed is the inverse matrix $\underset{\sim}{A}^{-1}$ from the TSS case solution. In the general case this matrix becomes complex-valued when the substitution in equation (11) is made. A simple algebraic decomposition of $\underset{\sim}{A}^{-1}$ into its real and imaginary parts for each special case then gives the necessary matrices for the expressions in equations (15) and (16). To illustrate the use of this method we now consider a particular problem.

MOVING LOAD ON A HALF-SPACE

A number of authors (refs. 4-7) have previously considered the response of an elastic half-space to loads traveling at a constant velocity on the plane surface. Here, we will solve for the waves generated in the half-space $\bar{y} \geq 0$, $-\infty < \bar{x} < \infty$, $-\infty < \bar{z} < \infty$ by a moving distributed load of intensity P(x) in the moving coordinates $x = \bar{x} + Ut$, $y = \bar{y}$, $z = \bar{z}$ (figure 1). Then the normal stress, t_{yy}, and shearing stress, t_{xy}, on the surface are given by

$$\left.\begin{aligned} t_{yy} &= -P(x)\sin\theta \\ t_{xy} &= P(x)\cos\theta \end{aligned}\right\} \tag{17}$$

where θ is the angle between the direction of the applied load and the half-space surface. In this case there are only two displacement potentials ϕ_1 and ϕ_2, which correspond to dilatational and shear wave disturbances, respectively, and two corresponding wavespeeds c_1 and c_2. Application of the boundary conditions (17) yields the matrix $\underset{\sim}{A}$ and vector $\underline{P}$ given by (ref. 8):

$$\underset{\sim}{A} = \begin{bmatrix} (M_2^2 - 2) & -2\beta_2 \\ -2\beta_1 & -(M_2^2 - 2) \end{bmatrix} \qquad \underline{P} = \begin{bmatrix} -P\sin\theta/\mu \\ P\cos\theta/\mu \end{bmatrix} \tag{18}$$

where μ is the shear modulus and $M_2 = U/c_2$. Then the inverse matrix $\underset{\sim}{A}^{-1}$ is given by

$$\underset{\sim}{A}^{-1} = \begin{bmatrix} (M_2^2 - 2)/D & -2\beta_2/D \\ -2\beta_1/D & -(M_2^2 - 2)/D \end{bmatrix} \tag{19}$$

where $D = (M_2^2 - 2)^2 + 4\beta_1\beta_2$. Table 1 shows the breakdown of this inverse matrix into its real and imaginary parts. In that table $D_1 = (M_2^2 - 2)^4 + 16\bar{\beta}_1\beta_2$ and $D_2 = (M_2^2 - 2)^2 - 4\bar{\beta}_1\bar{\beta}_2$. When those results are placed back into equations (15) and (16), the problem is then formally complete. To illustrate the use of these expressions for a particular loading, consider the case of a moving concentrated line load, i.e. $P(x) = P\delta(x)$ where P is a constant and $\delta(x)$ is the Dirac delta function. Then we obtain:

Totally Supersonic Case ($U > c_1 > c_2$)

$$\phi_1'' = (-a_{11}\sin\theta + a_{12}\cos\theta)P\delta(x - \beta_1 y)/\mu$$
$$\phi_2'' = (-a_{21}\sin\theta + a_{22}\cos\theta)P\delta(x - \beta_2 y)/\mu$$

Transonic Case ($c_2 < U < c_1$)

$$G_1'' = (a_{11}\sin\theta - a_{12}\cos\theta)P/i\pi\mu Z_1 + (b_{11}\sin\theta - b_{12}\cos\theta)P/\pi\mu Z_1$$
$$\phi_2'' = (-a_{21}\sin\theta + a_{22}\cos\theta)P\delta(x - \beta_2 y)/\mu$$
$$+ (b_{21}\sin\theta - b_{22}\cos\theta)P/\pi\mu(x - \beta_2 y)$$

Subsonic Case ($U < c_2$)

$$G_1'' = (a_{11}\sin\theta - ib_{12}\cos\theta)P/i\pi\mu Z_1$$
$$G_2'' = (-a_{22}\cos\theta + ib_{21}\sin\theta)P/i\pi\mu Z_2$$

Similar results to these have been derived by the traditional complex variable and characteristics approach in the treatise by Eringen and Suhubi (ref. 9).

CONCLUDING REMARKS

The correspondence principle developed above has led to a new unified form of the solution for steady-state interface problems (equations 15 and 16) which can be efficiently used to treat a number of problems. In addition, this principle clearly demonstrates the close relationship that exists between the structure of the general solution and the TSS case. This relationship is currently being extended to steady-state problems in anisotropic media.

REFERENCES

1. Friedlander, F. G.: On the Total Reflection of Plane Waves. Quart. Journ. Mech. Appl. Math, vol. 1, 1948, pp. 376-384.

2. Schmerr, L. W., Jr.: Pulse Distortion of an SV-Wave at a Free Surface. J. Appl. Mech., vol. 41, 1974, pp. 298-299.

3. White, J. E.: Seismic Waves-Radiation, Transmission, and Attenuation. McGraw-Hill Book Co., New York, 1965, pp. 26-38.

4. Sneddon, I. N.: The Stress Produced by a Pulse of Pressure Moving Along the Surface of a Semi-Infinite Solid. Rend. Cir. Mat. Palermo, vol. 2, 1952, pp. 57-62.

5. Cole, J.; and Huth, J.: Stresses Produced in a Half-Plane by Moving Loads. J. Appl. Mech., vol. 35, 1958, pp. 433-436.

6. Niwa, Y.; and Kobayashi, S.: Stresses Produced in an Elastic Half-Plane by Moving Loads Along its Surface. Mem. Fac. Engrg. Kyoto Univ., vol. 28, 1966, pp. 254-276.

7. Fryba, L.: Vibration of Solids and Structures Under Moving Loads. Noordhoff Int. Publishing Co., Groningen, 1970, pp. 269-305.

8. Fung, Y. C.: Foundations of Solid Mechanics. Prentice-Hall, Inc., Englewood Cliffs, New Jersey, 1965, pp. 259-268.

9. Eringen, A. C.; and Suhubi, E. S.: Elastodynamics - Volume Two: Linear Theory. Academic Press, New York, 1975, pp. 574-584.

TABLE I. - REAL AND IMAGINARY PARTS OF $\underset{\sim}{A}^{-1}$

CASES	MATRIX $\underset{\sim}{a}$		MATRIX $\underset{\sim}{b}$	
$U > C_1$	$\underset{\sim}{a} = \underset{\sim}{A}^{-1}$ (eq. (19))		$\underset{\sim}{b} = 0$	
$C_2 < U < C_1$	$(M_2^2 - 2)^3/D_1$	$-2\beta_2(M_2^2 - 2)^2/D_1$	$4\bar{\beta}_1\beta_2(M_2^2 - 2)/D_1$	$-8\bar{\beta}_1\beta_2^2/D_1$
	$-8\bar{\beta}_1^2\beta_2/D_1$	$-(M_2^2 - 2)^3/D_1$	$2\bar{\beta}_1(M_2^2 - 2)^2/D_1$	$-4\bar{\beta}_1\beta_2(M_2^2 - 2)/D_1$
$U < C_2$	$(M_2^2 - 2)/D_2$	0	0	$2\bar{\beta}_2/D_2$
	0	$-(M_2^2 - 2)/D_2$	$2\bar{\beta}_1/D_2$	0

$D_1 = (M_2^2 - 2)^4 + 16\bar{\beta}_1\beta_2$

$D_2 = (M_2^2 - 2)^2 - 4\bar{\beta}_1\bar{\beta}_2$

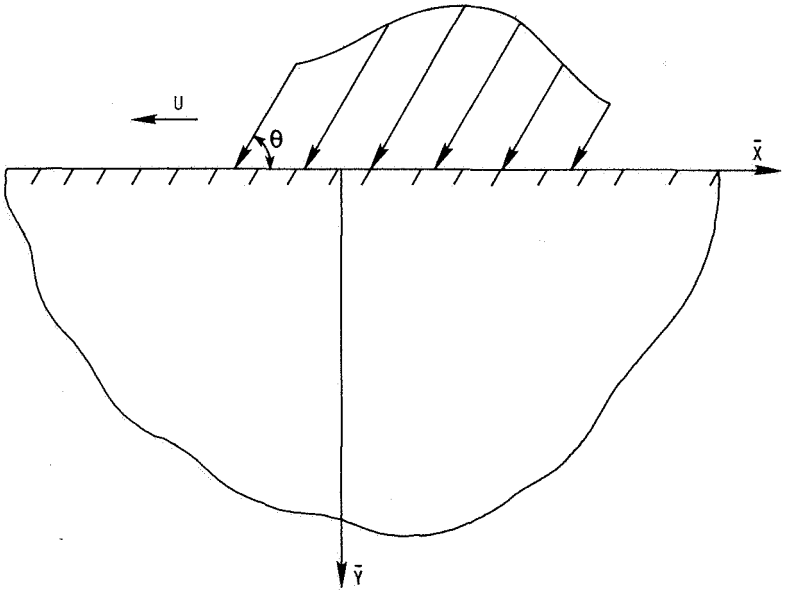

Figure 1.- Moving load on a half-space.

ACOUSTICAL PROBLEMS IN HIGH ENERGY PULSED E-BEAM LASERS

T. E. Horton and K. F. Wylie
University of Mississippi

SUMMARY

During the pulsing of high energy, CO_2, electron-beam (E-beam) lasers, a significant fraction of input energy ultimately appears as acoustical disturbances. The magnitudes of these disturbances are quantified by computer analysis. Acoustical and shock impedance data are presented on materials (Rayleigh type) which show promise in controlling acoustical disturbance in E-beam systems.

INTRODUCTION

The repetitively pulsed electron-beam (E-beam) laser, figure 1, has proven to be an efficient and compact means of achieving high power levels in CO_2 at atmospheric pressure, (ref. 1, 2, 3). In such a system the E-beam supplies high energy primary electrons which through secondaries produce a plasma in the laser cavity for a period τ_p, the time the gun is pulsed on. A sustainer voltage applied across the plasma supplies the energy for excitation of the laser states. By adjusting the sustainer field strength, the pumping of the laser state is optimized. As the lasing pulse duration approaches τ_1 (the relaxation time of the lower lasing state) optimum lasing output is achieved. For pulses less than τ_1 the lasing process is self-terminated by the incapacity of the lower state to relax; while for longer pulses the lower state capacity is reduced by gas heating. Practical values of τ_1 range from 1 to 10 μsec and are dependent upon gas composition and temperature. For the 1:2:3 (CO_2:N_2:He) mixture at 300 K considered in this work the value is 5 μsec.

In pulsed operation the sudden and sometimes nonuniform deposition of energy in the excited states of the laser media leads through vibrational energy cascading to pressure and temperature gradients which drive acoustical disturbances (ref. 4, 5, 6). Clearly, for efficient operation, these acoustical disturbances must be controlled since nonuniformity in the laser gas can lead to a reduction in beam quality and also to catastrophic arcing. To accommodate the heating of the laser gas, one must either execute a pulsed duty cycle of sufficient duration to allow dissipation of the energy or remove the energy from the cavity by flowing the gas through the cavity. The changes in gas properties and velocities which result from forced mass transport through the laser cavity and from heating the laser cavity have been designated as aero-acoustical effects.

The purpose of the present investigation is to quantify these effects and suggest promising means of controlling them. Constraints considered were

(1) power inputs up to 500 joules/liter of cavity gas, (2) laser cavity gas initially at standard temperature and pressure and composed of a 1:2:3 molar mixture of carbon dioxide, nitrogen, and helium, (3) the laser cavity has a 200-cm dimension along the optical axis, a 15-cm dimension between anode and cathode, and the discharge is considered to be 15 cm wide.

The first section of this paper delineates the magnitude of the problem created by bulk heating of the laser gas. The problem posed by nonuniform heating within the laser cavity, cathode waves, et al, have been treated in references 4, 5, and 6 and are not considered in this work. The second section treats the control of the discharge shocks by multiple reflection from low-pressure-drop, porous absorbers mounted in planes normal to the flow axis. In particular, the measured properties of Rayleigh materials, absorbers composed of thin walled tubers or honeycomb, are present in this second section. The paper concludes with a discussion of the feasibility of using the Rayleigh materials in a multiple reflection application.

MAGNITUDES FOR ACOUSTICAL DISTURBANCES

For optimum pulsed performance, the volumetric heating of the laser gas occurs by two relaxation paths. Initially during lasing, the rapid relaxation through the lower laser level results in a small temperature rise. The magnitude and time scale of this rise are insignificant acoustically. The primary heating takes place after lasing as the major fraction of the pumped energy cascades out of the upper states over the comparatively long period τ_u, the relaxation time of the upper laser level -- 60 μsec. Thus the acoustically significant temperature rise occurs on a time scale which is long for optimum lasing but which is short for significant changes in liter size systems. This justifies the assumption of constant volume heating of the gas in the laser cavity. These changes within the laser cavity lead to the formation of expansion and compression waves which are the source of acoustical problems in subsequent pulses.

For modeling the performance of an E-beam system, a computer program is desirable which, from a gasdynamic point of view, satisfies the coupled state, continuity, momentum, energy, and kinetic rate equations as a function of time over a three-dimensional array of points which includes the laser cavity and adjacent gas. When the gas is confined between two electrodes, as it is along the E-beam axis, and when some of the dimensions such as the optical axis are an order of magnitude or more greater than the other significant dimensions, then a one-dimension solution is a meaningful first approximation. Furthermore, with the short pulse condition argued above, the laser kinetics may be rationalized to be decoupled from the gasdynamic. The gasdynamics behavior is thus coupled to the kinetics in such a way that the problem can be posed as one of satisfying the one-dimensional mass, momentum, and energy conservation equations subject to a laser cavity heating rate predicted by constant volume laser code of reference 1.

A computer code incorporating the above assumptions is described in reference 7 and has been exercised to generate the results given below. Computations have been performed for a 1:2:3 mixture at power inputs ranging from 200 joules/liter to 500 joules/liter for beam turn-on times of 2 μsec and 10 μsec. For a 400-joule/liter input, the development of the compressive shock and expansion wave are illustrated over a 380-μsec interval in figure 2. Shortly after 140 μsec, the expansion wave will be reflected from the plane at the E-beam center, and a reduced density wave will propagate back through the 7.5-cm dimension of the discharge. The density minimum for the range of power inputs considered occurs at between 200 and 220 μsec. The variation of the minimum density in the reflected expansion wave with power input is illustrated in figure 3. These waves determine arcing limits for the sustainer field. For the energy inputs considered, the compressive waves were equivalent to the following Mach number shocks in air:

Energy Input (joules/liter)	Shock Mach Number	$\frac{\Delta P}{P}$
500	1.35	.960
400	1.28	.745
300	1.22	.570
200	1.15	.376

The strength of these shocks are far greater than the usual disturbances encountered in acoustics, with the equivalent sound intensities of 100 watts/cm^2 and 1000 watts/cm^2 for the 200-joule/liter and 500-joule/liter energy loadings. Thus the shocks listed above fall in the 180- to 190-db intensity range -- 40 to 50 db above the threshold of pain and 110 to 120 db above the normal speech level.

Another way to put the magnitude of the "acoustical problem" is to consider the amount of the energy input which is deposited in the adjacent gas as the laser cavity gas expands. A simple analysis based on constant volume heating with subsequent isentropic expansion back to atmospheric pressure yields the results given in figure 4. Clearly about one third of the energy input goes into "acoustical energy" while typically only 10% of the input goes into lasing.

ATTENUATOR CONCEPT AND MATERIALS

The problem is controlling disturbances of the magnitude discussed above in interpulse times at 10 to 100 μsec without causing excessive pressure drop in the flow. The concept considered is to dissipate the acoustical energy in multiple reflections from porous materials located on planes parallel to the E-beam axis and optical axis in close proximity to the discharge.

The intent below is to examine the properties of porous materials for this application. The properties of interest are the reflection coefficient and the attenuation coefficient. These properties are functions of the permeability and porosity of the material. The reflection coefficient is a strong function of the

frontal porosity. A high permeability is desired to reduce the steady flow pressure drop, but this means a reduced attenuation coefficient. Clearly what is desired is sufficient porosity to give rise to reflections of significant fractions of the acoustical energy with sufficient permeability and length to fully dissipate the energy ingested by the absorber.

The data of references 8, 9, 10, and 11 indicate that Rayleigh type materials may be ideally suited as acoustical absorbers for shocks. Three types of Rayleigh materials were used in this investigation. All were 7.5 cm long and made from Therma Comb ceramic. The size and corrugation geometries are shown in figure 5. For identification these have been referred to as fine, medium, and coarse.

For the data reported below the materials were mounted in a 7.5-cm diameter shock tube with the driver at atmospheric pressure. The small amplitude properties of the materials were determined by transmission-line standing-wave-ratio tests. For these measures the shock tube was fashioned into an acoustic transmission line with terminators of known impedance so that infinite thickness (front surface reflection only) impedances, W/pc, could be determined. The value for W found in this manner were real ($\theta_{max} = \pm 10^{o}$) and frequency independent ($\pm$ 10%). Typical values W/pc were 2.2 for the fine, 1.5 for the medium, and 1.3 for the coarse. Thus, for semi-infinite layers, the R_p^2 values would be 0.14, 0.04, and 0.017, respectively. Based upon Rayleigh's theory for impedance of small pipes, the reflectivity R_p is a function of the porosity σ. The values for R_p yield porosities of 0.45 for the fine, 0.67 for the medium and 0.77 for the coarse. These values are indicative of the flow areas to total area shown in figure 5.

Values of the attenuation constant α obtained in these experiments are shown in figure 6. The attenuation constant should correlate with the steady flow pressure drops. When the measured static flow resistivities of 5150, 2470, and 717 mks rayls/m (fine, medium, and coarse) are corrected to a common velocity base by multiplying by the porosity, they are in the ratio of 4.3:3.0:1.0. Similarly at 100 Hz the attenuation constants are in the ratio 4.0:2.7:1. The Rayleigh materials considered in this investigation all have acoustical properties which are of the same order of magnitude as those of the foametals which have previously been considered as shock absorbers (ref. 8).

Using the shock tube in its intended configuration, a series of tests were run on Rayleigh materials with velocities and pressure amplitudes of both reflected and transmitted waves being observed. As shown in figure 7, the reflected wave velocities for the medium Rayleigh materials are comparable to the foametal data of ref. 8. The results of the series of tests are depicted in figure 8 as the double cross-hatched area with extrapolation depicted by single cross-hatching. Here P_2 is the pressure behind the incident wave and ΔP is the pressure difference between the reflected and incident waves. In addition to tests on the Rayleigh type attenuators, a limited number of tests were made on stainless steel screens, 0-grade steel wool, and polyurethane foam. The tests on the foam and steel wool were not pursued because of adverse characteristics of these materials. The steel wool attenuator failed to transmit the

wave significantly but was deemed impractical, since after each shock small fragments of steel wool were found in the tube. The reflected wave properties of the steel wool (7 rolls compacted in a cylinder 14 cm long and 7.5 cm in diameter) were similar to foametal and hexcell ceramics as shown in figure 7. Screens appear to be quite promising materials from our limited testing. Screens can be easily stacked or tailored to achieve a prescribed set of properties.

CONCLUSIONS

The cogent question is: Can Rayleigh or other shock attenuators mounted in the flow of an E-beam system achieve reduction of shock and acoustical disturbances to sufficient amplitudes to assure good beam quality in repetitively pulsed operations? A conclusive answer to this question can be made by using the attenuator data of this study in a comprehensive analysis of a system taking into account reflection of waves back into the system after transmission through the attenuators. However, if these waves which are reflected back into the system are neglected, one finds that damping of Mach 1.35 waves to less than 1/10 their original value can be easily achieved in 4 reflections. This is a 20-db reduction and a reduction to small amplitude waves. A further 43-db reduction in 5 reverberations can be achieved if the fine Rayleigh material ($R_p^2 = 0.14$) is used. This 63-db reduction of a 500-joule/liter pulse in less than 10 reverberations is the order of reduction desired.

Further support for the use of the flow axis attenuation concepts is achieved by a comparison of the pressure traces in figure 9. In figure 9a the successive reflection of an initial Mach 1.35 pressure wave from the driver end of a shock tube is depicted. In figure 9b the 7.5-cm length of the fine Rayleigh material has been inserted 90 cm from the pressure gage. The damping of both the 5-msec reflected wave and the 12- to 20-msec retransmitted wave is quite dramatic. The 90-cm distance between the absorber and backplate of the driver and overall 3.3-m length of the system dictates a time scale which is far larger than that of the shorter E-beam flow axis dimensions.

REFERENCES

1. Kast, S. and Cason, C.: Performance Comparison of Pulsed Discharge and E-Beam Controlled CO_2 Lasers. J. Appl. Phys., Vol. 44, 1973, p. 1631.

2. Cason, C.: Review of CO_2 E-Beam Laser Operation and Heat Transfer Problems. AIAA Paper No. 74-686, AIAA/ASME Thermophysics and Heat Transfer Conference, Boston, MA, 1974.

3. Basov, N. G.; Danilychev, V. A.; et al.: Maximum Output Energy of an Electron-Beam-Controlled CO_2 Laser. Sov. J. Quantum Electronics, Vol. 4, 1975, p. 1414.

4. Pugh, E. R.; Wallace, J.; Jacob, J. H.; Northam, D. B.; and Daugherty, J. D. Optical Quality of Pulsed Electron-Beam Sustained Lasers. Appl. Optics, Vol. 13, 1974, p. 251.

5. McAllister, G. L.; Draggoo, V. G.; and Eguchi, R. G.: Acoustical Wave Effects on the Beam Quality of a High Energy CO Electric Discharge Laser. Appl. Optics, Vol. 14, 1975, p. 1290.

6. Culick, F. E. C.; Shen, P. I.; and Griffins, W. S.: Acoustical Waves Formed in an Electric Discharge CO Laser Cavity. AIAA Paper No. 75-851, 1975.

7. Horton, T. E.; Wylie, K. F.; Wang, S. Y.; and Rao, M. S.: Modeling the Acoustical Performance of E-Beam Systems, Oct. 1976.

8. Beavers, G. S. and Matta, R. K.: Reflection of Weak Shock Waves from Permeable Materials. AIAA J., Vol. 10, 1972, p. 959.

9. Schlemm, H.: Uber das Reflexionsverhalten Schwacher Stosswellen an Akustischen Absorben in Luft. Acustica, Vol. 13, 1963, p. 302.

10. Meyer, E. and Reipka, R.: Das Reflexions-und Durchlassverhalten von Stosswellen and porösen Absorben. Acustica, Vol. 16, 1965/66, p. 149.

11. Reipka, R.: Die Ausbreitung von Stosswellen in verengten Kanälen. Acustica, Vol. 19, 1967/68, p. 271.

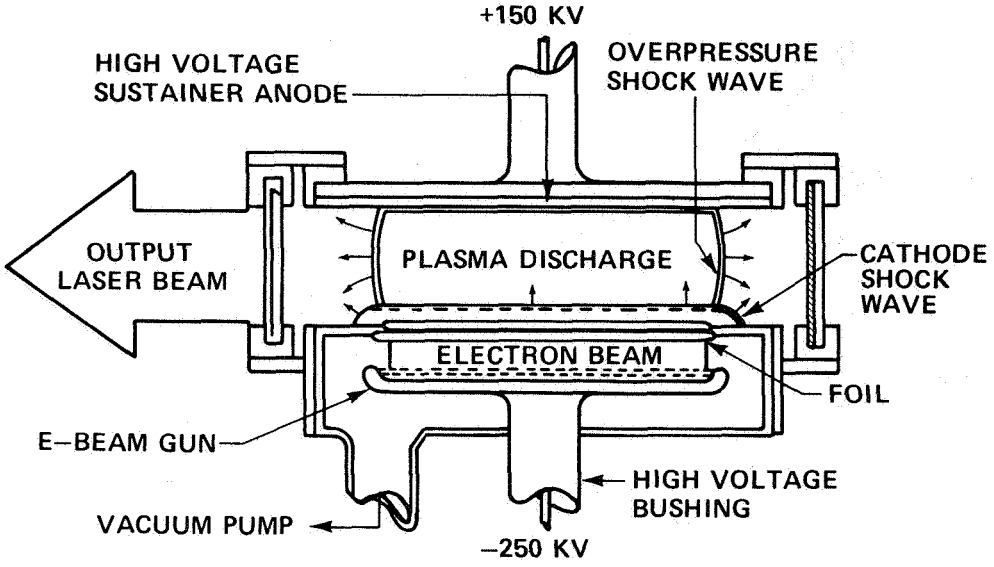

Figure 1.- Schematic views in optical and E-beam plane of an electron-beam laser. Overpressure waves typical of pulsed operation are shown.

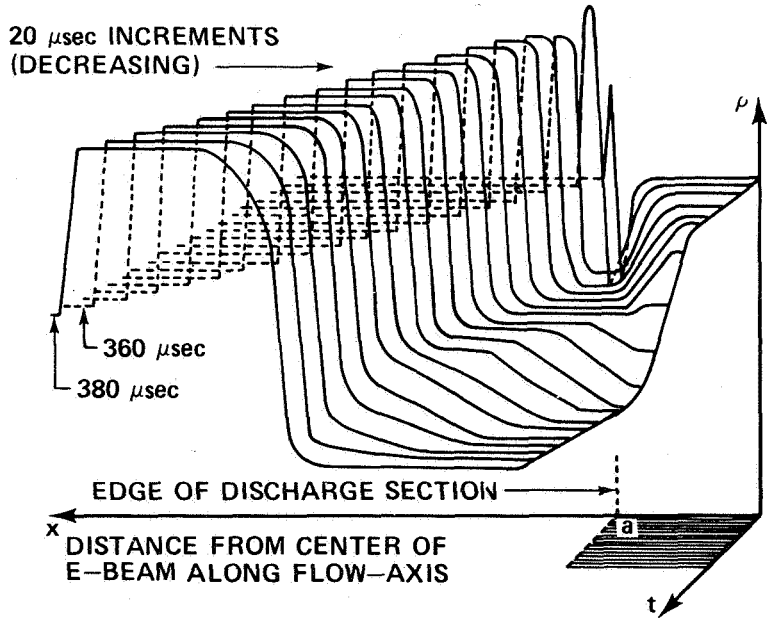

Figure 2.- Density variation at 20 μsec intervals for a 1:2:3 mixture and a power input of 400 J/liter. The expansion and compression waves start at the edge of the discharge (x = a). The expansion wave propagates to the E-beam center plane (x = 0) where it is reflected and propagates back through the discharge.

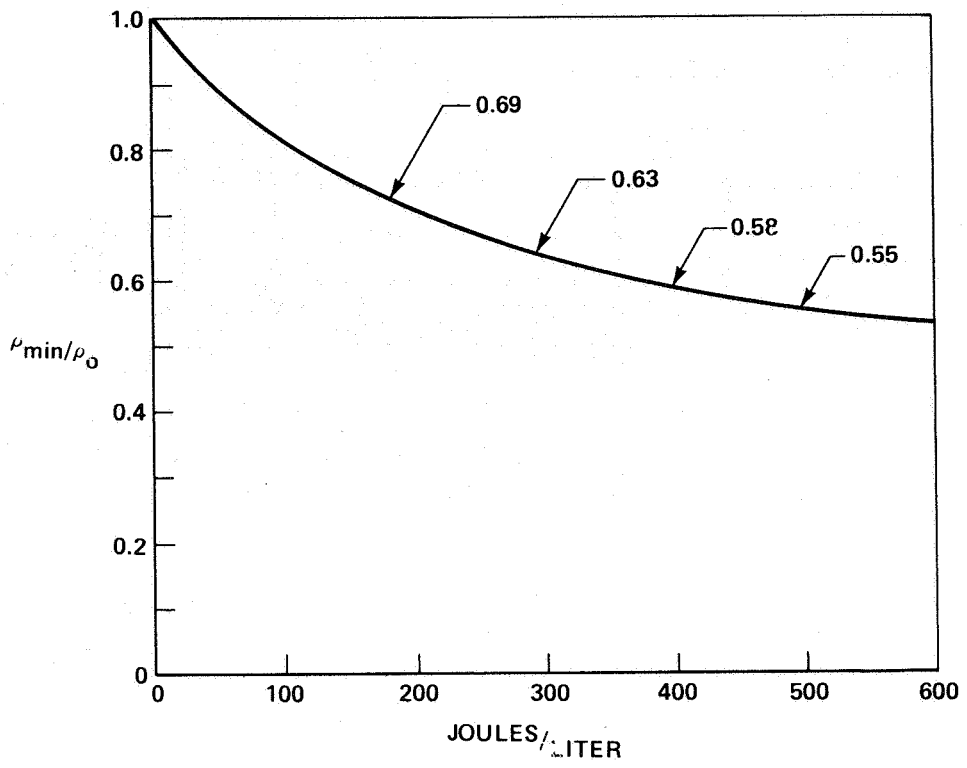

Figure 3.- Dependence of minimum density achieved at E-beam center plane on power input. The power input pulse length was 2 μsec. The mixture was 1:2:3.

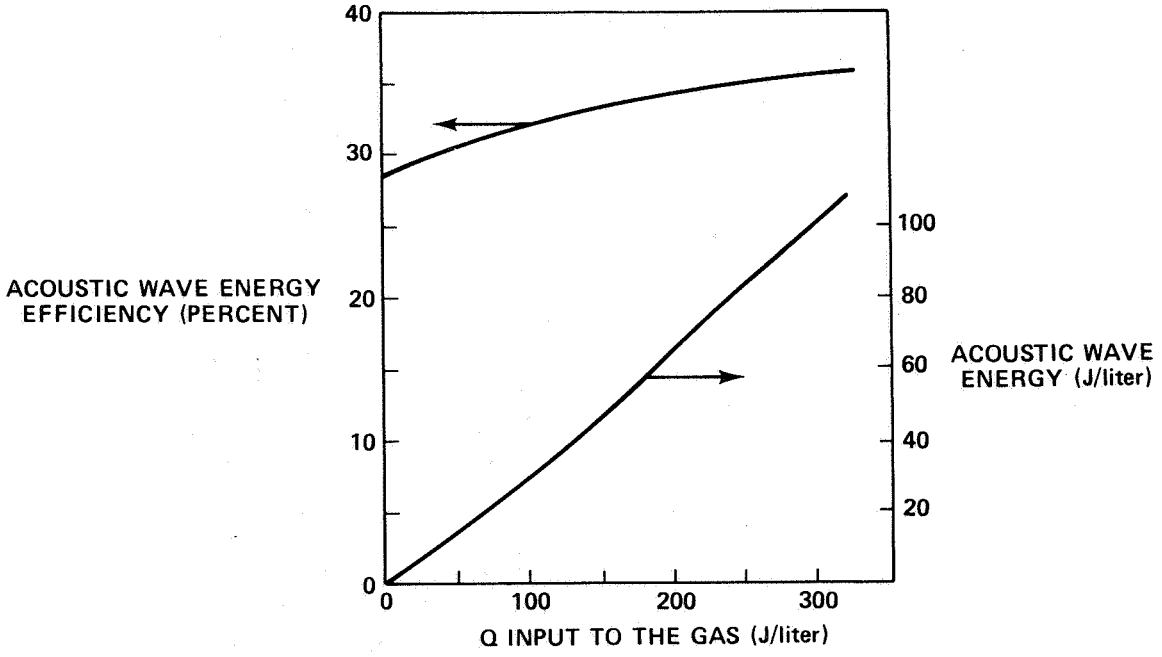

Figure 4.- Acoustical wave energy and conversion efficiency for a 1:2:3 mixture with 10% laser efficiency.

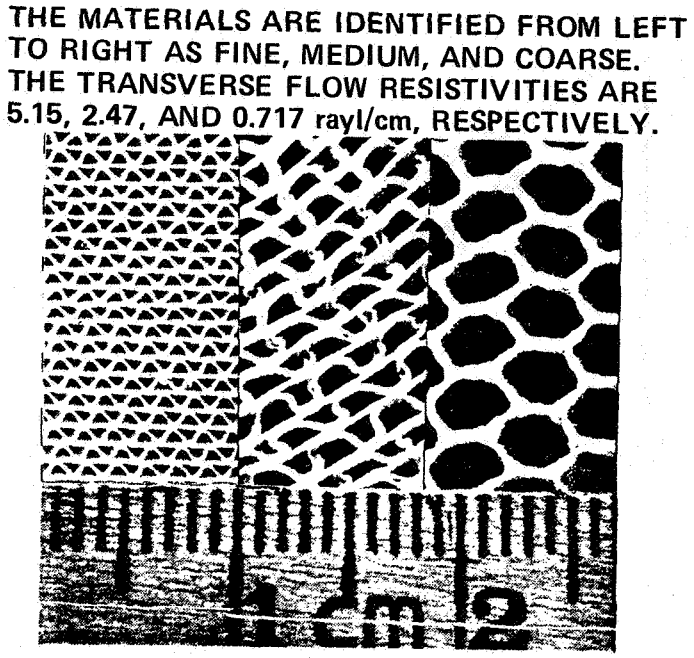

Figure 5.- Rayleigh absorber materials.

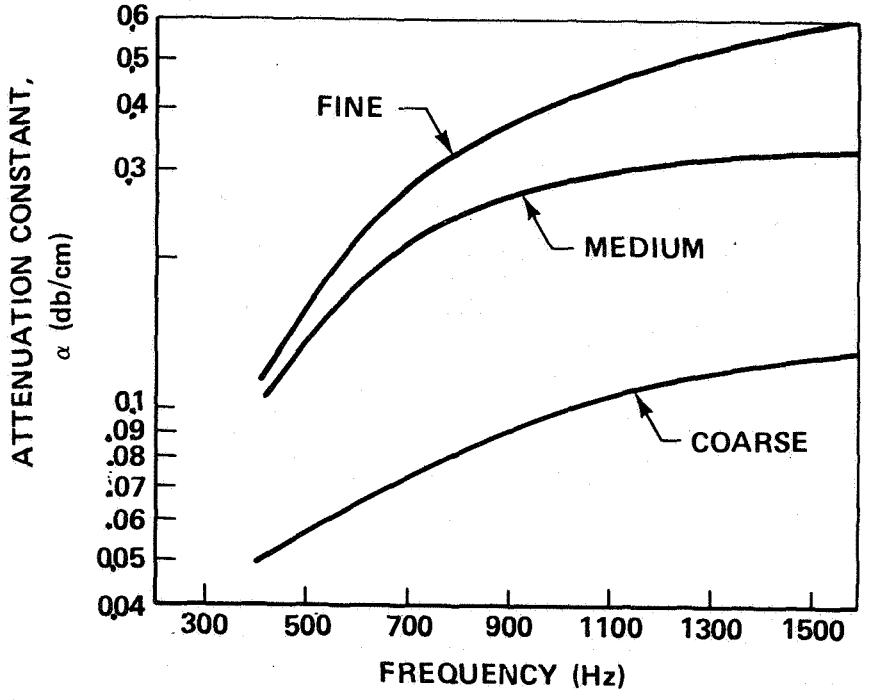

Figure 6.- Attenuation constant vs frequency for the three Rayleigh materials.

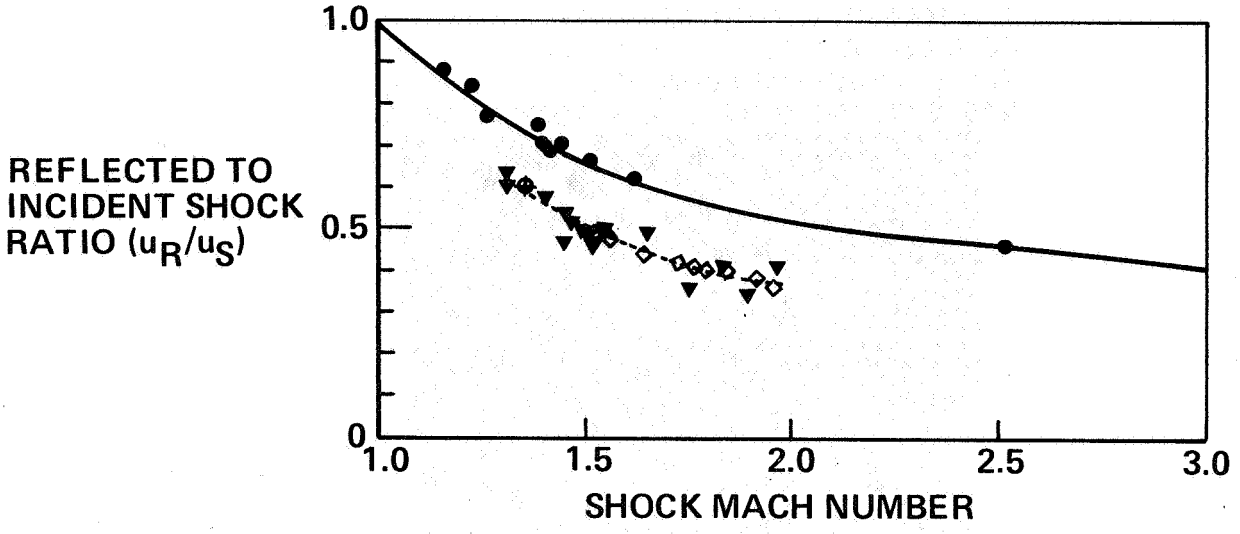

Figure 7.- Dependence of reflected shock velocity on incident shock Mach number. ● Solid boundary reflection, ▼ medium Rayleigh material, ⊕ steel wool between screens, ◇ foametal (ref. 8).

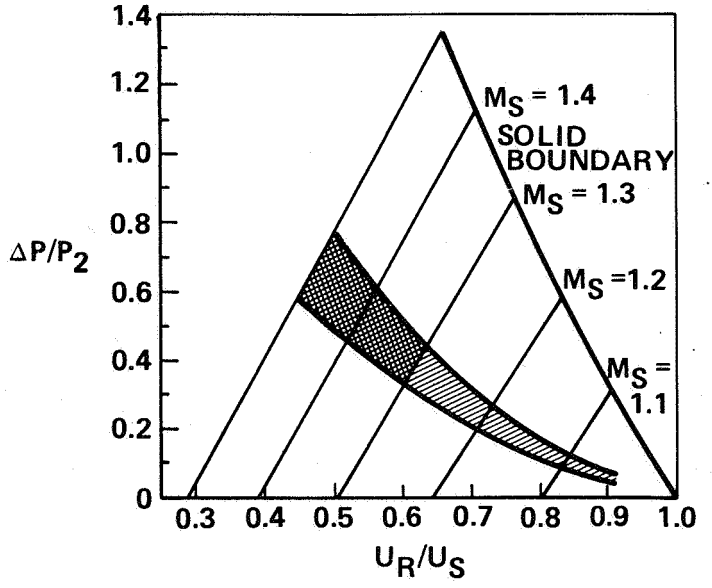

Figure 8.- Shock wave reflection properties. The dependence of reflected shock waves on incident Mach number is shown for attenuator materials listed in figure 7. The normalized reflected pressure increase, $\Delta P/P_2$, is shown as a function of normalized shock wave velocity.

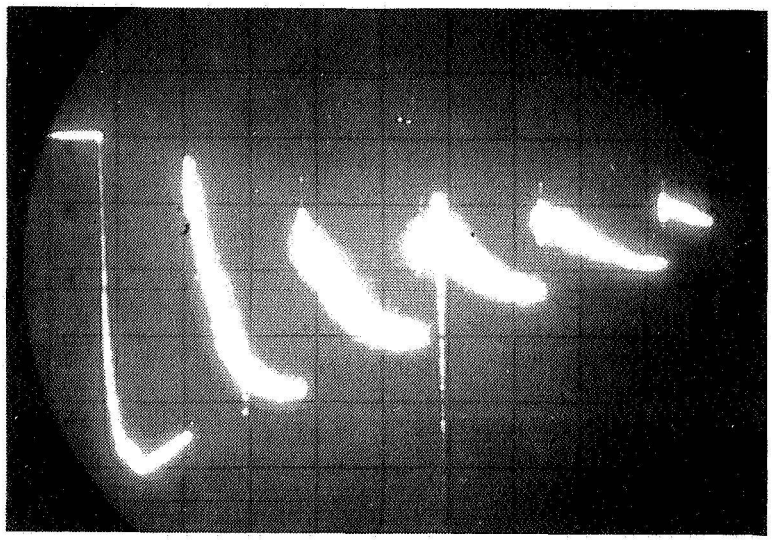

(a) Without attenuator.

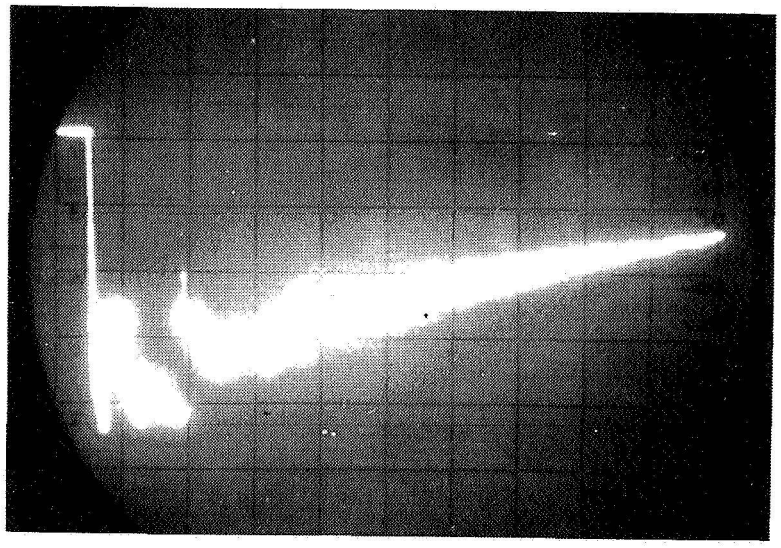

(b) With a 3-in. thickness of the "fine" Rayleigh attenuator located 8 in. from the driver diaphragm and 3 ft from the endplate pressure transducer.

Figure 9.- Pressure history at the driver endplate of a 11-ft closed shock tube with an initial shock of Mach number of 1.35 into air at standard temperature and pressure. Time base 10 msec/div.

A MICROSCOPIC DESCRIPTION OF SOUND ABSORPTION IN THE ATMOSPHERE

H. E. Bass
The University of Mississippi

SUMMARY

The various mechanisms which contribute to sound absorption in the atmosphere have been identified and a technique for computing the contribution from each is presented. The similarities between sound absorption, laser fluorescence measurements, and the opto-acoustic effect are discussed. Finally, experimental sound absorption results were compared to predictions to test the microscopic energy transfer approach.

INTRODUCTION

Perhaps the most attractive aspect of a comprehensive knowledge of basic physical phenomena is the capability of applying that knowledge to the solution of practical engineering problems. Too often, the physicist is so engrossed in his elegant esoteric theories that he neglects potential application. Too often, the engineer is so busy parameterizing his observations that he fails to identify the basic physics involved with a view towards a rigorous solution to his problems. Although these extremes are much too common, there are many cases where physicists and engineers have worked together to solve problems of mutual interest. The field of acoustics, due to the way in which it has evolved, is one of the best examples of this exchange of knowledge and interest.

This paper is going to deal with the topic of sound absorption in the atmosphere. The need for a reliable procedure to calculate sound absorption when predicting community noise around airports or when certifying aircraft is hopefully obvious to most of you. Perhaps not so familiar is the close relation between sound absorption and the design of high energy lasers or the study of the interaction potential between interacting molecules. So not only will this paper describe a procedure for computing sound absorption, it will also attempt to point out the close relation between these apparently quite different subjects.

SYMBOLS

a absorption coefficient, db - m^{-1}

c speed of sound, m - sec^{-1}

c_v specific heat at constant volume, J - $(kg\ mole)^{-1}$ - K^{-1}

c_v^{∞} specific heat at constant volume at frequencies well above the relaxation frequency, J - $(kg\ mole)^{-1}$ - K^{-1}

c_p^{∞} specific heat at constant pressure at frequencies well above relaxation frequency, J - $(kg\ mole)^{-1}$ - K^{-1}

c' relaxing specific heat, J - $(kg\ mole)^{-1}$ - K^{-1}

f acoustic frequency, Hz

f_r relaxation frequency, Hz

$f_{r,O}$ vibrational relaxation frequency of oxygen at atmospheric pressure, Hz

$f_{r,N}$ vibrational relaxation frequency of nitrogen at atmospheric pressure, Hz

h absolute humidity, percent

P ambient pressure, N - m^{-2}

P_o reference pressure, 1.01325×10^5 N - m^{-2}

R universal gas constant, 8.31432×10^3 J - $(kg\ mole)^{-1}$ K^{-1}

s relaxation strength

T temperature, K

T_o reference temperature, K

X mole fraction

Z_{rot} collision number

α attenuation coefficient, nepers - m^{-1}

α_{cl} attenuation coefficient for classical absorption, nepers - m^{-1}

α_{cr} combined classical and rotational relaxation attenuation coefficient, nepers - m^{-1}

α_{rot} rotational relaxation attenuation coefficient, nepers - m^{-1}

γ ratio of specific heats

κ coefficient of thermal conductivity, J - $(kg\ mole)^{-1}$ - K^{-1} - kg - m^{-1} - sec^{-1}

μ coefficient of viscosity, kg - m - sec^{-1}

τ relaxation time, sec^{-1}

ω angular acoustic frequency ($2\pi f$), rad - sec^{-1}

DISCUSSION

Sound absorption in the absence of turbulence can be divided into two categories: classical absorption due to viscosity, thermal conduction, and diffusion; and relaxation absorption due to vibrational and rotational relaxation of air molecules. Classical absorption can be rigorously computed for small amplitude pressure waves provided the coefficients of viscosity, thermal conduction, and diffusion are known (ref. 1). If these three quantities are considered on a microscopic basis, it is found that each can be expressed in terms of the potential of interaction between colliding molecules (ref. 2); hence, they are not independent quantities and need not be measured separately. As an example, the Eucken equation (ref. 3)

$$\kappa = (15R/4)[c_v/(15R) + 3/5] \qquad (1)$$

can be used to express the coefficient of thermal conductivity in terms of the coefficient of viscosity. Similar expressions exist for the diffusion coefficients. However, in air the masses of the constituent molecules do not differ appreciably; hence, diffusion need not be considered in absorption calculations (ref. 3).

By substituting numerical values into the equation for sound absorption in a viscous medium and using equation (1), the absorption due to classical mechanisms becomes

$$\alpha = [2\pi f^2/ Pc)](1.88) \qquad (2)$$

Equation (2) has been verified under a wide variety of pressures, frequencies, and temperatures (refs. 4 and 5) and has been found valid provided the wavelength of sound does not approach the mean free path (f/P<100MHz/atm). The study of sound absorption for cases where the frequency is the same as or less than the mean free path is still an active area of study (ref. 3) but for problems in atmospheric acoustics, classical absorption can be considered known.

The second source of sound absorption, the most variable and hence most difficult to predict, is that due to relaxation. When two or more atoms join to form a molecule, that molecule is free to rotate and vibrate as well as to move translationally. The translational degrees of freedom give rise to classical absorption; the rotation and vibration give rise to relaxation absorption. For now consider only a gas composed of one specie of diatomic molecules. Since the sound wave period is generally much shorter than the time required to establish thermal equilibrium with the surroundings, the wave propagates adiabatically. Under these conditions, as the positive pressure part of the sound wave impinges on a gas segment, the local temperature rises and the molecules seek to promote a larger number to a state of excitation in order to maintain a Boltzmann distribution. But molecules can only reach a higher state during collision and even then the probability of excitation is less than unity so some time is required for the gas to react to the change in temperature. The result is a phase lag which tends to dampen the acoustic signal if the period of the sound wave is of the same order or less than the time to achieve a new distribution of of excited molecules.

The time required for the molecules to reach a new equilibrium once disturbed is characterized by the relaxation time. The absorption due to a relaxation process can be written as (ref. 6)

$$\alpha = \frac{\omega s}{2c} \frac{\omega\tau}{1 + (\omega\tau)^2} \tag{3}$$

$$s = -Rc'/[c_{p\infty}(c_{v\infty} + c')]$$

The relaxation time for a specific internal mode (vibration or rotation) of a gas is proportional to the probability that a single collision will result in excitation and the frequency of collisions. Since the collision frequency is inversely proportional to the gas pressure, it is obvious that the relaxation time will vary inversely with pressure.

Each internal mode of the molecule will respond to changes in temperature at a different rate so, normally, each will have a separate relaxation time. The rotational energy levels, at reasonable temperature, are more closely spaced than vibrational levels; hence, a transition from one rotational state to another is generally more rapid than a vibrational transition. In fact, for atmospheric constituents, only about five collisions are necessary to establish rotational equilibrium (ref. 7). Hence, at atmospheric pressure, the rotational relaxation time is less than a nanosecond.

If, as is customary, we write the relaxation time as the value it has at atmospheric pressure, then the rotational relaxation time for air is on the order of a half of a nanosecond. For acoustic frequencies less than 10 MHz, equation 1 for rotational relaxation of air becomes

$$\alpha_{rot} = \alpha_{cl} \cdot .0681\, Z_{rot} \tag{4}$$

where the collision frequency has been expressed in terms of the viscosity

and Z_{rot} is the number of collisions necessary to establish rotational equilibrium. Using experimental values of Z_{rot}, it can be shown that to a good approximation, over the temperature range 213 K to 373 K, the combined classical and rotational relaxation absorption is given by

$$\alpha_{cr} = 18.4 \times 10^{-12} (T/T_o)^{1/2} f^2 (P/P_o) \qquad (5)$$

This equation has been thoroughly verified experimentally (ref. 4).

Vibrational relaxation represents a more formidable problem. The vibrational energy levels available in air are shown in figure 1. If each of these vibrational modes exchanged energy only with translation, the problem would be relatively simple. But that's not the way nature plays the game. Instead, if there are water vapor molecules around, oxygen vibration is more likely to gain a quantum of vibrational energy during a collision with a water molecule than it is directly from translation. If there is no water vapor in the air, oxygen is most likely to become excited by energy transfer from carbon dioxide during an oxygen-carbon dioxide collision. These different energy transfer paths make the resulting mathematical equations more complex. The equations and their solutions are quite similar to the treatment of coupled springs (ref. 8). In both cases, a normal mode analysis is appropriate.

Before continuing this discussion of sound absorption, consider the similarities between the above problem and that of designing a high power carbon dioxide laser. Efficient laser operation is achieved if the upper lasing level loses little energy through collisional processes; that is, if the relaxation time for the upper lasing level is long. The rate of energy transfer between, for example, carbon dioxide and nitrogen is the same no matter where the gas is. So many of the same relaxation times important in laser design are the same as those considered in sound absorption calculations (ref. 9). If is often most convenient to measure those rates using laser excitation of a test gas and then monitoring the fluorescence decay (ref. 10) rather than trying to determine the rates directly from sound absorption measurements. Another technique, the optoacoustic effect (ref. 11), involves the use of a pulse from a carbon dioxide laser which gives an acoustic pulse in the test gas. When determining a particular rate, the experimental approach which gives the rate most accurately should be employed without regard for what type of calculation the rate is going to be used for (e.g., sound absorption or laser design).

But now back to sound absorption. Table 1 lists the rate of energy transfer amongst various atmospheric constituents. The various rates were measured using a variety of techniques (ref. 12). It should also be noted that this table was taken from a theoretical paper on the rate at which a carbon dioxide laser beam will defocus due to atmospheric absorption and subsequent heating (ref. 13), another application of a complete kinetic description of energy transfer in the atmosphere. Once this list of rates is accurately known, one can predict sound absorption as well. When considering sound absorption, only reactions numbered 1-6 in Table 1 are important; the others affect the important relaxation times only by an immeasureably small amount.

The binary energy transfer rates from Table 1 can be substituted into a rigorous formalism for sound absorption in a multicomponent gas to give the relaxation times and strengths rigorously. This has been done (ref. 14) with the result that only two relaxation processes need be considered to calculate sound absorption in air. Further, it was found that the relaxation strengths of these two processes are given to within a fraction of a percent by the relaxing specific heats of nitrogen and oxygen. From the Planck-Einstein relation (ref. 15), the vibrational specific heat is given by

$$c' = X(\theta/T)^2 e^{-\theta/T}/(1 - e^{-\theta/T})^2 \qquad (6)$$

For the atmosphere, the mole fraction of nitrogen is close to 0.78 and from spectroscopic data (ref. 16), θ for nitrogen is 3352.0 K. The mole fraction of oxygen in the atmosphere is about 0.21 and θ is 2239.1 K. The remaining one percent is argon which does not contribute to the relaxation strength.

Referring back to equation (3), it can now be seen that for vibrational relaxation there are two terms which must be added to give the relaxation absorption. The strength of each process is also given by equation (3) with the relaxing specific heat from equation (6). The only quantity yet to be determined is the relaxation time for the two vibrational relaxation processes.

The relaxation times for nitrogen and oxygen in the atmosphere can be determined exactly from the binary energy transfer rates in Table 1. It turns out that due to reactions 3, 5, and 6, these relaxation times are strongly dependent on the water vapor concentration or relative humidity. As a result, the accuracy to which the relaxation times can be computed are limited by the accuracy of rate measurements for pure water vapor (reaction 6) and the rate at which nitrogen is deexcited by water vapor, (reaction 5). For this reason, the relaxation times as a function of humidity predicted from the rates in Table 1 must still be compared to values of absorption measured in moist air and the relaxation times refined to give the best agreement with laboratory air data (ref. 5). Defining the relaxation frequency, f_r, to be $1/2\pi\tau$, the best available values for the two relaxation frequencies are

$$f_{r,O} = (P/P_o)\{24 + 4.41 \times 10^4 h\,[(0.05 + h)/0.391 + h]\} \qquad (7)$$

$$f_{r,N} = (P/P_o)(T/T_o)^{-1/2}[9 + 350h \exp\{-6.142\,[(T/T_o)^{-1/3} - 1]\}].$$

$$\begin{aligned} a = 8.686 \cdot (T/T_o)^{1/2}[f^2/(P/P_o)]\{&1.84 \times 10^{-11} + 2.1913 \times 10^{-4} \\ &\times (T/T_o)^{-1}(P/P_o)(2239.1/T)^2[\exp(-2239.1/T)]/[f_{r,O} + (f^2/f_{r,O})] \\ &+ 8.1619 \times 10^{-4}(T/T_o)^{-1}(P/P_o)(3352/T)^2[\exp(-3352/T)]/[f_{r,N} + (f^2/f_{r,N})]\} \end{aligned} \qquad (8)$$

This expression, the procedure described previously, and supporting documentation is now being prepared for submission as a proposed American National Standards Institute Standard.

A comparsion of equation (8) to experimental results is given in figures 2, 3, and 4 for different ranges of frequency and atmospheric conditions. It is obvious that the agreement is quite good.

Concluding Remarks

Sound absorption in still air is now well understood. There is still a little problem with the relaxation frequency for moist nitrogen but that problem is now being resolved by studies in our laboratory and at Langley Research Center. Once that problem is resolved, there seems to be little need for further studies in air. However, for laser development, laser isotope separation, and other applications, sound absorption measurements in gases will continue to be a fruitful field of scientific study. Studies of sound propagation through the atmosphere should now focus on effects of ground cover and turbulence. Hopefully, these studies will again bring together physicists and engineers to the solution of pressing societal problems.

REFERENCES

1. Cottrell, T. L., and McCoubrey, J. C.: Molecular Energy Transfer in Gases, page 12 (Butterworths, London, 1961).

2. Hirschfelder, Joseph O., Curtiss, Charles F., and Bird, R. Byron: Molecular Theory of Gases and Liquids, pp. 523-541 (John Wiley & Sons, Inc., New York, 1954).

3. Bauer, H. -J.: Influences of Transport Mechanisms on Sound Propagation in Gases, Advances in Molecular Relaxation Processes, Vol. 2, 1972, pp. 319-376.

4. Bass, H. E.; and Keeton, Roy G.: Ultrasonic Absorption in Air at Elevated Temperatures, J. Acoust. Soc. Am., vol. 58, no. 1, July 1975, pp. 110-112.

5. Sutherland, Louis C.: Review of Experimental Data in Support of a Proposed New Method for Computing Atmospheric Absorption Losses, DOT-TST-75-87, 1975.

6. Herzfeld, K. F.; and Litovitz, T. A.: Absorption and Dispersion of Ultrasonic Waves, (Academic Press, New York, 1959).

7. Greenspan, M.: Rotational Relaxation in Nitrogen, Oxygen, and Air, J. Acoustical. Soc. Am., vol. 31, 1959, pp. 155-160.

8. Bauer, H. -J.; Shields, F. Douglas; and Bass, H.E.: Multimode Vibrational Relaxation in Polyatomic Molecules, J. Chem. Phys. vol. 57, no. 11, 1972, pp. 4624-4628.

9. Taylor, R. L.; and Bitterman, Steven: Survey of Vibrational Relaxation Data for Processes Important in the CO_2-N_2 Laser System, Rev. Mod. Phys., vol. 41, no. 1, Jan. 1969, pp. 26-47.

10. Rosser, W. A., Jr.; Wood, A. D.; and Gary, E. T.: Deactivation of Vibrationally Excited Carbon Dioxide (ν_3) by Collisions with Carbon Dioxide or Nitrogen, J. Chem. Phys., vol. 50, 1969, pp. 4996-5008.

11. Bauer, Hans-Jorg: Son et Lumiere or the Optoacoustic Effect in Multilevel Systems, J. Chem. Phys., vol. 57, no. 8, 15 Oct. 1972, pp. 3130-3145.

12. Evans, L. B.; Bass, H. E.; and Sutherland, L.C.: Atmospheric Absorption of Sound: Theoretical Predictions, J. Acoust. Soc. Am., vol. 51, no. 5, May 1972, pp. 1565, 1575.

13. Bass, H. E.; and Bauer, H. -J.: Kinetic Model for Thermal Blooming in the Atmosphere, Applied Optics, vol. 12, no. 7, June 1973, pp. 1506-1510.

14. Bass, H.E.; Bauer, H. -J.; and Evans, L. B. : Atmospheric Absorption of Sound: Analytical Expressions, J. Acoust, Soc. Am., vol. 52, no. 3,

Sept. 1972, pp. 821-825.

15. Holman, J.D.: Thermodynamics, page 199 (McGraw-Hill, New York, 1969).

16. American Institute of Physics Handbook, Dwight E. Gray, Ed., (McGraw-Hill, New York, 1972).

TABLE I. REACTION SCHEME

Reactions	Forward rate constants ($sec^{-1}\ atm^{-1}$)
$CO_2^*(\nu_3) + O_2 \rightleftharpoons CO_2^{***}(\nu_2) + O_2$	6.0×10^4
$CO_2^*(\nu_2) + O_2 \rightleftharpoons CO_2 + O_2$	3.0×10^4
$CO_2 + O_2^* \rightleftharpoons CO_2^*(\nu_2) + O_2$	3.0×10^5
$CO_2^*(\nu_1) + O_2 \rightleftharpoons CO_2^{**}(\nu_2) + O_2$	4.5×10^8
$CO_2^*(\nu_2) + CO_2 \rightleftharpoons CO_2 + CO_2$	1.8×10^5
$CO_2^*(\nu_3) + CO_2 \rightleftharpoons CO_2^{***}(\nu_2) + CO_2$	1.5×10^5
$CO_2^*(\nu_1) + CO_2 \rightleftharpoons CO_2^{**}(\nu_2) + CO_2$	4.5×10^8
$CO_2^*(\nu_2) + N_2 \rightleftharpoons CO_2 + N_2$	3.4×10^4
$CO_2 + N_2^* \rightleftharpoons CO_2 + N_2$	1.0
$CO_2^*(\nu_3) + N_2 \rightleftharpoons CO_2 + N_2^*$	1.8×10^7
$CO_2^*(\nu_3) + N_2 \rightleftharpoons CO_2^{***}(\nu_2) + N_2$	6.0×10^4
$CO_2^*(\nu_1) + N_2 \rightleftharpoons CO_2^{**}(\nu_2) + N_2$	4.5×10^8
$CO_2^*(\nu_2) + H_2O \rightleftharpoons CO_2 + H_2O$	4.2×10^8
$N_2^* + O_2 \rightleftharpoons N_2 + O_2^*$	1.5×10^2
$O_2^* + N_2 \rightleftharpoons O_2 + N_2$	4.0×10
$N_2^* + O_2 \rightleftharpoons N_2 + O_2$	1.0
$O_2^* + O_2 \rightleftharpoons O_2 + O_2$	6.3×10
$H_2O^*(\nu_2) + O_2 \rightleftharpoons H_2O + O_2^*$	4.6×10^7
$O_2^* + H_2O \rightleftharpoons O_2 + H_2O$	1.1×10^6
$H_2O^*(\nu_2) + O_2 \rightleftharpoons H_2O + O_2$	6.0×10^4
$N_2^* + N_2 \rightleftharpoons N_2 + N_2$	1.0
$N_2^* + H_2O \rightleftharpoons N_2 + H_2O$	1.1×10^5
$H_2O^*(\nu_2) + N_2 \rightleftharpoons H_2O + N_2$	1.4×10^6
$H_2O^*(\nu_2) + H_2O \rightleftharpoons H_2O + H_2O$	1.0×10^9

* DENOTES VIBRATIONAL EXCITATION

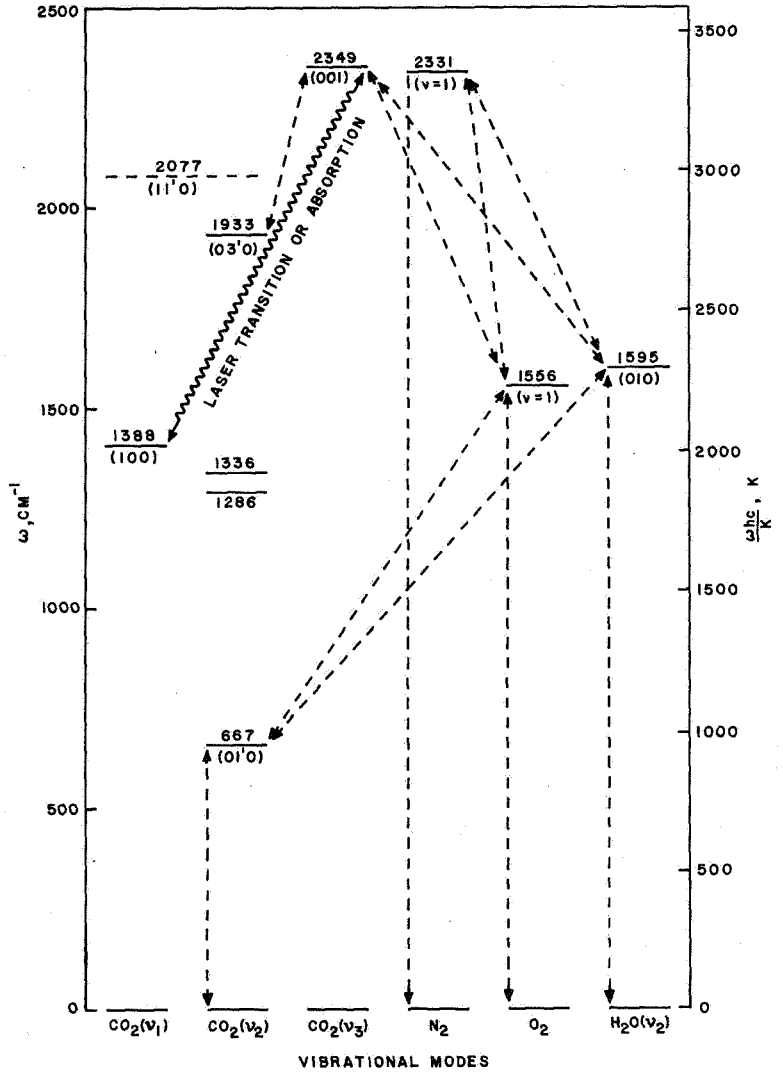

Figure 1.- Vibrational energy level diagram for air.

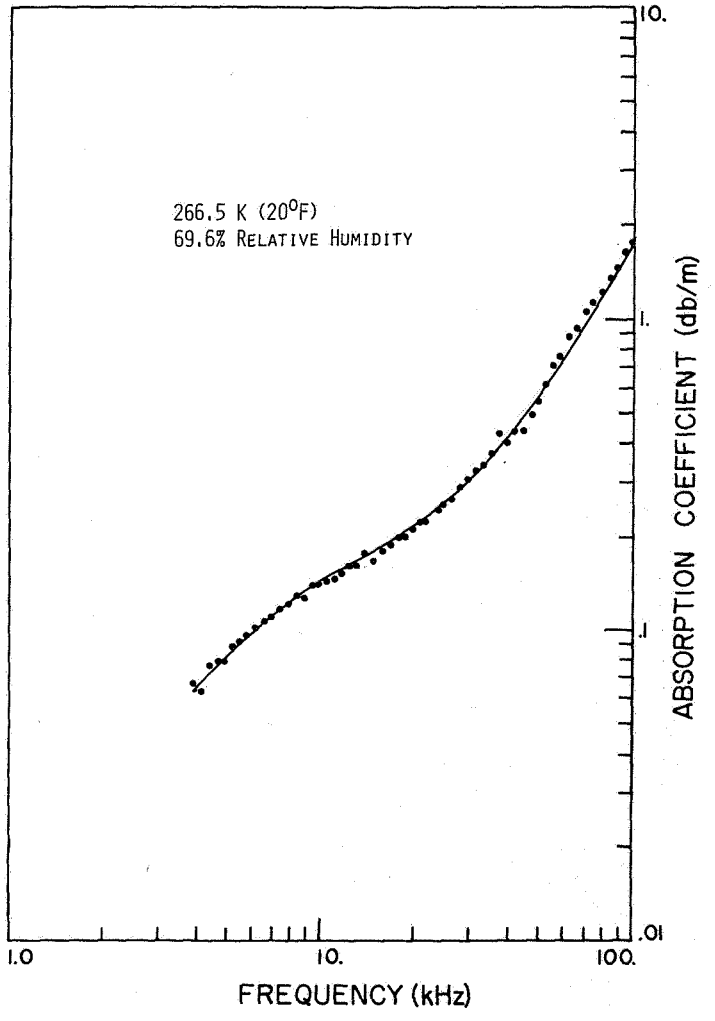

Figure 2.- Total absorption of sound in air at 266.5 K and 69.6% relative humidity.

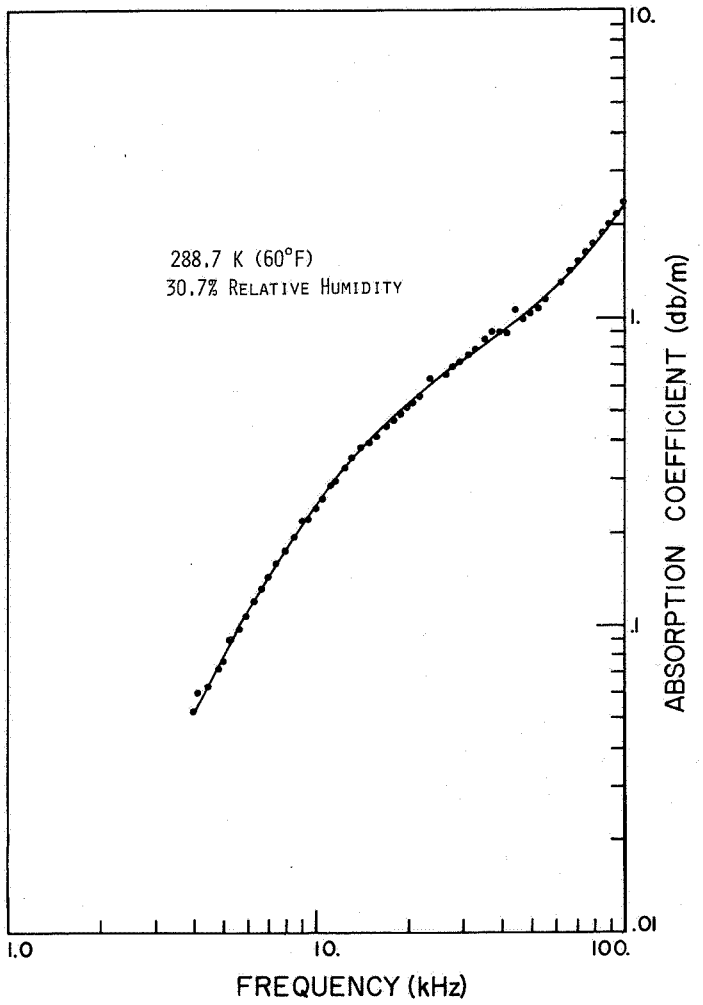

Figure 3.- Total absorption of sound in air at 288.7 K and 30.7% relative humidity.

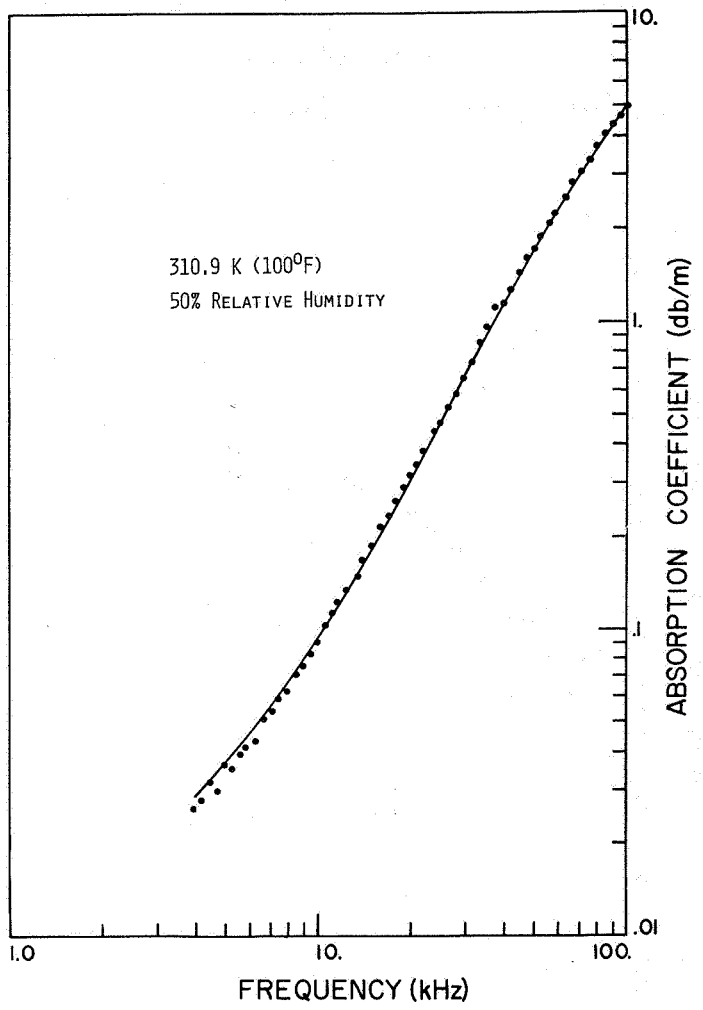

Figure 4.- Total absorption of sound in air at 310.9 K and 50% relative humidity.

PROPAGATION OF SOUND IN TURBULENT MEDIA*

Alan R. Wenzel
Institute for Computer Applications in Science and Engineering

SUMMARY

A review of some of the perturbation methods commonly used to study the propagation of acoustic waves in turbulent media is presented. Emphasis is on those techniques which are applicable to problems involving long-range propagation in the atmosphere and ocean. Characteristic features of the various methods are illustrated by applying them to particular problems. It is shown that conventional perturbation techniques, such as the Born approximation, yield solutions which contain secular terms, and which therefore have a relatively limited range of validity. In contrast, it is found that solutions obtained with the aid of the Rytov method or the smoothing method do not contain secular terms, and consequently have a much greater range of validity.

INTRODUCTION

In many real problems involving wave propagation in random media, such as those arising out of investigations of sound propagation in the atmosphere or ocean, the propagation medium may be regarded as weakly inhomogeneous in the sense that it deviates only slightly from a uniform state. This is convenient from a theoretical standpoint, since it allows such problems to be solved by perturbation methods. However, conventional perturbation methods, such as the Born method, suffer from the drawback that approximations obtained with them are generally limited in their range of validity. As a consequence, such methods are applicable only to problems involving relatively short-range propagation. For example, under conditions of moderately strong daytime turbulence, the Born approximation for acoustic propagation in the atmosphere may break down in as little as 100 meters.

The failure of the Born approximation in cases of long-range propagation arises from the fact that it is a finite-order approximation; i.e., it includes only a finite sum of terms of the complete perturbation expansion of the solution. Since such expansions usually involve secular terms (i.e., terms which increase indefinitely in magnitude with propagation distance), the Born approximation itself is secular, and hence can not generally be uniformly valid in the sense that the resulting error is bounded independently of propagation distance.

---

*This report was prepared as a result of work performed under NASA Contract No. NAS1-14101 while the author was in residence at ICASE, NASA Langley Research Center, Hampton, VA 23665.

It follows that any uniformly valid approximation must include at least the sum of an infinite subseries of the complete perturbation expansion. It is for the purpose of obtaining such approximations that infinite-order methods, such as the two-variable method, the Rytov method, the smoothing method, diagram methods, etc., have been applied to problems involving propagation in inhomogeneous and random media. Two of these methods, the Rytov method and the smoothing method, are discussed in this paper.

In section 1 the advantage of the Rytov method over the Born method in the case of long-range propagation is illustrated by applying both methods to a simple non-random problem which can be solved exactly. In section 2 the essential features of the smoothing method are brought out by first developing the method in a general context, and then applying it to a particular problem involving propagation of sound in a turbulent fluid.

1. COMPARISON OF THE BORN AND RYTOV METHODS

The precise nature of the failure of the Born method in the case of long-range propagation, as well as the improvement represented by the Rytov method, can best be illustrated by means of an example.

Consider the one-dimensional, non-random problem defined by the equation

$$u'' + k^2(1+\varepsilon)^2 u = 0 \ , \tag{1}$$

where the primes denote differentiation with respect to x. Here k and ε are real constants, with $k>0$ and ε a small parameter. We seek a solution of (1) representing rightward-propagating waves in the region $x>0$, subject to the boundary condition $u(0) = 1$. The exact solution of this problem can, of course, be written down immediately, and is

$$u(x;\varepsilon) = \exp\{ik(1+\varepsilon)x\} \ . \tag{2}$$

Now let us solve this problem by the Born method, with ε as the perturbation parameter. The procedure is as follows. We assume a solution of (1) of the form

$$u(x;\varepsilon) = u_0(x) + \varepsilon u_1(x) + \varepsilon^2 u_2(x) + \cdots \ , \tag{3}$$

substitute into (1), expand in powers of ε, and equate the individual coefficients of the resulting series to zero. This yields a sequence of differential equations and boundary conditions for the functions u_0, u_1, u_2, etc., which can be solved successively. By inserting the result into (3) we obtain the expansion

$$u(x;\varepsilon) = (1 + i\varepsilon kx - \tfrac{1}{2}\varepsilon^2 k^2 x^2 + \cdots)\exp(ikx) \ , \tag{4}$$

which we recognize as being just the series expansion in powers of ε of the exact solution. Termination of this procedure after the calculation of $n+1$ terms of the series yields the nth Born approximation for this problem. Note that the result is a finite-order expansion; i.e., it consists of a finite sum of terms of the complete perturbation expansion given by (4).

It is clear that, for any fixed, bounded range of x, the nth Born approximation can be made to approximate u as closely as we please by choosing n sufficiently large. However, for any fixed n, no matter how large, the nth Born approximation is not uniformly valid for all x. This is due to the presence of secular terms (i.e., terms which involve x raised to some positive power) in the expansion given by (4), which causes the resulting approximate expression for u to increase indefinitely in magnitude as $x \to \infty$. In contrast, the exact solution is obviously bounded as $x \to \infty$.

This secular behavior, which is characteristic of finite-order approximations and which limits their range of validity, constitutes the main drawback of this type of approach. This is a practical, as well as a theoretical, problem, since, for example, investigations of sound propagation in the atmosphere and ocean often involve propagation ranges that are greater than the range of validity of the Born approximation.

The analysis given above, in addition to delineating the difficulty arising from the presence of secular terms in the perturbation expansion, also furnishes a clue as to how this difficulty may be overcome. Comparison of equation (2) with equation (4) shows that the sum of an infinite series of secular terms may be non-secular. This suggests the general idea of avoiding secular behavior by summing infinite series of secular terms. Of course, when dealing with more complicated problems involving propagation in inhomogeneous or random media, we cannot expect, in general, to be able to sum the entire perturbation series, as we did in the simple example treated above, since that would be tantamount to writing down the exact solution. It may, however, be possible to sum an infinite sub-series of the complete perturbation series, thereby obtaining a non-secular approximation. This idea; i.e., the idea of summing an infinite sub-series of the complete perturbation series, is central to methods such as the two-variable method, the Rytov method, the smoothing method, diagram methods, etc., which we call infinite-order methods.

With these thoughts in mind we turn now to a discussion of the Rytov method. To apply this method to the problem considered above, we first write the solution of (1) in the form

$$u = \exp(i\psi) \quad , \tag{5}$$

where ψ, the new unknown function, is assumed to have an expansion of the form

$$\psi(x;\varepsilon) = \psi_0(x) + \varepsilon\psi_1(x) + \varepsilon^2\psi_2(x) + \cdots \quad . \tag{6}$$

The functions ψ_0,ψ_1,ψ_2,etc., can be determined by substituting (5) into (1), after which the resulting equation for ψ is transformed and then solved by a perturbation technique similar to that described above. The details of this procedure are given in reference 1 for the general case of propagation in a multi-dimensional random medium. (Note that Tatarski refers to the Rytov method as the method of smooth perturbations.) An alternate approach, which makes use of the corresponding Born series, has been suggested by Sancer and Varvatsis (ref. 2). In this approach equation (6) is substituted into equation (5), the right-hand side of which is then expanded in a power series in ε. Since the resulting series must be identical to that given by equation (3), we can equate coefficients to obtain

$$u_0 = \exp(i\psi_0) \ , \quad u_1 = i\psi_1 u_0 \ , \quad u_2 = (i\psi_2 - \tfrac{1}{2}\psi_1^2)u_0 \ ,$$

etc., from which it follows that

$$\psi_0 = -i\log u_0 \ , \quad \psi_1 = -i\frac{u_1}{u_0} \ , \quad \psi_2 = -i\left[\frac{u_2}{u_0} - \frac{1}{2}\left(\frac{u_1}{u_0}\right)^2\right] \ , \tag{7}$$

etc. The nth Rytov approximation is obtained by terminating this process after the calculation of $n+1$ terms in the expansion of ψ and substituting the resulting truncated series into (5).

The essential feature of the resulting nth Rytov approximation is that, for $n>0$, it is equivalent to the summation of an infinite sub-series of the complete perturbation expansion of u. For example, the first Rytov approximation,

$$u_1^{(R)} = \exp\{i(\psi_0+\varepsilon\psi_1)\} \ , \tag{8}$$

is obviously equivalent to the summation

$$u_1^{(R)} = (1+i\varepsilon\psi_1 - \tfrac{1}{2}\varepsilon^2\psi_1^2 + \cdots)\exp(i\psi_0) \ ,$$

which, from (7), is the same as

$$u_1^{(R)} = u_0 + \varepsilon u_1 + \tfrac{1}{2}\varepsilon^2 \frac{u_1^2}{u_0} + \cdots \tag{9}$$

It is for this reason that the range of validity of the Rytov approximation is, in general, much greater than that of the Born approximation. As an example, the first Rytov approximation for the problem treated above is, from (8), (7), and (4),

$$u_1^{(R)} = \exp\{ik(1+\varepsilon)x\} \quad , \tag{10}$$

which is the same as the exact solution. Thus, in this case, the first Rytov approximation is equivalent to the summation of the entire perturbation series for u, and consequently has an infinite range of validity.

More detailed discussions of the Rytov method can be found in references 1, 2, and 3.

2. THE SMOOTHING METHOD

One of the more useful perturbation techniques for treating problems involving wave propagation in random media is the smoothing method. It is, like the Rytov method, an infinite-order method, as we will show. However, the smoothing method is more convenient than the Rytov method for treating problems involving propagation in random media since it yields directly equations for the desired statistical properties of the wave field.

Our development of the method is quite general and follows closely that of Keller (ref. 4). We should emphasize here that the analysis which follows is entirely formal; except for some special cases, rigorous proofs of convergence of the series involved have not yet been given.

We begin our discussion of the smoothing method by considering the equation

$$(D+\varepsilon R)u = f \quad , \tag{11}$$

where D and R are linear operators on some vector space and ε is a small parameter. Here D is assumed to be deterministic with a known inverse, whereas R is assumed to be random with $\langle R \rangle = 0$ (the angular brackets denote an ensemble average). The source term f is assumed to be deterministic.

Since R is random, the solution u of (11) will also be random. We shall therefore be interested in solving the following type of problem: Given the operator D and the source term f, along with some appropriate statistical properties of the operator R, find some specified statistical properties of the solution u. In the analysis which follows we shall be concerned primarily with $\langle u \rangle$, the ensemble average of u.

We begin the analysis of $\langle u \rangle$ by multiplying equation (11) by D^{-1} and writing the resulting equation in the form

$$u = D^{-1}f - \varepsilon D^{-1}Ru \quad . \tag{12}$$

Solving (12) by iteration yields

$$u = D^{-1}f - \varepsilon D^{-1}RD^{-1}f + \varepsilon^2 D^{-1}RD^{-1}RD^{-1}f + \cdots \quad , \tag{13}$$

which is just the Neumann series for u. By averaging (13) and using the fact that $\langle R\rangle = 0$ we obtain

$$\langle u\rangle = D^{-1}f + \varepsilon^2 D^{-1}\langle RD^{-1}R\rangle D^{-1}f + \cdots \quad . \tag{14}$$

The series expansion for $\langle u\rangle$ given by equation (14) is analogous to the Born series (i.e., equation (4)) of section 1. It can be shown that, like the Born series, this series generally contains secular terms, and hence no finite sub-series of it can be expected to yield a uniformly valid approximation for $\langle u\rangle$.

In order to get a uniformly valid approximation for $\langle u\rangle$, we proceed as follows. First, we note that, from equation (14),

$$D^{-1}f = \langle u\rangle + O(\varepsilon^2) \quad .$$

It follows, by replacing the term $D^{-1}f$ in the second term on the right-hand side of (14) by $\langle u\rangle$, that

$$\langle u\rangle = D^{-1}f + \varepsilon^2 D^{-1}\langle RD^{-1}R\rangle\langle u\rangle + O(\varepsilon^3) \quad . \tag{15}$$

Now let w be a solution of the equation obtained by dropping the term of order ε^3 from (15); i.e., let w be a solution of

$$w = D^{-1}f + \varepsilon^2 D^{-1}\langle RD^{-1}R\rangle w \quad . \tag{16}$$

Then by writing w as a Neumann series; i.e., by writing

$$w = D^{-1}f + \varepsilon^2 D^{-1}\langle RD^{-1}R\rangle D^{-1}f + \varepsilon^4 D^{-1}\langle RD^{-1}R\rangle D^{-1}\langle RD^{-1}R\rangle D^{-1}f + \cdots \quad , \tag{17}$$

we see that w is the sum of an infinite series in ε , and also, by comparing (17) with (14), that $w - \langle u\rangle = O(\varepsilon^3)$. Thus, by solving equation (16) we obtain an approximation to $\langle u\rangle$ which is the sum of an infinite subseries of the complete perturbation expansion of $\langle u\rangle$, and which differs from $\langle u\rangle$ by terms of order ε^3 .

The procedure leading to equation (16) is called the smoothing method; the resulting equation is referred to as the first-order smoothing approximation for the mean field. The above analysis shows that the smoothing method is indeed an infinite-order method.

The approach described here can also be used to obtain higher-order statistics of u, such as the mean square, the correlation function, etc. These and other aspects of the smoothing method are discussed in more detail in reference 5.

We present now results obtained by applying the smoothing method to a problem involving propagation of acoustic waves in a turbulent fluid. The starting point of the analysis is equation (60) of reference 6 which is written here in the form

$$(c^{-2}D_t^2-\nabla^2)p = 0 \quad . \tag{18}$$

This is a convected wave equation governing the propagation of high-frequency acoustic disturbances in a moving, inhomogeneous fluid medium. Here p is the acoustic pressure, c is the sound speed of the medium, and $D_t = \partial_t + \underline{u}\cdot\nabla$, where $\underline{u}$ $[=(u_1,u_2,u_3)]$ is the fluid velocity. Also $\nabla = (\partial_1,\partial_2,\partial_3)$, where $\partial_t \equiv \frac{\partial}{\partial t}$, $\partial_i \equiv \frac{\partial}{\partial x_i}$; t is time and $\underline{x}$ $[=(x_1,x_2,x_3)]$ is the position vector. Since the basic flow is assumed here to be turbulent, both c and $\underline{u}$ are to be regarded as random functions of $\underline{x}$ and t.

We assume that the basic flow represents a small perturbation of a uniform fluid at rest. Accordingly we write

$$c = c_0(1+\tfrac{1}{2}\varepsilon\mu) \quad , \tag{19}$$

$$\underline{u} = \varepsilon c_0\hat{\underline{u}} \quad , \tag{20}$$

where μ and $\hat{\underline{u}}$ are dimensionless random functions with zero mean, c_0 is the average sound speed of the medium, and ε is a small parameter measuring the deviation of the medium from a uniform motionless state. By inserting (19) and (20) into (18), expanding in powers of ε, and (in accordance with the assumption of high-frequency waves) dropping derivatives of flow quantities, we obtain

$$[L_0+\varepsilon L_1+\varepsilon^2 L_2+O(\varepsilon^3)]p = 0 \quad , \tag{21}$$

where the operators L_0, L_1, and L_2 are given by

$$L_0 = c_0^{-2}\,\partial_t^2 - \nabla^2 \quad , \quad L_1 = 2c_0^{-1}(\hat{\underline{u}}\cdot\nabla)\partial_t - c_0^{-2}\mu\partial_t^2 \quad ,$$

$$L_2 = \hat{u}_i\hat{u}_j\partial_i\partial_j - 2c_0^{-1}\mu(\underline{\hat{u}}\cdot\nabla)\partial_t + \frac{3}{4}c_0^{-2}\mu^2\partial_t^2 \quad .$$

Equation (21) can be written in the same form as equation (11), provided we define

$$D = L_0 + \varepsilon\langle L_1\rangle + \varepsilon^2\langle L_2\rangle + O(\varepsilon^3) \ ,$$

$$R = L_1 - \langle L_1\rangle + \varepsilon(L_2 - \langle L_2\rangle) + O(\varepsilon^2) \quad .$$

It follows that the smoothing method, as described above, is applicable to this problem.

A detailed analysis of this problem based on the smoothing method is described in reference 6 . The main result of that analysis is an approximate expression for the quantity $\langle p\rangle$ (the coherent wave) which, for the case of a plane, time-harmonic wave propagating in the x_1 direction through a statistically homogeneous and isotropic medium which is slowly varying in time, can be written in the form

$$\langle p(x_1,t)\rangle = A\exp\{i(kx_1-\omega t)\} \ , \tag{22}$$

where A is an arbitrary amplitude factor, ω is the frequency, and

$$k = k_0 + \tfrac{1}{2}\varepsilon^2 k_0\,[4v^2(1+\tfrac{1}{2}im_0k_0\ell)+\langle\mu^2\rangle(1+\tfrac{1}{2}im_0'k_0\ell)] \ . \tag{23}$$

Here $k_0 = \omega/c_0$, $v^2 = \langle\hat{u}_1^2\rangle = \langle\hat{u}_2^2\rangle = \langle\hat{u}_3^2\rangle$, m_0 and m_0' are positive constants of order one, and ℓ is the correlation length of the turbulence.

Equation (23) shows that $\mathrm{Im}k > 0$ and also that $\mathrm{Re}k > k_0$. Thus, the turbulence causes an attenuation of the coherent wave as well as a reduction in its phase speed. The aspect of the solution given by equations (22) and (23) which is of most interest to us, however, in view of the preceding development, is that it is non-secular in the propagation distance x_1 . Note also that this solution can be written as the sum of an infinite sub-series of the complete perturbation series for $\langle p\rangle$, as can be seen by substituting (23) into (22) and expanding in powers of ε .

REFERENCES

1. Tatarski, V. I.: The Effects of the Turbulent Atmosphere on Wave Propagation. Keter Press, Jerusalem, 1971, p. 218. Available as TT68-50464 from the U. S. Department of Commerce, NTIS, Springfield, VA 22151.

2. Sancer, M. I., and Varvatsis, A. D.: A Comparison of the Born and Rytov Methods, Proc. IEEE 58, 140-141, 1970.

3. De Wolf, D. A.: Comments on "Rytov's Method and Large Fluctuations," J. Acoust. Soc. Am. 54, 1109-1110, 1973.

4. Keller, J. B.: Stochastic Equations and Wave Propagation in Random Media, Proc. Symp. Appl. Math. 16, 145-170, Amer. Math. Soc., 1964.

5. Frisch, U.: Wave Propagation in Random Media, in Probabilistic Methods in Applied Mathematics, A. T. Barucha-Reid, ed., Academic, New York, 1968, Vol. I.

6. Wenzel, A. R., and Keller, J. B.: Propagation of Acoustic Waves in a Turbulent Medium, J. Acoust. Soc. Am. 50, 911-920, 1971.

NOISE PROPAGATION IN URBAN AND INDUSTRIAL AREAS

Huw G. Davies
University of New Brunswick

SUMMARY

Simple acoustical ideas can be used to describe the direct and multiply reflected paths involved in the propagation of noise in regions with complicated shapes such as those found in urban and industrial areas. Several studies of propagation in streets, and the discrepancies between theoretical analyses and field measurements are discussed. Also a cell-model is used to estimate the general background level of noise due to vehicular sources distributed over the urban area.

INTRODUCTION

This paper describes some aspects of the propagation of sound in urban areas and in open industrial plants. Of the many factors that are important in determining noise levels due to various sources in such areas only the geometric or topographic effects will be discussed here. Sound propagation in urban areas involves multipath propagation, and reflection, absorption and scattering must all be taken into account. The geometries discussed are of interest for sources such as automobiles, construction sites, machinery in open industrial sites, and, in some cases for low-flying aircraft.

Factors such as wind and temperature gradients are not included. These are not thought to be of great importance over short distances. Atmospheric absorption is included only in the estimates of general background noise levels.

Much of the author's work that is described here was done at MIT as part of a program on Transportation Noise. The program was directed by R. H. Lyon. Much of the work of the group has been reviewed by Lyon (ref. 1); the present paper extends and complements Lyon's review. The author is grateful for the help and encouragement offered by Professor Lyon.

Each section of the paper deals with a particular approach to the problem of noise propagation. The topics include simple source models and eigenfunction models for estimating noise levels due to identifiable sources, and a cell-like model for estimating general background noise levels. Acoustic scale model experiments are discussed briefly.

Barriers such as earth berms are used quite extensively now for noise control along highways. Diffraction over barriers is a topic in itself and

is not discussed here.

SIMPLE SOURCE MODELS

Incoherent Point Sources

The most obvious and important geometric factor in sound propagation from a single point source is the 6dB/dd (dB per doubling of distance) due to geometric spreading. Salmon (ref. 2) has characterised the propagation from various shapes and arrays of incoherent point sources.

Manning and others (ref. 3) have shown how the very simple technique of adding the energies from incoherent point sources can be used very effectively in determining noise levels adjacent to certain types of open industrial plants. The technique has been used to help design new plant layouts to reduce noise levels in nearby communities.

Application to Propagation in City Streets

Noise propagation in city streets involves multiple reflections in the building facades bordering the streets. Typical field data taken by Delaney and others (ref. 4) is shown in figure 1. The L_{50} level is shown (the level exceeded 50% of the time). The source of sound is freely flowing traffic in the main artery. The variation of noise level with distance from the source is quite complicated.

Lyon's group at MIT has done considerable theoretical and experimental work on the propagation of sound in city streets, so called channel propagation (see, for example, refs.1, and 5 to 10). The results to date are encouraging yet no firm conclusions can be made about the important role that scattering seems to play in the propagation, and no theory can predict accurately all the features of experimental results such as those shown in figure 1. Several aspects of the problems involved are discussed below.

Wiener and others (ref.11), Schlatter (ref.5), and Lee and Davies (ref.6) have described the multiple reflections in channel propagation in terms of image sources along the line perpendicular to the street through the source position. None of them consider surface scattering. The noise level is estimated by adding the mean square sound pressure levels due to each source in a simple extension of Salmon's work. Sufficiently far down the street the decay must be at 6dB/dd except when the absorption coefficient α of the building walls equals one, in which case the decay (from an infinitely long line source) is only at 3dB/dd. Schlatter showed that both incoherent and pure-tone sources lead to essentially similar results provided an average of the sound level is taken for various receiver positions across the width of the street.

Lee and Davies (ref.6) summed the source and image fields numerically,

and included also the effects of propagation across intersections and around corners. All the data were reduced to a single nomogram for estimating noise levels.

Typical values obtained from the nomogram are shown in figure 1. A single source at the centre of the artery and side street intersection was used. The sound power output was chosen arbitrarily to be 105 dB. Two estimates using different values of the absorption coefficient are shown.

There are marked discrepancies between measured and estimated values particularly at large distances from the source. The houses along the street are typical British suburban two-storey semi-detached with gaps between the buildings. $\alpha = 0.2$ seems a reasonable number for the average value of the absorption coefficient of the building walls. Several factors should be included to improve the theoretical estimates. Donovan (ref.7) has suggested that the effect of scattering can be approximated by using an artificially high value for the effective absorption coefficient. But in this case the comparison between observed and estimated data for $\alpha = 0.5$ is hardly improved. The precise role that scattering plays is by no means clear. Certainly a considerable amount of scattering must be involved in Delaney's field situation.

Donovan's suggestion was made on the basis of scale model studies with artificially roughened building facades. Delaney and others (ref.12) comment that scale model experiments can only be made to reproduce full scale field data if the model building surfaces are made irregular. The role of scattering is an important one that needs further investigation.

An equally important effect not accounted for in the estimates shown in figure 1 involves the differences in spatial extents of the sources. Those sources with no line of sight along the side street are not included in the estimates. Such sources would increase markedly the sound field close to the artery but would have a negligible effect on noise levels further up the side street. Quantitative work on this aspect remains to be completed. However, preliminary estimates suggest that including no-line-of-sight sources does not explain the discrepancies completely.

In this context it is interesting to note that the nomogram of Lee and Davies predicts a drop of between 10 and 20 dB as the receiver "turns" a corner away from a source. This is consistent with measured values. However, the amount of the drop depends very much on the absorption coefficient; high absorption coefficients give large drops. This may well have a bearing on Donovan's scale model studies.

It is reasonable to ask if simple studies such as those above with stationary sources can estimate the noise levels due to flowing traffic. Kurze (ref.13) has estimated the mean and standard deviations of noise from freely flowing traffic when the receiver can see either a very long straight road or is shielded from part of the road by barriers. He showed that the value of the mean noise level can be estimated from stationary sources spaced

$1/\lambda$ apart where λ is the average number of vehicles per unit length of roadway. For long stretches of roadway the standard deviation is $1.8(\lambda d)^{-\frac{1}{2}}$ where d is the perpendicular distance from the observer to the road. The mean level is equivalent essentially to the L_{50} level. Higher levels such as the L_{10} level are important in determining noise intrusion. Kurze finds, as might be expected, that levels such as L_{10} and L_1 are far more sensitive than L_{50} to non-uniform traffic flows. Kurze's work did not include channel propagation, but it seems reasonable that here again mean levels at least can be estimated from stationary source distributions.

The geometry of Delaney's experiment (ref.4) is very similar to the geometry involved when a helicopter or V/STOL aircraft flies low over a city street. A receiver at street level is shielded from the noise until the aircraft is almost overhead. Pande (ref.8) and Pierce and others (ref.9) have shown that the sound level when the aircraft is overhead may be increased typically by 5 dB over the direct or open terrain level because of the multiple reflections.

OTHER MODELS FOR NOISE PROPAGATION IN STREETS

Sound propagation in corridors with absorbing walls has been discussed by Davies (ref.14). The results are applicable mainly to interior noise propagation. The sound field is described in terms of the eigenfunctions for a hard-walled corridor and each eigenfunction is expressed as a set of four plane waves. Each wave loses energy when it is reflected in absorbing material. This approximate ray tracing technique appears to work quite well close to the source. It works well also when only two opposite walls of the corridor absorb energy, and predicts correctly in this case a 3 dB/dd rate of decay at large distances from the source. However, when several walls are absorbing such as in a street (where the "top" of the corridor is open) the theory underestimates the attenuation quite considerably. Many of the results presented in reference 14 are for the most part neither adequate nor very appropriate to propagation in streets.

A different eigenfunction approach has been taken recently by Bullen and Fricke (ref.15). They attempt to account for some aspects of scattering at the building walls along the street. In particular, protrusions on buildings are regarded as constituting a change in the width of the street. An example of the geometry discussed is shown in figure 2. The walls are hard. Eigenfunction or modal expansions are written for each region with continuity of pressure and velocity used to match the expansions at the boundaries between regions. The assumption is made that coupling occurs only between a mode in region 1 and the mode in region 2 that has the closest wave number. The agreement obtained between their theory and scale model experiments is excellent for the range that was measured, namely up to eight street widths from the source. But the types of protrusions used still lead over most of the measured range to attenuation rates of less than 6 dB/dd. It remains to be seen whether the theory can be extended to include absorbing walls and a

stronger amount of scattering.

An interesting limiting case can be evaluated if the scattering is sufficiently strong that the sound field may be assumed diffuse at all points, that is, there is equal energy propagating in all directions down the street. In figure 3 only a fraction of the energy propagating in a given direction is reflected at the wall within the distance dx. From the results of reference 14 for equal energy in all directions the total power incident on the element dx is

$$P^+ \left(1 - \frac{2}{\pi} \tan^{-1} \frac{2L}{dx}\right) \simeq P^+ \frac{dx}{\pi L}$$

where P^+ represents the total input acoustic power at station x. It is assumed that a fraction α of this incident power is absorbed, and the remainder of the incident power is scattered equally in all directions so as to maintain the diffuseness of the sound field. An energy balance then gives

$$P^+ \Big|_{x+dx} = P^+ \Big|_x \left(1 - \frac{dx}{\pi L}\right) + \tfrac{1}{2}(1-\alpha)P^+ \Big|_x \frac{dx}{\pi L} + \tfrac{1}{2}(1-\alpha)P^- \Big|_{x+dx} \frac{dx}{\pi L}$$

where P^- represents power propagating in the negative x direction. A similar equation exists for P^-.

The solution of the resulting pair of differential equations for P^+ and P^- gives

$$P^+ = P_{IN} \exp\left(-\alpha^{\frac{1}{2}} \frac{x}{\pi L}\right)$$

where P_{IN} is the known power input at $x = 0$. The noise level decays linearly with distance. Attenuation such as this has been measured in coal mine tunnels by Leehey and Davies.

CELL MODEL FOR ESTIMATING BACKGROUND NOISE LEVELS

The studies above have all been concerned with estimating noise levels due to identifiable sources, even though the source may be out of sight around a corner. The residual background level that exists in any environment is that heard when no single source can be identified and when the noise seems to come from all around. Noise intrusion above this level due to isolated and specific events can cause annoyance. This residual background level corresponds approximately to the L_{90} level. A reasonable level is acceptable, and in fact

serves to mask sounds that would otherwise be intrusive.

Several field studies have been made of the background noise level. A particularly complete study is the Community Noise Survey of Medford, Massachusetts (ref.16). Theoretical estimates have been made by Shaw and Olson (ref.17) and Davies and Lyon (ref.18).

In the Shaw and Olson model the urban area is treated as a uniform, circular, spatially incoherent source of radius a that radiates power $NW/\pi a^2$ per unit area. N is the total number of sources each of power output W. Extensions to the results can be made easily to include source-free regions representing parks, for example, within an urban area. Since now contributing sources may be large distances from the receiver atmospheric absorption must be included in the model. The Shaw and Olson model leads to estimated values about 10 to 15 dB higher than the values they measured in Ottawa. The difference is attributed to a shielding factor due to buildings.

The Davies and Lyon cell model includes barriers and may be used to estimate this shielding factor. The urban area is modelled as a circular source region broken up into an array of square cells of dimension L. The cells each contain n sources of power output W. The cell walls are semi-permeable and reflect, absorb, and transmit sound. Figure 4 shows the cell-like structure in an urban area. The absorption is that due to the walls of the buildings; the average absorption coefficient of the walls of the cell is denoted by α. The transmission coefficient τ of the walls is given approximately by the ratio of street width to distance between streets. More accurate estimates would include diffraction. The reflection coefficient of the cell walls is $(1-\alpha-\tau)$.

The effective absorption coefficient $\bar{\alpha}$ for the cell accounts for both absorbed and transmitted power:

$$\bar{\alpha}A = L^2 + 4Lh(\alpha+\tau)$$

where $$A = 2L^2 + 4Lh$$

is the total surface area of a cell, and the room constant for a cell is $R = (1-\alpha)/(\bar{\alpha}A)$.

The noise level in each cell has both direct and reverberant components. The direct field can be calculated from Shaw and Olson's results. The intensity associated with the reverberant field in a cell is $p_m^2/4\rho c$ where p_m^2 is the mean square reverberant sound pressure in the m^{th} cell, ρ is density, and c is the speed of sound.

A power balance equation can be written as follows. The power removed from the reverberant field is $p_m^2 \bar{\alpha}A/4\rho c$. The power input is the contribution

$nW(1-\bar{\alpha})$ from the contained sources after the sound has undergone one reflection, plus the contributions $4nWLh\tau/A$ from the direct fields, and four contributions of the form $p_{m+1}^2 \, Lh\tau/4\rho c$ from the reverberant fields of the four adjoining cells.

If the number of cells in the source region is large the resulting power balance equation can be treated as a differential equation for the reverberant mean square sound pressure p^2 in the cells distant η cells from the centre of the source:

$$\frac{1}{\eta} \frac{d}{d\eta} \left(\eta \frac{d}{d\eta} p^2 \right) - \beta^2 p^2 = -nW \frac{4\rho c}{Lh\tau} \left(1 - \frac{L^2+4Lh\alpha}{A}\right)$$

$$\text{where} \quad \beta^2 = (L^2 + 4Lh\alpha)/Lh\tau \, .$$

Well within the source region the approximate solution is $p^2 = 4\rho cnW/R = 4\rho cNW/ M R$ where M is the total number of cells. MR represents the room constant for the whole urban area. When the direct field as calculated from Shaw and Olson is included the total mean square pressure is

$$p^2(\text{barrier}) = \rho c \left(\frac{NW}{\pi a^2}\right)\left(1 + \tfrac{1}{2}\ln N + \frac{4L^2}{R} - \tfrac{1}{2}\ln M\right).$$

The corresponding estimate from Shaw and Olson's work is

$$p^2 \ (\text{no barrier}) = \rho c \left(\frac{NW}{\pi a^2}\right)\left(1 + \tfrac{1}{2}\ln N\right).$$

The numerical difference in these estimates typically is not large, suggesting as might be expected that most of the noise is generated by nearby sources.

The situation when the receiver is outside the source region, for example in a park in an urban area is quite different. Davies and Lyon find

$$p^2 \ (\text{barrier}) = \rho cNW\left(\frac{\tau L^2}{\pi R}\right) \frac{e^{-\mu r}}{r^2} \, ,$$

where r is the distance from the source centre and μ represents the atmospheric absorption constant. Comparison with Shaw and Olson's work gives

$$\frac{p^2 \ (\text{barriers})}{p^2 \ (\text{no barriers})} = \frac{\bar{\alpha} \, A}{2\tau L^2(1-\bar{\alpha})} \, .$$

Numerical estimates of this ratio for typical values of α and τ give a barrier attenuation of 7 to 15 dB which is consistent with the values measured by Shaw and Olson.

The noise field in a traffic-free cell can be estimated, modelling, for example, the noise at an intersection when the traffic at the intersection is halted temporarily. The Davies and Lyon model gives the estimate

$$p^2 \text{ (barriers)} = \frac{16\ \rho c n W L h \tau}{R(L^2 + 4Lh\alpha)} .$$

Comparison with the corresponding Shaw and Olson result again suggests a building shielding factor on the order of 10 to 15 dB.

Finally it is of interest to estimate the noise field directly. For a source density N = 50 vehicles per square kilometer and a power level output from each source of 105 dB re 10^{-12} Watts, the Davies and Lyon model gives estimates of 67 dB and 51 dB when sources are and are not, respectively, present in the receiver cell. These levels are considered fairly representative of measured levels.

CONCLUSIONS

Little has been added to our knowledge of urban sound propagation since Lyon reviewed work in this area three years ago. Agreement between theoretical estimates and field data in general is quite poor. The discrepancies serve to emphasize quite strongly Lyon's conclusion that scattering plays a very important role in noise propagation. Work on this aspect of the problem is beginning. Work is needed also on the statistical aspects of traffic noise in urban areas.

Several groups are finding scale model studies of use (see for example DeJong and others, ref. 10). However in view of the comments of Delaney and others (ref.12) great care must be taken to ensure that scale model results compare accurately with field data.

REFERENCES

1. Lyon, R.H., Role of Multiple Reflection and Reverberation in Urban Noise Propagation. J. Acoust. Soc. Am. 55, 1974, p. 493.

2. Salmon, V., Sound Fields Near Arrays of Sources, 83rd Meeting of the Acoustical Society of America, paper 02, 1972.

3. Manning, J.E., contribution to Handbook of Industrial Noise, Cambridge Collaborative Inc., Cambridge, Mass., 1973.

4. Delaney, M.E., Copeland, W.C., and Payne, R.C., Propagation of Traffic Noise in Typical Urban Situation. NPL Acoustics Rpt. Ac 54, 1971.

5. Schlatter, W.R., Sound Power Measurements in a Semi-Confined Space, MS Thesis, MIT Dept. of Mech. Eng., 1971.

6. Lee, K.P., and Davies, H.G., Nomogram for Estimating Noise Propagation in Urban Areas, J. Acoust. Soc. Am. 57, 1975, p. 1477.

7. Donovan, P.R., and Lyon, R.H., Traffic Noise Propagation in City Streets. 89th Meeting of the Acoustical Society of America, paper Q8, 1975. See also Donovan, P.R., Ph.D. Thesis, MIT Dept. of Mech. Eng., 1975.

8. Pande, L., Model Study of Aircraft Noise Reverberation in a City Street, MS Thesis, MIT Dept. of Mech. Eng., 1972.

9. Pierce, A.D., Kinney, W.A., and Rickley, E.J., Helicopter Noise Experiments in an Urban Environment, J. Acoust. Soc. Am. 56, 1974, p. 332.

10. DeJong, R., Lyon, R.H., and Cann, R., Acoustical Modelling for Site Evaluation. 89th Meeting of the Acoustical Society of America, paper H5, 1975.

11. Wiener, F.M., Malme, C.I., and Gogos, C.M., Sound Propagation in Urban Areas. J. Acoust. Soc. Am. 37, 1965, p. 738.

12. Delaney, M.E., Rennie, A.J., and Collins, K.M., Scale Model Investigations of Traffic Noise Propagation. NPL Rept. Ac 58, 1972.

13. Kurze, U.J., Statistics of Road Traffic Noise. J. Sound Vibn. 18, 1971, p. 171.

14. Davies, H.G., Noise Propagation in Corridors, J. Acoust. Soc. Am. 53, 1973, p. 1253.

15. Bullen, R., and Fricke, F., Sound Propagation in a Street, J. Sound Vibn. 46, 1976, p. 33.

16. A Community Noise Survey of Medford, Mass. U.S. Dept. of Transportation Rept. No. DOT-TSC-OST-72-1, 1971.

17. Shaw, E.A.G., and Olson, N., Theory of Steady-State Urban Noise for an Ideal Homogeneous City, J.Acoust. Soc. Am. 51, 1972, p. 1781

18. Davies. H.G., and Lyon, R.H., Noise Propagation in Cellular Urban and Industrial Spaces, J. Acoust. Soc. Am. 54, 1973, p. 1565.

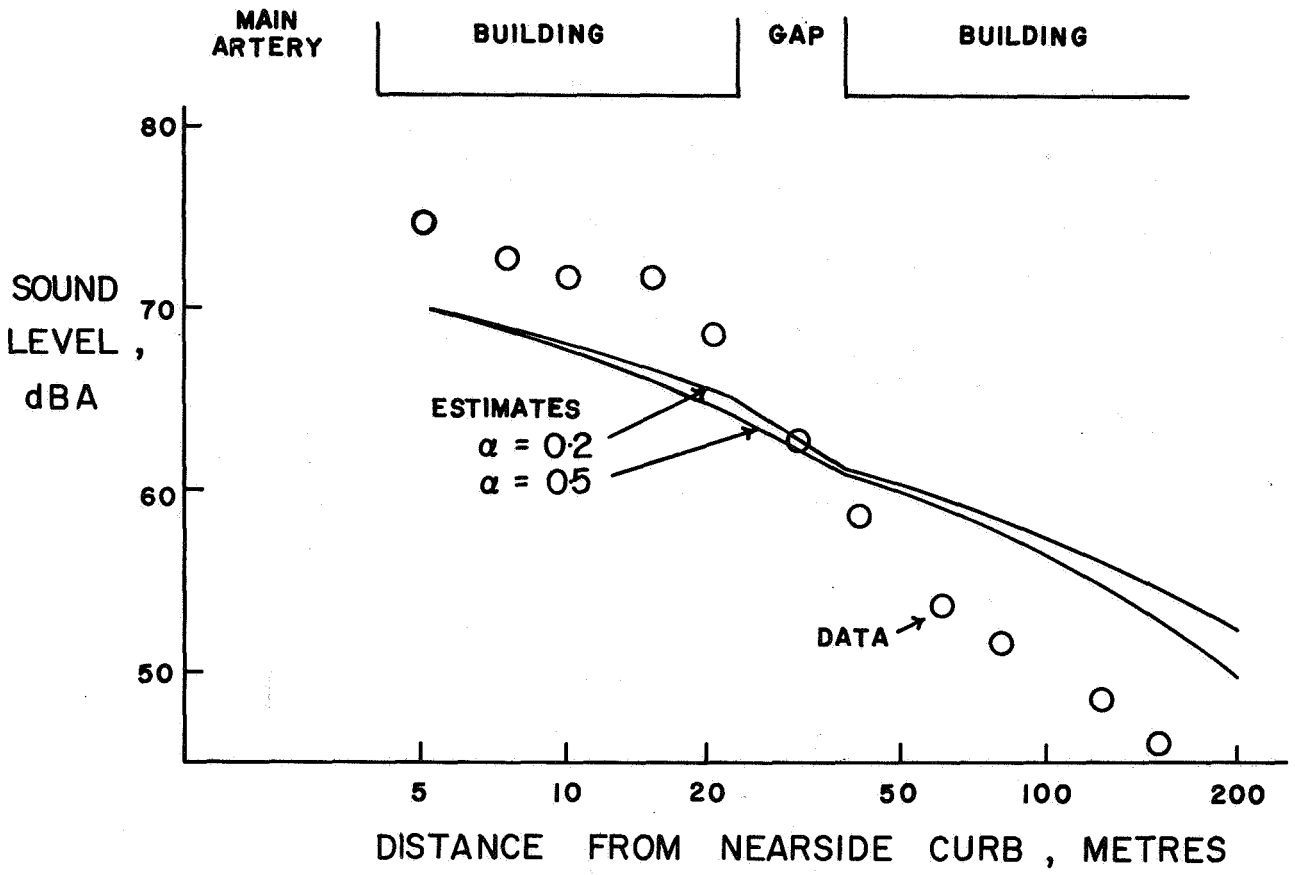

Figure 1.- Variation of noise level with distance along side street due to noise sources in main artery. Field data from reference 4; theoretical estimates from reference 6.

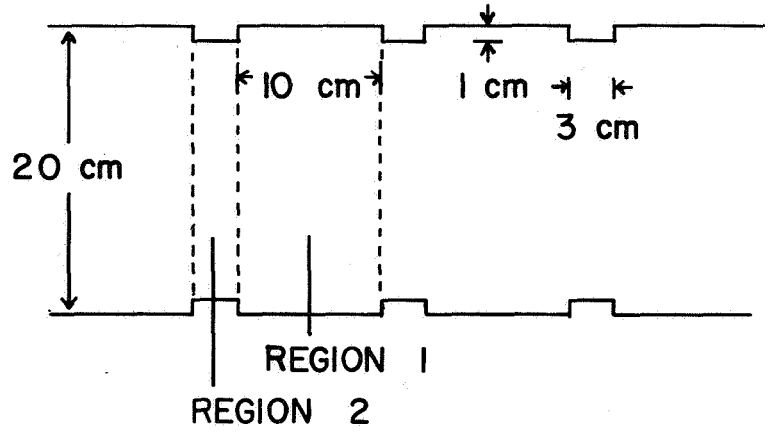

Figure 2.- Typical geometry of scale model street discussed in reference 15.

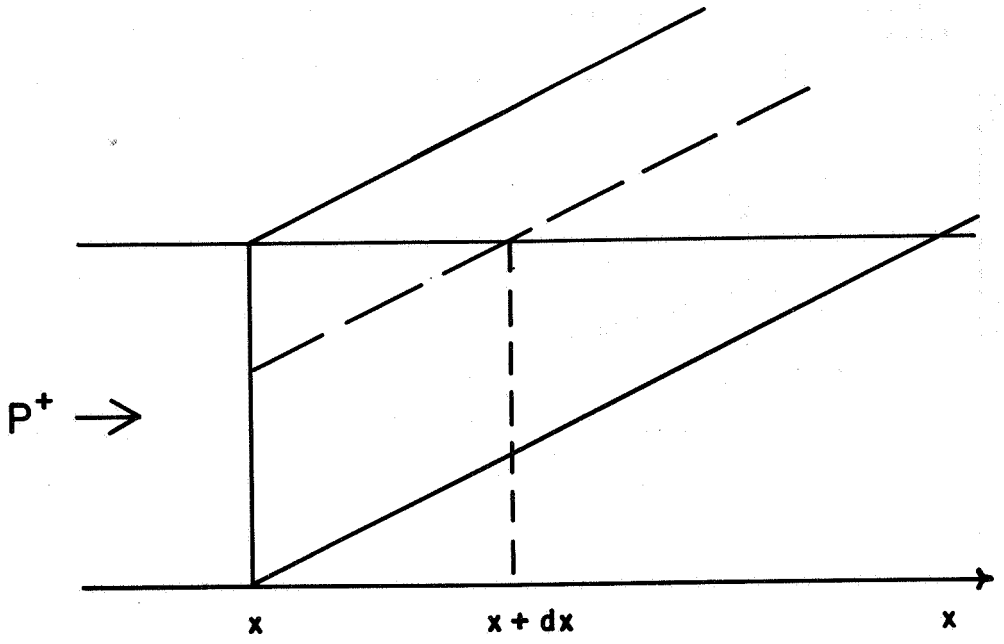

Figure 3.- Geometry to estimate power incident on wall element dx from given direction.

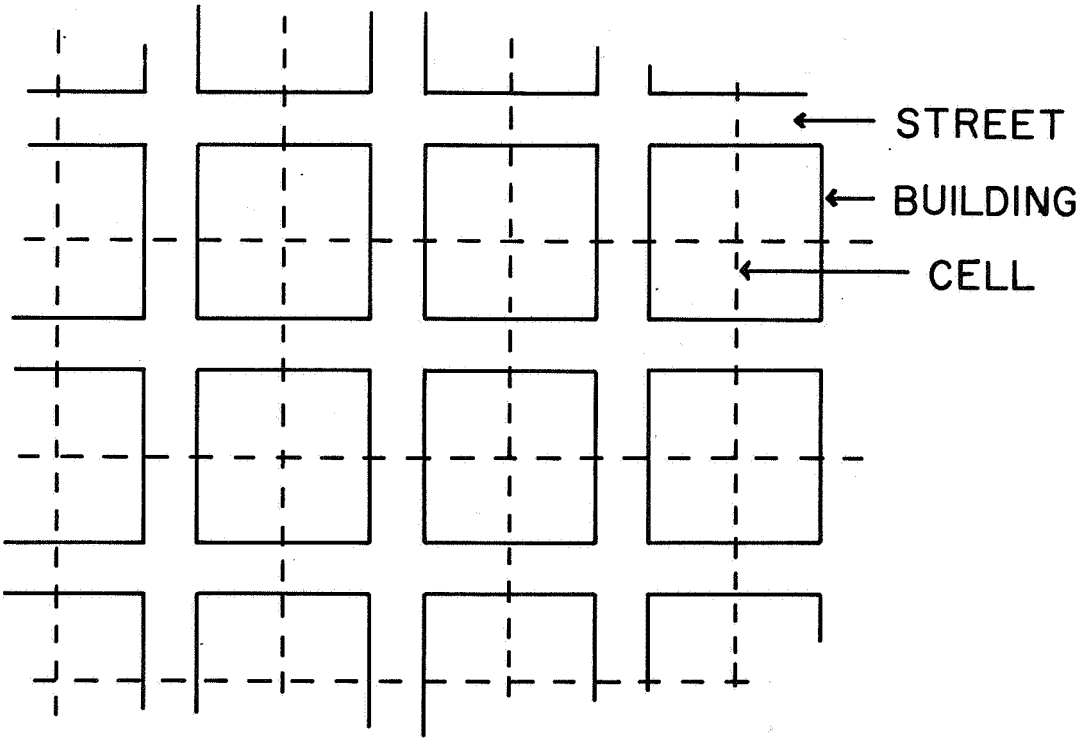

Figure 4.- Geometry of cell-like structure in urban area (ref. 18).

DIFFRACTION OF SOUND BY NEARLY RIGID BARRIERS

W. James Hadden, Jr., and Allan D. Pierce
Georgia Institute of Technology

SUMMARY

An analysis is presented of the diffraction of sound by barriers whose surfaces are characterized by large, but finite, acoustic impedance. The discussion is limited to idealized source-barrier-receiver configurations in which the barriers may be considered as semi-infinite wedges. Particular attention is given to situations in which the source and receiver are at large distances from the tip of the wedge. The expression for the acoustic pressure in this limiting case is compared with the results of Pierce's analysis of diffraction by a rigid wedge. An expression for the insertion loss of a finite impedance barrier is compared with insertion loss formulas which are used extensively in selecting or designing barriers for noise control.

INTRODUCTION

The desire for effective measures to protect residential areas from noise associated with various modes of transportation has led to a resurgence of interest in the problem of sound diffraction by barriers. Wedge-shaped barriers are of particular interest because of their ubiquity both as physical entities and as subjects of scientific investigations. Little attention has been given, however, to the effect of the finite acoustic impedance of a barrier's surfaces on its performance as a noise shield. The inclusion of the effect of large, but finite, acoustic impedance in calculations of the insertion loss for a barrier is consistent with current interest in better barrier design and selection procedures. This paper describes some of the results of a theoretical study of diffraction by hard wedges and suggests a method of adapting these results to widely used formulas (refs. 1 and 2) based on rigid wedges.

SYMBOLS

Values are given in dimensionless form.

p	acoustic pressure
r,θ,z	coordinate axes in cylindrical coordinates
ω	angular frequency
c	acoustic wave speed
k	acoustic wave number
η	normalized acoustic impedance (eq. (2))
β	exterior angle of wedge
L	modified spreading distance of diffracted ray (eq. (4))
R	spherical spreading distance (eq. (14))
α	complex angle (eq. (5))
γ	angle between source-receiver path and wedge vertex (eq. (6))
IL	insertion loss (eq. (12))

PROBLEM STATEMENT

We shall restrict our attention to an idealized case in which the source may be idealized as a point source and the barrier as a wedge whose faces occupy the planes $\theta=0$ and $\theta=\beta$. The geometrical configuration of source, wedge and receiver is depicted in figure 1. The acoustic pressure field must satisfy the reduced wave equation (exp (-iwt) time dependence suppressed throughout; k=w/c)

$$\left[\frac{\partial^2}{\partial r^2} + \frac{1}{r}\frac{\partial}{\partial r} + \frac{1}{r^2}\frac{\partial}{\partial \theta^2} + k^2 \sin^2 \gamma\right] p = 0 \qquad (1)$$

in the region $0 < \theta < \beta$ $(\pi < \beta \leq 2\pi)$. The impedance boundary conditions at the surfaces $\theta=0,\beta$ may be expressed as

$$\frac{\partial p}{\partial \theta} \pm (ikr/\eta)\, p = 0, \quad \theta = 0,\beta \qquad (2)$$

where the upper sign is taken for $\theta=0$ and η is a dimensionless impedance. In addition, the pressure field must obey a radiation condition (outgoing waves from the wedge).

The solution for the point source case has been obtained from the exact solution for the diffraction of plane electromagnetic waves, particularly useful versions of which have been given by Williams (ref. 3) and Malyuzhinets (ref. 4). The details of this analysis are presented in reference 5.

PRESSURE FIELD IN THE SHADOW ZONE

The plane wave solution can be modified, following Keller's geometrical theory of diffraction (ref. 6), to yeild a solution for the pressure field due to a point source. For situations in which both the source and receiver are many wavelengths away from the tip of the wedge, with the receiver located within the acoustic shadow of the wedge, the acoustic pressure at a point (r,θ,z) due to a source at (r_0,θ_0,z_0) may be approximated as

$$p(r,\theta,z) \simeq \frac{e^{ikL}\, e^{i\pi/4}}{L}\left(\frac{1}{2\ krr_0/L}\right)^{\frac{1}{2}} G(\theta,\theta_0,\alpha) \qquad (3)$$

which contains the modified spreading factor L,

$$L = \left[(z-z_0)^2 + (r+r_0)^2\right]^{\frac{1}{2}} \qquad (4)$$

which is interpreted as the net distance a wave travels along a line from the source to the wedge tip and then along a diffracted ray to the receiver. An additional condition for the validity of equation (3) is that the quantity $(krr_0/L\pi)$ be much larger than unity. The function $G(\theta,\theta_0,\alpha)$ in equation (3) describes the variation of the strength of the diffracted pressure field, with respect to source and receiver angles θ,θ_0, and with respect to the impedance through the parameter α which is defined by

$$\cos\ \alpha = (\eta \sin\ \alpha)^{-1} \qquad (5)$$

where γ is the angle the incident ray makes with the wedge axis

$$\cos\ \gamma = (z-z_0)/L\ ;\ \sin\ \gamma=(r+r_0)/L \qquad (6)$$

The functional form of $G(\theta,\theta_0,\alpha)$ for arbitrary values of the impedance is quite complicated; it is discussed fully in reference 5. It is possible to effect a considerable simplification in the case of a hard wedge.

NEARLY RIGID WEDGE

For a wedge with very large impedance η, the scattering function $G(\theta,\theta_0,\alpha)$ can be simplified to the form

$$G(\theta,\theta_0,\alpha) \simeq \left[\frac{1}{M_\nu(\theta+\theta_0)} + \frac{1}{M_\nu(\theta-\theta_0)}\right]\left[1 + \frac{S_\beta(\theta,\theta_0)}{\eta \sin\gamma}\right] \tag{7}$$

in which we have used

$$M_\nu(\theta) = \frac{\cos(\nu\pi) - \cos(\nu\theta)}{\nu \sin(\nu\pi)} \tag{8}$$

and

$$S_\beta(\theta,\theta_0) = 2\left[M_\nu(\theta+\theta_0) + M_\nu(\theta-\theta_0)\right]^{-1} - Q_\beta(-\theta) - Q_\beta(-\theta_0) \tag{9}$$

The function $Q_\beta(-\theta)$ takes on a rather simple form for wedge angles given by $\beta = p\pi/2q$, with p an odd integer and q and p relative primes. In such a case, we may use

$$Q_\beta(-\theta) = \sum_{n=1}^{\frac{p-1}{2}} \frac{-\nu \sin(\nu\pi)}{\sin \nu(2n\pi-\theta) \sin\left[\nu(2n-1)\pi-\theta\right]} + \sum_{m=0}^{q-1} \frac{\sin(\theta+2m\beta) + \sin\left[\theta+(2m+1)\beta\right]}{\sin(\theta+2m\beta)\sin\left[\theta+(2m+1)\beta\right]} \tag{10}$$

If we neglect the term involving $S_\beta(\theta,\theta_0)$ in equation (7), we recover the far-field limit of Pierce's expression for the diffracted pressure field of a rigid wedge (ref. 7).

PRACTICAL APPLICATIONS

The combination of equations (3) and (7) leads to an expression for the acoustic pressure in the shadow zone at large distances from the tip of the wedge which included a first-order correction for finite wedge impedance:

$$p(r,\theta,z) \approx \frac{e^{ikL}\, e^{i\pi/4}}{L}\left(\frac{1}{2\pi krr_0/L}\right)^{\frac{1}{2}}\left[\frac{1}{M_\nu(\theta+\theta_0)} + \frac{1}{M_\nu(\theta-\theta_0)}\right]\left[1 + \frac{S_\beta(\theta,\theta_0)}{\eta \sin\gamma}\right] \tag{11}$$

A particularly useful measure of a barrier's shielding effect is the insertion loss, defined as

$$IL \equiv 20 \log_{10} \frac{\left|p_{\text{No Barrier}}\right|}{\left|p_{\text{Barrier}}\right|} \tag{12}$$

For the present case we may take as $p_{\text{No Barrier}}$

$$p_{N.B.} = \frac{e^{ikR}}{R} \tag{13}$$

with

$$R = \left[r^2 + r_0^2 - 2rr_0 \cos(\theta-\theta_0) + (z-z_0)^2\right]^{\frac{1}{2}} \tag{14}$$

Thus we may express the insertion loss in terms of that for a rigid wedge

$$IL_{\text{Rigid}} = 20 \log_{10}(L/R) + 10 \log_{10}(2\pi krr_0/L) - 20 \log_{10}\left[M_\nu^{-1}(\theta-\theta_0) + M_\nu^{-1}(\theta+\theta_0)\right] \tag{15}$$

and the finite impedance correction

$$\Delta IL = -10 \log_{10} \left[\left| 1 + S_{\beta}(\theta,\theta_0)/(\eta \sin \gamma) \right|^2 \right] \qquad (16)$$

The restriction to barrier angles of the form $p\pi/2q$ presents no real problem: a desired barrier angle may be approximated closely enough by suitable choices of p and q, or one may interpolate for design purposes between the insertion losses for wedge angles with values of p,q which are convenient for computations. As an aid to the insertion loss computation values of the function $Q_{\beta}(-\theta)$, given by equation (10), may be computed for several wedge angles β and then plotted to provide the desire interpolation. A selection of the resulting curves is presented in figure 2. Numerical values for the finite-impedance correction to the insertion loss for an obtuse wedge with the interior angle 120° and surface admittance $\eta^{-1} = 0.1 - i0.05$ are presented in figure 3 for several combinations of source and receiver locations. As might be expected, the effect of the finite impedance is stronger for source and/or receiver locations nearer the surface of the wedge.

ADAPTATION TO CONVENTIONAL DESIGN PROCEDURES

The most widely used barrier design charts (ref. 1,2 and 8) consider only rigid barriers and generally deal only with the effective path difference, L-R, in the form of the Fresnel number $N = 2(L-R)/\lambda$. In reference 9, Pierce has shown that in general the insertion loss formula thus obtained (ref. 1, equation 7.15),

$$IL_{Rigid} \simeq 20 \log_{10} \left[\frac{\sqrt{2\pi N}}{\tanh \sqrt{2\pi N}} \right] + 5dB \qquad (17)$$

is valid primarily near the edge of the shadow boundary, which corresponds to having one of the functions M_{ν} (eq. (8)) very small.

In such cases it would seem to be an acceptable practice to add the correction term, equation (16), to the rigid wedge insertion loss computed from equation (17).

CONCLUDING REMARKS

The results of a theoretical study of the diffraction of sound into the shadow of a wedge with large but finite acoustic impedance have been presented. The finite-impedance correction for the insertion loss of the wedge is cast in a form which is amenable for some wedge angles to calculations using modern desk calculators. The insertion loss correction can be used in conjunction with other calculations for rigid barriers, although the rigid wedge insertion loss formula obtained here is of greater utility and involves little additional computational effort.

REFERENCES

1. Kurze, U. J. and Beranek, L. L.: Sound Propagation Outdoors. Noise and Vibration Control, ed. L. L. Beranek (McGraw-Hill, New York, 1971), pp. 174-178.

2. Kurze, U. J.: Noise Reduction by Barriers. J. Acoust. Soc. Am., vol. 55, no. 3, March 1974, pp. 504-518.

3. Williams, W. E.: Diffraction of an E-polarized Plane Wave by an Imperfectly Conducting Wedge. Proc. Roy. Soc. London, series A, vol. 252, 1959, pp. 376-393.

4. Malyuzhinets, G. D.: The Radiation of Sound by the Vibrating Boundaries of an Arbitrary Wedge. Soviet Physics-Acoustics, vol. 1, 1955, pp. 152-174 and 240-248.

5. Pierce, A. D. and Hadden, W. J., Jr.: Theory of Sound Diffraction around absorbing Barriers. Proc. Int'l. Conf. on Acoustic Protection of Residential Areas by Barriers. Centre National de la Recherche Scientifique, Marseilles 1975.

6. Keller, J. B.: Geometrical Theory of Diffraction. J. Opt. Soc. Am., vol. 52, no. 2, 1962, pp. 116-130.

7. Pierce, A. D. and Hadden, W. J., Jr.: Noise Diffraction around Barriers of Finite Acoustic Impedance. Proc. 3rd Interagency Symposium on University Research in Transportation Noise. U. S. Dept. of Transportation, November 1975, pp. 50-58.

8. Kurze, U. J. and Anderson, G. S.: Sound Attenuation by Barriers. Applied Acoustics, vol. 4, no. 1, 1971, pp. 35-53.

9. Pierce, A. D.: Diffraction of Sound Around Corners and Over Wide Barriers. J. Acoust. Soc. Am., vol. 55, no. 5, 1974, pp. 941-955.

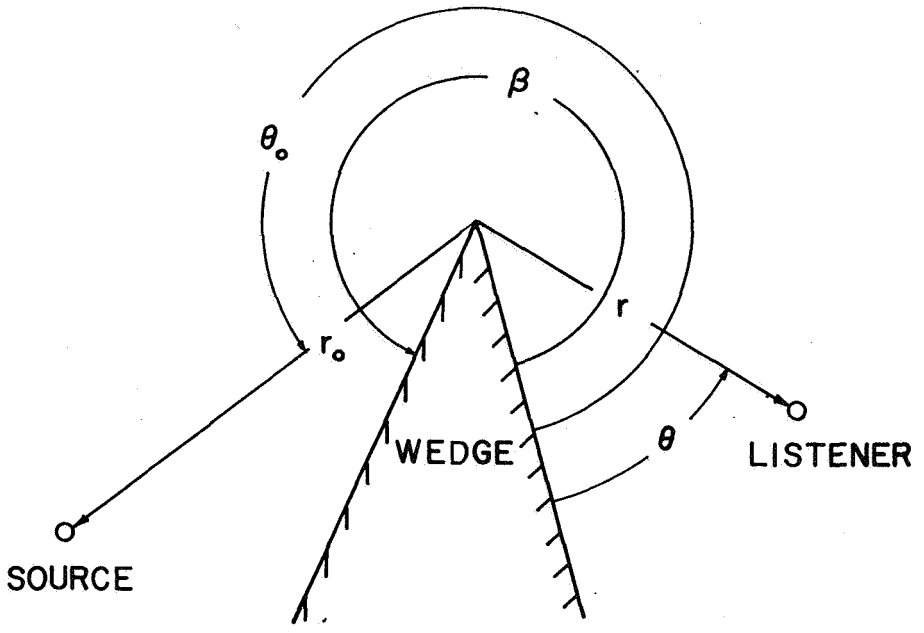

Figure 1.- Source-wedge-receiver configuration.

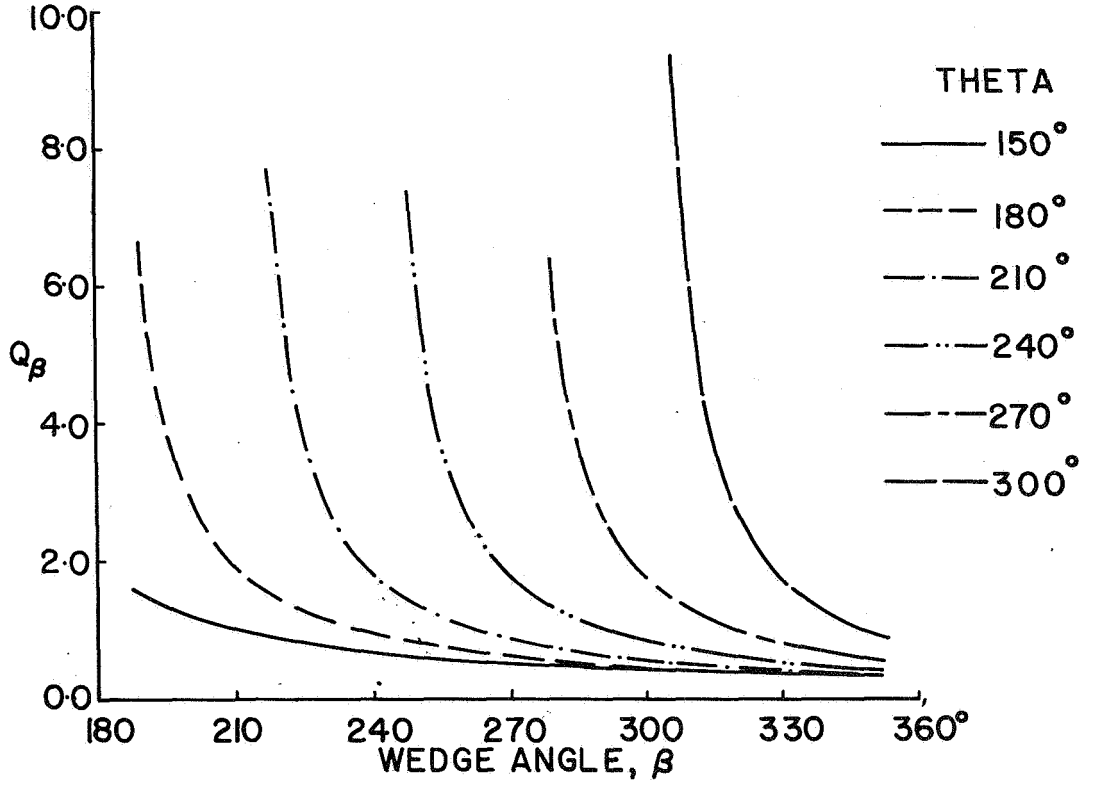

Figure 2.- Curves of Q_β $(-\theta)$.

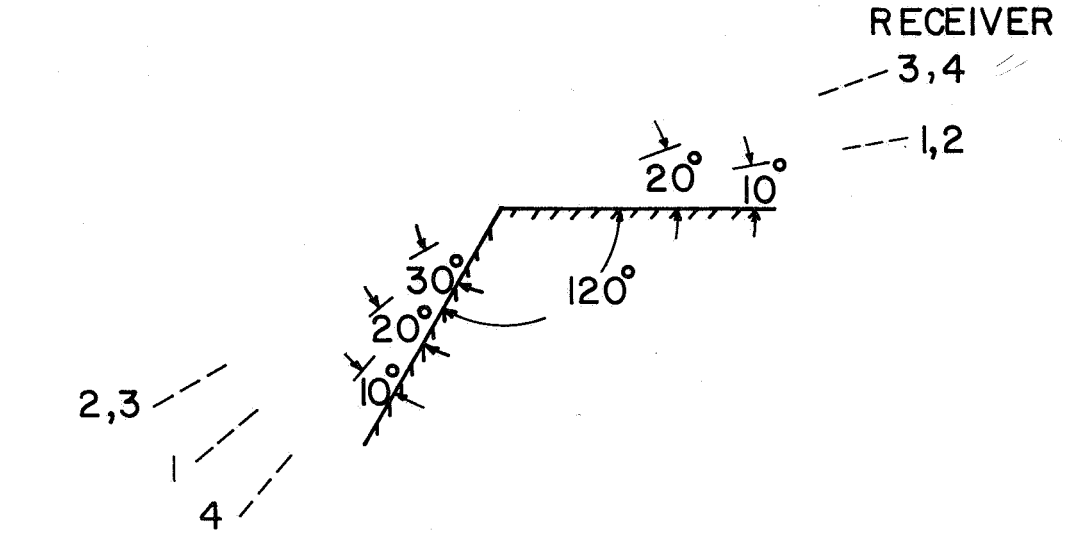

SOURCE CONFIGURATION

	1	2	3	4
Δ IL (DB)	6·1	4·6	1·8	6·9

Figure 3.- Finite-impedance correction to insertion loss. Surface admittance = 0.1 - 0.05i.

THE LEAKING MODE PROBLEM IN ATMOSPHERIC ACOUSTIC-GRAVITY WAVE PROPAGATION*

Wayne A. Kinney and Allan D. Pierce
Georgia Institute of Technology

SUMMARY

Previous attempts to predict the transient acoustic pressure pulse at long horizontal distances from large explosions in the atmosphere have adopted a model atmosphere bounded above by a halfspace of finite sound speed and have represented the waveform as a superposition of contributions from dispersively propagating guided modes. Certain modes at low frequencies decay exponentially (leaking modes) with increasing propagation distance. The practice up to now has been to neglect the contributions from such modes in such frequency ranges. The lower frequency cutoffs for such modes are extremely sensitive to the nature of the upper halfspace in contradiction to the reasonable supposition that energy ducted in the lower atmosphere should be insensitive to the assumed form of the upper halfspace. In the present paper the overall problem is reexamined with account taken of poles off the real axis and of branch line integrals in the general integral governing the transient waveform. Perturbation techniques are described for the computation of the imaginary ordinate of the poles and numerical studies are described for a model atmosphere terminated by a halfspace with c = 478 m/sec above 125 km. For frequencies less than 0.0125 rad/sec, the GR_1 mode, for example, is found to have a frequency dependent amplitude decay of the order of 10^{-4} nepers/km. Examples of numerically synthesized transient waveforms are exhibited with and without the inclusion of leaking modes. The inclusion of leaking modes results in waveforms with a more marked beginning rather than a low-frequency oscillating precursor of gradually increasing amplitude. Also, the revised computations indicate that waveforms invariably begin with a pressure rise, a result supported by other theoretical considerations and by experimental data.

INTRODUCTION

One of the standard mathematical problems in acoustic wave propagation is that of predicting the acoustic field at large horizontal distances from a localized source in a medium whose properties vary with height only. This problem, as well as its counterpart in electromagnetic theory, has received considerable attention in the literature (ref. 1), is reviewed extensively in various texts (refs. 2-7), and, for the most part, may be considered to be well understood.

A typical formulation of the transient propagation problem (refs. 8,9) leads (at sufficiently large horizontal distance r) to an intermediate result

*Work supported by Air Force Geophysics Laboratory

which expresses the acoustic pressure as a double Fourier integral over angular frequency ω and horizontal wave number k so that

$$p = S(r)\ \mathrm{Re}\ \{\int_0^\infty \hat{f}(\omega)e^{-i\omega t} \int_{-\infty}^{\infty} [Q/D(\omega,k)]e^{ikr}\,dk\,d\omega\}. \qquad (1)$$

Here S(r) is a geometrical spreading factor, which is $1/\sqrt{r}$ for horizontally stratified media and $1/[a_e \sin(r/a_e)]^{1/2}$ if the earth's curvature (a_e = radius of earth) is approximately taken into account. The quantity $f(\omega)$ is the Fourier transform of a time-dependent function that characterizes the source. Q is a function of receiver and source heights z_r and z_s, respectively, as well as of ω and k, and possibly of the horizontal direction of propagation if winds are included in the formulation. In any case, given z_r and z_s, Q should have no poles in the complex k-plane when ω is real and positive. The denominator $D(\omega,k)$ (which is termed the eigenmode dispersion function) may be zero for certain values $k_n(\omega)$ of k.

The k integration contour for Eq. (1) is chosen to lie along the real k-axis except where it skirts below or above poles which lie on the real axis (see Fig. 1a, where branch lines are identified by slash marks, poles are indicated by dots, and the k integration contour is marked by arrowheads that show the direction of integration). Let it suffice here to say that the placing of branch cuts and the selection of the contour must be such that the expression for the acoustic pressure dies out at long distance as long as a small amount of damping is included in the formulation. The guided-mode description in the formulation arises when the contour is deformed [permissible because of Cauchy's theorem and of Jordan's lemma (ref. 10)] to one such as is sketched in Fig. 1b. The poles indicated there above the initial contour are encircled in the counterclockwise sense, and there are contour segments which encircle (also in the counterclockwise sense) each branch cut that lies above the real axis. The integrals around each pole are evaluated by Cauchy's residue theorem so that what remains is a sum of residue terms plus branch line integrals. Each residue term is considered to correspond to a particular guided mode of propagation.

One approximation that was previously made in the guided-mode formulation was to neglect contributions from poles [i.e., the $k_n(\omega)$] which were located above the real k-axis (refs. 8,9). The thought behind this omission was that most of the contributions in the synthesis of waveforms for long propagation distances would come from poles which were on the real k-axis. Another approximation was that, for long distances, the contribution from branch line integrals could be neglected as well. Given these two approximations, the expression for the acoustic pressure in Eq. (1) can be approximated as follows:

$$p = \sum_n S(r) \int_{\omega_{Ln}}^{\omega_{Un}} A_n(\omega)\ \cos[\omega t - k_n(\omega)r + \phi_n(\omega)]\ d\omega, \qquad (2)$$

where $A_n(\omega)$ and $\phi_n(\omega)$ are defined in terms of the magnitude and phase of the residues of the integrand in Eq. (1) and the $k_n(\omega)$ are the real roots for $D(\omega,k)$ (which are numbered in some order with n = 1,2,3, etc.). It is understood that in Eq. (2), for any given n, $k_n(\omega)$ should be a continuous function of ω between the limits ω_{Ln} (lower) and ω_{Un} (upper). With this understanding, it should be possible to evaluate the resultant integral over ω approximately

by the method of stationary phase or by some numerical method.

In spite of the seeming plausibility of the above two approximations, there is a set of circumstances intrinsic to low-frequency infrasonic propagation for which they are not valid, even for distances of propagation of more than 10,000 km. It is these circumstances and their relation to the analytic synthesis of guided-mode atmospheric infrasonic waveforms that are of central interest in this discussion.

SYMBOLS FREQUENCY USED

A_{11}, A_{12}	defined in Eqs. (6)
c_T	sound speed for upper halfspace
$c(z)$	sound speed as a function of height
$D(\omega,k)$	eigenmode dispersion function defined in Eq. (5)
G	defined in Eq. (3)
GR_0, GR_1	gravitational modes
k, k_I, k_R	horizontal wave number and its imaginary and real parts, respectively
$k_n(\omega)$	ordered roots of $D(\omega,k)$
p	acoustic pressure
r	horizontal distance of propagation
R_{11}, R_{12}	[1,1] and [1,2] elements of the transmission matrix [R], respectively
t	time
v	phase velocity (ω,k)
$v^{(1)}$	complex phase velocity obtained by first iteration with Eq. (8a)
$v_a(\omega), v_b(\omega)$	roots of $R_{11}(\omega,v)$ and $R_{12}(\omega,v)$, respectively
$v_n(\omega)$	roots of $D(\omega,v)$
z	height
z_T	height of bottom of upper halfspace
α, β	derivatives of R_{11} and R_{12} with respect to v, respectively, and evaluated at v_a and v_b, respectively
ρ_o	ambient density
ω	angular frequency
ω_A, ω_B	characteristic frequencies used in Eq. (3)
(ω_L, v_L)	cutoff point in the (ω,v)-plane for a non-leaking mode.

INFRASONIC MODES

An atmospheric model that is frequently adopted in studies of infrasound is one in which the sound speed c(z) varies continuously with height z in some reasonably realistic manner up to a specified height z_T and is constant (value c_T) for all heights exceeding z_T (see Fig. 2). Should winds be included in the formulation, the wind velocities are also assumed to be constant in the upper halfspace $z > z_T$. It would seem reasonable to say that there is some choice in specifying the values for both z_T and c_T, even though the computations of such factors as Q and $D(\omega,k)$ in Eq. (1) become more lengthy with increasing z_T. Whatever the choice of z_T, it would seem reasonable to choose c_T to be $c(z_T)$ so that the sound-speed profile would then be continuous with height. Intuitively, it would also seem that if the source and receiver are both near the ground and if the energy actually reaching the receiver travels

via modes of propagation channeled primarily in the lower atmosphere, then the actual value of the integral in Eq. (1) would be somewhat insensitive to the choices of z_T and c_T. This idea, however, remains to be justified in any rigorous sense. In typical calculations performed in the past, z_T was taken as 225 km, and c_T was taken as the sound speed ($\approx$ 800 m/sec) at that altitude (ref. 8).

The formulation leading to that version of Eq. (1) which is appropriate to infrasound for frequencies at which gravitational effects are important (corresponding to periods greater than one to five minutes) is based on the equations of fluid dynamics with the inclusion of gravitational body forces, the associated nearly exponential decrease of ambient density and pressure with height, and a localized energy source. When c_T is taken to be finite, the incorporation of gravitational effects in this formulation leads to a dispersion relation for plane waves propagating in the upper halfspace which is (winds neglected) (refs. 8,9)

$$k_z^2 = -G^2 = [\omega^2 - \omega_A^2]/c_T^2 - [\omega^2 - \omega_B^2]k^2/\omega^2, \tag{3}$$

where the solution of the linearized equations of fluid dynamics for $z > z_T$ is of the form

$$p/\sqrt{\rho_o} = (\text{Constant})\ e^{-i\omega t}\ e^{ikx}\ e^{ik_z z}\ . \tag{4}$$

In these equations p is again the acoustic pressure, ρ_o is ambient density, x is the horizontal space dimension, and k_z is the vertical wave number (alternatively written as iG for inhomogeneous plane waves). ω_A and ω_B are two characteristic frequencies ($\omega_A > \omega_B$) for wave propagation in an isothermal atmosphere where $\omega_A = (\gamma/2)g/c_T$ and $\omega_B = (\gamma - 1)^{1/2}\ g/c_T$ ($g \approx 9.8$ m/sec^2 is the acceleration due to gravity and $\gamma \approx 1.4$ is the specific heat ratio for air). The values of k (positive and negative) at which G^2 is zero turn out to be the branch points in the k integration in Eq. (1). The branch lines extend upwards and downwards from the positive and negative branch points, respectively (recall Fig. 1).

The eigenmode dispersion function $D(\omega,k)$ in the case of atmospheric infrasound can be written in the general form (ref. 8)

$$D(\omega,k) = A_{12}R_{11} - A_{11}R_{12} - R_{12}G. \tag{5}$$

In this expression, R_{11} and R_{12} are the elements of a transmission matrix [R]. They depend on the atmospheric properties only in the altitude range zero to z_T, and are independent of what is assumed for the upper halfspace. In general, their determination requires numerical integration over height of two simultaneous ordinary differential equations [termed the residual equations (refs. 8,9,11)]. They do depend on ω and k (or, alternately, on ω and phase velocity $v = \omega/k$), but are free from branch cuts. The other parameters A_{12} and A_{11} depend on the properties of the upper halfspace, and on ω and k. A_{11} and A_{12} are given (winds excluded) as

$$A_{11} = gk^2/\omega^2 - \gamma g/[2c_T^2]; \tag{6a}$$

$$A_{12} = 1 - c_T^2 k^2/\omega^2. \qquad (6b)$$

It may be noted that, since every quantity in Eq. (5) (with the possible exception of G) is real when ω and k are real, the poles that lie on the real k-axis (recall that they are the real roots of D) must be in those regions of the (ω,k)-plane [or, alternatively, the (ω,v)-plane] where $G^2 > 0$. Since at heights above z_T, the integrand of Eq. (1) divided by $\sqrt{\rho_o}$ should vary with z as e^{-Gz_T}, there is no leakage of energy into the upper halfspace for those modes that correspond to the above poles. Such modes are termed fully ducted modes. Modes for which there is leakage of energy are termed leaking. If D is considered as a function of ω and phase velocity v, the locus of its real roots $v(\omega)$ (dispersion curves) has [as has been found by numerical computation with the program INFRASONIC WAVEFORMS (ref. 8)] the general form sketched in Fig. 3. The nomenclature for labeling the modes (GR for gravity, S for sound) is due to Press and Harkrider (ref. 12). It may be noted from Eq. (3) that there are two "forbidden regions" (slashed in the figure) in the (ω,v)-plane. Within these regions there are no real roots of the function $D(\omega,v)$ because G is imaginary. The existence of the high-frequency upper "forbidden region" implies that the phase velocities for propagating modes are always less than the sound speed chosen for the upper halfspace. The low-frequency lower-phase-velocity "forbidden region" appears to be due to the incorporation of gravitational effects into the formulation. However, if c_T is allowed to approach infinity, the lower "forbidden region" disappears. Thus, it can be seen that the fully ducted GR_0 and GR_1 modes both have a low-frequency cutoff [ω_L in Eq. (2)] which depends on c_T. In fact, the larger c_T becomes, the smaller this cutoff frequency becomes.

At this point, there should appear to be the following paradoxes. Given that frequencies below ω_B may be important for the synthesis of a waveform, an apparently plausible computational scheme based on the reasoning leading to Eq. (2) will omit much of the information conveyed by such frequencies. Also, in spite of the plausible premise that energy ducted primarily in the lower atmosphere should be insensitive to the choice for c_T, it can be seen that this choice governs the cutoff frequencies for certain modes and that certain important frequency ranges could conceivably be omitted by a seemingly logical choice for c_T. The resolution of these paradoxes seems to lie in the nature of the approximations made in going from Eq. (1) to Eq. (2). The latter equation may not be as nearly correct as earlier presumed, and it may be necessary to include contributions from poles off the real axis as well as from the branch line integrals. Even for the case when the propagation distance r is very long, it may be that the imaginary parts of the complex horizontal wave numbers are so small that the magnitude of e^{ikr} in Eq. (1) is still not small compared to unity. In addition, a branch line integral may be appreciable in magnitude at large r if there is a pole relatively close to the associated branch cut.

ROOTS OF THE DISPERSION FUNCTION

In light of the paradoxes mentioned, it would be desirable to modify the solution represented by Eq. (2) so as to remove the apparent artificial low-frequency cutoffs of the GR_0 and GR_1 modes. As a first step, the nature of the eigenmode dispersion function D in the vicinity of the dispersion curve for

a particular mode is examined. The curve of values $v_n(\omega)$ of phase velocity v versus ω for a given (n-th) mode is known for frequencies greater than the low cutoff frequency ω_L. Given this curve, analogous curves $v_a(\omega)$ and $v_b(\omega)$ can be found for values of the phase velocity ω/k at which the functions $R_{11}(\omega,v)$ and $R_{12}(\omega,v)$ in Eq. (5), respectively, vanish. One characteristic of the curves $v_n(\omega)$, $v_a(\omega)$, and $v_b(\omega)$ which has been checked numerically for $\omega > \omega_L$ (see Fig. 4) is that, for a given mode of interest, these curves all lie substantially closer to one another than to the corresponding curves for a different mode.

Given the definitions above of $v_a(\omega)$ and $v_b(\omega)$, the dispersion relation $D = 0$ for a single mode may be approximately expressed, through a simple expansion, as

$$D \approx (A_{12})(\alpha)(v - v_a) - [A_{11} + G](\beta)(v - v_b) = 0, \tag{7}$$

where $\alpha = dR_{11}/dv$, and $\beta = dR_{12}/dv$, evaluated at $v = v_a$ and v_b, respectively (for simplicity, D is considered here as a function of ω and $v = \omega/k$ rather than of ω and k). The above equation may also be written in the form

$$v^{(1)} = v_a + (v_a - v_b)X/[1-X], \tag{8a}$$

where

$$X = (\beta/\alpha)(A_{11} + G)/A_{12}. \tag{8b}$$

Eq. (8a) may be considered as a starting point for an iterative solution which develops v in a power series in $v_a - v_b$. With $v = v_a$ as the zeroth iteration, the right hand side of Eq. (8a) can be evaluated for the value of v required for the next iteration, etc. This iterative procedure should converge provided that v_a or v_b is not near a point at which G vanishes and provided that G in the vicinity of v_a or v_b is not such that the variable X is close to unity. Among other limitations, the iterative scheme is inappropriate for those values of ω in the immediate vicinity of ω_L.

As an illustration of the perturbation technique, detailed plots (for the GR_0 and GR_1 modes) versus angular frequency are given in Fig. 5 of ω/k_R (top portion of the figure) which is the reciprocal of the real part of $1/v^{(1)}$, and of k_I (bottom portion) which is the imaginary part of $\omega/v^{(1)}$ (k_R and k_I are the real and imaginary parts of k, respectively), where $v^{(1)}$ is the result of first iteration for the phase velocity using Eqs. (8). Note that k_I is zero above the corresponding cutoff frequencies. The values shown in Fig. 5 are appropriate to the case of a U. S. Standard Atmosphere (ref. 8; see also Fig. 2) without winds which is terminated at a height of 125 km by an upper halfspace possessing a sound speed of 478 m/sec. For frequencies at which v_n is computed, the agreement between $v^{(1)}$ and v_n has proven to be excellent. The ω/k_R serve as approximate extensions of the dispersion curves down to frequencies near zero, thus enabling the computation of waveforms with leaking modes included.

TRANSITION OF MODES FROM NON-LEAKING TO LEAKING

A more precise approximation to $D(\omega,v)$ in the vicinity of cutoff [i.e., near the point (ω_L,v_L)] reveals that a dispersion curve becomes tangential to

the line $G^2 = 0$ at (ω_L, v_L). For $\omega < \omega_L$, there is a very narrow gap in the frequency range in which there are no poles in the k- (or v-) plane corresponding to a given n-th mode. This gap is of the order 10^{-13} rad/sec for the GR_0 mode and 10^{-9} rad/sec for the GR_1 mode.

Since there is a gap in the range of frequencies for which a pole (corresponding to a mode) may exist, it is evident that evaluation of the integral over k in Eq. (1) by merely including residues may be insufficient for certain frequencies. Thus it would seem appropriate to include a contribution from branch line integrals. However, there is a line of reasoning which demonstrates that all contributions from branch line integrals are insignificant as previously assumed. Further details on this matter are provided in reference 13.

EXAMPLE (HOUSATONIC)

Values of ω/k_R and k_I calculated by the perturbation techniques outlined above were used [with a revised version of INFRASONIC WAVEFORMS (ref. 14)] to compute waveforms for the case of signals observed at Berkeley, California, following the Housatonic detonation at Johnson Island on October 30, 1962. A comparison of theoretical and observed waveforms for this case is given by Pierce, Posey, and Iliff (ref. 9). This case also serves as the main example in the 1970 AFCRL report by Pierce and Posey (ref. 8), and is discussed by Posey (ref. 15) within the context of the theory of the Lamb edge mode. The model atmosphere assumed here (winds included) is the same as in Fig. 3-12 of reference 8, except that in the present model the upper halfspace begins at 125 km rather than at 225 km. To avoid repeating tedious calculations of the k_I for the GR_0 and GR_1 modes for this model atmosphere, it was assumed that the k_I would be close in value to those shown in Fig. 5.

In Fig. 6, sets of plots for the Housatonic case are shown with and without leaking modes. The waveform that includes leaking modes is regarded as an improvement in that among other things, the spurious initial pressure drop shown in the original waveform is not present here. In Fig. 7 of reference 9 observed and theoretical waveforms are shown for the Housatonic case. On the basis of the calculations described above, this figure was redrawn and is given here as Fig. 7. The only difference between the two figures lies in the central waveform. The false precursor is absent in the waveform shown in Fig. 7, and the first peak to trough amplitude has been changed from 157 bar to 170 bar (less than a 10% increase). The remainder of the central waveform is virtually unchanged. The discrepancy with the edge-mode synthesis has not been diminished and remains a topic for future study.

CONCLUDING REMARKS

It was shown in this paper that, for a model atmosphere in which the sound speed is constant above some arbitrarily large height, the GR_0 and GR_1 modes have low cutoff frequencies and are leaking below that height. Given these facts, perturbation techniques were provided for the computation of the imaginary and real parts k_I and k_R, respectively, of the horizontal wave numbers for these modes. Knowledge of the k_I and k_R then made it possible to include, in a synthesis of waveforms, contributions from the GR_0 and GR_1 modes at frequencies where these modes were leaking. Finally it was demonstrated that this inclusion yielded waveforms that were more realistic than before.

REFERENCES

1. Thomas, J. E.; Pierce, A. D.; Flinn, E. A.; and Craine, L. B.: "Bibliography on Infrasonic Waves," Geophys. J. R. Astr. Soc. 26, 299-426 (1971).

2. Officer, C. G.: Introduction to the Theory of Sound Transmission with Application to the Ocean (McGraw-Hill, New York, 1958).

3. Wait, J. R.: Electromagnetic Waves in Stratified Media (Pergamon Press, Inc., New York, 1962).

4. Brekhovskikh, L. M.: Waves in Layered Media (Academic Press, New York, 1960).

5. Budden, K. G.: The Wave-Guide Mode Theory of Wave Propagation (Prentice-Hall, Inc., Englewood Cliffs, N. J., 1961).

6. Tolstoy, I. and Clay, C. S.: Ocean Acoustics (McGraw-Hill, New York, 1966).

7. Ewing, M.; Jardetzky, W.; and Press, F.: Elastic Waves in Layered Media (McGraw-Hill, New York, 1957).

8. Pierce, A. D. and Posey, J. W.: Theoretical Prediction of Acoustic-Gravity Pressure Waveforms generated by Large Explosions in the Atmosphere, Report AFCRL-70-0134, Air Force Cambridge Research Laboratories, 1970.

9. Pierce, A. D.; Posey, J. W.; and Iliff, E. F.: "Variation of Nuclear Explosion generated Acoustic-Gravity Waveforms with Burst Height and with Energy Yield," J. Geophys. Res. 76, 5025-5042 (1971).

10. Copson, E. T.: An Introduction to the Theory of Functions of a Complex Variable (Clarendon Press, Oxford, 1935) p. 137.

11. Pierce, A. D.: "The Multilayer Approximation for Infrasonic Wave Propagation in a Temperature and Wind-Stratified Atmosphere," J. Comp. Phys. 1, 343-366 (1967).

12. Press, F. and Harkrider, D.: "Propagation of Acoustic-Gravity Waves in the Atmosphere," J. Geophys. Res. 67, 3889-3908 (1962).

13. Pierce, A. D.; Kinney, W. A.; and Kapper, C. Y.: "Atmosphere Acoustic-Gravity Modes at Frequecies near and below Low Frequency Cutoff Imposed by Upper Boundary Conditions," Report No. AFCRL-TR-75-0639, Air Force Cambridge Research Laboratories, Hanscom AFB, Mass. 01731 (1 March 1976).

14. Pierce, A. D. and Kinney, W. A.: "Computational Techniques for the Study of Infrasound Propagation in the Atmosphere," Report No. AFCL-TR-76-0056, Air Force Geophysics Laboratory, Hanscomb AFB, Mass. 01731 (13 March 1976)

15. Posey, J. W.: "Application of Lamb Edge Mode Theory in the Analysis of Explosively Generated Infrasound," Ph.D. Thesis, Dept. of Mech. Engrg., Mass. Inst. of Tech. (August, 1971).

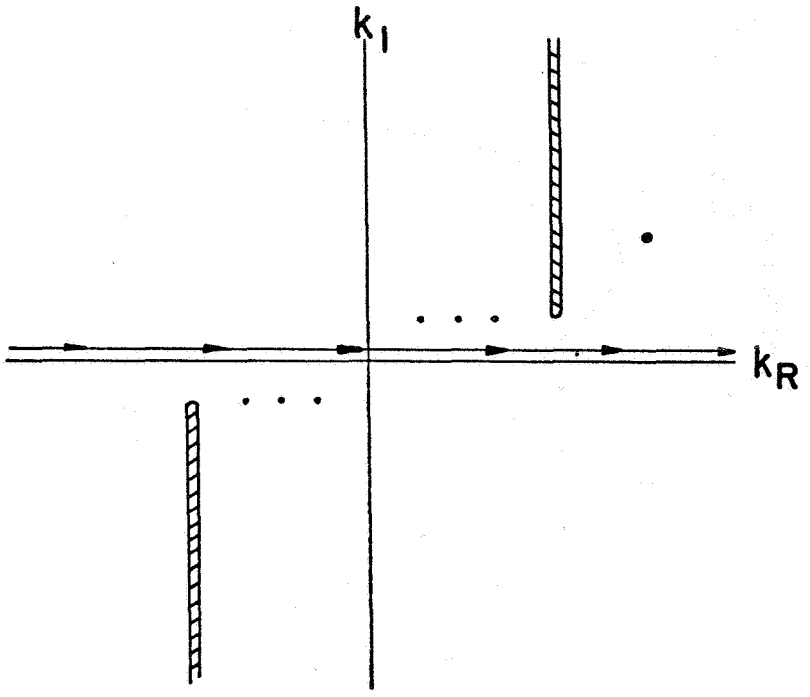

(a) Original.

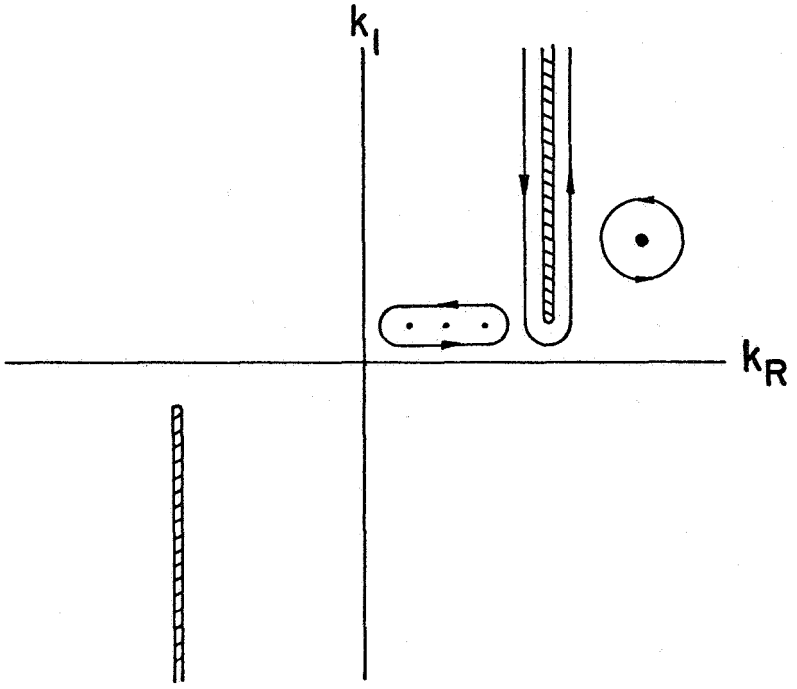

(b) Deformed.

Figure 1.- k-integration contours.

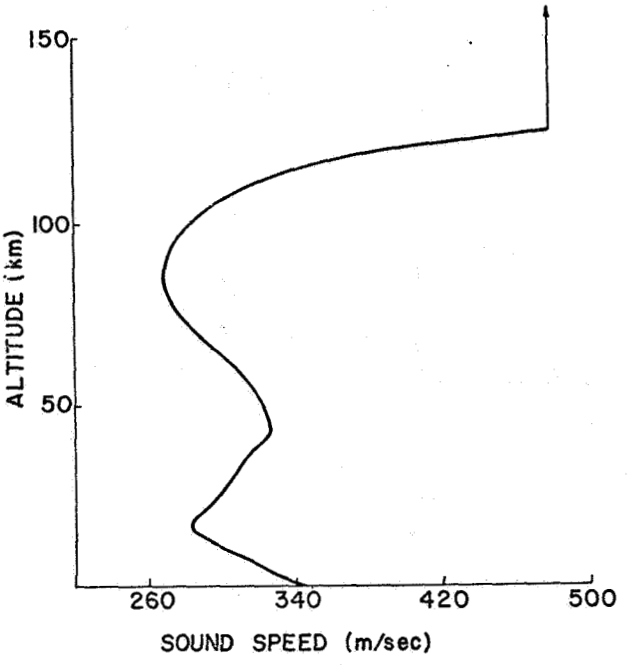

Figure 2.- Model atmosphere.

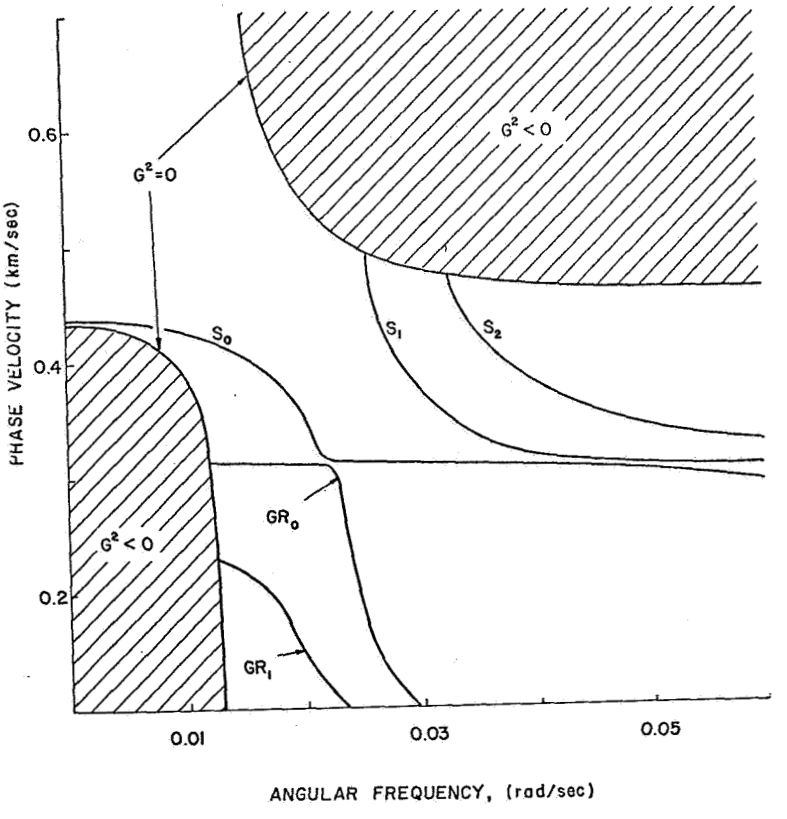

Figure 3.- Dispersion curves.

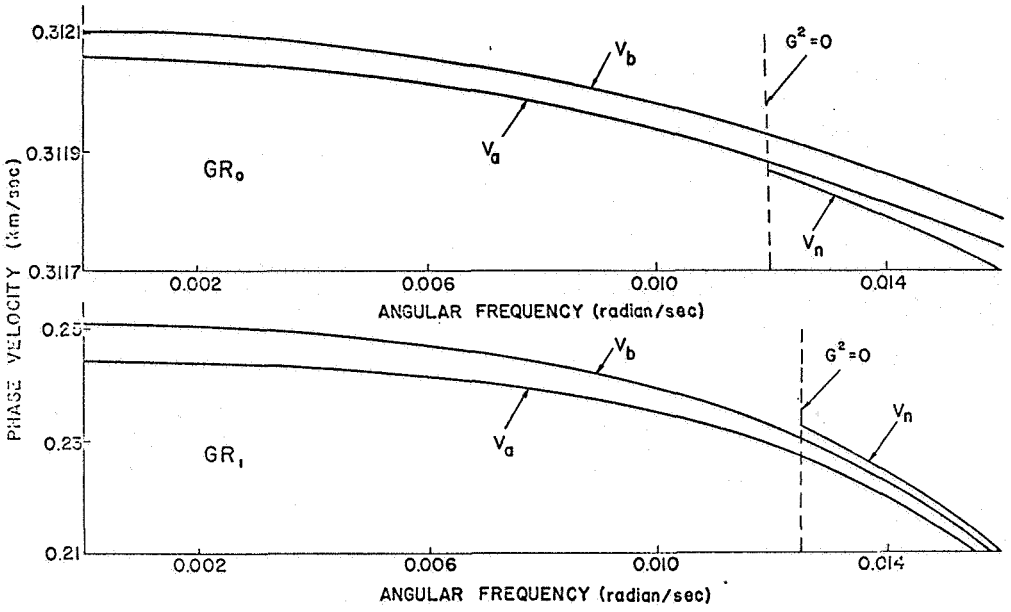

Figure 4.- Curves of v_n, v_a, and v_b.

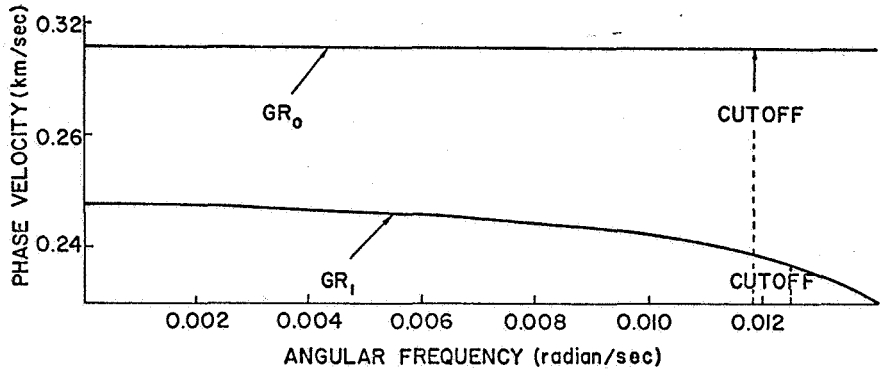

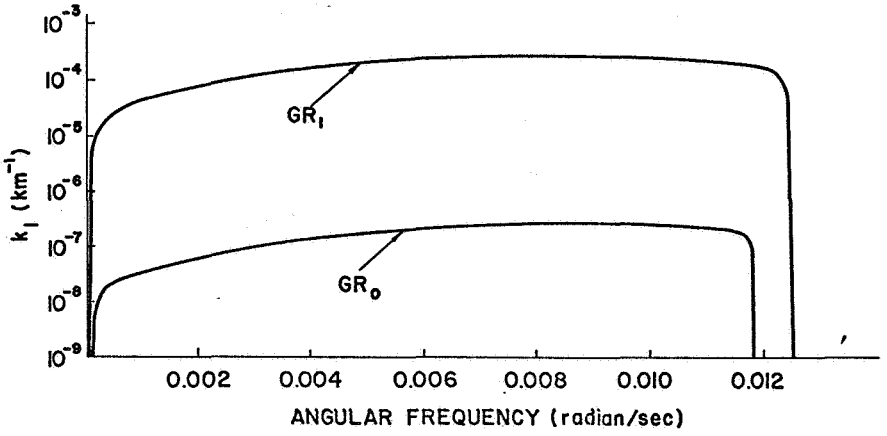

Figure 5.- Curves of ω/k_R and k_I.

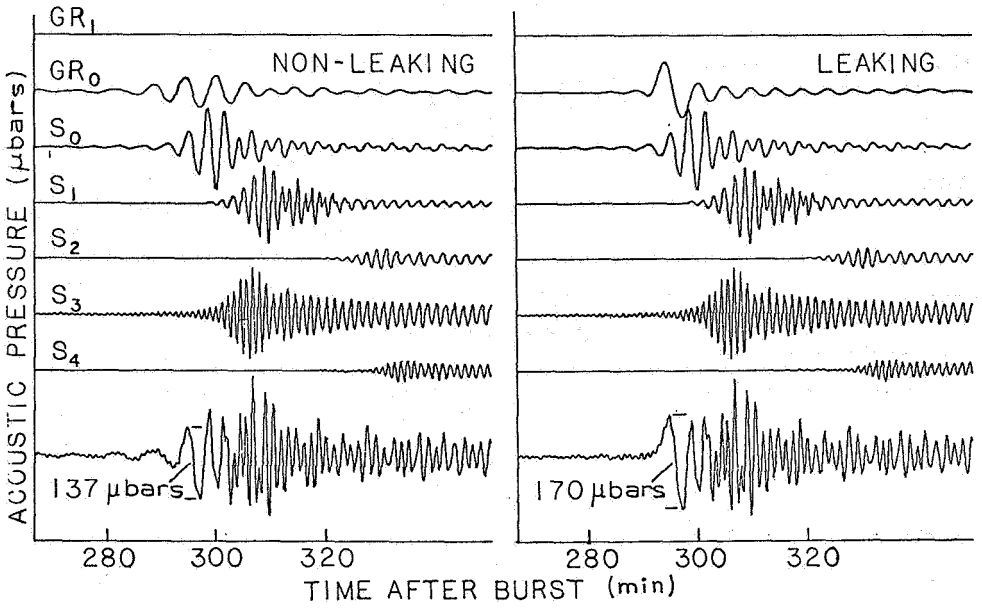

Figure 6.- Numerically synthesized waveforms (Housatonic).

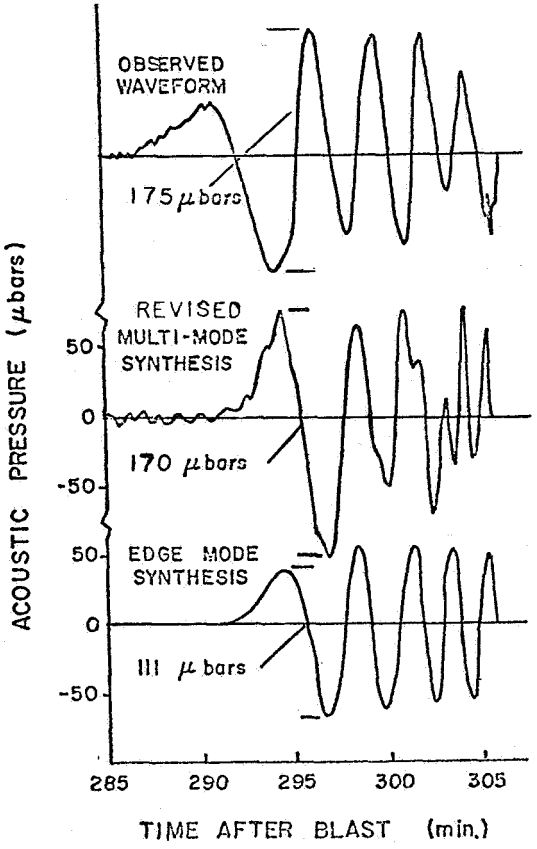

Figure 7.- Observed and theoretical waveforms (Housatonic).

THE PREDICTION AND MEASUREMENT OF SOUND RADIATED BY STRUCTURES

Richard H. Lyon and J. Daniel Brito
Massachusetts Institute of Technology

INTRODUCTION

This paper is a review of certain theoretical ideas about the radiation of sound and shows how these ideas have been implemented in strategies for explaining or measuring the sound produced by practical structures. We shall be especially interested in those aspects of the subject that relate to the determination of the relative amounts of sound generated by various parts of a machine or structure, which can be very useful information for noise reduction efforts. We will also point out areas in which significant uncertainties or questions remain in the theoretical and experimental aspects of the subject.

Intensity and Energy Density

Since the acoustical equations are first-order perturbations of the underlying fluid, dynamical, and state equations, it is not obvious that acoustical intensity, which is a second-order quantity, can be determined from the first-order quantities only. It is shown in advanced texts, however, that in a nonmoving ideal fluid, an energy conservation statement can be written in the form

$$\frac{\partial \varepsilon}{\partial t} + \nabla \cdot \vec{I} = 0, \qquad (1)$$

where $\varepsilon = \frac{1}{2}\rho_o u^2 + \frac{1}{2}p^2/\rho_o c^2$ is the acoustical energy density, $\vec{I} = p\vec{u}$ is the intensity, p and $\vec{u}$ are the first-order "acoustic" pressure and particle velocity respectively. This formulation, while internally consistent, does leave certain second-order terms out of the intensity and energy density which correspond to the transport of internal energy of the fluid by streaming flows. These terms are usually of little practical importance.

From eq. (1), it is clear that the addition to $\vec{I}$ of any solenoidal vector field will leave the conservation relation unchanged, but can greatly alter the intensity vector at any position (and time). Such solenoidal intensity fields do exist in reverberant fields (even when time averaged) and represent one way that reverberant sound can contaminate a measurement of sound intensity.

Simple Radiators

A simple radiator is a rigid plane surface, vibrating with a velocity u in a direction perpendicular to its own surface, set in an infinite rigid plane. When all dimensions of this vibrator are large compared to a wavelength, then the magnitude of the intensity is $I = u^2\rho_o c$. If the vibrator is a circular piston of radius a, then the total time-averaged radiated-sound power is

$$\Pi_{rad} = \langle u^2 \rangle \rho_o c S \sigma_{rad} \qquad (2)$$

where S is the area of the piston and σ_{rad} is the radiation efficiency, shown graphed in fig. 1.

The interesting feature of fig. 1 is that, as expected, σ_{rad} approaches unity at frequencies such that the wavelength is small compared to piston diameter, but also, this limit is essentially reached when the piston diameter is only about one-third of the wavelength of the sound wave. This geometric effect is very important in sound radiation by machines since many machines have sizes comparable to the wavelength of sound at frequencies of interest.

The radiation of sound by waves on a plane can be pictured as shown in fig. 2. Above the critical frequency, the flexural waves become supersonic (acoustically fast), and there is highly directed sound radiation. Below this frequency, the flexural wave is subsonic (acoustically slow), and there is no sound radiation from an infinite plate. The critical frequency is determined by elastic properties of the plate -- a simple formula for steel, aluminum, or glass is:

$$f_c = 500/h \text{ (in)}$$

where the thickness h is expressed in inches. This effect of bending wavespeed on radiation efficiency is very important for large flat structures, but less so for highly curved, segmented, or stiffened structures. Plate damping generally has a large effect on the amplitude of vibration (determines $\langle u^2 \rangle$), but has little practical effect on the radiation efficiency.

Above the critical frequency, the theoretical sound intensity is uniform over the surface. This is also the case for large finite supported plates, as shown in fig. 3. With a single mode of vibration, there are nodal lines in the intensity that correspond to zero velocity node lines on the plate. When the vibration is multimodal, the intensity pattern becomes more uniform.

Below the critical frequency, any interruption or discontinuity in the properties of an infinite plate (such as the line of support shown in fig. 4) will result in radiation of sound at frequencies less than the critical frequency. The normal component of intensity for such a support due to flexural waves reflecting from it at normal incidence is shown in fig. 4. Note the alternating regions of positive and negative intensity, with the region next to the support line being positive. The net radiation due to the line support is, of course, positive, but various regions of the plate are emitting and absorbing sound over an extended area.

When the plate is finite, it has been shown that below the critical frequency, the radiation efficiency is proportional to the perimeter of the plate. This has led to the concept of "edge radiation", with the strong implication that the sound is radiated from the edges of the plate. The average radiation efficiency for a supported plate is shown in fig. 5. A direct calculation of the sound intensity for a supported rectangular plate shows that the region very close to the edge is nearly always radiating, particularly for the edge modes that have trace wavelengths greater than the wavelength of sound. In fig. 6, we show a scan of intensity across a section of a simply supported plate for a single mode of vibration mode (17, 1), which clearly shows this edge radiation effect. In fig. 7, the case of multimodal radiation is shown. Thus, although the total radiated sound power from the plate is proportional to its edge length, the *pattern* of intensity is more like that of a set of surface radiators and absorbers with a line of radiation along the edge.

In addition to radiator size, plate thickness, and framing or support structure effects, curvature effects can also play an important role in radiation efficiency. Curved surfaces are stiffer than flat structures and may vibrate less, but their radiation efficiencies are generally higher. In fig. 5, we show the effect of curvature by comparing the radiation efficiency of a flat supported plate with that of a cylinder formed by rolling the plate.

EXPERIMENTAL METHODS

A number of experimental techniques are available for determining the amount of sound power radiated by a structure (or machine). Some methods simply give the total radiated power and possibly the directivity. Others allow one to measure, or infer, the amount of sound produced by various parts of the structure. Present concerns about machinery noise and noise reduction by design create special interest in techniques that allow one to scan the near field of the machine and determine noise radiated by various elements or surfaces.

The most commonly used technique is the reverberation method, in which the machine is placed in a room of fairly low absorption. In such a room, the reverberant mean square pressure $\langle p_R^2 \rangle$ is related to the radiated power Π_{rad}

$$\langle p_R^2 \rangle = \frac{4\Pi_{rad}\rho_o c}{R} \tag{3}$$

where $R = S\bar{\alpha}/(1-\bar{\alpha})$ is the "room constant", $\bar{\alpha}$ is the absorption coefficient in the room, and S is its interior area. The measurement of $\langle p_R^2 \rangle$ can only be done reliably when the wavelength of sound is less than half of a typical room dimension and if the source does not contain dominating pure tone components.

Another well known procedure employs a reflection free, or anechoic, room to measure the direct field $\langle p_D^2 \rangle$ from the radiator, which is related to the radiated power by

$$\langle p_D^2 \rangle = \frac{\Pi_{rad}\rho_o c}{4\pi r^2} Q \tag{4}$$

where Q is the directivity function and r is the distance from the "acoustic center" of the source. Since one does not know where the acoustic center of a source is, r must be large enough so that such uncertainties don't matter. Typically, r must be greater than the largest dimension of the source for the measurement to be in the "far field" or Frauenhofer zone of the radiator. This measurement technique allows one to determine the directivity function Q and the total power by an integration over solid angle.

A variation of the methods in the two preceding paragraphs is the "window" technique in which the machine is wrapped and then various positions of the machine are exposed. In this way, the contributions to the total noise power (and directivity) can be determined, if we assume that the process of wrapping does not disturb the relative roles of various elements in sound radiation. A sketch of a machine with its wrappings undergoing this process is shown in fig. 8. This procedure is conceptually simple, but the process of wrapping and unwrapping and the repetition of the sound measurements for each case can get quite time consuming and cumbersome.

The direct, or free field, method is essentially a measurement of sound intensity with a microphone. An intensity measurement close to the machine surface requires both a velocity and pressure measurement. The velocity measurement may be done using either a pressure gradient microphone or an accelerometer mounted to the surface of the structure, as shown in fig. 9. The required filtering, multiplication, and time averaging can be done by either analog or digital methods. The principal challenge is making sure that relative phase variations in the pressure and velocity channels are kept to a minimum.

Measurements of the intensity near the surface of a supported plate using a microphone-accelerometer scheme are shown in figs. 6 and 7. These measurements are in good agreement with the theoretical predictions shown in these figures, but these examples demonstrate one of the difficulties of applying this method. Since there are some areas of sound generation and others of sound absorption, a correct assessment of total, radiated-sound power requires

a very careful and accurate scan of the surface. Also, the requirement for two, phase-matched, measurement channels adds to the complication. Thus, its practical utility in measuring machine component noise is likely to be fairly limited.

Since measurements at the surface of a structure to determine relative sound generation of its various parts are so desirable, schemes have been developed which, although they lack a strict theoretical basis, are used because they seem to give useful answers, are very easy to implement, and the results are easy to interpret. The methods are the near field pressure scan and the acceleration, or radiation, efficiency method.

The near-field pressure scan takes note of the fact that the intensity of sound in a plane wave is $\langle p^2 \rangle / \rho_o c$ and in a diffuse field (over solid angle 2π) is $\langle p^2 \rangle / 2\rho_o c$ to assert that near a machine surface the intensity is $\langle p^2 \rangle / \delta \rho_o c$, where δ is to be determined. Each part of the machine has an area S_i and, consequently, the total power is

$$\Pi_{rad} = \sum_i \frac{\langle p_i^2 \rangle S_i}{\delta \rho_o c} \tag{5}$$

If Π_{rad} is known from a reverberant measurement, δ is determined. Most studies suggest a value of 4 for δ. In fig. 10, we show the total, sound-power output measured for a consumer sewing machine and the relative contribution to the total radiated power from its various surfaces as determined by this method. Also shown are the iso-pressure contours on this machine for the 500-Hz octave band.

The radiation efficiency method assumes that the sound radiation is dominated by vibrating structure. Mean square acceleration values $\langle a_i^2 \rangle$ are determined for various parts of the structure, and the radiated power is determined by a variant of eq. (2),

$$\Pi_{rad} = \sum_i \frac{\langle a_i^2 \rangle S_i}{\omega^2} \rho_o c \, \sigma_{rad,i} \tag{6}$$

One can assume that $\sigma_{rad,i}$ is the same for all surfaces and determine its value by a measurement of total radiated power. Then, the relative sound produced by each part of the machine is proportional to its contribution $\langle a_i^2 \rangle S_i$. This has been done for the sewing machine, and the result is shown in fig. 11. Obviously, this technique does not rank the sound output of the various elements in the same way that the pressure method does.

Of course, this last method can be improved by using the ideas presented in the section on "Simple Radiators" to make better estimates of

$\sigma_{rad,i}$. However, on balance, this vibration technique has several drawbacks compared to the pressure method. There is generally more variability to the acceleration field than in the pressure field so that an average is more difficult to determine. There is only a single, unknown parameter in the pressure method (δ) compared to several ($\sigma_{rad,i}$) in the acceleration method. Also, the acceleration method requires that structural vibration dominate the sound generation process, while no such assumption is made in the pressure method.

Clearly, more research and applications studies are required to define the basis for and limitations of these simplified methods for determining the sound produced by various parts of a machine or structure. Moreover, there is good reason to carry out these studies because of the importance of such measurements in developing noise reduction treatments for machines, particularly in the important area of redesign for reduced noise emission.

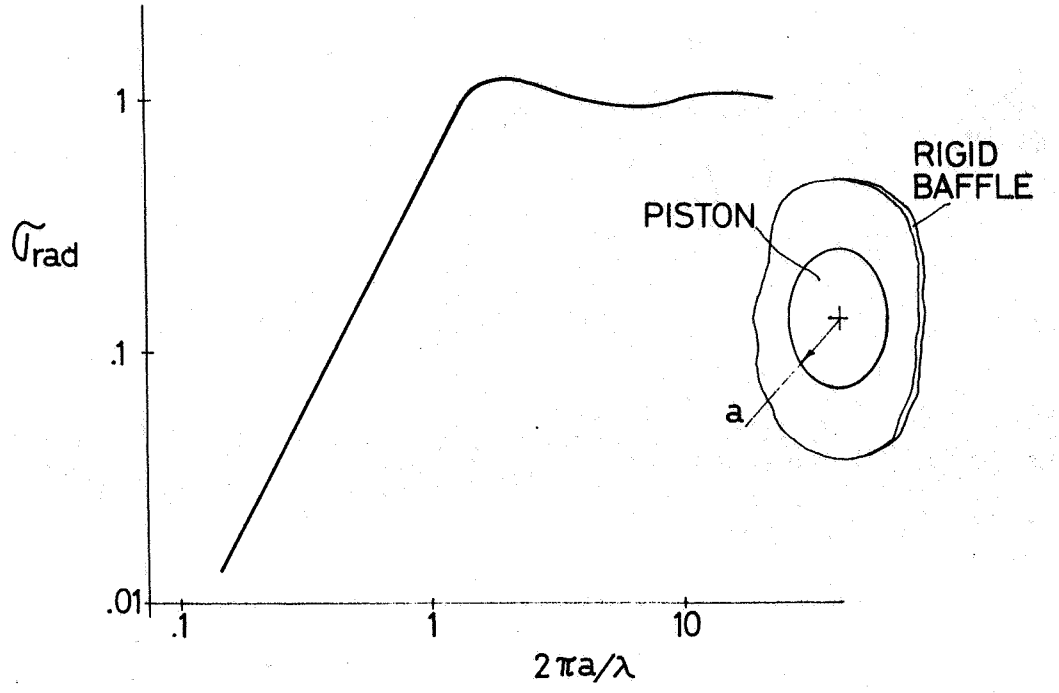

Figure 1.- Sketch of vibrating piston and theoretical radiation efficiency.

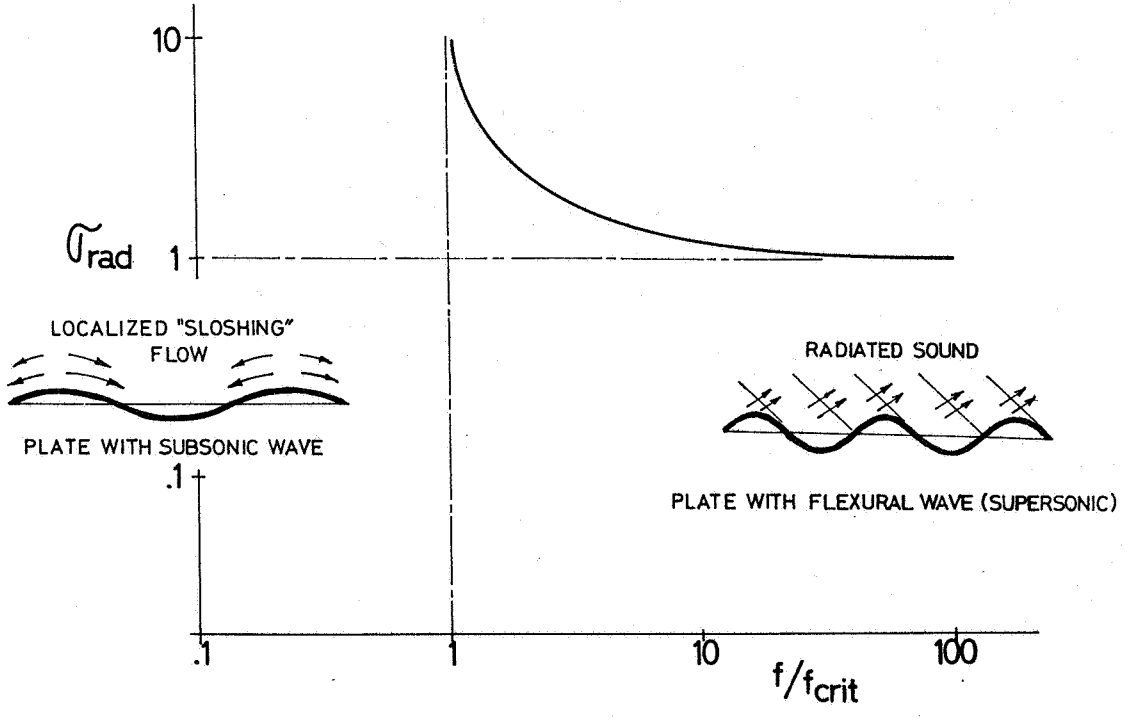

Figure 2.- Sketch of radiation of sound by vibrating plate, associated air motion, and resulting radiation efficiency.

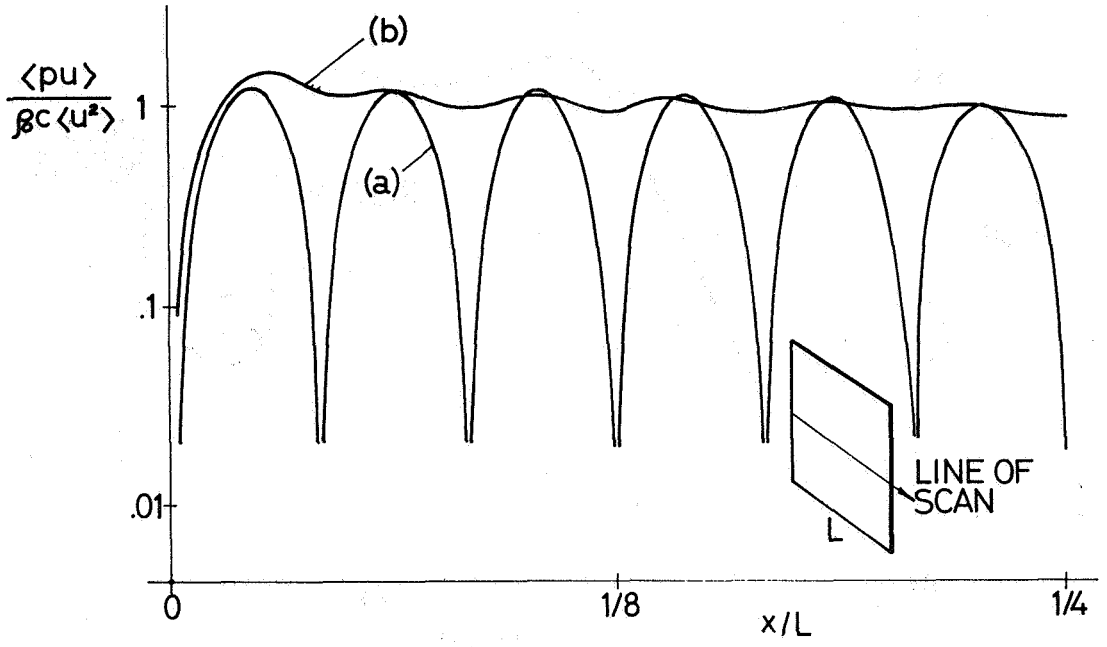

Figure 3.- Normal component of intensity vector at surface of vibrating, simply-supported plate above its critical frequency. (a) Single mode, (b) multi-modal.

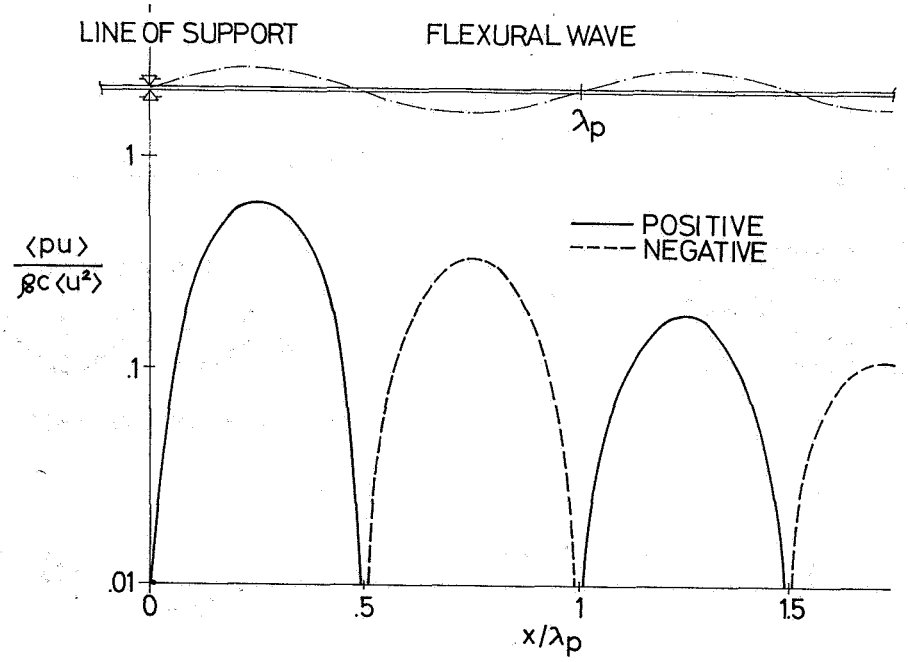

Figure 4.- Intensity near a line of support on an infinite plate showing regions of positive and negative intensity.

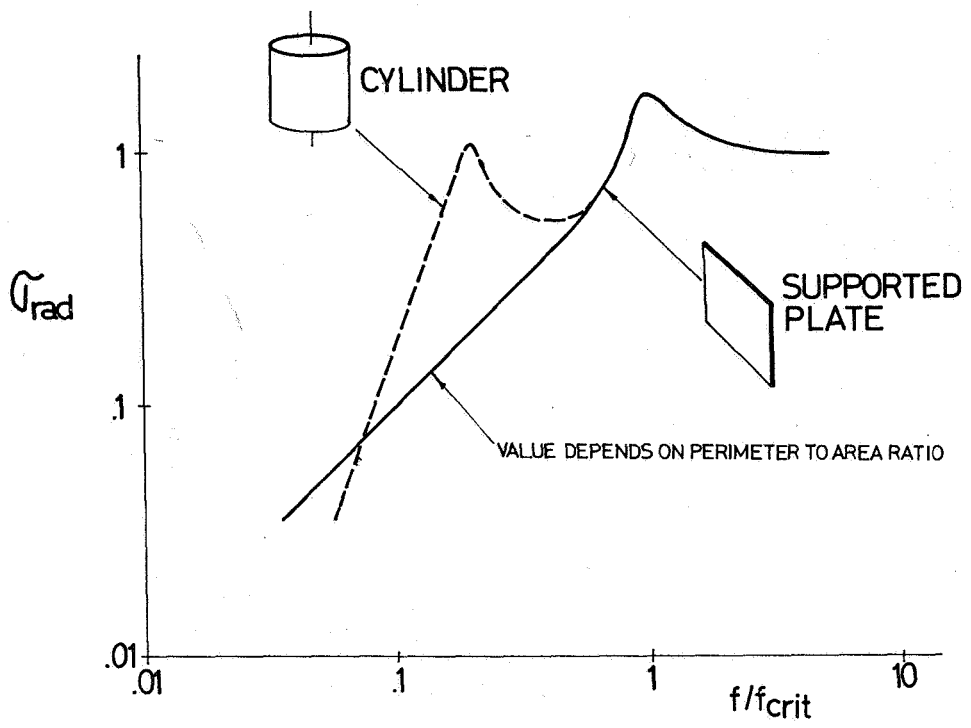

Figure 5.- Radiation efficiency of finite supported plate and cylinder of same area.

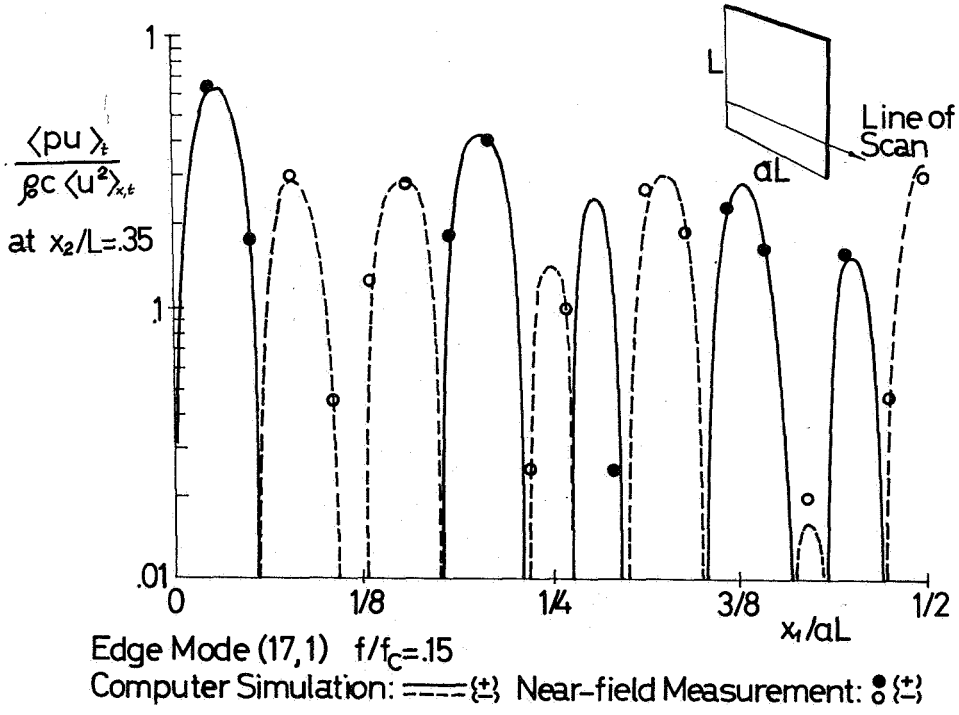

Figure 6.- Intensity scan across mid-section of rectangular supported plate showing region of sound absorption near the edge.

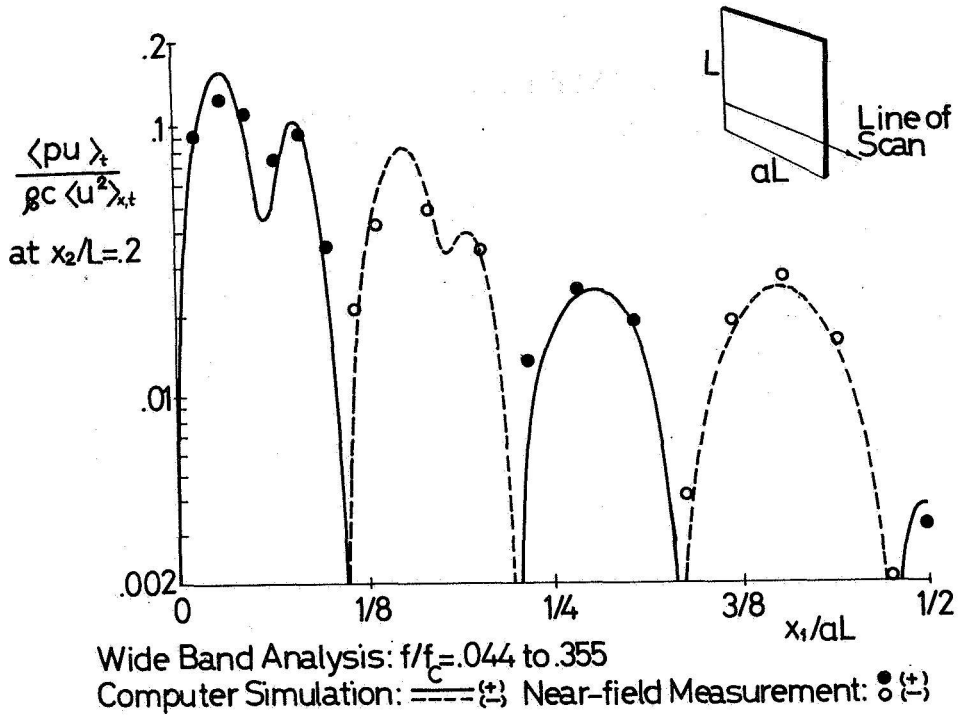

Figure 7.- Measured intensity along mid-section of simply-supported plate below the critical frequency.

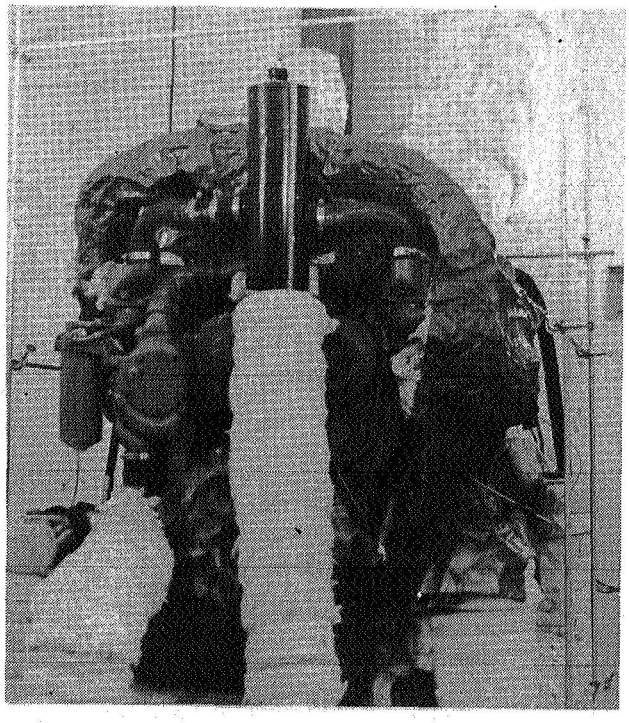

Figure 8.- In the window method, various parts of a wrapped machine are exposed for measurements of noise using either reverberant or anechoic methods.

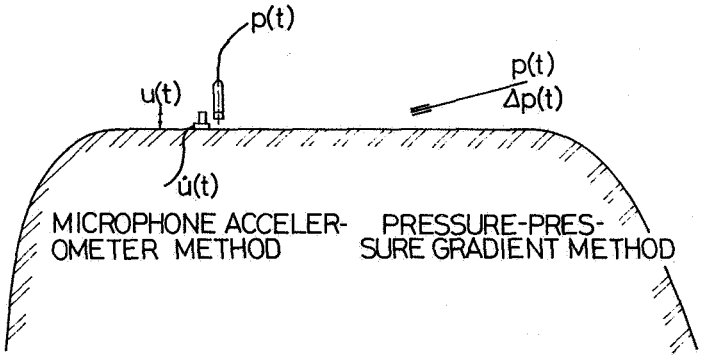

Figure 9.- Two methods for measuring the local sound intensity at the surface of a structure.

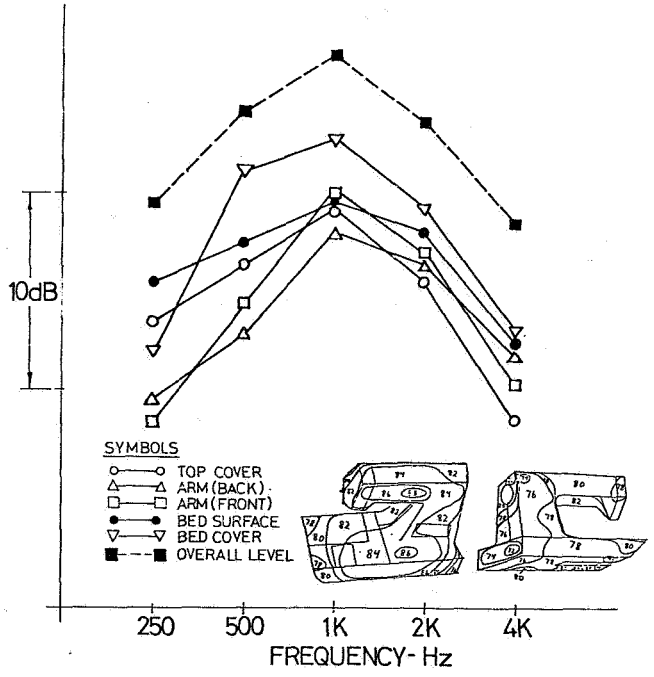

Figure 10.- Total and relative contributions of various machine surfaces to sound power radiated by a sewing machine as determined by the near field pressure method.

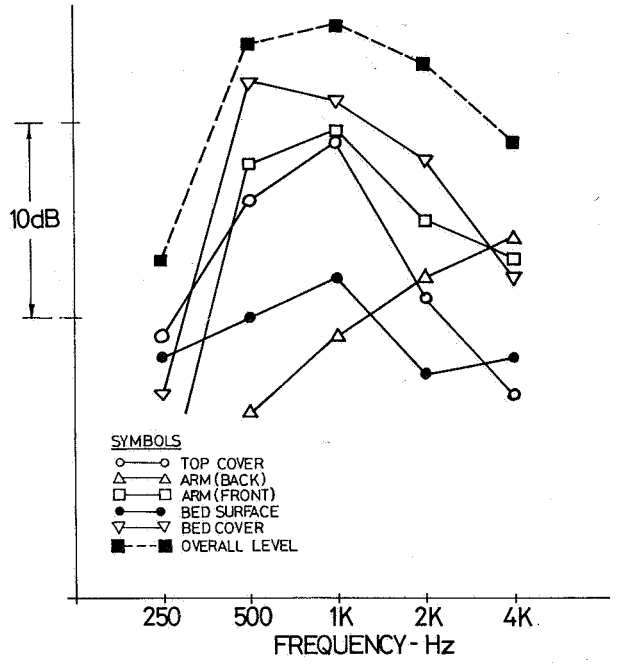

Figure 11.- Total and relative contributions to sound power radiated by sewing machine as determined by the acceleration method, assuming a uniform radiation efficiency for all surfaces.

ON THE RADIATION OF SOUND FROM BAFFLED FINITE PANELS*

Patrick Leehey
Acoustics and Vibration Laboratory
Massachusetts Institute of Technology

SUMMARY

This paper is a survey of some recent theoretical and experimental research on structural-acoustic interaction carried out at the M.I.T. Acoustics and Vibration Laboratory. The emphasis is upon the radiation from and acoustic loading of baffled rectangular plates and membranes. The topics discussed include a criterion for strong radiation loading, the "mass law" for a finite panel, numerical calculation of the radiation impedance of a finite panel in the presence of a parallel mean flow, and experimental determination of the effect of vibration amplitude and Mach number upon panel radiation efficiency.

INTRODUCTION

The problem of sound radiation from a baffled finite panel is fundamental to our understanding of problems of radiation from structures and of the influences of the acoustic field upon the structural vibration itself. A rectangular panel is a reasonable representation of a structural element of an aircraft fuselage, a machine casing, or of a ship's hull or sonar dome. These are all cases where the question of acoustic radiation is of engineering significance. More generally, this structural element forms a basis for the development of techniques for dealing with multi-modal excitation of complex structures.

In the 1940's Lothar Cremer recognized that acoustic radiation from panels becomes important when the bending wave speed of the panel vibration equals or exceeds the sound speed in the adjacent medium. For an infinite plate, when the bending wave speed is less than the sound speed there is no radiation whatsoever. Modal radiation from finite panels can be classified according to the characteristics of the component traveling waves which make up the standing wave pattern of the mode. Thus, if the speed of the traveling waves is greater than the sound speed one speaks of an acoustically fast mode. It is possible for a traveling wave to have a speed less than the sound speed, but to have a trace of its wave front traveling along a panel

---

*Work supported by the Sensor Technology Program, Office of Naval Research.

edge at a speed exceeding the sound speed, see figure 1. Such a mode is called an edge mode. Finally, we have the case where no traces on any edge have speeds which exceed the sound speed. Such modes are called corner modes. One might say whimsically that the trace becomes supersonic as it turns a panel corner.

The efficiency of radiation from a finite panel follows this classification. Essentially the entire surface area of the panel contributes to the radiation for an acoustically fast mode. We say that such a mode has a radiation efficiency σ_{RAD} of unity. Strips along two parallel edges of a panel, each one quarter of a bending wave length wide, contribute to the radiation from an edge mode. Here the radiation efficiency is of the order 10^{-2}. Lastly, for a corner mode, small rectangles in each panel corner about a quarter of a bending wave length on edge contribute to the radiation with an efficiency of approximately 10^{-4}.

Although the physical concepts of modal radiation resistance are straightforward to grasp, the precise calculations of radiation impedance including radiation resistance, added mass, and mode coupling terms presents a non-trivial problem in numerical analysis. The double integrals involved are improper, have integrands that are highly oscillatory, and contain lines of indeterminacy. Wallace (ref. 1) has calculated modal radiation resistance; Sandman (ref. 2) has calculated modal added mass as well. We have extended these calculations to include the capability for computing modal coupling terms for zero mean flow. In addition we can compute the effect upon modal radiation resistance and added mass of a subsonic mean flow over a panel in a direction parallel to one pair of edges. A slip flow boundary condition is imposed. Thus, the effect of the boundary layer over the panel is ignored as are also any interaction effects with flow resulting from finite amplitude displacements. A physical interpretation of the effect of mean flow upon radiation resistance is given.

It is customary to analyze the problem of panel response and radiation using *in vacuo* mode shapes. When this is done the back reaction of the acoustic field upon the panel vibration results in an infinite set of linear equations in an infinite number of unknown modal coefficients. The presence of modal coupling precludes the diagonalization of this system. For light fluid loading such as in air, the coupling terms are on one hand ignored but on the other hand are treated as the mechanism by which one obtains equipartition of vibratory energy among panel modes resonant in a narrow frequency band. This concept is fundamental to the method of statistical energy analysis of multi-modal systems as developed by Lyon and Maidanik (ref. 3) and Smith and Lyon (ref. 4). When multi-modal responses are important, statistical energy methods permit the use of average radiation resistances. Such usage appears in some of the experiments to be discussed later.

Building acousticians have long utilized the so called "mass law" in calculations of transmission losses through room partitions. This law states that the acoustic power transmitted through a panel is reduced by 6 decibels

per frequency doubling or per mass doubling. The law was originally derived for the case of an infinite panel without stiffness, see London (ref. 5). Practically the mass law is found to apply for reasonably damped plates at frequencies below that for coincidence of free bending wave speed with the sound speed.

For finite panels the mass law is demonstrated here to apply to those panel modes which are driven at frequencies well above their resonant frequencies. The responses of these modes are mass-like and eventually becomes acoustically fast. These considerations have particular importance in high frequency radiation for they set a limit on the effectiveness of panel damping treatments in reducing radiated sound. One must keep in mind that the mass law applies to radiated power levels, not to sound pressure levels. For a finite panel we shall discuss the implications of the effect of directivity upon the interpretation of the mass law.

If the fluid loading is heavy it may so affect the panel vibration that the *in vacuo* modes lose their physical significance. Intuitively one would define heavy loading as that condition when a layer of fluid over a panel, an acoustic wave length in thickness, has a mass of the same order as the panel surface mass. Davies (ref. 6) has quantified this idea by analyzing the problem of a free wave on a semi-infinite membrane normally incident on a rigid baffle in the presence of an acoustic medium. He finds that there is a sharp division between heavy and light fluid loading when the parameter $\mu = \omega m/\rho c$ is equal to unity.

We conclude this review by a brief discussion of some recent experimental results of Chang (ref. 7) on the influence of mean flow Mach number and vibration amplitude upon panel radiation efficiency.

SYMBOLS

A	$= \ell_1 \ell_2$, panel area
c	sound speed
c_b	bending wave speed
c_m	membrane wave speed
c_t	trace wave speed
D	plate flexural rigidity
k	$= \omega/c$, acoustic wave number
k_1, k_2	longitudinal and transverse wave numbers
k_{mn}	$= [(m\pi/\ell_1)^2 + (n\pi/\ell_2)^2]^{1/2}$, modal wave number

k_p	resonant wave number
ℓ_1, ℓ_2	rectangular panel longitudinal and transverse lengths
M	= U/c, Mach number
m	panel mass per area
N	number of panel resonances in a frequency band
P_{mn}	modal acoustic pressure at panel
R_{mnpq}	modal coupling impedance
T	membrane tension
U	mean flow in x_1 direction
u_τ	friction velocity
$\langle V(\omega) \rangle_{PLATE}$	vibration velocity spectral density, averaged over panel
v_{pq}	modal vibration velocity of panel
x_1, x_2	longitudinal and transverse coordinates
y^+	vibration amplitude in viscous lengths ν/u_τ
λ_b	bending wave speed
μ	= $\omega m/\rho c$, ratio of membrane mass impedance to fluid characteristic impedance
μPa	micro-Pascal, 1 Pa = 1 newton/(meter)^2
ν	fluid kinematic viscosity
Π_{RAD}	radiated sound power spectral density
ρ	fluid density
σ_{mn}	modal radiation efficiency
σ_{RAD}	panel radiation efficiency
σ_{rad}	non-dimensional radiated power (Davies)
χ_{mn}	modal added mass coefficient
ω	frequency, radians/second

MODAL RADIATION IMPEDANCE

A useful classification of panel modes in terms of their radiation characteristics is given in figure 2. This graphical representation, due originally to Maidanik, shows panel modes as a lattice of points in a wave number plot. For a given frequency, wave numbers are inversely proportional to wave speeds. Hence any mode whose wave number k_{mn} is greater than the acoustic wave number k is a slow mode. The slow modes are further subdivided into edge and corner modes. The edge mode radiation shown in figure 1 is typified by the k_{23} mode in figure 2.

We have tacitly assumed sinusoidal mode shapes. This assumption is quite good, even for a fully clamped plate, beyond the lowest few mode number pairs. For a plate, the resonantly responding modes are those for which $k_{mn} = k_p$ where k_p satisfies the dispersion relation

$$k_p^4 = m\omega^2/D \tag{1}$$

Obviously, the greatest radiation response will occur when a mode is both resonant and acoustically fast, i.e. when one also has $k_p \leq k$. The lowest frequency for which this can occur is the acoustical critical frequency

$$\omega = c^2 \, (m/D)^{1/2} \tag{2}$$

For a membrane, $k_p = \omega/c_{mn}$ where $c_m = (T/m)^{1/2}$ is the fixed membrane wave speed. Thus all resonant membrane modes are either fast ($c_m > c$) or slow ($c_m < c$).

By performing frequency transforms and modal expansions of the governing differential equations for the panel and the acoustic field, one obtains a relation

$$P_{mn}(\omega) = \sum_{p,q=1}^{\infty} v_{pq}(\omega) \, R_{mnpq} \qquad m,n = 1,2,3,... \tag{3}$$

between the modal coefficients v_{pq} of normal panel velocity and the corresponding modal coefficients $P_{mn}(\omega)$ of the acoustic pressure field at the panel. The modal coupling impedance R_{mnpq} is a function of the acoustic wave number k and the panel geometry. The (self) radiation impedance may be written

$$R_{mnmn} = \rho c(\sigma_{mn} - i \, \chi_{mn}) \tag{4}$$

where ρc is the characteristic impedance of the field. Typical plots of the modal radiation efficiency σ_{mn} and the modal added mass coefficient χ_{mn} as functions of the ratio of acoustic wave number to modal wave number are shown in figures 3 and 4, respectively. Both peak in the neighborhood of $k/k_{mn} = 1$. At high wave numbers all modes become acoustically fast with efficiencies of unity and disappearing added mass. It is further true that modal couplings disappear at high wave numbers.

EFFECT OF MEAN FLOW UPON RADIATION IMPEDANCE

An analytical treatment of the effect of mean flow U over a vibrating plate has been given by Chang (ref. 7). The mean flow is in the positive x_1 direction at a Mach number M = U/c less than one. A linearized solution is obtained in which both the kinematic and dynamic boundary conditions are satisfied at the mean position of the panel. Viscous effects and the presence of a boundary layer are neglected. The transient version of this problem was solved earlier by Dowell (ref. 8).

The principal physical feature of the effect of mean flow upon radiation efficiency is readily grasped by reference to figure 5. The circle of radius k in figure 2 is replaced here by an ellipse centered on the negative x_1 axis. The upstream traveling longitudinal bending wave component of a mode need only exceed c - U in speed in order for that mode to become (half) fast. Except for those modes that are converted from slow to fast by the mean flow, the influence of mean flow upon radiation efficiency is quite small at moderate Mach numbers as is evident in figure 3. Much more significant increases in added mass are obtained as the Mach number is increased (see figure 4).

MASS LAW FOR A BAFFLED RECTANGULAR PANEL

Since the radiation impedances are computable, it is possible to express the modal response coefficients as a linear system of equations driven by the modal excitations. Once the modal response velocities are obtained, the radiation field can then be predicted using Rayleigh's equation. We shall not write these expressions here. It will suffice to say that the system is one of an infinite number of equations in an infinite number of unknowns. Customarily an approximate solution is obtained by truncating the system and inverting the coefficient matrix. This method works well for frequencies corresponding to the first few modal resonances. Variational techniques are available, Morse and Ingard (ref. 9), but they appear to offer no significant advantage in treating this case.

From earlier remarks, it is evident that the coefficient matrix becomes diagonal in the high frequency limit. All terms of the radiation impedance matrix vanish except for the radiation resistances, all of which represent unity efficiencies. Moreover, these modes respond as masses for they are being driven well above their resonant frequencies. Closed formed solutions for panel vibration and acoustic radiation can be obtained because the series involved may be summed explicitly.

The results of one of a series of experiments by Sledjeski (ref. 10) are shown in figure 6. A nearly plane acoustic wave was directed normally through a baffled rectangular membrane. The membrane dimensions were $\ell_1 = 0.305$ m, $\ell_2 = 0.203$ m. Its surface density was 0.36 kg/m^2, and it was tensioned uniformly to produce an *in vacuo* wave speed c_m of 100 m/sec. The measuring

microphone was placed one meter away directly over the membrane center on the side opposite the sound source. Measurements were taken of the sound transmitted through the membrane while the input to the sound source was very slowly swept in frequency with output controlled to provide an incident sound pressure level of 84 dB at the membrane.

Figure 6 shows a successive pattern of resonances and "anti-resonances". The resonances occur at the loaded natural frequencies of each odd/odd mode. Both the frequency of resonance and the transmitted level can be predicted from a simple single degree of freedom analysis using the calculated radiation impedance and the measured total loss factor for the mode and frequency in question. The "anti-resonances" occur at approximately the *in vacuo* resonant frequencies of modes such as (2,2), (3,2), (2,3) (i.e. modes with at least one even mode number). Such modes cannot be excited by a normally incident plane wave. The response at these "anti-resonances" comes from the non-resonant responses of adjacent odd/odd modes and is greatly weakened by the fact that the contributions of those driven above resonance are out of phase with those driven below resonance. Here the computed contributions of only a few of these adjacent modes are required to achieve a good correlation with experiment.

At high frequencies, the "anti-resonances" become less and less pronounced and there is a tendency for the sound pressure level to asymptote to a fixed value. This is the mass law regime where the level is maintained almost entirely by the lower non-resonant acoustically fast modes.

Such behavior seems anomalous in terms of the classical mass law. However, as remarked earlier, it is the sound power, not the on-axis sound pressure, which must decrease by 6 dB per frequency doubling. In fact, our closed form solution for the sum of all non-resonant modes yields precisely the vibration of a rigid rectangular piston. At high frequencies, the directivity index for this case is well-known to be 20 log $(k\sqrt{A})$ plus a constant. The mass law is not violated, for although the on-axis pressure level approaches a constant value, the directivity increases by this rule, insuring that the radiated power decreases by 6 dB per frequency doubling. This conclusion was verified experimentally by measuring the directivity patterns of the membrane radiation.

EFFECT OF FLUID LOADING

Davies (ref. 6) has solved the problem of an acoustically slow wave on a semi-infinite membrane normally incident on the edge of a semi-infinite rigid baffle in the presence of an acoustic medium. A Wiener-Hopf technique was used to obtain the reflection coefficient at the edge and the acoustic power per span radiated from a neighborhood of the edge, both as functions of the parameter $\mu = \omega m/\rho c$, the ratio of the membrane mass impedance to the characteristic impedance of the fluid. His results for a non-dimensional radiated power σ_{rad} as a function of μ and the ratio c_m/c are shown in

figure 7. His σ_{rad} is not directly a radiation efficiency, rather σ_{rad} μ is an effective radiation efficiency for a zone of the order of an acoustic wavelength wide along the edge. Note, as figure 7 shows, that it is possible for the *in vacuo* membrane wave speed $c_m = (T/m)^{1/2}$ to be supersonic. The fluid loaded free membrane wave speed, however, must remain subsonic.

It is clear by comparison of the exact calculations with the asymptotic limits for large and small μ that there is a clear demarkation at $\mu = 1$ between the heavy and light fluid loading regimes. Davies shows further that for $c_m/c << 1$ and $\mu >> 1$, the acoustic power is radiated by a line source of a quarter membrane wave length volume velocity. The inference is strong that fluid loading effects upon mode shapes are negligible for $\mu > 1$.

EFFECT OF VIBRATION AMPLITUDE

We concluded this survey with a brief mention of a few experimental results of Chang (ref. 7) on the effects of vibration amplitude and Mach number upon panel radiation efficiency. A rectangular steel plate, 0.33 m by 0.28 m, 0.152 mm thick was mounted flush in one wall of our wind tunnel test section. The back side of the plate was enclosed in a highly absorbent and damped box which also housed a non-contact solenoid exciter and non-contact Fotonic optical displacement sensors. The opposite wall of the test section was removed in the neighborhood of the plate. When the plate was excited essentially all of its radiation was directed through the opening into a fairly large reverberant chamber enclosing the test section. The plate was excited by various 50 Hz bands of white noise at mean flow Mach numbers M = 0 and M = 0.23.

The results of these experiments are shown in figure 8. The radiation efficiencies σ_{RAD} for each of the bands were determined from the expression.

$$\Pi_{RAD}(\omega) = \rho c A \sigma_{RAD} \langle V(\omega) \rangle_{PLATE} \tag{5}$$

where Π_{RAD} is the spectral density of radiated sound power and $\langle V(\omega) \rangle_{PLATE}$ is the vibratory velocity spectral density, averaged over the plate surface. This radiation efficiency can be related to the modal radiation efficiencies σ_{mn} by

$$\sigma_{AVG} = \frac{1}{N} \sum_{m,n} \sigma_{mn} \tag{6}$$

where N is the number of resonant modes in the band and the summation extends over these modes. Equations (5) and (6) are for multi-modal resonance dominated radiation. Their validity is based on the statistical energy arguments referred to in the introduction. For this plate approximately 10 modes are resonant in a 50 Hz band.

At Mach number 0.23 we see a significant increase in radiation efficiency with increasing vibration amplitude y^+ measured in viscous lengths ν/u_τ. Both boundary layer thickening and amplitude change were used to vary y^+. The computed values are from the linear "slip flow" theory for resonantly responding modes. The no flow results corresponded closely with the $y^+ = 128$ data and with the no flow computations. Some calculations were made which indicated that changes in non-resonant mode contributions with Mach number were also too small to account for the increases in radiation efficiency. It thus appears likely that a non-linear interaction with the boundary layer is involved. Unfortunately, it was not possible to vary M independently of y^+ over a sufficient range to determine whether or not there was an independent Mach number effect.

REFERENCES

1. Wallace, C. E., Radiation Resistance of a Rectangular Panel, J. Acoust. Soc. Am., 51, 3, (2), March 1972, pp 946-952.

2. Sandman, B. E., Motion of a Three-Layered Elastic-Viscoplastic Plate Under Fluid Loading, J. Acoust. Soc. Am., Vol. 57, No. 5, May 1975, pp 1097-1107.

3. Lyon, R. H. and Maidanik, G., Power Flow Between Linearly Coupled Oscillators, J. Acoust. Soc. Am., 34, (5), May 1962, pp 623-639.

4. Smith, P. W., Jr. and Lyon, R. H., Sound and Structural Vibration, Bolt, Beranek and Newman, Inc., Report No. 1156, September 1964.

5. London, A., Transmission of Reverberant Sound Through Single Walls, Journal of Research of the National Bureau of Standards, Vol. 42, Paper RP 1998, June 1949.

6. Davies, H. G., Natural Motion of a Fluid-Loaded Semi-Infinite Membrane, J. Acoust. Soc. Am., 55, (2), February 1974, pp 213-219.

7. Chang, Y. M., The Mean Flow Effect on the Acoustic Impedance of a Rectangular Panel, Ph.D. Disertation, MIT, May 1976.

8. Dowell, E. H., Generalized Aerodynamic Forces on a Flexible Plate Undergoing Transient Motion, Quart. Appl. Math., 24, 1967, pp 331-338.

9. Morse, P. M. and Ingard, K. U., Theoretical Acoustics, McGraw-Hill Book Co., New York, 1968.

10. Sledjeski, L., Sound Transmission Through a Rectangular Membrane, M.Sc. Thesis, MIT, May 1973.

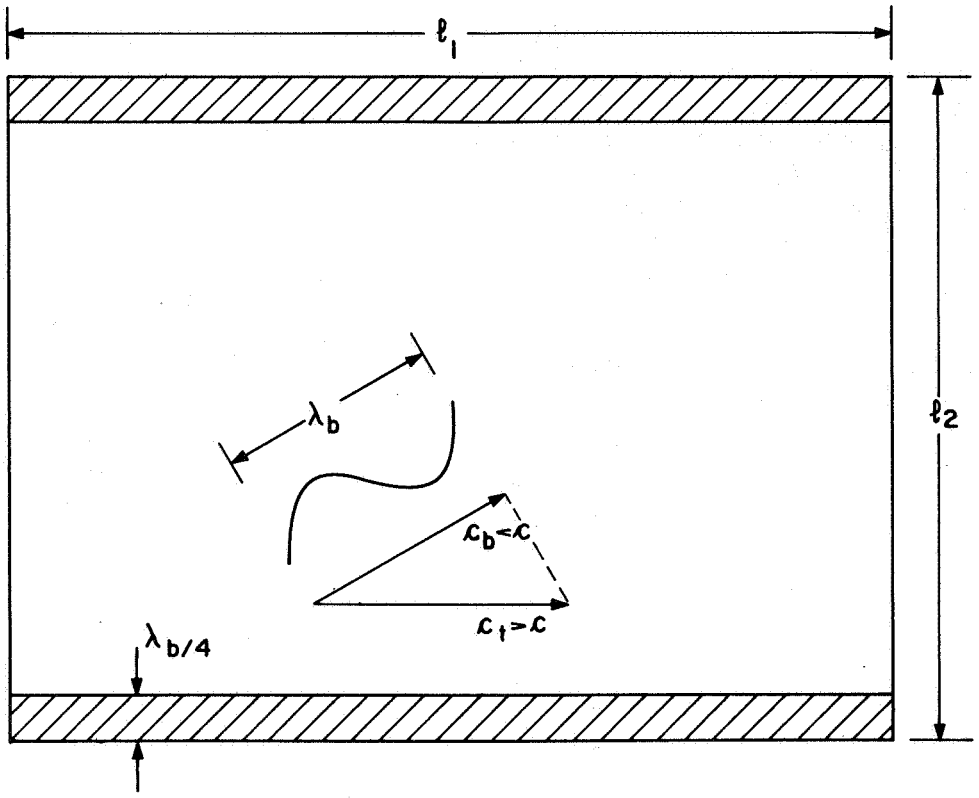

Figure 1.- Edge mode radiation.

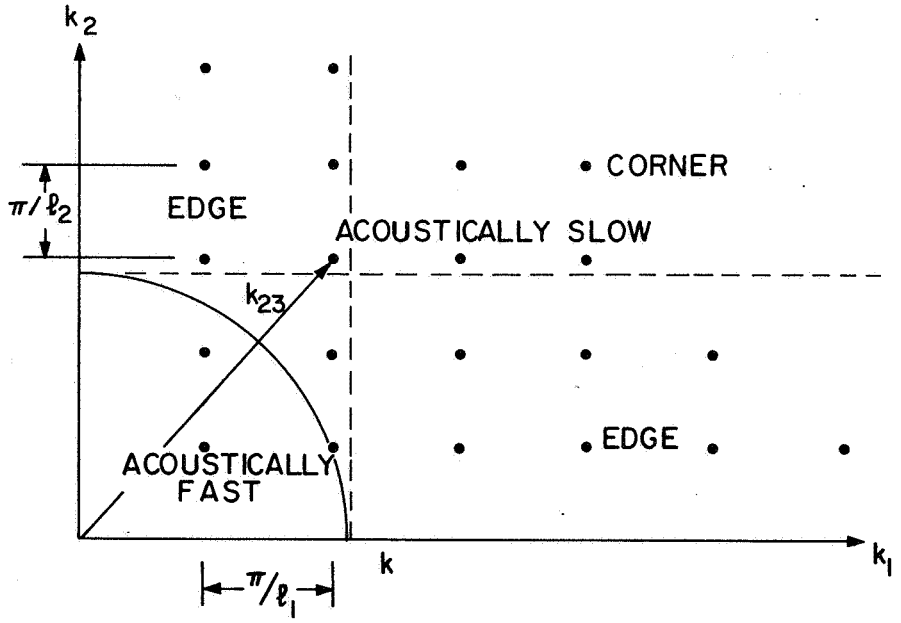

Figure 2.- Classification of panel modes in wavenumber space.

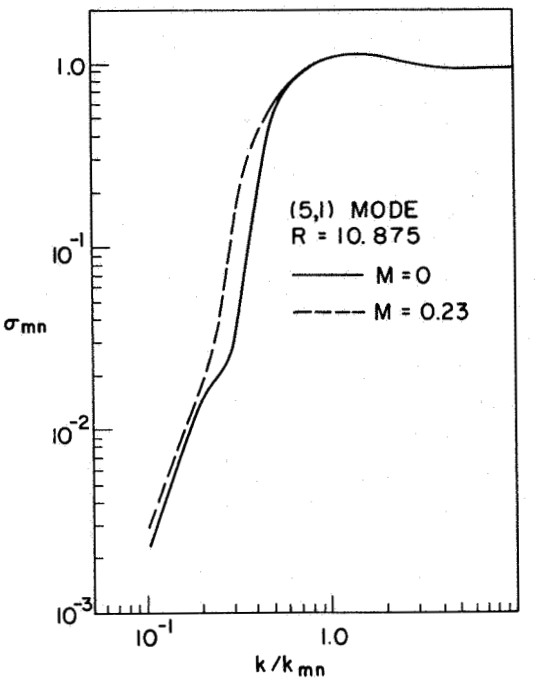

Figure 3.- Modal radiation efficiency, from Chang (ref. 7).

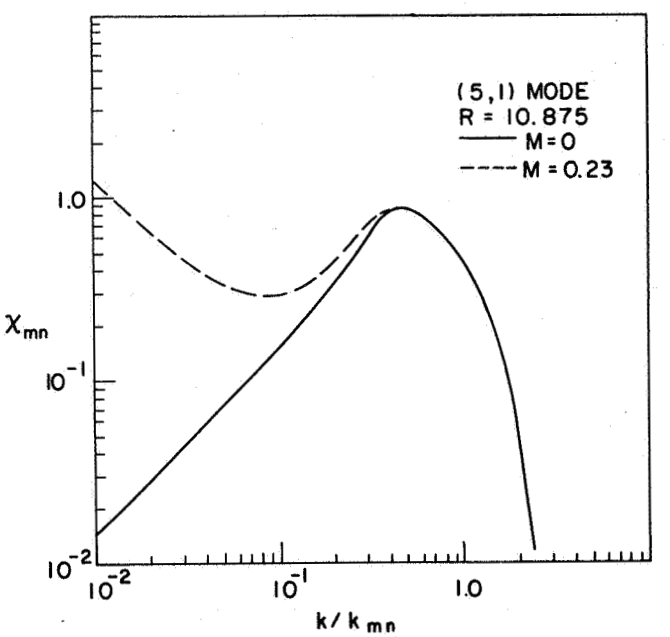

Figure 4.- Modal added mass coefficient, from Chang (ref. 7).

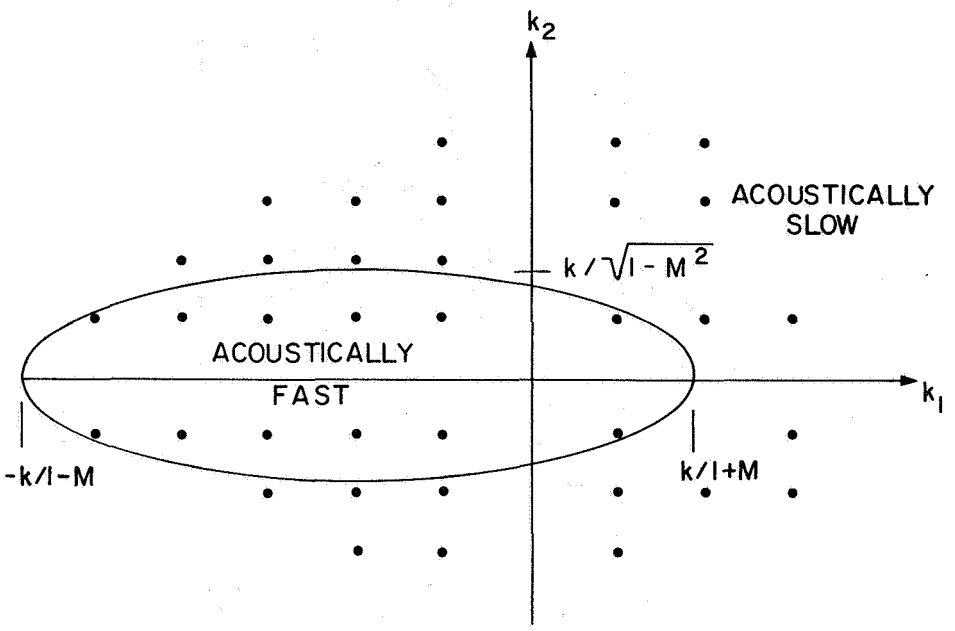

Figure 5.- Effect of mean flow Mach number upon radiation classification of modes, M = 0.6.

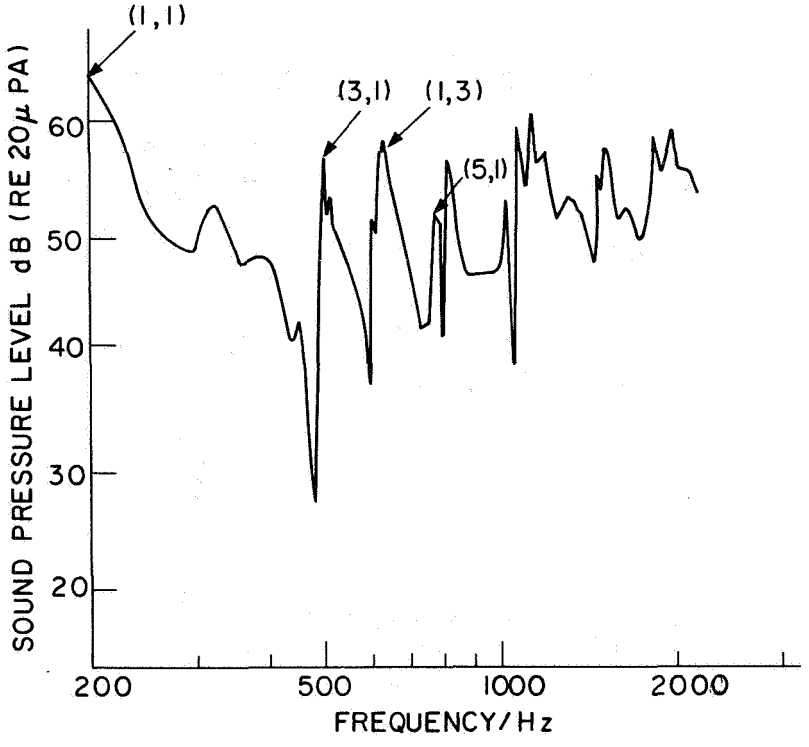

Figure 6.- Sound transmissed through a rectangular membrane, from Sledjeski (ref. 10).

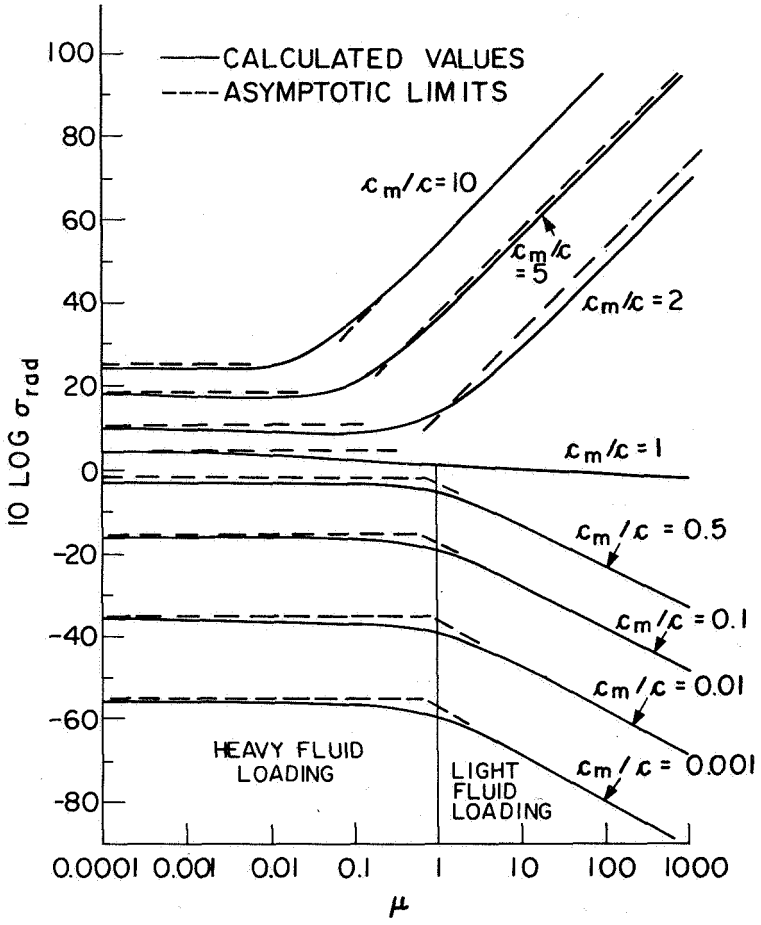

Figure 7.- Radiated power for a semi-infinite membrane, from Davies (ref. 6).

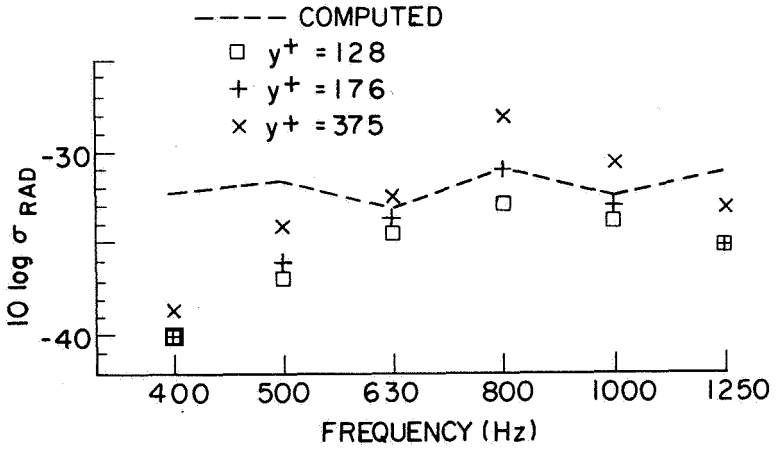

Figure 8.- Effect of vibration amplitude upon radiation efficiency, M = 0.23, from Chang (ref. 7).

ACOUSTOELASTICITY*

Earl H. Dowell
Princeton University

INTRODUCTION

We consider internal sound fields. Specifically the interaction between the (acoustic) sound pressure field and the (elastic) flexible wall of an enclosure will be discussed. A good introduction to this subject is given in "Sound, Structures and their Interaction" by Junger and Feit (ref. 1). Also the author has briefly discussed this subject in his book, "Aeroelasticity of Plates and Shells" (ref. 2). This paper is a highly condensed version of reference 3.

Such problems frequently arise when the vibrating walls of a transportation vehicle induce a significant internal sound field. The walls themselves may be excited by external fluid flows. Cabin noise in various flight vehicles and the internal sound field in an automobile are representative examples.

Briefly considered are mathematical model, simplified solutions, and numerical results and comparisons with representative experimental data. An overall conclusion is that reasonable grounds for optimism exist with respect to available theoretical models and their predictive capability.

MATHEMATICAL MODEL

Here the essentials of the mathematical noise transmission model will be summarized. No mathematical derivations are included, however. A complete description of the analysis is contained in reference 3. A modal representation of the structural wall(s) and acoustic cavity(ies) is used. For the structural wall

$$w(x,y,t) = \sum_m q_m(t)\, \psi_m(x,y) \tag{1}$$

w - physical wall deflection

q_m - modal coordinate; function of time

ψ_m - natural mode shape (in vacuum); defined over an appropriate area with coordinates x, y

Associated with the ψ_m are natural mode frequencies, ω_m, and generalized masses, M_n.

$$M_m \equiv \iint m(x,y)\, \psi_m^2 \, dxdy \qquad m \text{ - structural mass per unit area} \tag{2}$$

*This work was performed under NASA Grant NSG 1253, Langley Research Center.

For the acoustic cavity

$$p(x,y,z,t) = \rho c^2 \sum_n \frac{P_n(t)}{M_n^A} F_n(x,y,z) \qquad (3)$$

p - physical acoustic pressure — P_n - acoustic modal coordinate

ρ - air density — F_n - acoustic natural mode (for rigid walls)

c - air speed of sound — Z_a - absorbent wall impedance

Associated with the F_n are acoustic natural frequencies, ω_n^A, and generalized masses

$$M_n^A \equiv \frac{\iiint F_n^2}{V} dxdydz \qquad V \equiv \text{total cavity volume} \qquad (4)$$

The external pressure field, p^E, is represented in terms of its generalized forces

$$Q_m^E \equiv -\iint_{\text{on area, } A_{EW}} p^E(x,y,t)\, \psi_m(x,y)\, dxdy \qquad A_{EW} \equiv \text{(external) structural wall area} \qquad (5)$$

The minus sign arises from the sign convention that w is positive outward and p^E is positive inward with respect to the cavity. See Figure 1.

The data given are:

p^E for the external sound field — Q_m is determined from (5)

m, ψ_m, ω_m for the structural wall — ρ, c, F_n, ω_n^A, Z_a for the cavity(ies)

M_m is determined from (2) — M_n^A is determined from (4)

q_m, P_n are then determined from the modal equations of motion, i.e.

$$M_m [\ddot{q}_m + 2\zeta_m \omega_m \dot{q}_m + \omega_m^2 q_m] - \rho c^2 A_{EW} \frac{\sum_n P_n L_{nm}}{M_n^A} = Q_m^E \qquad (6)$$

$$\ddot{P}_n + \omega_n{}^A{}^2 P_n + A_A \rho c^2 \sum_r \frac{\dot{P}_r C_{nr}}{M_r^A} = \frac{-A_{EW}}{V} \sum_m \ddot{q}_m L_{nm} \qquad (7)$$

where

$$L_{nm} \equiv \frac{\iint_{\text{over } A_{EW}} F_n \psi_m dxdy}{A_{EW}}, \quad C_{nr} \equiv \frac{\iint_{\text{over } A_A} \frac{F_n F_r}{Z_a} dA}{A_A}, \quad A_A \equiv \text{absorbent cavity wall area}, \quad \zeta_m - \text{modal damping}$$

These are two coupled systems of spring-mass-damper-oscillators and (6) and (7) are familiar and computationally efficient descriptions of their dynamics.

Moreover multiple walls or cavities may be readily included in a similar fashion. For two connected cavities, see Figure 1, the common wall between the two cavities may be treated as a (common) structural wall and in an obvious notation (where we have cavities a and b) (6) and (7) are replaced by

$$M_m[\ddot{q}_m + 2\zeta_m\omega_m\dot{q}_m + \omega^2{}_m q_m] - \rho c^2 A_{CW} \sum_n \frac{P^a{}_n L^a{}_{nm}}{M_n{}^{Aa}} + \rho c^2 A_{CW} \sum_n \frac{P_n{}^b L^b{}_{nm}}{M_n{}^{Ab}} = 0 \quad (8)$$

$$\ddot{P}^a{}_n + \omega_n{}^{Aa2} P_n{}^a + A^a{}_A \rho c^2 \sum_r \dot{P}_r{}^a \frac{C^a_{nr}}{M_r^{Aa}} = \frac{-A_{CW}}{V_a} \sum_m \ddot{q}_m L^a{}_{nm} \quad (9)$$

$$\ddot{P}^b{}_n + \omega_n{}^{Ab2} P_n{}^b + A^b{}_A \rho c^2 \sum_r \dot{P}_r{}^b \frac{C^b_{nr}}{M_r^{Ab}} = + \frac{A_{CW}}{V_b} \sum_m \ddot{q}_m L^b{}_{nm} \quad (10)$$

where $L^a{}_{nm} \equiv \iint_{A_{CW}} \frac{F_n{}^a \psi_m}{} \, dxdy$, etc. and the subscript CW denotes common wall.

For simplicity we have considered the external walls rigid. However, clearly (6), (7), (8), (9), (10) can be combined to allow for both external and (internal) common wall motion with multiple cavities.

Once q_m and P_n are determined, the physical deflection, w, and sound pressure, p, are known from (1) and (3). The flexibility in the model is in treating ω_m, ψ_m and $\omega^A{}_n$, F_n as given. For simple shapes, these are known analytically. In some cases it will be possible to approximate the structural wall and cavity by a simple shape or several component simple shapes. In other cases it will be necessary to determine the natural modes by numerical methods (finite element analysis) or experiment (scale models).

Before leaving the mathematical model, two of its widely applicable consequences should be noted. Firstly, the coupling of the acoustic cavity-structural wall is gyroscopic. This can be seen directly by replacing the acoustic pressure, p, by the corresponding velocity potential. These are related through Bernoulli's equation (ref. 2 and 3). The importance of recognizing that the coupling is gyroscopic is that one can then invoke Meirovitch's algorithm for determining the eigenvalues of the acoustic-structural system using standard numerical techniques (ref. 4). This is preferable to alternative formulations which lead to trial and error solutions to transcendental equations, e.g. ref. 5. For additional detail, see reference 3. Fortunately the coupled acoustic-structural wall natural frequencies are normally little changed from their rigid wall acoustic mode and in vacuum structural wall mode counterparts. This simplifies matters considerably, of course, and will often permit one to avoid a completely coupled analysis altogether. More will be said of this in the next section.

The second theoretical consequence and one of more practical importance is the direct way in which two interacting cavities can be treated. (Recall

Fig.1.) If there is a pure opening between two cavities, i.e. one of zero mass, damping, and stiffness, then (8) becomes

$$\sum_n \frac{P^a_n L^a_{nm}}{M^{Aa}_n} - \sum_n \frac{P^b_n L^b_{nm}}{M^{Ab}_n} = 0 \qquad (11)$$

To determine the natural frequencies of this two cavity system, one assumes simple harmonic motion, solves for P^a_n, P^b_n from (9), (10) in terms of q_m and substitutes the result into (11) to obtain (for $Z_a \to \infty$)

$$\sum_m q_m Q_{rm} = 0 \quad \text{where} \quad Q_{rm} \equiv \frac{1}{V_a} \sum_n \frac{L^a_{nr} L^a_{nm}}{M^a_n[-\omega^2+\omega^{Aa^2}_n]} + \frac{1}{V_b} \sum_n \frac{L^b_{nr} L^b_{nm}}{M^b_n[-\omega^2+\omega^{Ab^2}_n]} \qquad (12)$$

The natural frequencies are determined by the condition that the determinant of Q_{rm} must vanish. This is a non-standard eigenvalue problem because of the form that ω^2 takes in Q_{rm}, see (12). However it has one overwhelming advantage: The size of the matrix is determined by the number of <u>two-dimensional</u> pure opening modes, ψ_m, rather than the number of <u>three-dimensional</u> cavity modes, F^a_n, F^b_n. The former will be much smaller in number than the latter for a given desired accuracy. This advantage will persist even when the opening is a structural member of finite stiffness, etc., or there are more than two cavities (ref. 3).

Once the natural frequencies of the multiple cavities have been determined, they may be treated as an equivalent single cavity so far as determination of interior sound levels is concerned.

SIMPLIFIED SOLUTIONS FOR INTERNAL SOUND LEVELS

The mathematical model may be solved numerically without further approximation. Indeed one of its advantages is that the calculation would be no more (nor less!) tedious than is frequently performed today for structural vibration response. However it is of interest to make further simplifications <u>if</u> little accuracy is lost and/or substantial computational reduction is possible. Here a summary of highlights from analytical and numerical studies is provided.

It is usually true that complete coupling between the structural wall and acoustic cavity can be neglected. Hence it is normally permissible to first calculate the external wall motion due to an external pressure loading (neglecting the acoustic cavity) and then determine the internal acoustic cavity pressure due to the now known wall motion.

There are two known circumstances where the complete coupling must be taken into account (see ref. 3 for details):

(1) If the fundamental wall resonant frequency is well below the fundamental acoustic resonant frequency (in the direction perpendicular to the wall), the Helmholtz mode of the cavity will provide a spring stiffness which may

substantially raise the panel wall mode frequency above its in vacuum value. But then only the single Helmholtz mode of the cavity need be considered. An example is discussed in the following section.

(2) If a structural wall mode and acoustic cavity resonant frequency are in close proximity, then again a fully coupled analysis may be required. But then only the two closely coupled modes need be examined.

Assuming that the more usual situation applies, one may make further progress analytically if one considers simple harmonic external excitation at either a structural wall or cavity resonant frequency. Also for broad band random excitation, similar results may be obtained by invoking power spectral analysis since for small damping the internal cavity response will be dominated by the wall and/or cavity resonances. However if the external field has its own dominant harmonics then the following simple results will not hold and one must return to the full analysis (but hopefully still being able to neglect full wall-cavity coupling). There is one advantage in such a situation, however, and that is a precise knowledge of damping will not be so important in these off resonant conditions and hence the basic mathematical model should be a more accurate representation of the physical system. Here only the simplest type of external excitation will be considered.

External Exciting Frequency, ω^E, = Structural Resonant Frequency, ω_s

The response will be dominated by the s^{th} structural mode and the cavity pressure is given by

$$|p^c| = \frac{\rho c^2 A_F Q_s^E}{2\zeta_s V M_s} \sum_n \frac{F_n^A}{M_n^A} \frac{1}{[-\omega_s^2+\omega_n^{A2}]} \tag{13}$$

If $\omega_s < \omega_n^A$ for all $\omega_n^A \neq 0$, then typically $|p^c| > p^E$ and conversely.

External Exciting Frequency, ω^E, = Cavity Resonant Frequency, ω_c^A

The cavity response will be dominated by the c^{th} cavity mode, and if in addition there is a dominant structural mode (say s^{th}), the cavity pressure is given by

$$p^c = \frac{F_c \int_{\text{on } A_F} p^E \psi_s dA}{\int_{\text{on } A_F} F_c \psi_s dA} \tag{14}$$

From (14), at most $p^c \simeq p^E$. For $p^E \sim F_c$ on A_F, $p^c = p^E$. In particular if F_c and p^c are approximately uniform over A_F, then $p^c \simeq p^E$.

It is interesting to note that neither (13) nor (14) involve the impedance or damping of the cavity. This is true under even broader circumstances, i.e. the wall absorbtion is not important in determining internal sound levels due to external sources (ref. 3).

NUMERICAL RESULTS AND COMPARISONS WITH EXPERIMENTS

For a single cavity with a flexible wall and an external sound source, the theoretical model has been verified experimentally by several authors (refs. 6-11). Hence we first assess the capability of the model to describe accurately the acoustic natural modes in multiply connected cavities. Once the combined natural modes of the multiply connected cavities are determined and verified experimentally, they may be treated as one single cavity. Then the earlier work for a single cavity may be taken as experimental verification for the forced excitation of multiply connected cavities as well.

Acoustic Natural Modes in Multiply Connected Cavities

The experimental studies discussed here were conducted by Smith (ref. 12). A representative configuration consists of two acoustic cavities, one twice the dimensions of the other, with rigid walls and a partial opening between them. In Figure 2, the longitudinal pressure distributions (along with their resonant frequencies) are shown for the first six (symmetric with respect to height) acoustical modes with a full opening between cavities. The agreement between theory and experiment is very good.

In these experiments, c_o = 343.5 m/sec, a = d = 25.4 cm and the width dimension was 10.16 cm to provide two-dimensional conditions in the frequency range of interest. The thickness of the partition (assumed zero in the theoretical calculations) is 1.27 cm as is the thickness of all external walls. The cavity is constructed from plexiglass.

Forced Response of a Single Cavity with a Flexible Wall

Experimental Arrangement:

For this discussion, Gorman's work (refs. 8, 9) is used; however, also see references 6, 7, 10 and especially 11. The flexible wall panel was 25.4 cm x 50.8 cm x .127 cm aluminum alloy plate that was bonded onto a stiff rectangular frame. By bonding the plate in this way, a clamped edge boundary condition was approximated. A sealed cavity, also 25.4 cm x 50.8 cm, was constructed beneath the panel so that the cavity depth could be varied. The cavity enclosure was made of 1.27 cm thick plexiglass.

The panel was excited acoustically by a Wolverine LS15, 20 watt loudspeaker driven by a B & K Beat Frequency Oscillator, type 1022. By using a single speaker, an external field distribution that was modestly variable in space was obtained. Measurements were made of panel deflections and cavity pressures due to a pure tone. Only the latter are considered here.

Cavity Pressure Measurement:

The sound pressure level within the cavity was measured using a B&K 1/4" microphone, type 4136 with a type 2615 cathode follower with type UA0035 connector

In Figure 3 the cavity pressure is plotted against frequency. This pressure is the difference between the dB level inside the cavity and that outside the cavity on the upper surface of the panel. The dominant features are the three primary resonant peaks occurring at 113 cps, 210 cps, and 518 cps. The first two resonances correspond to the first and third panel modes, and thus indicate that the panel is driving the cavity at these frequencies. The resonance at 518 cps is the fundamental cavity depth mode. Theoretically, if the external pressure were uniform over the flexible panel, it should be motionless, and the pressure level difference between the external and internal measurements should be zero when the external frequency equals the cavity resonant frequency. This is nearly the case, see Figure 3.

Results:

Panel Resonant Frequency Changed by Cavity

In Figure 4, a comparison between theory and experiment is made. The ratio of panel frequency (modified by coupling with the cavity) to "in-vacuo" panel frequency is plotted against panel length to cavity depth ratio, a/d. The "in-vacuo" panel frequencies were computed from Warburton's theory, (ref. 13) and the panel frequencies' variation with cavity depth were computed from Dowell and Voss' theory (ref. 10) which is an earlier version of the present analysis. There is excellent agreement between theory and experiment at the large cavity depths, with some variation from theory occurring at shallow cavity depths. Again it should be emphasized that this interesting change in panel frequency occurs only for flexible panels and stiff (shallow) cavities.

Panel Damping

Three types of damping will be referred to in this discussion: constant damping, frequency damping, and experimental damping. Constant damping is the value measured for a 30.48 cm cavity depth and assumes that there is no variation of panel modal damping ratio with cavity depth. Frequency damping allows for variation of damping ratio with frequency and employs the data measured at a 30.48 cm cavity depth for various panel resonances. Thus, the only effect changing this type of damping is the variation of panel modal frequency with cavity depth (Fig. 4 and ref. 8). Experimental damping is that measured for the exact conditions under study.

Cavity Pressure and Damping Effects

Figure 5 plots the variation of cavity pressure with cavity depth for the three different theoretical damping models, i.e. constant damping, frequency damping, and experimental damping. The exciting external frequency is equal to the fundamental panel resonant frequency. Recall that the damping ratios used in these calculations are those of the panel and not of the cavity; the latter were neglected. Even though cavity damping has not been considered, there is excellent agreement between experiment and the theoretical model using experimental damping.

Similar results have been obtained for random external pressure excitation (ref. 9). Pretlove (ref. 7) has made measurements of panel natural frequency

variation with cavity depth; Guy and Bhattacharya (ref. 11) have measured cavity pressures and panel natural frequencies. Generally good agreement with theory has also been shown in references 7, 9 and 11.

CONCLUDING REMARKS

A comprehensive theoretical model has been developed for interior sound fields which are created by flexible wall motion resulting from exterior sound fields. Included in the model are the mass, stiffness and damping characteristics of the flexible wall and of the acoustic cavity. Full coupling between the wall and cavity is permitted although detailed analysis, numerical results and experiment suggest that it is the exceptional case when the structural wall dynamic characteristics are significantly modified by the cavity.

Based upon the general theory, an efficient computational method is proposed and used to determine acoustic natural frequencies of multiply connected cavities. Simplified formulae are developed for interior sound levels in terms of in-vacuuo structural wall and (rigid wall) acoustic cavity natural modes.

Comparisons of theory with experiment show generally good agreement. The principal uncertainty remains the structural and/or cavity damping mechanisms. For external sound excitation, cavity damping is demonstrated to be generally unimportant; however it may be of importance for interior sound sources. The results of Wolf, Nefske and Howell (ref. 14) and Petyt, Lea and Koopman (ref. 15) using finite element techniques and Howlett and Morales (ref. 16) using modal analysis also suggest that effective analytical models are available.

REFERENCES

1. Junger, M. and Feit, D., "Sound, Structures and Their Interaction," M.I.T. Press, 1972

2. Dowell, E.H., "Aeroelasticity of Plates and Shells," Noordhoff International Publishing, Leyden, 1974.

3. Dowell, E.H., "Acoustoelasticity," Princeton University AMS Report 1280, May 1976.

4. Meirovitch, L., "A New Method of Solution of the Eigenvalue Problem for Gyroscopic Systems," AIAA Journal, 12, pp. 1337-1342, 1974.

5. Cockburn, J.A., and Jolly, A.C., "Structural-Acoustic Response, Noise Transmission Losses and Interior Noise Levels of an Aircraft Fuselage Excited by Random Pressure Fields," Air Force Flight Dynamics Laboratory Technical Report, AFFDL-TR-68-2, August 1968.

6. Dowell, E.H. and Voss, H.M., "The Effect of a Cavity on Panel Vibrations," AIAA Journal, 1, pp. 476-477, 1963.

7. Pretlove, A.J., "Free Vibrations of a Rectangular Panel Backed by a Closed Rectangular Cavity," J. Sound Vib. 2, pp. 197-209, 1965.

8. Gorman, III, G.F., "An Experimental Investigation of Sound Transmission Through a Flexible Panel into a Closed Cavity," Princeton University AMS Report No. 925, July 1970.

9. Gorman, III, G.F., "Random Excitation of a Panel-Cavity System," Princeton University AMS Report No. 1009, July 1971.

10. Dowell, E.H. and Voss, H.M., "Experimental and Theoretical Panel Flutter Studies in the Mach Number Range of 1.0 to 5.0," AIAA Journal, 3, pp. 2292-2304, 1965.

11. Guy, R.W. and Bhattacharya, M.C., "The Transmission of Sound Through a Cavity-Backed Finite Plate," J. Sound Vib. 27, pp. 207-223, 1973.

12. Smith, D.A., "An Experimental Study of Acoustic Natural Modes of Interconnected Cavities," Princeton University AMS Report No. 1284, August 1976.

13. Warburton, G.B., "The Vibration of Rectangular Plates," Proc. Inst. Mech. Engrs. (London), 1968, pp. 371-384, 1954.

14. Wolf, Jr., J.A., Nefske, D.J., and Howell, L.J., "Structural-Acoustic Finite Element Analysis of the Automobile Passenger Compartment," SAE Paper 760184, Presented at the Automotive Engineering Congress and Exposition, Detroit, Michigan, February 1976.

15. Petyt, M., Lea, J. and Koopman, G.H., "A Finite Element Method for Determining the Acoustic Modes of Irregular Shaped Cavities," J. Sound Vib. 45, pp. 495-502, 1976.

16. Howlett, J.T. and Morales, D.A., "Prediction of Light Aircraft Interior Noise," NASA TM X-72838, April 1976.

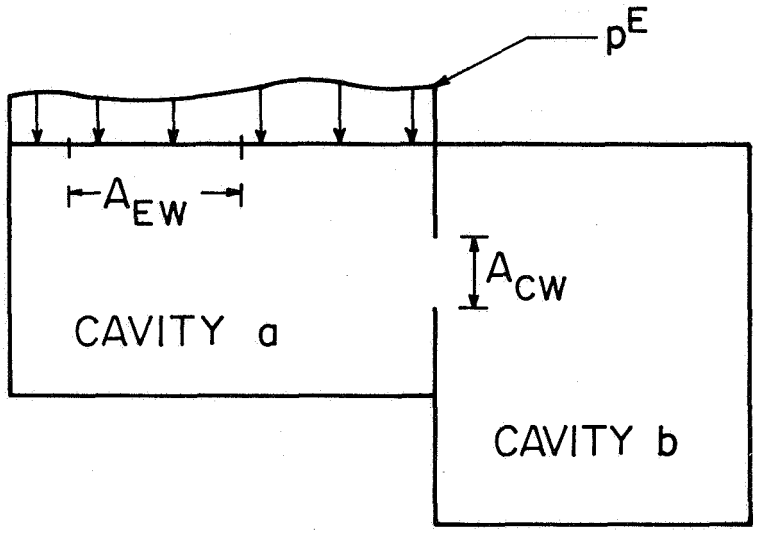

Figure 1.- Acoustic cavity-structural wall geometry.

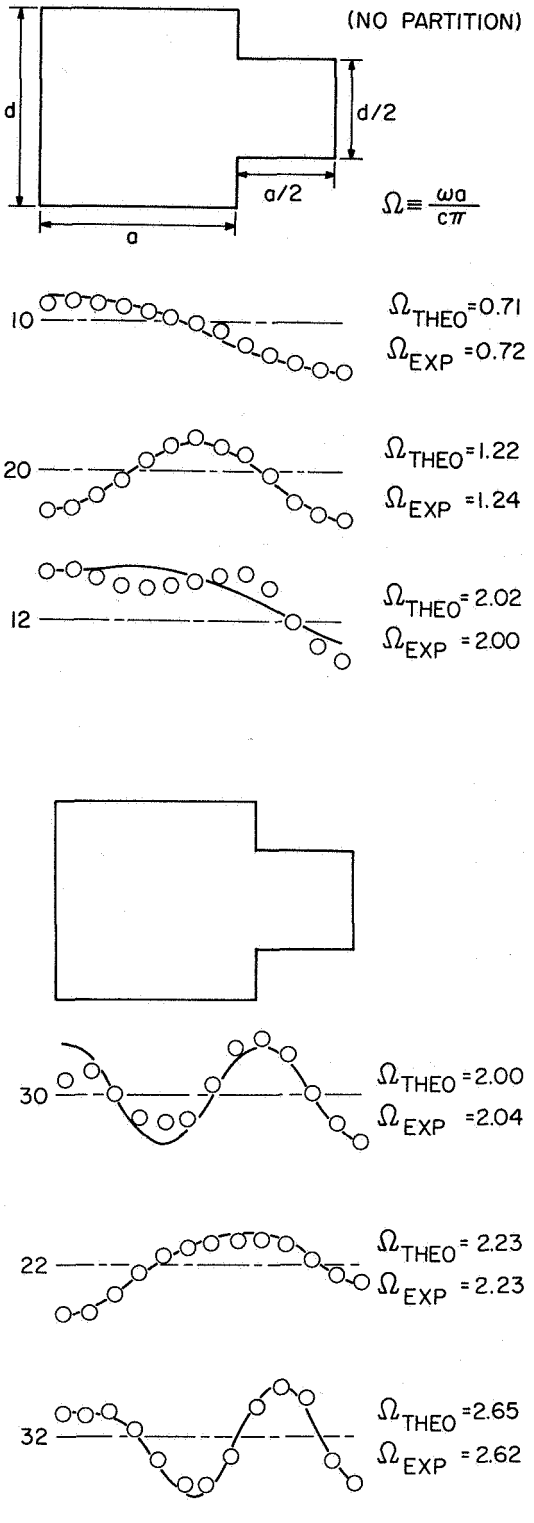

Figure 2.- Comparison of theoretical and experimental cavity acoustic modes.

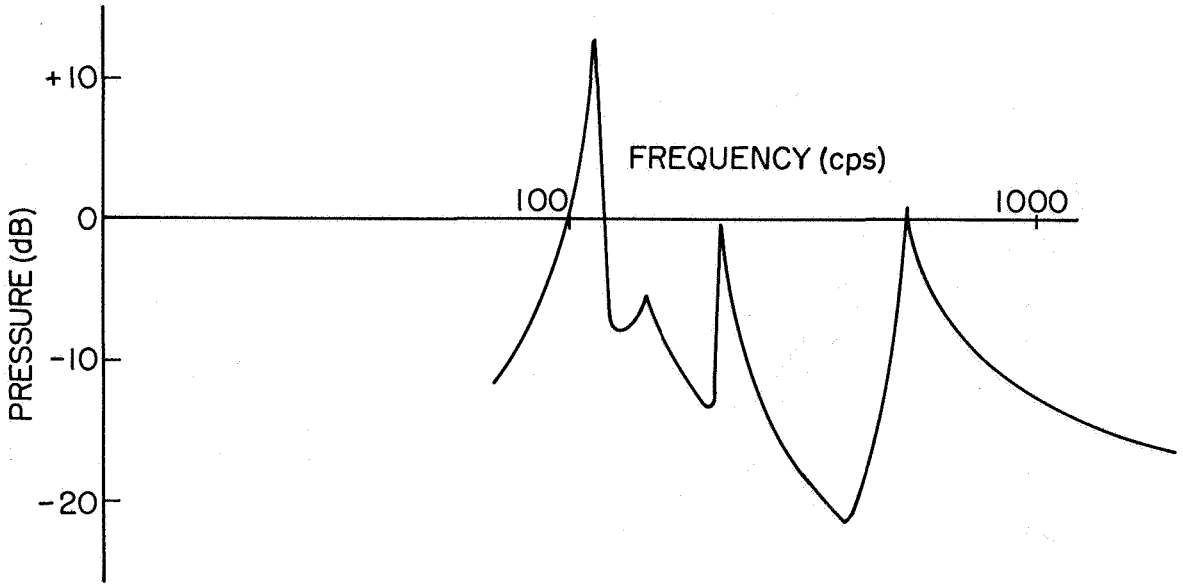

Figure 3.- Cavity response to sinusoidal external field.

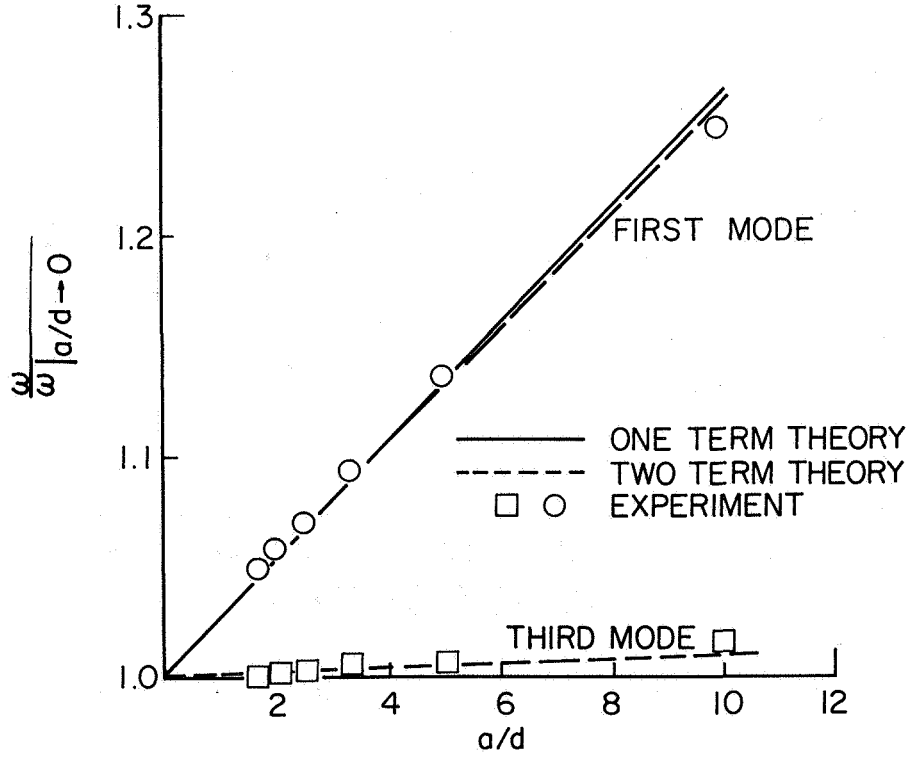

Figure 4.- Cavity effect on panel natural frequencies.

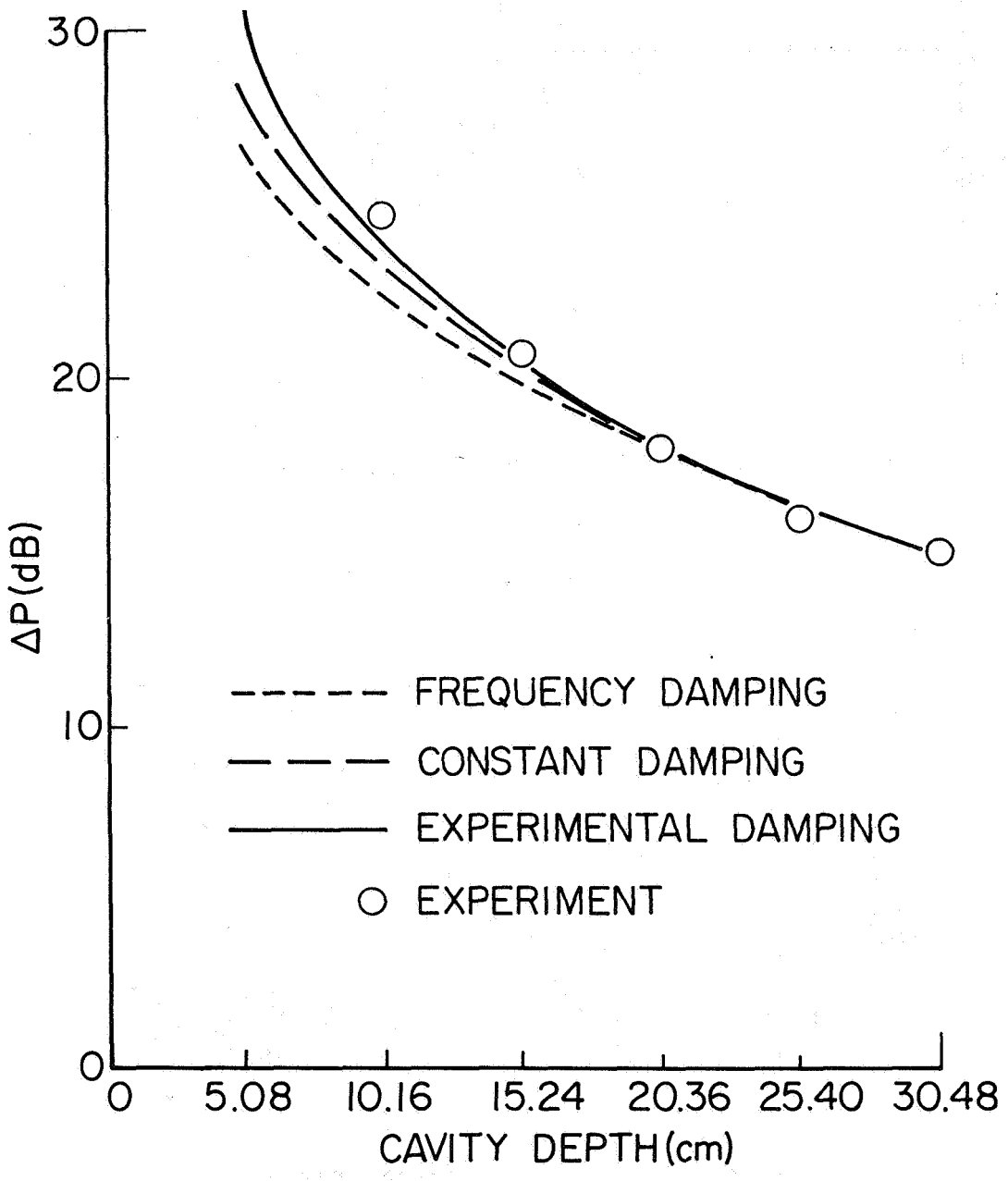

Figure 5.- Cavity pressure versus cavity depth.

SOUND RADIATION FROM RANDOMLY VIBRATING BEAMS OF FINITE CIRCULAR CROSS SECTION

M.W. Sutterlin
Bolt Beranek and Newman Inc.

A.D. Pierce
Georgia Institute of Technology

INTRODUCTION

Previous studies of the radiation of sound from vibrating cylindrical beams have been concerned with radiation from resonant modes of these finite beams, with specified end boundary conditions. These include studies by Yousri and Fahy (ref. 1) and Kuhn and Morfey (ref. 2). The radiation efficiency or radiation loss factor determined in this manner represents the contribution of a single mode to the radiation at a given frequency. More recently, Yousri and Fahy have presented (ref. 3) a more general derivation which shows that the radiation efficiency for a cylindrical beam is a summation of terms that represent contributions from various modes. This summing over modes is necessary whenever more than one mode is excited in the frequency band of interest.

The results of the present study are given in a form which depends only on the frequency of the beam vibrations and the physical characteristics of the beam and its surroundings. A statistical consideration of random beam vibrations allows this result to be independent of the boundary conditions at the ends of the beam. The acoustic power radiated by the beam can be determined from a knowledge of the frequency band vibration data without a knowledge of the individual modal vibration amplitudes.

A practical example of the usefulness of this technique is provided by the application of the theoretical calculations to the prediction of the octave band acoustic power output of the picking sticks of an automatic textile loom. Calculations are made of the expected octave band sound pressure levels based on measured acceleration data. These theoretical levels are subsequently compared with actual sound pressure level measurements of loom noise.

THEORY

A beam of finite length is modelled as a cylinder of infinite length situated on the z axis (see Fig. 1). The transverse velocity of the beam vibrations is assumed to be zero except on the segment of the cylinder which lies between the points $z = \ell/2$ and $z = -\ell/2$. On this vibrating segment the transverse velocity consists of x and y components, v_x and v_y, which are expanded in a Fourier series of arbitrary fundamental time period ω

$$\vec{v}(z,t) = \sum_{n=-\infty}^{\infty} \vec{v}_n(z)\ e^{in\omega_o t} \tag{1}$$

The individual components of the Fourier series are represented as the superposition of two traveling waves moving in opposite directions on the beam

$$\vec{v}_n(z) = \vec{v}_n\ (e^{ik_b z} + e^{-i(k_b z + \psi)}) \qquad -\frac{\ell}{2} \le z \le \frac{\ell}{2} \tag{2}$$

where k_b is the wave number of the beam vibrations, and ψ represents the relative phase between the two traveling waves. Furthermore, $v_n(z)$ can be written as

$$\vec{v}_n(z) = \int_{-\infty}^{\infty} \vec{v}(\alpha)\ e^{i\alpha z}\ d\alpha \tag{3}$$

and the radial or normal velocity is

$$v_r(\theta,z) = (\cos\theta\ \hat{i} + \sin\theta\ \hat{j}) \cdot \int_{-\infty}^{\infty} \vec{v}(\alpha)\ e^{i\alpha z}\ d\alpha \tag{4}$$

The acoustic pressure due to these transverse vibrations is found by applying the acoustic boundary condition at the surface of the cylinder to the solution of the linear acoustic wave equation in cylindrical coordinates. The partial differential equation and the appropriate boundary condition are

$$\frac{\partial^2 P}{\partial r^2} + \frac{1}{r}\frac{\partial P}{\partial r} + \frac{1}{r^2}\frac{\partial^2 P}{\partial \theta^2} + \frac{\partial^2 P}{\partial z^2} - \frac{1}{c^2}\frac{\partial^2 P}{\partial t^2} = 0 \tag{5}$$

$$\left.\frac{\partial P}{\partial r}\right|_{r=r_o} = in\omega_o \rho\ v_r \tag{6}$$

The solution to Eq. 5 can be written as a general linear combination of the seperable solutions (see ref. 4). The solution for outgoing waves of fixed frequency $\omega_n = n\omega_c$ can be written

$$P(r,\theta,z) = \sum_{m=0}^{\infty} \int_{-\infty}^{\infty} [A_m(\alpha)\cos(m\theta) + B_m(\alpha)\sin(m\theta)] H_m^{(1)}(k_r r) e^{i\alpha z}\, d\alpha \qquad (7)$$

where $k_r = (k^2 - \alpha^2)$, $k = \omega/c$ and $H_m^{(1)}$ is the Hankel function of the first kind and of order m. Applying the boundary condition of Eq. 6 to the above expression, one finds that

$$P(r,\theta,z) = (\cos\theta\, \hat{i} + \sin\theta\, \hat{j}) \cdot \int_{-\infty}^{\infty} Z(\alpha,r)\vec{v}(\alpha) e^{i\alpha z}\, d\alpha \qquad (8)$$

where

$$Z(\alpha,r) = i\omega_n \rho \frac{H_1^{(1)}(k_r r)}{k_r H_1^{(1)'}(k_r r_o)} \qquad (9)$$

The time average acoustic power radiated by the beam at a given frequency is found by taking the time average of the integral over the surface of the cylinder of the product of the acoustic pressure at the surface of the cylinder $P(r_o,\theta,z)$ and the normal velocity $v_r(\theta,z)$

$$W = \frac{1}{2} \mathrm{Re}\left\{ \int_{-\infty}^{\infty} \int_{0}^{2\pi} P(r_o,\theta,z)\, v_r^*(\theta,z)\, r_o\, d\theta\, dz \right\} \qquad (10)$$

where Re denotes the real part, and * indicates the complex conjugate. The ensemble average acoustic power radiated in a given frequency band is found by taking the ensemble average of a sum over the frequencies within the band of the result of Eq. 10. The ensemble average is performed assuming all relative phases to be equally probable.

The result of the θ integration in Eq. 10 is π, and the z integration produces a dirac delta function $2\pi\delta(\alpha-\alpha')$. This allows one of the α integrations to be performed by inspection, yielding

$$W = \pi^2 r_o \int_{-\infty}^{\infty} \mathrm{Re}\{Z_o(\alpha)\} \left(|v_x(\alpha)|^2 + |v_y(\alpha)|^2\right) d\alpha \qquad (11)$$

where

$$Z_o(\alpha) = Z(\alpha,r_o) = i\omega_n \rho \frac{H_1^{(1)}(k_r r_o)}{k_r H_1^{(1)'}(k_r r_o)} \qquad (12)$$

This expression for the acoustic power radiated by a finite cylinder can be simplified by applying some of the properties of Hankel functions. For

$k^2 < \alpha^2$ the argument for the Hankel functions is imaginary and $\mathrm{Re}\{Z_o(\alpha)\}$ is zero. For $k^2 > \alpha^2$ the argument is real and the Wronskian relation for the Hankel functions gives (ref. 5)

$$\mathrm{Re}\{Z_o(\alpha)\} = \frac{2\omega\rho}{\pi r_o} \frac{1}{k_r^2 |H_1^{(1)'}(k_r r_o)|^2} \tag{13}$$

Referring back to Eqs. 2 and 3, one can write $\vec{v}(\alpha)$ as the inverse transform of $\vec{v}(z)$, which when evaluated gives

$$\vec{v}(\alpha) = \frac{\vec{v}_n}{\pi} \left[\frac{\sin(k_b + \alpha)\frac{\ell}{2}}{(k_b + \alpha)} e^{-i\psi} + \frac{\sin(k_b - \alpha)\frac{\ell}{2}}{(k_b - \alpha)} \right] \tag{14}$$

Therefore

$$|v_x(\alpha)|^2 + |v_y(\alpha)|^2 = \frac{|v_{nx}|^2 + |v_{ny}|^2}{\pi^2} \left[\frac{\sin^2(k_b + \alpha)\frac{\ell}{2}}{(k_b + \alpha)^2} + \right.$$

$$\left. \frac{\sin^2(k_b - \alpha)\frac{\ell}{2}}{(k_b - \alpha)^2} + 2\cos\psi \frac{\sin(k_b + \alpha)\frac{\ell}{2} \sin(k_b - \alpha)\frac{\ell}{2}}{(k_b^2 - \alpha^2)} \right] \tag{15}$$

The $\cos\psi$ term goes to zero in taking the average assuming all ψ to be equally probable. It can be shown, by taking the time average of $\vec{v} \cdot \vec{v}$, that the mean square velocity in a given frequency band is equal to a sum over the frequencies in the band of the magnitude squared of $\vec{v}_n$

$$\langle v_x^2 \rangle = \sum |v_{nx}|^2 \qquad \text{and} \qquad \langle v_y^2 \rangle = \sum |v_{ny}|^2 \tag{16}$$

assuming x and y vibrations to be uncorrelated.

All these results are incorporated into Eq. 11 with the result that the acoustic power radiated in a given frequency band is

$$W = \frac{2\omega\rho}{\pi} (\langle v_x^2 \rangle + \langle v_y^2 \rangle) \int_{-K}^{K} \frac{1}{k_r^2 |H_1^{(1)'}(k_r r_o)|^2} \left[\frac{\sin^2(k_b + \alpha)\frac{\ell}{2}}{(k_b + \alpha)^2} + \frac{\sin^2(k_b - \alpha)\frac{\ell}{2}}{(k_b - \alpha)^2} \right] d\alpha \tag{17}$$

where all frequency terms are evaluated at the center frequency of the band.

This result can be written in the form of a radiation efficiency for the

beam. For a cylinder the radiation efficiency is

$$\sigma = \frac{W}{\rho c \pi r_o \ell (\langle v_x^2 \rangle + \langle v_y^2 \rangle)} \tag{18}$$

With the change of variables $\beta = \alpha/k$ and the above expression, one can write the radiation efficiency for a cylindrical beam

$$\sigma = \frac{4}{\pi^2 k^2 r_o \ell} \int_{-1}^{1} \frac{1}{(1-\beta^2)\left|H_1^{(1)\prime}(\sqrt{1-\beta^2}kr_o)\right|^2} \frac{\sin^2(\varepsilon+\beta)\frac{k\ell}{2}}{(\varepsilon+\beta)^2} d\beta \tag{19}$$

where $\varepsilon = k_b/k$ and a symmetry of the integral was used to simplify the expression.

RESULTS

In the low frequency or small radius limit, kr_o is small. An approximation may be used in place of the Hankel function in order to simplify the integral in Eq. 19. The first term in the series expansion for the derivative of the Hankel function gives

$$\left|H_1^{(1)\prime}(z)\right|^2 = \frac{4}{\pi^2} \frac{1}{z^4} \tag{20}$$

With this approximation and the change of variables $u = (\varepsilon+\beta)k\ell/2$, one gets

$$\sigma = \frac{(kr_o)^3}{2} \int_{(\varepsilon-1)\frac{k\ell}{2}}^{(\varepsilon+1)\frac{k\ell}{2}} \left[1 - \left(\frac{2u}{k\ell} - \varepsilon\right)^2\right] \frac{\sin^2 u}{u^2} du \tag{21}$$

Well below the coincidence frequency ($k_b = k$), u^2 in the denominator can be approximated as $u^2 = (k\ell/2)^2$. The result of this approximation is

$$\sigma = \frac{2}{3} (kr_o)^2 \left(\frac{r_o}{\ell}\right) \left(\frac{k}{k_b}\right)^2 \left[1 - \frac{3\cos k_b \ell}{(k\ell)^2} \left\{\frac{\sin k\ell}{(k\ell)} - \cos k\ell\right\}\right] \tag{22}$$

This expression is directly comparable to the results of Kuhn and Morfey (ref. 2) in their low frequency approximation of the Yousri and Fahy (ref. 1) expression for the radiation efficiency of a simply supported beam. The radiation efficiency for the simply supported case gives a result which is exactly twice that given by Eq. 22 when evaluated at the same resonance frequency. The

reason for this difference lies in the fact that the simply supported boundary condition implies a specific phase ψ in Eq. 2. This phase happens to be one which maximizes the radiation efficiency. Other possible phase relationships result in lower values for the radiation efficiency. It will be shown later that these differences disappear at higher frequencies.

At high frequencies the major contribution to the integral in Eq. 19 comes from the vicinity of $\beta = -\varepsilon$. Expanding the Hankel function term in a Taylor series about that point and keeping only the first term one gets

$$\sigma = \frac{2}{\pi k r_o} \frac{1}{(1-\varepsilon^2)\left|H_1^{(1)'}(\sqrt{1-\varepsilon^2}\,k r_o)\right|^2} \tag{23}$$

This is the radiation efficiency for a cylinder of infinite length. If $(1-\varepsilon^2)^{1/2} k r_o >> 1$, then the derivative of the Hankel function may be expressed in terms of its asymptotic limit and

$$\sigma = \frac{\sqrt{1-\varepsilon^2}\,(k r_o)^2}{(1-\varepsilon^2)(k r_o)^2+1} \tag{24}$$

For purposes of a numerical evaluation of Eq. 19, the radiation efficiency is considered as a function of three independent variables only one of which is frequency dependent. These are $k r_o$, ℓ/r_o and

$$\varepsilon(k r_o)^{1/2} = \left(\frac{m}{B}\right)^{1/4} (c r_o)^{1/2} \tag{25}$$

where m is the mass per unit length of the beam and B is the bending stiffness. This last parameter is chosen so as to eliminate the frequency dependence of $\varepsilon = k_b/k$. Figs. 2 and 3 show the results of a numerical calculation of the radiation efficiency. Each graph shows σ as a function of $k r_o$ for several values of $\varepsilon(k r_o)^{1/2}$ and for one value of ℓ/r_o. A valid comparison with the modal approach can be made by leaving the phase angle in Eq. 15 and continuing the derivation of the radiation efficiency. The result is

$$\sigma = \frac{4}{\pi^2 k^2 r_o \ell} \int_{-1}^{1} \frac{1}{(1-\beta^2)\left|H_1^{(1)'}(k r_o\sqrt{1-\beta^2})\right|^2} \left[\frac{\sin^2(\varepsilon+\beta)\frac{k\ell}{2}}{(\varepsilon+\beta)^2} + \cos\psi \, \frac{\sin(\varepsilon+\beta)\frac{k\ell}{2} \sin(\varepsilon-\beta)\frac{k\ell}{2}}{(\varepsilon^2-\beta^2)} \right] d\beta \tag{26}$$

Fig. 4 gives this comparison for the two extreme cases, where the $\cos\psi$ term is either always positive or always negative at the modal resonance frequencies. It is clear from the figure that the contribution from the second term to the

integrand in Eq. 26 diminishes at higher frequencies, as the two extreme cases converge towards the average.

APPLICATION TO TEXTILE LOOM PICKING STICKS

In order to apply these results to the picking sticks of an automatic textile loom, it is necessary to generalize them to allow for different radiation efficiencies and perhaps different effective radii for the x and y vibrations. This is necessary to account for the fact that the picking stick is more nearly rectangular in cross section than circular. With this in mind one can write the acoustic power as

$$W = \rho c \pi \ell \quad [r_{ox} \langle v_x^2 \rangle \sigma_x + r_{oy} \langle v_y^2 \rangle \sigma_y] \tag{27}$$

Values for the parameters were chosen to correspond to the characteristics of the picking sticks. The numerical technique used to evaluate σ and measured vibration data were used to determine the octave band acoustic power output for each of the two picking sticks on a loom. Fig. 5 shows a graph of the resulting power levels.

From these power levels, octave band sound pressure levels were calculated at a reference point one meter from the front of the loom, assuming symmetric cylindrical spreading,

$$SPL = 10 \log_{10} \frac{\langle p^2 \rangle}{p_{ref}^2} \qquad \langle p^2 \rangle = \frac{\rho c}{2\pi R \ell} [W_{left} + W_{right}] \tag{28}$$

where R is the distance to the reference point and $P_{ref} = 2 \times 10^{-5}$ N/m^2 is the reference pressure. A comparison of this predicted sound pressure level with sound pressure levels actually measured at this position is shown in Fig. 6. This graph shows good agreement between theoretical and experimental results for frequencies above 125 Hz. The agreement is particularly close in the range of frequencies which have the highest sound pressure levels. Both curves in the figure represent an overall A-weighted level of 94 dBA. It is clear however that the low frequency predicted result falls short of the measured values. It is thought that there may be other noise sources on the loom which contribute to the higher levels at these low frequencies.

REFERENCES

1. Yousri, S. N.; and Fahy, F. J.: Sound Radiation from Transversely Vibrating Unbaffled Beams. J. Sound Vib., vol. 26, 1973, pp. 437-439.

2. Kuhn, G. F.; and Morfey, C. L.: Radiation Efficiency of Simply Supported Slender Beams Below Coincidence. J. Sound Vib., vol. 33, 1974, pp. 241-245.

3. Yousri, S. N.,; and Fahy, F. J.: Acoustic Radiation by Unbaffled Cylindrical Beams in Multi-Modal Transverse Vibration. J. Sound Vib., vol. 40, 1975, pp. 299-306.

4. Morse, P. M.; and Ingard, K. U.: Theoretical Acoustics. McGraw Hill, New York, 1968, pp. 356-357.

5. Junger, M. C.: The Physical Interpretation of the Expression for an Outgoing Wave in Cylindrical Coordinates. J. Acoust. Soc. Am., vol. 25, 1953, pp. 40-47.

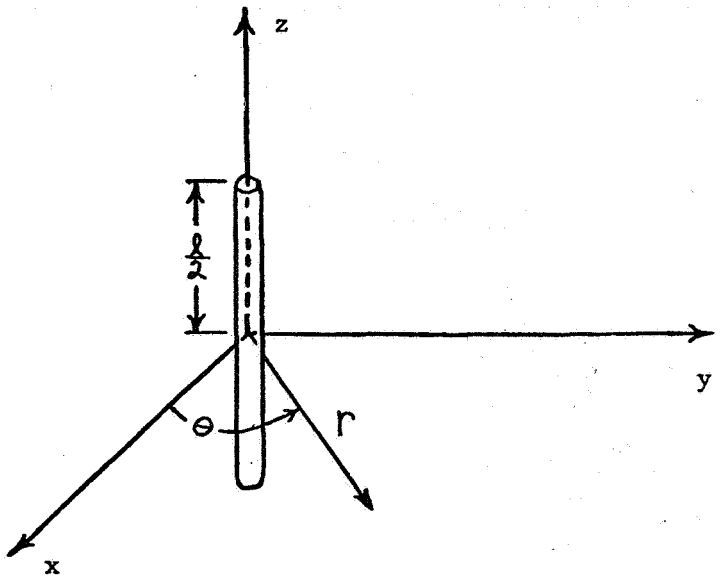

Figure 1.- Beam location and coordinate system.

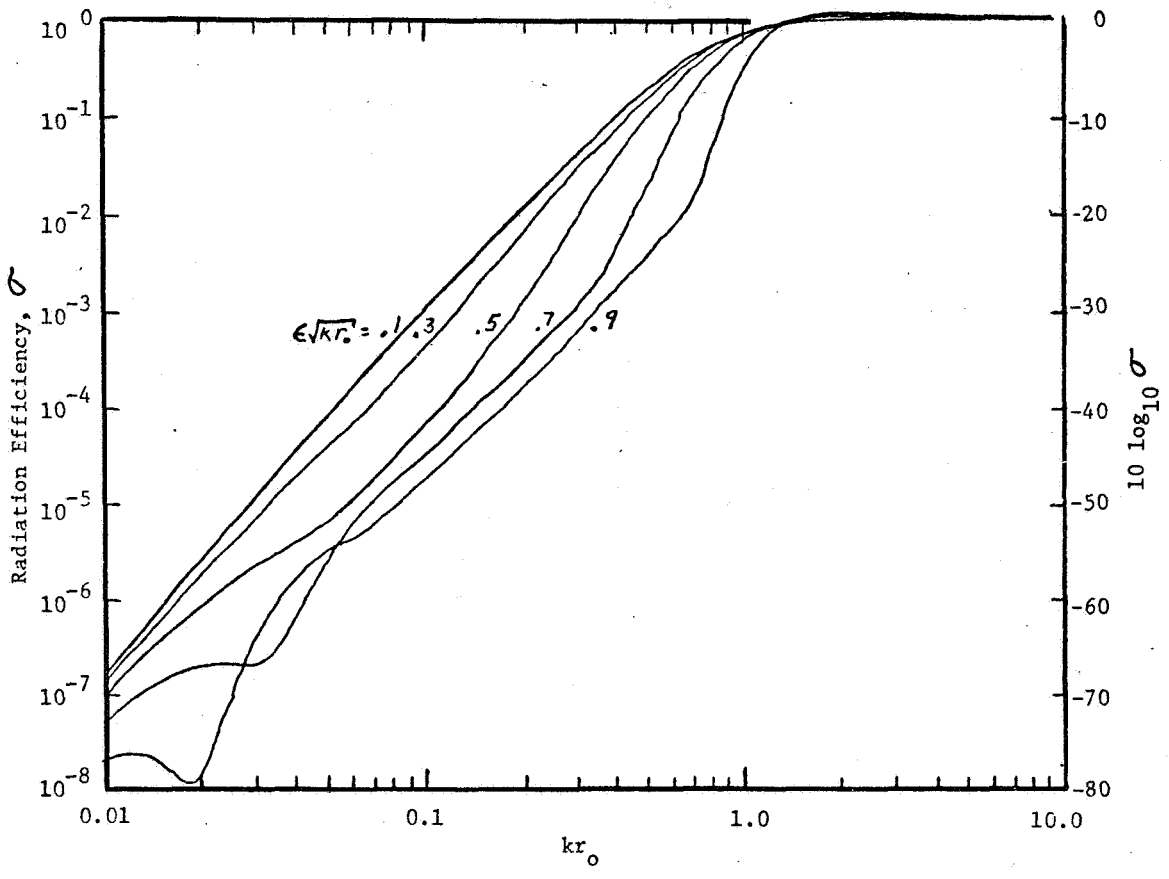

Figure 2.- Radiation efficiency of a beam for $\ell/r_o = 50$.

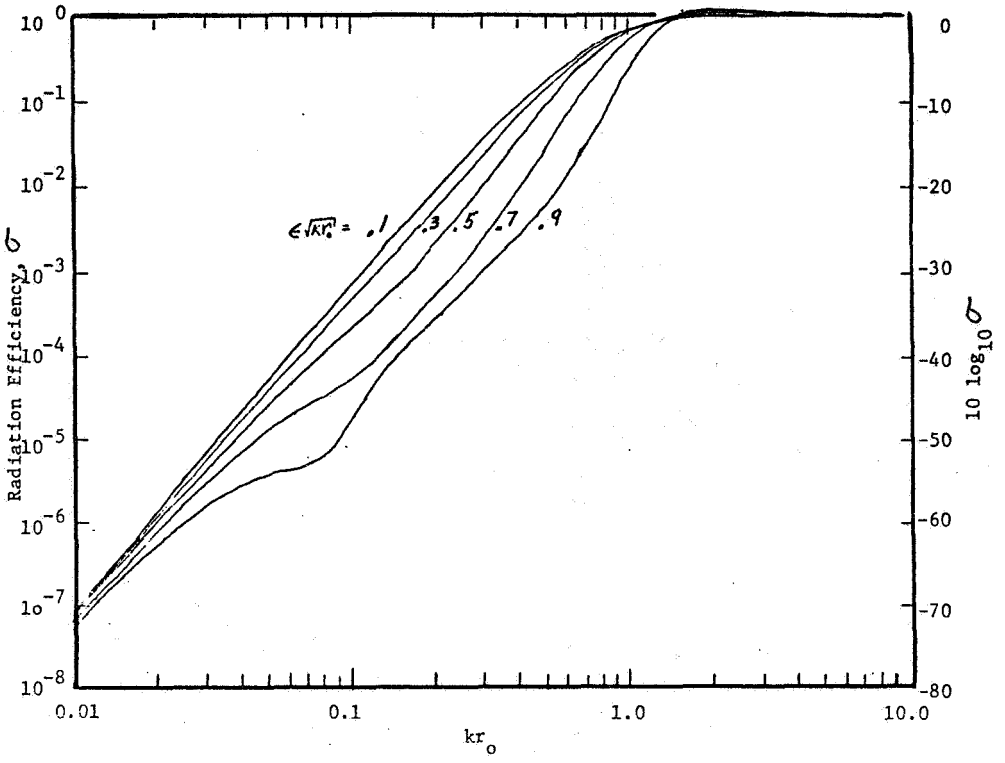

Figure 3.- Radiation efficiency of a beam for $\ell/r_o = 25$.

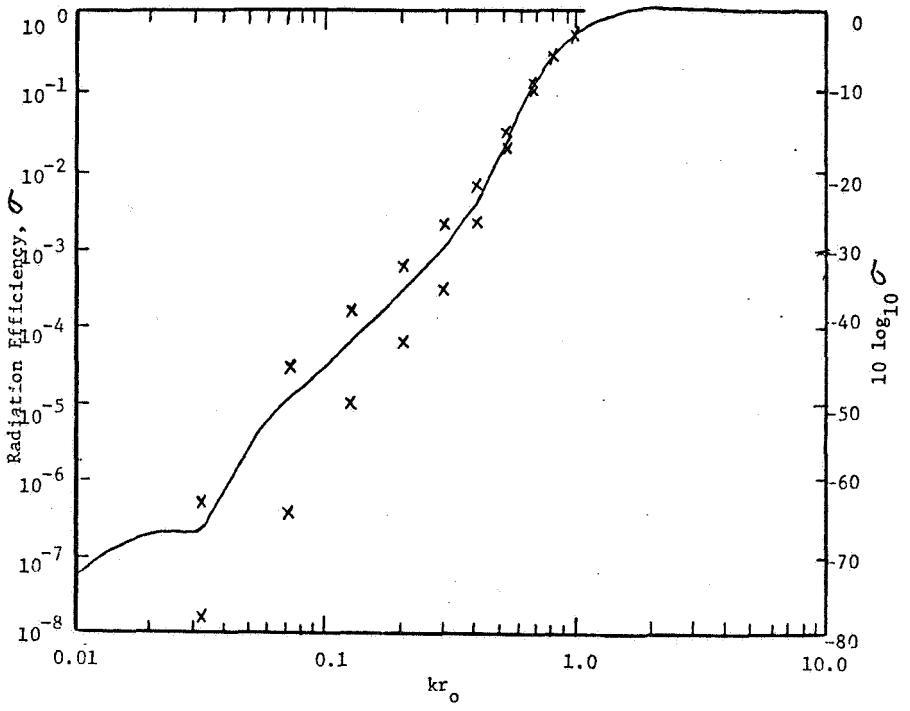

Figure 4.- A comparison of radiation efficiencies, — averaging technique, $\ell/r_o = 50$, $\varepsilon\sqrt{kr_o} = 0.7$, x modal approach.

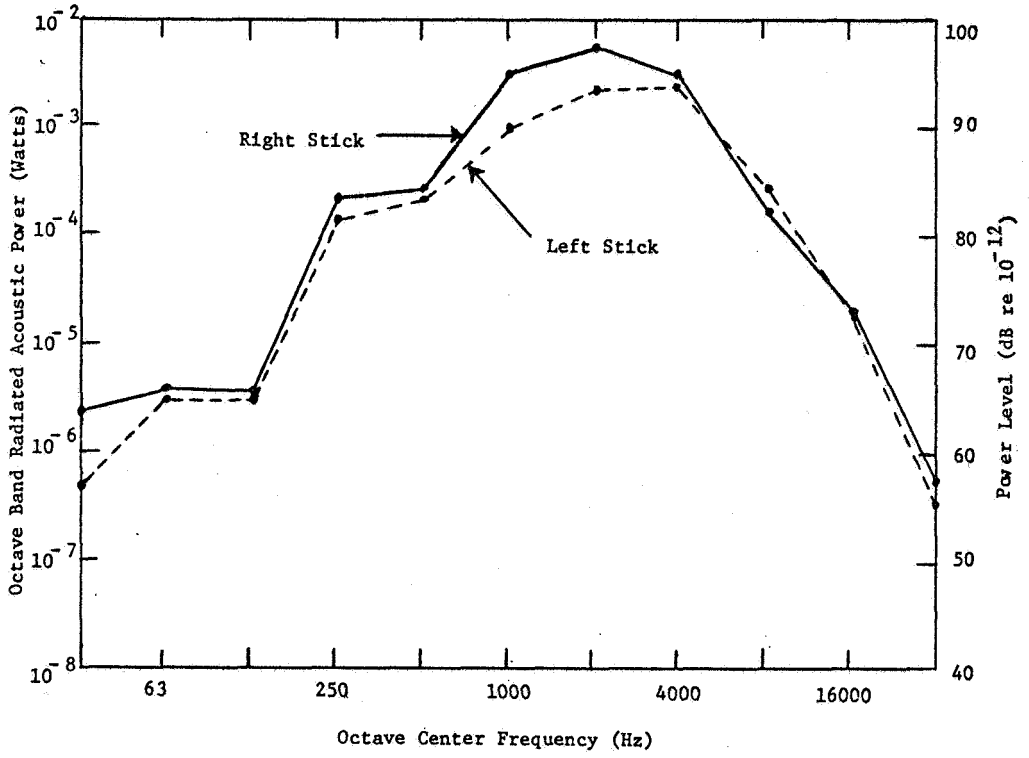

Figure 5.- Theoretical acoustic power output.

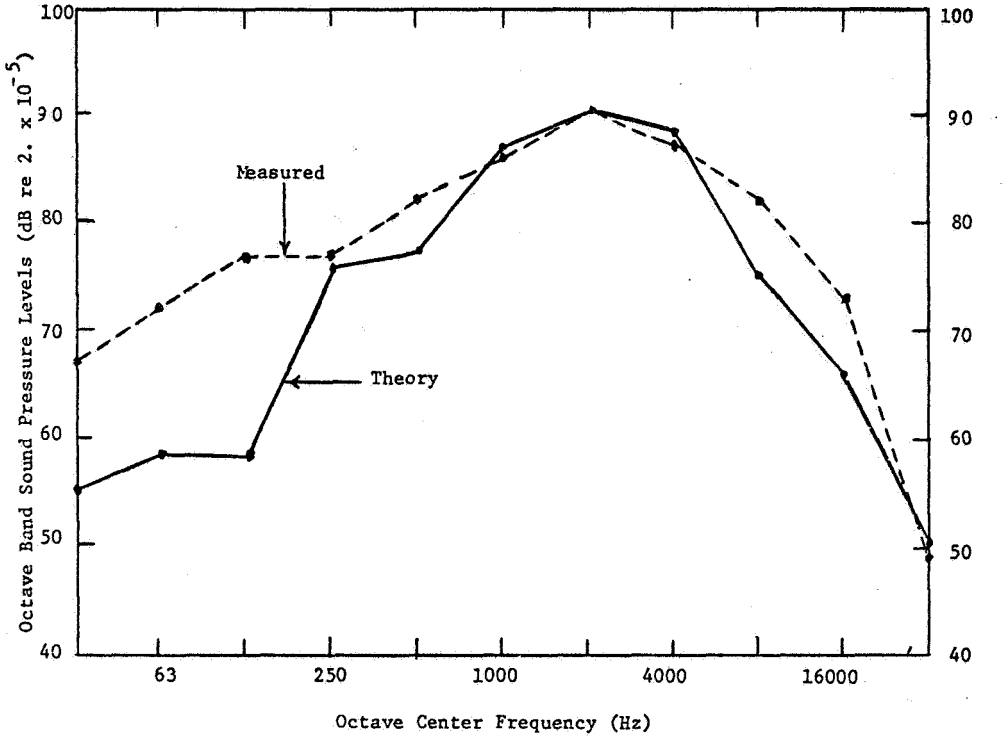

Figure 6.- Theoretical and experimental sound pressure levels.

A PHENOMENOLOGICAL, TIME-DEPENDENT TWO-DIMENSIONAL PHOTOCHEMICAL MODEL OF THE ATMOSPHERE

George F. Widhopf
The Aerospace Corporation

ABSTRACT

A two-dimensional atmospheric model which describes the time-dependent distribution of the trace species O_3, $O(^3P)$, $O(^1D)$, NO, NO_2, N_2O, HNO_3, OH, HO_2, H_2O_2, CH_4, CO, N, and H throughout the entire yearly seasonal cycle has been developed. The two-dimensional atmospheric transport coefficients used in the model have been tested by calculating the time-dependent distributions of atmospheric nuclear debris resulting from past nuclear weapon tests and the results are in good agreement with observations. The resulting calculated model distributions of O_3, NO_2, NO, N_2O and HNO_3 in the natural atmosphere are in good agreement with available measurements of these species. The monthly variation of the ozone column is in good agreement with observations throughout the year, as are the individual calculated vertical ozone profiles at all latitudes. The seasonal and latitudinal variations of these trace species are significant.

THE DIFFUSION APPROXIMATION - AN APPLICATION TO RADIATIVE TRANSFER IN CLOUDS

Robert F. Arduini and Bruce R. Barkstrom
Joint Institute for Advancement of Flight Sciences
The George Washington University

INTRODUCTION

Water droplets and ice crystals, the constituents of clouds, are very nearly transparent (i.e. they absorb almost no radiation in the visual wavelengths (400 nm to 700 nm)). Clouds are also optically thick with optical depths for a one kilometer path ranging from 10 to 50, depending upon droplet size and number density of droplets. Therefore, visible light which enters a cloud is scattered many times before being absorbed or exiting the cloud. This type of process is well described by a diffusion model.

In this paper it is shown how the radiative transfer equation reduces to the diffusion equation. To keep the mathematics as simple as possible, the approximation is applied to a cylindrical cloud of radius R and height h. The diffusion equation separates in cylindrical coordinates and, in a sample calculation, the solution is evaluated for a range of cloud radii with cloud heights of 0.5 km and 1.0 km.

The simplicity of the method and the speed with which solutions are obtained give it potential as a tool with which to study the effects of finite-sized clouds on the albedo of the earth-atmosphere system.

THE DIFFUSION APPROXIMATION

The diffusion approximation has long been used in nuclear reactor theory (refs. 1-3) and has recently been applied to the transfer of visual radiation in snow (ref. 4). In the diffusion approximation, the radiation is assumed to have an almost isotropic angular distribution, so that the specific intensity at space point $\underline{r}$ for radiation traveling in direction $\underline{\Omega}$ is

$$I(\underline{r}, \underline{\Omega}) \simeq J(\underline{r}) - 3D\underline{\Omega} \cdot \underline{\nabla} J(\underline{r}) \tag{1}$$

$$J(\underline{r}) = \frac{1}{4\pi} \int I(\underline{r}, \underline{\Omega}) d\underline{\Omega} \tag{2}$$

is the mean intensity, D is the diffusion coefficient, and $\underline{\nabla}$ is the gradient operator. Because the net vector flux

$$\underline{\Phi} \equiv \int \underline{\Omega} I \, d\underline{\Omega} \tag{3}$$

is proportional to the gradient of J:

$$\underline{\Phi} = - 4\pi D \, \underline{\nabla} J \tag{4}$$

it follows that J satisfies the diffusion equation

$$\nabla^2 J - L^{-2} J = 0 \tag{5}$$

where the diffusion length, L, is related to D according to

$$L^2 = D/\kappa \tag{6}$$

κ is the absorption coefficient.

The net flux through a surface with normal $\hat{n}$ is

$$\Phi_n = \hat{n} \cdot \underline{\Phi} = - 4\pi D \frac{\partial J}{\partial n} \tag{7}$$

where $\partial/\partial n$ denotes the directional derivative. The flux in the direction of $+\hat{n}$ is

$$\Phi_n^{(+)} = \pi J - 2\pi D \, \partial J/\partial n \tag{8a}$$

and the flux in direction $-\hat{n}$ is

$$\Phi_n^{(-)} = \pi J + 2\pi D \, \partial J/\partial n \tag{8b}$$

The plus and minus signs indicate the positive and negative senses of $\hat{n}$.

The diffusion coefficient and the diffusion length are related to the extinction coefficient χ and the phase function of the cloud droplets according to

$$D = 1/[3\chi(1 - \omega g)] \tag{9}$$

and

$$L^2 = 1/[3\chi(1 - \omega)(1 - \omega g)] \tag{10}$$

In these equations, ω is the single scattering albedo (or fraction of light scattered in a single interaction with a cloud droplet) and g is the mean cosine of single scattering. Equations (9) and (10) are essentially approximations to the dispersion relation derived by Mika (ref. 5) for the largest singular eigenvalue in the singular eigenfunction solution for a plane-parallel atmosphere and expanded by van de Hulst (refs. 6 and 7) in his scaling laws. It may be noted that the diffusion equation (5) is identical to the Eddington approximation in a plane-parallel medium, in that for this geometry, the second moment of the radiation field, K, in a conservative atmosphere is equal to one-third of the mean intensity

$$K \equiv \frac{1}{2}\int_{-1}^{1} \mu^2 \, I \, d\mu \simeq \frac{1}{3} J \tag{11}$$

deep in the medium. Equation (11) uses the assumption of the plane-parallel atmosphere and describes the direction of propagation $\underline{\Omega}$ in terms of a polar coordinate system with a polar angle $\theta = \cos^{-1}\mu$ such that $\theta = 0$ is perpendicular to the plane of symmetry.

THE CYLINDRICAL CLOUD

Clouds in the atmosphere vary markedly in shape and size. To keep the mathematics as simple as possible, we have applied the diffusion approximation to a cylindrical cloud of radius R and height h. The cloud is illuminated from the top by a diffuse source, which is normalized to unit flux. It is assumed that none of the radiation that escapes the cloud returns.

With this choice of geometry and boundary conditions, the diffusion equation (5) separates. The solution for the mean intensity may be found as an expansion of standard mathematical functions in the form

$$J(r, z) = \sum_{m=0}^{\infty} [A_m \exp(\alpha_m z) + B_m \exp(-\alpha_m z)] J_0(\beta_m r) \tag{12}$$

with $J_0(\beta_m r)$ being the zeroth order Bessel function of the first kind. The separation constants α_m and β_m are related through the diffusion length in the following manner:

$$\alpha_m^2 = \beta_m^2 + L^{-2} \tag{13}$$

β_m is the solution of the transcendental equation that results from the application of the boundary condition at the sides:

$$\beta_m R\, J_1(\beta_m R) - C\, J_0(\beta_m R) = 0 \tag{14}$$

where

$$C = \frac{R}{2D} \tag{15}$$

Equation (14) is solved numerically using a Newton-Raphson method of root finding. The application of the boundary conditions at the top and bottom yields expressions for the expansion coefficients

$$B_m = \frac{2}{\pi \beta_m R\, J_1(\beta_m R)} \cdot \frac{1+2D\alpha_m}{[(1+2D\alpha_m)^2 - (1-2D\alpha_m)^2 \exp(-2\alpha_m h)]} \cdot \frac{1}{[1+(\frac{\beta_m R}{C})^2]} \tag{16}$$

and

$$A_m = \frac{(2D\alpha_m - 1)}{(2D\alpha_m + 1)} \exp(-2\alpha_m h)\, B_m \tag{17}$$

Our primary interest in this study is in the fate of the energy incident on the cloud. As one might expect, the energy may be reflected back out the top, may be transmitted out the bottom, escape out the sides, or be absorbed within the cloud. The power incident on the cloud top is

$$F^{\downarrow}_{TOP} = \int_0^{2\pi} d\phi \int_0^R r \Phi_z^{(-)}(z=0)\, dr = \pi R^2 \tag{18}$$

If we normalize the reflected and absorbed power by this amount, we find that they may be expressed in terms of the expansion coefficients and geometrical properties of the cloud in the form

$$E^{\uparrow}_{TOP} = 2\pi \sum_{m=0}^{\infty} [A_m(1+2D\alpha_m) + B_m(1-2D\alpha_m)]J_1(\beta_m R)/\beta_m R \tag{19}$$

$$E_{SIDE} = 2\pi \sum_{m=0}^{\infty} [A_m(\exp(\alpha_m h)-1) + B_m(1-\exp(-\alpha_m h))]$$

$$[J_0(\beta_m R) + 2D\beta_m J_1(\beta_m R)]/\alpha_m R \tag{20}$$

$$E^{\downarrow}_{BOTTOM} = 2\pi \sum_{m=0}^{\infty} [A_m \exp(\alpha_m h)(1-2D\alpha_m) + B_m \exp(-\alpha_m h)$$

$$(1+2D\alpha_m)]\ J_1(\beta_m R)/\beta_m R \tag{21}$$

and

$$E_{ABS} = 8\pi\kappa \sum_{m=0}^{\infty} [A_m\ (\exp(\alpha_m h)-1) + B_m(1-\exp(-\alpha_m h))]\cdot$$

$$J_1(\beta_m R)/\alpha_m \beta_m R \tag{22}$$

A SAMPLE CALCULATION

In a sample calculation the above expressions were evaluated for clouds of heights 0.5 and 1.0 km and a range of cloud radii from 0.5 to 10.0 km. The cloud droplet radius was assumed to be 10 microns with a number density of 100 cm^{-3}. The mean cosine g was assumed to be 0.8516 and the single scattering albedo ω was chosen to represent nearly conservative scattering ($1-\omega = 10^{-8}$) and non-conservative scattering ($1-\omega = 10^{-2}$). These values are typical of cumulus clouds as seen in Deirmendjian's model C1 (ref. 8).

The effect of the finite radius is marked, as can be seen in Figs. 1 and 2. The albedo of an isolated cloud, 1 km thick, may be reduced by 5 percent or more if the radius is less than 5 km. This reduction in albedo is due to the leakage of energy out the sides of the cloud. As the radius becomes smaller, the escape out the sides becomes more and more important. Clouds

whose radii are about equal to their height lose nearly as much energy out the sides as is reflected back out the top.

As the radius increases we expect the results to closely approach those from a plane-parallel treatment. Table 1 shows the difference between the results using the diffusion approximation for a cylindrical cloud and those using the Eddington approximation for a plane-parallel layer. The difference is quite small for clouds whose horizontal extent is much larger than the vertical.

It is generally known that Monte Carlo techniques, which are currently being used to study the effects of finite-sized clouds (refs. 9 and 10), consume great amounts of computer time. The above results using the diffusion approximation required less than 30 seconds execution time on a CDC CYBER 175 computer. The simplicity of the approximation and the speed with which results are obtained give the diffusion approximation potential as a tool to study the effects of finite-sized clouds on the earth-atmosphere system.

CONCLUDING REMARKS

Clouds represent an optically thick medium for visible radiation in which the internal radiation field is very nearly isotropic. Such a medium is well-suited to a description by a diffusion model. Applying the diffusion approximation to a cloud of cylindrical geometry, the fraction of the incident energy emerging from each of the cloud's surfaces has been calculated. The amount of radiation escaping from the sides becomes significant when the cloud's horizontal extent is less than ten times its vertical extent. The speed and simplicity of the method argue for its use to study the effects of finite-sized clouds on the earth's albedo.

REFERENCES

1. Glasstone, S. and Edlund, M. C.: The Elements of Nuclear Reactor Theory. D. Van Nostrand, 1952, 416 pp.

2. Meghreblian, R. V. and Holmes, D. K.: Reactor Analysis. McGraw-Hill, 1960, 808 pp.

3. Case, K. M. and Zweifel, P. F.: Linear Transport Theory. Addison-Wesley, 1967, 342 pp.

4. Bohren, C. F. and Barkstrom, B. R.: Theory of the Optical Properties of Snow. J. Geophys. Res., 1974, 4527-4535.

5. Mika, J. R.: Neutron Transport With Anisotropic Scattering. Nucl. Sci. Eng., 1961, 415-427.

6. van de Hulst, H. C.: The Spectrum of the Anisotropic Transfer Equation. Astron. Astrophys., 1970, 366-373.

7. van de Hulst, H. C.: High Order Scattering in Diffuse Reflection From A Semi-Infinite Atmosphere. Astron. Astrophys., 1970, 374-379.

8. Deirmendjian, D.: Electromagnetic Scattering on Spherical Polydispersions. American Elsevier, 1969, 290 pp.

9. McKee, T. B. and Cox, S. K.: Scattering of Visible Radiation By Finite Clouds. J. Atmos. Sci., 1974, 1885-1892.

10. Davies, R.: Three Dimensional Transfer of Solar Radiation In Terrestrial Clouds. Am. Meteor. Soc., Second Conference on Atmospheric Radiation, Oct. 29-31, 1975.

TABLE I.-COMPARISON BETWEEN EDDINGTON (PLANE-PARALLEL) AND DIFFUSION (CYLINDRICAL) APPROXIMATIONS
(Cloud Height = 1 km)

		Plane-Parallel	Cylindrical				
			R = 10 km	5 km	2 km	1 km	0.5 km
$1-\omega = 10^{-8}$	Albedo	0.875	0.848	0.821	0.744	0.631	0.464
	Transmission	0.125	0.114	0.104	0.076	0.040	0.009
$1-\omega = 10^{-2}$	Albedo	0.549	0.538	0.528	0.498	0.450	0.361
	Transmission	0.009	0.009	0.008	0.007	0.005	0.002

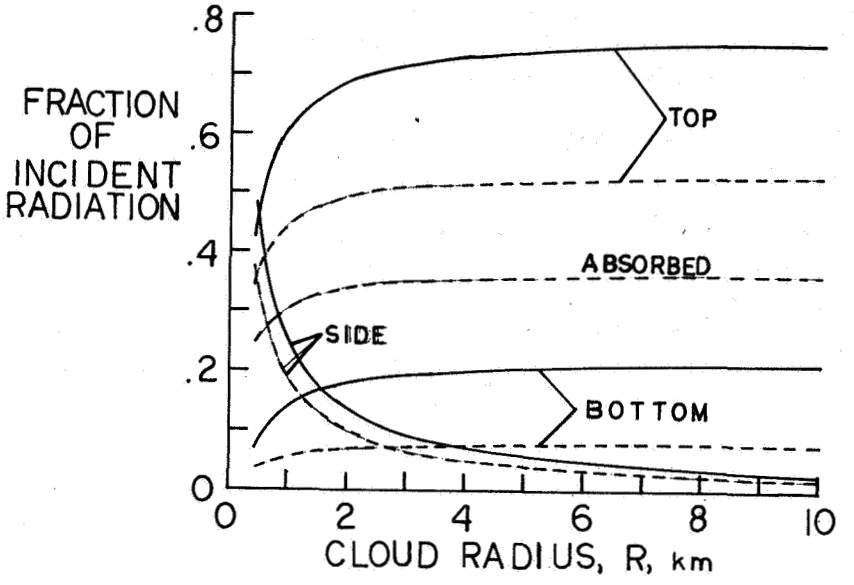

Figure 1.- Fate of energy incident upon a cylindrical cloud of height 0.5 km as a function of radius (solid line: $1-\omega = 10^{-8}$; broken line: $1-\omega = 10^{-2}$).

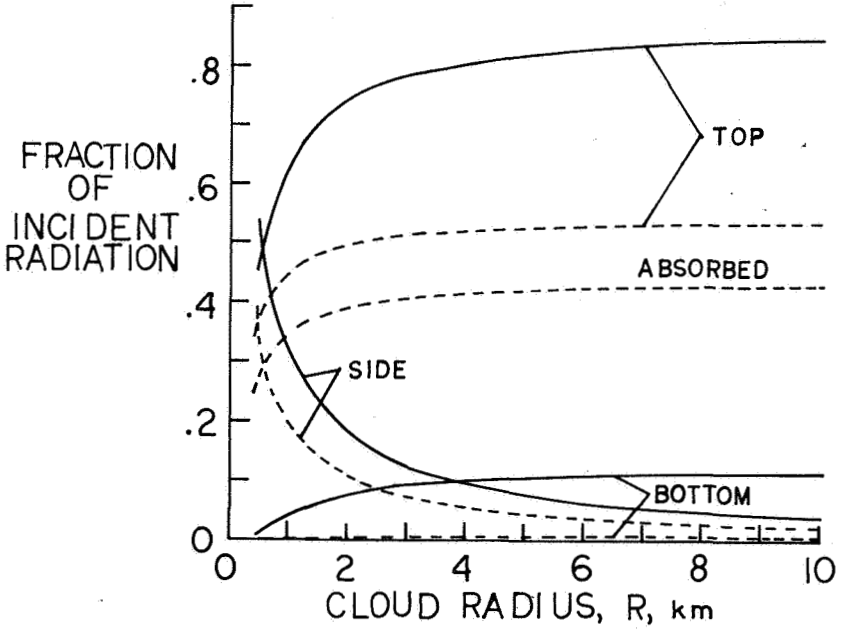

Figure 2.- Fate of energy incident upon a cylindrical cloud of height 1.0 km as a function of radius (solid line: $1-\omega = 10^{-8}$; broken line: $1-\omega = 10^{-2}$).

CALIBRATION AND VERIFICATION OF ENVIRONMENTAL MODELS

Samuel S. Lee, Subrata Sengupta,
Norman Weinberg, and Homer Hiser
University of Miami

INTRODUCTION

One of the weakest links in developing viable numerical models for environmental transport processes is the need for large comprehensive data bases for calibration and verification. The specific needs vary with the characteristics of the model under consideration. However, it has been found that the more complex the model is, the more difficult it is to obtain the adequate data base. In fact, often even before calibration and verification, the problem manifests itself in terms of specification of adequate boundary conditions for a well posed mathematical formulation. This paper deals with the unique problems of calibration and verification of mesoscale models applied to investigating power plant discharges.

Policastro (refs.1,2,3) in a series of reports has calibrated and verified a large number of thermal plume models with field data. He used a single data base to obtain comparative results from different models. Very few studies of this nature have been done primarily owing to the lack of comprehensive data bases. Lee et al (ref.4) summarized the importance of remote-sensing data in thermal pollution studies. Sengupta et al (ref.5) have demonstrated the important role of remote-sensing data in the development of numerical models. However, remote-sensing data usually provide only the surface conditions. For three-dimensional modelling it is imperative to have variations with depth. The role of in-situ measurements is therefore essential until remote-sensing techniques are developed for vertical profile measurement. Some studies of thermal plumes have been made using ground truth and remote-sensing data. Madding et al (ref.6) used a Texas Instrument RS-18A scanner mounted on a DC-3 together with in-situ measurements made by Argonne National Laboratory to study plumes from Point Beach Nuclear Power Plant located on the shoreline of Lake Michigan. Dinelli et al (ref.7) have discussed the use of thermal infrared scanner data in evaluating predictive models for thermal plumes. They studied the power plant sites at Vado Ligure and Porto Tolle in Italy. They discussed the use of IR data to develop plume models as well as verify them.

The thermal pollution group at the University of Miami is developing a package of three-dimensional models to predict and monitor thermal anomalies caused by power plant discharges. Remote-sensing IR data from satellites and airborne radiometers in conjunction with ground truth and in-situ measurements are used to calibrate and verify the models. The application sites are Biscayne Bay and Hutchinson Island in South Florida where a number of power plants are located. The details of the effort are presented in a series of reports by Lee et al (refs. 8 and 9). Hiser et al (ref.10) have presented the remote sensing effort. A brief description of the overall study is presented by Sengupta et al (ref. 11). Figure 1 shows the relationship between the data acquisition effort and modelling effort from the model development stage to verification and application stages.

THE MATHEMATICAL MODELS

The hydro- and thermodynamic behavior of a body of water in an ecosystem is affected by natural influences as characterized by the meteorological and hydrological characteristics of the domain as well as the anthromorphic disturbances generated by industry, agriculture and urban activity. The method of numerical modelling is to describe the system in terms of governing equations and boundary conditions that express the relevant physical laws and domain characteristics and then to simulate or solve the equations with numerical techniques, after approximations are made regarding variables as well as dimensions. We will consider three-dimensional "complete" models only, the data requirements being less stringent for simpler models.

The governing equations are the conservation of total mass, momentum and energy. The constitutive equation describing density as a function of temperature completes the set. The system consists of coupled, non-steady, non-linear, secondary, three-dimensional partial differential equations. The equations are presented by Sengupta et al(ref.5). Turbulence is modelled by eddy transport coefficients.

The rigid-lid assumption is made, thereby eliminating surface gravity waves and therefore the restrictive Courant-Levy Fredrichs' condition. This assumption has been used extensively in oceanic modelling by Bryan (ref.12) and others. Sengupta and Lick (ref.13) developed this idea for ecosystem modelling. However, where surface height fluctuations are dominant, a free-surface model has to be used. Therefore two sets of models, namely, rigid lid and free surface, have been developed by the University of Miami group to study thermal pollution.

The details of the rigid-lid model have been presented by Sengupta and Lick (ref.13) and Lee et al (ref. 9). The governing equations are continuity, two horizontal momentum equations, the hydrostatic equation, the energy equation and the equation of state. A predictive equation for surface or lid pressure (no longer atmospheric) derived from the vertically integrated momentum equations completes the system of equations. The boundary conditions are no-slip and no-normal velocity at solid surfaces. At the air-water interface wind stress and heat transfer coefficients are specified. The solid surfaces are considered adiabatic. Influx conditions for velocity and temperature are specified at open boundaries. Explicit schemes are used to integrate the momentum and energy equations. Iterative schemes are used to calculate the surface pressure from the predictive equation for pressure. Forward time, central space schemes are used for the diffusion terms which use the Du Fort-Frankel scheme. Single-sided schemes are used at the boundaries. A vertical normalization with respect to local depth is used to map a variable depth domain to constant depth.

The free-surface model uses essentially the same set of equations as the rigid lid except that height is now a variable. Therefore an equation for surface height is obtained from the vertically integrated continuity equation. The pressure at the surface is atmospheric. The boundary conditions at the air-water interface are obtained from wind stress and surface heat transfer coefficient. At solid walls slip conditions are used except for the bottom. All solid walls are assumed adiabatic. An open boundary, temperature and either height or velocities are specified. Explicit schemes with central diffuse in time and space are used.

Both the rigid-lid and free-surface models are applied to far-field and near-field situations. The near field is that region affected by thermal discharges. The far field affects the near field and not vice versa. Specifically, in Biscayne Bay the whole bay is considered far field whereas the near field is those regions where significant thermal anomalies are caused by discharges. Thus we have four sub-models (1) free-surface far field, (2) free-surface near field, (3) rigid-lid far field, and (4) rigid-lid near field.

DATA REQUIREMENTS

Table I shows the data requirements for the models for initialization, specification of boundary conditions, calibration and verification. It is necessary to specify values of all dependent variables throughout the three-dimensional domain as initial conditions. Remote sensing can at present provide sur-

face temperatures throughout the domain but vertical profiles have to be obtained by in-situ measurements, which are usually sparce and non-synoptic. Therefore compromises in specification of initial conditions have to be made. One of the common assumptions is to start with isothermal domain and zero velocity field. Where data is available, interpolation schemes are used to approximate conditions in the domain using available measurements. Boundary conditions on closed boundaries are easier to specify since they can be derived from strict requirements of no-slip and no-normal velocity. Adiabatic conditions are commonly used. Boundary conditions on open boundaries are considerably more difficult to prescribe. For the free-surface model, values or gradients of any three velocity components and surface heights are required. Surface height variations may be obtained for tide gauge stations. For the rigid-lid model at open boundaries all velocities and temperatures have to be specified. For open boundaries which separate near field from far field the boundary conditions are specified from far-field calculations in conjunction with remote sensing and interpolated in-situ measurements. The surface conditions for both models consist of surface wind stresses and heat transfer coefficients. For calibration and verification the requirements are similar to those for specification of initial conditions. At discharge locations the values of all dependent variables have to be specified at all times, except for surface height which can be calculated subsequently from the velocity field. The eddy transport coefficients have to be specified; they are not isotropic. These are obtained either from empirical relations or by trial and error during the calibration process.

DATA GATHERING PROCEDURE

The thermal IR data used for the study is received at Wallops Island, Virginia, from the NOAA-2 and NOAA-3 satellites and is processed at the National Environmental Satellite Services (NESS) facility in Suitland, Maryland. Data for the Florida area are available on southbound passes at approximately 0945 EDT (1345 Z) and on northbound passes at 2100 EDT (0100 Z)(ref.14).

The NASA-6 system is a Daedalus scanner which uses the 8-14 micron window for water surface temperature measurement. It's field of view is 2-5 milliradians and it scans through 77° 20' degrees of arc normal to flight path. It has an 10°C useable dynamic range and for this study is calibrated to measure temperatures from 24°C to 34°C. The analog readout is recorded on magnetic tape aboard the aircraft. Data is later transferred to 70 mm film at Kennedy Space Center. A calibration of the film gray scale density in terms of temperature is provided.

The major functions for in-situ measurements are to provide (1) ground truth for evaluation of remotely sensed measurements, (2) boundary conditions and verification of the mathematical model, particularly vertical profiles, and (3) assistance in the development of new techniques for remote sensing.

The most significant measurements are those of current magnitude and direction, horizontal and vertical temperature profiles, surface temperatures using infrared detectors and salinity. Current is measured by an impeller type instrument, the Endeco 110. It has been modified to measure low flows. Direct contact temperatures are measured using thermistors accurate to within $0.2^{o}C$. Salinity is measured using an induction type meter.

CALIBRATION AND VERIFICATION

The calibration and verification procedure for the rigid-lid model far-field application will be discussed here. The application site was Biscayne Bay in South Florida. This is a shallow bay open on the northeast side to the Atlantic Ocean. At the north end a causeway effectively isolates the bay; at the south end a series of banks enclose the bay. Figure 2 shows a map of Biscayne Bay. At the middle is the Featherbed Banks which is a shallow region. There are a number of creeks in the south bay open to the ocean.

The procedure for obtaining an adequate data base was to use thermal scanner flights on a north-south route. Figure 2 shows the flight lines. The coverage is not exactly synoptic since the time lapse between the eastern most flight and the western most flight is around 3 hours. The IR data was corrected using ground truth data from boats. The resulting data was then interpolated to draw surface isotherms for the whole bay. The boat measurements also provided vertical profiles.

Many different meteorological conditions were modelled. The details are presented by Lee et al (ref. 9). The conclusions indicated that tidal flows dominate wind driven effects. The tide flows primarily into and out of the south bay. The creeks only play a localized role. The velocities are small over the Featherbed Banks. They are high in the deeper regions adjacent to these banks. The temperature distribution is predominantly determined by bottom topography. Vertical diffusion is the dominant heat transfer mechanism.

After values for eddy viscosities and heat transfer coefficients were calibrated, the model was ready for verification. The vertical eddy diffusion coefficient was 5 cm^{2}/sec. The

surface heat transfer coefficient was 176 W/m^2-^oC (750 BTU/day-^oF-ft^2). The tide was taken as incoming at 10 cm/sec and the wind was from the southeast at 4.8 m/sec (10 MPH). On April 15, 1975 a field experiment was made. NASA-6 IR data was used to draw surface isotherms. The model was run for 6 hours with an isothermal initial temperature of 24.5^oC at 8 A.M. Figure 3 shows a comparison between the surface isotherms from model prediction and IR data. The model not only accurately predicts the qualitative nature of the temperature field, but the actual difference is within 1^oC throughout the bay. This is remarkable considering that the IR data is not truly synoptic. The comparison of vertical temperature profiles obtained from in-situ measurements and model agreed to within 1^oC (ref. 11).

CONCLUDING REMARKS

It is imperative that model development be integrated with adequate data acquisition effort. Remote sensing is the only way to obtain required data bases, for most complex models. Satellite data is not directly useable at present for mesoscale studies. However, airborne radiometer data is invaluable. It has been demonstrated that even with incomplete data bases a three-dimensional model has been calibrated and verified to give results within 1^oC accuracy for Biscayne Bay in South Florida.

REFERENCES

1. Policastro, A.J. and Tokar, J.W.: Heated-Effluent Dispersion in Large Lakes. State of the Art of Analytical Modelling. Part I Critique of Model Formulations. Report No. ANL/ES-11, Argonne National Laboratory, Argonne, Illinois, 1972.

2. Policastro, A.J.: Heated Effluent Dispersion in Large Lakes. State-of-the Art of Analytical Modelling, Surface and Submerged Discharges. Presented at the Topical Conference, Water Quality Considerations. Siting and Operating of Nuclear Power Plants, Atomic Industrial Forum, Inc., 1-4 October 1972.

3. Policastro, A.J. and Paddock, R.A.: Analytical Modeling of Heated Surface Discharges with Comparisons to Experimental Data. Interim Report No. 1. Presented at the 1972 Annual Meeting of the A.I.Ch.E., 26-30 November 1972.

4. Lee, S.S., Veziroglu, T.N., Sengupta, S., and Weinberg,N.: Remote Sensing Applied to Thermal Pollution. Proceedings of the Symposium on Remote Sensing Applied to Energy-Related Problems, 1974.

5. Sengupta, S., Lee, S.S., and Veziroglu, T.N.: Application of Remote Sensing to Numerical Modelling, Proceedings of the Symposium on Remote Sensing Applied to Energy-Related Problems, 1974.

6. Madding, R.P., Tokar, J.V. and Marmer, G.J.: A Comparison of Aerial Infra-red and In-Situ Thermal Plume Measurement Techniques, Environmental Effects of Cooling Systems at Nuclear Power Plants, International Atomic Energy Agency, Vienna, 1975.

7. Dinelli, G., Parrini, F.,Hodder, D.T.: Use of Thermal Infra-red Scanning in Evaluating Predictive Models for Power-plant Thermal Plume Mixing in Italian Coastal Waters. Proc. No. 17 Remote Sensing and Water Resources Management, American Water Resources Association, 1973.

8. Lee,S.S., Veziroglu, T.N., Sengupta, S., Hiser, H.W., and Weinberg, N.: Application of Remote Sensing for Prediction and Determination of Thermal Pollution, NASA-CR-139182, 1974.

9. Lee, S.S., Veziroglu, T.N., Hiser, H.W., Weinberg, N. and Sengupta, S.: The Application of Remote Sensing to Detecting Thermal Pollution, Final Report NASA CR-139188, 1976.

10. Hiser, H.W., Lee, S.S., Veziroglu, T.N., and Sengupta, S.: Application of Remote Sensing to Thermal Pollution Analysis, Presented at the Fourth Annual Remote Sensing of Earth Resources Conference, University of Tennessee Space Institute, Tullahoma, Tennessee, 1975.

11. Sengupta, S., Lee, S.S., and Bland, R.: Three Dimensional Model Development for Thermal Pollution Studies, presented and published in proceedings at the EPA Conference on Modelling, Cincinnati, 1976.

12. Bryan, K.: A Numerical Method for the Study of the World Ocean. J. Comp. Phys. 4, 1969.

13. Sengupta, S. and Lick, W.: A Numerical Model for Wind-Driven Circulation and Heat Transfer in Lakes and Ponds. FTAS/TR-74-98. Case Western Reserve University, 1974.

14. Schwalt, A.: Modified Version of the Improved TIROS Operational Satellite (ITOS D-G), NOAA Technical Memorandum NESS 35, U.S. Department of Commerce, Washington, D.C., April 1972.

TABLE I

DATA REQUIREMENTS

	Initial Conditions	Boundary Conditions		Surface Conditions	Calibration and Verification
		(Open)	(Closed)		
Free-Surface Model	All velocity components Surface pressure Surface heights Temperature	Specify conditions on any three of the velocity components and surface height. Surface pressure, temperature density		Wind stress Heat transfer coefficient Atmospheric pressure	Three-dimensional fields for velocities and temperature, Surface heights at some selected locations.
Rigid-Lid Model	All velocity components Surface pressure Temperature, Density	Specify conditions on velocities, temperature density		Wind stress Heat transfer coefficient No vertical velocities	Three-dimensional fields for velocities and temperature

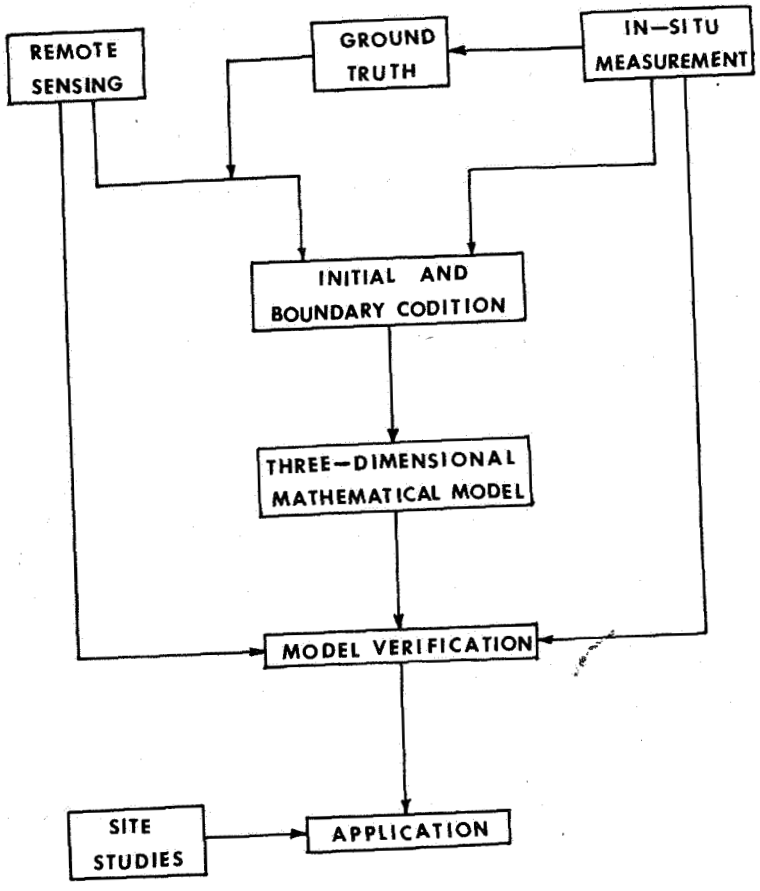

Figure 1.- Relations between various phases of the study.

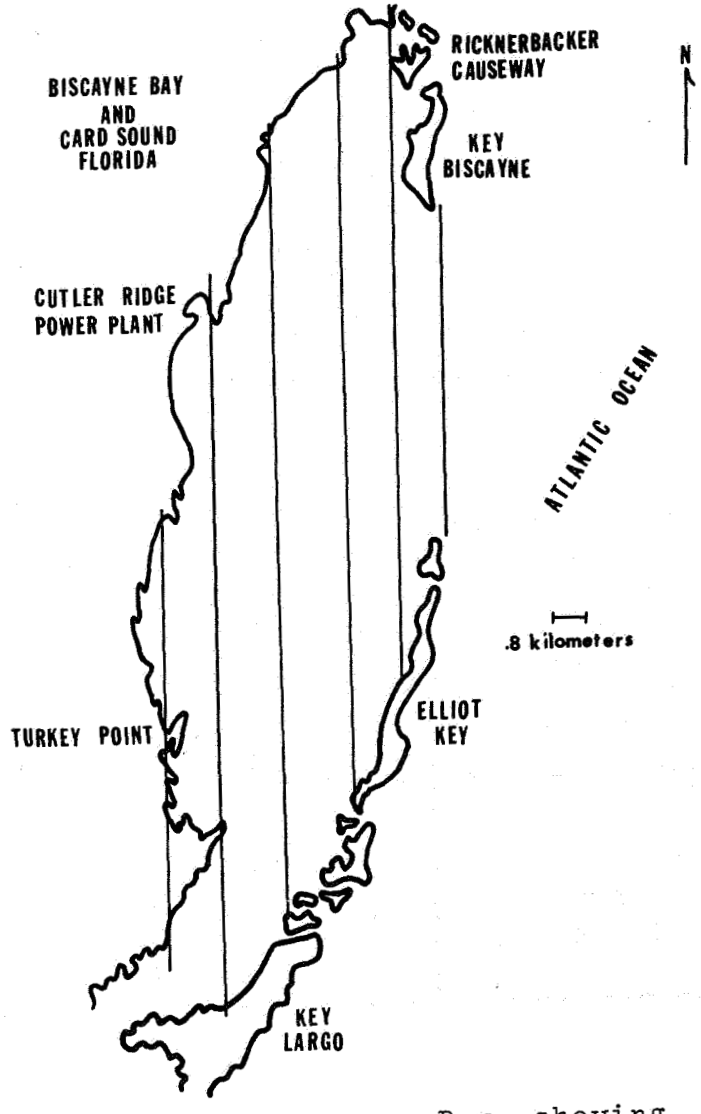

Figure 2.- Biscayne Bay, showing NASA-6 flight lines.

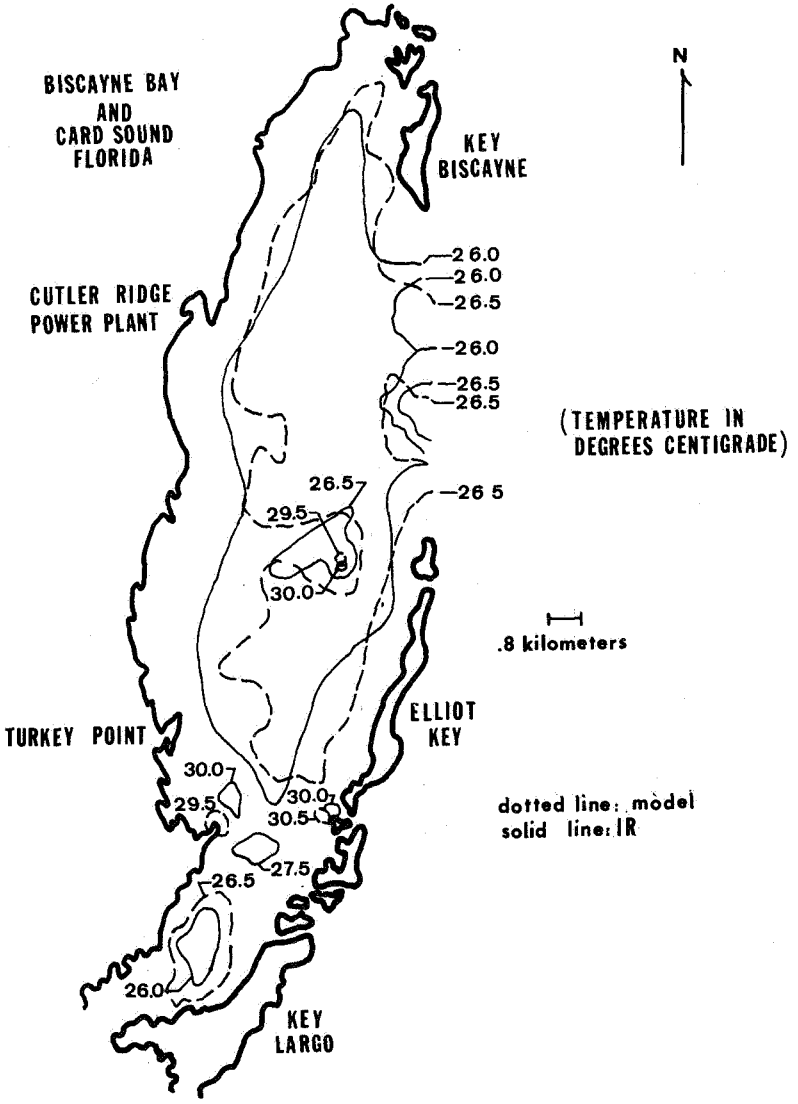

Figure 3.- Comparison of IR data with predicted results (4/15/75).

ON THE ABSORPTION OF SOLAR RADIATION IN A LAYER OF OIL BENEATH A LAYER OF SNOW

Jack C. Larsen and Bruce R. Barkstrom
Joint Institute for Advancement of Flight Sciences
The George Washington University

SUMMARY

Calculation of solar energy deposition in oil layers covered by snow is performed for three model snow types, using radiative transfer theory. It is suggested that excess absorbed energy is unlikely to escape, so that some melting is likely to occur for snow depths less than about 4 cm.

INTRODUCTION

The increase in Arctic oil exploration has raised concern about the effect of a large oil spill on Arctic sea ice or tundra. Weir (ref. 1) has shown that when oil covers Arctic sea ice, it will absorb sufficient sunlight during the Arctic summer day that the ice may be destroyed within one or two years, leaving open ocean. A large oil spill on tundra also will reduce the albedo of the surface and increase the absorbed energy, perhaps to the point that the permafrost would melt. Although the amount of absorbed energy is easily measured or calculated when the oil lies atop the surface, such a calculation becomes much more difficult and uncertain when the oil is covered by a layer of snow. Because snowstorms may deposit snow on spilled oil and because spilled oil may spread under an existing snow pack, such absorption is of more than academic interest. This paper provides some calculations of the amount of visual radiation that is absorbed by oil and overlying snow for three different types of snow.

SYMBOLS

$a(\mu_o)$	albedo of a surface under collimated light incident at a zenith distance θ_o = arc cos (μ_o)	
D	mean snow grain diameter	cm
κ	absorption coefficient for snow (eq. (1))	cm^{-1}
κ_i	absorption coefficient for ice	cm^{-1}

μ_o	cosine of solar zenith distance	
ρ_s	snow density	g cm^{-3}
ρ_i	solid ice density	g cm^{-3}
σ	scattering coefficient for snow	cm^{-1}

OPTICAL PROPERTIES OF SNOW AND OIL

Solutions to the radiative transfer equation in snow have been shown to give reasonable agreement with a number of features of reflection of sunlight from snow layers (ref. 2 and 3). Use of this equation requires specification of absorption and scattering coefficients κ and σ, as well as the phase function p. According to a preliminary theory developed by Bohren and Barkstrom (ref. 4), κ and σ are related to the mean grain diameter D, and the specific density of snow ρ_s/ρ_i, according to

$$\kappa = 1.26\kappa_i(\rho_s/\rho_i) \tag{1}$$

and

$$\sigma = 1.5D^{-1}(\rho_s/\rho_i) \tag{2}$$

Three kinds of snow have been modeled here. The first is "new-fallen powder", for which we assume a grain diameter of 0.01 cm and a specific density of 0.2. The second is "clean, Antarctic snow", whose grain diameter is 0.03 cm and whose specific density is 0.43, corresponding to the measurements of Liljequist (ref. 5). The third is "old, weathered snow" with $D = 0.1$ cm and $\rho_s/\rho_i = 0.5$. To convert these properties to absorption and scattering coefficients, we need the absorption coefficient for pure ice. The values we have adopted are given in table 1.

The phase function for snow appears to be considerably more uncertain. Barkstrom and Querfeld (ref. 3) have given a phase function based on matching the bidirectional reflectance measured by Middleton and Mungall (ref. 6). The mean cosine of single scattering for this phase function is about 0.51. Bohren and Barkstrom (ref. 4), on the other hand, have suggested that geometrical optics could be used to calculate the phase function because the grains are so large. When geometrical optics is used to calculate the phase function for spheres of ice, the mean cosine is considerably larger, about 0.84. In this paper, we have adopted the phase function given in Barkstrom and Querfeld because it seems to give better agreement with observations of snow albedos.

The absorption coefficient for oil is much greater than 5 cm^{-1} (ref. 7) in the visual, so that none of the energy reaching an oil layer thicker than a few mm will be transmitted through it. This allows us to treat the oil

layer as a layer that absorbs all of the energy it does not reflect. Because oil's index of refraction is different than air, ice or water, it does reflect light. The dependence of oil albedo upon angle of solar incidence is given by Weir (ref. 1) for a layer of oil on ice. Approximating this dependence by a linear relation in μ_o, we find that the hemispherical albedo of an oil layer

$$a = 2\int_0^1 d\mu_o \mu_o a(\mu_o) \tag{3}$$

is 0.1197. In this expression, $a(\mu_o)$ is the albedo of the oil for a solar zenith angle $\theta_o = \arccos(\mu_o)$. This albedo has been used in the computations reported below as the albedo of a Lambert reflector at the base of the snow layer.

RESULTS OF NUMERICAL SIMULATION OF RADIATIVE TRANSFER IN SNOW

The radiation field within and emerging from a layer of snow was calculated using the finite difference method described in reference 8. The transfer problem in snow is linear with respect to incident radiation, so that energy balances under any conditions of incidence may be found by suitably weighing the solutions for a given wavelength and angle of incidence by the amount of flux incident and adding the weighted properties. Collimated radiation at five wavelengths between 0.45 μm and 0.65 μm was incident at the four μ_o values 0.0694, 0.33, 0.67 and 0.031. To compute the changes in energy balance of a snow surface due to the addition of an oil layer, we may begin by computing the difference in hemispherical albedo between a deep snow layer and a thinner layer with oil underneath. If this albedo difference is then multiplied by the flux incident on the snow, we have the power per unit area which is to be absorbed either in the snow or in the underlying oil. Finally, the power deposited in the oil is the product of the excess power put into the upper surface of the snow and the transmission through the snow.

The calculated frequency integrated albedos are listed in table 2 for new, Antarctic, and old snow as functions of layer depth and μ_o. The values are summarized in figure 1 which shows the hemispherical albedo (eq. (3)) as a function of depth for various kinds of snow. The hemispherical albedos are nearly independent of wavelength. The calculated values are markedly higher than those given by Liljequist (ref. 5) and Rusin (ref. 9) for Antarctic snow, which have hemispherical albedos between 0.75 and 0.80, and they are somewhat higher than those observed by Grenfell, who has hemispherical albedos near 0.97. We have been unable to lower the hemispherical albedos to the Antarctic values except by introducing an additional absorber with an absorption coefficient amounting to about 0.3 cm^{-1}. This would be consistent with 10^9 completely absorbing particles of radius 0.1 μm in each cubic cm of snow. The mass mixing ratio for such a substance would be about 10^{-4} kg per kg of snow, which is probably undetectable except by microscopic examination.

In the calculations the fraction of incident net flux that is transmitted through a snow slab depends only upon the snow properties and the physical depth of the slab. It is independent of angle of incidence. Figure 2 shows the transmission of net flux through a snow slab as a function of depth for various types of snow. The predicted $\rho_s/\sqrt{D}$ dependence suggested by Bohren and Barkstrom (ref. 4) is followed. The effect of increasing the absorption coefficient as seems to be needed to match the Antarctic data will be to increase the extinction coefficient and decrease the transmission. Thus, the transmission values given in figure 2 may be somewhat high.

ENERGY ABSORBED BY THE OIL

Because we have no way of knowing when an oil spill will occur, we cannot calculate the history of the energy balance and predict how soon the snow will melt. However, we can examine the amount of solar energy deposited in the layer of oil at various depths to determine whether so much will be absorbed that melting is nearly certain or so little will be absorbed that melting is unlikely. Accordingly, we have calculated the excess energy deposited in the oil as a function of time of year for each of the three kinds of snow. When snow overlying an oil layer is compared with deep snow in a surrounding region, we can see from figure 1 that the albedo of the oil covering snow is decreased. Because the decrease is small compared with the surrounding medium, the incoming shortwave flux is not greatly affected. As a result, the oil covering snow receives an excess flux given by

$$\begin{aligned} \Delta F &\simeq F_o(1-a_{\text{oil covering}}) - F_o(1-a_{\text{surrounding}}) = \\ &= F_o(a_{\text{surrounding}} - a_{\text{oil covering}}) \end{aligned} \tag{4}$$

where F_o is the shortwave flux in unperturbed conditions. Of this excess flux a fraction T, given in figure 2, is transmitted through to the oil. The excess flux absorbed by the oil is

$$\Delta F_{\text{oil}} = T(a_{\text{surrounding}} - a_{\text{oil covering}})F_o \tag{5}$$

We have taken the shortwave fluxes quoted in Weir from Fletcher (ref. 10) and used these to calculate the excess energy deposited in the oil. The energy deposited in the oil during a given month is listed in table 3 together with the equivalent number of grams of ice per cm^2 that would be melted by this amount of energy.

The precise fate of the absorbed energy is uncertain because there are a number of pathways by which it might escape such as conduction or latent heat loss. However, we expect that the energy exchange at the surface of the snow

is not appreciably altered by the underlying oil, and that conduction into underlying ice is insufficient to remove large quantities of heat. As a result, the excess energy deposited in the oil is likely to cause a temperature rise to 0°C followed by melting. It is clear from table III that oil layers deeper than 8 cm are unlikely to be affected by absorbed solar energy. However, if an oil spill were to occur during April or May, or if oil were on the surface in August or September, it appears likely that any new snow with a depth less than three to four cm would not survive. As a result, a large oil spill opens the possibility of not only melting the Arctic ice but of shortening the time required to do so by lengthening the summer season.

REFERENCES

1. Weir, C. R.: Oil Contamination in the Arctic and Its Relation to the Heat Budget. M.S. Thesis, Dept. of Oceanography, Fla. State University, June 1975.

2. Barkstrom, B. R.: Some Effects of Multiple Scattering on the Distribution of Solar Radiation in Snow and Ice. J. Glaciology, Vol. 11, No. 63, 1972, pp. 357-368.

3. Barkstrom, B. R.; and Querfeld, C. W.: Concerning the Effect of Anisotropic Scattering and Finite Depth on the Distribution of Solar Radiation in Snow. J. Glaciology, Vol. 14, No. 70, 1975, pp. 107-124.

4. Bohren, C. F.; and Barkstrom, B. R.: Theory of the Optical Properties of Snow. J. Geophys. Res., Vol. 79, No. 30, Oct. 20, 1974, pp. 4527-4535.

5. Liljequist, G. H.: Energy Exchange of An Antarctic Snow-field. Shortwave Radiation (Maudhein 71° 03'S, 10° 56'W). Norwegian-British-Swedish Antarctic Expedition, 1949-52. Scientific Results, Vol. 2, Pt. 1A, 1956.

6. Middleton, W. E. K.; and Mungall, A. G.: The Luminous Directional Reflectance of Snow. J. Opt. Soc. Amer., Vol. 42, No. 8, 1952, pp. 572-579.

7. Klemas, V.: Detecting Oil On Water: A Comparison of Known Techniques. AIAA Paper No. 71-1068 from Proc. of a Joint Conf. on Sensing Env. Pollut., Palo Alto, Nov. 8-10, 1971.

8. Barkstrom, B. R.: A Finite Difference Method of Solving Anisotropic Scattering Problems. J. Quant. Spect. and Rad. Transf., in press, 1976.

9. Rusin, N. P.: Meteorological and Radiational Regime of Antarctica. Translated from the Russian by the Israel Program for Scientific Translation. Wash. D.C., U.S. Dept. of Commerce, 1964.

10. Fletcher, J. O.: Energy Fluxes in the Central Arctic. From Maykut, G. A. and Untersteiner, N.: Numerical Prediction of the Thermodynamic Response of Arctic Sea Ice to Environmental Changes, Report RM-6093-PR, The Rand Corporation, Santa Monica, California, November 1969, p. 27.

TABLE I. - ABSORPTION COEFFICIENT FOR ICE

Wavelength	κ_i
μm	cm^{-1}
.45	.000774
.50	.001032
.55	.001472
.60	.002299
.65	.004068

TABLE II. - WAVELENGTH INTEGRATED ALBEDOS UNDER COLLIMATED LIGHT FOR SNOW SLABS OF VARIOUS THICKNESSES

Slab Depth	Wavelength Integrated Albedo			
cm	μ_o=.069	.33	.67	.931
	New-Fallen Snow			
1	.9600	.9405	.9168	.8988
2	.9785	.9681	.9558	.9466
4	.9881	.9823	.9755	.9705
8	.9924	.9887	.9844	.9812
16	.9938	.9907	.9872	.9846
32	.9940	.9911	.9877	.9852
	Antarctic Snow			
1	.9461	.9196	.8870	.8630
2	.9702	.9556	.9385	.9253
4	.9827	.9743	.9645	.9573
8	.9886	.9822	.9754	.9704
16	.9894	.9843	.9784	.9740
32	.9897	.9847	.9789	.9746
	Old Snow			
1	.8766	.8138	.7423	.6905
2	.9261	.8895	.8451	.8133
4	.9573	.9365	.9115	.8925
8	.9735	.9606	.9457	.9346
16	.9797	.9699	.9585	.9502
32	.9811	.9720	.9614	.9537

TABLE III. - EXCESS ENERGY DEPOSITED IN OIL BENEATH LAYERS OF SNOW IN THE CENTRAL ARCTIC

Layer Depth	Excess Energy Deposited, in 10^6 J m^{-2} (Melted Water Equivalent, gH_2O cm^{-2})							
cm	March	April	May	June	July	August	September	October
New-Fallen Snow								
1	.56(1.7)	2.90 (8.7)	5.18(15.5)	5.62(16.8)	3.18(11.9)	2.63 (7.9)	1.08 (3.2)	.12 (.3)
2	.24 (.7)	1.26 (3.8)	2.26 (6.8)	2.45 (7.3)	1.74 (5.2)	1.02 (3.4)	.47 (1.4)	.05 (.2)
4	.08 (.2)	.43 (1.3)	.76 (2.3)	.83 (2.5)	.59 (1.8)	.39 (1.2)	.16 (.5)	.02 (.1)
8	.02 (.1)	.08 (.2)	.14 (.4)	.15 (.5)	.11 (.3)	.07 (.2)	.03 (.1)	.00 (.0)
Antarctic Snow								
1	.71(2.1)	3.71(11.1)	6.64(19.8)	7.20(21.5)	5.10(15.2)	3.37(10.1)	1.39 (4.1)	.15 (.4)
2	.30 (.9)	1.56 (4.7)	2.79 (8.3)	3.03 (9.0)	2.15 (6.4)	1.42 (4.2)	.58 (1.7)	.06 (.2)
4	.09 (.3)	.46 (1.4)	.83 (2.5)	.90 (2.7)	.64 (1.9)	.42 (1.3)	.17 (.5)	.02 (.1)
8	.01 (.0)	.07 (.2)	.12 (.4)	.13 (.4)	.09 (.3)	.06 (.2)	.02 (.1)	.00 (.0)
Old Snow								
1	1.71(5.1)	8.92(26.7)	13.31(47.7)	17.30(51.7)	12.26(36.6)	8.11(24.2)	3.33(10.0)	.36(1.1)
2	.89(2.7)	4.63(13.8)	8.27(24.7)	8.97(26.8)	6.36(19.0)	4.21(12.6)	1.73 (5.2)	.19 (.6)
4	.35(1.1)	1.85 (5.5)	3.30 (9.9)	3.58(10.7)	2.54 (7.6)	1.68 (5.0)	.69 (2.1)	.07 (.2)
8	.08 (.3)	.44 (1.3)	.79 (2.4)	.86 (2.6)	.61 (1.8)	.40 (1.2)	.17 (.5)	.02 (.1)

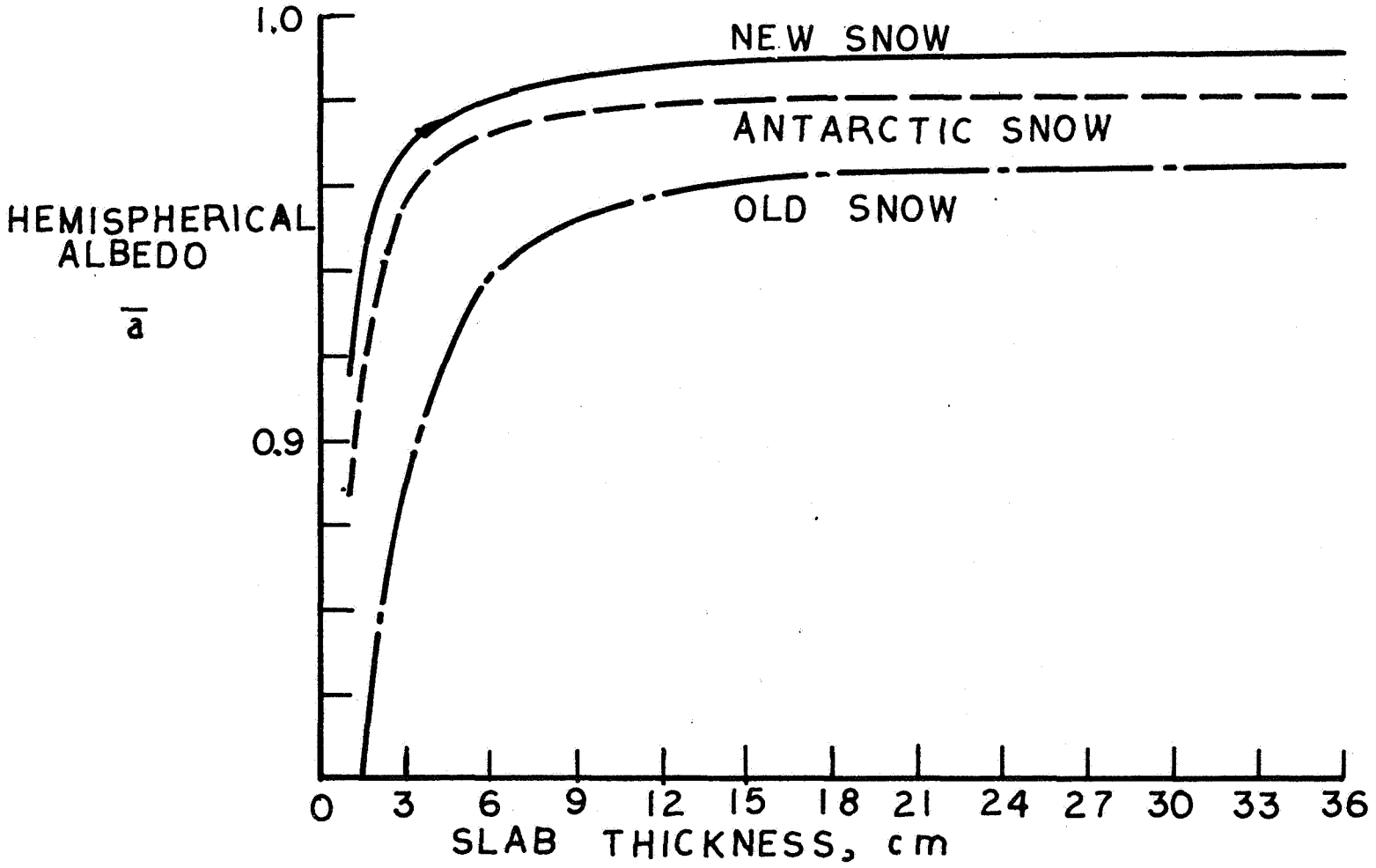

Figure 1.- Hemispherical albedo of snow slabs.

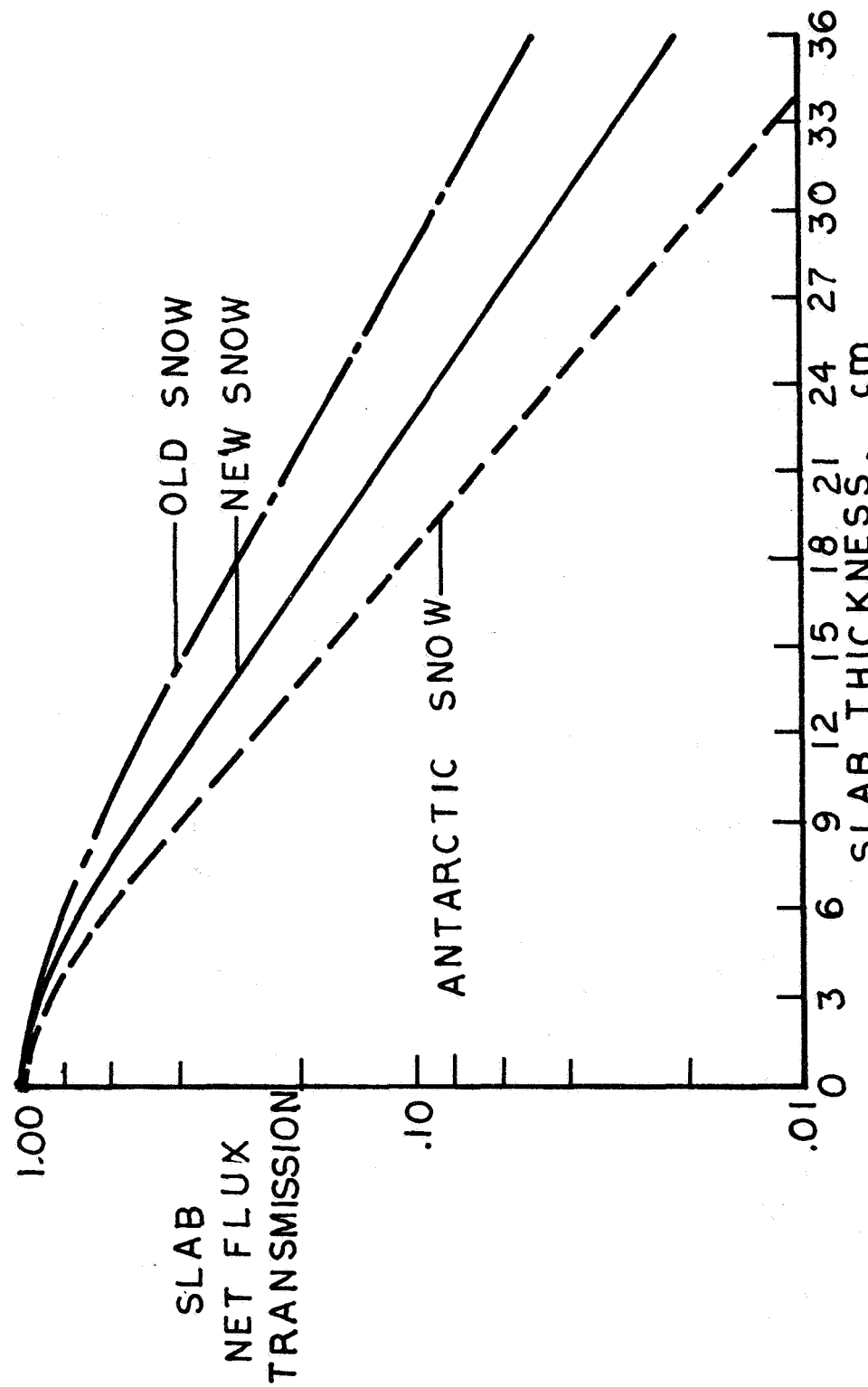

Figure 2.- Snow slab net flux transmission.

THE INFLUENCE OF THE DIABATIC HEATING IN THE TROPOSPHERE ON THE STRATOSPHERE

Richard E. Turner, Kenneth V. Haggard,
and Tsing Chang Chen

NASA Langley Research Center

SUMMARY

In order to simulate the seasonal variation of the stratospheric circulation in a zonal mean circulation model, a Newtonian heating function and a detailed heating function are applied to the troposphere and stratosphere, respectively. The purpose of this study is to investigate the response of stratospheric circulation to alterations of the radiative equilibrium temperature of the troposphere.

INTRODUCTION

A time-dependent, zonal, mean circulation model of the atmosphere was developed at the Langley Research Center to study the mutual interactions of dynamics, radiation, and photochemistry in the stratosphere, and the possible impact of stratospheric circulation on the Earth's climate.

It was found (Charney and Drazin, ref. 1, and Dickinson, refs. 2 and 3), that the circulation of the lower stratosphere is mainly driven by the upward propagation of energy from the troposphere. The purpose of this study is to investigate to what extent the stratospheric circulation is affected by tropospheric circulation in a zonal mean circulation model.

The study is performed by imposing a specified increment on the horizontal gradient of the radiative equilibrium temperature in the troposphere. The resulting change in the stratospheric circulation would indicate how alterations of physical variables in the troposphere propagage into the stratosphere.

SYMBOLS*

A_E	eddy available potential energy
A_Z	zonal available potential energy
$C(A_E,A_Z)$	conversion rate of A_E to A_Z
$C(K_Z,A_Z)$	conversion rate of K_Z to A_Z

*cgs units are used throughout unless specifically denoted otherwise.

$C(K_E,K_Z)$ conversion rate of K_E to K_Z

K_E eddy kinetic energy

K_Z zonal kinetic energy

P pressure

Q diabatic heating

T temperature

$T(A_Z)$ transformation of A_Z by transport

$T(K_Z)$ transformation of K_Z by transport

V northerly velocity

W vertical velocity

Operators:

$\bar{(\ )}$ zonal average of ( )

$(\ )'$ departure of ( ) from $\bar{(\ )}$, $(\ )' = (\ ) - \bar{(\ )}$

$[(\ )]$ vertical average of ( )

$\langle(\ )\rangle$ latitudinal average of ( )

ϕ latitude

DESCRIPTION OF MODEL

The model is developed in primitive equations on a pressure-latitude coordinate system (MacCracken, ref. 4). The prognostic variables are distributed on a 10° grid with zonal velocity and meridional velocity defined at the poles and at 10° intervals pole to pole. Temperature and specific humidity are defined at grid points 5° from the poles and at 10° intervals. Vertical velocity is staggered in the vertical direction between the prognostic variables on 19 pressure levels of approximately equal altitude increments, from 1000 mb to 0.1 mb.

The eddy transport of potential temperature and specific humidity is treated in the manner of Stone (ref. 5) in the troposphere and in the manner of Reed and German (ref. 6) in the stratosphere. For pressure levels above 30 mb, where Reed and German (ref. 6) data are not given, the 30-mb data are used. The eddy

transport of angular momentum is specified from observed data following Harwood and Pyle (ref. 7).

The flux of thermal energy, water vapor, and angular momentum into the atmosphere through the lower boundary is treated following MacCracken (ref. 4).

The governing equations of motion are approximated by second-order finite differences and integrated temporally by the leap frog technique.

The tropospheric heating function is a simple Newtonian type that is particularly well suited for simulating variations in heating rates that result from variations in radiative equilibrium temperatures. The stratospheric heating function is a detailed heating function developed by Ramanathan (ref. 8). It incorporates a detailed treatment of the solar heating and infrared cooling from CO_2, water vapor, and O_3.

NUMERICAL EXPERIMENTS

Two numerical experiments were performed. The first experiment, Run A, used radiative equilibrium temperatures in the tropospheric heating function compiled by Trenberth (ref. 9). The second numerical experiment, Run B, used radiative equilibrium temperatures obtained by adding a latitudinally dependent temperature increment (5 K at the Equator and multiplied by the cosine of the latitude) to Trenberth's (ref. 9) radiative equilibrium temperature. This particular variation was chosen for two reasons: First, the generally higher radiation equilibrium temperature in the troposphere would increase the tropospheric temperature; second, the additional latitudinal temperature gradient in the midlatitudes would create additional dynamic motions in the troposphere to drive the stratosphere. The comparison of Runs A and B would then show how the stratosphere responds to altered thermal and dynamic states in the troposphere.

The initial conditions for the model temperatures were taken to be observed mean temperatures in the troposphere and radiative equilibrium temperatures in the stratosphere (Trenberth, ref. 9). The initial zonal winds were balanced geostrophically and the meridional flow was set to zero. Both experiments were begun at a heating condition corresponding to August 15 and run for 16 months, by which time near periodicity was established in the prognostic variables.

Although the model vertical structure extends to 0.1 mb, experience has shown that predicted flow fields in the top three layers are dependent on the top boundary conditions; furthermore, it has been found the flow fields are distorted near the poles by the large 10° grid spacing. Thus, comparisons are made only from 1000 mb to 1.5 mb pressure and through the midlatitudes and at a model time corresponding to December 15. The control run, Run A, was previously found to compare favorably (Turner et al., ref. 10) with the observed atmosphere, as compiled by Newell (ref. 11) and with the U.S. Standard Atmosphere (ref. 12), relative to the pressure-latitude distributions of temperature, zonal wind, and meridional flow lines. Herein, Run A is compared with Run B, relative to the pressure-latitude distributions of temperature, zonal wind, and

the meridional flow to demonstrate the response of the model stratosphere to alterations in the model troposphere. Also, the model stratosphere alterations are interpreted in terms of boundary conditions (at the tropopause) and internal reactions of the stratosphere.

RESULTS OF EXPERIMENTS AND DISCUSSION

In general, both runs have well-developed tropospheric circulation below 150 mb with the characteristic temperature decline from 1000 mb to the tropopause. The observed tropospheric temperature gradient from the tropics to the polar regions is also properly represented. The tropospheric temperature distributions from Run A and Run B, differ by an amount which is similar to the difference in the radiative equilibrium temperatures. The vertical lapse rates are approximately equal for both runs. The latitudinal temperature difference for Run B, is about 2 K larger than for Run A (less than half of the 5 K increment in the latitudinal gradient of the radiation equilibrium temperature).

The tropospheric zonal winds show two well-developed midlatitude jets. The maximum velocity of the Run B jet winds (about 30 m/sec) is about 1.5 m/sec higher than Run A, but the jet cores for both runs are located at identical positions.

The meridional flow from both runs is essentially identical, each having the characteristic six-cell structure observed in the real atmosphere.

The prime driving force in the altered model troposphere is the increased latitudinal gradient in the radiation equilibrium temperature distribution. The model troposphere responds directly to increased tropical radiation equilibrium temperatures by developing higher tropical temperatures to prevent larger tropical diabatic heating rates. The resulting stronger latitudinal temperature gradient causes stronger tropospheric jet winds by the thermal wind effect and increases the midlatitude eddy heat transport into the polar regions. Consequently, the increase in polar temperatures tends to decrease the latitudinal temperature gradient to stabilize the model troposphere. The increased eddy heat flux from the tropics must be balanced by a drop in tropical temperature to decrease the latitudinal temperature gradient further. The net result is that the model latitudinal temperature gradient for Run B is greater than for Run A but the increment is less than the latitudinal gradient of the increment in radiation equilibrium temperatures. The increase in tropospheric jet winds is directly attributed to the thermal wind effect. The weakness of zonal mean circulation models is evident in the weak response of the model meridional flow to the altered radiation equilibrium temperature field. Because of the dominance of the eddy transport of angular momentum and Coriolis acceleration in the zonal velocity equation, the prespecification of eddy transport of angular momentum is tantamount to the specification of the meridional flow. The model meridional transport of heat and angular momentum is essentially invariant between the two runs.

The model tropospheric response to the altered radiation equilibrium temperature causes a tropopause temperature increment of about 5 K in the tropics,

about 3-1/2 K in the midlatitudes, and about 2-1/2 K in the polar regions. The model tropopause zonal winds are strengthened through the thermal wind effect while the tropopause meridional velocity is nearly invariant due to the prespecification of eddy transport of angular momentum. These alterations in the tropopause conditions directly affect the stratosphere along the tropopause where the flow is from the troposphere into the stratosphere. A second source affecting the stratosphere is the diabatic heating term. The alteration in the tropospheric thermal state in turn causes an alteration in the radiative heat flux from the troposphere into the stratosphere and, consequently, alters the radiative equilibrium temperature in the stratosphere.

The alteration in the stratospheric temperature is similar to the alteration observed in the tropospheric temperature but diminishing with distance from the tropopause at 150 mb and nearly vanishing at 10 mb. The zonal wind alterations in the stratosphere penetrate the entire stratosphere with a slight enhancement from the increased latitudinal temperature gradient through the thermal wind effect. This enhancement is approximately twice as strong in the summer hemisphere (3 m/sec or 3 percent) as in the winter hemisphere (1.5 m/sec or 1.5 percent). The alteration in the meridional flow is small near the tropopause but increases to about 0.05 m/sec (or 10 percent) at the stratopause.

The relative roles of dynamics and radiation in maintaining the alterations in the stratospheric thermal state can be inferred by considering the prognostic equation for potential temperature which equates the total time derivative of potential temperature to the diabatic heating (which, in this case, arises solely from radiation). If the diabatic heating for the potential temperature alteration were zero, then the dynamic motions within the stratosphere would uniformly mix the alteration throughout the stratosphere. If radiation is dominant in sustaining the alteration, then there would be no differences that could be attributed to circulation. The summer stratosphere (having a generally rising air mass) has a 3 K potential temperature alteration at the tropopause and a 1 K alteration at 0.15 mb. The winter stratosphere (having a generally sinking air mass) has a 3 K potential temperature alteration at the tropopause, vanishing at the midstratosphere and going 3 K negative in the upper stratosphere. The deeper penetration of the potential temperature alteration into the rising air mass indicates a strong dependence on both heat advection and radiation to sustain the alteration. The stronger penetration of the tropopause zonal wind alteration into the summer stratosphere is consistent with the temperature alteration and the thermal wind effect. The alteration of the meridional flow in the stratosphere is interesting but should be viewed with suspicion because it is near the top boundary.

In summary, the perturbed radiative equilibrium temperature (in the troposphere) gives rise to a smaller alteration in the tropospheric thermal state with alterations in the zonal wind field which are consistent with the thermal wind effect. The tropospheric meridional flow remains essentially constant due to the prespecification of eddy transport of angular momentum. These alterations are carried into the stratosphere principally by thermal energy transport with energy advection and radiation having large influences. Alteration in the stratospheric temperature vanishes near the 10-mb level, with alterations in zonal wind penetrating the whole stratosphere consistent with the thermal wind effect. Alterations of the meridional wind increase in the upper stratosphere,

probably to balance mass transport in the troposphere. Surface and volume integrals of the model prognostic equations verify the apparent model interactions.

A net increase in heat transported through the midlatitudes by eddys of 10 percent (see table I) as opposed to a small increase in heat transported by meridional flow indicates that the eddy heat opposes an increase in latitudinal temperature gradient while the meridional flow remains essentially steady as was observed in the prognostic variables. The peak diabatic cooling and heating in the tropics and polar regions (see table I) is significantly strengthened. The vertically averaged prognostic equation for meridional velocity shows a close geostrophic balance that establishes the thermal wind effect in maintaining the zonal wind field alteration. The vertical integral of the zonal wind kinetic energy prognostic equation shows a general balance between the eddy advection of zonal wind and the Coriolis force; this verifies that the eddy transport of angula momentum controls the meridional flow. The horizontal integral along the tropopause of thermal energy transported out of the stratosphere by eddys and by meridional flow (see table I) shows a net reduction of about 1.5 percent. The horizontal integral of the diabatic heating (see table I) shows a 10-percent reduction near the tropopause to compensate for decreased cooling from thermal energy advection out of the stratosphere. Volume integrals of the available potential energy and kinetic energy prognostic equations (see table II) help to further determine the internal reaction of the model atmosphere to the altered tropospheric radiation balance.

The tropospheric zonal available potential energy is increased by about 20 percent in Run B over Run A, reflecting the increased latitudinal temperature gradient. The cause is attributed directly to a 20-percent increase in the generation term $G(A_Z)$. The increased generation of zonal available potential energy is primarily balanced by an increased conversion of zonal available potential energy to the eddy available potential energy; this infers a growth of tropospheri eddy activity consistent with the previously observed midlatitude heat transport into the polar regions. In the lower stratosphere, the zonal available potential energy is decreased by about 5 percent (probably due to the increased temperature transport through the tropopause in the tropics which acts to reduce temperature gradients in the stratosphere).

The tropospheric zonal kinetic energy is observed to increase by about 10 percent with energy from the zonal available potential energy acting as source and eddy kinetic energy acting as a sink. The joint increase of zonal available potential energy and zonal kinetic energy are mutually consistent and are consistent with the thermal wind effect. The stratospheric zonal kinetic energy is seen to decrease about 5 percent as is consistent with the observed decrease in the zonal available potential energy.

CONCLUDING REMARKS

In general, the model response to increased tropospheric radiation equilibrium temperature suggests that temperature alterations in the stratosphere decrease with distance from the tropopause, and that the zonal wind alterations

penetrate through the entire stratosphere. Unfortunately, the model prediction of meridional flow response is not thought to be reliable because of the prespecification of angular momentum transport.

It would seem proper (since zonal vorticity is generally transported up gradient) that the increased eddy activity in the tropopause would act to strengthen the tropospheric jet stream as well as the meridional circulation (because of the dominance of eddy transport of angular momentum and Coriolis force in the zonal wind prognostic equation). Stronger jet streams would in turn cause stronger latitudinal temperature gradients through the northerly geostrophic balance. The net effect would be a stronger penetration of zonal wind alteration into the stratosphere.

Based upon the work presented here, one must conclude that thermal alterations in the tropospheric thermal state penetrate into the stratosphere mildly, but zonal wind alteration penetrates the stratosphere completely. Meridional flow alterations have not been illuminated.

REFERENCES

1. Charney, J. G.; and Drazin, P. G.: Propagation of Planetary Scale Disturbances From the Lower Into the Upper Atmosphere. J. Geophys. Rev., 1961, Vol. 66, pp. 83-109.

2. Dickinson, R. E.: On the Exact and Approximate Linear Theory of Vertically Propagating Planetary Rossby Waves Forced at a Spherical Lower Boundary. Mon. Wea. Rev., 1968, No. 96, pp. 405-415.

3. Dickinson, R. E.: Planetary Rossby Waves Propagating Vertically Through Weak Westerly Wind Wave Guides. J. Atmos. Sci., 1968, No. 25, pp. 989-1002.

4. MacCracken, M. C.: A Zonal General Circulation Model. UCRL-50594, Lawrence Livermore Radiation Laboratory (1969).

5. Stone, P. H.: The Meridional Variation of Eddy Heat Fluxes by Baroclinic Waves and Their Parameterization. J. Atmos. Sci., Vol. 31, Sept. 1973, pp. 444-455.

6. Reed, R. J.; and German, K. E.: A Contribution to the Problem of Stratospheric Diffusion by Large-Scale Mixing. Mon. Wea. Rev., May 1965, pp. 312-321.

7. Harwood, R. S.; and Pyle, J. A.: A Two-Dimensional Mean Circulation Model for the Atmosphere Below 80 km. Quart. J. R. Met. Soc., May 1965, pp. 312-321.

8. Ramanathan, V.: Radiative Transfer Within the Earth's Troposphere and Stratosphere: A Simplified Radiative-Convective Model. J. Atmos. Sci., 33, 1976.

9. Trenberth, K.: Global Model of the Atmosphere Below 75 Kilometers With an Annual Heating Cycle. Mon. Wea. Rev., 1973, pp. 287-305.

10. Turner, R. E.; Haggard, K. V.; and Chen, T. C.: A Numerical Study of the Radiative-Dynamic Interaction in the Stratosphere by a Time-Dependent Zonal Mean Circulation Model. Joint DMB/AMS International Conference on Simulation of Large-Scale Atmospheric Processes, Hamburg, Germany, Aug. 30-Sept. 4, 1976.

11. Newell, R.: Radioactive Contamination of the Upper Atmosphere. Progress in Nuclear Energy. Series XII, Health Physics (1969), Vol. 2, A. M. Francis Duhamel, Ed., Pergamon Press, pp. 535-550.

12. U.S. Standard Atmosphere Supplement, 1966. U.S. Government Printing Office, Washington, D.C., 20402.

TABLE I. ELEMENTS OF THERMAL ENERGY TRANSPORT

	Run A	Run B
$[Q]_{\phi=0}$	0.475 K/day*	0.499 K/day*
$[Q]_{\phi=\pi/2}$	-.221 K/day*	-.318 K/day*
$[\overline{T'V'}]_{\phi=\pi/4}$	$+.704 \times 10^{3}$*	$+.802 \times 10^{3}$*
$[\bar{T}\ \bar{V}]_{\phi=\pi/4}$	$+.255 \times 10^{3}$*	$+.260 \times 10^{3}$*
$\langle\overline{T'\omega'}\rangle_{p=150\ mb}$	$.797 \times 10^{-1}$	$.780 \times 10^{-1}$
$\langle\bar{T}\ \bar{\omega}\rangle_{p=150\ mb}$	$.147 \times 10^{-1}$	$.138 \times 10^{-1}$
$\langle\bar{Q}\rangle_{p=125\ mb}$	$.770 \times 10^{-1}$ K/day	$.683 \times 10^{-1}$ K/day

*Stratosphere plus troposphere.

TABLE II. ENERGETIC DIAGNOSTIC VARIABLES

	Run A*	Run A**	Run B*	Run B**
A_Z	0.369×10^{10}	0.631×10^{8}	0.444×10^{10}	0.591×10^{8}
$C'(K_Z,A_Z)$	$-.862 \times 10^{2}$	$.526 \times 10^{2}$	$-.110 \times 10^{3}$	$.517 \times 10^{2}$
$C(A_E,A_Z)$	$-.263 \times 10^{4}$	$.505 \times 10^{2}$	$-.318 \times 10^{4}$	$-.502 \times 10^{2}$
$G(A_Z)$	$.287 \times 10^{4}$	$.413 \times 10^{1}$	$.344 \times 10^{4}$	$.414 \times 10^{1}$
$T(A_Z)$	$-.131 \times 10^{3}$	$-.562 \times 10^{1}$	$-.144 \times 10^{3}$	$-.568 \times 10^{1}$
K_Z	$.590 \times 10^{9}$	$.213 \times 10^{9}$	$.654 \times 10^{9}$	$.206 \times 10^{9}$
$C(K_Z,A_Z)$	$-.862 \times 10^{2}$	$.526 \times 10^{2}$	$-.110 \times 10^{3}$	$.517 \times 10^{2}$
$C(K_E,K_Z)$	$-.752 \times 10^{2}$	$.353 \times 10^{2}$	$-.101 \times 10^{3}$	$.335 \times 10^{2}$
$T(K_Z)$	$.331 \times 10^{0}$	$.262 \times 10^{2}$	$.373 \times 10^{0}$	$.257 \times 10^{2}$

*Troposphere.

**Stratosphere.

USE OF VARIATIONAL METHODS IN THE DETERMINATION OF WIND-DRIVEN OCEAN CIRCULATION

Roberto Gelós
Instituto Argentino de Oceanografia

Patricio A. A. Laura
Instituto de Mecánica Aplicada

SUMMARY

Simple polynomial approximations and a variational approach are used to predict wind-induced circulation in rectangular ocean basins. Stommel's and Munk's models are solved in a unified fashion by means of the proposed method. Very good agreement with exact solutions available in the literature is shown to exist. The method is then applied to more complex situations where an exact solution seems out of the question.

INTRODUCTION

Stommel (ref. 1) has performed an interesting study of the "wind-driven ocean circulation in a homogeneous rectangular ocean under the influence of surface wind stress, linearized bottom friction, horizontal pressure gradients caused by a variable surface height and Coriolis force." In the case of a flat rectangular ocean Stommel shows that his model is governed by the differential system:

$$\nabla^2\psi + \alpha \frac{\partial \psi}{\partial x} = \gamma \sin \frac{\pi y}{b} \tag{1}$$

$$\psi(a,y) = \psi(-a,y) = \psi(x,0) = \psi(x,b) = 0 \tag{2}$$

where ψ is the stream function; 2 a and b are the sides of the rectangle in the x and y directions, respectively; $\gamma = F.\pi/R.b$; R is the coefficient of friction; F is the Coriolis parameter (in general it is a function of y); $\alpha = D/R\ \partial F/\partial y$; and D is the constant depth of the ocean when at rest.

In equation (1) it is assumed that the wind stress is defined by the simple functional relation $-F.\cos \pi y/b$.

Consider the case of Munk's model governed by the partial differential equation (ref. 2):

$$A \nabla^4 \psi(x,y) - \beta \frac{\partial \psi}{\partial x} = - (\nabla x \tau) . \overset{\vee}{k} \tag{3}$$

where A and β are constant parameters; ψ is the stream function; and τ is the tangential wind stress.

Since the boundary constitutes a streamline one has:

$$\psi = 0 \quad \text{on the boundary} \tag{4}$$

As a second boundary condition one may have:

a) no slippage against the boundary (ref. 2):

$$\frac{\partial \psi}{\partial n} = 0 \tag{5a}$$

where n denotes the normal to the boundary, or

b) free slippage (no lateral shear against the boundary):

$$\frac{\partial^2 \psi}{\partial n^2} = 0 \tag{5b}$$

Equations (5) constitute highly idealized situations. As an intermediate condition one must take:

$$\frac{\partial \psi}{\partial n} = \alpha_1 \frac{\partial^2 \psi}{\partial n^2} \quad \text{on the boundary} \tag{6}$$

For $\alpha_1 = 0$ one obtains equation (5a) and

for $\alpha_1 = +\infty$ one has the free slippage condition.

Since the solution of the differential system governed by equations (3) and (6) is quite complicated, even in the case of a rectangular ocean basin, it seems reasonable to make use of an approximate method to solve it.

Taking the approximate solution:

$$\psi \simeq \psi_A = \sum_{j=0}^{N} \sum_{k=0}^{N} A_{jk}[a_j x^{4+j} + b_j x^{2+j} + x^j][c_k y^{4+2k} + d_k y^{2+2k} + y^{2k}] \qquad (7a)$$

where each coordinate function satisfies identically the boundary conditions, and substituting in equation (1) one obtains a residual function $\varepsilon(x,y)$.

Galerkin's method is used to minimize the error or residual function $\varepsilon(x,y)$ and a linear system of equations in the A_{jk}'s is then obtained.

In order to assess the accuracy of the method, it is used first in a few cases where an exact solution is available.

Some new problems are then studied. A similar approach is followed in the case of Stommel's model. The stream function is approximated by the functional relation:

$$\psi(x,y) \simeq \sum_{j=0}^{N} A_j \, (a^2 - x^2) \, x^j \sin \frac{\pi y}{b} \qquad (7b)$$

where each coordinate function satisfies identically the boundary conditions in equation (2).

STOMMEL'S MODEL

Substituting equation (7b) in equation (1) one obtains the error or residual function:

$$\varepsilon_N(x,y) = \sin\left(\frac{\pi y}{b}\right)\left\{ \sum_{j=0}^{N} A_j \left[j(j-1)a^2 x^{j-2} - (2+j)(1+j)x^j - \left(\frac{\pi}{b}\right)^2 (a^2 x^j - x^{2+j}) + \right.\right.$$
$$\left.\left. \alpha(j\, a^2 x^{j-1} - (2+j)\, x^{j+1})\right] - \gamma \right\} \qquad (8)$$

Galerkin's orthogonalization condition requires that:

$$\int_0^b dy \int_{-a}^{a} \varepsilon_N(x,y) \, \psi_K(x,y) \, dx = 0 \quad (k=0,1,\ldots N) \qquad (9)$$

where

$$\psi_k = A_k \, (a^2 - x^2) \, x^k \sin \frac{\pi y}{b} \qquad (10)$$

From equations (8), (9) and (10) one finally obtains:

$$\sum_{j=0}^{N} A'_j \left\{ \frac{j(j-1)}{j+k-1} \left(1-(-1)^{j+k-1}\right) - \frac{2(1+j+j^2)}{j+k+1} \left(1-(-1)^{j+k+1}\right) + \frac{(2+j)(1+j)}{3+j+k} \right.$$

$$\left(1-(-1)^{j+k+3}\right) - \lambda^2 \left[\frac{1}{1+j+k} \left(1-(-1)^{j+k+1}\right) - \frac{2}{j+k+3} \left(1-(-1)^{j+k+3}\right) + \frac{1}{j+k+5} \right.$$

$$\left. \left(1-(-1)^{j+k+5}\right) \right] + \alpha a \left[\frac{j}{j+k} \left(1-(-1)^{j+k}\right) - \frac{2+2j}{2+j+k} \left(1-(-1)^{2+j+k}\right) + \frac{2+j}{j+k+4} \left(1-(-1)^{4+j+k}\right) \right]$$

$$= \frac{1}{k+1} \left(1-(-1)^{k+1}\right) - \frac{1}{3+k} \left(1-(-1)^{3+k}\right) \qquad (11)$$

where:

$$A'_j = A_j \frac{a^j}{\gamma} \; ; \; \lambda^2 = \frac{\pi^2 a^2}{b^2}$$

A system of (N+1) linear equations in the A_j's is then obtained.

Numerical and graphical results are shown in table I and figure 1. Table I depicts results obtained making $\alpha = 0$ (analogous to the torsion problem of a bar of rectangular cross section).

Three terms of equations (7) have been used. The agreement with the exact solution is very good. It is important to point out that the case $\alpha_1 = 0$ corresponds to a nonrotating ocean. It is also a valid approximation at high latitudes.

The case where α is a constant (in other words, the Coriolis parameter is a linear function of latitude) is presented in figure 1. One can easily see that the approximate solution converges to the exact, known solution in a convenient fashion.

MUNK'S MODEL

Munk's model yields a differential system similar to the one governing the static bending of a rectangular plate subjected to uniformly distributed loading when the Coriolis parameter is a constant and the wind shear stress obeys a linear law:

$$\tau_x = \tau_o / b_1 \; y$$

Then equation (3) becomes:

$$A \nabla^4 \psi = \tau_{o/b_1} \tag{12}$$

Equations (12), (4) and (5a) are equivalent to the mathematical relations governing the plate problem previously referred to. It has already been shown (ref. 3) that the polynomial approach yields excellent accuracy for this situation.

Consider now the case where β is a constant and the wind shear stress is given by a functional relation of the type

$$\vec{\tau} = F. \frac{y}{b} \left(\frac{y^2}{3b^2} - 1\right) \hat{i} \tag{13}$$

Equation (4) becomes now:

$$\nabla^4 \psi - \frac{\beta}{A} \frac{\partial \psi}{\partial x} = - \frac{F}{A.b} \left(1 - \frac{y^2}{b^2}\right) \tag{14}$$

The boundary conditions are given by equations (4) and (6) which in the case of a rectangular ocean of sides 2 a x 2 b become:

$$\psi\Big|_c = 0 \tag{15a}$$

$$\frac{\partial \psi}{\partial x}\Big|_{x=a} = K_1 \frac{\partial^2 \psi}{\partial x^2}\Big|_{x=a} \tag{15b}$$

$$\frac{\partial \psi}{\partial y}\Big|_{y=b} = K_2 \frac{\partial^2 \psi}{\partial y^2}\Big|_{y=b} \tag{15c}$$

For x= -a and y= -b one obtains functional relations similar to equations (15b) and (c).

The stream function ψ is now approximated using the polynomial expansion of equation (7a).

As shown in tables II through VIII the effect of the coefficients K_1 and K_2 on the values of the stream function ψ is quite appreciable which, on the other hand, was to be expected.

It is important to point out that the determination of the velocity components requires obtaining partial derivatives of the stream function. It has already been shown (ref. 3) that sufficient accuracy may be attained working with a rather small number of polynomials.

REFERENCES

1. Stommels, H.: The Westward Intensification of Wind-Driven Ocean Circulation. Wind-Driven Ocean Circulation (A Collection of Theoretical Studies, Edited by A. R. Robinson) Blaisdell Publishing Company, Division of Random House, Inc., 1963, pp. 13-21.

2. Munk, W. H.: On the Wind-Driven Ocean Circulation. Wind-Driven Ocean Circulation (A Collection of Theoretical Studies, Edited by A. R. Robinson) Blaisdell Publishing Company, Division of Random House, Inc., 1963, pp. 25-56.

3. Laura, P. A. A.; and Duran, R.: A Note on Forced Vibrations of a Clamped Rectangular Plate. J. Sound & Vib., vol. 42, no. 1, 1975, pp. 129-135.

Table I.- Values of $\frac{\psi}{\gamma} \times 10^{-16}$

[Stommel's model, $\alpha = 0$. First number is exact value; second number is the result obtained by the present approach.]

$\frac{x}{A}$	Values of $\frac{\psi}{\gamma} \times 10^{-16}$ for y/b of —				
	0.1	0.2	0.3	0.4	0.5
0	-1.033 -1.031	-1.965 -1.961	-2.705 -2.699	-3.180 -3.172	-3.343 -3.336
0.1	-1.027 -1.025	-1.953 -1.950	-2.688 -2.684	-3.160 -3.155	-3.323 -3.317
0.2	-1.007 -1.007	-1.916 -1.916	-2.637 -2.637	-3.100 -3.100	-3.260 -3.259
0.3	-0.973 -0.975	-1.851 -1.855	-2.548 -2.554	-2.996 -3.002	-3.150 -3.157
0.4	-0.923 -0.927	-1.755 -1.764	-2.416 -2.428	-2.840 -2.854	-2.987 -3.001
0.5	-0.853 -0.859	-1.622 -1.634	-2.233 -2.248	-2.625 -2.643	-2.760 -2.780
0.6	-0.759 -0.765	-1.443 -1.455	-1.996 -2.003	-2.335 -2.355	-2.455 -2.476
0.7	-0.635 -0.640	-1.207 -1.217	-1.661 -1.676	-1.953 -1.970	-2.053 -2.071
0.8	-0.473 -0.476	-0.899 -0.906	-1.237 -1.247	-1.455 -1.466	-1.529 -1.542
0.9	-0.263 -0.266	-0.500 -0.506	-0.688 -0.697	-0.809 -0.819	-0.850 -0.862

Table II.- Values of $\frac{\psi A}{Fa^3} \times 10^3$

$[K_1/a = 0;\ K_2/b = 0;\ \beta = 0;\ \lambda = \frac{a}{b} = 1.5]$

$\frac{x}{A}$	Values of $\frac{\psi A}{F.a^3\lambda} \times 10^3$ for y/b of —					
	0	0.2	0.4	0.6	0.8	1.0
0	6.012	5.701	4.744	3.143	1.182	0
0.2	5.541	5.254	4.372	2.897	1.089	0
0.4	4.242	4.022	3.347	2.218	0.834	0
0.6	2.462	2.335	1.943	1.287	0.484	0
0.8	0.779	0.739	0.615	0.407	0.153	0
1.0	0	0	0	0	0	0

Table III.- Values of $\frac{\psi A}{F.a^3\lambda} \times 10^3$

$[K_1/a = K_2/b = \infty;\ \beta = 0;\ \lambda = \frac{a}{b} = 1.5]$

$\frac{x}{A}$	Values of $\frac{\psi A}{F.a^3\lambda} \times 10^3$ for y/b of —					
	0	0.2	0.4	0.6	0.8	1.0
0	19.826	19.020	16.581	12.484	6.812	0
0.2	18.880	18.113	15.790	11.889	6.487	0
0.4	16.121	15.465	13.482	10.151	5.539	0
0.6	11.775	11.296	9.848	7.415	4.046	0
0.8	6.224	5.971	5.205	3.919	2.132	0
1.0	0	0	0	0	0	0

Table IV.- Values of $\frac{\psi A}{F.a^3\lambda} \times 10^3$

$[K_1/a = 0;\ K_2/b = 2;\ \beta = 0;\ \lambda = \frac{a}{b} = 1.5]$

$\frac{x}{A}$	Values of $\frac{\psi A}{F.a^3\lambda} \times 10^3$ for y/b of —					
	0	0.2	0.4	0.6	0.8	1.0
0	15.879	14.825	11.801	7.309	2.532	0
0.2	15.176	14.169	11.279	6.986	2.420	0
0.4	13.101	12.232	9.737	6.031	2.089	0
0.6	9.756	9.109	7.251	4.491	1.555	0
0.8	5.310	4.958	3.946	2.444	0.847	0
1.0	0	0	0	0	0	0

Table V.- Values of $\frac{\psi A}{F.a^3\lambda} \times 10^3$

$[K_1/a = 0;\ K_2/b = \infty;\ \beta = 0;\ \lambda = \frac{a}{b} = 1.5]$

$\frac{x}{A}$	Values of $\frac{\psi A}{F.a^3\lambda} \times 10^3$ for y/b of —					
	0	0.2	0.4	0.6	0.8	1.0
0	13.260	12.880	10.644	6.183	2.191	0
0.2	12.628	12.266	10.137	5.888	2.086	0
0.4	10.782	10.473	8.655	5.028	1.781	0
0.6	7.875	7.650	6.322	3.672	1.301	0
0.8	4.163	4.043	3.341	1.941	0.608	0
1.0	0	0	0	0	0	0

Table VI.- Values of $\frac{\psi A}{F.a^3\lambda} \times 10^3$

$[K_1/a = \infty;\ K_2/b = 0;\ \beta = 0;\ \lambda = \frac{a}{b} = 1.5]$

$\frac{x}{A}$	Values of $\frac{\psi A}{F.a^3\lambda} \times 10^3$ for y/b of —					
	0	0.2	0.4	0.6	0.8	1.0
0	6.751	6.560	5.928	4.698	2.701	0
0.2	6.222	6.046	5.463	4.329	2.489	0
0.4	4.764	4.629	4.183	3.315	1.906	0
0.6	2.765	2.687	2.428	1.924	1.106	0
0.8	0.875	0.850	0.768	0.609	0.350	0
1.0	0	0	0	0	0	0

Table VII.- Values of $\frac{\psi A}{F.a^3\lambda} \times 10^3$

$[K_1/a = \infty;\ K_2/b = 2;\ \beta = 0;\ \lambda = \frac{a}{b} = 1.5]$

$\frac{x}{A}$	Values of $\frac{\psi A}{F.a^3\lambda} \times 10^3$ for y/b of —					
	0	0.2	0.4	0.6	0.8	1.0
0	28.264	24.350	18.147	15.261	9.603	0
0.2	27.013	23.272	17.344	14.505	9.178	0
0.4	23.320	20.090	14.973	12.591	7.923	0
0.6	17.365	14.961	11.150	9.376	5.900	0
0.8	9.451	8.143	6.068	5.103	3.211	0
1.0	0	0	0	0	0	0

Table VIII.- Values of $\frac{\psi A}{F.a^3\lambda} \times 10^3$

$[K_1/a = 2;\ K_2/b = 2;\ \beta = 0;\ \lambda = \frac{a}{b} = 1.5]$

$\frac{x}{A}$	Values of $\frac{\psi A}{F.a^3\lambda} \times 10^3$ for y/b of —					
	0	0.2	0.4	0.6	0.8	1.0
0	26.331	25.270	22.072	16.717	9.258	0
0.2	25.165	24.151	21.095	15.977	8.848	0
0.4	21.725	20.849	18.211	13.793	7.638	0
0.6	16.178	15.526	13.561	10.271	5.688	0
0.8	8.805	8.450	7.381	5.590	3.095	0
1.0	0	0	0	0	0	0

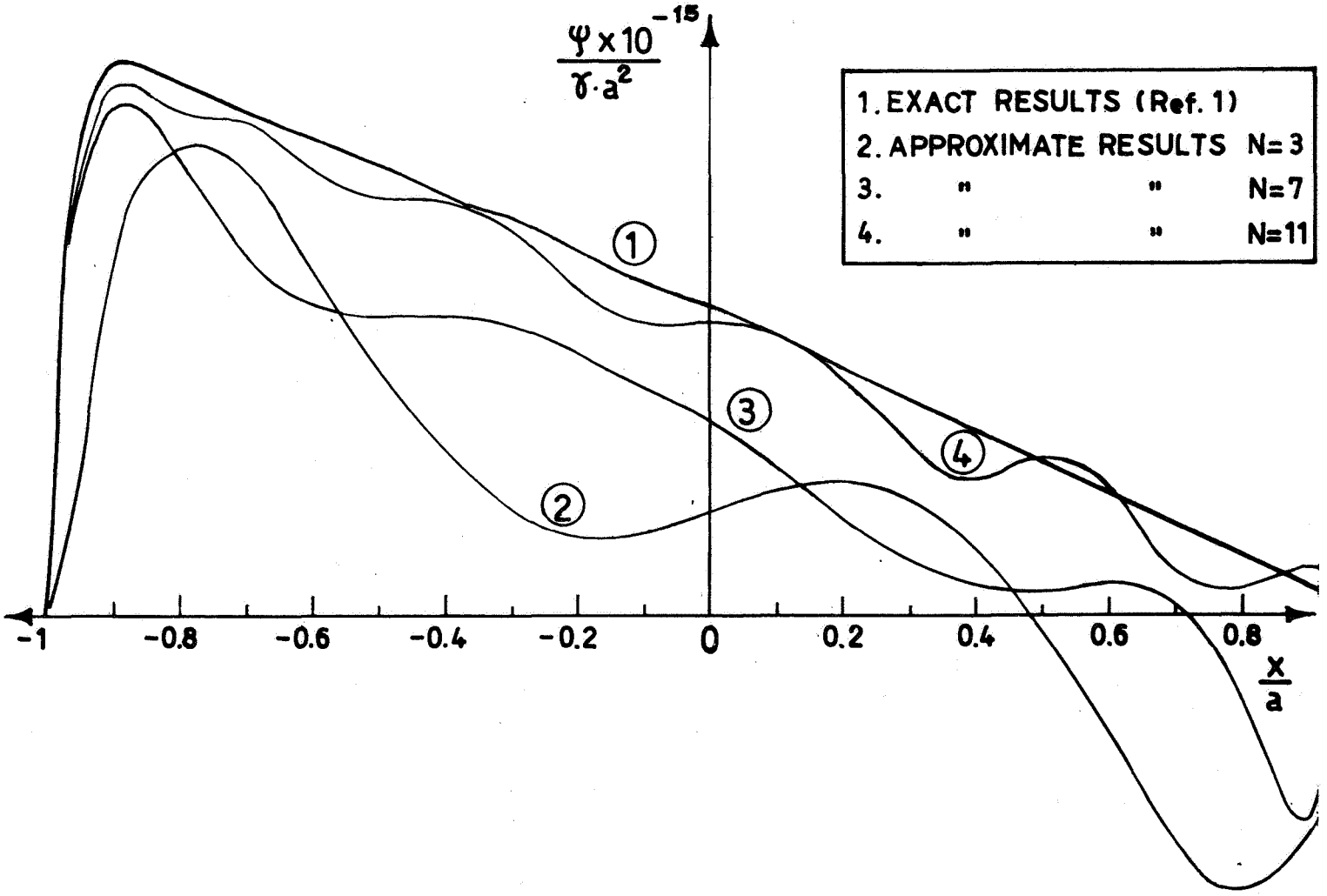

Figure 1.- Variation of the stream function as a function of x/a for y = b/2 (α = constant).

OPTICALLY RELEVANT TURBULENCE PARAMETERS IN THE MARINE BOUNDARY LAYER*

K. L. Davidson and T. M. Houlihan
Naval Postgraduate School

SUMMARY

Shipboard measurements of temperature and velocity fluctuations were performed to determine optical propagation properties of the marine boundary layer. Empirical expressions describing the temperature structure parameter, C_T^2, in terms of the Richardson Number, Ri, overland were used to analyze data obtained for open ocean conditions. Likewise, profiles of mean wind and velocity fluctuation spectra derived from shipboard observations were utilized to calculate associated boundary layer turbulence parameters. In general, there are considerable differences between the open-ocean results of this study and previously determined overland results.

INTRODUCTION

Optical propagation through the atmosphere is affected by the refractive nature of the medium. In addition to the regular variation of atmospheric refractive index with height, there exist small inhomogeneities in the refractive index associated with fluctuations in the temperature of the air. These cause random phase and amplitude distortions in propagating wave fronts and thus degrade spatial and temporal coherence in the transmission. The magnitude of these effects places limitations on optical system performance and must be included in design considerations. It is desirable to have a theory sufficiently well-developed to permit derivation of propagation statistics from bulk measurement of meteorological variables.

Descriptions of small scale fluctuations which affect laser propagations have not been as complete nor in the quantity for the overwater regime as for the overland regime. Overwater descriptions are necessary, even though considerable progress has been made in overland investigations (ref. 1). The necessity exists

*This work was supported by the Navy High Energy Laser Project (PMS-22), CAPT A. Skolnick, Director.

because of the increasing evidence of the influence on atmospheric motions by oceanic waves (ref. 2). This wave influence has been observed to be significant enough to warrant re-examination of empirical expressions relating small scale properties of the atmosphere to mean wind and temperature profiles.

SYMBOLS

C_z	drag coefficient for given height (z)
C_q	moisture exchange coefficient for given height
C_H	temperature exchange coefficient for given height
C_N^2	refractive index structure function parameter $(m^{-2/3})$
C_T^2	temperature structure function parameter $(K/m^{-2/3})$
C_{10}	drag coefficient value at 10 meter height
C_{10p}	drag coefficient value calculated using mean wind profile data
$C_{10\varepsilon}$	drag coefficient calculated using velocity variance spectral estimates of ε
L	Monin-Obukhov length (m)
P	barometric pressure (mb)
$\bar{Q}_a$	average water vapor density (g/m^3)
$\bar{Q}_s$	average water vapor density at surface (g/m^3) (assuming saturated air at surface)
ΔQ	$(\bar{Q}_s - \bar{Q}_a)$
q	water vapor density fluctuation (g/m^3)
Ri	Richardson Number (dimensionless)
$\bar{\theta}$ or $\bar{\theta}_a$	Average potential temperature (K)
$\bar{\theta}_s$	Average sea surface temperature (K)
$\Delta\theta$	$(\bar{\theta}_s - \bar{\theta}_a)$
θ_v	Virtual potential temperature (K)

T'	temperature fluctuation (K)
$\overline{U}$	average wind speed at height Z (m/s)
$\overline{U}_{10}$	average wind speed at 10 meter height (m/s)
(u,w)	horizontal and vertical velocity fluctions (m/s)
U_*	friction velocity (m/s); = $(\overline{-uw})^{1/2}$
T_*	characteristic temperature (K); = $\overline{-wT'}/U_*$
T_{*_v}	characteristic virtual temperature (K)
ε	dissipation rate of turbulent kinetic energy (m^2/s^3)
U_{*_p}	friction velocity calculated using mean wind profile data (m/s)
U_{*_ε}	friction velocity calculated using ε data (eq. (18))
R_3	constant determined by bulk aerodynamic exchange coefficients
Z	measurement height (m)
β	empirical constant (3.20), (eq. (4))
κ	Von Karman constant (0.35)
χ	dissipation rate of temperature variance (K^2/s)
g	gravitational acceleration (9.80 m/sec)
γ	kinematic molecular viscosity (cm^2/s)
f_i	empirical functions of Z/L (i = 1, 2, 3)
ϕ_i	empirical functions of Ri (i = 1, 4)
X	bulk aerodynamic stability parameter (eq. (11))
Z_o	profile roughness parameter (m)
L_o	outer turbulence scale
ℓ_o	inner turbulence scale
T	ambient atmospheric temperature (K)

THEORETICAL CONSIDERATIONS

General expressions for C_T^2

On the basis of the isotropic nature of small scale fluctuations, only one parameter is necessary to describe the intensity of the atmospheric refractive index fluctuations over many scales (ref. 3). It is the refractive index structure function parameter, C_n^2, where

$$C_n^2 = [n'(x) - n'(x + r)]^2/r^{2/3} \tag{1}$$

Here, $n'(x)$ and $n'(x + v)$ are refractive index fluctuations at two points on a line oriented normal to the mean wind direction separated by the distance, r. This distance, r, is less than the outer scale, L_o, (the lower end of the inertial subrange) and greater than the inner scale, ℓ_o (the smallest scale of naturally occurring turbulence.) The brackets in equation (1) designate an RMS evaluation of the quantities contained therein.

A parallel expression, which defines the temperature structure function parameter, C_T^2, is

$$C_T^2 = [T'(x) - T'(x + r)]^2/r^{2/3} \tag{2}$$

where $T'(x)$ and $T'(x + r)$ are temperature fluctuations at two points separated by the distance r.

Fortunately, C_n^2 is related to the temperature structure function parameter, C_T^2, as

$$C_n^2 = (79 \times 10^{-6}\ P/T^2)^2 C_T^2 \tag{3}$$

where P is the barometric pressure and T is the atmospheric temperature. Equally fortunate is the fact that both C_N^2 and C_T^2 are readily measurable by optical and meteorological means, respectively.

An alternate relationship for C_T^2, which involves measurement of the rates of dissipation of turbulent kinetic energy (ε) and temperature variance (χ) is

$$C_T^2 = \beta \chi \varepsilon^{-1/3} \tag{4}$$

β is an empirical constant with a value of 3.20. This last form enables indirect estimates of C_T^2 to be made from mean conditions, since ε and χ are easily related to boundary layer

fluxes and profiles if steady, horizontally homogeneous conditions exist. Expressions which relate C_T^2 to mean properties of the boundary layer are desirable because the small scale measurements are impractical to obtain in most operational or tactical situations.

Since turbulence is nearly synonymous with temperature fluctuations, it is ultimately desirable to describe mean thermal stratification in terms of the atmospheric bulk stability parameters such as the Richardson Number (Ri) or Monin-Obukhov Length (L). In this regard, measurements of both atmospheric mean profiles and fluxes are required for a complete determination of atmospheric transmission behavior. Profile ($\partial\bar{\theta}_v/\partial Z$ and $\partial\bar{U}/\partial Z$) and boundary flux ($U_*$ and T_*) parameters appear in the following expressions for Ri and L,

$$\mathrm{Ri} = \frac{g\,\partial\bar{\theta}_v/\partial Z}{\bar{\theta}\,(\partial\bar{U}/\partial Z)^2}$$

$$L = \frac{\bar{\theta}\,U_*^2}{g\,\kappa\,T_{*v}} \qquad (5)$$

In unstable conditions (Ri and L<0) the ratio Z/L is approximately equal to the Richardson number.

The following similarity predictions for the dependence of ε and χ on momentum and heat fluxes and height were considered by Wyngaard, et al. (ref. 1) in deriving an empirical expression for estimating C_T^2 from mean stability parameters,

$$\varepsilon Z/U_*^3 = f_1(Z/L) \quad (a)$$

$$\chi Z/T_* U_* = f_2(Z/L) \quad (b) \qquad (6)$$

The form of the empirical expression for C_T^2 is obtained by direct substitution of equation (6) into equation (4) which yields

$$C_T^2 = T_*^2 Z^{-2/3} f_3(Z/L) \qquad (7)$$

Furthermore, since (Z/L) and Ri can be functionally related, a parallel dependence on Ri can be obtained, viz.,

$$C_T^2 = Z^{4/3}(\partial\bar{\theta}/\partial Z)^2 \phi_3(\mathrm{Ri}) \qquad (8)$$

The functions f_1, f_2, f_3 and ϕ_3 in equations (6), (7), and (8) are empirical and formulated on the basis of observations of both temperature fluctuations, momentum and heat fluxes and mean gradients of wind speed, temperature and humidity.

The relation expressed by equation (8) provides a desired dependence of C_T^2 on more readily measured mean stability (Z, $\partial\bar{\theta}/\partial Z$ and Ri). The forms for f_3 and ϕ_4 and the data obtained from the extensive AFCRL study of turbulence structure over a flat, unobstructed Kansas plain are presented in reference 1. As will be shown later, available marine data does not appear to agree for f_3 as well as expected with the overland predictions. The overland predictions, based on the separate, empirical expressions for f_1 and f_2 in equation (6), were as follows for unstable (Z/L<0) and stable (Z/L>0) conditions,

$$f_3(Z/L) = 4.9\ (1 - 7\ (Z/L))^{-2/3},\ Z/L \leq 0$$
$$f_3(Z/L) = 4.9\ (1 + 2.75\ (Z/L)),\ Z/L \geq 0 \qquad (9)$$

The utility of equations (7) or (8) for estimating C_T^2 from routine observation is not satisfactory in most cases, since they require mean measurements of either the boundary fluxes (eq. (7)) or profile gradients (eq. (8)). Therefore, it is desirable to obtain general expressions for C_T^2 which are based on bulk formulae for estimating the fluxes.

A bulk aerodynamic formula relates boundary fluxes to the wind speed at one level and the temperature difference between that level and the surface. The derivation of such formulae involves several assumptions regarding the stability conditions of the boundary layer and the turbulent processes within it. If valid, however, this type of formulation is very useful for most practical needs.

The form of bulk aerodynamic formulae for momentum, temperature and humidity fluxes are, respectively,

$$U_*^2 = C_z U^2$$
$$\overline{wT'} = C_H \bar{U}\ (\bar{\theta}_s - \theta_a) \qquad (10)$$
$$\overline{wq} = C_q \bar{U}\ (\bar{Q}_s - Q_a)$$

Friehe (ref. 4) combined Wyngaard, et al.'s (ref. 1) general expressions for C_T^2 (eqs. (7) and (9)) with bulk aerodynamic formulae to obtain an alternate expression for the estimation of C_T^2. This derivation yielded the following expression for the nondimensional

temperature structure function parameter $(C_T^2\ Z^{2/3}/(\Delta\bar{\theta})^2)$,

$$\frac{C_T^2\ Z^{2/3}}{(\Delta\bar{\theta})^2} = \begin{cases} 3.12 \times 10^{-3}\ (1 + 1.62X)^{2/3} & \text{stable} \\ 3.12 \times 10^{-3}\ (1 - 0.64X) & \text{unstable} \end{cases} \tag{11}$$

where

$$X = \frac{Z\ \Delta\bar{\theta}}{\bar{U}^2}\ (1 + 0.21\ R_3\ \frac{\Delta\bar{Q}}{\Delta\bar{\theta}}).$$

X is a bulk aerodynamic stability parameter and R_3 is a constant determined by the values of the exchange coefficients (C_Z, C_H and C_q) in the bulk aerodynamic formulae and depends on the height of the measurement in the air.

General expression for small scale properties of velocity fluctuation

Small scale velocity fluctuation properties are of interest in optical propagation because image resolution has been empirically related to the inner scale ℓ_o which is defined as

$$\ell_o = (\frac{\gamma^3}{\varepsilon})^{1/4} \tag{12}$$

where γ is the kinematic molecular viscosity and ε is the dissipation rate of turbulent kinetic energy similar to C_T^2. ε can be obtained from either one-dimensional velocity variance spectral estimates in the inertial subrange or from velocity structure function estimates.

ε and hence ℓ_o can be functionally related to mean profile and flux estimates (U_* and Ri or Z/L) on the basis of an empirical expression presented previously (eq. (6a)). For the purpose of examining overwater ε results from different stability conditions described by Richardson numbers (Ri), equation (6a) can be expressed in the following form,

$$\varepsilon = \frac{U_*^3}{\kappa Z}\ \phi_1(\mathrm{Ri}) \tag{13}$$

since Z/L and Ri are functionally related.

Overwater ε values can also be evaluated on the basis of U_* values estimated from them. Such estimates can be evaluated by comparing them with U_* estimates computed from mean wind profile measurements. Both U_* estimates utilize the following expression

for the mean wind gradient,

$$\frac{\partial \bar{U}}{\partial Z} = \frac{U_*}{\kappa Z} \phi_1(Ri) \tag{14}$$

where $\phi_1(Ri)$ is the same as that appearing in equation (13) and is equal to 1.0 under neutral conditions. U_* is assumed to be constant with height in this expression.

Integration of equation (14) for neutral conditions yields

$$\bar{U} = \frac{U_*}{\kappa} \text{Ln} \frac{Z}{Z_o} \tag{15}$$

where U_o is assumed to be zero, Z_o is the roughness parameter and κ is the von Karman constant equal to .35. One must realize that both unstable and stable conditions alter the logarithmic profile suggested by equation (15). Z_o can be eliminated from equation (15) by selecting mean winds at two appropriate levels so that

$$U_* = \kappa(\bar{U}_2 - \bar{U}_1)/\text{Ln}(\frac{Z_2}{Z_1}) \tag{16}$$

It is important to note that this expression relating U_* to mean wind values (U_2 and U_1) at two levels (Z_2 and Z_1) is applicable only for near neutral conditions (Ri ≈ 0).

In near neutral conditions, turbulent kinetic energy production is assumed to be equal to the rate of molecular dissipation of turbulent kinetic energy and yields the following relation,

$$\varepsilon = U_*^2 \, (\partial \bar{U}/\partial Z). \tag{17}$$

Combining equations (14) and (17), assuming $\phi_1(Ri) = 1$ and solving for U_*, yields

$$U_* = (\varepsilon \kappa Z)^{1/3} \tag{18}$$

Thus, under neutral conditions, the friction velocity (U_*) can be estimated from either mean wind profiles using equation (16) or from fluctuation data (involving turbulent energy dissipation, ε), using equation (18).

Having determined values for U_* it is possible to calculate a momentum drag coefficient, C_Z, that corresponds to a given height in the surface layer

$$C_Z = \frac{U_*^2}{\bar{U}^2} \tag{19}$$

Studies have been conducted to determine a representative value of C_z at a 10 meter height, (e.g., Cardone (ref. 5)). Check calculations of C_{10} employing U_* determined from both mean wind profiles and dissipation rates were performed in this study.

EXPERIMENTS

Shipboard observational experiments to describe the small scale properties of atmospheric turbulence were performed aboard the Naval Postgraduate School research vessel, ACANIA, anchored off Pt. Pinos in Monterey Bay. The shipboard sensor arrangement appears in figure 1.

Mean wind measurements were made with a cup anemometer wind profile register system. The set has a characteristic low starting speed with a small amount of internal friction which aids in checking inertial overshoot. Quartz crystal probes were used to measure mean temperatures at each level. The resolution for each probe was 0.005°C. Lithium chloride sensors were used to measure relative humidity valves. Both mean temperature and humidity sensors were housed in aspirated shelters at each measurement level.

Data logging for the mean system was accomplished using an NPS developed micro-processor based data acquisition system. This MIDAS (Microprocessing, Integrated Data Acquisition System) utilizes a central processing unit to control the sampling, averaging and recording of mean meteorological data. The operator is interfaced with the system via a teletype unit for full duplex input/output communication and program control. Once initiated, the system is fully automated in sampling the tailored list of sensors every 30 seconds and periodically printing output values averaged over the selected interval of from one minute to one hour. Output values are printed on the teletype in columnized format with the time of print as the leader. The teletype features a paper tape punch to produce a data copy concurrent with the printout.

Velocity fluctuation measurements were performed using a hot-wire anemometer system. The system featured a linear frequency response from DC to 2KHz. Temperature fluctuations were measured using resistance wire bridges with platinum wires. The baseband portion of this system is a balanced bridge excited by a 3KHz signal with a synchronous detector on the output. The system featured a response to temperature variations as small as 0.004°C in magnitude and up to 1KHz in frequency. Both wind and temperature fluctuation data were recorded on a 14-channel FM Analog tape recorder. Real time readout on an 8-channel chart recorder was used to check the quality of the signals from the instruments. The charts were also used to select the periods analyzed for the investigation.

ANALYSIS

In the analysis of the recorded data, first the individual mean wind ($\bar{U}$), mean temperature ($\bar{\theta}$), and mean humidity ($\bar{Q}$) values were plotted on a logarithmic scale. From best fit lines drawn through the data points, values were chosen and applied to the expressions developed by Wyngaard. Secondly, values of $\bar{U}$, $\bar{\theta}$ and $\bar{Q}$ from individual levels were applied to the bulk aerodynamic expressions developed by Friehe. Variance spectra were interpreted to estimate C_T^2 and ε values. The spectra of temperature and velocity signals were obtained by processing recorded signals on an analog spectrum analyzer.

Friction velocity values, U_*, were calculated in two ways. In the first method, profiles of Log Z versus mean wind were plotted and the best fit profiles were determined subjectively. After the profiles were thus developed, five and ten meter wind speeds were abstracted and were used to solve equation (16) for U_*p. In the second method, turbulent kinetic energy dissipation rates (ε) were determined from velocity spectra and together with measurement height values, were used in equation (18) to solve for $U_{*\varepsilon}$ values. Finally, friction velocity results were used to compute the momentum drag coefficients, C_{10p} and $C_{10\varepsilon}$. Equation (19) was solved for C_Z at the ten meter level for both U_{*p} and $U_{*\varepsilon}$ values.

RESULTS

A comparison of overwater and overland results is presented in figure 2. The solid curve therein represents overland determination based upon Wyngaard's results. Overwater data appear as dots while averages over Ri intervals of 0.25 appear as dots within a larger circle. The error bars are standard deviations from the means within each interval, while the number at the top of the error bars is the number of observations defining the mean value.

For both stable (+Ri) and unstable (-Ri) stratification cases, there appears to be little agreement. However, the trend for the unstable conditions appears to be correlated. The scatter in the observed results can be attributed to scatter in both C_T^2 and $(\partial\bar{\theta}/\partial z)$ measurements. Deviation of temperature spectra from the predicted (-5/3) slope in the inertial subrange caused errors in C_T^2 estimates. Likewise, deviations in temperature gradient measurements caused severe distortions in final results since these generally small gradient values are squared and entered into the denominator of the normalized ordinate value.

In figure 3, C_T^2 results are evaluated with regard to their predictability by bulk aerodynamic parameters. The curve in figure (3) represents Friehe's (ref. 4) bulk aerodynamic expression (eq. (11)) of Wyngaard et al.'s overland empirical expression. Again, there is considerable scatter in the observed results. The agreement is as satisfactory as that found by Friehe with overwater results but both sets indicate a significant difference between the overland and overwater regimes.

In figure 4, ε results are compared with predictions based on equation (13) expressed in its logarithmic form. In the latter form, the coordinates in figure 4 would yield the indicated -1 slope for the ε values. The function $\phi_1(Ri)$ corrects the ε plots to the expected -1 slope in figure 4a but not in figure 4b. The latter could have been due to improper specification of Ri. In plotting "not-corrected" results in figure 4, $\phi_1(Ri)$ was set equal to 1.

Figure 5 is a plot of friction velocities computed from profiles (U_{*_p}, eq. (16)) and dissipation estimates (U_{*_ε}, eq. (18)). The scatter is not too large, considering the errors inherent in both methods, e.g., assuming neutral conditions. Further evaluation of the ε estimates can be made on the basis of resulting C_{10} values. In figures 6a and 6b, plots of $\bar{U}_{10}$ versus C_{10p} and $C_{10\varepsilon}$, respectively, are compared with a curve (Cardone, ref. 5) which summarizes considerable overwater results. Both sets of results agree satisfactorily with the summary curve but the scatter, indicated by error bars, is less for the $C_{10\varepsilon}$ results. The latter feature lends more credence to the U_{*_ε} values and, hence, the ε estimates.

CONCLUSION

Correlation of spectrally derived C_T^2 results with stability parameters (Ri and χ) was not good for the data obtained in this study of the marine environment. Likewise, verification evaluations for friction velocity results from mean (profile) and turbulent (dissipation) data were inconclusive. However, credible agreement between previously derived results and present turbulent data for drag coefficient values was obtained.

It is concluded that the turbulent temperature field in the marine layer is subjected to several anomalous effects which can cause the disruption of the inertial subrange. Thus, empirically, expressions for describing overland transmission characteristics (C_T^2) will undoubtedly have to be altered to provide operational determinations for utilization in the marine environment.

REFERENCES

1. Wyngaard, J. C., Izumi, Y., and Collins, S. A.: Behavior of the Refractive Index Structure Parameter Near the Ground. Jour. Opt. Soc. America, no. 61, 1971, pp. 1646-1650.

2. Davidson, K. L.: Observational Results on the Influence of Stability and Wind-Wave Coupling on Momentum Transfer and Turbulent Fluctuations Over Ocean Waves. Boundary-Layer Meteorology, vol. 6, 1974, pp. 305-331.

3. Tatarski, V. I.: Wave Propagation in a Turbulent Medium. McGraw-Hill, 1961.

4. Friehe, C. A.: Estimation of the Refractive-Index Temperature Structure Parameter in the Atmospheric Boundary Layer Over the Ocean. Applied Optics, 1976, (in press).

5. Cardone, V.J.: Specification of the Wind Distribution in the Marine Boundary Layer for Wave Forecasting. Report GSL-TR69-1, New York University, 1969.

6. Hughes, M. M.: An Investigation of Optically Relevant Turbulence Parameters in the Marine Boundary Layer. M.S. Thesis, Naval Postgraduate School, 1976.

7. Atkinson, H. E.: Turbulent Flux Estimates from Shipboard Mean Wind and Temperature Profiles and Dissipation Rates. M.S. Thesis, Naval Postgraduate School, 1976.

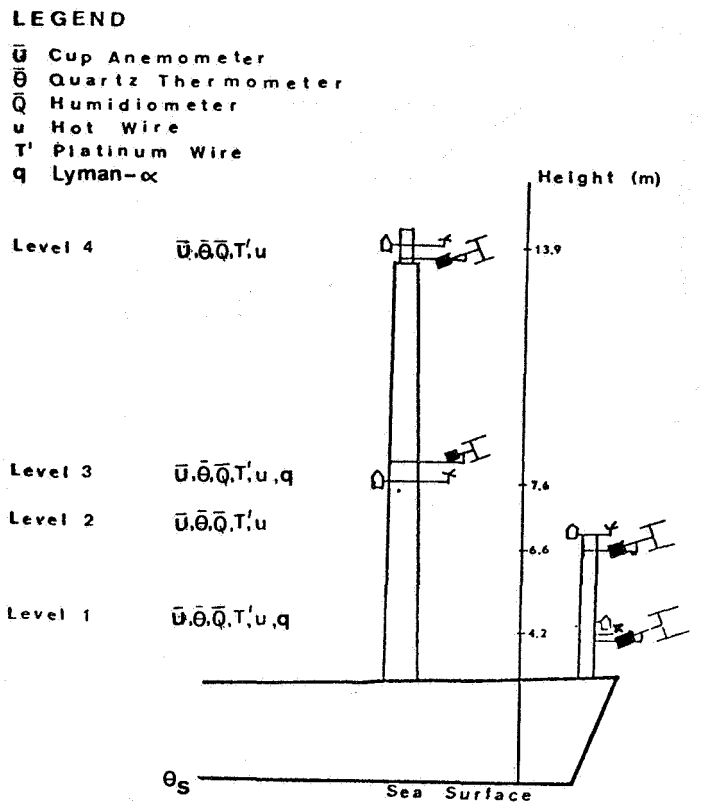

Figure 1.- Mounting arrangements aboard the R/V ACANIA.

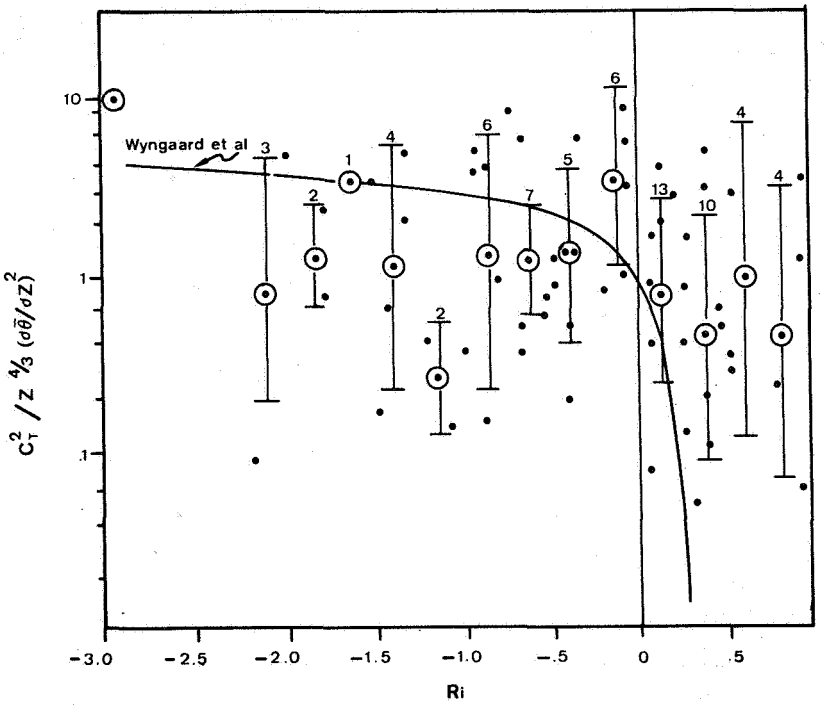

Figure 2.- Overwater results for nondimensional temperature structure function parameter versus Ri. (From reference 6).

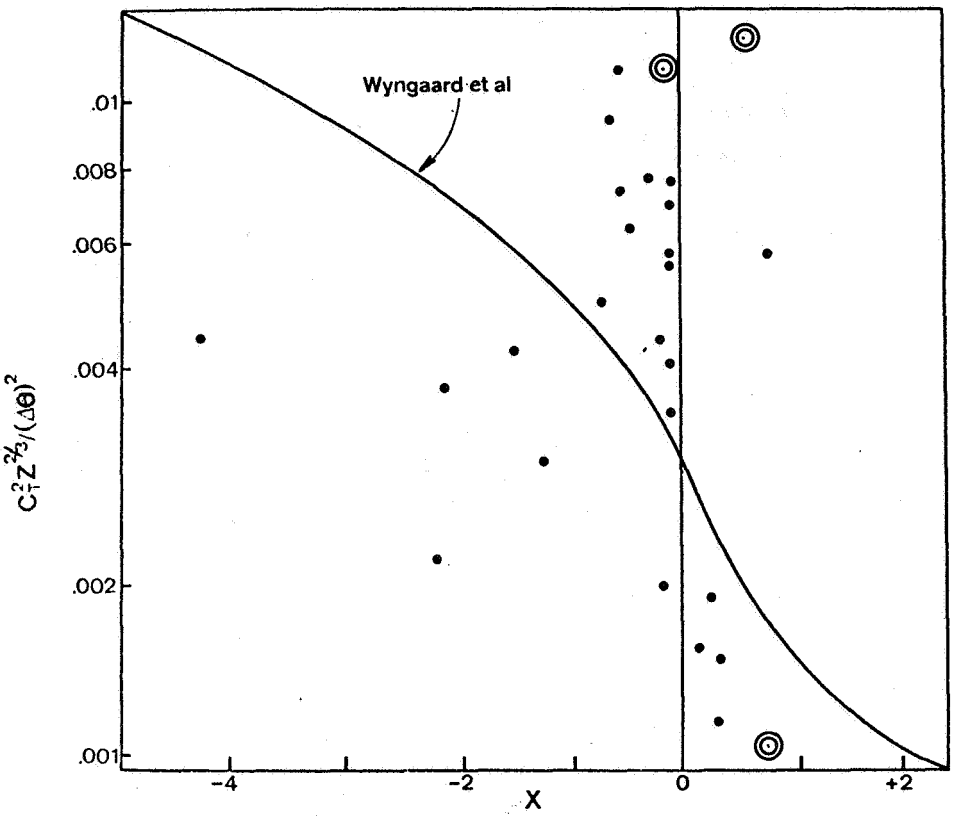

Figure 3.- Overwater results for nondimensional temperature structure function parameter versus bulk aerodynamic parameter; points enclosed by concentric circles are from Friehe (ref. 4). (From reference 6).

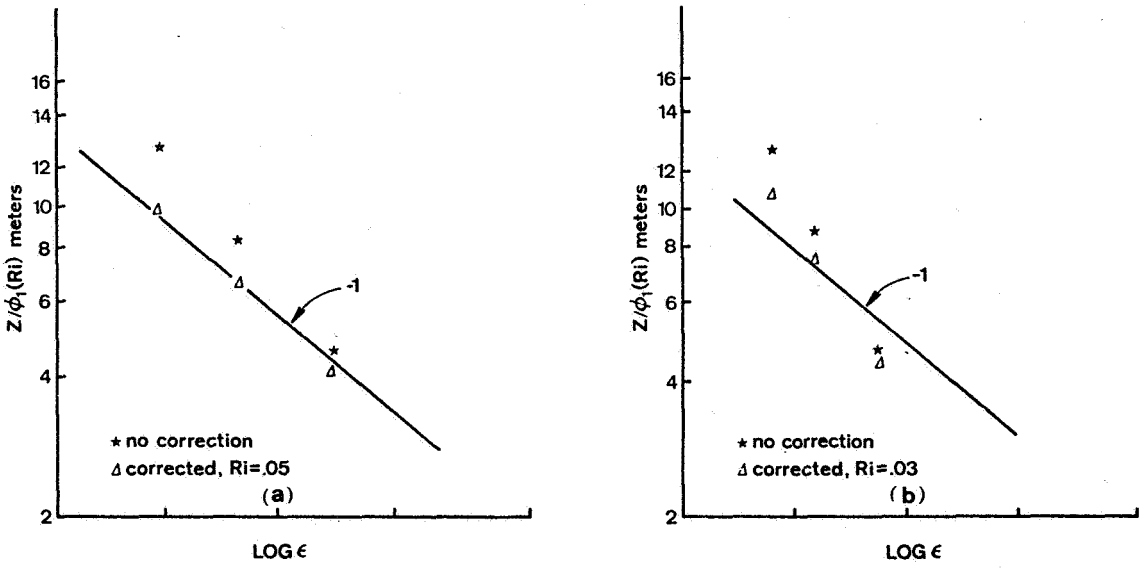

Figure 4.- ε versus Z/ϕ, (Ri) results; (a) Ri = .05 and (b) Ri = .03.

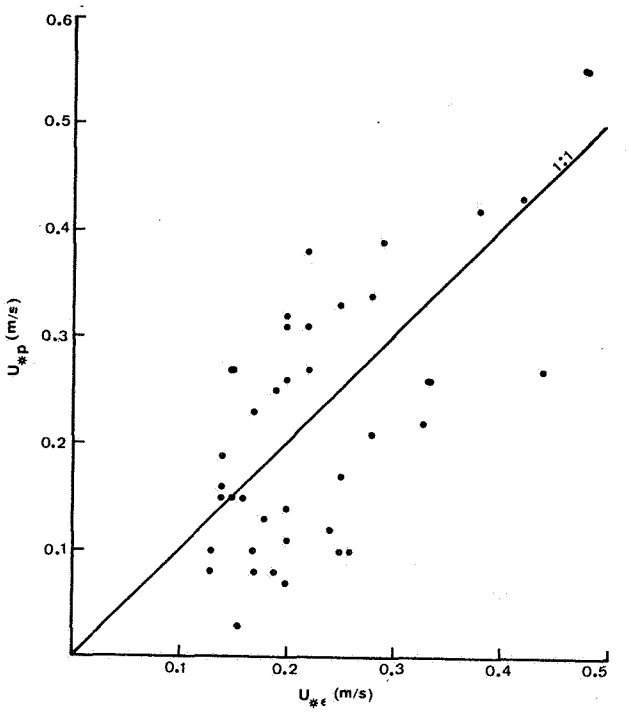

Figure 5.- Friction velocity results. (From reference 7).

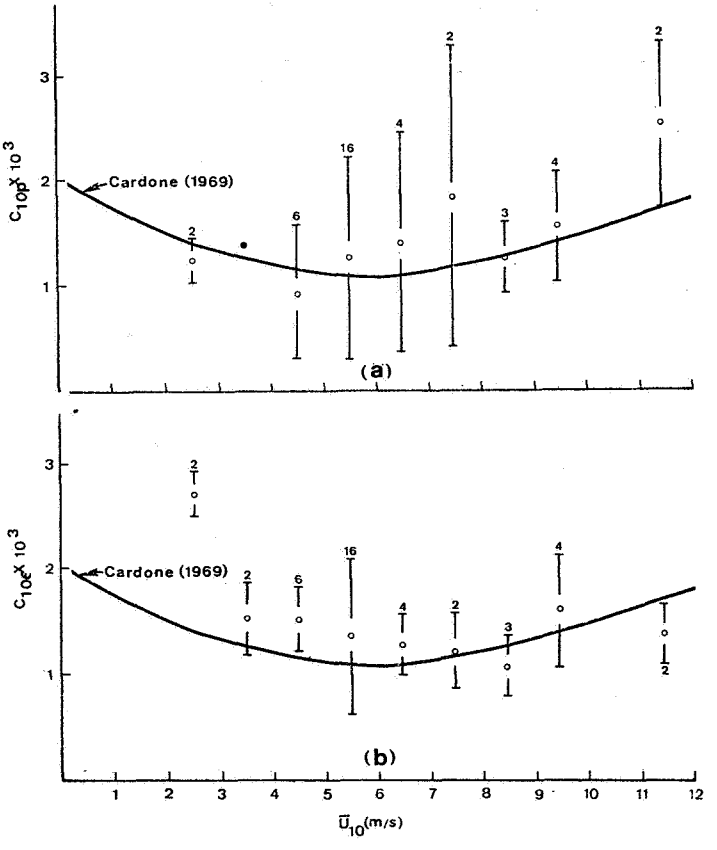

Figure 6.- Drag coefficient results; (a) C_{10p} and (b) $C_{10\epsilon}$. (From reference 7).

THE NUMERICAL PREDICTION OF TORNADIC WINDSTORMS

Douglas A. Paine
Cornell University

Michael L. Kaplan
Joint Institute for Advancement of Flight Sciences
The George Washington University

SUMMARY

The numerical prediction of localized, severe weather events such as tornadoes bred by squall lines is being sought by extending foundational concepts of turbulence theory. Rather than treat such turbulent bursts as being purely statistical in nature, a mathematical framework has been founded upon the concept of a deterministic cascade of energy-momentum which bridges the gap between the longest and shortest of atmospheric wave phenomena. This cascade relieves macroscale wavelengths (>1000 km) of mass-momentum imbalances by exciting convective phenomena (<10 km) through a sophisticated transfer process involving intermediate, mesoscale wavelengths.

INTRODUCTION

Atmospheric dynamics has traditionally been approached from a particular spatial and temporal scale. Scalar analysis became a primary mathematical tool which was often employed to study the dominant forcing functions at a given wavelength (frequency). This concept served to simplify the governing set of conservation equations as one attempted to numerically simulate a given dynamical process.

To numerically model a tornado, one must be able to simulate the efficient transfer of energy momentum beginning with wavelengths greater than 1000 km and ending at those less than 1 km. We may approach the complexity of this scale interaction problem from the vector form of the three-dimensional equation of motion:

$$\frac{d\vec{V}}{dt} = g + 2\vec{\Omega}x\vec{V} - \alpha\nabla P + \eta\nabla^2\vec{V} \qquad (1)$$

Momentum is conserved when the four righthand forcing functions sum to zero. We note the first two terms involving the gravitational acceleration and Coriolis force are spatially independent and both are known at any given height or latitude, respectively. The remaining two forcing functions, namely the pressure gradient force weighted by the specific volume plus the friction term expressed as the Laplacian of velocity weighted by the coefficient of eddy viscosity, are both highly scale dependent. If the local temporal derivative of momentum is equated to the spatial derivatives of momentum advection, we may set these spatial derivatives equal to their respective summation of forces in x-, y-, and z-space:

$$\alpha_1 u + \beta_1 v + \gamma_1 w = \frac{F_x}{u} \qquad \text{where} \quad u = u_o e^{i\alpha_1 x} e^{i\beta_1 y} e^{\gamma_1 z} \tag{2a}$$

$$\alpha_2 u + \beta_2 v + \gamma_2 w = \frac{F_y}{v} \qquad \text{where} \quad v = v_o e^{i\alpha_2 x} e^{i\beta_2 y} e^{\gamma_2 z} \tag{2b}$$

$$\alpha_3 u + \beta_3 v + \gamma_3 w = \frac{F_z}{w} \qquad \text{where} \quad w = w_o e^{i\alpha_3 x} e^{i\beta_3 y} e^{\gamma_3 z} \tag{2c}$$

with $\alpha \equiv \partial/\partial x$, $\beta \equiv \partial/\partial y$, and $\gamma \equiv \partial/\partial z$. We are mathematically stating, given the gravitational, Coriolis, and pressure gradient terms as known quantities, that

$$\frac{d\vec{V}}{dt}^{o} = \eta \nabla^2 \vec{V} \tag{3}$$

and hence $\eta \nabla^2 \vec{V} = 0$ or $\nabla^2 \vec{V} = 0$. Thus internal viscosity becomes the localized, self-cancelling accelerations/decelerations within the fluid system manifested at inflection points in the curvature of the momentum field. In this closed atmospheric dynamic, external viscosity is neglected. A graduate student at Cornell, Miguel Larsen, first suggested, and now is studying the fluid properties which emerge when momentum conservation is expressed in the resultant form of the following tensor matrix:

$$\begin{vmatrix} \alpha_1 & \beta_1 & \gamma_1 \\ \alpha_2 & \beta_2 & \gamma_2 \\ \alpha_3 & \beta_3 & \gamma_3 \end{vmatrix} \begin{vmatrix} u \\ v \\ w \end{vmatrix} = \begin{vmatrix} F_x(u^{-1}) \\ F_y(v^{-1}) \\ F_z(w^{-1}) \end{vmatrix} \tag{4}$$

The scale dependence mentioned with regard to the Newtonian equations of motion may be alternatively expressed as the divergence of both the pressure and velocity gradients, a mathematical measure of the geometry of the mass and momentum fields taken together. In equation (4), the scale dependence of the former forcing functions cited in equation (1) is now reflected in the scale dependent spatial gradients of momentum. Apparently, as evidenced by the dimensions of sec^{-1} expressed in the righthand column of the tensor matrix, a given kinematic flow regime characterized by its advection of momentum evokes a particular configuration to both the mass and momentum fields to yield a preferred class of waves. Furthermore, as the strength of momentum advection within an atmospheric volume changes, the fluid will undergo a rapid rotation of its preferred axis of spin which may be evaluated as an exchange through time between the horizontal and vertical components of relative vorticity (sec^{-2}). As we shall see in the following case study, extreme gradients of momentum and momentum advection evoke a chain reaction toward ever decreasing wavelengths which culminates in a severe family outbreak of tornadoes.

Data Base

The data base for this particular study will include radiosonde data collected at 1200 GMT (Greenwich Mean Time) 11 April and 2400 GMT 12 April, 1965. We will also engage observed hourly surface data for the sixteen hour period beyond 1200 GMT 11 April during which 37 tornadoes devastated portions of Iowa, Wisconsin, Illinois, Michigan, Indiana, and Ohio.

THE INITIAL STATE PRECEDING THE TORNADO OUTBREAK OF PALM SUNDAY 1965

At 1200 GMT 11 April there is a modest surface depression of 986 mb (1013 millibar = 101.3 kPa = 1 atm) near the border of Iowa and Nebraska. A large upper vortex extends northwestward to the distended tropopause boundary over southwestern South Dakota. The region between the upper vortex over South Dakota and an elongated ridge of high pressure over the Gulf of Mexico is dominated by a zonal pressure pattern with relatively large meridional gradients of pressure. These gradients are most significant across Nebraska, Iowa, Kansas, Missouri, and Oklahoma.

The jet stream wind maximum, comprised dominantly of zonal kinetic energy, lies near 350 mb as shown in Figure 1. The jet maximum centered near south-central Kansas is unusual not only because of its magnitude in excess of 75 m sec^{-1} and its relatively low elevation of 8 km, but most markedly because of the extraordinary meridional shearing of the u-velocity component between Dodge City (#) and North Platte (@). The former station has a u-component of 60 m sec^{-1}, the latter station has a u-component of 6 m sec^{-1}, representing one order of magnitude shear in 400 km. This meridional shear yields a relative vorticity due to $-\partial u/\partial y$ alone between these two stations of approximately $+14 \times 10^{-5}$ sec^{-1}.

The atmosphere's response within the next few hours south and east of this shear zone is to generate: 1) an elongated mesoscale high pressure ridge; 2) a major dust storm; 3) a low-level shearline associated with mesoscale divergence in excess of 10^{-4} sec^{-1} and microscale divergence in excess of 10^{-3} sec^{-1}; 4) two mesoscale low pressure troughs; 5) and several large tornadoes embedded within a rapidly moving squall line.

TOTAL TIME TENDENCIES OF DIVERGENCE GOVERNING TROPOSPHERIC FRONTOGENESIS

To understand what triggers this response, we turn to the two-dimensional (2-D) divergence equation in a z vertical coordinate system:

$$\frac{d\,Div}{dt} = (Div)^2 - \dot{\nabla}\alpha\cdot\nabla P - \alpha\nabla^2 P - 2\left(\frac{\partial v}{\partial x}\frac{\partial u}{\partial y} - \frac{\partial u}{\partial x}\frac{\partial v}{\partial y}\right) - \nabla w\cdot\frac{\partial \vec{V}}{\partial z} - \frac{\partial f}{\partial y}u + f\zeta - f\frac{\partial v}{\partial x} - \nabla\cdot\vec{F} \quad (5)$$

Classically, both in scale analysis work and in conjunction with initialization for synopticscale dynamical prediction models, the total time tendency of divergence on the lefthand side of equation (5) is assumed to be of trivial significance and a quasi-balance is assumed to exist between the following terms:

$$\underset{1}{-\nabla\alpha\cdot\nabla P} \quad \underset{2}{-\alpha\nabla^2 P} \quad \underset{3}{-2\left(\frac{\partial v}{\partial x}\frac{\partial u}{\partial y} - \frac{\partial u}{\partial x}\frac{\partial v}{\partial y}\right)} \quad \underset{4}{+f\zeta} \quad \underset{5}{-\frac{\partial f}{\partial y}u} \quad (6)$$

This group of terms represents the so-called non-linear balance expression. Computations at the Langley Research Center have indicated a substantial scale-dependence built into the terms in this expression. More specifically, when this expression is evaluated using finite-difference operators at several different space scales it becomes apparent that the terms $-\alpha\nabla^2 P$ and $-2(\partial v/\partial x\ \partial u/\partial y - \partial u/\partial x\ \partial v/\partial y)$ display the most significant scale-dependent variation.

For example: within the crucial shearing region below the tropopause, over the central Plains, the orders of magnitude of the above terms evaluated with a 168 km (½ global mesh) space operator are:

TERM	1	2	3	4	5	UNITS
Typical Order of Magnitude	$+10^{-10}$ to $+10^{-9}$	$+10^{-9}$	$+10^{-9}$	$+10^{-9}$	-10^{-10}	sec^{-2}

...and with a 42 km (1/8 global mesh) space operator:

Order of Magnitude and Sign	$+10^{-9}$	$+10^{-8}$ to $+10^{-7}$	$+10^{-8}$ to $+10^{-7}$	$+10^{-9}$	-10^{-9}	sec^{-2}

The NASA Langley capability of color coding the magnitudes of such meteorological quantities has proven invaluable in interpreting these multivalued forcing functions at their respective spatial scales. As a specific instance of scale dependent quantitative information being reduced to an effective visual display of information, we cite the following example. The term, $\alpha\nabla^2 P$, which evaluates the geometry of the mass field at a particular height in the atmosphere, varied from .025 at 1/16th mesh (21 km) to .000036 at full mesh (336 km) in absolute magnitudes (x 10^6) when diagnosed at 2750 m. To illustrate the term's scale dependence more effectively, the term's variation in magnitude at the 1/16th mesh was assigned the full range of 64 colors. Strong gradients from deep blue to brilliant red were evident just upstream of the eventual zone of tornado formation.

In contrast, the range of colors weighted against the absolute variance from 0 to 64 at the 1/16th mesh required to depict the diagnosed values of $\alpha\nabla^2 P$ at the other mesh lengths are listed within parentheses as a function of fractions of the full mesh length: 1/8th (10 to 50 colors); 1/4 (34 to 38); 1/2 (35.5 to 37.0); and full mesh (36.6 to 36.7). The lack of forcing exhibited by the geometry of the mass field at the longer length scales was easily discerned by the unaided eye as an unvarying color scheme which saturated the display screen at both the 1/2 and full mesh diagnostic evaluations. In lieu of the inability to provide color prints in this paper, illustrative samples of the diagnosed amplified imbalances in the 2-D divergence equation will be used to establish the mesoscale order of magnitude increase in terms 2 and 3 above.

The diagnosed positive imbalance in the region of the aforementioned strongly shearing flow forces the divergence dependent terms in equation (5) to increase and compensate, as would be expected from the terms $-u\partial u/\partial x$ and $-v\partial v/\partial y$ in the 2-D Navier-Stokes equations. Thus the appropriate kinematic flow regime will lead to the production of divergence approximating $+10^{-4}$ sec^{-1} over a period of 1 to 3 hours. Figure 2 shows the inversion which develops in this atmospheric volume as isentropes become compacted in the vertical. This marks the result of mid- to upper-tropospheric frontogenesis influencing the 320-328 K isentropes, as found over Peoria, Illinois 12 hours later at the break in the tropopause. This same cross section also captures the distended isentropes along a dashed line located where the tornado-producing squall line is approaching Flint, Michigan at 2400 GMT 12 April. In the next section, we will discuss

this frontogenesis and resultant extrusion of stratospheric air feeding into the squall line from the perspective of potential vorticity theory.

THE GENERATION OF POTENTIAL VORTICITY BY THE SOLENOID TERM TRIGGERING THE EXTRUSION OF STRATOSPHERIC AIR INTO THE TROPOSPHERE

The scale dependence associated with terms 2 and 3 mentioned above may be linked to another equation synthesizing atmospheric dynamics into a single mathematical statement for the conservation of mass, energy, and momentum. Ertel's potential vorticity theorem (ref.1) states:

$$\underset{a}{\frac{d}{dt}(\alpha\nabla\theta\cdot\vec{q}_a)} = \underset{b}{\alpha\,\vec{q}_a\cdot\nabla\frac{d\theta}{dt}} + \underset{c}{\alpha\nabla\theta\cdot\nabla\times\vec{F} - \alpha\nabla\theta\cdot\nabla\alpha\times\nabla P} \qquad (7)$$

where the quantity $\alpha\nabla\theta\cdot q_a$ represents potential vorticity and terms a-c are the diabatic heating, curl of friction, and solenoid terms, respectively. Terms a-c are source/sink terms for potential vorticity. In the absence of substantial diabatic heating, it seems consistent to expect the solenoid term to be a major source of kth-component potential vorticity and the curl of friction term a major sink in the mid- to upper-troposphere. It also is consistent from a mathematical perspective to expect an increased role to be played by term b when parcels, <u>already</u> having large potential vorticity values within the strong cyclonically shearing region, encounter a region of substantial potential vorticity increase generated by the solenoid term. Thus significant local increases in potential vorticity can occur when there is a large three-dimensional transport of potential vorticity in proximity to a maximization of the solenoid term.

If we return to the 350 mb jet maximum configuration, a possible link may be made between the total time tendencies of divergence and potential vorticity. First, the maximization of $-\nabla\cdot\nabla P$ in equation (5) is linked to the kth component of $-\alpha\nabla\theta\cdot\nabla\alpha\times\nabla P$. Large mesoscale values of $-\nabla\cdot\nabla P$ occur where the $\nabla_y\cdot\nabla_y P$ field changes substantially over a short distance such as in diffluent zones imbedded within the broad pressure field. Likewise, negative values of $\hat{k}\cdot\nabla\alpha\times\nabla P$ are enhanced where $\partial P/\partial x$ is substantially smaller than $\partial P/\partial y$ and of the appropriate sign, namely negative, and the fluid is stably stratified, i.e. $\partial\theta/\partial z>>0$. One would then expect large positive values of the solenoid term to be highly scale-dependent in order of magnitude as is $\nabla\cdot\nabla P$.

Calculations of $-\alpha\nabla\theta\cdot\nabla\alpha\times\nabla P$ indicate a one to two order of magnitude increase when evaluated on a 42 km mesh as opposed to 168 km mesh. This represents a variation from 10^{-9} to 10^{-7} as an extreme example. The positioning of the maximum positive solenoid term is displaced 100-300 km to the south and east of the maximum positive values of $(-\nabla\cdot\nabla P)$ sloping back towards the northwest between the 1200 and 7650 m levels. Thus the positioning of the maximum potential vorticity source term shown in Figure 3 is just to the southeast of maximum kinetic energy, cyclonic vorticity, potential vorticity, and divergence equation imbalance.

Parcels high in potential vorticity while experiencing substantial positive divergence equation imbalances will be deflected to the south and east of their original quasi-geostrophic trajectories. The downward component of motion due

to large d Div/dt in this volume characterized by the southeastward deflection will cause parcels to carry their tropopause momentum downward while generating high potential vorticity in the region of large positive ($-\alpha\nabla\theta\cdot\nabla\alpha x\nabla P$), thereby tapping the fluid's available potential energy, and thus forcing the curl of friction term to rapidly mix the fluid and act as a sink of potential vorticity. These processes are further amplified if: 1) there is a component of diabatic heating parallel to the maximum component of absolute vorticity, forcing the diabatic term to act as a potential vorticity source mechanism; 2) the depth through which vertical wind shear exists is quite shallow, thus enhancing the $w\partial w/\partial z$ term in the vertical equation of motion; 3) $\partial/\partial z\ \partial P/\partial z$ is substantial, as is often the case near the tropopause because of local potential temperature stratification.

In short, the total time tendency of the three-dimensional divergence is important and the fluid is effectively forced to be a compressible medium, implying unusually efficient energy-momentum transfer. It is thus acoustically-modified, leading to a maximization of $\nabla w\cdot\partial\vec{V}/\partial z$. Under circumstances such as these in which terms a and b play an important source/sink role, the total time tendency of $(\alpha\nabla\theta_E\cdot\vec{q}_a)$ or <u>equivalent</u> potential vorticity is a more complete representation of the total dynamics within the fluid (See ref.2, Paine and Kaplan). Figure 4 depicts the strongly deformed equivalent potential temperature isentropes at 1200 GMT 11 April leading to large negative gradients of $\partial\theta_E/\partial z$ over the stippled region. Such gradients yield atmospheric columns which will become absolutely convectively unstable as moisture convergence beginning within the next few hours saturates narrow mesoscale zones leading to squall-line formation.

THE PRESSURE TENDENCY EQUATION AS A LINK BETWEEN SEVERE TURBULENCE GENERATED NEAR THE TROPOPAUSE/TOPOGRAPHIC BOUNDARIES

It is the mechanism of the low-level pressure tendency which acts as the final link between the folding and eventual break of the tropopause boundary and the planetary boundary layer mesogenesis. The pressure tendency equation states:

$$\frac{\partial P}{\partial t} = -g\int_h^\infty \nabla\cdot\vec{V}\ \rho\ dz - g\int_h^\infty \vec{V}\cdot\nabla\rho\ dz + g(\rho w)_h \qquad (8)$$

At 1100 CST (Central Standard Time), 5 hours after the 1200 GMT sounding, the maximum low-level divergence and surface pressure rises are in NE Kansas. The southeastward and downward deflection of zonal kinetic energy which began over NW Kansas beneath the tropopause forces parcels towards the right of the mid- and upper-tropospheric jet maximum, leading to integrated velocity convergence and surface mesoscale pressure rises across NE Kansas.

For the previous 6 hours very low visibilities associated with blowing dust from southwest of Wichita, Kansas to northeast of Kansas City, has been the signature of the aforementioned downward transport of high potential vorticity values into the large solenoid term region in the lower troposphere. The surface wind vector at this time at Kansas City is blowing nearly perpendicular to the surface isobars with a sustained value in excess of 20 m sec^{-1}. This isallobaric flow carries low values of specific volume northeastward towards the tornado outbreak zone in NE Iowa. This process sustains super-

adiabatic lapse rates over a substantial portion of the lower troposphere as microscale eddies of heat and moisture are mixed into the downward extension of high potential vorticity values. Thus low Richardson number regimes are maintained as the mesoscale pressure rise pattern accelerates northeastward.

Hourly surface pressure, wind, and dewpoint observations shown in Figures 5a-d indicate a continuance of this process for the next eleven hours, culminating an extraordinarily occluded low-level frontal structure. (See ref. 3.) Mesopressure rises proceed northeastward from NW Missouri, NE Iowa, to NW Illinois, northern and central Indiana, southern Wisconsin and Michigan, and northern Ohio. As the mesoridge builds northeastward under the integrated convergence there is accompanying divergence of the isodrosotherms, lines of constant dewpoint, while the enhanced surface velocity convergence along the leading edge of the rise area associated with the intensification of the isallobaric wind is increased.

The tornadic storms are organized when this rapidly moving dry momentum surge forces a negative slope in the frontal structure. This allows enough vertical variation of convergence coupled with large vertical gradients of θ_e to permit the maximization of vortex tube stretching, i.e., $w\,\partial w/\partial z$ within the moist layer. (A situation in which the term $\nabla w \cdot \partial \vec{V}/\partial z$ in the divergence equation is maximized and the source/sink terms in the equivalent potential vorticity theorem are also maximized.)

In the area of the mesoscale trough formation ahead of the ageostrophic momentum surge, surface pressure falls have occurred due to integrated divergence. This, in turn, enhances low-level convergence. The maximization of low-level convergence ahead of the surge-line is a function of the proper juxtaposition of low-level $-\nabla \cdot \nabla P$ and $-2J(u,v)$ as well as negative solenoid fields. The maximum negative solenoid value in the lower troposphere is in western Illinois in close proximity to the surface mesotrough formation, intensification, and insipient tornado development beginning at 1300 CST.

CONCLUSIONS

In summary, it has been hypothesized that mesoscale pressure, kinetic energy, and moisture distributions are the product of hydro-thermodynamic processes which involve the nonconservation of both 2-D velocity divergence and potential vorticity following parcels. These deep, quasi-hydrostatic, divergence-convergence patterns flanking the jet stream are amplified over short time periods when the appropriate phasing occurs between the configuration of the velocity components and the divergence of the pressure gradient force per unit mass. The final stages of family tornado development arise where energy-momentum from the longer class of atmospheric wavelengths enters its smallest spatial and temporal envelope to be characterized as internal viscosity.

REFERENCES

1. Ertel, H.: Ein neuer hydrodynamischer Wirbelsatz. Meteor.Z., Vol. 59, 1942, pp. 277-281.

2. Paine, D. A.; and Kaplan, M. L.: An Equivalent Potential Vorticity Theory Applied to the Analysis and Prediction of Severe Storm Dynamics. Preprint Am. Meteor. Society 6th Conf. on Weather Forecasting and Analysis, May 1976, pp. 98-104.

3. Fujita, Tetsuya T.; Bradbury, Dorothy L.; and Van Thullenar, C. F.: Palm Sunday Tornadoes of April 11, 1965. Mon. Weather Rev., vol. 98, no. 1, Jan. 1970, pp. 29-69.

TABLE OF SYMBOLS

$\alpha_n, \beta_n, \gamma_n$	spatial derivatives
α	specific volume
θ	potential temperature
θ_e	equivalent potential temperature
η	eddy viscosity coefficient
ρ	density
ζ	kth-component relative vorticity, $\partial v/\partial x - \partial u/\partial y$
∇	spatial gradient operator $\hat{i}\partial/\partial x + \hat{j}\partial/\partial y + \hat{k}\partial/\partial z$
∇^2	Laplacian, second order spatial gradient operator
$\hat{i}, \hat{j}, \hat{k}$	unit vectors along x,y,z
$\partial/\partial t$	local time derivative
d/dt	total time derivative
∇x	spatial curl operator
$2\vec{\Omega} x \vec{V}$	Coriolis force
e	exponential
f	Coriolis parameter
g	gravitational acceleration
h	height
i	imaginary component
$\vec{q}_a$	3-D absolute vorticity
u,v,w	velocity components along i,j,k
$\vec{F}$	friction
$F_x F_y F_z$	summation of forces x,y,z-space
$\vec{V}$	3-D velocity vector
Div	$\nabla \cdot \vec{V}, \partial u/\partial x + \partial v/\partial y$, 2-D horizontal velocity divergence
P	pressure

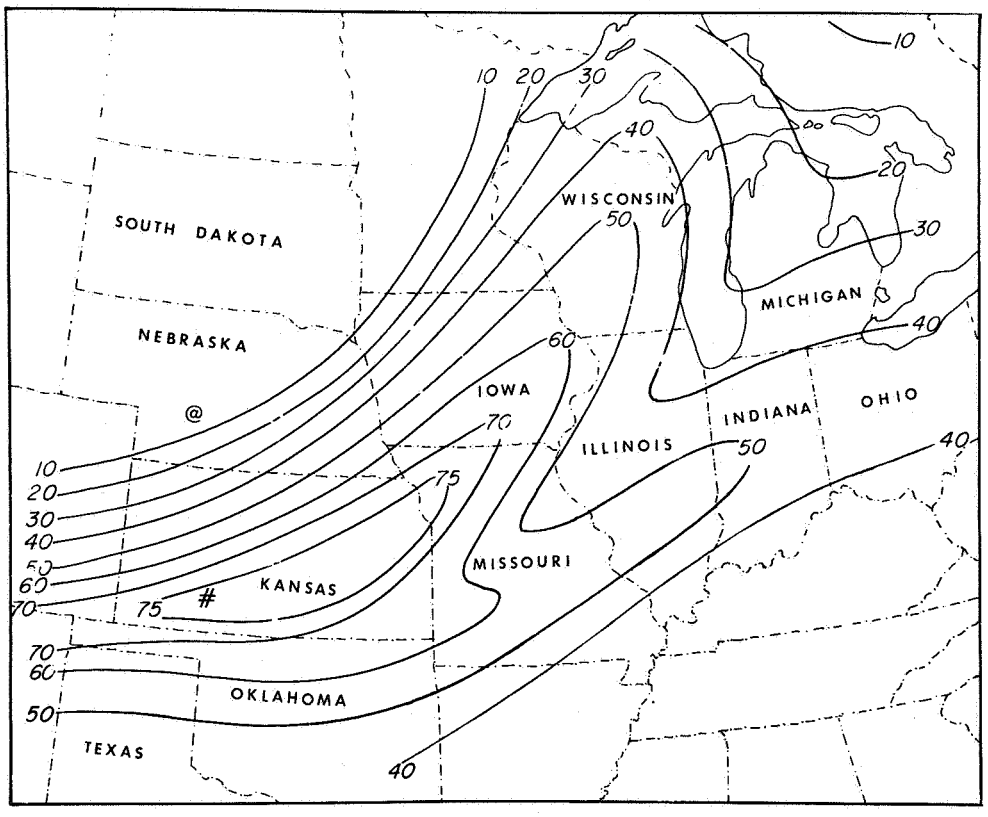

Figure 1.- 350 mb (≃ 8 km) wind isotachs in m sec^{-1} for 1200 GMT 11 April 1965.

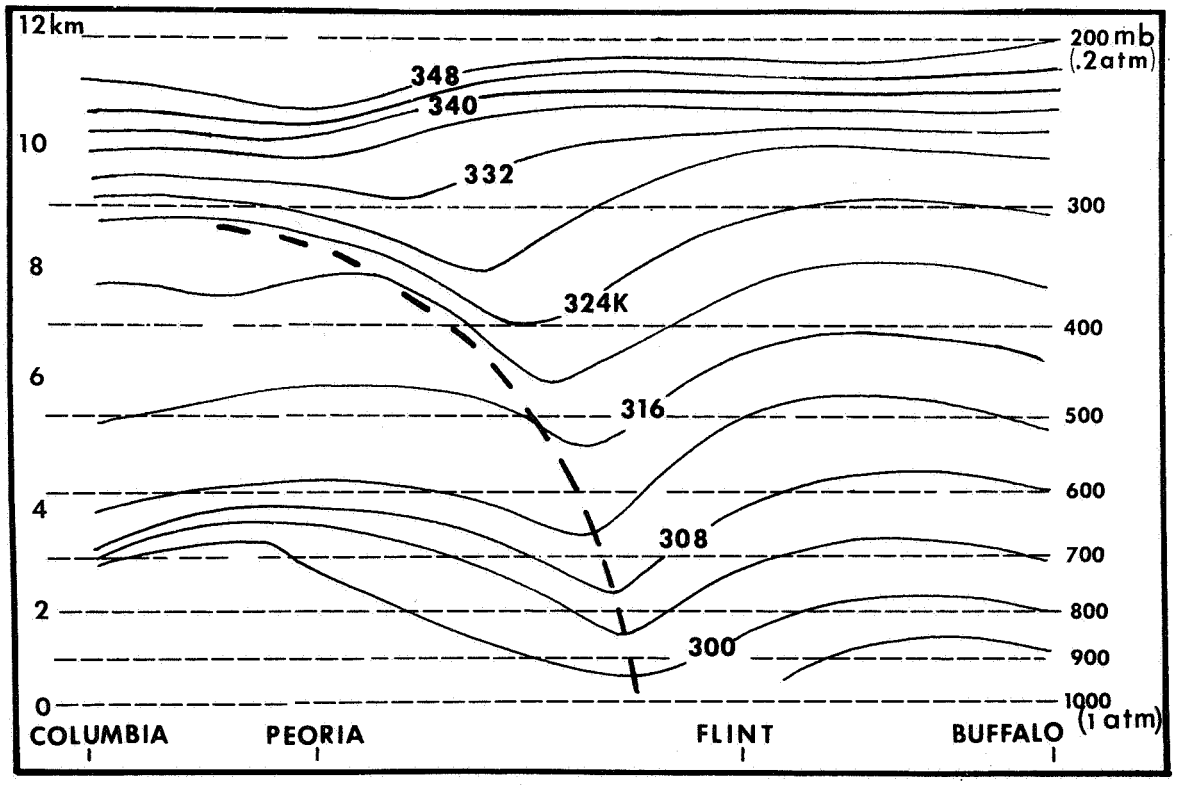

Figure 2.- Potential temperature (4 K intervals) vertical cross section for 2400 GMT 12 April 1965.

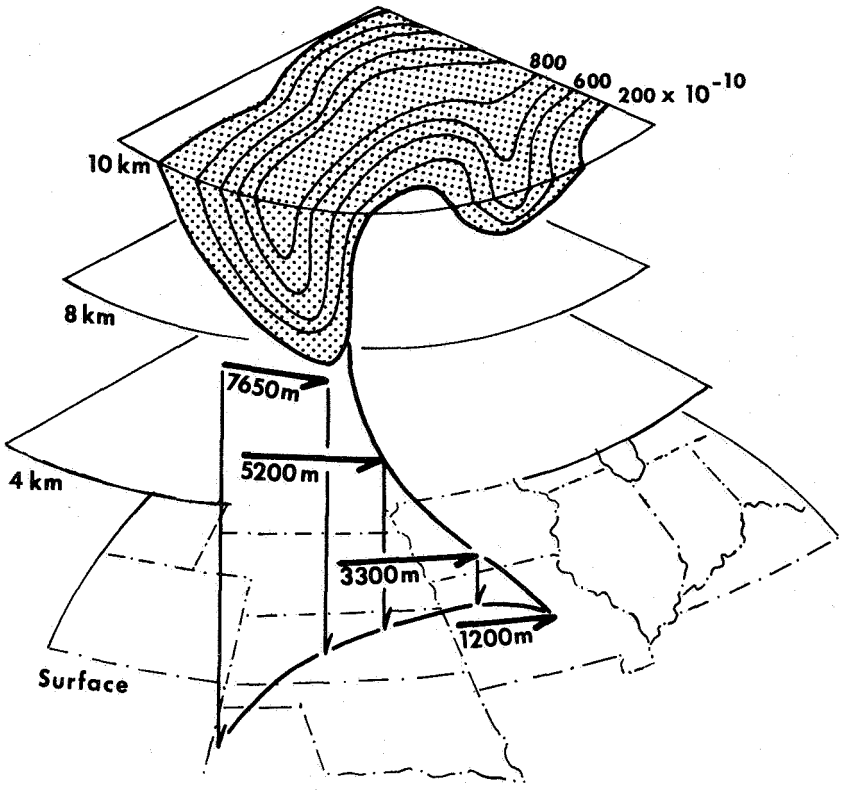

Figure 3.- Potential vorticity (x 10^{-10} $cm^2 g^{-1}$ K s^{-1}) plus solenoid source term.

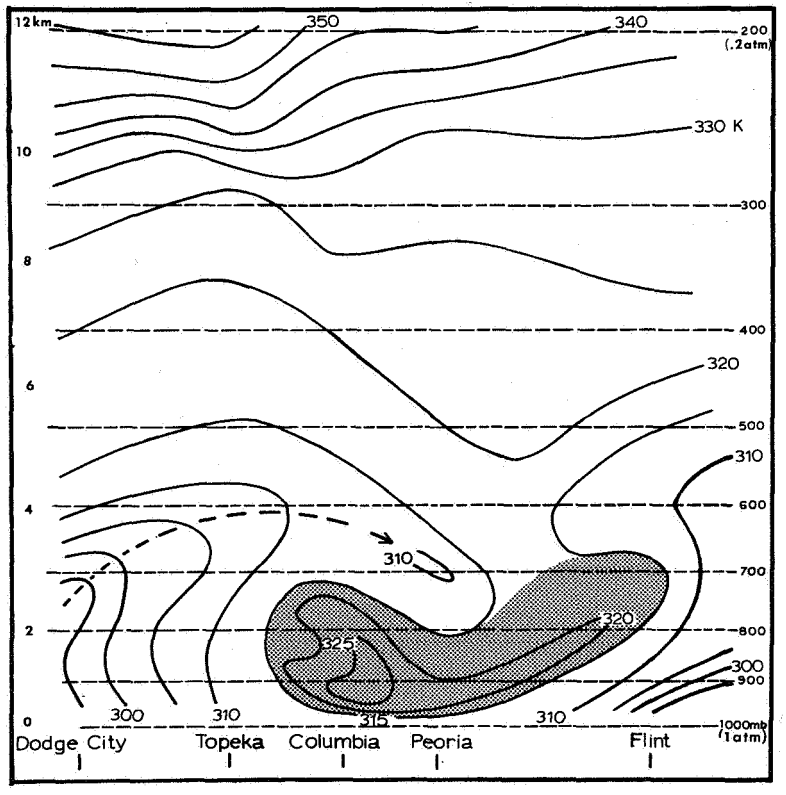

Figure 4.- Equivalent potential temperature (5 K intervals) vertical cross section for 1200 GMT 11 April 1965.

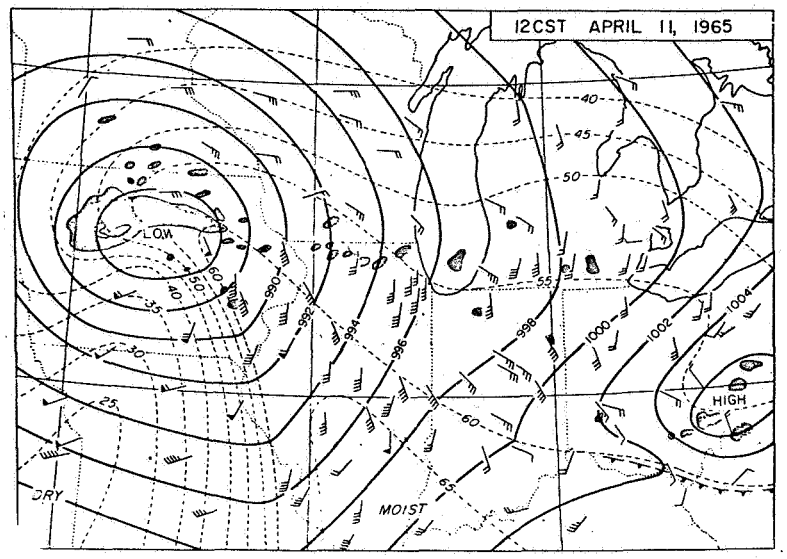

(a) Surface charts with sea level isobars (mb) as solid lines.

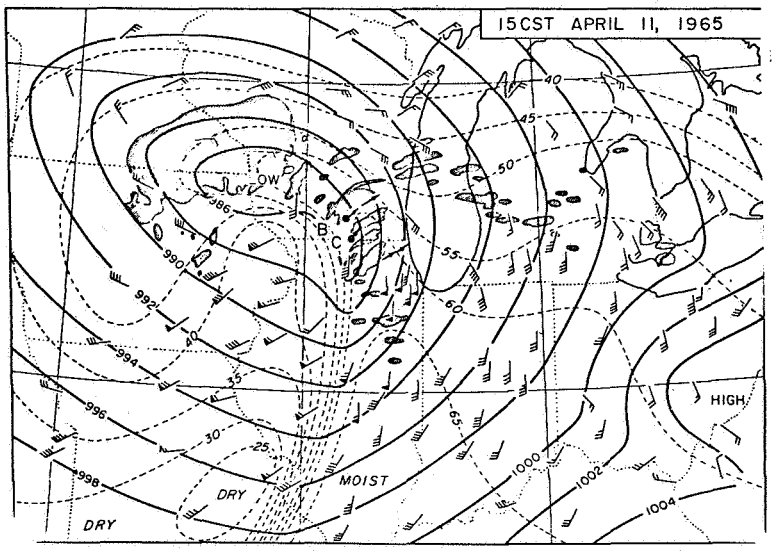

(b) Dashed isodrosotherms (^{o}F), and winds (full barb = 2.5 m sec^{-1}; flag = 12.5 m sec^{-1}).

Figure 5.- Surface weather during the Palm Sunday tornado outbreak.

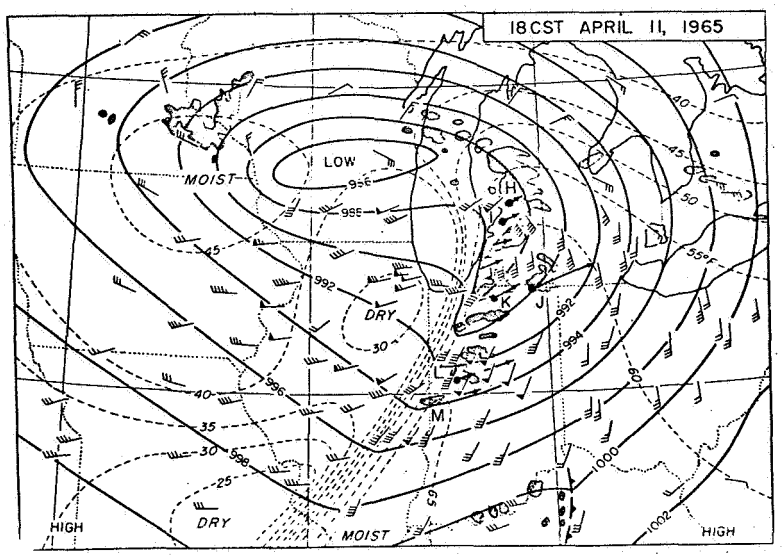

(c) Stippled areas indicate radar echoes and arrows show direction of motion of tornado echoes.

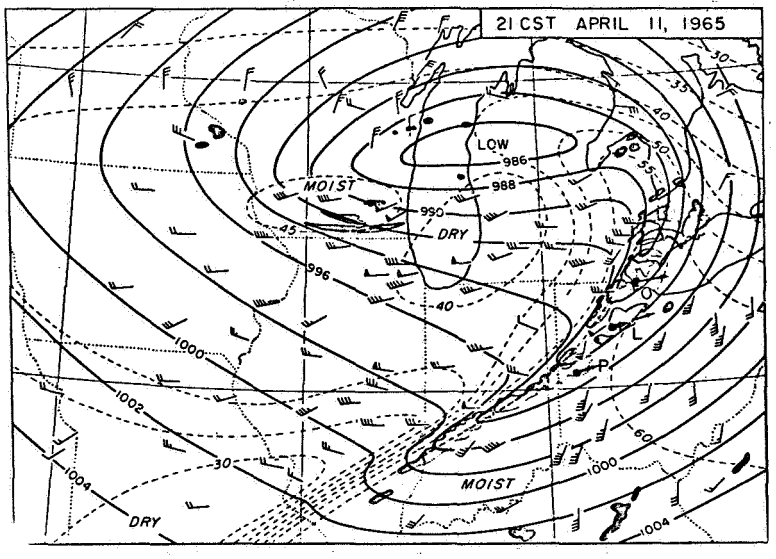

(d) Palm Sunday tornadoes of April 11, 1965. (See ref. 3.)

Figure 5.- Concluded.

SIMULATION OF THE ATMOSPHERIC BOUNDARY LAYER IN THE WIND TUNNEL FOR MODELING OF WIND LOADS ON LOW-RISE STRUCTURES

Henry W. Tieleman and Timothy A. Reinhold
Virginia Polytechnic Institute and State University

Richard D. Marshall
National Bureau of Standards

SUMMARY

In this paper a description is given of the simulation of the lower part of the atmospheric boundary layer (strong wind conditions) in the low-speed wind tunnel for the modeling of wind loads on low-rise structures. The turbulence characteristics of the turbulent boundary layer in the wind tunnel are compared with full-scale measurements described in the open literature and with measurements made at NASA Wallops Flight Center. Wind pressures measured on roofs of a 1:70 scale model of a small single-family dwelling are compared with results obtained from full-scale measurements. The results indicate a favorable comparison between full-scale and model pressure data as far as mean, r.m.s. and peak pressures are concerned. In addition, results also indicate that proper modeling of the turbulence is essential for proper simulation of the wind pressures.

INTRODUCTION

It has become clear that damage to low-rise structures is not usually due to wind loads acting over the entire structure, but it is initiated locally as a result of peak fluctuating pressures. The repeated application of these loads on small exterior areas may result in local failure of windows, cladding and roofing. These fluctuating pressures are associated with local separation and reattachment of the flow and the formation of strong vortices along the roof edges. The intensities of the pressure fluctuations are dependent on the turbulence intensity and the direction of the oncoming flow. Modeling of the pressures on scaled models in the wind tunnel can only be successful if the turbulence intensity and the turbulence integral scale in the approach flow are modeled adequately (ref. 1). Full-scale pressure measurements show that under certain conditions the amplitude probability distribution of the local pressures has a marked skewness in the negative direction (refs. 2 and 3).

In recent times, the results from research concerned with wind loads on high-rise buildings and other large structures have significantly influenced design practice. Full-scale measurements of wind loads and comparison of these results with data obtained from model studies in low-speed wind tunnels have confirmed the validity of design coefficients for load and struc-

tural response. A similar approach needs to be taken for wind load problems for low-rise structures, and eventually this should result in the update of those sections of building codes dealing with these problems.

SYMBOLS

$C_{\bar{p}}$	Mean pressure coefficient $\bar{p}/\frac{1}{2}\rho U_R^2$
C_p^{σ}	r.m.s. pressure coefficient $\sigma_p/\frac{1}{2}\rho U_R^2$
$C_{\hat{p}}$	Negative peak pressure coefficient $\hat{p}/\frac{1}{2}\rho U_R^2$
c, k	Weibull coefficients
L_u^x	Turbulence integral scale
n	Frequency
$\bar{p}$	Mean pressure
p_{max}	Negative peak pressure
$\hat{p}$	$p_{max} - \bar{p}$
P(>x)	Probability distribution function
$S_u(n)$	Power spectral density of the streamwise turbulence components
$S_p(n)$	Power spectral density of pressure signals
u, v, w	Turbulence components in x, y and z directions, respectively
$\overline{uw}$	Correlation between x and z turbulence components
U	Mean velocity
U_R	Mean velocity at the reference height z_R
U*	Shear velocity
X	Reduced variate, $(p_{neg} - \bar{p})/\sigma_p$
x, y, z	Coordinate directions (see figure 1)
z_R	Reference height (10 m full-scale and 14.3 cm for model)
α	Power index of the mean-velocity profile
β	Mean wind direction relative to the direction normal to the length of the model measured counter-clockwise

σ_p Standard deviation of the fluctuating pressure

ρ Air density

WIND TUNNEL MODEL TECHNIQUE AND SIMULATION OF THE FLOW

In order to achieve adequate simulation of the wind loads on low-rise structures, the following problems need to be considered:

a. Simulation of the approaching flow in the wind tunnel appropriate to a particular site.
b. Reproduction of the actual site and the prototype structure at the chosen geometric scale.
c. Measurement of the exterior surface-pressures (static component as well as dynamic component) on the model.
d. Statistical description of the fluctuating pressures which should include mean, r.m.s. and peak pressure coefficients, cross-correlation coefficients of pressures at various points, probability distribution of the peak pressures and pressure spectra.
e. Comparison of the statistical quantities representing the fluctuating pressures on the model with those obtained from full-scale measurements.

Preferably, the flow simulated in the wind tunnel should be compared with velocity measurements made near the prototype. In most cases, however, the full-scale velocity data are limited to measurements at one point. As an alternative one has to rely on wind data taken over similar terrain or results from review articles (refs. 4 and 5).

In short test-section wind tunnels, a thick turbulent boundary layer needs to be developed over a short distance. This can be achieved with the use of a system which depletes the momentum close to the tunnel floor and introduces large scale vorticity at the test section entrance. This flow is then allowed to pass over a fetch of boundary-layer roughness elements (fig. 1) which should create the appropriate simulation of the atmospheric boundary layer.

Models (1:70 scale) with different building geometries, including variations in roof slope (0, 10, 20 and 30 degrees), length to width ratio, length of roof overhang, as well as single- and two-story models were investigated for mean and fluctuating roof pressures with six pressure transducers. One of the test models is a 1:70 scaled model of a full-scale test house at Quezon City (ref. 6; fig. 2). The location of the test house is not the most ideal site, because several large structures are located nearby. However, some full-scale data are compared with model results and discussed in this paper.

EXPERIMENTAL TECHNIQUES AND MEASUREMENTS

Mean velocity and turbulence measurements were made initially at the model location (fig. 1) of the flow generated by the spire-roughness method. The flow was checked for two-dimensionality and for homogeneity in the direction of the flow. The experimental techniques used for the measurement of the mean velocity and the turbulence as well as the data analysis are described in

reference 7. Similarly, the full-scale as well as the model pressure measurements and their analysis are described in reference 6.

The free-stream dynamic pressure at a height of 1.5 m above the tunnel floor is maintained at 3.81 cm of water which corresponds to a velocity of 27 m/s. The reference velocity, U_R = 12.8 m/s, used throughout this paper is the mean velocity at the scaled reference height, z_R, of 14.3 cm corresponding to a full-scale height of 10 m.

DISCUSSION OF FLOW MEASUREMENTS

The mean-velocity profile measured at the model location (x,y = 0,0 cm) is shown in power-law form in figure 3 and semi-logarithmic form in figure 4. The results show a "smooth" velocity profile (α = 0.117 and z_o = 9.5 x 10^{-5} cm) up to a height of z/z_R = 0.2, and for heights 0.2 < z/z_R < 0.7 a "transition" profile. For heights of z/z_R = 0.7 and up to z/z_R = 4.5, the mean velocity profile shows a power index of α = 0.286 and a roughness length z_o = 0.69 cm. Figure 5 shows the turbulence-intensity distribution for the longitudinal velocity component measured at the model location. At the reference height z/z_R = 1.0, the intensities for the x, y and z turbulence components are 19.5%, 21.5% and 18.75%, respectively. Full-scale measurements show longitudinal turbulence intensities of 30% and 19.5% at the 10 m reference height for a power index of 0.29 and 0.125, respectively. The wind tunnel results show a 19.5% turbulence intensity for a power index of 0.29. This observation indicates that reproduction of the velocity profile does not automatically mean a correct turbulence intensity. As a matter of fact the simulation of the velocity profile needs to be relaxed if the primary requirement is the simulation of the turbulence intensity. In order to achieve a certain turbulence intensity in the wind tunnel simple geometric scaling of the upstream roughness is not sufficient. To the contrary, the upstream roughness elements need to be exaggerated in size which will result in a larger power index.

The turbulent shear-stress distribution (fig. 6) indicates a constant-stress layer up to a height of z/z_R = 1.75 (17.5 m full scale). The constant stress layer should be thicker according to full-scale measurements. This could be achieved by increasing the length of the fetch of upstream roughness-elements. In this case this length was limited because of the location of the turntable which was used for rotation of the models through 360 degrees.

The vertical distribution of the measured turbulence integral-scales, L_u^x, is shown in figure 7 for several positions near the model location. Using the mean-velocity power index of 0.29 and 0.125 the full-scale turbulence integral scale at the 10 m reference height should be 50 m and 150 m, respectively (ref. 5). For the 1:70 geometric scale ratio, a model integral-scale of 0.71 m and 2.14 m, respectively would be required. These requirements are impossible to achieve in a wind tunnel whose test section has a cross section of 1.8 m x 1.8 m. The actual measured integral scale at the reference height is 0.23 m which is nearly twice as large as the largest model dimension.

Spectra of the longitudinal turbulence component at heights of z/z_R = 0.2, 0.55, 1.0, 2.12, 2.88 and 4.27 at the model location are shown as a composite in figure 8. The spectra compare quite well with the von Karman spectrum-function which also provides an excellent fit to full-scale velocity spectra. The

parameters defining the flow obtained with the spire-roughness method and obtained in a long test-section wind tunnel with smooth floor are compared with the full-scale data from references 4 and 5 and independent measurements made at NASA, Wallops Island. These data are listed in Table 1.

COMPARISON OF THE PRESSURE MEASUREMENTS

Results of the full-scale and model tests on the building configuration shown in figure 2 are discussed in the following paragraphs. The wind directions do not correspond exactly. The full-scale wind data for the four available runs are listed in table 2.

The pressure coefficients, based on the dynamic pressure at 10 m for the full-scale data and based on the dynamic pressure at the scaled reference height in the wind tunnel, are shown in table 3. The agreement between model and full-scale for the mean pressure coefficients is fair. Some of the discrepancies can be explained to be a result of long-term drift of the transducers. Considerably more confidence can be placed in the full-scale pressure fluctuations, and the agreement between full-scale r.m.s. coefficients for nearly identical wind directions is significantly better. The agreement of the negative peak pressure coefficients is fair. The values of $C_{\hat{p}}$ for the wind tunnel data were obtained from stripchart recordings taken during rotation of the model and, therefore, are not associated with any specific record length.

The output signals from the six pressure transducers were recorded on a strip chart while the model was exposed to the simulated flow and rotated through 360 degrees at the same time. The mean pressure coefficients, $C_{\overline{p}}$, and the negative peak-pressure coefficients, $C_{\hat{p}}$, obtained from the strip charts are shown in figure 9. The results clearly indicate that the negative peak pressure coefficients are much larger in magnitude than the mean pressure coefficients. Wind loads on small areas needed for design of cladding are governed by the peak pressures and not by the mean pressures. The results indicate that these peak pressures occur near the edges of the roof with the wind normal to the roof edge and deviating $\pm$ 60 degrees from this normal direction.

It is well-known that the fluctuating pressures show larger negative peaks than positive peaks. Similar results are obtained for both model and full-scale measurements as shown by the pressure records in figure 10. As a result, the amplitude probability distribution associated with the negative pressure fluctuations depart substantially from a gaussian distribution at large amplitudes. For both full-scale and model, the negative pressure fluctuations can be described by a Weibull distribution (figure 11)

$$P(>x) = \exp[-(x/c)^k] \qquad (1)$$

where c and k are coefficients determined by curve fitting.

Two spectra of the fluctuating pressures which are matched at the low frequency end of the spectrum show the similarity of the model and full-scale results (fig. 12). This matching procedure leads to a scale ratio of 1:45, which compares favorably with the geometric scale ratio of 1:70.

A great deal of attention was paid to the simulation of the turbulent structure of the flow. In order to show that this is necessary, one of the models was tested in a smooth flow as well. The results show that the mean

pressure coefficients for smooth and turbulent flow are very similar (fig. 13). However, the negative peak pressure coefficients for smooth flow are negligible when compared with the negative peak pressure coefficients for turbulent flow (fig. 14). Consequently, the proper simulation of the turbulence is essential for the simulation of the fluctuating pressures.

CONCLUSIONS

The spire-roughness method is an excellent method for the reproduction of the flow of the atmospheric surface layer in a short test-section wind tunnel for the simulation of wind pressures on models of small-rise structures with a model scale of the order of 1:70. Based on the agreement between the dimensionless pressure coefficients, probability distributions and power spectra, it can be concluded that valid roof-pressure data can be obtained from models with relatively large geometric scale ratios. It is not possible to accurately model all flow features of the atmospheric surface layer with the technique described in this report. However, results obtained from this study and comparison with results from previous investigations suggest that the simulation of the turbulence intensity with a sufficiently large turbulence integral scale are the key factors for the success of the simulation of the fluctuating roof pressures.

REFERENCES

1. Marshall, R. D., "A Study of Wind Pressures on a Single-Family Dwelling in Model and Full-Scale", Journal of Industrial Aerodynamics, Vol. 1, No. 2, October 1975, pp. 177-199.
2. Eaton, K. J. and Mayne, J. R., "The Measurement of Wind Pressures on Two-Story Houses at Aylesbury", Journal of Industrial Aerodynamics, Vol. 1, No. 1, June 1975, pp. 67-109.
3. Eaton, K. J., Mayne, J. R. and Cook, N. J., "Wind Loads on Low-Rise Buildings - Effects of Roof Geometry", Building Research Establishment Current Paper CP1/76, Garston, Watford, U.K., January 1976.
4. Counihan, J., "Adiabatic Atmospheric Boundary Layers: A Review and Analysis of Data from the Period 1880-1972", Atmospheric Environment, Vol. 9, No. 10, pp. 871-905, October 1975.
5. Engineering Sciences Data Unit, "Characteristics of the Atmospheric Turbulence near the Ground, Part II: Single Point Data for Strong Winds (Neutral Atmosphere)", ESD Item No. 74031, October 1974.
6. Marshall, R. D., Reinhold, T. A. and Tieleman, H. W., "Wind Pressure on Single Family Dwellings", ASCE-EMD Specialty Conference; Dynamic Response of Structures: Instrumentation, Testing Methods and System Identification, UCLA Extension, March 30-31, 1976.
7. Tieleman, H. W., Reinhold, T. A. and Marshall, R. D., "On the Wind Tunnel Simulation of the Atmospheric Surface Layer for the Study of Wind Loads on Single Family Dwellings", ASCE-EMD Specialty Conference; Dynamic Response of Structures: Instrumentation, Testing Methods and System Identification, UCLA Extension, March 30-31, 1976.

TABLE 1 - Flow Characteristics for Wind Tunnel Simulation and Full Scale

Flow Characteristics	Full Scale References 4 and 5 (1)	(2)	Wallops Island Virginia (3)	Model Short Wind Tunnel Spire-Roughness Method (4)	Long Test-Section Wind Tunnel Smooth Floor (5)
Power Index α	0.29	0.125	0.13	0.29	0.15
Roughness Length, z_o (cm)	250	3.0	1.50	0.69	0.0013
$\sqrt{\overline{u^2}}/U^*$	2.5	2.5	1.22	1.67	1.62
$\sqrt{\overline{v^2}}/U^*$	1.875	1.875	1.34	1.89	—
$\sqrt{\overline{w^2}}/U^*$	1.25	1.25	—	1.68	1.29
$\sqrt{\overline{u^2}}/U_R$, %	30.0	19.5	17.4	19.5	6.25
$\sqrt{\overline{v^2}}/U_R$, %	23.0	13.0	19.0	21.5	—
$\sqrt{\overline{w^2}}/U_R$, %	15.0	8.5	—	18.8	5.0
$\overline{uw}/\sqrt{\overline{u^2}}\sqrt{\overline{w^2}}$	-0.32	-0.32	—	-0.36	-0.48
$(L_u^x)_R$ (m)	50	150	125	0.23	0.10

Reference height for data in column 3 is 15.2 m

Table 2. Full-Scale Flow Properties, Quezon City

Run	β Degrees	U_R m/s	$\sqrt{\overline{u^2}}$ m/s	$\sqrt{\overline{u^2}}/U_R$ %	$(L_u^x)_R$ m
3-2A	85.5	10.5	2.4	22.4	24.4
3-6A	81.5	7.3	1.9	26.5	
1-4	54.5	11.5	2.1	18.7	28.0
1-2	53.5	9.3	2.2	23.5	

Table 3. Comparison of Pressure Coefficients Model and Full Scale, Quezon City

	Tap No.	1	2	3	4	5	6
Run No.	β			Mean Pressure Coefficients, $C_{\bar{p}}$			
	0	-0.125	-0.119	-0.281	-0.230	-0.113	-0.189
Wind	20	-0.295	-0.139	-0.309	-0.289	-0.028	-0.198
	45	-0.641	-0.213	-0.257	-0.684	-0.120	-0.108
Tunnel	70	-0.657	-0.263	-0.120	-0.826	-0.623	-0.017
	90	-0.701	-0.138	-0.046	-0.704	-0.756	-0.022
Tests	225	-0.223	-0.189	-0.169	-0.135	-0.173	-0.189
3-2A	85.5	-0.20	-0.11	0.01	-0.33	-0.59	-0.42
3-6A	81.5	-0.72	-0.46	-0.31	-0.69	-0.95	-0.20
1-4	54.5	-0.34	-0.24	-0.03	-0.53	-0.64	-0.19
1-2	53.5	-0.57	-0.37	-0.23	-0.82		0.02
Run No.	β			R.M.S. Pressure Coefficients, C_p^{σ}			
	0	0.106	0.075	0.144	0.118	0.115	0.166
Wind	20	0.172	0.077	0.144	0.203	0.125	0.183
	45	0.254	0.122	0.111	0.377	0.311	0.148
Tunnel	70	0.287	0.150	0.097	0.387	0.473	0.094
	90	0.365	0.220	0.098	0.387	0.365	0.097
Tests	225	0.144	0.159	0.087	0.089	0.087	0.094
3-2A	85.5	0.22	0.12	0.11	0.36	0.27	0.10
3-6A	81.5	0.32	0.17	0.16	0.43	0.46	0.14
1-4	54.5	0.23	0.13	0.09	0.27	0.34	0.07
1-2	53.5	0.27	0.17	0.15	0.51	0.50	0.11
Run No.	β			Peak Pressure Coefficient, $C_{\hat{p}}$			
Wind	85.5	-1.85	-0.93	-0.35	-1.50	-1.27	-0.47
Tunnel	81.5	-1.70	-0.93	-0.33	-1.31	-1.20	-0.42
	54.0	-1.75	-0.70	-0.50	-1.93	-1.78	-0.81
Tests	53.5	-1.75	-0.70	-0.50	-1.93	-1.78	-0.81
3-2A	85.5	-1.32	-0.56	-0.35	-1.69	-1.94	-0.53
3-6A	81.5	-1.79	-1.05	-0.72	-2.34	-3.10	-0.64
1-4	54.5	-1.12	-0.54	-0.50	-1.20	-1.76	-0.37
1-2	53.5	-1.90	-0.87	-0.57	-2.75		-0.82

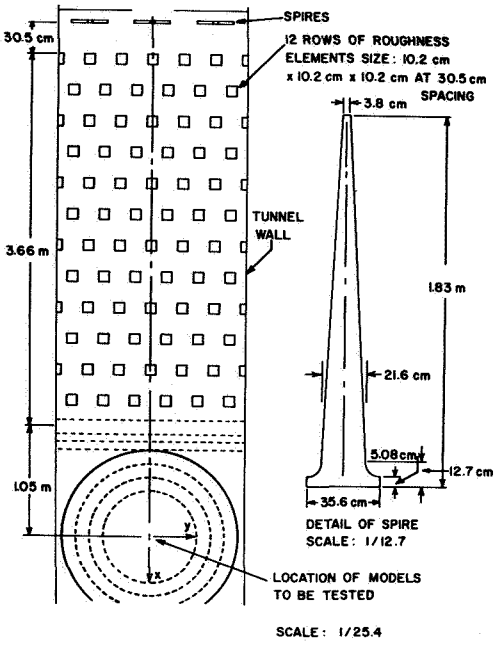

Fig. 1 - Wind Tunnel Configuration (Plan) and Spire Geometry

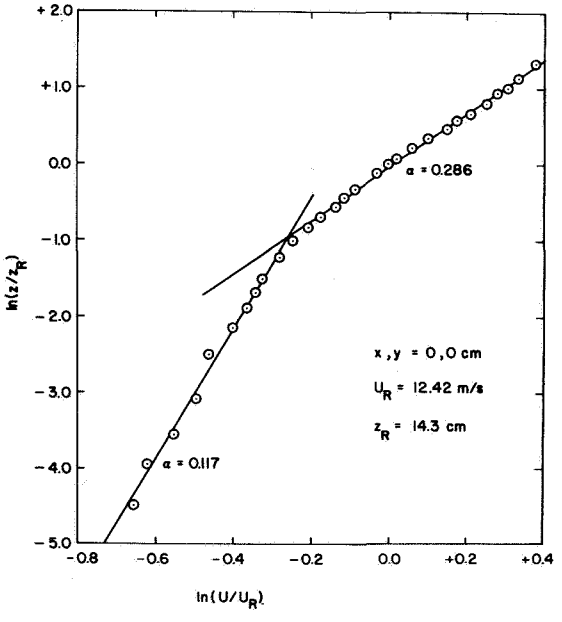

Fig. 3 - Mean Velocity Profile - Power Law Representation

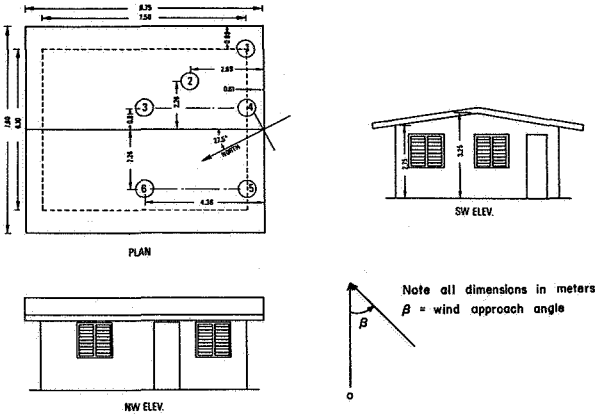

Fig. 2 - Experimental Building, Quezon City, Philippines

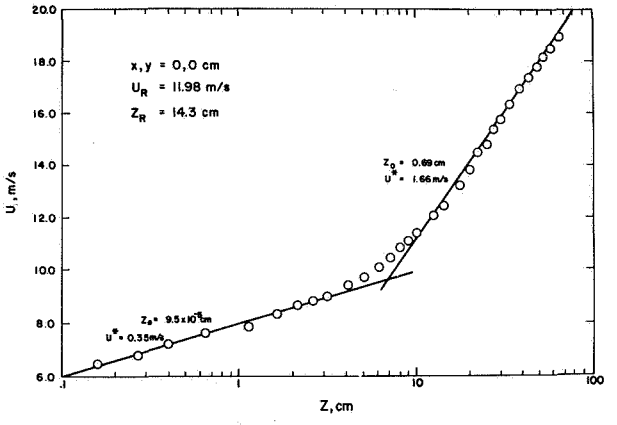

Fig. 4 - Mean Velocity Profile - Semilogarithmic Representation

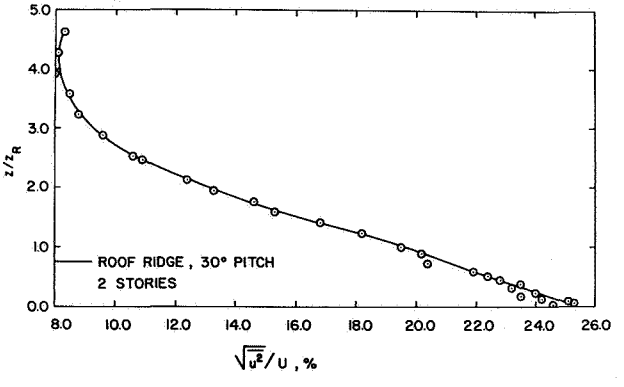

Fig. 5 - Turbulence Intensity - Streamwise Component - x,y = 0,0 cm

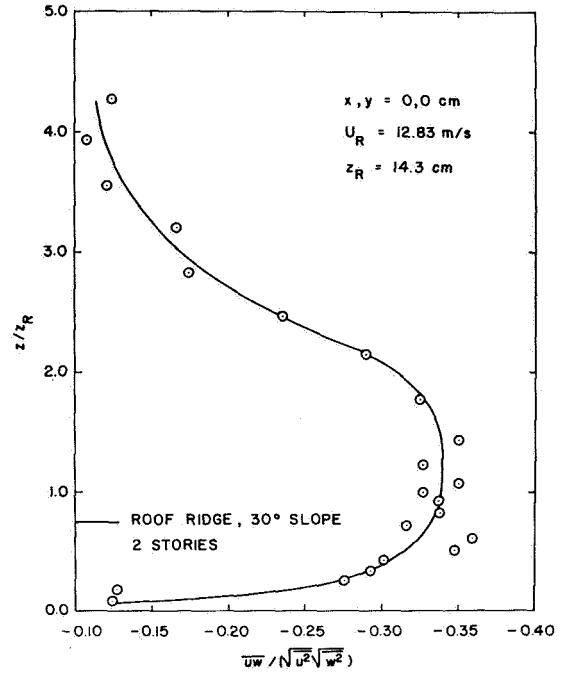

Fig. 6 - Turbulence Shear-Stress Distribution

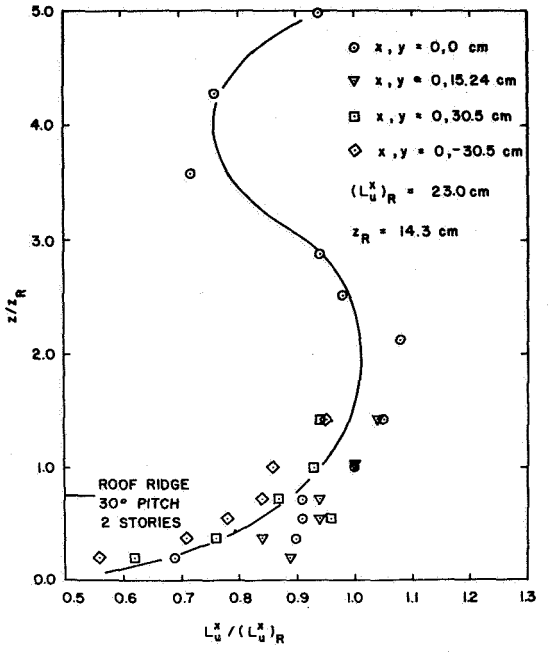

Fig. 7 - Variation of Integral Length Scale with Height

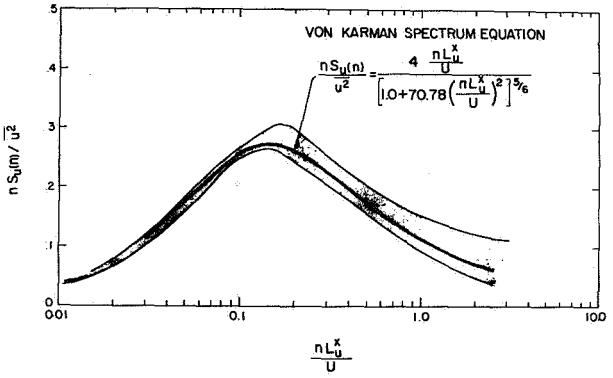

Fig. 8 - Turbulence Spectra - x,y = 0,0 cm

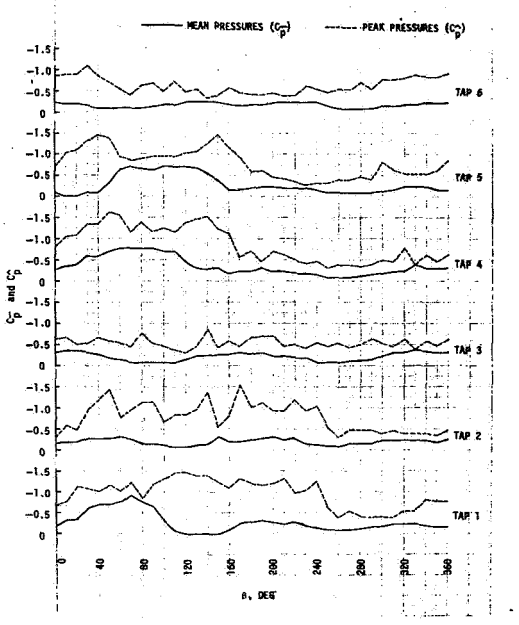

Fig. 9 - Mean and Negative Peak Pressure Distributions as a Function of Wind Approach Angle (Pitch 10°, L/W = 1.2, Eaves, 1 Story)

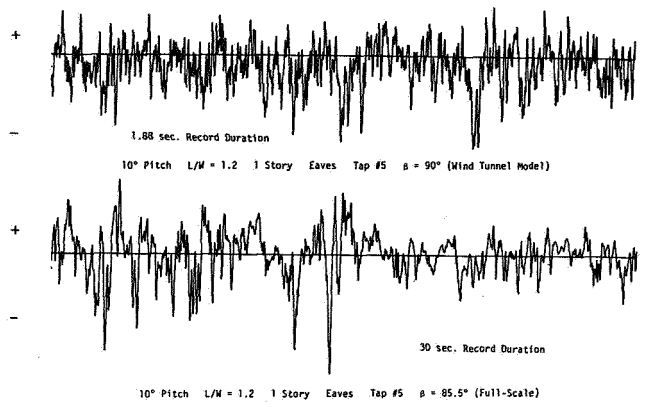

Fig. 10 - Records of Pressure Signals, Model and Full-Scale, Quezon City

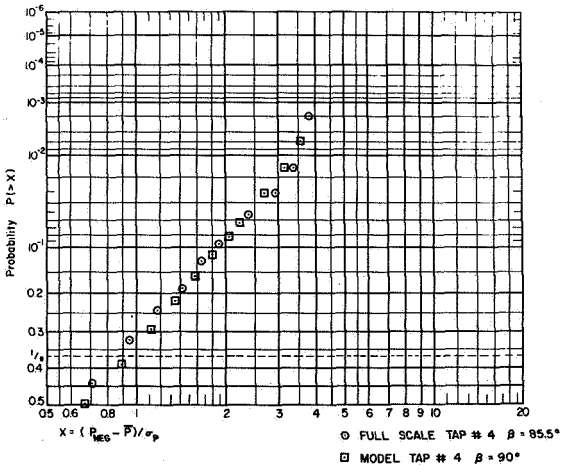

Fig. 11 - Probability Distribution of Negative Pressure Fluctuations

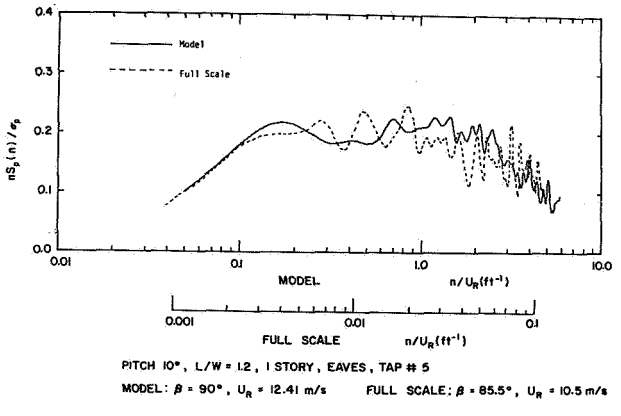

Fig. 12 - Pressure Spectra, Comparison of Model and Full-Scale, Quezon City

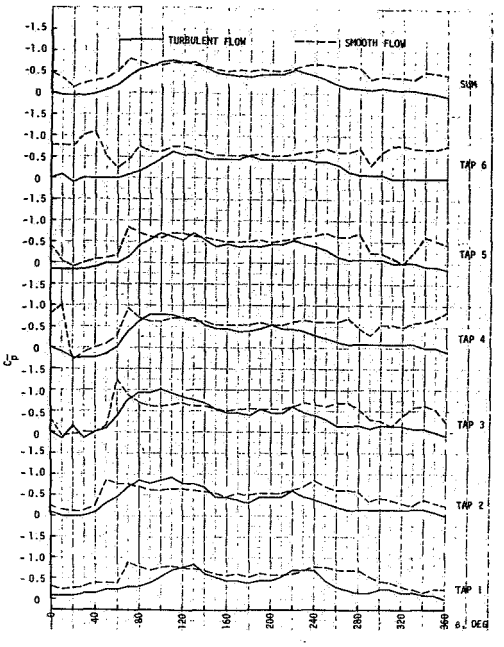

Fig. 13 - Mean Pressure Distribution for one of the Models (Pitch 30°, L/W = 1.2, 2 Stories, No Eaves) for Turbulent and Smooth Flow

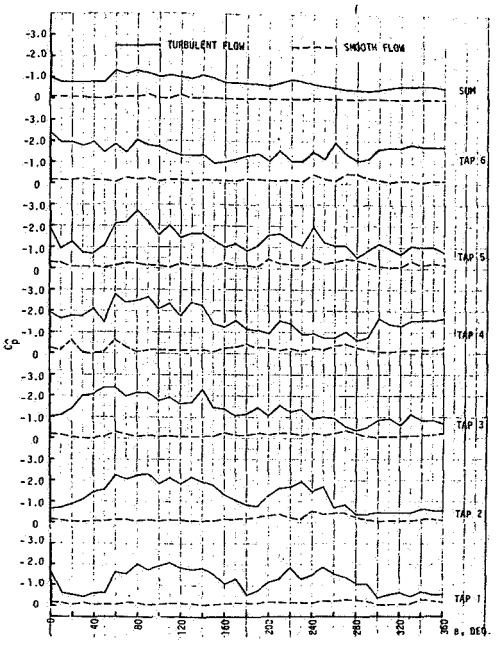

Fig. 14 - Peak Pressure Distribution for one of the models (Pitch 30°, L/W = 1.2, 2 Stories, No Eaves) for Turbulent and Smooth Flow

NUMERICAL SIMULATION OF TORNADO WIND LOADING ON STRUCTURES

Dennis E. Maiden
Lawrence Livermore Laboratory

SUMMARY

A numerical simulation of a tornado interacting with a building was undertaken in order to compare the pressures due to a rotational unsteady wind with that due to steady straight winds currently used in design of nuclear facilities. The numerical simulations were performed on a two-dimensional compressible hydrodynamics code. Calculated pressure profiles for a typical building is then subjected to a tornado wind field and the results are compared with current quasi-steady design calculations. The analysis indicates that current design practices are conservative.

INTRODUCTION

A major concern in the nuclear industry in the design of power, fuel fabrication, and fuel reprocessing plants is that the Nuclear Regulatory Commission (ref. 1) requires that the plants remain safe in the event of the most severe tornado that is likely to occur. Tornados are difficult to predict, and a geographical frequency-of-occurrence distribution is commonly used. Their physical properties have largely been based on eye-witnesses, movies, photographs, and damage assessment. The most important is the curve fitting of the results of Hoecker (ref. 2) for the Dallas tornado of 1957. Determination of wind speeds in tornados are only rough approximations (Mehta ref. 3). As a result of these studies, however, tornados have been characterized by a set of properties that are useful for purposes of structural design and siting. These properties are defined in Table 1 (ref. 1 and 3) for a regionalized Design Basis Tornado (DBT). (See ref. 4.)

PURPOSE OF NUMERICAL ANALYSIS

The meteorologists provide information on the validity of vortex models, their interaction with the ground, and the maximum attainable wind speeds. With this information they have constructed a simple vortex model of a tornado. They assume that the rotational component acts as a straight wind on interaction with a structure and thus they can compute the aerodynamic pressures with the aid of experimentally determined pressure coefficients. The pressure drop is treated independently and added to the previous result only to obtain the worst case. This is called the quasi-steady or "ANSI" (ref. 5) approach. The purpose of this paper is to bridge the gap between the vortex models and the structural design criteria by utilizing two-dimensional numerical fluid mechanical models in a self-consistent manner.

Wen (ref. 6) calculated significant dynamic loads on a structure due to a translating vortex by employing an empirical relation that accounted for the

"added mass" or acceleration effect as the fluid is forced around the structure. Hunt (ref. 7) later disproved Wen's analysis by computing exactly the loads on a cylinder and found them to be much less. He attributes them to lift in a rotating fluid. A further critique of tornado modeling is provided by Redmann et al. (ref. 8) in which they point out that Hoecker's data requires careful interpretation, that scaling relations for other tornados have little or no physical basis, and that the simple models are not physically consistent with fluid mechanical equations of motion and continuity.

Therefore the important questions to be considered are: based on fluid mechanics, does the ANSI approach give a reasonable approximation to the forces due to the tornado model described by the meteorologists? What are the engineers missing by taking the simplified approach? What are the limitations of the fluid mechanics?

TORNADO WIND MODEL

The simple vortex model is described fully in McDonald et al. (ref 9) and Rotz et al. (ref. 10). The parameters or the model are given in Table 1. The tangential velocity V_θ is assumed to be a combined Rankine vortex defined by

$$V_\theta = \begin{cases} \frac{r}{R_m} V_{\theta m} & 0 \le r \le R_m \\ \frac{R_m}{r} V_{\theta m} & R_m \le r < \infty \end{cases} \qquad (1)$$

where r is the radius from the center of the core, R_m is the radius at maximum tangential velocity, and $V_{\theta m}$ is the maximum tangential wind velocity. The radial velocity $V_r = V_\theta/2$ and the vertical velocity $V_v = 0$ for our purposes. The rotational velocity is defined as $V_{ro} = \sqrt{V_r^2 + V_\theta^2} = 1.12\ V_\theta$, V_t is defined as the translational velocity, and the maximum velocity is $V_{max} = V_{ro} + V_t$.

The atmospheric pressure drop P_a is obtained by integration of the cyclostrophic wind equation $dP_a/d_r = \rho V_\theta^2/r$ where P is the air density. The results are:

$$P_a = \begin{cases} \frac{\rho V_m^2}{2}\left(2 - \frac{r^2}{R_m^2}\right) & 0 \le r \le R_m \\ \frac{\rho V_m^2}{2}\left(\frac{R_m^2}{r^2}\right) & R_m \le r < \infty \end{cases} \qquad (2)$$

The vortex model is depicted in figure 4.

NUMERICAL ANALYSIS

The numerical simulation was performed on the two-dimensional hydrodynamic code BBC (ref. 11). Equations (1) and (2) along with the parameters of Table 1 were taken as initial conditions. This allowed a DBT to translate and interact with a typical structure. BBC is first order accurate with a numerical viscosity $D = V\Delta x/2$ and the diffusion distance of the velocity is approximately $d = \sqrt{Dt}$ where V is the velocity, Δx is the mesh spacing, and t is the time. In a typical

case V = 80 m/sec, Δx = 10 m, t = 1 sec and d = 20 m.

DESIGN ANALYSIS FOR TORNADO WINDS

Physical damage to buildings and structures is caused by two types of tornado-induced forces: (1) forces due to aerodynamic effects and (2) forces due to atmospheric pressure change.

Aerodynamically, buildings experience an inward acting force on the windward wall, and outward acting forces on the roof and on leeward and side walls as shown in figure 1. Forces due to atmospheric pressure change cause outward acting forces on all surfaces of a tightly closed building as shown in figure 1, and could cause explosive failure. With the exception of nuclear facilities, conventional facilities have sufficient openings to allow inside air to escape and hence do not experience forces due to atmospheric pressure change.

Essentially the design procedure (ref. 9 and 10) is to calculate wind loadings on structure by the ANSI Standard (ref. 5) method. Utilizing the parameters of Table 1 the velocity is imposed on the building in the manner depicted in figure 1. The velocity pressures are then calculated by

$$P_v = .5\, C_p\, C_s\, \rho\, V_{max}^2 \tag{3}$$

where C_p are aerodynamic pressure coefficients obtained from wind tunnel data for straight winds, C_s is the size coefficient, (ref. 9 or 10), ρ is the density of air, and V_{max} is the maximum horizontal velocity component. The maximum pressure drop from equation (2) is

$$P_a = \rho\, V_{\theta m}^2 \tag{4}$$

Equation (4) predicts a pressure less than that of Table 1 so the latter value is used for design. The design pressures are (ref. 9 or 10):

$$P = \max\,(P_a,\ P_v,\ P_v + 1/2\ P_a) \tag{5}$$

RESULTS AND DISCUSSION

Problem 1

In order to check out BBC a sample problem is considered of flow around a building 100 x 70 m (328 x 230 ft.). The results of BBC are shown in figures 2 and 3 for the case of a uniform velocity of 89.4 m/sec (200 mph). Good agreement with experimental pressure data is shown in Table 2. Apparently the numerical viscosity provides a fortuitous pressure drop on the leeward side.

Problem 2

This is a typical design problem of a tornado interacting with the building of Problem 1. This example was taken from reference 9 in which the tornado is translating toward the shorter side (side A). The parameters of the problem are from Table 1 with exception of the pressure drop in which equation (2) is used. Design pressures computed from equations (3) to (5) are given in Tables 3.1 to 3.3. BBC results for this example are shown in figures 4 to 6. Care should be taken in interpretation of the results since the tail on the free vortex was cut off at 150 m from the vortex center. This will lead to short time transient effects. The tornado is 160 m from the building and it will take 5 sec to get

there and 3 sec more to pass over. Therefore, the total pressures will be a sum of the aerodynamic pressure and atmospheric pressure drop. The pressure profiles taken at various times (fig. 5), however, are more representative of the aerodynamic forces since the building destroys the vortex and the pressure drop. The two-dimensional nature does not allow maintenance of the pressure drop. The corresponding velocity vector plots are shown in figure 6. Interpretation of the results should be made in conjunction with each other.

A comparison of BBC with design calculations are provided in Table 3.1 and 3.2. The values of average pressure are comparable for the windward acting force and 50 per cent lower for the leeward and side forces. The individual wall and roof panel results are low. Table 3.3 are the final design loads for the frame. The atmospheric pressure drop controls. Furthermore, there are no high values at the wall corners as there are in the straight wind calculations. The importance of this is that the design of the corner framing and edges of the building is costly due to the high loads predicted by a straight wind analysis. It is interesting to note that recent experiments by Cermak and Akins (ref. 12) show that the pressure coefficients are reduced by 50 per cent in a gradient wind field.

Figures 4 to 6 are the velocity vector plots as the tornado translates into the building at 31.3 m/sec (70 mph). The vortex is peeled off and the flow is redirected around the building. The strength of vortex is thus reduced along with the pressure drop. This result corresponds to the dissipation of a tornado by a tall building. In reality the tornado would have the bottom part of the funnel clipped off but the pressure drop would continue to translate and the rotating flow would recover due to shear by the time the tornado passed over the building. In the absence of a three-dimensional calculation it does appear that the superposition technique (i.e., aerodynamics and pressure drop treated independently) is reasonable because the building itself tends to decouple the flow.

Finally, one may argue that the flow is too complicated to be captured by BBC. However, Hunt (ref. 7) provides the argument that if the time scale of the tornado translation $T_t = R_m/V_t$ is greater than the time scale of the flow $T_f = L/V_{max}$ past the building then the separated flow region in the wake tends to shrink and potential flow model is a good approximation. For our case $T_t/T_f = V_{max}/L \cdot R_m/V_t = 360/240 \cdot 150/70 = 3.5$. Furthermore, the C_p values at the corners should be the standard values.

Problem 3

This is an interesting example where the tornado is directed toward side B but more head on as opposed to a glancing flow of problem 2. The results are shown in figures 7 and 8. It should be noted that the free vortex tail is out to 150 m and should be much larger. Note that the wall B (or the top T) experiences a negative pressure as in an airfoil.

Problem 4

The building of problem 2 was reduced to 40 x 40 m (131 x 131 ft.). The results were similar to problem 2.

CONCLUDING REMARKS

A two-dimensional numerical model was developed for the study of dynamic wind effects on structures.* A number of qualitative conclusions can be drawn from the numerical examples. They are summarized as follows.

1. Calculated pressure profiles for steady flow with straight winds are in good agreement with experimental data.

2. Calculated pressure profiles for rotational winds reveal no serious unsteady dynamic effects. The results are within the bounds of the ANSI approach.

3. The quasi-steady engineering approach of uncoupling the aerodynamic forces and the pressure drop is conservative. This conclusion is further supported by recent work of Cermak and Akins (ref. 12) who have performed wind experiments on a three-dimensional building placed in a turbulent boundary layer and also in a flow with a linear velocity gradient. In reference to tornado flows they say:

> "In the meantime wind loading for these more complex flows may be estimated by using force and moment coefficients determined in two-dimensional turbulent boundary layer flows and the maximum wind speed that is probable (see ANS proposed standard, 1976) for the meteorological event. On the basis of evidence presented in this paper such a procedure will lead to a conservative estimate."

4. The results in the paper represent the first calculation of a tornado like vortex interacting with a structure. Further calculations and refinements will be made in the future. A three-dimensional computer model would, however, provide a better representation of the flow field and corresponding pressures. These calculations should be done in conjunction with planned experiments of the type suggested by Cermak and Akins (ref. 12).

*This work was performed under the auspices of the U.S. Energy Research and Development Administration, under contract No. W-7405-Eng-48.

REFERENCES

1. Stevenson, J. D. "Application of Tornado Technology to the Nuclear Industry, Symposium on Tornadoes: Assessment of Knowledge and Implications for Man. Texas Tech University, Lubbock, Texas. (June 1976).

2. Hoecker, Jr. W. H., "Wind Speed and Air Flow Patterns in the Dallas Tornado of April 2, 1957," Mon. Weather Rev. 88, 167-180 (1960).

3. Mehta, K. C. "Windspeed Estimates: Engineering Analysis," (see ref. 1).

4. "Design Basis Tornado for Nuclear Power Plants," Regulatory Guide 1.76, Directorate of Regulatory Standards, U.S. Atomic Energy Commission (April 1974).

5. "American National Standard Code Requirements for Minimum Design Loads in Buildings and Other Structures," American National Standards Institute, A58.1 (1972).

6. Wen, Yi-Kwi "Dynamic Toradic Wind Loads on Tall Buildings," Jn. of the Structural Div., ASCE, p. 169 (Jan. 1975).

7. Hunt, J. C. R., Discussion on the paper by Wen, Jn. of the Structural Div., ASCE, p. 2448 (Nov. 1975).

8. Redmann, G. H., Radbill, J.R., Marte, J.E., Dergarabedian, P.,and Fendell, F.E. "Wind Field and Trajectory Models for Tornado-Propelled Objects EPRI Rept. 308 Electric Power Research Institute, Palo Alto, CA. (Feb. 1976).

9. McDonald, J.R., Mehta, K.C., and Minor, J.E. "Engineering for Tornados," Institute for Disaster Research and Dept. of Civil Engr. Texas Tech. University, Lubbock, Texas (Feb. 1975).

10. Rotz, J.V., Yeh, G.C., and Bertwell, W. "Tornado and Extreme Wind Design Criteria for Nuclear Power Plants," Bechtel Power Corporation Rept. BC-TOP-3-A Rev. 3, San Francisco, CA (Aug. 1974).

11. Sutcliffe, W.G., "BBC Hydrodynamics" Lawrence Livermore Laboratory Rept. UCID-17013, Livermore, California (1974). This code was developed in collaboration with R. Litterst and S. Warshaw; the latter provided the tornado initial conditions.

12. Cermak, J.E. and Akins, R.E. "Wind Loads on Structures," (see ref. 1).

TABLE 1 - DESIGN BASIS TORNADO CHARACTERISTICS, REGION 1

V_{max} = 160.9 m/sec (360 mph)	V_{ro} = 129.6 m/sec (290 mph)
V_m = 115.8 m/sec (259 mph)	$P_a(0)$ = .207 bars (432 psf
V_t = 31.3 m/sec (70 mph)	R_m = 45.7 m (150 ft)

*Region 1 is East of the Rocky Mountains

TABLE 2 - COMPARISON OF EXPERIMENTALLY DERIVED DESIGN PRESSURE WITH BBC FOR STEADY FLOW (Problem 1)

Location	C_p	Design Pressure		BBC (Figure 2)	
		bars	psf	bars	psf
Windward	.8	+.039	+81.5	+.032	+66.8
Roof or Side	-.7	-.034	-71.0	-.07	-146.
Leeward	-.5	-.025	-52.2	-.04	-83.5
Windward Side Wall Corner	-2.0	-.098	-205.	-.10	-208.9

TABLE 3.1 - COMPARISON OF AVERAGE PRESSURES WITH BBC FOR FRAME DESIGN (Problem 2)

Location	Wind Direction	L		P_{max}/P_{ave} C_s	C_p	Design Pressure		BBC		
		m	ft			bars	psf	bars	psf	
Windward	A*	73.2	240	0.512	0.8	+.065	+136	±.05	±104	
	B*	99.1	325	0.425	0.8	+.054	+113			
Leeward	A	73.2	240	0.512	-0.5	-.041	-85	-.02	-42	
	B	99.1	325	0.425	-0.5	-.034	-72		(±63)	T
Roof or Side	A	73.2	240	0.512	-0.7	-.057	-119	(±.03)	125	B
	B	99.1	325	0.425	-0.7	-.047	-99	+.06		

*A = Toward short side of building.
*B = Toward long side of building.

TABLE 3.2 - COMPARISON OF LOCAL PEAK PRESSURES WITH BBC FOR LOCAL MEMBER DESIGN. (Problem 2).

Location	C_p	Local Design Pressure		BBC	
		bars	psf	bars	psf
Wall Corners	-2.0	-.318	-664	-.07	-146
Eaves	-2.4	-.382	-797		
Roof Corners	-5.0	-.795	-1660		
Design for Individual Wall and Roof Panels					
Windward Wall	+0.8	+.127	+266	+.07	+146
Leeward Wall	-0.5	-.079	-166	-.06	-125
Side Wall	-0.7	-.111	-232	-.05 (+.1)	-104 T (+209) B
Roof Panel	-0.7	-.111	-232		

TABLE 3.3 - TYPICAL TORNADIC DESIGN LOADS FOR FRAME DESIGN (EQ.5)

Load Combination Weight	Wind Direction	Windward		Leeward		Roof or Side	
		bars	psf	bars	psf	bars	psf
P_v	A *	+.065	+136	-.041	-85	-.095	-199
	B *	+.054	+113	-.034	-72	-.047	-99
P_a	A	-.207	-432	-.207	-432	-.207	-432
	B	-.207	-432	-.207	-432	-.207	-432
$P_v + .5\ P_a$	A	-.038	-80	-.144	-301	-.160	-335
	B	-.049	-103	-.138	-288	-.151	-315

*A = Toward short side of building.
*B = Toward long side of building.

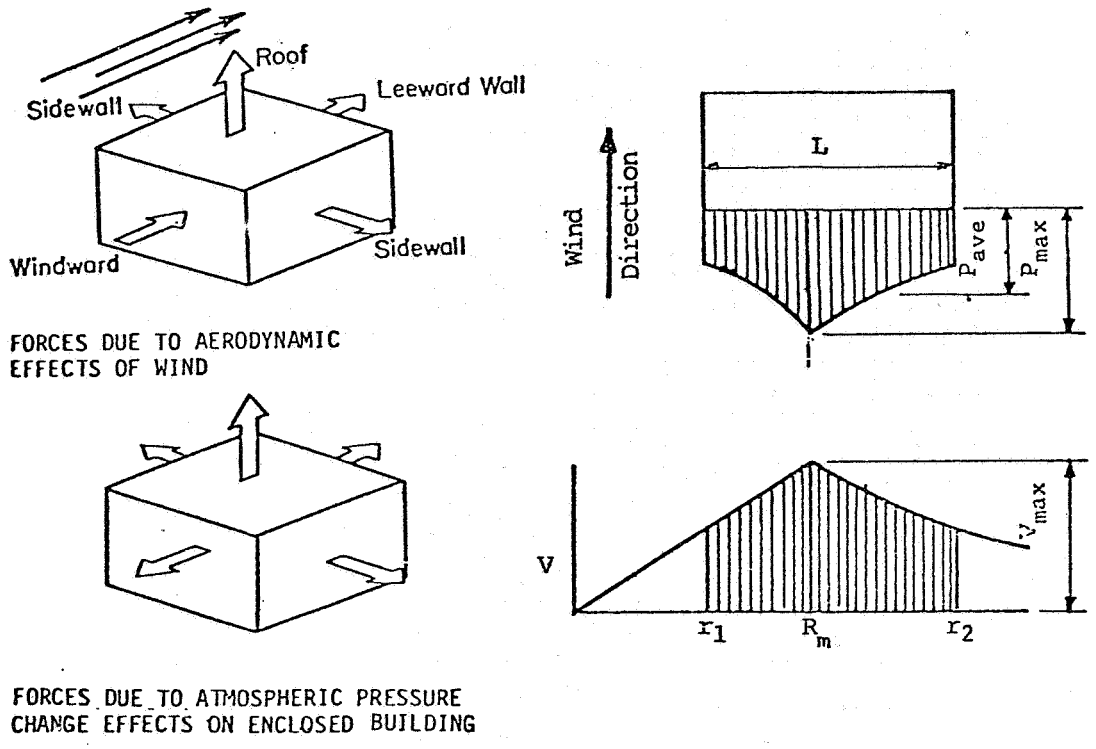

Figure 1.- Decomposition of tornado wind forces into aerodynamic and pressure drop force components; also shown is a typical velocity pressure loading diagram.

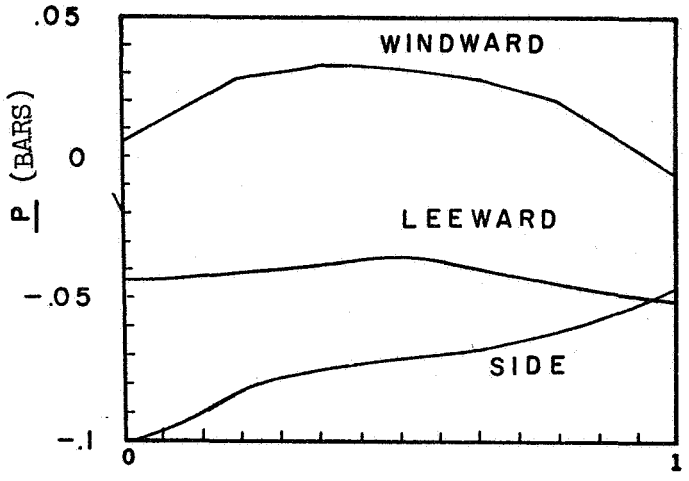

Figure 2.- Steady state pressure profiles for problem 1. (Distance is normalized.)

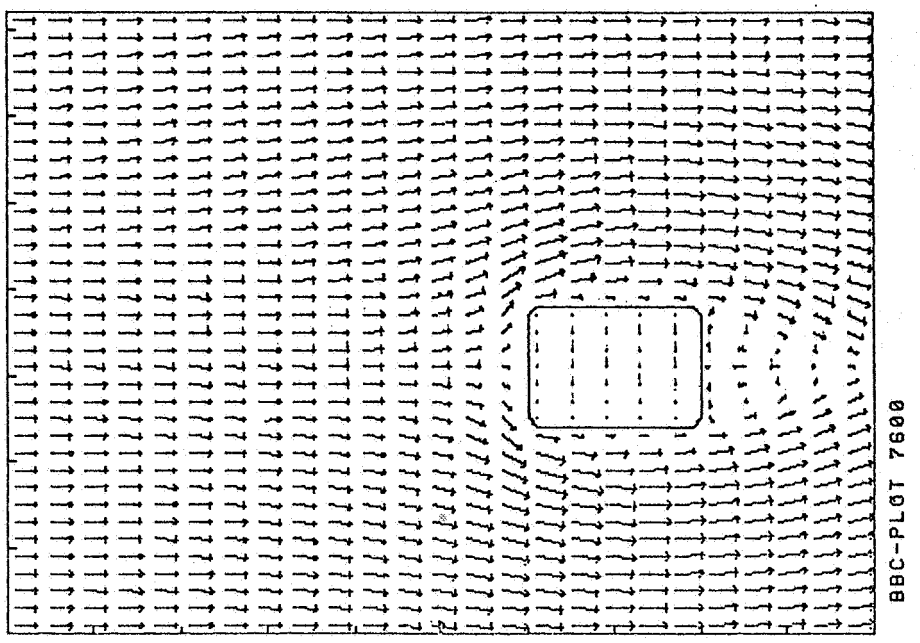

Figure 3.- Steady state velocity vectors for problem 1 with V_{max} = 114. m/sec (255 mph) at T = 2.0 sec.

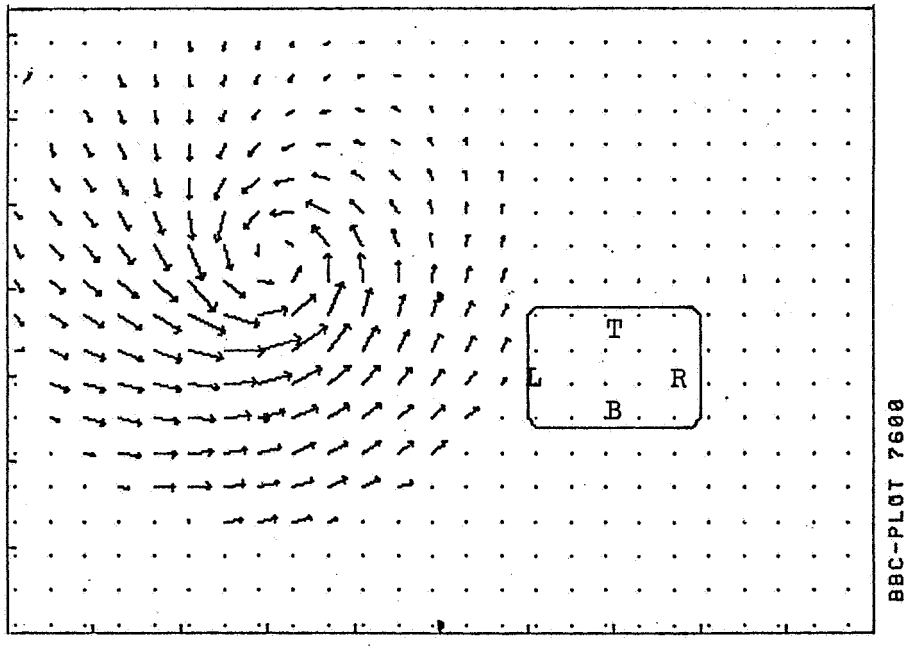

Figure 4.- Initial velocity vectors for the tornado of problem 2 with V_{max} = 156. m/sec (350 mph) and T = 0.0 sec.

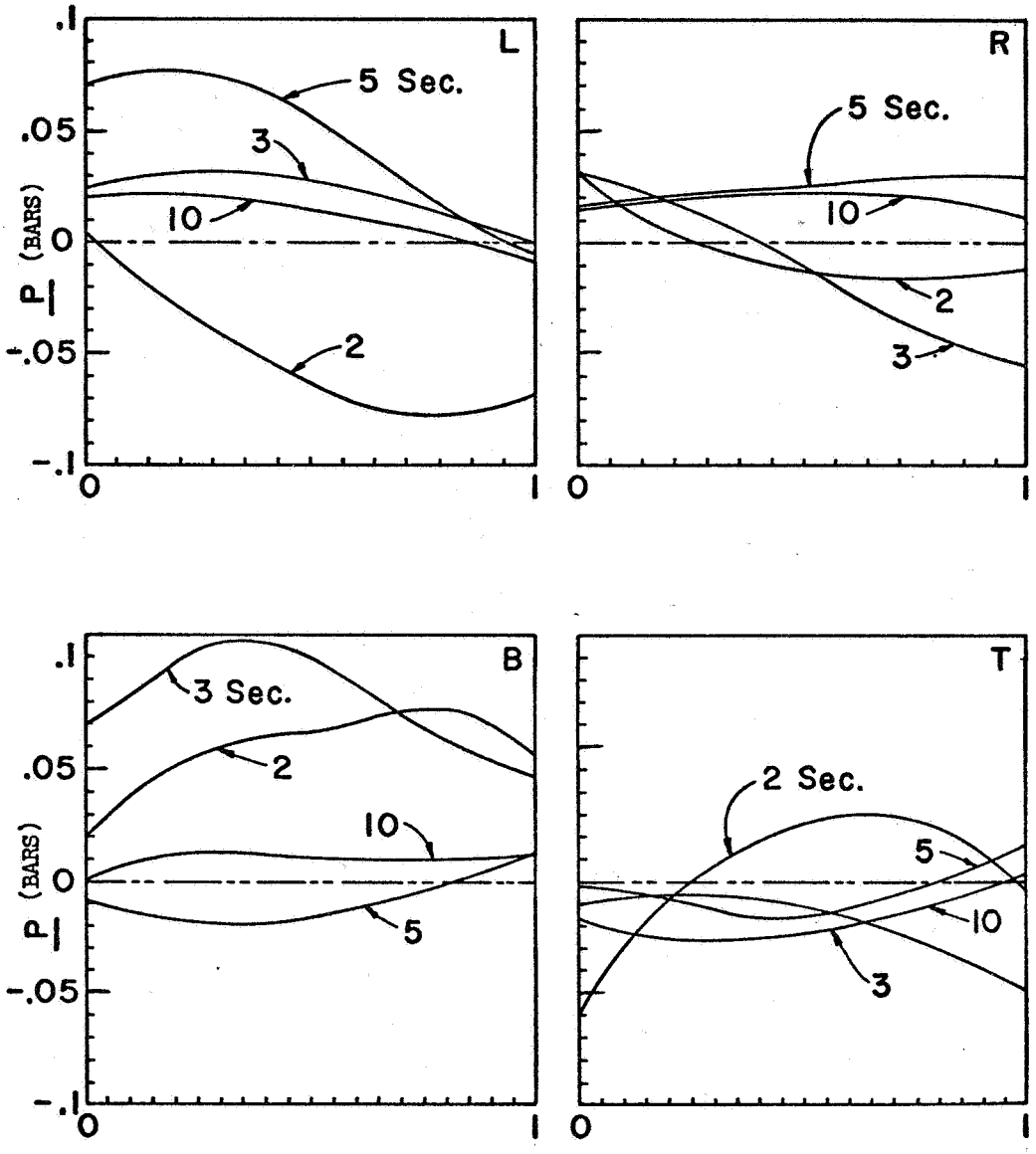

Figure 5.- Pressure profiles for problem 2 taken at various times and on the sides indicated in figure 4 (distance is normalized).

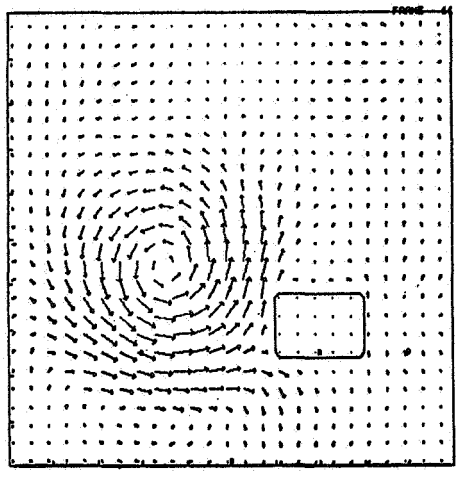

V_{max} = 76.4 m/sec (171 mph)
at t = 2 sec.

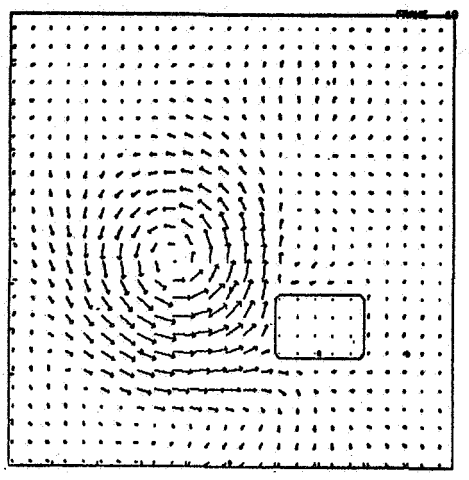

V_{max} = 73.7 (165 mph)
at t = 3 sec.

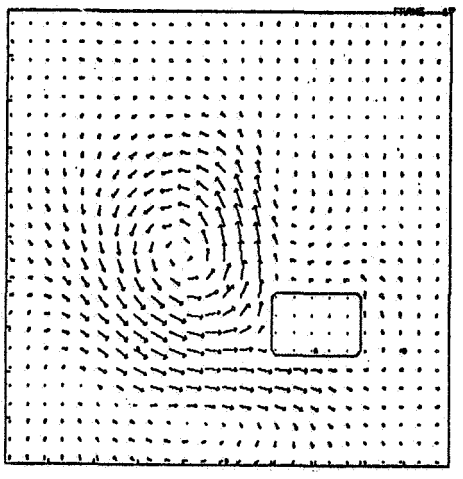

V_{max} = 72.4 m/sec (162 mph)
at t = 5 sec.

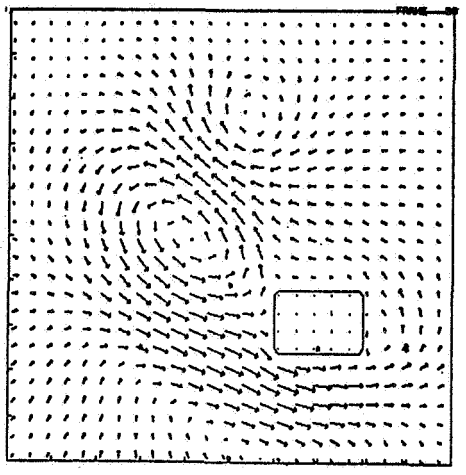

V_{max} = 48.2 (108 mph)
at t = 10 sec.

Figure 6.- Velocity vector plots for problem 2.

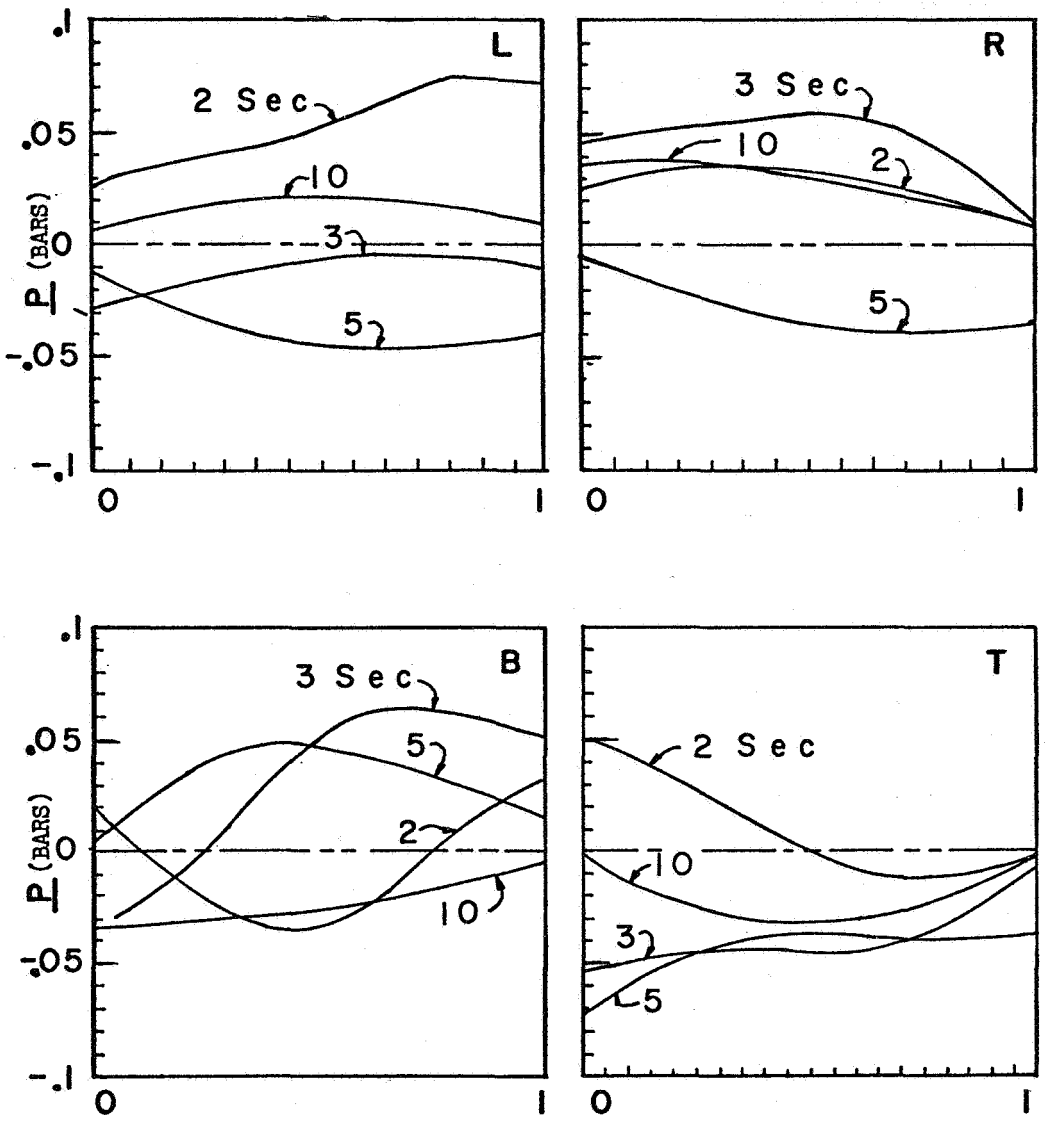

Figure 7.- Pressure profiles for problem 3 taken at various times and on the sides indicated in figure 4 (distance is normalized).

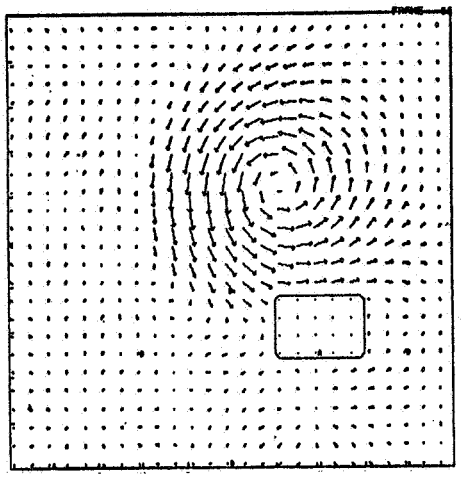

V_{max} = 83.7 (187 mph)
at t = 2 sec.

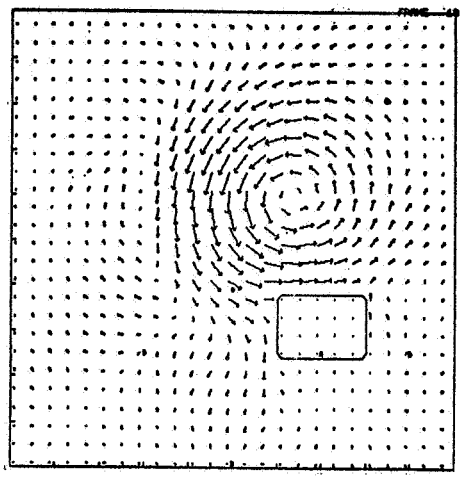

V_{max} = 74.9 (168 mph)
at t = 3 sec.

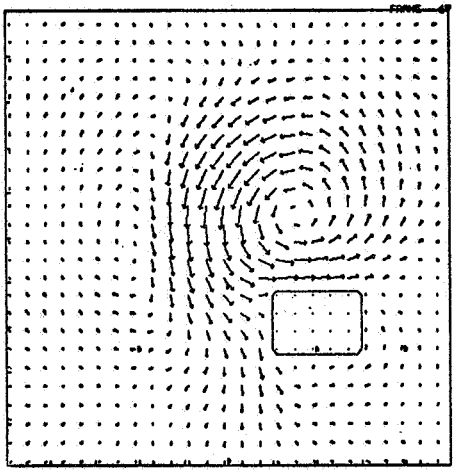

V_{max} = 68.5 (153 mph)
at t = 5 sec.

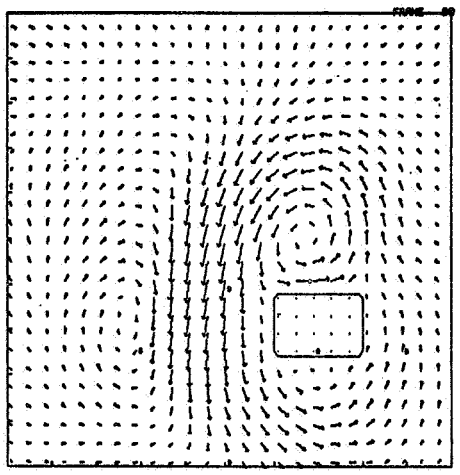

V_{max} = 49.9 (112 mph)
at t = 10 sec.

Figure 8.- Velocity vector plots for problem 3.

THE MAKING OF THE ATMOSPHERE

Joel S. Levine
NASA Langley Research Center

SUMMARY

The Earth's atmosphere and oceans are assumed to have accumulated as a result of volatile outgassing from the Earth's interior. The bulk of the outgassed volatiles were originally trapped within the solid Earth during the planetary accretion process, while other volatiles resulted from radiogenic decay within the solid Earth. Atmospheric oxygen resulted from the photodissociation of water vapor during the Earth's early history and from photosynthetic activity in more recent times. The origin and evolution of atmospheric ozone is closely related to the growth of oxygen. The rise of ozone and the evolution of life is discussed in terms of an evolving oxygen atmosphere.

THE ATMOSPHERES OF VENUS, EARTH AND MARS: A COMPARISON

Before we can accurately assess and critically evaluate the effects of anthropogenic activities on the atmosphere (i.e., the possible inadvertent depletion of stratospheric ozone, increased concentrations of atmospheric carbon dioxide, etc.), we must understand the natural variability, as well as the longer-term evolution of the atmosphere. Two of the constituents of the Earth's atmosphere most relevant to living systems, oxygen and ozone, are both recent additions to the atmosphere on a geological time-scale.

To consider the complexities of the question of the evolution of the Earth's atmosphere consider the atmospheric composition of our two neighboring worlds - Venus and Mars. The atmospheric composition of Venus, Earth and Mars is summarized in table I and references 1 to 8. It is generally believed that all three planets formed from the same material at about the same time (about 4.5×10^9 years ago). Yet table I shows the atmospheric composition of these neighboring worlds to be quite dissimilar. The atmospheres of both Venus and Mars are almost devoid of nitrogen and oxygen, the two major constituents of the Earth's atmosphere. Furthermore, carbon dioxide, the major atmospheric constituent of both Venus and Mars is only a trace constituent of the Earth's atmosphere.

In this paper a scenario for the evolutionary history of the Earth's atmosphere will be discussed. Recently scenarios for the evolutionary history of the atmospheres of Venus (Reference 9) and Mars (Reference 10) have been discussed.

THE OUTGASSING HISTORY OF EARTH:

TRAPPED VOLATILES

There is considerable and varied evidence (astronomical, aeronomical, geological, geochemical and biological) to suggest that the Earth's atmosphere and hydrosphere formed over geological time due to volatile outgassing from the interior, as opposed to being a remnant of the primordial solar nebula that enveloped the Earth during its formation (References 11-17). The outgassed volatiles were either originally trapped in the solid Earth during the planetary accretion process or resulted from radiogenic decay. The presence of oxygen in the Earth's atmosphere is an important exception to the outgassing hypothesis and will be treated separately in a later section.

The gases trapped in the solid Earth during the planetary accretion process reflected the cosmic abundance of the primordial solar nebula that gave birth to the solar system: $H = 2.6 \times 10^{10}$; $He = 2.1 \times 10^{9}$; $O = 2.4 \times 10^{7}$; $C = 1.4 \times 10^{7}$; and $N = 2.4 \times 10^{6}$, normalized with respect to $Si = 1 \times 10^{6}$ (Reference 18). The conditions in the primordial solar nebula must have been highly reducing due to the overwhelming presence of excess hydrogen. It has been suggested that in the early history of the Earth, before the migration of metallic iron to the core, the outgassed volatiles were highly reduced consisting of methane (CH_4) and smaller amounts of ammonia (NH_3), molecular hydrogen (H_2) and water vapor (H_2O) (References 14, 15). This early methane-ammonia atmosphere appears to be the most suitable environment for initiating the development of complex biological molecules and the chemical evolution of life (References 19-23). The formation of the Earth's metallic core had the effect of increasing the average degree of oxidation of the materials outside the core because the core formation removed free metal, mainly iron, from the remaining material, which became the mantle. Hence, after core formation the outgassed volatiles should have been much less reduced - methane was replaced by carbon dioxide (CO_2), ammonia was replaced by molecular nitrogen (N_2) and molecular hydrogen was replaced by water vapor (References 14, 15). The time of the formation of the Earth's core is uncertain. The best estimates suggest that core formation occurred at least 3.5×10^{9} years ago during the Earth's first billion years (Reference 17). The stability of an early methane-ammonia is another unresolved question. It may have lasted from only 10^{5} to 10^{8} years (Reference 13) to as long as 10^{9} years (Reference 24).

The total volatile outgassing inventory of Earth in grams-cm^{-2} over its history has been estimated as: $H_2O = 3.25 \times 10^{5}$; total C as $CO_2 = 1.78 \times 10^{4}$; $Cl = 5.88 \times 10^{3}$; $N = 8.23 \times 10^{2}$; $S = 4.31 \times 10^{2}$; $H = 1.96 \times 10^{22}$ and B, Br, A, and F = 78.43 (References 12 and 13). The most abundant gas released from the Earth's interior, water vapor has condensed out of the atmosphere and is present mainly in liquid form in the Earth's extensive oceans. The bulk of the carbon dioxide, the next most plentiful outgassed volatile, precipitated out in the presence of liquid water in the form of calcium carbonate ($CaCO_3$) on the ocean floor and to a much lesser degree formed fossil fuels. Nitrogen, being quite chemically inert, has largely remained in the atmosphere and forms the bulk of the Earth's present atmosphere. About 10% of atmospheric nitrogen

has been removed from the atmosphere and placed in geological deposits and a fraction (10^{-8}) of atmospheric nitrogen is fixed each year, mainly by biological processes. The nitrogen that undergoes fixation is mostly returned to the atmosphere within a few years or decades (Reference 17).

OUTGASSING OF RADIOACTIVE VOLATILES

In addition to the outgassing of trapped volatiles discussed in the last section, radiogenic volatiles (argon-40 and helium-4) constitute an important class of outgassed species in the Earth's atmosphere. On the cosmic abundance scale, the isotopic abundance ratios of argon-36, argon-38, and argon-40 are 84.2%, 15.8%, and 0%, respectively (Reference 18), while the isotopic abundance ratios of argon in the Earth's atmosphere are 0.33%, 0.063%, and 99.6%, respectively (Reference 2). Therefore, the bulk of the argon in the Earth's atmosphere has resulted from the radioactive decay of potassium-40. Since argon is a relatively heavy atom it cannot escape from the Earth's atmosphere and argon-40 has accumulated over geological time to become the third most abundant permanent constituent of the Earth's atmosphere.

Helium-4, resulting from the radiogenic decay of uranium and thorium, is the major source of atmospheric helium on Earth (the ratio of radiogenic helium-4 to helium-3 in the Earth's atmosphere is about 8×10^5). The radiogenic decay of uranium and thorium results in a helium-4 surface mixing ratio of about 5 ppm by volume. Since helium is such a light gas it readily escapes from the Earth's upper atmosphere resulting in an accumulation time of only about 2×10^6 years for the helium-4 abundance presently in the Earth's atmosphere.

THE ORIGIN AND EVOLUTION OF OXYGEN

From a geochemical point of view, the presence of large amounts of free oxygen in the Earth's atmosphere is puzzling. The solid Earth is under-oxidized and outgassed volatiles do not contain free oxygen - in fact the interaction with surface material and volcanic gases is actually a sink for oxygen. Crustal rock weathering and the continual exposure of fresh minerals that are under-oxidized is a significant drain on the atmospheric oxygen supply.

Free atmospheric oxygen results from the photodissociation of atmospheric water vapor with the subsequent atmospheric escape of the hydrogen atom. However, this is a self-limiting process, since as oxygen builds up in the atmosphere it shields water vapor, which is confined to the troposphere, from further photodissociation. It has been shown that the limiting oxygen concentration that can evolve from the photodissociation of water vapor before the process shuts itself off is about one-thousandth of the present atmospheric level (P.A.L.) of oxygen (Reference 25). However, a reexamination of this problem suggests that the photodissociation of water vapor may account

for as much as 1/4 P.A.L. or more of the oxygen in the Earth's atmosphere (Reference 26).

Another source of atmospheric oxygen is photosynthesis. In the photosynthetic process carbon dioxide, water and energy yield free oxygen and a carbohydrate. The beginning of photosynthetic activity has been established at about 2.7 billion years ago (Reference 25). The first photosynthetic organisms were probably photosynthetic protozoa or green algae or their evolutionary predecessors.

The history of the growth of atmospheric oxygen and ozone (the evolution of ozone is discussed in the following section) and its relation to the evolution of life on Earth has been investigated (Reference 25). The basic assumption in this study is that the growth of oxygen from the primitive levels (10^{-3} P.A.L.) resulting from the photodissociation of atmospheric water vapor is due to photosynthetic activity. The important stages in this sequence (Reference 25) are summarized below:

(1) The Pre-Cambrian Period (prior to 600 million years ago):

The atmospheric oxygen level resulting from the photodissociation of water vapor could not exceed 10^{-3} P.A.L. Ample solar ultraviolet radiation was available in the waters for the synthesis of amino acids, enzymes, etc., since the total oxygen and ozone content was too small for significant absorption above 2100 Å (1 Å = 1^{-10} m). By the same token solar ultraviolet was lethal to living organisms even through 5 to 10 meters of water. Consequently, the ecology for the origin of life and photosynthesis by organisms would appear very restrictive limited to water, below the penetration of lethal solar ultraviolet radiation and, consistent with this limitation, as shallow as possible to maximize photosynthetic activity. This primitive ecological restriction lasted a very long time - probably about 3/4 of the Earth's history. Life may conceivably have arisen independently in a large number of disconnected localities that were well insulated, ecologically from one another.

(2) "The First Critical Level" - The Cambrian Revolution (600 million years ago):

The total rate of photosynthetic production of oxygen finally exceeded its rate of photodissociation loss and rose to about 10^{-2} P.A.L. At this level oxygen and ozone restricted the ultraviolet zone of lethality to a thin layer at the water's surface which greatly enhanced photosynthetic activity through new opportunities near the surface and permitting life to spread to the entire ocean.

(3) "The Second Critical Level" - The Late-Silurian Revolution (420 million years ago):

Due to the spread of living organisms and enhanced photosynthetic activity in the oceans oxygen rapidly rose to about 10^{-1} P.A.L. This level of oxygen with an increase in the ozone content of the atmosphere permitted the evolution of life on dry land now shielded from lethal ultraviolet radiation. With the opening of the land, a new ecological niche, evolutionary activity

was again explosive. This enhancement of photosynthetic activity caused atmospheric oxygen levels to rise unstably to present or even higher levels possibly associated with the lush life of the carboniferous period (350 million years ago). Thereafter, the oxygen level may have fluctuated slightly to reach the present, presumably stable level. The stability of oxygen in the Earth's atmosphere has been investigated (Reference 27).

THE ORIGIN AND EVOLUTION OF OZONE

Closely related to the evolution of free oxygen in the Earth's atmosphere is the origin and evolution of atmospheric ozone (References 25 and 28). The photochemistry of atmospheric ozone has recently received considerable attention due to the possibility of inadvertent modification or depletion of the Earth's ozone layer by anthropogenic activities, i.e., exhaust gases from high-flying supersonic transports; the release of chlorofluoromethanes from aerosol spray cans; and increased world-wide use of agricultural nitrogen fertilizer (Reference 29). NASA's upper atmospheric research programs within the Offices of Space Science and Applications were created to foster a better understanding of the physical and chemical processes occurring in the Earth's upper atmosphere, with immediate emphasis on the question of possible inadvertent depletion of atmospheric ozone.

At the Langley Research Center we have been investigating the detailed photochemistry and evolution of atmospheric ozone over geological time using a photochemical model for ozone developed within the Aeronomy Section, Planetary Physics Branch, Environmental and Space Sciences Division and the Flight Applications Section, Computer Mathematics and Programming Branch, Analysis and Computation Division. We will summarize our calculations on the rise of ozone for an evolving oxygen atmosphere using the classical Chapman photochemical equilibrium scheme given below:

(1) $O_2 + h\nu \rightarrow O + O$; $\lambda < 2424$ Å

(2) $O + O_2 + M \rightarrow O_3 + M$

(3) $O_3 + h\nu \rightarrow O_2 + O$; $\lambda < 11{,}800$ Å

(4) $O_3 + O \rightarrow 2O_2$

(5) $O + O + M \rightarrow O_2 + M$

The vertical distribution of ozone corresponding to oxygen levels of 5, 1, 10^{-1}, 10^{-2}, 10^{-3} and 10^{-6} P.A.L. is shown in Figure 1. The total ozone column density for these levels of oxygen is shown in Figure 2. All calculations are for a solar zenith angle of 57.3°, the mean global daytime value. For oxygen levels of 5, 1 and 10^{-1} P.A.L., the U.S. Standard Atmosphere 1966 Spring/Fall Mid-Latitude temperature profile was used. For oxygen levels less than 10^{-1} P.A.L., it was assumed that there is no temperature rise in the

stratosphere and that temperature decreases linearly from the tropopause to the mesopause, as suggested by radiative equilibrium temperature calculations for reduced stratospheric ozone levels (Reference 30).

The profiles in Figures 1 show that the rise of atmospheric ozone to present levels is a recent event on a geological time scale. For more reduced levels of oxygen, the ozone distribution peaked lower and lower in the atmosphere. This is due to the fact that for reduced oxygen levels solar ultraviolet radiation could penetrate deeper and deeper into the atmosphere to initiate the ozone formation chemistry via the photodissociation of molecular oxygen. As already mentioned, the ozone profiles for oxygen levels of 10^{-2}, 10^{-3} and 10^{-6} P.A.L. were calculated using a primordial temperature profile with no stratospheric temperature increase. At the stratopause (50 km) the primordial temperature profile is about 60 K cooler than the present stratopause. The lower temperatures within the primordial stratosphere result in increased ozone concentrations at these altitudes. Therefore, we find comparable ozone concentrations between 50 and 60 km for oxygen levels of 10^{-1} P.A.L. with the present atmospheric temperature profile and for oxygen levels of 10^{-2} P.A.L. with the primordial temperature profile.

The variation in total ozone column density or total ozone burden for an evolving oxygen atmosphere is given in Figure 2. Our calculations indicate that the total ozone burden reaches a maximum at about 10^{-1} P.A.L. and actually decreases somewhat for 1 and 5 P.A.L. This is a surprising result and contrary to the results of Reference 25 which are also shown. This interesting result was also reported in Reference 28. Also of particular interest are the total ozone burdens corresponding to the pre-photosynthetic activity level of oxygen, and the "first critical level" and the "second critical level" of oxygen evolution (Reference 25). According to our calculations, these total ozone burdens were achieved for significantly lower oxygen levels than given in Reference 25. For example, our pre-photosynthetic activity level of oxygen was achieved for 10^{-5} P.A.L. compared to 10^{-3} P.A.L. for Reference 25. Our total ozone burdens corresponding to the two critical levels of oxygen also correspond to much lower oxygen levels than reported in Reference 25. Our results indicate that comparable total ozone burdens existed for much smaller oxygen levels than reported in Reference 25. Our results, also supported by calculations presented in Reference 28, indicate that ozone evolved earlier in the Earth's history than suggested in Reference 25.

We are just beginning to better understand the evolutionary history of ozone in the Earth's atmosphere. Knowledge of ozone's past history will hopefully lead to a better understanding of its future evolution in the Earth's atmosphere.

REFERENCES

1. Kumar, S.: The Ionosphere and Upper Atmosphere of Venus. Atmospheres of Earth and the Planets (edited by B. M. McCormac), D. Reidel Publishing Co., 1975, pp. 385-399.

2. Banks, P. M.; and Kockarts, G.: Aeronomy, Part A, Academic Press, 1973, pp. 18-25.

3. Keating, G. M.; and Levine, J. S.: Response of the Neutral Upper Atmosphere to Variations in Solar Activity. Solar Activity Observations and Predictions (edited by P. S. McIntosh and M. Dryer), The MIT Press, 1973, pp. 313-340.

4. Dalgarno, A.; and McElroy, M. B.: Mars: Is Nitrogen Present? Science, 170, 1970, pp. 167-168.

5. Owen, T.: What Else Is Present in the Martian Atmosphere? Comments Astrophys. Space Phys., 5, 1974, pp. 175-180.

6. Levine, J. S.; and Riegler, G. R.: Argon in the Martian Atmosphere. Geophys. Res. Lett., 1, 1974, pp. 285-287.

7. Anderson, D. E.; and Hord, C. W.: Mariner 6 and 7 Ultraviolet Spectrometer Experiment: Analysis of Hydrogen Lyman Alpha Data. J. Geophys. Res., 76, 1971, pp. 6666-6673.

8. Levine, J. S.; Keating, G. M.; and Prior, E. J.: Helium in the Martian Atmosphere: Thermal Loss Considerations. Planet Space Sci., 22, 1974, pp. 500-503.

9. Walker, J. C. G.: Evolution of the Atmosphere of Venus. J. Atmos. Sci., 32, 1975, pp. 1248-1256.

10. Levine, J. S.: A New Estimate of Volatile Outgassing on Mars. Icarus, 28, 1976, pp. 165-169.

11. Brown, H.: Rare Gases and the Formation of the Earth's Atmosphere. The Atmospheres of the Earth and Planets (edited by G. P. Kuiper), The Univ. of Chicago Press, 1949, pp. 260-268.

12. Rubey, W. W.: Geologic History of Sea Water: An Attempt to State the Problem. Geol. Soc. of Amer., Bulletin, 62, 1951, pp. 1111-1147.

13. Rubey, W. W.: Development of the Hydrosphere and Atmosphere, With Reference to Probable Composition of the Early Atmosphere. Geol. Soc. Amer. Special Paper 6Z, 1955, pp. 631-650.

14. Holland, H. D.: Models for the Evolution of the Earth's Atmosphere. Petrologic Studies: A Volume to Honor A. F. Buddington, Geol. Soc. Amer., 1962, pp. 447-477.

15. Holland, H. D.: On the Chemical Evolution of the Terrestrial and Cytherean Atmospheres. The Origin and Evolution of Atmospheres and Oceans (edited by P. J. Brancazio and A. G. W. Cameron), John Wiley and Sons, 1964, pp. 86-101.

16. Cloud, P. E.: Atmospheric and Hydrospheric Evolution on the Primitive Earth. Science, 1968, 160, pp. 729-736.

17. Johnson, F. S.: Origin of Planetary Atmospheres. Space Sci. Rev., 1969, 9, pp. 303-324.

18. Cameron, A. G. W.: Abundances of the Elements in the Solar System. Space Sci. Rev., 1973, 15, pp. 121.

19. Oparin, A. I.: Origin of Life. MacMillan, 1938.

20. Miller, S. L.: Production of Amino Acids Under Possible Primitive Earth Conditions. Science, 1953, 117, pp. 528-529.

21. Miller, S. L.; and Urey, H. C.: Organic Compound Synthesis on the Primitive Earth. Science, 1959, 130, pp. 245-251.

22. Urey, H. C.: Primitive Planetary Atmospheres and the Origin of Life. The Origin of Life on Earth, Vol. I (Symp. of Intern. Union of Biochemistry), MacMillan, 1959, pp. 16-22.

23. Ponnamperuma, C.; and Gabel, N. W.: Current Status of Chemical Studies on the Origin of Life. Space Life Sci., 1968, 1, pp. 64-96.

24. McGovern, W. E.: The Primitive Earth: Thermal Models of the Upper Atmosphere for a Methane-Dominated Environment. J. Atmos. Sci., 1969, 26, pp. 623-635.

25. Berkner, L. V.; and Marshall, L. C.: On the Origin and Rise of Oxygen Concentrations in the Earth's Atmosphere. J. Atmos. Sci., 1965, 22, pp. 225-261.

26. Brinkmann, R. T.: Dissociation of Water Vapor and Evolution of Oxygen in the Terrestrial Atmosphere. J. Geophys. Res., 1969, 74, pp. 5355-5368.

27. Walker, J. C. G.: Stability of Atmospheric Oxygen. Amer. J. of Sci., 1974, 274, pp. 193-214.

28. Ratner, M. I.; and Walker, J. C. G.: Atmospheric Ozone and the History of Life. J. Atmos. Sci., 1972, 29, pp. 803-808.

29. Stratospheric Ozone Depletion: Hearings before the Subcommittee on the Upper Atmosphere of the Committee on Aeronautical and Space Sciences of the United States Senate, Ninety-fourth Congress, First Session, September 8, 9, 15 and 17, 1975, Part I. U.S. Government Printing Office, 1975, 554 pages.

30. Manabe, S.; and Strickler, R. F.: Thermal Equilibrium of the Atmosphere with a Convective Adjustment. J. Atmos. Sci., 1964, 21, pp. 361-385.

TABLE I.- THE ATMOSPHERES OF THE TERRESTRIAL PLANETS

	Venus	Earth	Mars
Distance from Sun (A.U.)	0.723	1.000	1.524
Lower Atmosphere			
Surface pressure (mb)	~90×10^3	~10^3	~6
Surface temperature (K)	~750	~288	~225
N_2	~1% (Ref. 1)	78.08% (Ref. 2)	<5% (Ref. 4)
O_2	<1 ppm (1)	20.95% (2)	1100 ppm (5)
Ar	?	0.93% (2)	0 to 28% (5,6)
CO_2	~95% (1)	330 ppm (2)	>95% (5)
CO	~1% (1)	0.06-1 ppm (2)	1600 ppm (5)
H_2O	<1 ppm (1)	$1\text{-}28\times10^3$ ppm (2)	300 ppm (5)
O_3	?	0.01-.1 ppm (2)	0.03 ppm (5)
Upper Atmosphere			
Exospheric temperature (K)	400 (1)	700-2000 (3)	350 (7)
Composition:			
H (250 km)(cm^{-3})	~10^4 (1)	~10^4 (3)	3×10^4 (7)
He (250 km)(cm^{-3})	~10^7 (1)	~10^7 (3)	~10^7 (8)

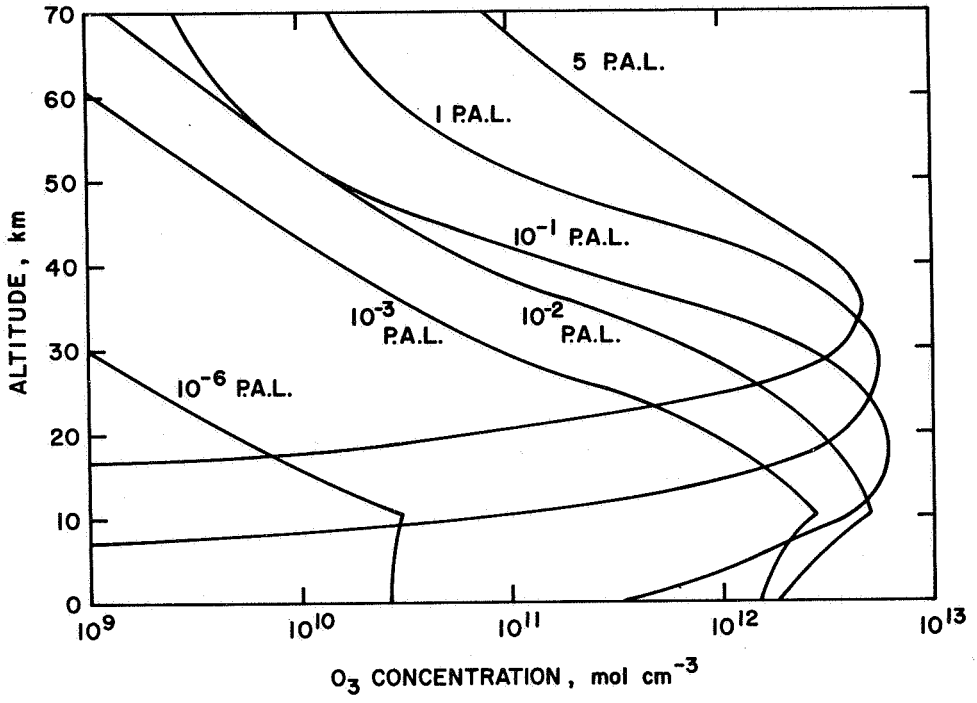

Figure 1.- The vertical distribution of atmospheric ozone for oxygen levels of 5, 1, 10^{-1}, 10^{-2}, 10^{-3} and 10^{-6} present atmospheric level (P.A.L.).

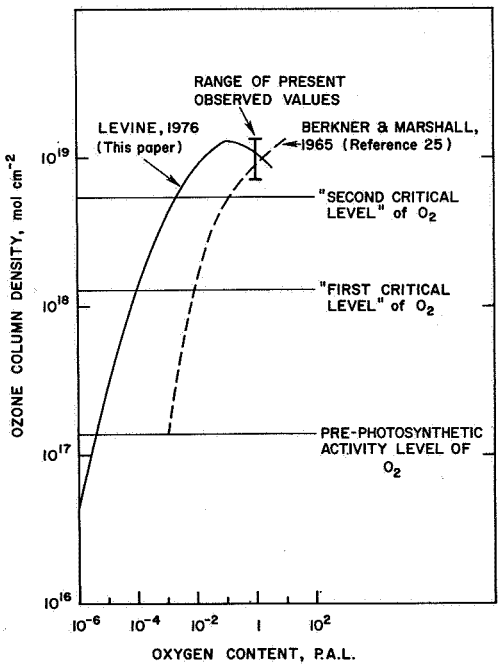

Figure 2.- The total ozone burden above the surface for evolving oxygen levels and comparison with calculations of Berkner and Marshall, 1965 (Reference 25).

ATMOSPHERIC ENGINEERING OF MARS

R. D. MacElroy and M. M. Averner
Ames Research Center, NASA

SUMMARY

Considerations have been made of the feasibility of creating a breathable atmosphere on Mars. Assuming that indigenous life is absent, and that human habitation will prove economically justifiable, several methods of introducing oxygen were considered. On the basis of energy requirements, photosynthetic oxygen production appears to be reasonable, assuming that the amounts of water, carbon dioxide, and mineral nutrients available on the Martian surface would be adequate for the growth of photosynthetic microorganisms. However, optimum rates of O_2 formation could occur only after a significant increase in average temperature and in atmospheric mass. The generation of a runaway greenhouse/advective effect was considered. However, neither the energy requirement nor the time constant for initiation could be calculated. There appear to be no insuperable obstacles to the conversion of the Martian atmosphere to one containing oxygen, but the conversion would require many thousands of years.

INTRODUCTION

As a close neighbor to Earth, Mars has long been the object of speculation concerning the presence of life on its surface. Percival Lowell's observations of the planet, and particularly his generation of popular interest in the "canals," laid the base for ready public acceptance of the possibility of intelligent life on Mars (ref. 1). As more solid information about Mars becomes available, the less likely it seems that intelligent life can exist there. What we know now of the atmosphere and of the surface, thanks to the Mariners and Viking, suggests that conditions are very hostile indeed, and that even simple life forms may have difficulty surviving. However, the possibility of finding life on Mars cannot be eliminated. Automated exploration of Mars will continue and, with the passage of time, Mars will become more accessible and more thoroughly explored because of improved, more powerful booster rockets and more sophisticated equipment. It seems inevitable that man will one day set foot on the planet, explore it, and set up temporary, enclosed stations on it.

During the period of exploration, consideration will be given to exploitation of Mars. The decision to colonize the planet will depend upon economic factors, as have all similar decisions in the history of civilization on Earth. The economic factors to be considered will include assessment of mineral deposits, industrial possibilities, and perhaps even of room for population expansion. Our present knowledge of the Martian environment tells us that man will require enclosed life support systems to survive on the planet. But if

colonization becomes economically feasible, the question arises whether man will always be confined to protective enclosures, or whether the Martian environment can be altered to allow eventual unencumbered human habitation.

STUDY RESULTS

We have considered whether the conversion of Mars to a planet habitable by humans is feasible by determining some requirements for conversion of the atmosphere. Specifically, optimal final conditions were estimated, energy needs were calculated, and the kinds of information required for a decision chain were identified. We were also most interested in whether preliminary exploration of Mars could inadvertently compromise such an engineering project.

The study was conducted during the summer of 1975 with the participation of Drs. S. Berman, W. Kuhn, P. Langhoff, and S. Rogers. A short report of the study has been released (ref. 2) and a final report will be published shortly (ref. 3).

The physical characteristics of Mars are shown in table I. Of specific interest are the temperature at the surface (table I(f)), and the atmospheric composition (table I(c)). The low level of O_2 in the atmosphere prevents the formation of appreciable ozone, so that the flux of ultraviolet light (table I(e)) at the surface is sufficient to kill even the most resistant terrestrial microorganisms within minutes. The density of the atmosphere and the concentration of H_2O are too low to permit the development of significant advective or greenhouse effects.* For this reason the temperatures over the surface exhibit large diurnal variations (fig. 1) and are too low to support continuous metabolic activity by terrestrial organisms. Thus a fundamental requirement is to increase the mass of the atmosphere and, particularly, the mass of atmospheric O_2 and H_2O: O_2 for respiration and ozone production, and H_2O for increasing the average temperature.

What methods could be used to build up O_2 in the Martian atmosphere? The approach suggested by Ehricke (ref. 4), nuclear mining of O_2, was investigated, and an energy requirement was calculated. This technique has been considered by Vondrak (refs. 5,6) for the formation of a stable-lunar atmosphere. Assuming a similar crustal composition for Mars, the need for an input of about 4×10^{24} J is indicated. This would involve an amount of energy equivalent to 10 million 1-megaton bombs, an enormous amount of energy. The actual use of

---

*Atmospheric greenhouse effect refers to a condition of increased warming caused by the presence of certain gases in the atmosphere. These gases, CO_2 and H_2O vapor among them, absorb some of the thermal radiation (heat) rising from the surface of the planet, so that not all the radiation is lost to space but is re-emitted down from the atmosphere, thereby heating the planet's surface. Advection is the term used by meteorologists to denote horizontal transport of air.

nuclear bombs would also pose a severe radiation hazard and would certainly alter the surface sufficiently to destroy its scientific value.

As an alternative, the possibility of generating a suitable atmosphere photosynthetically was considered since the present terrestrial atmosphere is the product of such a process. The amount of solar energy intercepted by Mars (table I(d)), and the amount of energy in the wavelengths used for green plant photosynthesis were calculated. Utilization of photosynthesis as a means of producing O_2 requires not only light, but CO_2 and water as well:

$$CO_2 + H_2O \xrightarrow{h\nu} \underset{\text{(carbohydrate)}}{(CH_2O)_x} + O_2 \qquad (1)$$

Although the Martian atmosphere consists of 74 to 98 percent CO_2, the total amount (2×10^{19}g) is insufficient to support photosynthesis for a significant period of time. The amount of water in the atmosphere (3×10^{15}g), even if condensed on the surface, could support growth of terrestrial organisms for an even shorter time. To summarize, the production of an O_2-containing Martian atmosphere is necessary for two reasons: to provide O_2 for breathing, and to produce O_3 to protect from lethal uv. The energy necessary to produce sufficient O_2 could be imported, but at a totally prohibitive cost. Solar energy could be utilized by biological systems to produce O_2, but insufficient water and CO_2 and low temperatures are important constraints. It is worthwhile to consider whether any of these constraints could be relieved, and how.

The polar caps apparently contain solid CO_2 and, judging by the degree of their seasonal recession, solid H_2O. The arguments of Levine (refs. 7, 8) describing the genesis of the Martian atmosphere suggest that water has been a major constituent of the crust of Mars. Measurements by Houck et al. (ref. 9) indicate adsorbed water in the surface, and estimates by Fanale (ref. 10) suggest major ice deposits below the surface. Metal carbonates might also be considered as a crust constituent in the absence of liquid water. Thus there may be large reservoirs of H_2O and CO_2 on or under the Martian surface.

An increase in the average planetary temperature of Mars could have several effects, ranging from an increase in the amount of atmospheric CO_2 by the melting of the polar caps, to increasing the amount of water vapor due to the melting of water ice at the caps and at the surface. Since increased CO_2 and H_2O in the atmosphere can cause an increase in surface temperature by greenhouse/advective heating, and because increased temperature can cause an increase in atmospheric CO_2 and H_2O content, the possibility exists for a runaway effect, a self-generating increase in atmospheric mass and an average temperature increase of about 30 K. Such a runaway greenhouse and advective effect has been discussed by Sagan (ref. 11).

Triggering such a temperature increase will require extensive studies of model atmospheres; such studies have not been done to date. Intuitive dissection of the problem suggests that introduction of energy for a sufficient

period into the polar caps could initiate a greenhouse/advective effect. Direct, explosive energy might be used, as could more slowly released reactor energy, but again the available solar energy could also be utilized by decreasing the albedo of the caps and allowing them to absorb more solar energy. A complex, detailed analysis will be required to determine the time period required to induce such an event.

Even though some modified terrestrial forms might grow on Mars in the absence of an altered atmosphere, the physical generation of a more massive atmosphere, and the concomitant temperature increase, would also increase the availability of liquid water and produce a many-fold increase in the rate of photosynthetic oxygen generation. Even in the absence of a polar cap melting program, seeding the planet with photosynthetic organisms is not unreasonable. The question arises as to which terrestrial photosynthetic organism might be best suited to survive, grow, and produce oxygen on Mars in the planet's present state. Two members of our study group, W. Kuhn and S. Rogers, constructed a model of a terrestrial lichen mat which suggests that such an organism might survive the Martian environment and produce O_2 at a slow rate. This model has encouraged us to consider other kinds of organisms that might be candidates for seeding operations. It has also stimulated consideration of genetically engineering organisms to fit the environment. A genetically engineered organism might have increased capability of withstanding ultraviolet insult, or of growing maximally at low temperatures, or of avoiding desiccation. Perhaps all of these attributes might be incorporated into a single organism.

The use of organisms to modify the atmosphere of Mars deserves some additional comment and clarification. The present atmosphere of the Earth was formed and is maintained by organisms, and represents the product of a transition from an oxygenless environment that existed prior to about 600 million years ago. It is generally assumed that anaerobic organisms, mostly bacteria which did not require O_2, were predominant before oxygen accumulated on Earth, and that the evolution of a mechanism to directly use solar energy, photosynthesis, led to the ability to produce oxygen. The vast lengths of time that were required for the development of an oxygen atmosphere need not discourage us excessively, if we remember that we would start a Mars atmospheric conversion project with organisms that have already evolved photosynthetic mechanisms; more significantly, we will be able to transfer genetic information from one organism to another and in this way build the most efficient organism for our purposes.

The production of oxygen, however, is just one part of the problem. Whether on Earth or on Mars, organisms are living in a large, but closed biochemical system. This fact requires that recycling of materials must occur, or the system will cease functioning. The specific constraints that we can identify already on Mars include limitations of carbon dioxide as well as of nitrogen, an element essential for life. While we have every reason to suppose that other elements, such as phosphorous, sulfur, or magnesium, are available on the surface of Mars, the absence of any indications of nitrogen in the atmosphere may signal a severe problem for biology.

Assuming that the requirements for photosynthetic life can be met on Mars, and that water, CO_2, sunlight, and nutrient elements are available, oxygen could be produced in the temperate regions; however, the organisms selected for this task must have sufficient protective or repair mechanisms to prevent decimation by the ultraviolet flux. A simultaneous accumulation of oxygen and organic material, and a depletion of water and CO_2 will occur (see eq. (1)). To allow continuation of the process, it will be necessary to recycle the carbon in the organic material back to CO_2. On Earth this is done by organisms that use the organic material as food. Some of these organisms utilize oxygen in this process and if they were introduced on Mars, they could deplete the newly-formed oxygen. By selecting organisms carefully, it is possible to obtain some that will feed on the organics without utilizing oxygen. These anaerobic organisms could release CO_2 and molecular hydrogen. The escape of the hydrogen from the planet would result in a net conversion of H_2O to O_2.

$$H_2O + CO_2 \xrightarrow{h\nu} (CH_2O) + O_2 \quad \text{Photosynthesis}$$

$$(CH_2O) + H_2O \longrightarrow CO_2 + 2H_2 \quad \text{Anaerobic (}\underline{\text{Clostridium}}\text{) Metabolism}$$

$$2H_2O \xrightarrow{h\nu} O_2 + 2H_2 \quad \text{Sum}$$

It is obvious from this simple case that at the minimum a two-component biological system will be needed. As considerations are made of other nutritional requirements, enlargement of the ecological system to be formed on Mars will be necessary. In a balanced system, the organisms acting as the collectors of energy and nutrients must be offset by the organisms that release the nutrients back into the system. The formation of a specific new Martian atmosphere will require an unbalanced system initially, one which will favor the accumulation of O_2; in time, with the accumulation of sufficient oxygen, it will be reasonable to introduce oxygen using organisms, and to stop the loss of hydrogen from the planet. On Earth it would seem that excessive hydrogen loss is limited by the fact that anaerobic organisms are inhibited by O_2 and that other organisms can use and conserve hydrogen. Any system that involves interactions between two or more organisms is very complex. On a planetary scale, the management of such an ecosystem will require first, a major research effort just to describe it, and second, extensive modeling to understand it.

The possibility presents itself that inadvertent introduction of organisms could disrupt or negate any attempt to develop an oxygen-containing atmosphere on Mars. Such biological contamination could also hamper the exploration of the planet. Exploration must be completed before any scheme such as we have described could begin. If indigenous organisms exist on Mars, a scheme of ecosynthesis should not be attempted unless overwhelming reasons are marshalled to justify the disruption of the native population. However, indigenous organisms might also be incorporated into the formation of a new ecosystem.

A major question arises as to the time required to form an atmosphere that would provide sufficient O_2 for breathing. The answer to the question is

dependent upon so many factors that specific times cannot be quoted. For example, if the planet were ideal for the growth of algae, and all of the surface could be utilized, with unlimited water and CO_2, a period of less than 100 years might be needed. On the other hand, an O_2 production rate consistent with present conditions, and assuming that major physical engineering changes would not be done, would suggest a time period of several million years. The most realistic time frame, assuming the selection of an efficient organism, some increase in temperature, availability of water, CO_2, and nitrogen, and an exponential increase in O_2 production rate, would seem to be several thousand years.

The preceding speculations will probably not be considered in a serious way for at least a century, and the scenario developed then will undoubtedly include the simultaneous use of long-term enclosed stations, coupled with the development of an external atmosphere. The conclusions of this feasibility study are: (1) that while much more information about Mars is essential for a reasonable consideration of ecosynthesis, there are no insuperable obstacles, identifiable at this time, that would prevent the conversion of the Martian atmosphere into one that could eventually support human life; and (2) that lack of proper concern now for biological contamination of Mars may seriously obstruct future efforts at Martian planetary engineering.

REFERENCES

1. Lowell, P.: Mars as the Abode of Life. MacMillan, New York, 1910.

2. MacElroy, R. D., et al.: On the Habitability of Mars. In: Final Report, NASA-ASEE Summer Institute. 1975, Stanford-Ames Research Program, D. Bershader, J. Leveen and J. Mayers, eds., 1975.

3. Averner, M. M. and MacElroy, R. D.: On the Habitability of Mars: An Approach to Planetary Ecosynthesis. NASA SP 406, 1976.

4. Ehricke, K.: Extraterrestrial Imperative. Bull. Atomic. Sci., Nov., 1971, pp. 18-26.

5. Vondrak, R.: Creation of an Artificial Lunar Atmosphere. Nature, 248, 1974, pp. 657-659.

6. Vondrak, R.: Artificial Creation of a Stable Lunar Atmosphere on the Moon. EOS. Trans. Am. Geophys. Union, 54, 389, 1973.

7. Levine, J. S.: Argon on Mars! Where is the Water? EOS. Trans. Am. Geophys. Union, 56, 405, 1975.

8. Levine, J. S.: A New Estimate of Volatile Outgassing on Mars. Icarus, 28, 1976, pp. 165-169.

9. Houck, J. R., Pollack, J. B., Sagan, C., Schaak, P., and Dekker, J. A.: High-Altitude Infrared Spectroscopic Evidence for Bound Water on Mars. Icarus, 18, 1973, pp. 470-480.

10. Fanale, F. P.: Martian Volatiles: Their Degassing History and Geochemical Fate. Icarus, 28, 1976, pp. 179-202.

11. Sagan, C.: The Long Winter Model of Martian Biology: A Speculation. Icarus, 15, 1971, pp. 511-514.

12. Goody, R. M., and Walker, J. C. G.: Atmospheres. Prentice-Hall, Inc., Englewood Cliffs, New Jersey, 1972.

13. Noll, R. B., and McElroy, M. B.: Models of Mars' atmosphere. NASA Space Vehicle Design Criteria (Environment), NASA SP-8010, 1974.

14. McCormac, B. M., ed.: Introduction to the Scientific Study of Atmospheric Pollution. D. Reidel Publishing Company, Dordrecht-Holland, 1971.

15. Barth, C. A.: The Atmosphere of Mars. Ann. Rev. Earth and Planet. Sci., 2, 1974, pp. 333-367.

16. Levine, J. S., Kraemer, D. R., and Kuhn, W. R.: The distribution of solar radiation incident on Mars and the Jovian Planets. EOS. Trans. Am. Geophys. Union, 55, 343, 1974.

17. Nawrocki, P. J., and Papa, R.: Atmospheric Processes. Prentice Hall, Inc., Englewood Cliffs, New Jersey, 1963.

18. Crutcher, H. L.: Temperature and Humidity in the Troposphere. In: A World Survey of Climatology, vol. 4: Climate of the Free Atmosphere. Rex, D. F., ed., Elsevier, Amsterdam, 1969, pp. 45-83.

19. Woiceshyn, P. M.: Global Seasonal Atmospheric Fluctuations on Mars. Icarus, 22, 1974, pp. 325-344.

20. Conrath, B., Curran, R., Hanel, R., Kunde, V., Maguire, W., Pearl, J., Pirraglia, J., and Welker, J.: Atmospheric and Surface Properties of Mars Obtained by Infrared Spectroscopy on Mariner 9. J. Geophys. Res., 78, 1973, pp. 4267-4278.

21. Kliore, A. J., Fjeldbo, G. F., Seidel, B. L., Sykes, M. J., and Woiceshyn, P. M.: S Band Radio Occultation Measurements of the Atmosphere and Topography of Mars with Mariner 9: Extended Mission Coverage of Polar and Intermediate Latitudes. J. Geophys. Res., 78, 1973, pp. 4331-4351.

22. Hanel, R. A., Conrath, B. J., Hovis, W. A., Kunde, V. G., Lowman, P. D., Pearl, J. C., Prabhakara, C., and Schlachman, B.: Infrared Spectroscopy Experiment on the Mariner 9. Mission: Preliminary Results. Science, 175, 1973, pp. 305-308.

23. Fanale, F. P., and Cannon, W. A.: Exchange of Absorbed H_2O and CO_2 Between the Regolith and Atmosphere of Mars Caused by Changes in Surface Insolation. J. Geophys. Res., 79, 1974, pp. 3397-3402.

24. Ingersoll, A. P.: Mars: The Case Against Permanent CO_2 Frost Caps. J. Geophys. Res., 79, 1974, pp. 3403-3410.

TABLE I.- PHYSICAL CHARACTERISTICS OF EARTH AND MARS

(a) Planetary and Orbital Parameters

Parameter	Earth	Mars
Mass, g	5.98×10^{27}	6.43×10^{26}
Mean density, g/cm^3	5.52	3.94
Mean radius, km	6371	3394
Surface gravity, cm/sec^2	981	373
Length of day, Earth-days	1	1.026
Length of year, Earth-days	365	687
Obliquity, deg	23.5	23.9
Orbital eccentricity	0.017	0.093
Mean distance from Sun, km	150×10^6	228×10^6
Solar constant, $cal/cm^2/min$	2.00	0.866
Planetary albedo	0.30-0.35	0.15-0.25
Effective temperature, K	253	216

Source of data: Goody and Walker (ref. 12)

(b) Atmospheric Parameters

Parameter	Earth	Mars
Atmospheric mass, g	5.3×10^{21}	2.4×10^{19}
Surface air pressure, mbar	1000	5
Surface air density, g/cm	1.2×10^{-3}	1.2×10^{-5}
Scale height, km	8.4	10.6
Adiabatic lapse rate, K/km	9.8	4.5
Average optical thickness	2	0.1[a]
Tropopause height, km	10	30?
Turbopause height, km	80	150

[a]Much higher in duststorms.

Sources of data: Goody and Walker (ref. 12);
Noll and McElroy (ref. 13)

TABLE I.- Continued.

(c) Atmospheric Composition (% by volume)

Gas	Earth	Mars
N_2	78	?
O_2	20	0.1
H_2O	1[a]	<0.1[a]
Ar	0.93	1-25 } 99
CO_2	0.03	98-74 }
CO	10^{-5}	0.1
O_3	$<10^{-5}$	$<6\times10^{-5}$ a

[a]Displays large variations with latitude and season.

Sources of data: McCormac (1971) (ref. 14); Noll and McElroy (ref. 13); Barth (ref. 15); Levine (ref. 7)

(d) Average Solar Radiation Incident at the Surface (cal/cm^2/day)

Latitude, deg	Earth[a] Northern Hemisphere		Mars Northern Hemisphere	
	Summer	Winter	Summer	Winter
90 N	327?	0	320	0
45 N	520	112	315	100
0	380	419	250	365
45 S	99	513	100	450
90 S	0	341?	0	450

[a]Includes attenuation due to atmospheric turbidity and cloudiness.

Sources of data: Unpublished notes of H. H. Lettau (Univ. of Wisconsin) (Earth values); Levine, Kraemer, and Kuhn (ref. 16) (Martian values).

(e) Average Ultraviolet Radiation Incident at the Surface (cal/cm^2/day)

UV Band	Earth	Mars
2000-3000 Å	≈ 0	10.6[a]

[a]This figure is equal to 6×10^3 erg/cm^2/sec.

Source of data: Nawrocki and Papa (ref. 17).

TABLE I.- Concluded.

(f) Average Surface Temperature, K

Latitude, deg	Earth[a] Northern Hemisphere		Mars Northern Hemisphere	
	Summer	Winter	Summer	Winter
90 N	279	235	185	145
45 N	289	261	220	175
0	297	297	200	240
45 S	279	287	162	265
90 S	226	263	145	200

Sources of data: Crutcher (ref. 18) (Earth values); Woiceshyn (ref. 19); Conrath et al. (ref. 20); Kliore et al. (ref. 21); Hanel et al. (ref. 22) (Mars values).

(g) A Chemical Inventory (g/cm^2)

Species	Earth	Mars
CO_2		
atmosphere:	0.3	15
crust:	10^5	$10-10^3$?
H_2O		
atmosphere:	2	0.01
crust:	10^6	$1-10^3$?
O_2		
atmosphere:	200	0.01
crust:	10^7	?
N_2		
atmosphere:	780	0.5 ?
crust:	10^2 ?	1-4 ?
O_3		
atmosphere:	10^{-3}	2×10^{-7}

Sources of data: Barth (ref. 15); Noll and McElroy (ref. 13); Fanale and Cannon (ref. 23); Sagan (ref. 11); Ingersoll (ref. 24)

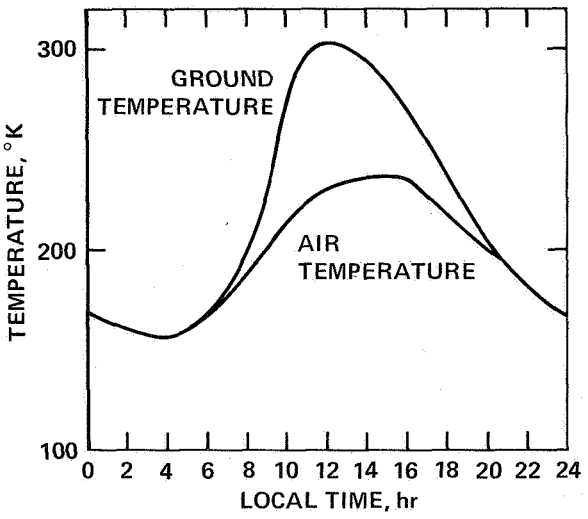

Figure 1.- Diurnal surface temperature for Mars; at the equator at equinox.

CREATION OF AN ARTIFICIAL ATMOSPHERE ON THE MOON

Richard R. Vondrak
Stanford Research Institute

SUMMARY

At the present time the solar wind is able to rapidly remove gases added to the thin lunar atmosphere. However, if the lunar atmosphere were to become more dense, loss to the solar wind would be ineffective and thermal escape would become the dominant loss mechanism. The lunar atmosphere would then be long-lived since thermal escape lifetimes are thousands of years. Evaluation of possible methods of gas production indicates that it is technologically feasible to create an artificial long-lived lunar atmosphere.

INTRODUCTION

The present lunar atmosphere is a collisionless exosphere with surface number densities less than 10^7 cm^{-3} and a total mass less than 10^4 kg. This tenuous state is maintained by the solar wind, which promptly removes ionized gas from the lunar vicinity through the action of the interplanetary electric field As shown in figure 1, an atmospheric ion formed through photoionization by the solar ultraviolet or by collisional ionization by the solar wind is accelerated initially in the direction of the interplanetary electric field. Half of the ions are thus lost into space and half are driven into the surface. The mean residence time of an atom or molecule is the ionization lifetime (typically 10^6 to 10^7 sec). The accelerated atmospheric ions have been directly detected for both the natural lunar atmosphere and gases released during the Apollo missions (refs. 1 and 2). Exponential decay times of the order of one month were observed for the Apollo exhaust gases.

The solar-wind loss mechanism is the dominant process only so long as the solar wind has direct access to the majority of the atmosphere. As the atmosphere becomes more dense, newly formed ions of atmospheric origin load down the solar wind and cause it to be diverted around the Moon (see figure 2). Thermal escape then becomes the dominant loss mechanism and the atmosphere becomes long-lived, since thermal escape times are thousands of years for gases heavier than helium.

In this paper I examine quantitatively the effectiveness of the lunar atmospheric loss mechanisms. It is found that it is possible to artificially increase the density of the lunar atmosphere so that the atmospheric source

rate exceeds the ability of the solar wind to carry off the gas. Thus, the present lunar "vacuum" is a fragile state that could be modified by human activity, and that should be treated carefully if it is to be preserved.

ATMOSPHERIC LOSS MECHANISMS

A quantitative evaluation of the lunar-atmosphere loss mechanisms is shown in figure 3 for an oxygen atmosphere. The exospheric loss rate to the solar wind was calculated by assuming that the total ionization rate was 5×10^{-6} ion per atom s^{-1} and that half of the exospheric mass was on the day-side. The limit to mass lost to the solar wind for a thick atmosphere is taken as equal to the solar-wind mass flux through the lunar cross section (≈ 30 g-s^{-1}), since critical mass loading of the solar wind occurs if ions are added at a rate comparable to the solar wind flow (ref. 3). Venus and Mars each lose about 10 g-s^{-1} to the solar wind (refs. 3 and 4), which is 1% (Venus) and 20% (Mars) of the mass flux of the solar wind through their cross-sectional areas. The thermal escape rate (ref. 5) was calculated with 300 K as the weighted average of the lunar surface temperature. Absorption of the solar wind and ultraviolet by a thick atmosphere results in exospheric heating and more effective thermal evaporation. However, as the atmospheric density is increased, the exospheric base rises above the surface and the mass lost to thermal evaporation becomes constant.

Details of the transition from a thin to a thick atmosphere are still uncertain because of incomplete understanding of the mechanisms by which the solar wind is deflected and the exosphere is heated. In particular, the thick atmosphere thermal loss has probably been overestimated in figure 3, since it is unlikely that exospheric heating occurs as rapidly as indicated. However, it is expected that a crossover will occur between solar-wind loss and thermal loss. More importantly, both loss rates will approach constant values so that atmospheric loss becomes essentially linear rather than exponential.

Other features of atmospheric loss, such as possible absorption of gases by the lunar soil, have been examined in detail in ref. 6.

If gases are added to the lunar atmosphere, the atmospheric size will increase until the source rate is equal to the loss rate. Figure 4 shows the atmospheric masses that result from various constant gas addition rates, Q. The effect of inducing a transition from an exosphere with rapid loss to a thick atmosphere with slow loss is illustrated by considering the result when the gas source is shut off (Q = 0). The thick atmosphere decays with an exponential lifetime of several hundred years, whereas the thin atmosphere decays in a few weeks. Although the transition to a long-lived atmosphere requires a total mass of 10^8 kg, the surface density would still be low compared to densities in the terrestrial atmosphere. For atmospheres in excess

of 10^8 kg the loss rate cannot increase substantially and, in principle, the atmosphere can grow indefinitely if the source rate exceeds 60 kg-s^{-1}.

ATMOSPHERIC SOURCES

The total lunar atmospheric mass is at present less than 10^4 kg and is maintained by a natural source rate less than 10 g-s^{-1} (ref. 7). A larger gas addition rate will result in an artificial lunar atmosphere in which the gases of natural origin are only trace components. As discussed above, an increase to 10^8 kg, such as could be accomplished by a sustained release rate exceeding 60 kg s^{-1}, would result in a long-lived lunar atmosphere.

Each Apollo mission deposited nearly 10^4 kg of rocket exhaust into the lunar environment. However, since they occurred infrequently, no long-lived increase in the lunar atmosphere was produced. A permanent lunar base would probably release gas at a rate equivalent to 10^{-2} kg-s^{-1} per man, assuming supply traffic equal to one Apollo mission $month^{-1}$ per man. Therefore, small lunar colonies would seem to present no lasting hazard to the lunar environment. Another potential source of gas contamination is mining of the lunar surface. Examination of the lunar samples indicates that about 10^{-4} of the mass of the lunar soil consists of trapped gases. Perhaps 10% of these gases will be released during upheaval and heating of the soil in normal mining operations. Construction of large structures in space have been proposed by O'Neill (ref. 8) that would require the removal of about 10^9 kg of soil from the lunar surface. Mining this amount would yield only about 10^4 kg of gases, so this does not appear to be a significant source of atmospheric contamination. However, vigorous lunar colonization and mining could result in more substantial release rates.

If one wanted intentionally to create an artificial lunar atmosphere, gases could be obtained by vaporization of the lunar soil. Approximately 25 MW is needed to produce 1 kg-s^{-1} of oxygen by soil vaporization. An efficient mechanism for gas generation is subsurface mining with nuclear explosives, as shown in figure 5. K. Ehricke (ref. 9) estimates that a 1-kt nuclear device will form a cavern approximately 40 m in diameter from which 10^7 kg of oxygen can be recovered. Application of this technique can easily generate the 10^8 kg of gas needed to drive the Moon into the long-lived atmosphere state.

An obvious speculation is the feasibility of creating an artificial lunar atmosphere that would be "breathable" or as dense as the surface terrestrial atmosphere. Such a lunar atmosphere would have a total mass of 2×10^{18} kg. Obtaining this much oxygen by vaporization of lunar soil requires an amount of energy equal to 2×10^{11} kt of TNT. Since this is approximately 10^4 times larger than the total U.S. stockpile of nuclear weapons (ref. 10), it seems impractical that such an amount of gas could be generated by current technology.

Since there are no known natural gas reservoirs on the Moon, it would be necessary to import gases. For example, a cometary nucleus of radius 80 km contains 2×10^{18} kg of oxygen.

The desirability of intentionally increasing the density of the lunar atmosphere is highly questionable, since the primary applications of a lunar laboratory involve utilization of the present lunar "vacuum." But the artificial generation of an atmosphere can be considered as another potential method for modification of planetary environments.

CONCLUSIONS

The principal results of this study are:

(1) An increase in the mass of the present lunar exosphere could result in an atmosphere with a relatively long lifetime.

(2) Such a long-lived atmosphere could be created inadvertently through active lunar colonization, or intentionally, if desired, by technological methods presently feasible. Even modest lunar exploration results in a lunar atmosphere in which the gases of natural origin are only trace components.

(3) Creation of a dense lunar atmosphere comparable to the terrestrial atmosphere is not feasible with current technology.

REFERENCES

1. Lindeman, R.; Freeman, J.; and Vondrak, R.: Ions from the Lunar Atmosphere. Proceedings of the Fourth Lunar Science Conference. Geochim. Cosmochim. Acta, Suppl. 4, vol. 3, 1973, pp. 2889-2896.

2. Freeman, J.; Fenner, M.; Hills,H.; Lindeman, R.; Medrano, R.; and Meister, J.; Suprathermal Ions near the Moon. Icarus, vol. 16, 1972, pp. 328-338.

3. Michel, F. C.: Solar-Wind-Induced Mass Loss from Magnetic Field Free Planets. Planet. Space Sci., vol. 19, 1971, pp. 1580-1582.

4. Cloutier, P. A.; Daniell, R. E.; and Butler, D. M.: Atmospheric Ion Wakes of Venus and Mars in the Solar Wind. Planet. Space Sci., vol. 22, 1974, pp. 967-990.

5. Johnson, F. S.: Lunar Atmosphere. Rev. Geophys. Space Phys., vol. 9, 1971, pp. 813-823.

6. Vondrak, R.: Creation of an Artificial Lunar Atmosphere. Nature, vol. 248, no. 5450, April 19, 1974, pp. 657-659.

7. Vondrak, R.; Freeman, J.; and Lindeman, R.: Measurements of Lunar Atmospheric Loss Rate. Proceedings of the Fifth Lunar Science Conference. Geochim. Cosmochim. Acta, Suppl. 5, vol. 3, 1974, pp. 2945-2954.

8. O'Neill, G. K.: The Colonization of Space. Physics Today, vol. 28, no. 9, 1974, pp. 32-43.

9. Ehricke, K. A.: Lunar Industries and Their Value for the Human Environment on Earth. Acta Astronautica, vol. 1, 1974, pp. 585-622.

10. Symington, S.: Address to the General Assembly of the United Nations, New York, 21 October 1974.

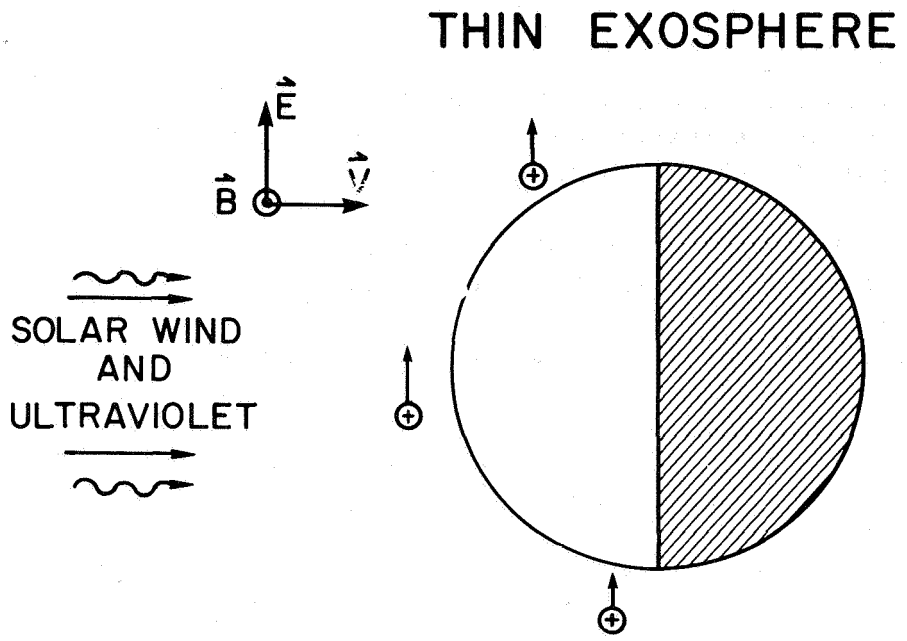

Figure 1.- Interaction between a thin exosphere and the solar wind. Ions are formed by photoionization or collisional ionization and are then accelerated by the interplanetary electric field E that results from the convection of the interplanetary magnetic field B past the moon at the solar wind velocity V.

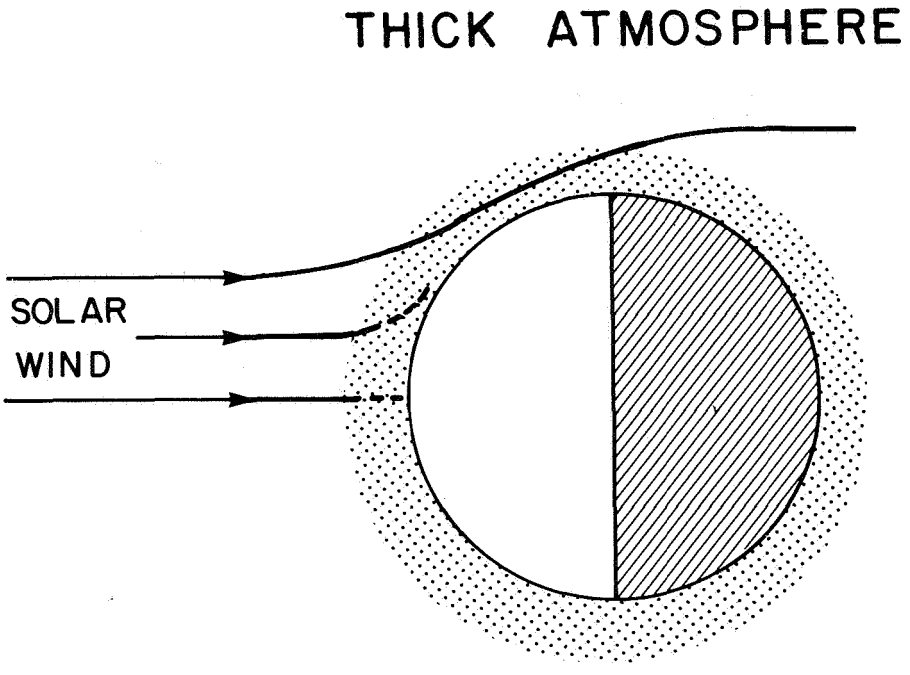

Figure 2.- Interaction between a thick atmosphere and the solar wind. Solar-wind flow is diverted around the planet by the formation of an ionopause.

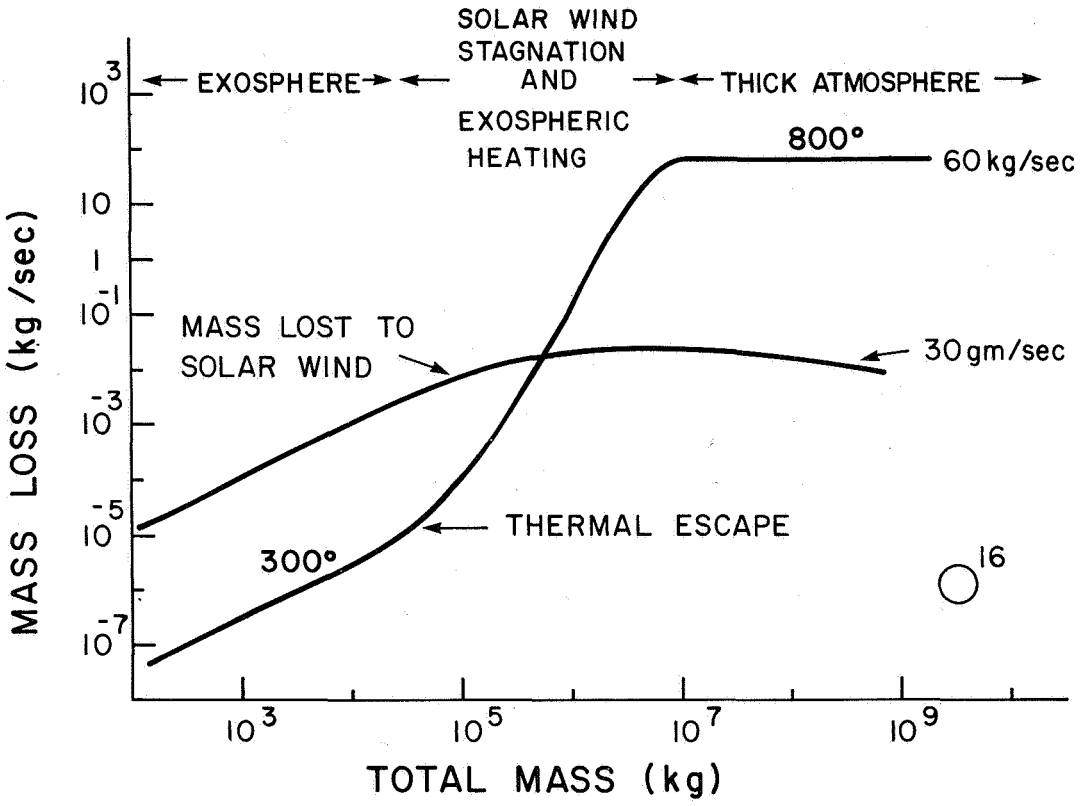

Figure 3.- Loss rates for an oxygen (mass 16 a.m.u.) atmosphere of varying size.

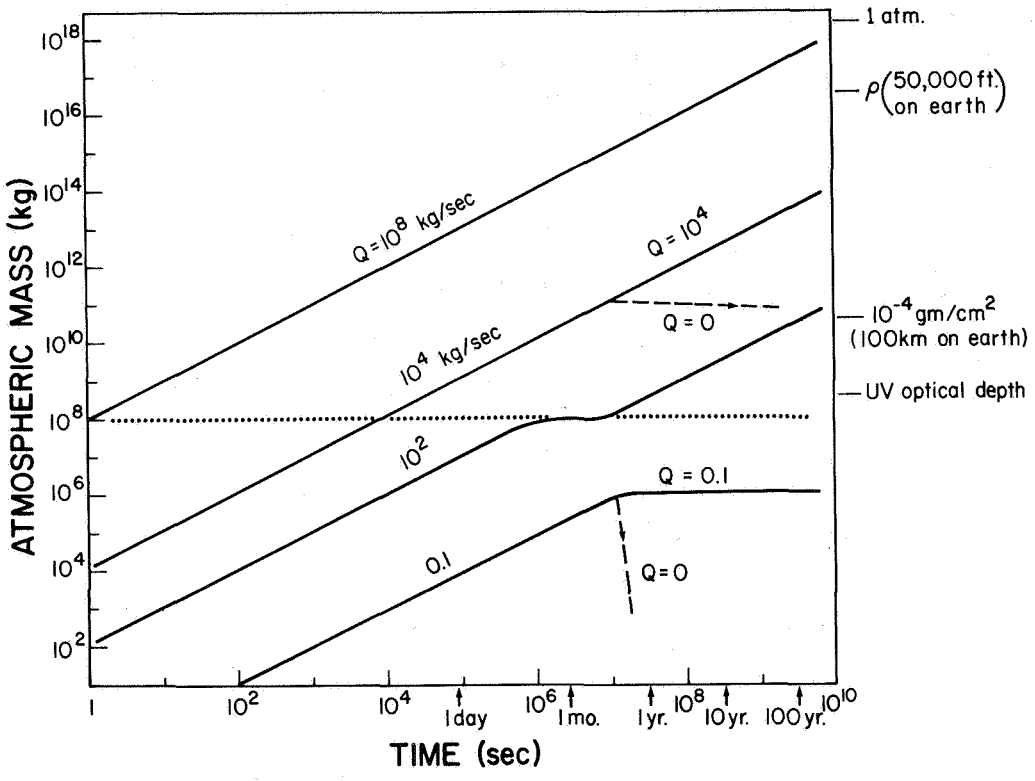

Figure 4.- Growth curves of the lunar atmosphere for various constant gas addition rates, Q. Comparable densities in the terrestrial atmosphere are indicated. Dashed lines indicate decay in the total mass if the gas source is shut off.

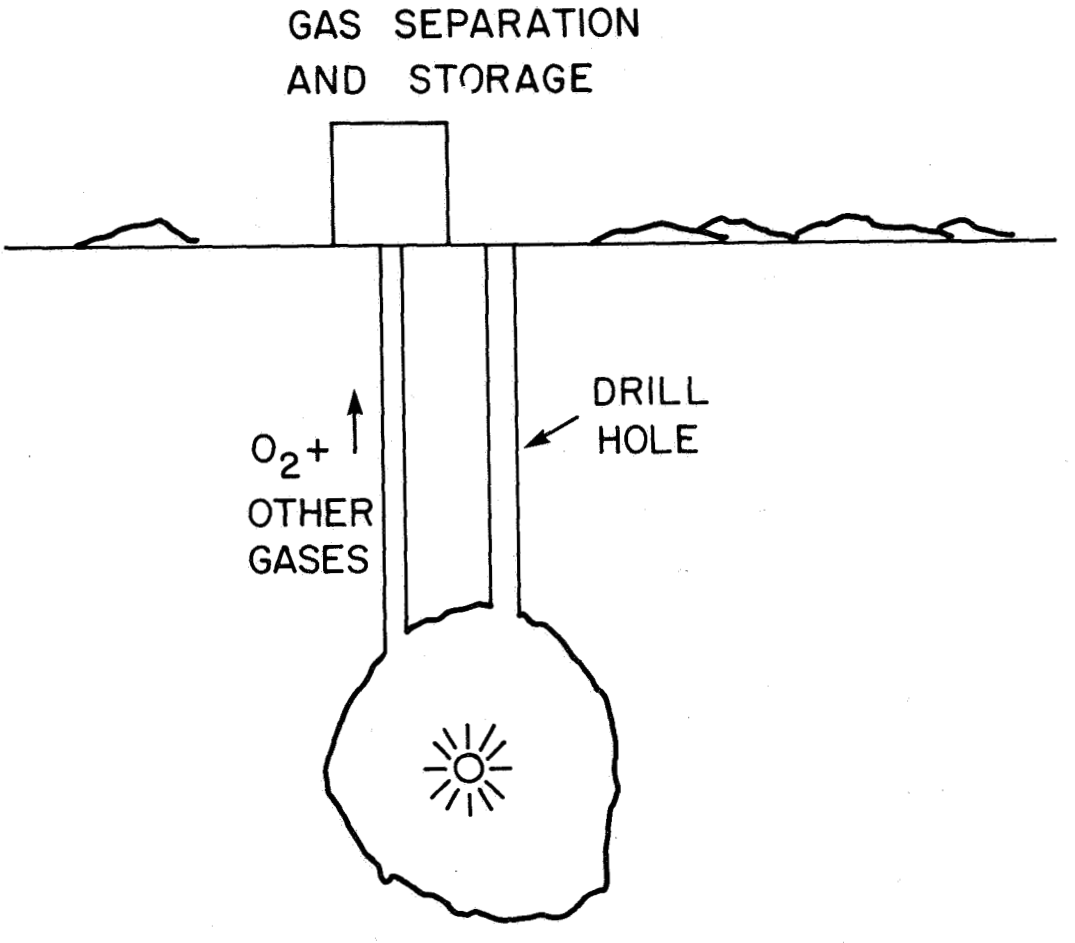

Figure 5.- A method, proposed by Ehricke (ref. 9), for obtaining oxygen from underground nuclear explosions. Ehricke estimates that 1 kt of TNT will yield about 10^7 kg of recoverable oxygen.

A TWO-DIMENSIONAL STRATOSPHERIC MODEL OF THE DISPERSION OF AEROSOLS FROM THE FUEGO VOLCANIC ERUPTION

Ellis E. Remsberg
Langley Research Center

Carolyn F. Jones*
Vought Corporation

Jae Park
College of William and Mary

SUMMARY

The eruption of the Volcan de Fuego in Guatemala (15°N) in October 1974 provides an excellent opportunity to study the effects of a major incursion of volcanic aerosols into the stratosphere. Observational data of the pre- and post-volcanic aerosols are used in conjunction with predictions of a 2-D circulation model to gain better understanding of the transport, chemical, and sedimentation processes which determine the stratospheric aerosol layer.

INTRODUCTION

Knowledge of the distribution of the volcanic aerosols is important not only for a better understanding of the stratospheric circulation, but also for estimating decreases of the mean temperature of the Earth's surface due to increases in aerosol amounts. Stratospheric aerosols are predominantly sulfate particles—possibly SO_2 converted through a series of reactions to SO_3 and then hydrolyzed to H_2SO_4. The major portion of all stratospheric aerosols is due to volcanic eruptions. Other natural and anthropogenic aerosol sources occur through troposphere-stratosphere exchange processes which may be responsible for the background concentrations of 0.5 particles per cm^3 with sizes ranging from about 0.1 to 1.0 micrometer in radius. The properties of the stratospheric aerosols and their effects on the radiation balance can be found in Cadle and Grams (ref. 1).

Remote sensing techniques have been used to monitor stratospheric aerosols at fixed locations and from aircraft. One such technique, the laser radar (lidar), has been successfully utilized since 1963 to give vertical profiles of aerosol layers. The principle of the lidar and the lidar calibration have been described by Northam, et al. (ref. 2). A lidar measure of the aerosol mixing ratio is the scattering ratio R_s

*Presently employed by Old Dominion University

$$R_s = 1.0 + \frac{f_a}{f_m} \tag{1}$$

where f_a and f_m are the aerosol and molecular backscattering functions, respectively. The f-values are products of the species cross section and number density. Any R_s value greater than one represents backscattering from aerosols. If the aerosol cross section is constant with height, the scattering ratio profile is a direct measure of aerosol number density.

Figure 1 shows two R_s profiles obtained by lidar at Hampton, Virginia. The plot for January 2, 1975, represents an enhanced aerosol layer due to volcanic activity in Guatemala in October 1974. The February 19, 1976, profile resembles a near-background aerosol level and shows the depletion of the January 2 layer over 13 months.

As a result of the substantial quantity of lidar data available from a semi-global observation network, an analysis of theoretical models of the latitudinal and vertical dispersion of the stratospheric aerosol layer can be conducted. This paper specifically concerns the Fuego volcanic eruptions in Guatemala (15°N) in October 1974 (ref. 3). Chemical processes, atmospheric transport, and particle sedimentation processes are evaluated for that event. The aerosol property in equation (1) is then compared for both observations and theory.

MODEL DESCRIPTION

The rate of change of aerosol mixing ratio is defined by

$$\frac{dN}{dt} = \left(\frac{\partial N}{\partial t}\right)_{ch} + \left(\frac{\partial N}{\partial t}\right)_{tr} + \left(\frac{\partial N}{\partial t}\right)_{gr} \tag{2}$$

where N is aerosol mixing ratio, $\left(\frac{\partial N}{\partial t}\right)_{ch}$ is the chemical term, $\left(\frac{\partial N}{\partial t}\right)_{tr}$ is the transport term, and $\left(\frac{\partial N}{\partial t}\right)_{gr}$ is the aerosol growth rate term.

The SO_2 to aerosol conversion chemistry was initially considered with a one-dimensional model to determine its importance in the long-term aerosol dispersion. A simple SO_2 to H_2SO_4 gas chemistry follows the route

$$SO_2 \rightarrow HSO_3 \rightarrow SO_3 \rightarrow H_2SO_4 \tag{3}$$

The $SO_2 \rightarrow H_2SO_4$ conversion is estimated to take place within about 100 days. Since aerosol chemistry is not well understood, the modeling attempt in this paper neglects the term $\left(\frac{\partial N}{\partial t}\right)_{ch}$.

The dynamical model developed by Louis (ref. 4) includes advection by the mean meridional circulation and diffusion by large-scale eddies. The model extends from 0 to 50 km in altitude with a grid spacing of 1 km and from 90°N to 90°S with a grid spacing of 5 degrees. The continuity equation for the aerosol mass mixing ratio is integrated at specified time steps using a semi-implicit, centered-difference scheme. For simulations presented in this paper, the circulation has been specified by monthly mean winds and eddy diffusion parameters derived from the seasonal circulation in Louis' Model II. Louis' model has successfully approximated the distributions of trace gases and radioactive debris in the stratosphere. In particular, the analysis of a volcanic event represents dispersion from a point source, similar to that for radioactive bomb debris.

The transport term also includes the sedimentation of aerosol. Hunten (ref. 5) has discussed the importance of aerosol sedimentation rates for determining the residence times of volcanic aerosol layers. Aerosol fall speeds for various aerosol sizes tabulated by Kasten (ref. 6) for particle densities of $1.5 g/cm^3$ have been applied to an initial aerosol size distribution. An estimate of the Fuego aerosol size distribution has been adopted from the 1963 measurements by Mossop (ref. 7) obtained 1 month after the eruption of Mount Agung. The total size distribution has been divided into four size ranges with mean radii of 0.16, 0.32, 0.53, and 0.93μ. Distributions of mass mixing ratios of four different sizes are then calculated as functions of altitude and time.

Aerosol growth by both coagulation and condensation mechanisms has been evaluated by Hamill, et al. (ref. 8). Coagulation processes would be noted by a change in the size distribution with time, where larger particles grow at the expense of smaller ones. Observations, however, show a relative decrease in the number of large particles as a function of time, thus indicating that sedimentation dominates coagulation in its effect on the total aerosol mass profile. Conversely, condensation, or H_2SO_4 gas to aerosol conversion, actually, adds to the total aerosol mass. The condensation process varies directly with H_2SO_4 gas number density and, for a volcanic event, would be a function of altitude. For a layer of aerosol and gas injected at 20 km, the net effect of growth by condensation on the aerosol profile would be to prolong the existence of the aerosol layer. Because the effects of aerosol growth are only understood qualitatively, they have not been incorporated into the model calculations at this time.

Initially then, it is assumed that any substantial deviations between the model results and the observed aerosol profiles can be accounted for within the uncertainties in the aerosol sedimentation growth rates and chemistry. As mentioned before, the transport model by Louis is assumed reasonable for studying the dispersion of stratospheric aerosol.

COMPUTATIONAL METHOD

The aerosol distribution is predicted by the model in the form

$$N(t) = N(t_o) + \frac{dN}{dt} \tag{4}$$

where $\frac{dN}{dt}$ is defined in equation (2). Initial conditions of aerosol distribution $N(t_o)$ for the model were estimated from several data sources. High resolution infrared satellite photographs (released by the National Oceanic and Atmospheric Administration in Rockville, Maryland) were employed to estimate the initial size and direction of the dust clouds for several days after the eruptions of October 14 and 17, 1974. Since the photographs and local wind profiles indicate that the October 17 event was responsible for the bulk of the 20-km layer, a grid based on that event is used in the model. The model is started on October 19 at 1200Z to allow for some spread of the cloud. Data taken by lidar at Hawaii (ref. 9) on October 29 were applied to verify the initial vertical profile of the dust layer. The vertical width of the layer at half maximum as computed by the model for October 29 at 20°N was compared with the observations (half-width of 0.8 km) at Mauna Loa Observatory in Hawaii for that date. The shape of the model profiles at all latitudes where aerosol had been transported in that 10-day period was adjusted to agree with the Hawaii observations. These adjusted profiles then represent the initial conditions for the aerosol source. Amounts of injected material were determined from estimates by Cadle, et al. (ref. 10).

A constant mass mixing ratio of 2×10^{-10} was assumed for the model at a lower boundary of 10 km. Dustsonde data from Wyoming (ref. 11) support this assumption that the aerosol mixing ratio remains almost constant with time after the eruption in the troposphere.

RESULTS AND DISCUSSION

Figure 2 displays the integrated aerosol mass density between 16 and 21 km as a function of time after the eruption. The solid line represents the lidar data from Hampton, Virginia (37°N), and considerable variability is present in the early returns. The lidar data were obtained by summations over 1-km increments of

$$(\bar{R}_s(Z) - 1)\, N_m(Z) \tag{5}$$

where $\bar{R}_s(Z)$ is the average scattering ratio and $N_m(Z)$ is the molecular number density (see eq. (1)). Thus, the relative aerosol column density applies to a 5-km column of 1-cm^2 cross section. The quantity on the ordinate is then equivalent to $(\sigma_a/\sigma_m)\, N_a(Z)$ where σ_a and σ_m are aerosol and molecular cross sections, respectively, and $N_a(Z)$ is the aerosol number density which is directly proportional to aerosol mass density. No attempt

has been made to actually compute mass densities from the lidar data. That is, no adjustment has been made for possible variations of σ_a with time.

The model results in figure 2 are an average for 35° and 40°N latitude. The model quantity is a little different from observed quantities (eq. (5)) because it does not contain the additional effects of various size distributions as does the scattering ratio lidar measurements which are more sensitive to larger size particles. The circles in the figure are for a log-normal background type aerosol size distribution (ref. 12) where the mean radius is 0.0725μ (see later discussion). The triangles are for a volcanic aerosol size distribution taken from Mossop (ref. 7).

The peak magnitudes of the lidar and model data have been arbitrarily adjusted to afford a better comparison of the time rate of change of the aerosol column load. The time of the occurrence of the maximum aerosol load has been simulated very well by the model, indicating that the meridional transport for the first few months is correct. The 1/e decay time for the integrated aerosol column density from lidar measurements (16-21 km) after February 1965 is about 10 months.

The data for aerosol column density both with and without sedimentation acting on the log-normal background distribution compare almost exactly, and verify that sedimentation has little effect on aerosols with radii less than 0.1 micrometer. However, inclusion of sedimentation for a volcanic aerosol size distribution indicates rapid aerosol depletion with time.

Figure 3 shows the initial size distribution adopted from Mossop for the Agung eruption for 20 km and 15° to 35°S latitude and then compares subsequent measured size distributions with those determined from the model by including sedimentation processes. In general, the comparison is reasonable; however, in all cases observed size distributions possess steeper slopes. This trend could be affected by the growth of small aerosols by condensation of H_2SO_4 gas. A size distribution of Fuego dust at 18 km obtained by G. Ferry on April 30, 1975, over Northern California (40°N) is also shown. This measurement, taken some 195 days after the Fuego event, indicates a size distribution slope steeper than both the model result and the Agung measurements. Therefore, the initial size distribution employed in this model may contain too many large particles and the sedimentation rates would have been too rapid and therefore would have affected the results shown in figure 2 as well. That is, the rapid depletion of aerosol column density after January is due to depletion of larger size particles. This rapid depletion is also caused by the fixed lower boundary condition of minimum background value at 10 km, forcing more aerosol mass into the troposphere.

Figure 4 displays aerosol profiles for 35 to 40°N for February and May 1975; the lidar data are plotted in terms of aerosol mass mixing ratios while the dustsonde profiles from the University of Wyoming (ref. 11) are in terms of aerosol number density mixing ratios for particles greater than 0.15 micrometer in radius. Although there are some amplitude variations between the lidar and dustsonde data, the mean altitudes of the layer peaks and the widths at half-maximum are comparable. The corresponding model profiles are presented both with and without sedimentation effects. The model results clearly show

the effects of sedimentation. The width at half-maximum is overestimated for the case with no gravitational settling. This latter result means that either the transport is too rapid or that there is considerable chemical production of aerosol mass in the layer itself. These same trends are also evident in comparisons between model profiles at 20°N and lidar data from the Mauna Loa Observatory, Hawaii (19°N). The profiles showing sedimentation effects indicate a very low peak aerosol load at 13 km. Again, this is probably due to the boundary condition imposed and too many large particles in the size distribution chosen.

This initial study into the dispersion of volcanic particles has shown that transport alone does not account for the spread to other latitudes and altitudes. In order to obtain more accurate sedimentation rates, it will be necessary to have more post-volcanic particle size distribution data. The aerosol chemistry may be of importance and should be included in further studies. Quantitative knowledge of aerosol growth by gas condensation must also be considered.

REFERENCES

1. Cadle, R. D.; and Grams, G. W.: Stratospheric Aerosol Particles and Their Optical Properties. Rev. of Geophys. and Space Phys., vol. 13, 1975, pp. 475-501.

2. Northam, G. B.; Rosen, J. M.; Melfi, S. H.; Pepin, T. J.; McCormick, M. P.; Hofmann, D. J.; and Fuller, W. H., Jr.: A Comparison of Dustsonde and LIDAR Measurements of Stratospheric Aerosols. Appl. Opt., vol. 13, 1974, pp. 2416-2421.

3. Remsberg, E. E.; and Northam, G. B.: A Comparison of Dustsonde and LIDAR Measurements of Stratospheric Aerosols. Proceedings of the Fourth Conference on the Climatic Impact Assessment Program (CIAP). Department of Transportation, 1976.

4. Louis, J. F.: A Two-Dimensional Transport Model of the Atmosphere. Ph.D Thesis, Univ. of Colorado, 1974.

5. Hunten, D.: Residence Times of Aerosols and Gases in the Stratosphere. Geophys. Res. Let., vol. 2, 1975, pp. 26-28.

6. Kasten, F.: Falling Speed of Aerosol Particles. J. Appl. Meteor., vol. 7, 1968, pp. 944-947.

7. Mossop, S. C.: Volcanic Dust Collected at an Altitude of 20 Km. Nature, vol. 203, 1964, pp. 824-827.

8. Hamill, P.; Toon, O.B.; and Kiang, C. S.: A Physical Model of the Stratospheric Aerosol Particles. Submitted for publication in J. Atmospheric Sci., 1976.

9. Fegley, R. W.; and Ellis, H. T.: Lidar Observations of a Stratospheric Dust Cloud Layer in the Tropics. Geophys. Res. Let., vol. 2, 1975, pp. 139-141.

10. Cadle, R. D.; Kiang, C. S.; and Louis, J. F.: The Global-Scale Dispersion of the Eruption Clouds From Major Volcanic Eruptions. J. Geophys. Res., vol. 81, no. 18, June 1976, pp. 3125-3132.

11. Hofmann, D. J.; and Rosen, J. M.: Balloon Observations of the Time Development of the Stratospheric Aerosol Event of 1974-75. Report AP-36, Dept. of Phys. and Astronomy, Univ. of Wyoming, 1976.

12. Pinnick, R. G.; Rosen, J. M.; and Hofmann, D. J.: Stratospheric Aerosol Measurements III: Optical Model Calculations. J. Atmos. Sci., vol. 33, 1976, pp. 304-314.

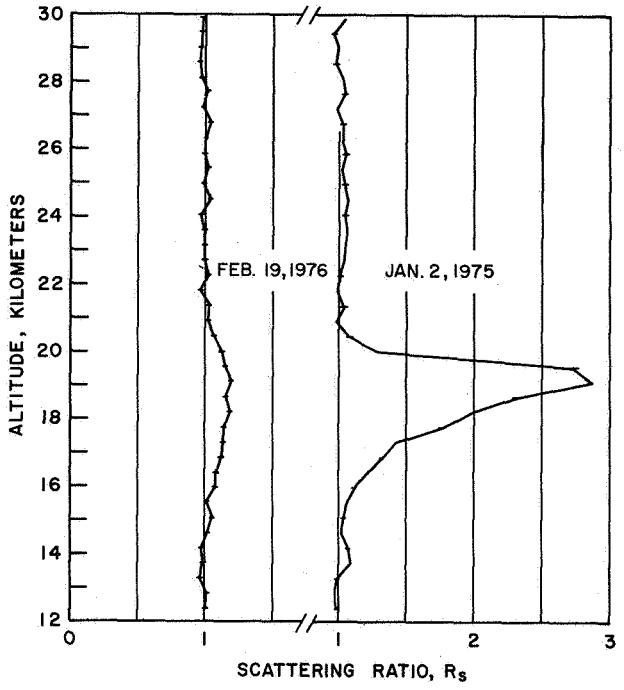

Figure 1.- Aerosol scattering ratios from lidar at Hampton, Va., following the eruption of Volcan de Fuego in October 1974.

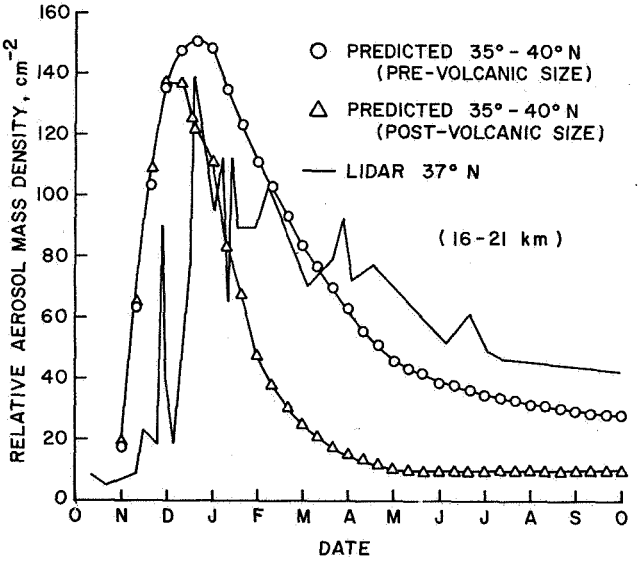

Figure 2.- Observed lidar aerosol number densities at Hampton, Va., and relative model aerosol mass densities calculated for the column 16 to 21 km.

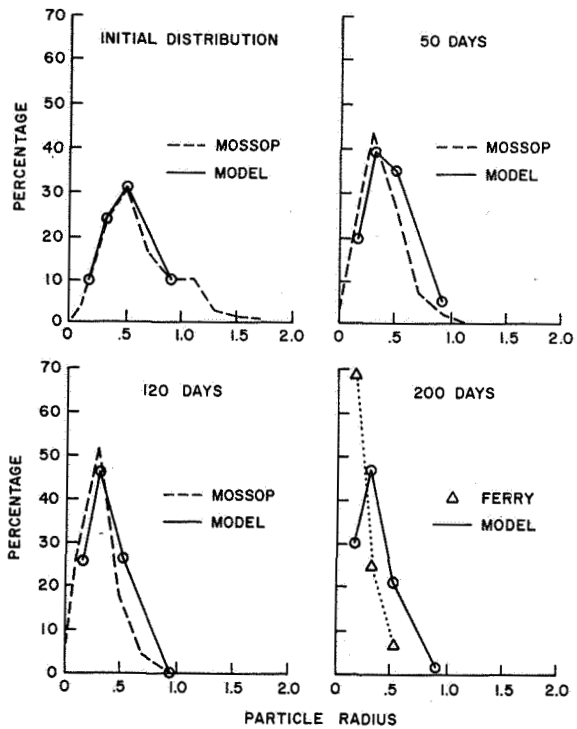

Figure 3.- Aerosol size distributions determined by Mossop (ref. 7) after the Agung eruption, by Ferry following the Fuego eruption, and model predictions employing Mossop's initial size distribution.

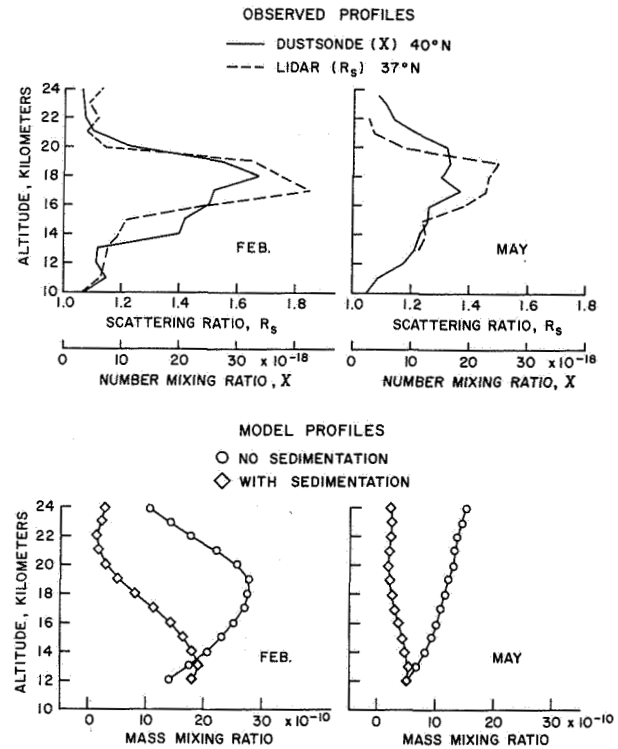

Figure 4.- Vertical profiles of aerosols from observations and model results for February and May. Units: lidar (scattering ratios); dustsonde (number mixing ratios); model (mass mixing ratios).

SOLAR ENERGY STORAGE & UTILIZATION

S. W. Yuan and A. M. Bloom
The George Washington University

The critical shortcoming in many recent schemes for using solar energy to heat buildings resides in their incapacity to store more than a few days' worth of heat. This leads to reliance on fossil-fuel backup systems and to the loss of most of the sun's energy because that energy is most available when the storage reservoir cannot accept additional heat. The most striking such example is during the period from April through September; not only collection efficiencies can be much greater because of higher outdoor ambient temperatures, but heat loss to air is much less than that of winter months.

This paper presents the concept of a heat reservoir with the ability to store solar energy for long-duration which can be used subsequently. The earth, as a thermal storage reservoir, has several interesting attributes. First, heat capacities are extremely large due to the large masses available. For example, in a volume of one acre of area by fifteen feet deep, at a temperature difference of 50°F,

$$\text{ENERGY} = \rho C \Delta T = 1.47 \times 10^9 . \text{BTU}$$

Assuming a winter heating requirement of 60×10^6 BTU for a small home, this reservoir has the capacity to supply approximately 25 homes.

Another attribute of earth is its extremely low thermal conductivity. Since the system may be unbounded in the downward and sideward directions, it is just this low conductivity that restricts losses in those directions. Since the total energy in the solar flux over one acre of area for one summer season, approximately 1.2×10^{10} BTU, is the heating load of approximately 200 houses, the energy flux that is theoretically available is extremely high.

Briefly, the ground surface would absorb the solar heat, which would then be rapidly transferred several feet downward by the use of heat exchanger piping arrays with a circulating fluid. Additional movement of heat would occur by conduction, perhaps aided by some convective flow of earth water, until the total volume (one acre by about ten feet in depth) would stabilize into a near isothermal condition. Calculations of a first order nature indicate that losses downward (assuming no flowing ground water) as well as sideward can be kept within reason, and losses upward reduced by multiple glazing techniques as well as by keeping the surface temperature as low as possible through unidirectional heat-pipe and circulator systems.

Heat is extracted from earth storage by use of heat exchange piping arrays with a circulating water located below the ground. Low temperature water is pumped into the heat exchanger and is heated by the high temperature earth. The theoretical analysis is formulated by assuming that the heat transfer in

the pipe flow is governed by conduction and convection. Furthermore, the heat transfer in the pipe is assumed to be two-dimensional and unsteady. The fluid flow through the pipe is taken to be an incompressible fully developed turbulent pipe flow. The soil region is assumed to have cylindrical symmetry about the pipe. Therefore, the heat transfer in the soil is a process of two-dimensional unsteady heat conduction.

At some initial time t=0 the soil and fluid are taken to be at the same heated temperature due to the action of solar collectors on the ground level. For t>0 the bulk fluid temperature entering the pipe is assumed to be lower than the soil temperature. This represents a simulated demand load from a house. In order to determine the temperature distributions in the fluid and soil downstream of the pipe entrance, the interface temperature distributions between the fluid and soil must be given. This requires an iteration between the soil and fluid equations. The procedure has been carried out numerically using the method of finite differences on an IBM 370 digital computer for various design conditions.

Design calculations were made for the space heating requirements of a typical house in the Washington-Baltimore area for the year 1954. Weather data was used in conjunction with an empirical house heat requirement curve to determine a simulated demand load based on the outside dry bulb temperature. The unsteady heat transfer analysis is used to compute the fluid temperature increase and soil temperature decrease through one acre of earth storage ten feet deep. 20,000 ft. of pipe was used in the ground heat exchanger. The results show that for 15,000 sq. ft. of house floor area and an initial fluid and soil temperature of 200°F (fully heated), six months of winter operation reduce the fluid and soil temperatures at the heat exchanger exit to T_f=149°F and T_s=152°F, respectively.

Therefore, it can be concluded that one acre of earth storage is adequate to provide space heating for twelve average size houses in most areas of the United States.

SOLAR HOT WATER SYSTEMS APPLICATION TO THE SOLAR BUILDING TEST FACILITY AND THE TECH HOUSE

Ross L. Goble, Ronald N. Jensen, and Robert C. Basford
NASA Langley Research Center

SUMMARY

Two projects have recently been completed by NASA which relate to the current national thrust toward demonstrating applied solar energy. One project has as its primary objective the application of a system comprised of a flat plate collector field, an absorption air conditioning system, and a hot water heating system to satisfy most of the annual cooling and heating requirements of a large commercial office building. The other project addresses the application of solar collector technology to the heating and hot water requirements of a domestic residence. In this case, however, the solar system represents only one of several important technology items, the primary objective for the project being the application of space technology to the American home.

INTRODUCTION

Energy systems employing flat plate collectors have been used for years in various parts of the world as a means of converting readily available solar energy to commercial and domestic needs. Such use has been less predominant in countries such as the United States, where electric power has been inexpensive. However, the rising cost of energy available from centralized supplies has now reached the point where interest in broader application of solar systems is also increasing. It is not surprising, therefore, that NASA became involved several years ago in this area of technology, given its capability to evolve needed systems, and its need to mitigate the impact of an increasing energy bill on its own operation.

These factors, coupled with the objectives of not only technology demonstration but also technology transfer to the public sector, led to two programs which have recently been completed - the Solar Building Test Facility and the Tech House.

In this paper, an overview of the technical aspects of each program is presented. Preliminary data comparing expected results with those achieved to date are also provided.

SOLAR BUILDING TEST FACILITY (SBTF)

System Description

The SBTF is a joint project of NASA Langley, NASA Lewis, and the Energy Research and Development Agency. The 4 645 square meter (m^2) (53 000 ft^2) Systems Engineering Building and its 1 189 m^2 (12 800 ft^2) Solar Energy Field constitute the SBTF which represents an operational system housing over 300 engineering personnel. The collector field is made up of 12 rows of collectors with 50 collectors in each row utilizing configurations from five manufacturers in the initial test program. The collectors are mounted facing due south at an angle of 0.6 rad (32^o) from the horizontal, the angle representing an optimum for a fixed flat plate collector system since the hot water from the system is used not only for baseboard heat in winter but also as input to a 170-ton lithium bromide absorption air conditioner for summer cooling. The system is designed to supply water at 104^o C (220^o F) at a flow rate of 1.6 m^3/min (350 gal/min). A 136 m^3 (25 000 gal) hot water storage tank will provide a constant temperature for approximately four hours during periods when insolation is minimum. It should be noted that the solar/absorption chiller system can be operated without the use of the stored water since the design permits direct use of solar heated water from the field to the chiller during periods when adequate insolation is available. An auxiliary steam converter provides backup for all other required periods. In other words, the building heating, ventilating, and air conditioning system can operate completely independent of the solar system when necessary. A schematic showing the system elements is given in Figure 1.

During the design phase of the SBTF, "NASA's Energy Cost Analysis Program" (NECAP) was used. All energy conservation concepts were evaluated and fairly reasonable estimates of the expected energy consumption were made. Initial project estimates indicated that approximately 75 percent of the year round heating requirements could be supplied by the solar field. The projections of the building requirements compared with the solar system energy available are given in Figure 2. From such information, system economics were developed in the early design phase. Design features such as the nighttime setback or shutoff were determined to be the best and simplest cost/energy saving, yielding a 30 percent energy saving in the simulation case. Other features such as the thickness of wall and roof insulation, economy cycles (use of outside air for cooling), type of air conditioning system, and window shading were also incorporated.

Because the SBTF represents an ongoing R&D program, the solar field has been installed at ground level for accessibility such that additional panel configurations may be evaluated. An aerial view of the total configuration is given in Figure 3.

Since energy efficiency is one of the objectives of this program, it is important to note that the steam requirements for a building like the Systems Engineering Building when operated in a non-energy efficient mode would be

approximately 1 800 000 kilograms (kg) (4 X 10^6 pounds) annually. By utilizing energy conservative design in the building itself, this annual requirement can be reduced to about 1 035 000 kg (2.3 X 10^6 pounds). Further, when operated with the solar system, NASA expects to require only 270 000 kg (6 X 10^5 pounds) of steam annually. This amounts to a savings of about 1 500 000 kg (3.4 X 10^6 pounds) annually, which, in terms of the fuel oil required to generate steam, equates to a savings of 104 m^3 (23 000 gal).

General System Data Methods

The SBTF is designed to test in an actual field application the effectiveness of different solar collectors and system components. Temperatures, flows, and pressures will be recorded through an automatic data processing system. The data will be reviewed on a continuing basis to determine component abnormalities, and to assist in making corrective actions to the system as well as to validate the system "math model." The ultimate goal of this developmental project is to develop the realistic math models of components and systems. When this has been successfully carried out, high speed computers will be used to optimize the operation of Langley's SBTF and to provide design data for other proposed projects.

System Results to Date

The initial operation of the SBTF began in early summer. Since that time, its operation has been quite successful with some significant operational characteristics being determined.

Up to the latter part of August, a partial field area of 929 m^2 (10 000 ft^2) has been used. This is about three-fourths of the originally sized solar field. Due to this size reduction, discharge water temperatures from the solar field, which is used to operate the chiller, run between 77 and 88° C (170 and 190° F). Minor problems, such as low pump flow characteristics, have occurred. By a natural balance of components, to date an 11 to 14° C (52 to 58° F) chilled water temperature has been obtained, yielding 80 to 90 tons of cooling. This is a substantial decrease from the computed 110-ton cooling load to be supplied, but as explained earlier, only a portion of the solar field is operational at this time.

The maximum summer discomfort level of 26° C (79° F) and 62 percent relative humidity has been established. With the reduced solar field, the ability to maintain the building within this criterion exceeds expected results. The SBTF is located in an eastern coastal region having a fairly high humidity during the summer. Thus, dehumidification has always been a design criterion. The system, however, is maintaining comfort conditions by discharging 18 to 20° C (64 to 69° F) supply air to the occupied space, which requires practically no dehumidification. One possible reason for the acceptable internal humidity condition is the low fresh air rate per person of 0.14 m^3/min (5 ft^3/min) coupled with the nighttime shutdown.

During the month of July, the projected energy consumption required for the cooling and heating system was 3.58×10^{11} joules (340×10^{6} Btu). Although the actual consumption rate must be estimated because the instrumentation is not yet fully operational, the system used about 2.95×10^{11} joules (280×10^{6} Btu). Of this, about 1.62×10^{11} joules (154×10^{6} Btu) were obtained from the solar field or 55 percent of building requirements. Thus, as additional solar collectors are added to the solar array, the prediction of 75 percent of the energy from the solar system should be met, if not well exceeded.

The required solar system temperatures are usually developed at 10:30 to 11:00 a.m. DST, at which time the system is switched over to the solar field. No supplemental heat is provided during the remainder of the day. Adequate operating temperatures are usually available beyond shutoff time due to the mass of the solar collectors in the field. This has led to the conclusion that the field should be facing somewhat east of south. Since this is not possible with our fixed arrangement, preheating of the collectors from storage is being investigated to provide earlier morning operation.

These results, coupled with findings for numerous other system elements and operational characteristics, should provide improved systems for subsequent design of commercial-type buildings.

TECH HOUSE

System Description

The Tech House project, which began several years ago, has culminated in the recent completion of a domestic residence embodying many space technology elements which appear to have utility in the home-buying market. It was felt that the home selected should be consistent with what housing authorities expected to see as the single family residence of approximately five years from now. The set of guidelines established is as follows: (1) 140 m^2 (1500 ft^2) floor area, one story, attractive and economical; (2) latest current technology (technology that may be commercially available in approximately five years), some custom made components; (3) systems selection where any extra cost would be recovered within lifetime of system; (4) total energy management of all heat sinks and sources in house; (5) best modern practices in construction, electrical, plumbing, and materials; (6) water/sewage partial reclamation; and (7) solar heating/cooling considerations.

In order to ensure that considerations from a broad spectrum of interests were incorporated in the project, an ad hoc review committee was established. It was comprised of representatives from the National Association of Home Builders (NAHB), the National Bureau of Standards (NBS), NASA's Technology Utilization Office, Department of Housing and Urban Development (HUD), Consumer Products Safety Commission, Architect-Engineers, and other NASA Centers. This committee helped shape the house design by making many helpful suggestions leading to the final configuration.

Before selecting the technology to be incorporated, a careful analysis was performed to ensure that the items used would have identifiable benefits, whether tangible or intangible, to the future homeowner. Those items finally selected are as follows: (1) heat pipe skewer, (2) low-voltage light, (3) black-chrome collector coating, (4) solar cell, (5) thermistor, (6) flat conductor cable, (7) vibrational security detector, (8) self-locking hinge, (9) foams, (10) water reclamation system, (11) NASA control and instrumentation technology, and (12) fire resistant materials. However, only those aspects of the Tech House which fit the general intent of this paper will be discussed further.

Solar System

The solar hot water system employs flat plate collectors very similar in configuration to those of the SBTF discussed earlier, except that the system here is designed to supply only the heating requirements of the residence. One hundred percent of these requirements will be met with this system. A NASA engineering analysis was performed to optimize the total energy design, yielding panel area requirements of 40 m^2 (432 ft^2). This array is located on a south-facing roof designed with an inclined angle of 1.01 rad (58^o) (different from the SBTF because the winter sun angle is the most important for heating). The house exterior is shown in Figure 4 and the solar schematic in Figure 5.

Since the solar system is designed to operate in conjunction with a heat pump, which can also use well water as a heat source, a rather unusual coefficient of performance results as can be seen in Figure 6. Note that when water in the storage tank is below 13^o C (55^o F), which indicates that the output of the solar collectors is minimum, the heat pump extracts heat from the well water. If the system water temperature is between 13 and 40^o C (55 and 105^o F), the heat pump extracts heat from the stored solar-heated water. Above 43^o C (105^o F), the solar hot water can be piped directly to the heat exchanger in the forced air system, thus permitting the heat pumps to be shut down. Coefficient of performance results are thereby achieved which are quite unlike those of any commercially available systems.

Design

Other aspects of the Tech House energy design which represent a departure from the standard home construction techniques are as follows: (1) foam insulation, (2) 15 cm (6 in.) thick exterior walls, (3) multi-zoned interior, (4) south-facing roof overhang with glass exposure, (5) exterior thermal shutters, and (6) nighttime radiator.

The foam insulation was selected over fiberglass because of its superior resistivity as well as its improved fire safety. Engineering studies showed that 15 cm (6 in.) exterior walls with the tripolymer foam insulation would lead to a significant overall cost benefit when coupled with the other

system energy elements. Also, the foam insulation can be installed after the dry walls are in place. (This is not an installation requirement, however, and was used only for the interior walls. Exterior walls were sprayed with the foam from the inside after the exterior siding was in place.)

The multi-zoned interior consists of four zones. Each zone is programmed independently by inputting the desired mode of motorized damper operation to the computer/controller. The control system is designed to permit a given program for year round operation to be developed, thus lending adaptability to any life style. The programmed operation can be adjusted at will or can be bypassed by manual override if desired.

The south-facing overhang is designed to preclude the summer sun reaching the living space but permits winter insolation through the large glass areas. Individually operated exterior shutters improve the insulation qualities of the double-glazed windows by providing two insulating cavities, one between the window and the shutter, and one in the shutter panel itself.

The nighttime radiators have been employed to permit evaluation of this method of cooling the storage tank water during summer operation. The stored water is used as the condensing medium for the heat pump. The procedure is to pump the stored water through the radiators permitting radiation to the night sky of the heat removed from the house during the day by the refrigeration cycle. Since a cool condensing medium is required primarily for the summer mode to provide increased coefficient of performance for the system, satisfactory night cooldown of the tank water by the radiators may obviate the well requirement, thus yielding a more cost effective system.

The above system elements, in conjunction with savings from other technology, are expected to yield a reduction of two-thirds in the amount of energy required for this residence as compared to a similar home with standard construction.

System Instrumentation

To measure actual results against estimated performance, the house has been heavily instrumented. In addition to data desired from other technology items, it is desirable to determine the hourly temperature patterns for the home through the diurnal cycle. To effect this measurement, thermocouples have been installed at three lateral positions across each wall and at three vertical positions near each wall face. Additional temperature data are recorded for the attic and crawl spaces to establish total system performance.

System Results to Date

During the current period, only a portion of the solar system is being operated. Of the 40 m^2 (432 ft^2) of solar collectors installed in the house, 4.5 m^2 (48 ft^2) are utilized for domestic hot water preheat. The

preheat system is currently operational flowing 0.004 m^3/min (1 gal/min) through the collectors with a maximum discharge water temperature of 75° C (167° F) being recorded at a maximum solar intensity of 2 500 000 joules/hr-m^2 (220 Btu/hr-ft^2). The domestic water temperature in the preheat tank averages 49° C (120° F). Since there has not been a demand for domestic hot water as a result of the house not being occupied, actual performance of the system has not been evaluated at this time. Total system results await the the onset of winter and the occupancy of the house such that the heating system performance can be tested.

CONCLUDING REMARKS

Two projects at NASA Langley Research Center, both embodying solar hot water systems, have been completed and are currently providing measured data. These data indicate that such systems are certainly feasible from a technology standpoint, and it is expected that long term results will provide valuable information for the practical application of solar systems for both commercial and domestic uses.

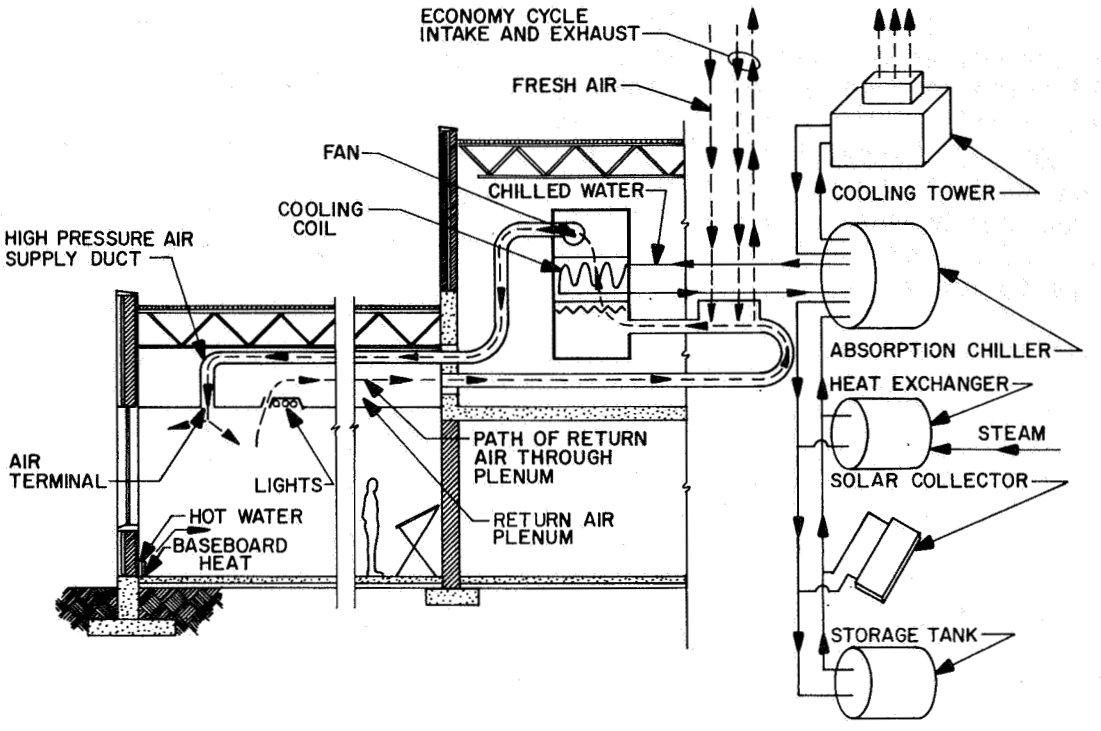

Figure 1.- SBTF solar system flow diagram.

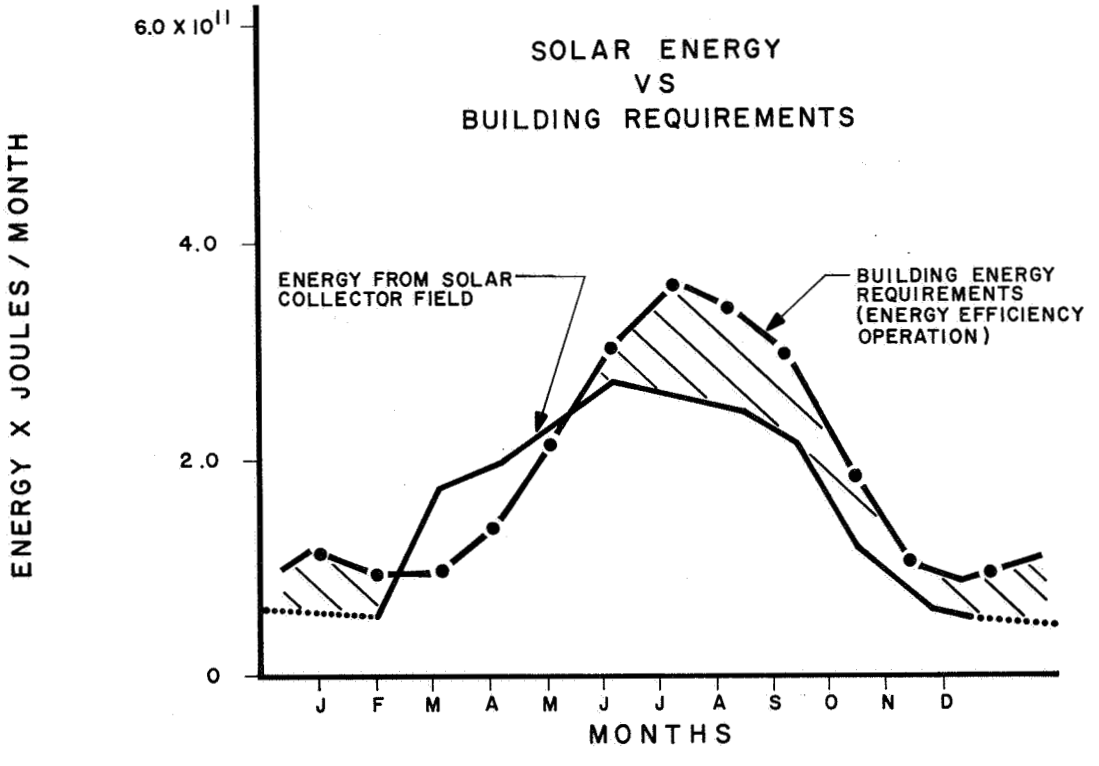

Figure 2.- Energy available versus energy required.

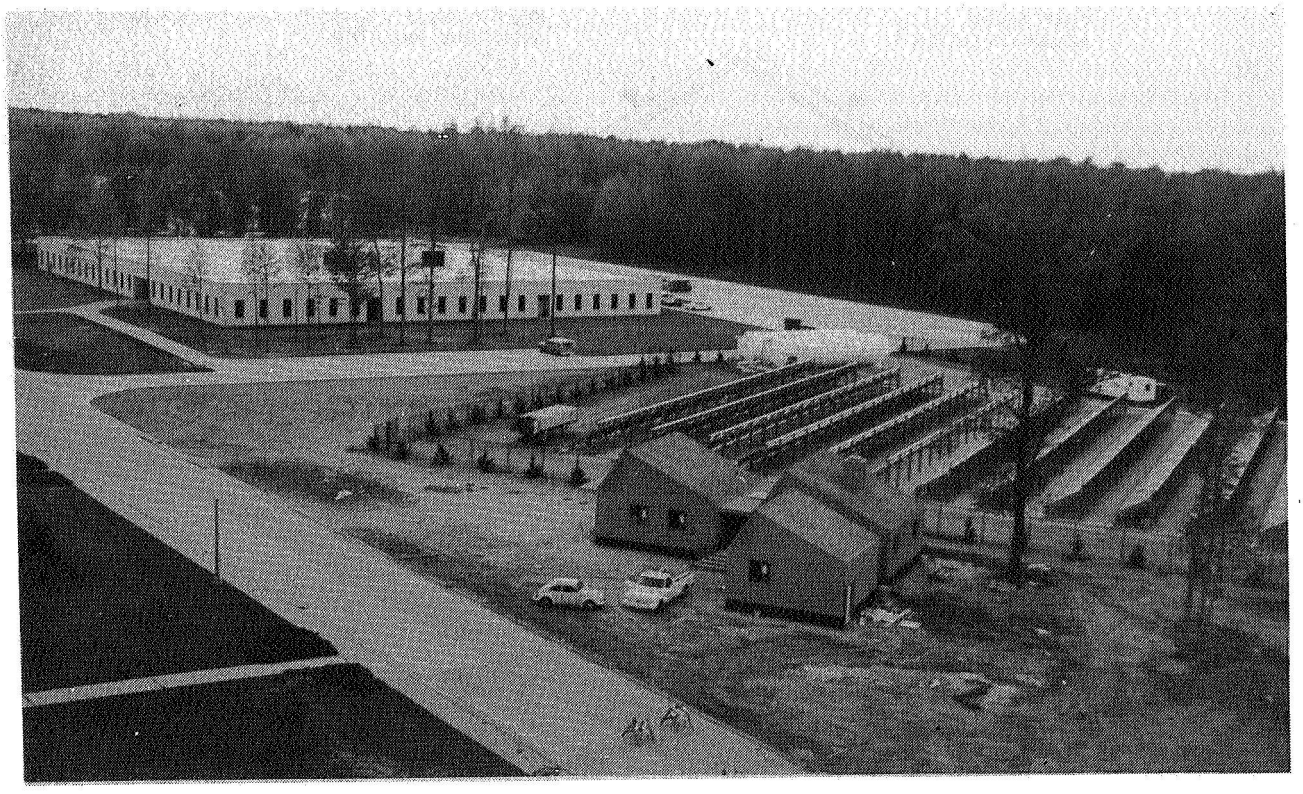

Figure 3.- Aerial view of solar building test facility.

Figure 4.- Tech house.

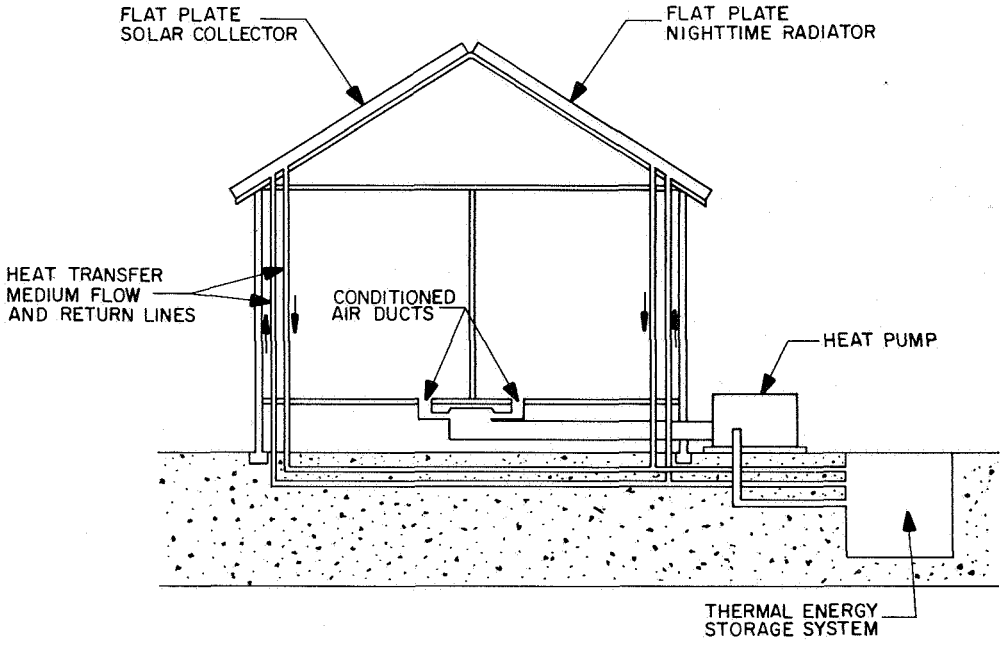

Figure 5.- Tech house solar system schematic.

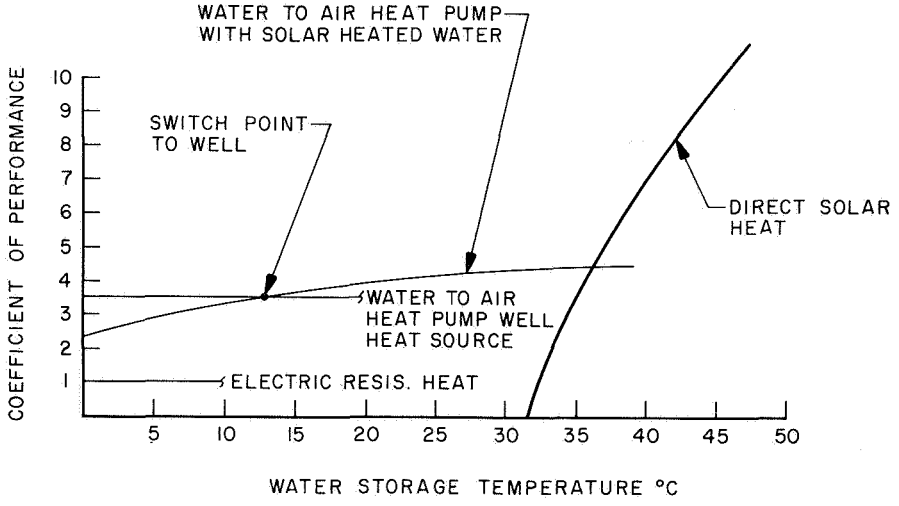

Figure 6.- Hybrid system performance curve.

D.C. ARC CHARACTERISTICS IN SUBSONIC ORIFICE NOZZLE FLOW*

Henry T. Nagamatsu and Richard E. Kinsinger
General Electric Research and Development Center

SUMMARY

The cold air flow field for a 1.27 cm orifice nozzle was determined for subsonic flow velocities. In addition, d.c. arc voltage, current, and diameter measurements were made for a range of velocities and arc gaps. Average voltage gradient increased rapidly as an arc extinguishing velocity was approached. Measured values of current and diameter were used as an input for relaxation solution of an energy balance equation to compute radial temperature profiles. Calculated arc voltage gradients compare favorably with measured average voltage gradients.

INTRODUCTION

The performance of gas blast circuit breakers depends on the extinction of the arc near current zero. The arc cooling rate is governed at low currents primarily by the following physical parameters: flow velocity, pressure, type of gas, and character of the arc, laminar or turbulent. The turbulent convection heat transfer rate from the arc to the surrounding cold gas in the nozzle is much greater than for the laminar arc as observed by Frind (ref. 1) and Hermann et al (ref. 2). In both of these investigations the arc near the upstream electrode was laminar and became turbulent as the arc length increased in the direction of the flow. The transition from laminar to turbulent arc is similar but not identical to the transition of the laminar boundary layer in subsonic flow (ref. 3) and hypersonic Mach 14 flow (ref. 4) which indicated bursts in the transition region.

Malghan et al (ref. 5) have investigated the high current arc behavior in an orifice nozzle and correlated the measurements with analytical predictions. Arc characteristics in a dual orifice nozzle interrupter configuration at very high peak currents were investigated by Thiel (ref. 6) who postulated that arc behavior was completely controlled by the turbulence phenomena.

To increase the knowledge regarding the effects of flow velocity on the arc transition at low currents, an investigation was conducted with an orifice nozzle in a steady flow facility with a low current d.c. arc. The orifice diameter was 1.27 cm and the flow velocity was varied up to sonic velocity. For

* Work supported in part by Electric Power Research Institute through Contract No. RP246-1.

various arc gaps, the arc voltage, current, resistance and diameter were determined. The final section of the paper describes a theoretical model for the low current d.c. arc. The calculated voltage gradient is compared with the experimental measurement with good agreement.

SYMBOLS

c_p	specific heat at constant pressure
D	arc diameter
E	electric field (axial)
I	electric current
j	electric current density
L	arc length
P	pressure
Δp	difference in upstream and downstream pressure
P_{rad}	net radiation power density
Q_{rad}	radiation power flux
r	radius
R	arc radius
t	time
T	temperature
U	axial velocity
V	radial velocity
ε	frequency dependent coefficient of radiative emission
κ	laminar thermal conductivity
ν	radiation frequency
π	3.14159
ρ	gas density
σ	electrical conductivity

EXPERIMENTAL APPARATUS

Orifice Nozzle and Electrodes

An orifice nozzle with a throat diameter of 1.27 cm was constructed out of Lexan for electrical insulation, as well as for visible observation of the arc at the upstream electrode. Hemispherical upstream and downstream electrodes were made from 1.27 cm diameter copper-tungsten rod. Both electrodes are adjustable relative to the orifice throat. A drawing of the nozzle and electrodes arrangement is shown in figure 1. The air flow through the nozzle discharges into an exhaust vent.

Electrical connection from the MG power supply to the electrode is made to the metal plate which holds the upstream cathode, and the downstream anode is mounted to a movable insulated probe holder. To initiate the arc after steady flow is established the electrode gap is bridged by a 0.25 mm copper wire.

Flow System

The high pressure air is supplied by a 200 hp compressor with a large storage tank through a 5.08 cm diameter, 500 psi piping system. A 15.24 cm diameter reservoir section with screens is used to smooth the flow before entering the contraction section to which the orifice nozzle is attached. The pressure in the reservoir is controlled by a Fisher valve in the supply line. With this system it is possible to maintain steady air flow for detailed static and impact pressure measurements to define the flow field, as discussed in reference 7.

Power Supply

A 250 volt MG set supplies the d.c. current to the arc through the network represented in figure 1. One side of the generator is grounded, and an external resistance of 1.4 Ω is connected in series to limit the current to 150A. To establish the arc with the fuse wire and flow through the orifice, two coils with total inductance of 0.033 Henry were added to the circuit. After the flow is established in the nozzle, the open circuit voltage for the generator is set at the desired value and the solenoid operated contact is closed for approximately 500 milliseconds. A steady d.c. arc is established in approximately 40 milliseconds. The arc voltage across the electrodes and the current are measured with Tektronix scopes.

FLOW PROPERTIES

The flow velocity through the orifice nozzle is varied by adjusting the reservoir pressure, while the temperature of the air supplied remains close to ambient. A static pressure tap is located in the throat of the nozzle. This pressure is used to calculate the Mach number in the orifice from the isentropic flow relationship. The flow velocity and Mach number are presented in figure 2 as functions of the pressure drop across the nozzle.

Static pressures were measured along the nozzle surface and on the axis of the nozzle with a movable static pressure probe (ref. 7). The axial flow Mach number distributions for different pressure drops across the nozzle with the upstream electrode placed 0.89 cm from the nozzle exit are shown in figure 3. At low nozzle pressure drops the flow does not accelerate appreciably from the electrode to the orifice. But at high pressure drops, the acceleration of the flow from the electrode through the orifice is appreciable. Downstream of the nozzle the flow velocity along the axis, where the arc is located, is nearly constant.

Besides the static pressure measurements, impact pressure probe surveys were conducted along the nozzle axis and across the exit of the orifice for various nozzle pressure drops. For all nozzle pressure drops the axial impact pressures were close to the reservoir pressure due to the subsonic speed of the flow. In addition, the flow velocity determined from the radial impact pressure measurements across the orifice exit were uniform, except at the outer edge of the orifice.

Static pressures over the upstream electrode surface were measured with the electrode placed 0.89 cm from the nozzle exit. Maximum flow velocity occurs at approximately 30° from the axis and the flow decelerates to lower velocity towards the axis, with flow separating from the electrode in a stagnation region.

Schlieren photographs of the subsonic and supersonic flows downstream of the orifice nozzle were taken with a 0.4 microsecond spark source. For subsonic flows the turbulent mixing region of the jet flow with the ambient air without shock wave is clearly visible. Shock waves are present for the supersonic flow conditions.

D.C. ARC CHARACTERISTICS

Arc Voltage and Current

After the desired flow velocity is established in the orifice, the circuit is closed and the voltage and current are recorded on the Tektronix scopes. Typical oscillograms are shown in figure 4 for an arc gap of 1.27 cm and various flow velocities. Three arc gap distances of 1.27, 1.59 and 2.22 cm were investigated with the upstream electrode located 0.89 cm from the nozzle exit.

The d.c. arc is established in approximately 40 milliseconds using the 0.25 mm copper trigger wire and the circuit is closed for a total time of approximately 500 milliseconds.

At low flow velocities arc voltage and current oscillogram traces are quite smooth, indicating steady laminar arcs. Fluctuations in the voltage trace are evident for a flow velocity of 108 m/s, indicating that the arc is no longer laminar. The magnitude of the voltage fluctuations increases with the flow velocity. At the maximum velocity of 300 m/s, where the arc is finally extinguished, the voltage fluctuations are appreciable with fluctuations present also in the current trace.

Frind (ref. 1) observed similar optical variations of a long d.c. arc in a quartz tube with argon at low currents. High speed photographs of his arc with exposure time of 1.35 microseconds indicated a steady undisturbed arc at low flow velocities. As the flow velocity was increased, disturbances appeared in the outer layer of the arc. At high velocities the arc column broke into globules, similar to the observations by Hermann et al (ref. 2) in a Laval nozzle near current zero. The question of whether the laminar to turbulent arc transition is similar to the transition of a laminar to turbulent boundary layer on a surface (refs. 3, 4) is not answered by available knowledge of the behavior of the arc column. Further investigations must be conducted to resolve this problem.

The mean arc column voltage and current variation with the flow velocity are presented in figures 5a and 5b for electrode gaps of 1.27, 1.59 and 2.22 cm. For these tests the voltage for the generator was set at 250 volts. With no flow the arc current is approximately 105 amperes and the arc voltage increases from 64 to 92 volts with increasing electrode gap. For the electrode gap of 1.27 cm the arc voltage increases slowly while the current decreases from 108 to 84 amperes with increasing flow velocity up to approximately 256 m/s. The voltage increases and current decreases rapidly for higher velocities as the arc extinction velocity is approached. Similar arc voltage and current variation with flow velocity are observed for electrode gap spacings of 1.59 and 2.22 cm; however, the arc extinction velocity decreases drastically with the arc column length. With a longer arc column the arc cooling is increased providing a corresponding increase in the arc resistance. To extend the investigation to longer arc columns at supersonic velocities, a solid state rectified d.c. power supply of 2000 volts has recently been installed.

Arc Voltage Gradient

The mean arc column voltage gradient, including the voltage at the cathode and anode, was calculated from the arc voltage data. The results are shown in figure 6a as functions of the flow velocity and the arc gap. The arc voltage gradient over the flow velocity range of 0 to 75 m/s remains nearly constant for each arc gap and the average gradient decreases with the arc column length. Topham (ref. 8) observed a similar decrease in the voltage gradient with arc column length in a uniform air flow in a shock tube. For the shortest arc gap of 1.27 cm, the voltage gradient increases slowly up to a

velocity of approximately 250 m/s. At higher flow velocities the voltage gradient increases rapidly as the arc extinction velocity is approached.

The cooling of the arc column by the high velocity flow constricts the arc and increases the resistance. This in turn decreases the current with a fixed supply voltage. An analysis of the arc voltage gradient for the constricted arc, based upon Kinsinger's model (ref. 9), is presented in the next section. Cooling and constriction are just the processes which occurs in the gas blast circuit breakers. Hermann et al (ref. 2) observed a rapid increase in the voltage gradient as current zero was approached in a supersonic nozzle. The arc voltage gradient with the flow velocity is similar for all three arc gaps with the rapid increase in the voltage gradient occurring at lower arc extinction velocity for longer arcs.

Arc Diameter

To measure the arc diameter and the fluctuations in the arc column, high speed pictures were taken with a Dynafax camera with an exposure time of 8 microseconds. Photographs of the arc column were obtained through optical filters after the arc was established at various subsonic flow velocities in arc gaps of 1.27, 1.59, and 2.22 cm. For low subsonic flow velocities with a laminar arc and steady voltage trace (figure 4), the photographs show a steady arc column without any fluctuation in the arc boundary, similar to that observed by Frind (ref. 1) in argon at low flow velocities. At higher flow velocities the arc column becomes irregular with fluctuations in the arc boundary, and the fluctuations become appreciable as the arc extension velocity is approached for each arc gap. From the high speed photographs, arc diameters were measured and the results are shown in figure 6b. The arc diameter constricts slowly as the flow velocity is increased, but the constriction becomes rapid as the current quenching velocity is approached for each arc gap. These arc diameters are used to calculate the arc voltage gradient in the next section.

STEADY STATE ARC CALCULATIONS AND CORRELATION WITH EXPERIMENTAL DATA

Arc Equations

A theoretical model has been developed for the time dependent behavior of low current arcs. The original purpose of the model was the determination of both the transient behavior of axially blown arcs at current zero and the importance of various energy loss mechanisms to this behavior. Both as a check on the results of this model and as a determination of the sensitivity of d.c. arc properties to the constricted arc diameter, the numerical program was run to give results for selected steady state arcs as reported in previous section. To do this, the arc temperature profiles were permitted to relax (numerically) with fixed current and arc radius until a time independent solution was obtained. Results for electric field (and temperature profile) can then be compared with experiment.

The equations and method of solution for the numerical model have been given earlier (refs. 9, 10) and will be summarized here. The Navier-Stokes equations for gas flow fields are simplified by the following approximations. Local thermodynamic equilibrium (L.T.E.) is assumed for all gas properties. Cylindrical geometry is adopted and both the axial gradients (temperature and flow speed) and the axial convective energy transfer are neglected in comparison with radial gradients and radial convective energy transfer. Kinetic energy density is neglected in comparison with enthalpy density. Temporal and spatial variations in pressure are neglected, as are viscous and magnetic field effects.

With these simplifications the momentum equation is decoupled from the continuity and energy equations. These later equations may then be written:

$$\frac{\partial \rho}{\partial t} = \frac{\partial}{\partial r^2} (2\rho r V) \tag{1}$$

$$\rho c_p \frac{\partial T}{\partial t} = -2rV\rho c_p \frac{\partial T}{\partial r^2} + \frac{\partial}{\partial r^2} (4r^2 \kappa \frac{\partial T}{\partial r^2}) - \frac{\partial}{\partial r^2} (2r Q_{rad}) + \sigma E^2 \tag{2}$$

The first three terms on the right side of the energy equation, eq. (2), represent power loss density due to convection, conduction, and radiation, respectively. The fourth term on the right of eq. (2) represents Joule or Ohmic heating.

To relate the current and electric field of the arc, we integrate the Ohm's law implicit in eq. (2), $j = \sigma E$, to get:

$$I = \pi E_o \int^{R^2} \sigma dr^2, \tag{3}$$

where R is a large enough radius that the conducting region of the arc is contained therein. Equations (1) to (3) then form a closed set to give the temporal history of the arc profile, $T(r,t)$, given the L.T.E. gas properties ($\rho(T;p)$, $c_p(T;p)$, $\kappa(T;p)$, $\sigma(T;p)$), a technique for calculating the radiation flux, a current or electric field history, and an outer boundary condition on the arc.

In the program used to solve these equations, called ARC, the temperature is interchanged with the radius as an independent variable. That is, the gas properties are tabulated at a fixed set of temperatures, T_j, and the locations of these temperatures as functions of time, $r_j(t)$, are the solution developed by the program. This transformation, which assumes a monotonic temperature profile, was suggested by Ragaller et al (ref. 11).

To avoid the numerical instability associated with the heat conduction term in eq. (2), that term is handled using a six point implicit numerical

technique. This technique permits time steps which can be as large as several microseconds for typical high pressure arc calculations.

For steady state calculations to compare with the d.c. arc measurements reported in previous section, the program was used to relax the temperature profile with given and fixed values of current, I, and arc radius, R (defined as the location of the 500K temperature point). The temperature profile at the start of the calculation was taken as parabolic, with T = 500K at the fixed arc radius and some chosen temperature at the center, T_c, generally 30000K. The program was run with fixed I through a number of time steps sufficient to relax the temperature profile to the point that the further change in any grid point in one time step was less than 0.01 percent. The electric field at each time step was adjusted in accordance with eq. (3). The final temperature profile and electric field can be used to compare with experiment.

Calculated Arc Properties

For comparison with experiment, three points from the measured arc characteristics were selected for calculation. These points are labeled 1 , 2 , and 3 in the curves of figures 5b, 6a and 6b. The arc properties associated with these points are listed in table 1.

Since the measurements of arc diameter in figure 6b were made downstream of the orifice in an ambient of one atmosphere, the properties of one atmosphere of air were used for the ARC calculation. These properties were calculated in separate programs which solve for L.T.E. compositions using either minimization of free energy (CHEME) or the coupled set of Saha equations (SAHA). The temperature grid points and the property values used for the calculations are listed in table 2.

For the calculations we have assumed that turbulence does not play a strong role in the radial energy transfer of the measured arcs so the radial heat conduction may be modeled using the laminar thermal conductivity as given in table 2.

The calculation of radiation power losses is difficult since at one atmosphere for the arcs of this study, significant power is radiated in regions of the spectrum both for which the arc is optically thick and optically thin. Since detailed calculations of radiation transfer in all appropriate spectral regions are not justified by their expected accuracy, it was decided to bracket the radiation power density by calculations for two extreme cases.

In one extreme, solutions of eq. (2) were found for no radiation power loss by setting $\partial/\partial r^2\ (2r\ Q_{rad}) = 0$. These solutions correspond to the limit in which all radiation emitted is locally absorbed - zero radiation mean free path.

In the other extreme, the emitted radiation escapes from the arc with no further interaction - infinite radiation mean free path. Solutions for this limit were found using

$$\frac{\partial}{\partial r^2}(2r\,Q_{rad}) = P_{rad} = \int 4\pi\,\varepsilon(\nu)\,d\nu$$

where $\varepsilon(\nu)$ is the frequency dependent coefficient of emission. Values of P_{rad} then depend only on temperature and pressure and may be calculated from equilibrium compositions, continuum radiation formulae, and data for the oscillator strengths of important lines.

The radiation emitted in the actual arc will in part escape and in part be reabsorbed. Therefore, except at the edge of the arc where there may be an actual net radiation absorption, the two extreme calculations should bracket the actual radiation power density. The calculated results for arc center temperature and electric field may, therefore, be expected to bracket the actual values.

Using the above information and techniques, we have calculated steady state arc profiles for cases 1 , 2 , and 3 , both for no net radiation and for no radiation absorption. The temperature profiles calculated for case 2 , with current of 84A and an arc diameter of 0.12 cm are shown in figure 7. As can be seen, the presence or absence of radiation losses makes a large difference with respect to the calculated center temperature and the character of the temperature profile in the core of the arc. A measurement of the central temperature for such an arc could provide useful information on the importance of radiation transfer.

The values of center temperature and electric field from the above calculations are given in table 1. Since we do not yet have measurements of arc temperature, comparison with experiment must be made on the basis of arc voltage gradient. Although the calculated and measured gradients are in rough agreement, the calculated values are somewhat higher (for cases 1 and 3 the experimental value falls below the lower calculated bracket value). Since the measured average voltage gradient includes electrode falls, it is probably an overestimate of the actual gradient at the downstream location. Therefore, the disagreement appears to be systematic.

The effect of arc diameter on the calculated voltage gradient is shown in figure 8 and further data for case 2 in table 1. From this data, it can be seen that voltage gradients equal to or slightly less than the measured value would be calculated for arc diameters only slightly greater than the measured value. Since the photographic measurements probably give a value of arc diameter corresponding to the location of an elevated temperature (for radiation cut off), the effective arc diameter (at cold gas temperatures) may indeed be somewhat larger. As an example, compare the radius at ~10000K (0.052-0.054 cm) with the nominal arc radius (0.06 cm) for the profiles for case 2 shown in figure 7.

Since the sensitivity against arc diameter is large, the comparison of experimental and calculated voltage gradients is as good as can be expected. In

addition, this sensitivity suggests the importance of constriction of the arc by convective energy removal in the gas flow field in determining the properties of low current (precurrent zero) arcs.

CONCLUDING REMARKS

A steady air flow facility capable of sustaining .450 kg/sec at 6.80 atm has been used to produce subsonic flows of various nominal Mach numbers (0.1 - 0.95) through an orifice of 1.27 cm diameter. After characterization of the cold flow field by static and impact pressure measurements, d.c. arc voltage and current measurements were made for a range of flow velocities and arc gaps. High speed photography was used to determine arc diameters at the orifice exit for the same range of conditions. Average arc voltage gradient and resistance increased rapidly with flow velocity as an arc extinguishing velocity was approached for a given gap.

Measured values of current and diameter were used as input for a relaxation solution of an arc energy balance equation (modified Elenbaas-Heller equation) for the radial temperature profile. Calculations were performed for extremes of radiation power loss. Calculated arc voltage gradients compare reasonably well with measured average voltage gradients when consideration is given to the large sensitivity of voltage gradient to arc diameter.

REFERENCES

1. Frind, G.: Electric Arcs In Turbulent Flows, II. USAF Aerospace Res. Labs. Rep. ARL66-0073, 1966.

2. Hermann, W.; Kogelschatz, U.; Niemeyer, L.; Ragaller, R.; and Schade, E.: Investigation on the Physical Phenomena Around Current Zero in HV Gas Blast Breakers. IEEE Trans. Paper F 76-061-2, 1976.

3. Schlichting, H.: Boundary Layer Theory. McGraw-Hill, 1960, pp. 375-456.

4. Nagamatsu, H. T.; Sheer, R. E. Jr.: and Graber, B. C.: Hypersonic Laminar Boundary Layer Transition on 8-Foot-Long, 10° Cone, M_1 = 9.1-16. AIAA Jour., vol. 5, no. 7, July 1967, pp. 1245-1252.

5. Malghan, V. R.; M. T. C. Fang; and Jones, G. R.: High Current Arcs In An Orifice Air Flow. University of Liverpool, Rep. ULAP-T30, February 1975.

6. Thiel, H. G.: Turbulence Controlled High-Power Arcs With Different Electron and Gas Temperatures. Proc. IEEE, vo.. 59, no. 4, April 1971, pp. 508-517.

7. Nagamatsu, H. T.; Sheer, R. E. Jr.; and Bigelow, E. C.: Flow Properties of Air and SF_6 In Supersonic Circuit Breaker Nozzles. IEEE Conf. paper C74 184-8, 1974.

8. Topham, D. R.: Measurements of the Current-Zero Behavior of Constant-Pressure Axial-Flow Electric Arcs In Nitrogen. Proc. IEEE, vol. 120, no. 12, December 1973, pp. 1568-1573.

9. Kinsinger, R. E.: A Numerical Model For Current-Zero Arc Interruption Processes. IEEE Trans. Power App. Syst., vol. 93, 1974, pp. 1143-1152.

10. Frind, G.; Kinsinger, R. E.; and Sharbaugh, A. H.: First Quarterly Report on Fundamental Investigation of Arc Interruption In Gas Flows. EPRI Contract No. RP 246-0-0, September 1974.

11. Ragaller, K.; Schneider, W. R.; and Hermann, W.: A Special Transformation of the Differential Equations Describing Blown Arcs. Z.A.M.P., vol. 22, 1971, pp. 1321-1328.

TABLE I.- COMPARISON OF EXPERIMENTAL AND CALCULATED DATA FOR ORIFICE NOZZLE ARCS

For all cases: $P_{downstream}$ = 1 atm, L = 1.27 cm

		Calculated Data	
	Experimental Data	No Radiation	Full Radiation Loss
1	Δp = 1.0 psi		
	U = 122 m/sec		
	I = 104 A		
	D = 0.15 cm	T_c = 31200K	T_c = 20900K
	$\bar{E}$ = 56 V/cm	E = 67 V/cm	E = 94 V/cm
2	Δp = 5.2 psi		
	U = 256 m/sec		
	I = 84 A		
	D = 0.12 cm	T_c = 31400K	T_c = 22200K
	$\bar{E}$ = 88 V/cm	E = 84 V/cm	E = 110 V/cm
	D = 0.10 cm	T_c = 34600K	T_c = 24600K
		E = 109 V/cm	E = 136 V/cm
	D = 0.14 cm	T_c = 29000K	T_c = 20600K
		E = 68 V/cm	E = 94 V/cm
3	Δp = 7.0 psi		
	U = 290 m/sec		
	I = 50 A		
	D = 0.066 cm	T_c = 32700K	T_c = 26700K
	$\bar{E}$ = 120 V/cm	E = 158 V/cm	E = 181 V/cm

TABLE II.- CALCULATED PROPERTIES FOR ONE ATMOSPHERE OF AIR (80% N - 20% O)

(K)	ρ (gm/cm^3) $\times 10^{-6}$	c_p (J/gm K)	σ (mho/cm)	κ (W/cm K) $\times 10^{-4}$
500	703.7	1.05	0.	5.
1000	351.8	1.14	0.	7.0
2000	175.3	1.38	0.	12.7
3000	114.5	2.75	0.	40.1
4000	76.76	3.14	0.021	58.5
5000	58.40	3.03	0.214	61.0
6000	44.80	7.76	0.893	203.
7000	31.54	13.39	2.71	351.
8000	23.28	8.69	8.19	197.
9000	19.61	4.63	17.23	118.
10000	17.20	5.12	27.4	126.
11000	15.08	7.60	37.7	157.
12000	13.05	11.36	47.7	195.
14000	9.197	19.85	66.6	252.
16000	6.536	18.53	82.2	249.
18000	5.207	10.35	94.7	233.
20000	4.507	6.05	106.0	245.
22000	4.030	6.18	116.3	282.
24000	3.627	9.75	124.3	331.
26000	3.218	17.25	127.5	387.
28000	2.784	25.33	127.5	441.

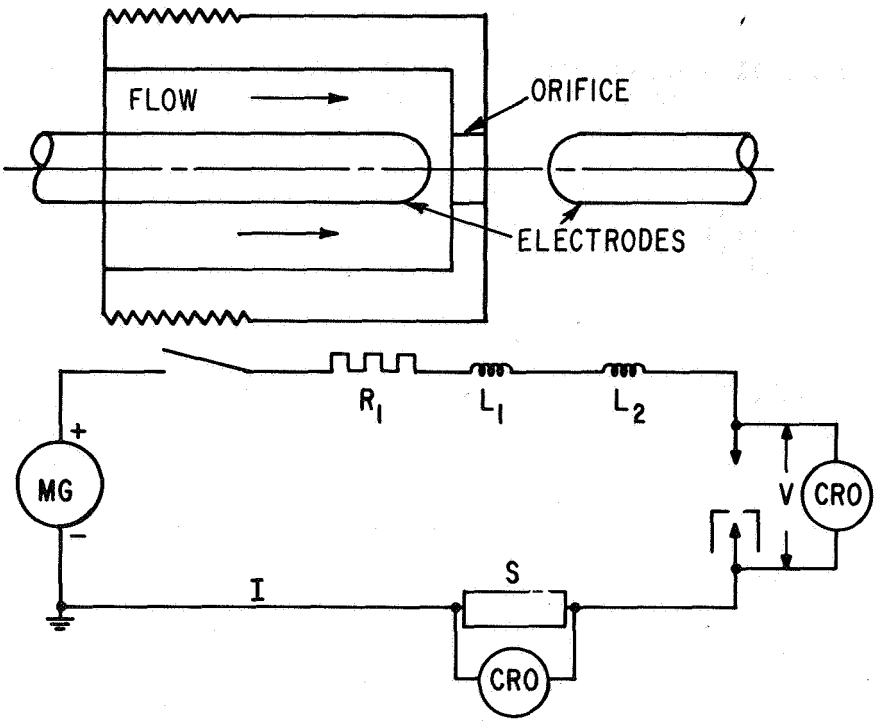

Figure 1.- Schematic of orifice nozzle and electrical network.

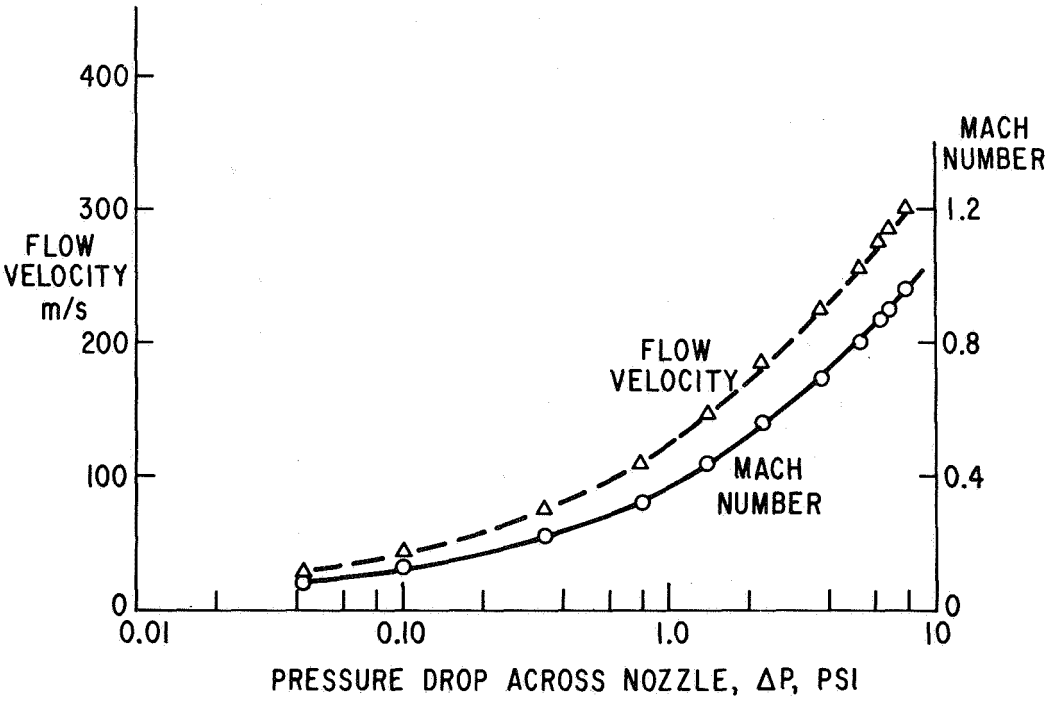

Figure 2.- Flow velocity and Mach number as function of pressure drop.

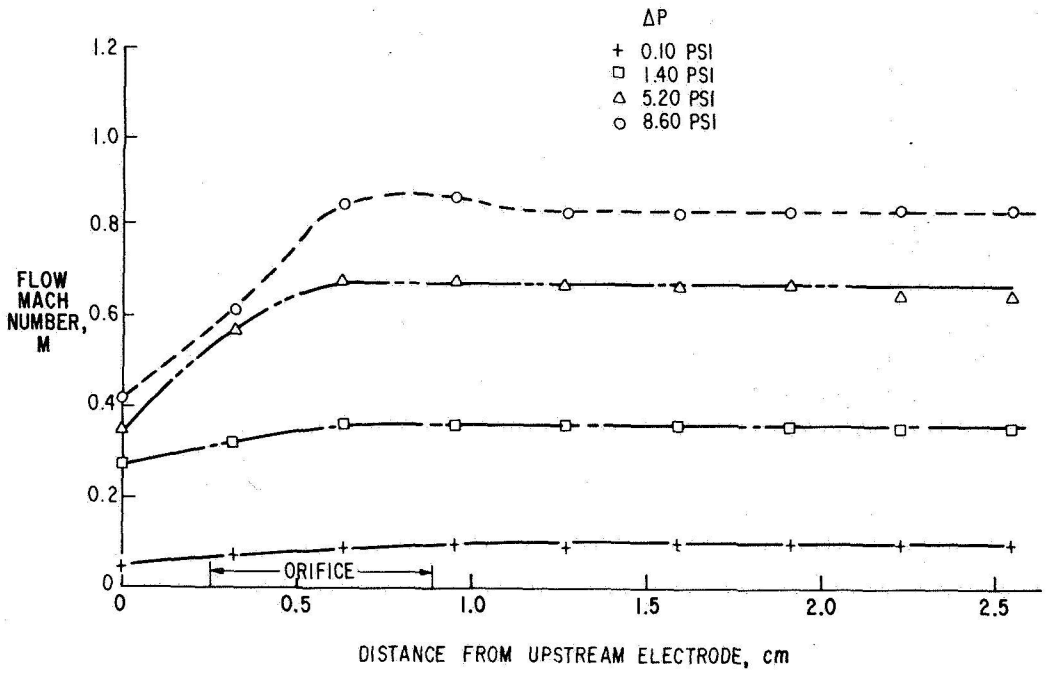

Figure 3.- Axial flow Mach number as function of distance from upstream electrode and nozzle pressure drop with electrode at X_e = 0.89 cm.

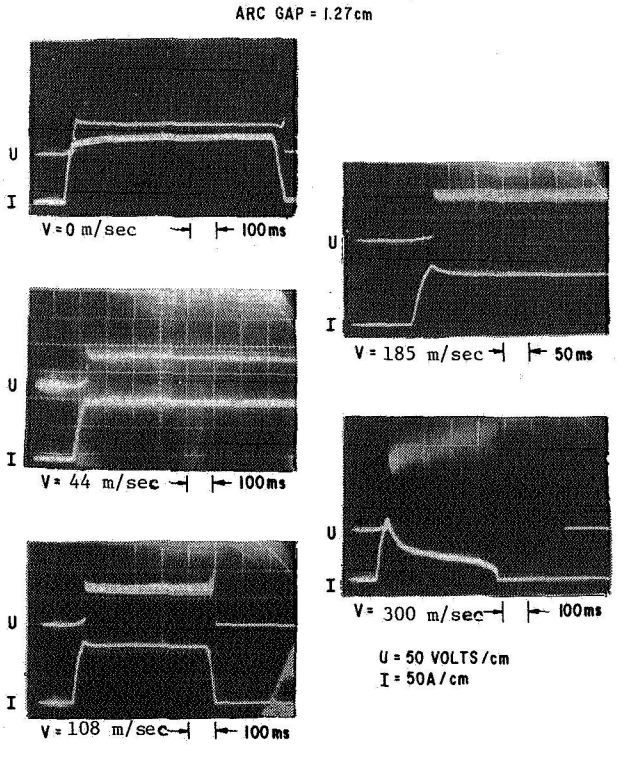

Figure 4.- Typical arc voltage and current traces at various flow velocities for gap distance of 1.27 cm.

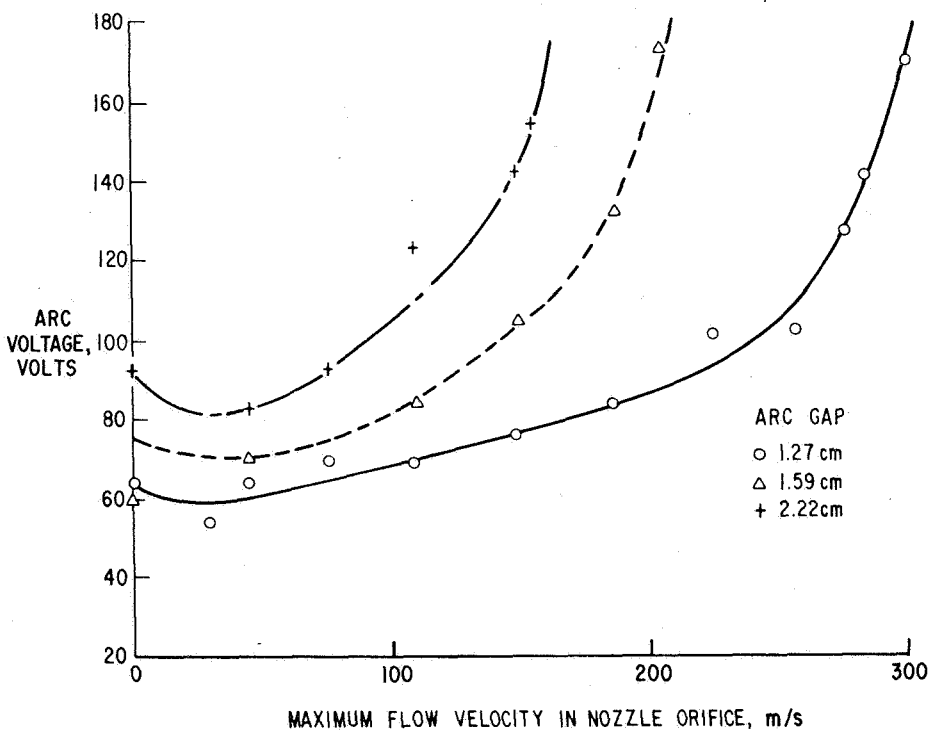

Figure 5a.- Arc voltage as function of maximum flow velocity in nozzle orifice and gap distance.

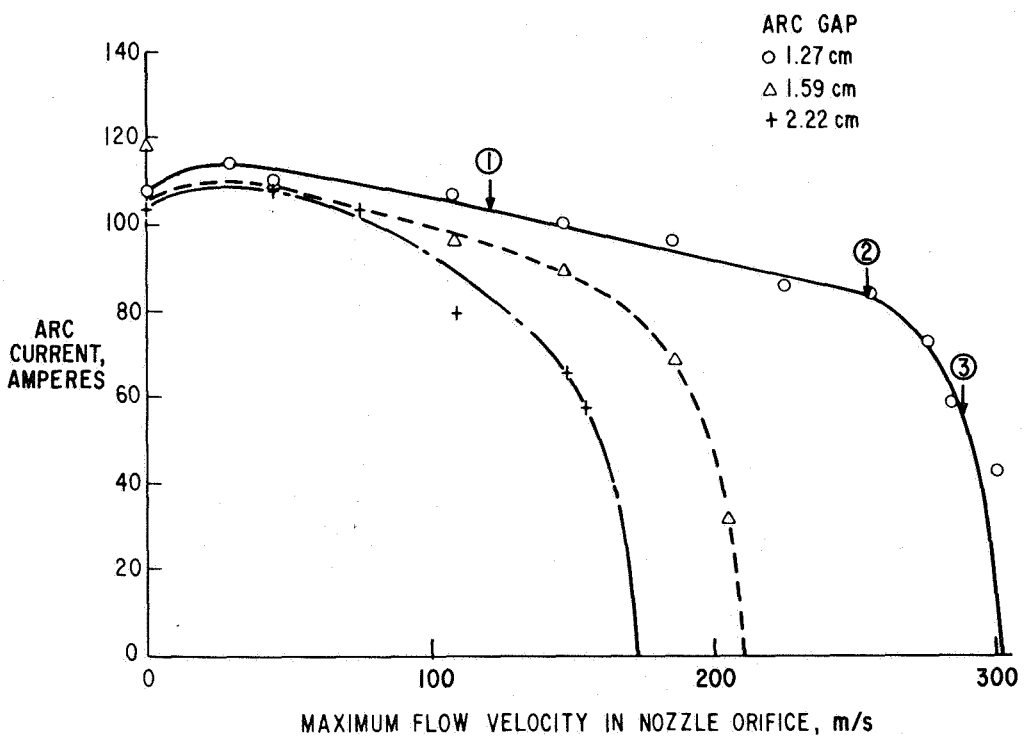

Figure 5b.- Arc current as function of maximum flow velocity in nozzle orifice and gap distance.

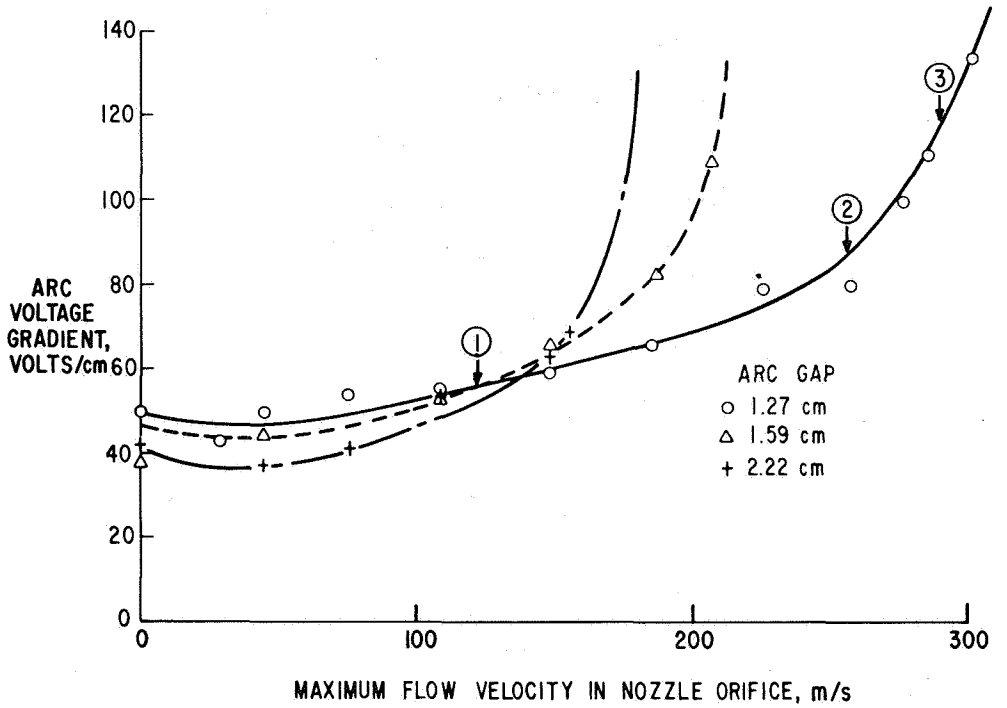

Figure 6a.- Arc voltage gradient as function of maximum flow velocity in nozzle orifice and gap distance.

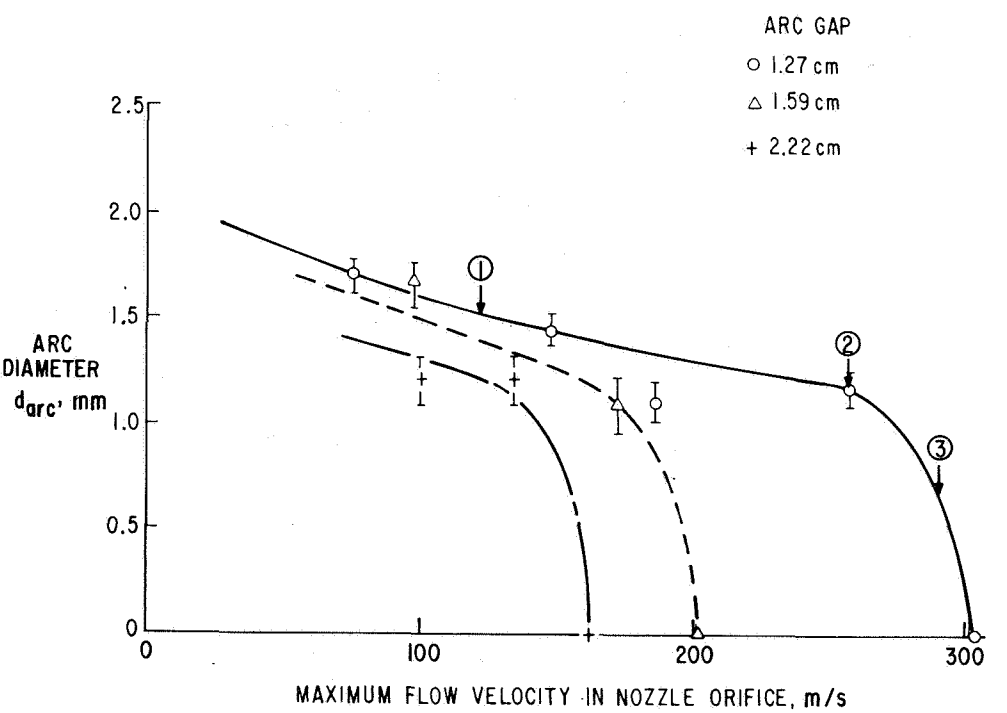

Figure 6b.- Arc diameter at orifice exit as function of maximum flow velocity in nozzle orifice and gap distance.

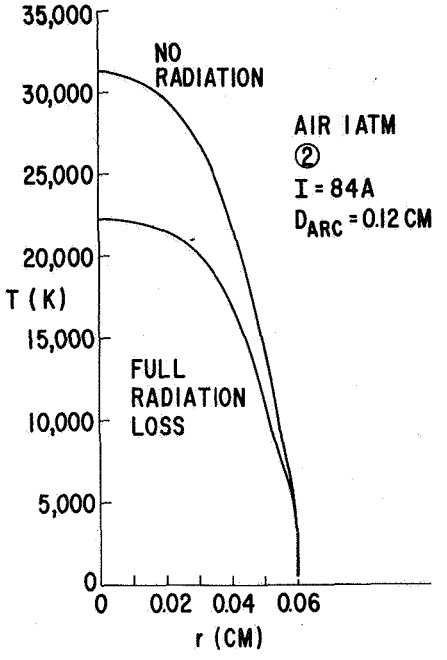

Figure 7.- Calculated temperature profiles for arc in one atmosphere of air with 84A and 0.12 cm diameter, both assuming no radiation losses and assuming no radiative reabsorption.

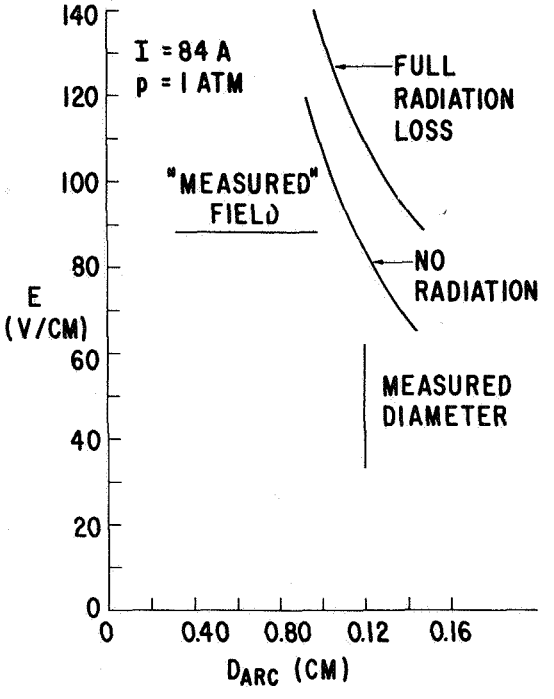

Figure 8.- Dependence of calculated voltage gradient on arc diameter for arc in one atmosphere of air with 84A.

HYDROGEN-FUELED SUBSONIC AIRCRAFT — A PERSPECTIVE

Robert D. Witcofski
NASA Langley Research Center

SUMMARY

Liquid hydrogen, a very light, environmentally superior fuel which can be produced from virtually any primary source of energy, is being considered by the NASA as a candidate fuel for aircraft of the future. This paper compares the performance characteristics of hydrogen-fueled subsonic transport aircraft to those using conventional aviation kerosene. Additional aspects discussed include potential improvements in the exhaust emissions characteristics of aircraft jet engines, problems associated with onboard fuel containment, results of recent NASA-sponsored studies of the impact of hydrogen-fueled aircraft on the airport and associated ground-support equipment, and estimates of the cost and thermal efficiency of producing synthetic aviation fuels from coal.

INTRODUCTION

The first aircraft-related use of hydrogen began in the 19th century when, because of its very low density, it was used in the gas bags of balloonists for buoyancy. The early part of the 20th century saw the construction of huge Zeppelin airships, which also used hydrogen for buoyancy. Zeppelins utilized internal combustion (I.C.) engines to drive the propellers which provided forward motion, and the engines used liquid fuels, typically diesel fuel. As is well described in reference 1, as the liquid fuel was burned, corresponding quantities of hydrogen had to be vented in order to hold the ship at the optimum altitude. In 1928, part of the hydrogen which would have been vented was used as an engine performance booster (typically 5 to 30 percent hydrogen-diesel fuel), the principle of which has been recently redemonstrated in an automobile engine and an aircraft piston engine by the Jet Propulsion Laboratory (ref. 2). Preignition and backfire prevented the total use of hydrogen in I.C. engines of the Zeppelins until it was found (ref. 1) that increasing the compression ratio of the I.C. engines to 16:1 allowed the use of almost all hydrogen for fuel without preignition. Burning this hydrogen as fuel not only reduced the fuel load for a given range and thus increased the payload, but would also facilitate vertical navigation, especially when landing with limited water ballast. As a result, a typical voyage from Northern Europe to Egypt would require almost 5 tons less fuel oil (ref. 1).

It is not a rebirth of Zeppelins that has caused a resurgence of the interest in hydrogen as an aviation fuel, but the growing concern over the depletion of our natural petroleum reserves.

About a year ago the United States Energy Research and Development Administration (ERDA) released an overview of the U.S. energy situation, including a prospectus on the domestic oil situation. Figure 1 is reproduced from the ERDA

report (ref. 3) and shows that even with enhanced recovery methods, the production of domestic oil in the U.S. may never surpass that which occurred during 1970 and will constantly decline after the 1980's. This estimate includes already identified resources and estimated undiscovered resources.

The ERDA document of reference 3 also includes estimates of the remaining recoverable domestic energy resources in the U.S., and these estimates are reproduced in figure 2. As can be seen in figure 2, natural gas and oil resources are dwarfed by oil shale, coal, and uranium.

Nuclear power has the potential of dwarfing all of the other energy resources noted in figure 2 but is greatly dependent upon the successful development of the breeder reactor. Successful development of nuclear fusion would offer an almost endless supply of energy. Although not included in figure 2, solar energy is expected to play an increasingly large role in the long-range energy future of the United States.

Oil shale and coal can be converted to a variety of fuels for both stationary and transportation needs. Such is not the case with nuclear and solar energy. Hydrogen, an environmentally superior fuel, can be produced from virtually any primary source of energy. The most promising alternate fuels for aviation are generally regarded as synthetic Jet-A derived from either oil shale or coal, liquid methane derived from coal, and liquid hydrogen which can be derived from many primary energy sources.

The NASA's Langley Research Center is conducting a Hydrogen-Fueled Aircraft Technology Program which is aimed at investigating the potentials of liquid hydrogen as an alternate aviation fuel of the future. This paper is an overview of the results of the program to date and addresses the areas of aircraft performance, engine emissions, cryogenic insulation for onboard fuel storage, ground requirements at the airport, the production of hydrogen from coal, and the subsequent liquefaction of the hydrogen.

U.S. Customary Units were used for the principal calculations in this paper but the results are presented in the International System of Units.

AIRCRAFT STUDIES

The NASA's Langley Research Center, as part of its Hydrogen-Fueled Aircraft Technology Program, selected the Lockheed-California Company to perform studies (refs. 4 and 5) of the performance potentials of subsonic transport aircraft when designed to utilize liquid hydrogen (LH_2) as a fuel. The study considered the performance characteristics of both LH_2 and Jet-A fueled aircraft and considered a variety of design ranges and payloads. Both passenger and cargo aircraft were considered in the study. The design range-payload characteristics of the aircraft considered in the Lockheed study are shown in table 1. The passenger aircraft shown in table 1 as having a 9265-kilometer radius were designed to carry 400 passengers 9265 kilometers, land, take off unrefueled, and carry 400 passengers another 9265 kilometers. The maximum nonstop ranges

for these aircraft were 19 590 kilometers for the LH_2 aircraft and 19 980 kilometers for the Jet-A aircraft.

A kilogram of hydrogen contains about 2-3/4 times the energy contained in a kilogram of conventional aviation fuel (Jet-A). Hydrogen, because of its low energy density when in its gaseous form, must be liquefied (a cryogen at 20° K) in order to increase its energy content per unit volume. Even after liquefaction, 4 liters of hydrogen are required in order to have the same energy content as 1 liter of aviation kerosene. In other words, to have the same energy content as a given quantity of Jet-A requires a mass of liquid hydrogen about one-third that of the Jet-A and the volume of liquid hydrogen about four times that of the Jet-A.

A variety of approaches for housing the low-density LH_2 were investigated by Lockheed, the most promising concepts being those shown in figure 3. The configuration in the foreground of figure 3 would house the LH_2 within the fuselage, whereas the configuration in the background would house fuel in tanks mounted on the wings. The drag penalties associated with the wing-mounted tanks caused the performance of such aircraft to be inferior to the configuration with the fuel housed in the fuselage. For that reason, the fuel-in-fuselage configuration is the favored configuration.

Hydrogen's high-energy content per kilogram of fuel is reflected in figure 4 where the gross take-off masses and onboard fuel masses of the passenger aircraft of the Lockheed study are shown as a function of design range. Aircraft having longer ranges and/or higher payloads require more fuel. The greater the amount of fuel required to perform the mission, the greater the mass-saving advantages of hydrogen fuel. In figure 4, the lower fuel masses of the LH_2 aircraft are reflected by lower gross take-off masses. Although hydrogen's low-energy density per unit volume, again one-fourth that of Jet-A, causes additional drag which the airplane's engines must overcome, less lift must be generated to support the airplane because the LH_2 airplane has less mass. Lift is generated at the expense of drag incurred; and overall, the drag increases associated with the low energy per unit volume of LH_2 are overshadowed by the fact that less lift must be generated, smaller wings are required, and thus less total drag is incurred. This shows up in the area of fuel consumption.

Figure 5 shows the relative energy requirements of the LH_2 and Jet-A aircraft of the Lockheed study. The energy requirements are shown as the ratio of kilojoules per seat-kilometer of the LH_2 aircraft to the kilojoules per seat-kilometer of Jet-A aircraft, as a function of design range. The energy requirements for the cargo aircraft (ref. 4) are shown as a ratio of the LH_2-to-Jet-A values for kilojoules per kilogram-kilometer. The energy consumption analysis of figure 4 considers both the onboard energy consumption (exclusive of the energy required to produce the fuels) and the total energy consumption (including the energy required to produce the fuels). The total energy consumption will be discussed in a later section.

Figure 5 shows, for the payloads considered in the Lockheed study, that for an airplane having a design range greater than about 4000 kilometers, the LH_2 fueled aircraft will use less onboard energy than would its Jet-A fueled counterpart. The greater the range, the greater the fuel savings associated with the LH_2 aircraft.

Environmental Emissions

Hydrogen-fueled aircraft would have as their only emission, water vapor and oxides of nitrogen (NOX). Water vapor emissions should be about 2-1/4 times those of Jet-A fueled aircraft. Studies are currently underway at NASA to attempt to determine the effect of water vapor emissions from LH_2 aircraft on the upper atmosphere.

There is every reason to believe that the NOX emissions of hydrogen-fueled jet engines could be reduced to levels well below that of Jet-A fueled engines. The flame speed associated with the combustion of hydrogen is about 10 times that of hydrocarbon fuels and, therefore, shorter combustion zones should be permissible in the LH_2 fueled jet engines. Shorter combustion zones mean less dwell time in the combustion zone, and shorter dwell times mean lower NOX formations (ref. 6).

Because of the very low flammability limit of hydrogen when mixed with air, (4 percent hydrogen, by volume, for an upward burning flame and 8.5 percent hydrogen for a downward burning flame), there is a potential for further NOX emissions reductions. If the maximum temperature in the engine can be reduced, the formation of NOX can be reduced. Lower maximum flame temperatures should be obtainable via lean burning. Currently, jet engines combine about 25 percent of the airflow (fan air excluded) with the fuel in the primary combustor where burning occurs. The remaining three-fourths of the air is then used to dilute the combustion products gases, the combination of the two producing the turbine inlet temperature from whence the power is derived. The lean flammability limit of hydrogen offers the possibility of enlarging the diameter of the primary combustor and allowing more air to be mixed with the fuel and burned in the primary combustion zone (lean burning). As a result of the lean burning, lower temperatures will occur in the primary combustion zone and, thus, lower NOX formation (order of magnitude) will occur. There will be less air to dilute the combustion products and a proper balance of primary combustor and diluent air could be struck to maintain the turbine inlet temperature required to power the aircraft.

Cryogenic Insulations

Perhaps the most critical technology item associated with the LH_2 aircraft is that of obtaining a cryogenic insulation system for storage of the LH_2 aboard the aircraft. Insulation concepts must be very light, safe, reliable, economically practical, and have a long service life. Insulation concepts developed for use in space may not have the useful life required for aircraft application.

Insight into the problem of finding a suitable insulation may be gained by examining the approach where a foam insulation is bonded to the exterior surface of the fuel tank.

If the foam insulation is porous, the gases surrounding the tank will enter the insulation and liquefy, causing cryopumping to occur. If the insulation is sufficiently porous to allow the liquefied gases to flow downward along the

outside wall of the tank and to drip off the bottom of the tank, continuous cryopumping will occur. If the gas surrounding the tank is air, selective liquefaction of oxygen may occur and an oxygen-rich environment in the area surrounding the tanks is a most undesirable situation from the standpoint of safety. NASA-sponsored studies of the broader aspects of hydrogen safety are currently underway.

Regardless of what the compositon of the gas surrounding the insulation may be, if the gas enters the insulation and liquefies, it may quickly gasify within the insulation when the tank is emptied and warms up, and may cause the insulation to pop off.

Another problem with external foam insulation is the difference between the coefficient of thermal contraction of most foam insulations and that of 2219 aluminum, which is generally regarded as the best material for tank construction. The thermal contraction of most foam insulations is from two to four times that of 2219 aluminum. The difference causes high tension stresses in the insulation near the tank wall and compressive stresses in the outer portion of the insulation. Such stresses may lead to structural failure of the insulation.

NASA-sponsored efforts are currently underway to advance the technology status of cryogenic insulation systems for LH_2 aircraft tankage. These efforts involve the testing of available foam insulations and the formulation of additional foam insulations.

Our major effort during the next year will be to make an engineering analysis of the characteristics of the total fuel system requirements for LH_2 aircraft. The analysis will include consideration of all components of the aircraft fuel system, from the lid on the fuel tank to the combustion chamber of the engine.

LH_2 AT THE AIRPORT

As another part of NASA's Hydrogen-Fueled Aircraft Technology Program, we selected The Boeing Commercial Airplane Company (ref. 7) and the Lockheed-California Company (ref. 8) to assess the impact of the use of LH_2 as a fuel for all wide-body jets at two major airports in the United States (O'Hare International in Chicago, Illinois, and San Francisco International in San Francisco, California). It was assumed that a supply of gaseous hydrogen was available at the gates of the airports. Boeing and Lockheed were supported by a team of experts in hydrogen liquefaction and storage and in airport planning and operation. The results of the studies (refs. 7 and 8) were most encouraging. The major conclusions were:

1. Such a conversion was technically feasible and there were no technical problems which did not lend themselves to straightforward engineering solutions.

2. Sufficient real estate is available for the necessary liquefaction plant and storage tanks.

3. Relatively conventional ground-support setups and passenger loading facilities could be used.

4. Turn-around times for LH_2 aircraft are consistent with those of Jet-A aircraft.

It was estimated that the necessary liquefaction, storage, and distribution facilities would cost approximately $\$470 \times 10^6$ for O'Hare and $\$340 \times 10^6$ for San Francisco.

The method of financing was found to have profound effect upon the cost of the delivered hydrogen product. Figure 6, taken from reference 7, shows the LH_2 cost of fuel delivered to the airlines as a function of the cost of the gaseous feedstock. Also shown is the effect of the cost of the electrical power required to liquefy the hydrogen on the cost of the liquid hydrogen. It is assumed in figure 6 that about 15 percent of the LH_2 delivered to the airlines is vaporized during fuel loading and that the gas is returned to the liquefaction plant and credited to the airline accounts. On the left side of figure 6, airport financing which is typical in the United States, assumes that the airlines ultimately absorb the financial costs through user fees over a period of time consistent with the payoff schedule for revenue bonds issued by the airport authority. On the right side of figure 6, the cost reflects private financing. Figure 6 illustrates that the method of financing can make 20 cents/kg difference in the cost of the product delivered to the airplane.

As a point of reference, the current price of Jet-A fuel in the U.S. is about 6.6 cents per liter (30 cents per gal) which is the equivalent of 28 cents per kilogram for LH_2.

HYDROGEN PRODUCTION AND LIQUEFACTION

As was stated earlier in this paper, coal is one of the more plentiful remaining energy resources in the United States. The NASA asked the Institute of Gas Technology (IGT) to perform a study of the cost and thermal efficiency of producing hydrogen, methane, and synthetic aviation kerosene from coal (ref. 9). These results were combined with those from a study done for the NASA by the Linde Division of Union Carbide (ref. 10) to determine the cost and energy requirements for the liquefaction of hydrogen. The combined results of the IGT and Linde studies are shown in table 2 and figure 7.

Table 2 (ref. 9) summarizes the thermal efficiencies of the coal conversion processes analyzed, where thermal efficiency is defined as the total useful energy products of a particular process divided by the total energy required by the process.

The most thermally efficient hydrogen-from-coal process was the Steam-Iron process. The reason for the high thermal efficiency of the Steam-Iron process

is that a large quantity of low-energy gas (low kilojoule per kilogram) at 1100° K and at a pressure of 1000 kN/m^2 is a byproduct of the process. The heating value plus sensible heat of this byproduct gas (after energy requirements internal to the process have been satisfied) represents about 39 percent of the heating value of the coal used in the process. Depending upon whether the byproduct gas (heating value plus sensible heat) or electrical power generated from the gas is credited as the byproduct energy, the thermal efficiency of liquid hydrogen produced via the Steam-Iron process is 49 percent or 44 percent.

Synthetic aviation kerosene, produced by hydrocracking and hydrogenating the heavy oil product of the Consol Synthetic Fuel process is seen in table 2 to have a thermal efficiency of 54 percent. Production of the large quantities of hydrogen required to hydrocrack and hydrogenate the heavy oil consumes a large portion of the high-energy gas coproduct from the Consol Synthetic Fuel process and lowers the overall thermal efficiency of the aviation kerosene product.

Liquid methane produced via the Hygas® process and subsequently liquefied had the highest thermal efficiency, 64 percent. The performance of subsonic aircraft when designed to utilize methane fuel has not yet been addressed in depth.

If one chooses to determine how efficiently coal might be utilized as an aircraft fuel, the Lockheed aircraft study results can be combined with the IGT/Linde fuel production studies. Returning to figure 5, the energy requirements for producing LH_2 and aviation kerosene from coal have been combined with the Lockheed aircraft performance data to produce the curve shown on the right of figure 5. The curve indicates that aircraft must have design ranges in excess of 8000 kilometers before coal-derived LH_2 fueled aircraft are more energy efficient than coal-derived aviation kerosene-fueled aircraft.

Transfer and storage losses are not considered in figure 5, but as pointed out in reference 9, such losses should be larger for LH_2 than for aviation kerosene.

The reader is cautioned against making hard decisions based on the curve presented on the right in figure 5, because of the sensitivity of the results to changes in technology. For instance, a 20-percent decrease in the energy requirements for the liquefaction of the hydrogen would move the total energy curve back over to the 4000-kilometer crossover point. Such a 20-percent improvement potential has already been identified in the Linde study (ref. 10).

Cost estimates for coal-derived fuels (fig. 7) are taken from reference 9 where the IGT results on fuel production were combined with those of Linde (ref. 10) on hydrogen liquefaction. For the Steam-Iron process, it is assumed that electrical power from the process can be sold for 2 cents per kilowatt hour. It is likewise assumed that electrical energy for liquefaction can be purchased for the same price as the byproduct electric power is sold.

Advanced hydrogen liquefaction technology would drop the cost of LH_2 about 50 cents per gigajoule. Liquid hydrogen produced via the Steam-Iron process is seen to be economically competitive with coal-derived aviation kerosene particularly at higher coal costs but considerably more expensive than liquid methane produced via the Hygas® process. Hydrogen liquefaction costs of $3.00 to $3.50 per gigajoule are the cause of the higher LH_2 costs. (For reference purposes, 6.6 cents/liter or 30 cents/gal Jet-A corresponds to $2.30/GJ.)

CONCLUDING REMARKS

Studies conducted under the NASA's Hydrogen-Fueled Aircraft Technology Program have indicated that liquid hydrogen is an attractive alternate fuel for future subsonic transport aircraft. Such aircraft have the potential of consuming less onboard energy when the design range is in excess of about 4000 kilometers. Studies indicate that the greater the fuel requirement for a particular design mission, the greater will be the onboard fuel savings associated with the use of liquid hydrogen fuel.

Liquid hydrogen is an environmentally superior fuel, having combustion products of only water vapor and oxides of nitrogen. Lean burning offers the potential of sizable reductions in the oxides of nitrogen.

A suitable cryogenic insulation system for housing the LH_2 fuel is perhaps the major technology gap which must be filled.

Studies have indicated that the introduction of liquid hydrogen for use as a fuel for wide-body jets at two major U.S. airports is feasible and offers no technical problems which do not lend themselves to straightforward engineering solutions.

If coal is to be utilized as the source of future jet aircraft fuel, studies indicate that liquid methane is less expensive and more thermally efficient to produce from coal than are liquid hydrogen or synthetic aviation kerosene.

The sensitivity of the parameters used in assessing the potentials of liquid hydrogen as an aircraft fuel to potential changes in the technology status of fuel production, fuel handling, and fuel use precludes a decision at this time regarding the future of liquid hydrogen as an aviation fuel.

REFERENCES

1. Weil, Kurt H.: The Hydrogen I.C. Engine — Its Origins and Future in the Emerging Energy-Transportation-Environment System. Seventh Intersociety Energy Conversion Engineering Conference, 1972. San Diego, California, September 25-29, 1972.

2. Menard, W. A.; Moynihan, P. I.; and Rupe, J. H.: New Potentials for Conventional Aircraft When Powered by Hydrogen-Enriched Gasoline. First World Hydrogen Energy Conference, Volume III. Miami Beach, Florida, March 1-3, 1976.

3. A National Plan for Energy Research, Development, and Demonstration: Creating Energy Choices for the Future. United States Energy Research and Development Administration, Washington, D.C., ERDA-48, Volume 1, June 28, 1975.

4. Brewer, G. D.; Morris, R. E.; Lange, R. H.; and Moore, J. W.: Study of the Application of Hydrogen Fuel to Long-Range Subsonic Transport Aircraft. NASA CR-132559, prepared by Lockheed-California Company and Lockheed-Georgia Company under Contract NAS1-12972, January 1975.

5. Brewer, G. D.; and Morris, R. E.: Study of LH_2 Fueled Subsonic Passenger Transport Aircraft. NASA CR-144935, prepared by Lockheed-California Company under Contract NAS1-12972, January 1976.

6. Grobman, J.; Anderson, D. N.; Diehl, L. A.; and Niedzwiecki, R. W.: Combustion and Emissions Technology. Aeronautical Propulsion, NASA SP-381, 1975.

7. An Exploratory Study to Determine the Integrated Technological Air Transportation System Ground Requirements of Liquid-Hydrogen-Fueled Subsonic, Long-Haul Civil Air Transports. NASA CR-2699, prepared by The Boeing Commercial Airplane Company under Contract NAS1-14159, May 1976.

8. LH_2 Airport Requirements Study. NASA CR-2700, prepared by Lockheed-California Company under Contract NAS1-14137, March 1976.

9. Witcofski, R. D.: The Thermal Efficiency and Cost of Producing Hydrogen and Other Synthetic Aircraft Fuels From Coal. First World Hydrogen Energy Conference, Volume III. Miami Beach, Florida, March 1-3, 1976.

10. Survey Study of the Efficiency and Economics of Hydrogen Liquefaction. NASA CR-132631 prepared by The Linde Division of Union Carbide Corporation under Contract NAS1-13395, April 1975.

TABLE 1.- RANGE-PAYLOAD CHARACTERISTICS OF AIRCRAFT CONSIDERED IN PERFORMANCE STUDY

Range, kilometers	Payload	
	No. passengers	kilograms
Passenger aircraft		
2 780	130	
5 560	200	
5 560	400	
10 190	400	
9 265 (radius)	400	
Cargo aircraft		
5 560		56 700
10 190		113 400

TABLE 2.- THERMAL EFFICIENCY OF PRODUCING SYNTHETIC FUELS FROM COAL (BASED ON NET HEATING VALUES OF ALL FUELS)

Product	Process	Thermal efficiency, percent	
		Coal to gas	Coal to liquid
Hydrogen	Koppers-Totzek	51	38
	U-Gas™	59	42
	Steam-Iron	[a]77, [b]62	[a]49, [b]44
Methane	Hygas®	67	64
Aviation kerosene	Consol Synthetic Fuel, hydrocracking, and hydrogenation		54

[a]If heating value plus sensible heat of low Btu gas is byproduct.

[b]If electrical power is byproduct.

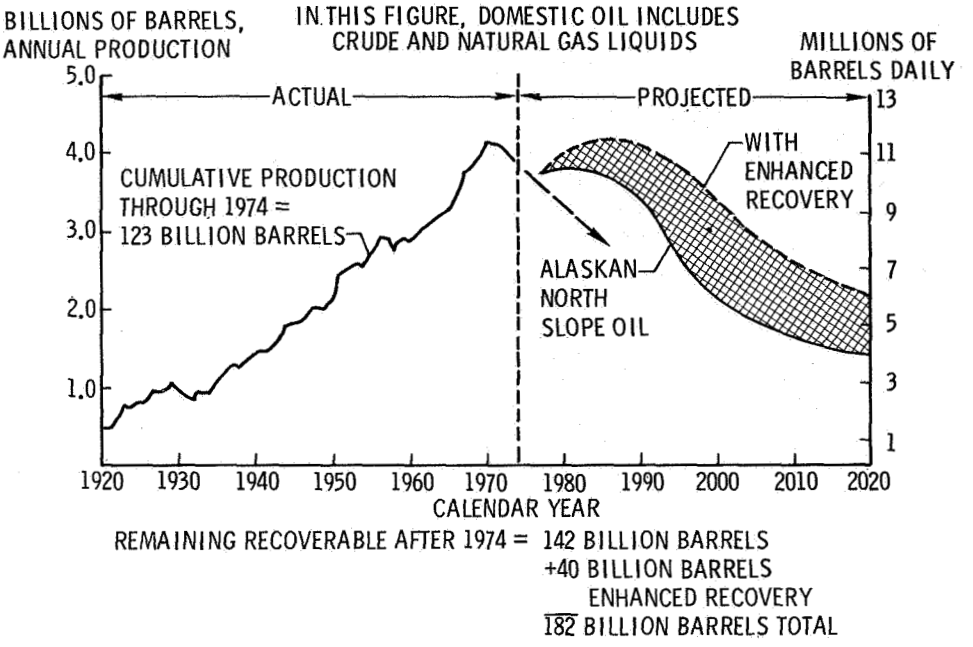

Figure 1.- Projected U.S. domestic oil production (ref. 3).

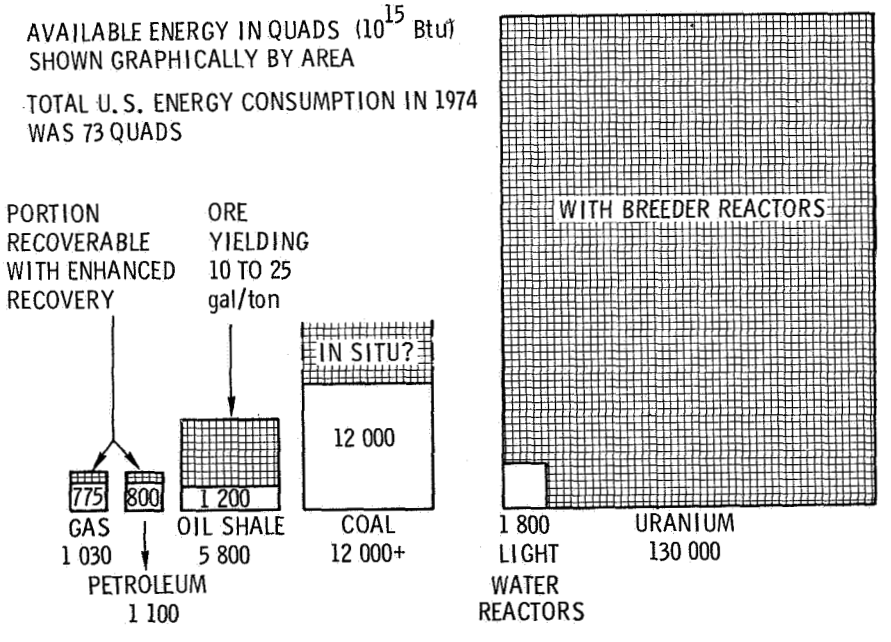

Figure 2.- Available energy from recoverable U.S. domestic energy resources (ref. 3).

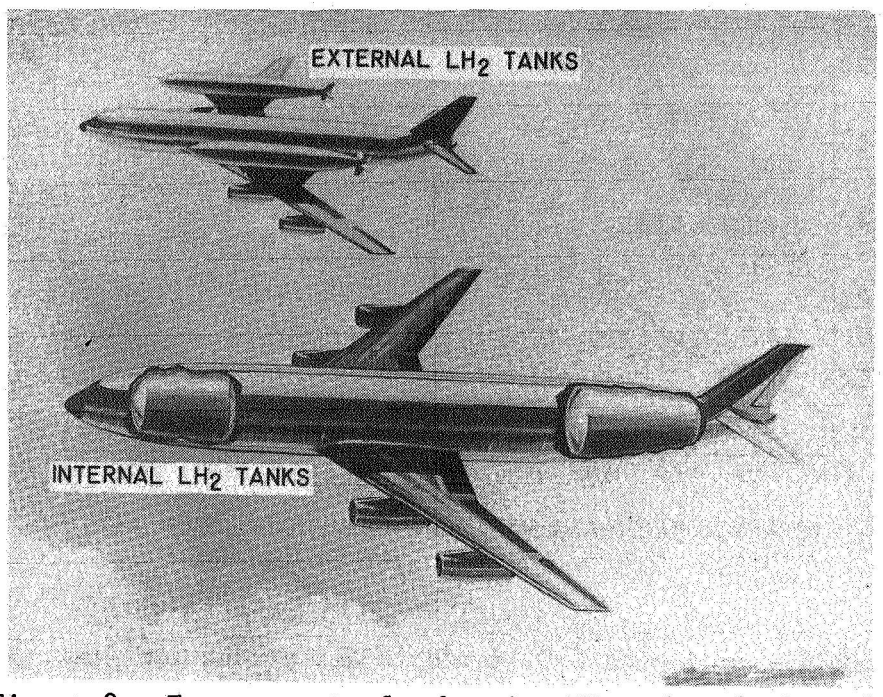

Figure 3.- Two concepts for housing LH_2 onboard aircraft.

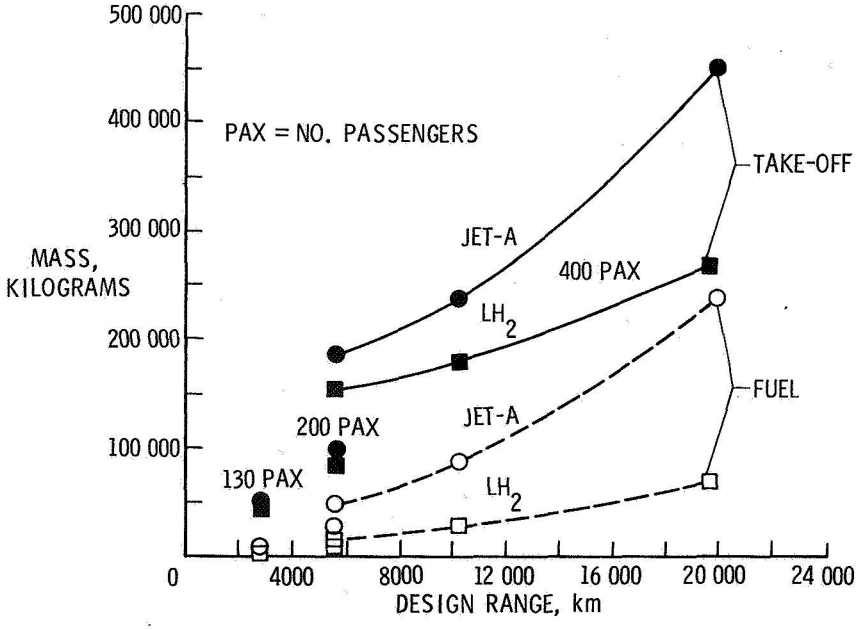

Figure 4.- Mass characteristics of LH_2 and Jet-A passenger transport aircraft.

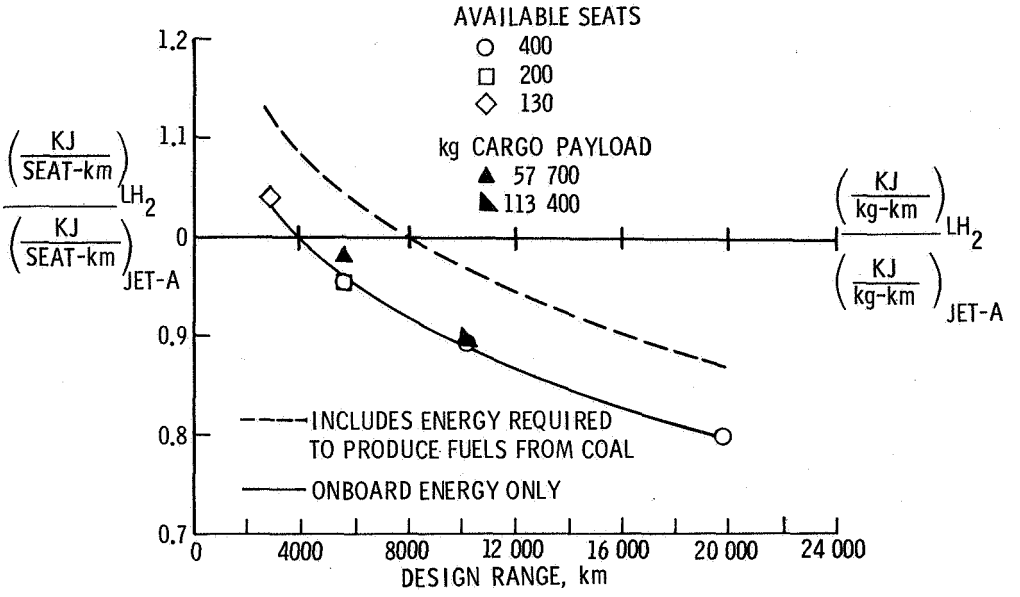

Figure 5.- Relative energy consumption of LH_2 and Jet-A aircraft (net heating values).

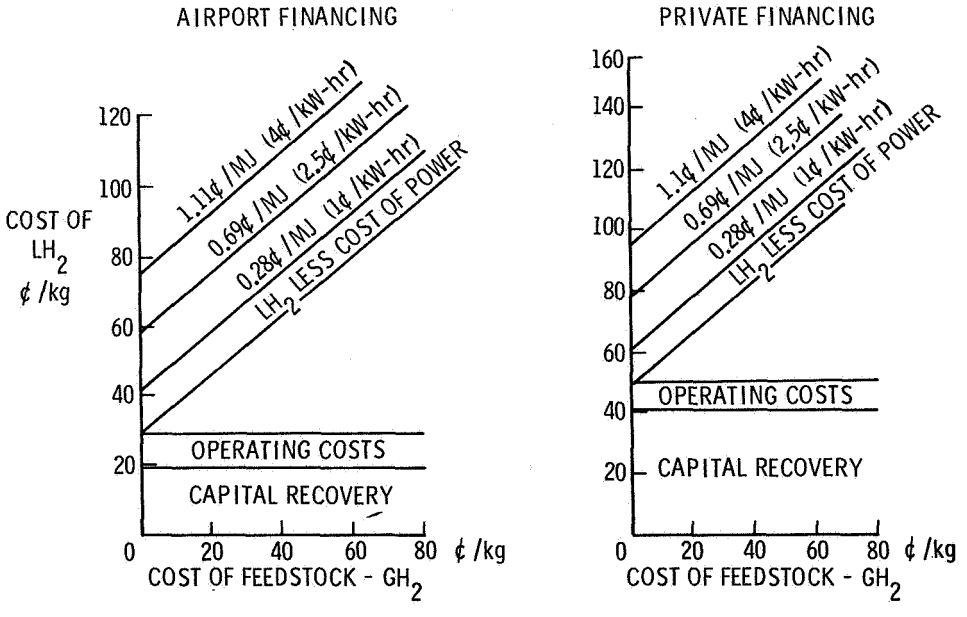

Figure 6.- Liquid hydrogen fuel costs, delivered to the airlines (1975 $).

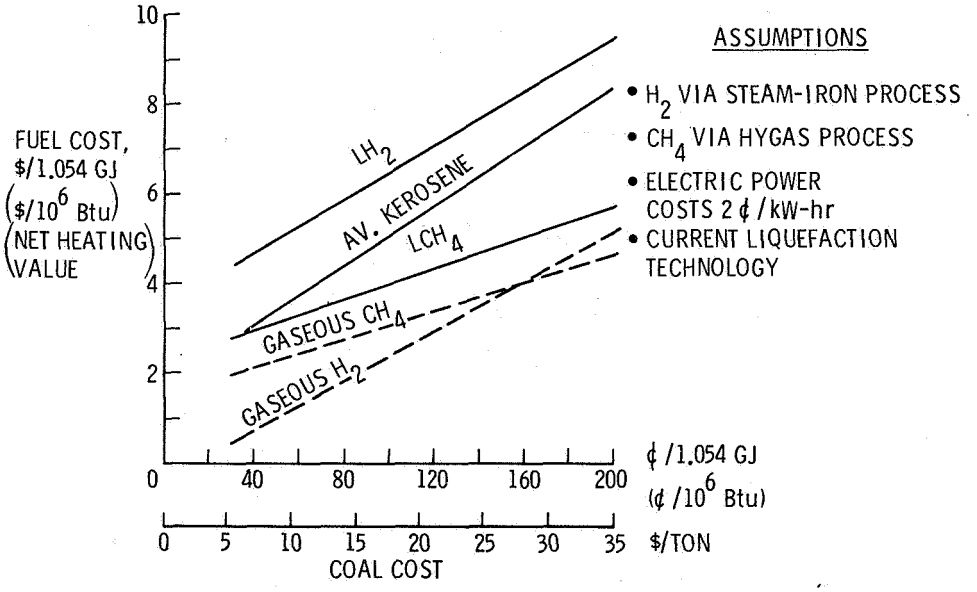

Figure 7.- The effect of coal cost on synthetic fuel cost.

NASA-Langley, 1976

NATIONAL AERONAUTICS AND SPACE ADMINISTRATION
WASHINGTON, D.C. 20546

OFFICIAL BUSINESS
PENALTY FOR PRIVATE USE $300

SPECIAL FOURTH-CLASS RATE
BOOK

POSTAGE AND FEES PAID
NATIONAL AERONAUTICS AND
SPACE ADMINISTRATION
451

U.S.MAIL

POSTMASTER: If Undeliverable (Section 158 Postal Manual) Do Not Return

"The aeronautical and space activities of the United States shall be conducted so as to contribute . . . to the expansion of human knowledge of phenomena in the atmosphere and space. The Administration shall provide for the widest practicable and appropriate dissemination of information concerning its activities and the results thereof."

—NATIONAL AERONAUTICS AND SPACE ACT OF 1958

NASA SCIENTIFIC AND TECHNICAL PUBLICATIONS

TECHNICAL REPORTS: Scientific and technical information considered important, complete, and a lasting contribution to existing knowledge.

TECHNICAL NOTES: Information less broad in scope but nevertheless of importance as a contribution to existing knowledge.

TECHNICAL MEMORANDUMS: Information receiving limited distribution because of preliminary data, security classification, or other reasons. Also includes conference proceedings with either limited or unlimited distribution.

CONTRACTOR REPORTS: Scientific and technical information generated under a NASA contract or grant and considered an important contribution to existing knowledge.

TECHNICAL TRANSLATIONS: Information published in a foreign language considered to merit NASA distribution in English.

SPECIAL PUBLICATIONS: Information derived from or of value to NASA activities. Publications include final reports of major projects, monographs, data compilations, handbooks, sourcebooks, and special bibliographies.

TECHNOLOGY UTILIZATION PUBLICATIONS: Information on technology used by NASA that may be of particular interest in commercial and other non-aerospace applications. Publications include Tech Briefs, Technology Utilization Reports and Technology Surveys.

Details on the availability of these publications may be obtained from:

SCIENTIFIC AND TECHNICAL INFORMATION OFFICE

NATIONAL AERONAUTICS AND SPACE ADMINISTRATION

Washington, D.C. 20546